

VOLUME 77

MARCH 15, 1973

NUMBER 6

JPCA_x

THE JOURNAL OF

PHYSICAL
CHEMISTRY

PUBLISHED BIWEEKLY BY THE AMERICAN CHEMICAL SOCIETY

THE JOURNAL OF PHYSICAL CHEMISTRY

BRYCE CRAWFORD, Jr., *Editor*

STEPHEN PRAGER, *Associate Editor*

ROBERT W. CARR, Jr., FREDERIC A. VAN-CATLEDGE, *Assistant Editors*

EDITORIAL BOARD: A. O. ALLEN (1970-1974), C. A. ANGELL (1973-1977), J. R. BOLTON (1971-1975), F. S. DAINTON (1972-1976), M. FIXMAN (1970-1974), H. S. FRANK (1970-1974), R. R. HENTZ (1972-1976), J. R. HUIZENGA (1969-1973), W. J. KAUZMANN (1969-1973), R. L. KAY (1972-1976), W. R. KRIGBAUM (1969-1973), W. J. MOORE (1969-1973), R. M. NOYES (1973-1977), J. A. POPLE (1971-1975), B. S. RABINOVITCH (1971-1975), H. REISS (1970-1974), S. A. RICE (1969-1975), F. S. ROWLAND (1973-1977), R. L. SCOTT (1973-1977); W. A. ZISMAN (1972-1976)

AMERICAN CHEMICAL SOCIETY, 1155 Sixteenth St., N.W., Washington, D. C. 20036

Books and Journals Division

JOHN K CRUM *Director*

RUTH REYNARD *Assistant to the Director*

CHARLES R. BERTSCH *Head, Editorial Processing Department*

D. H. MICHAEL BOWEN *Head, Journals Department*

BACIL GUILLEY *Head, Graphics and Production Department*

SELDON W. TERRANT *Head, Research and Development Department*

©Copyright, 1973, by the American Chemical Society. Published biweekly by the American Chemical Society at 20th and Northampton Sts., Easton, Pa. 18042. Second-class postage paid at Washington, D. C., and at additional mailing offices.

All manuscripts should be sent to *The Journal of Physical Chemistry*, Department of Chemistry, University of Minnesota, Minneapolis, Minn. 55455.

Additions and Corrections are published once yearly in the final issue. See Volume 76, Number 26 for the proper form.

Extensive or unusual alterations in an article after it has been set in type are made at the author's expense, and it is understood that by requesting such alterations the author agrees to defray the cost thereof.

The American Chemical Society and the Editor of *The Journal of Physical Chemistry* assume no responsibility for the statements and opinions advanced by contributors.

Correspondence regarding accepted copy, proofs, and reprints should be directed to Editorial Processing Department, American Chemical Society, 20th and Northampton Sts., Easton, Pa. 18042. Head: CHARLES R. BERTSCH. Assistant Editor: EDWARD A. BORGER. Editorial Assistant: JOSEPH E. YURVATI.

Advertising Office: Centcom, Ltd., 142 East Avenue, Norwalk, Conn. 06851.

Business and Subscription Information

Remittances and orders for subscriptions and for single copies,

notices of changes of address and new professional connections, and claims for missing numbers should be sent to the Subscription Service Department, American Chemical Society, 1155 Sixteenth St., N.W., Washington, D. C. 20036. Allow 4 weeks for change of address. Please include an old address label with the notification.

Claims for missing numbers will not be allowed (1) if received more than sixty days from date of issue, (2) if loss was due to failure of notice of change of address to be received before the date specified in the preceding paragraph, or (3) if the reason for the claim is "missing from files."

Subscription rates (1973): members of the American Chemical Society, \$20.00 for 1 year; to nonmembers, \$60.00 for 1 year. Those interested in becoming members should write to the Admissions Department, American Chemical Society, 1155 Sixteenth St., N.W., Washington, D. C. 20036. Postage to Canada and countries in the Pan-American Union, \$5.00; all other countries, \$6.00. Single copies for current year: \$3.00. Rates for back issues from Volume 56 to date are available from the Special Issues Sales Department, 1155 Sixteenth St., N.W., Washington, D. C. 20036.

This publication and the other ACS periodical publications are now available on microfilm. For information write to MICROFILM, Special Issues Sales Department, 1155 Sixteenth St., N.W., Washington, D. C. 20036.

THE JOURNAL OF
PHYSICAL CHEMISTRY

Volume 77, Number 6 March 15, 1973

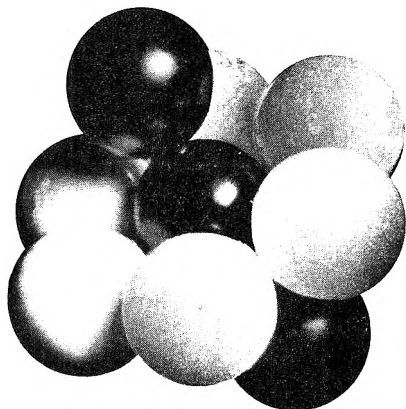
JPCHAx 77(6) 725-862 (1973)

- Hydrogen Fluoride and Deuterium Fluoride Elimination Reactions of Chemically Activated
1,1,1-Trideuterio-2,2-difluoroethane, 1,1-Difluoroethane,
and 1,1,1-Trideuterio-2-fluoroethane **K. C. Kim, D. W. Setser,* and B. E. Holmes** 725
- Kinetics of the Thermal Dissociation of Tetrafluorohydrazine
. **E. Tschuikow-Roux,* K. O. MacFadden, K. H. Jung, and D. A. Armstrong** 734
- Flash Photolysis of Chlorine Dioxide in Aqueous Solution
. **J. C. Mialocq, F. Barat,* L. Gilles, B. Hickel, and B. Lesigne** 742
- Reactions of Fluorinated Benzenes with Hydrated Electrons and Hydroxyl Radicals in
Aqueous Solutions **R. Köster and K.-D. Asmus*** 749
- The Yields of Fragment Ions in the Radiolysis of Liquid *n*-Butane
. **Noboru Fujisaki, Toshinori Wada, Shoji Shida,* and Yoshihiko Hatano** 755
- Methylene Produced by Vacuum-Ultraviolet Photolysis. V. Energy Partitioning in the Reaction
cis-Dimethylcyclopropane + $h\nu(123.6 \text{ nm}) \rightarrow 2\text{-Butene} + {}^1\text{CH}_2$ **K. Dees and R. D. Koob*** 759
- Studies on the Formation of Primary Yields of Hydroxyl Radical and Hydrated Electron in
the γ -Radiolysis of Water **Z. D. Draganić and I. G. Draganić*** 765
- An Electron Spin Resonance Study of the Photolysis of Aqueous Sulfite Solutions
. **Om P. Chawla, N. L. Arthur, and Richard W. Fessenden*** 772
- An Electron Spin Resonance Study of Radicals Produced in the Photolysis of α -Keto Acids
and Esters **A. Samuni, D. Behar, and R. W. Fessenden*** 777
- Electron Paramagnetic Resonance Evidence for a Peroxy Type Superoxide Ion on Surfaces
. **Y. Ben Taarit and J. H. Lunsford*** 780
- Electron Spin Resonance Spectra of Interlamellar Copper(II)-Arene Complexes on
Montmorillonite **J. Paul Rupert** 784
- Oxidation-Reduction Properties of Copper- and Nickel-Substituted Hydroxyapatites
. **Makoto Misono and W. Keith Hall*** 791
- Raman Spectra of the Products of Rubidium and Cesium Atom Argon Matrix Reactions with
Oxygen Molecules **Richard R. Smardzewski and L. Andrews*** 801
- A Redetermination of the Crystal Structure of Dehydrated Zeolite 4A
. **Russell Y. Yanagida, Allen A. Amaro, and Karl Seff*** 805
- Application of the Polanyi Adsorption Potential Theory to Adsorption from Solution on
Activated Carbon. IV. Steric Factors, as Illustrated by the Adsorption of Planar and
Octahedral Metal Acetylacetonates **Cary C. T. Chiou and Milton Manes*** 809
- Use of the Nonpolar Analog Model in Predicting the Effects of Solvents on Molecular Complex
Formation Equilibria **Sherril D. Christian,* Roger Frech, and Kwang Ok Yeo** 813
- Conductance and Ion Pair Formation of Bis(2,9-dimethyl-1,10-phenanthroline)copper(I)
Perchlorate. III. In Acetonitrile-Carbon Tetrachloride and Water-Dioxane Mixtures
. **Katsuhiko Miyoshi* and Toshihiro Tominaga** 819

ห้องสมุด กรมวิทยาศาสตร์

Molecular Sieve Zeolites

ADVANCES IN CHEMISTRY SERIES No. 101 and 102



Seventy-seven papers from a symposium co-sponsored by the Divisions of Colloid and Surface Chemistry, Petroleum Chemistry, and Physical Chemistry of the American Chemical Society and Worcester Polytechnic Institute, Edith M. Flanigen and Leonard B. Sand, co-chairmen.

Do you need a group of substances that can remove radioactive isotopes from nuclear wastes, remove ammonia from secondary sewage effluents, remove sulfur dioxide from waste gases, foster formation of actinides, or disrupt bacterial cells? These and many other possibilities are available through research on molecular sieve zeolites. For example, they are used for separating hydrogen isotopes . . . solubilizing enzymes . . . carrying active catalysts in curing of plastics . . . transporting soil nutrients in fertilizers . . . filtering tars from cigarette smoke.

“Molecular Sieve Zeolites” reports recent advances in this rapidly developing field. Volume I offers 41 papers devoted to the synthesis, structure, mineralogy, and modification of sieve zeolites. These are followed in Volume II by 36 papers discussing sorption and catalysis.

Volume I: 526 pages with index	Cloth (1971)	\$16.00
Volume II: 459 pages with index	Cloth (1971)	\$16.00
No. 101 and 102 ordered together		\$30.00

Postpaid in U.S. and Canada; plus 40 cents elsewhere.
Set of L.C. cards with library orders upon request.

Other books in the ADVANCES IN CHEMISTRY series on colloid chemistry include:

No. 95 Cellulases and Their Applications

Twenty-five papers stress the practical application of cellulolytic systems in biochemistry, animal nutrition, textiles, forest product utilization. Topics include new mechanisms for cellulose degradation, the cellulase complex, structure and morphology of cellulase, a commercial enzyme process and wood-derived products as nutritional sources.

470 pages with index Cloth (1969) \$14.50

No. 87 Interaction of Liquids at Solid Substrates

Twelve papers survey recent research on solid/liquid interaction, including work on “coupling agents,” adhesion of polymers, organic/inorganic interfaces, ultrasonic impedance. Four more papers are concerned with heparinized surfaces at the blood/material interface.

212 pages with index Cloth (1968) \$9.50

No. 84 Molecular Association in Biological and Related Systems

Nineteen articles survey and report new work on molecular association in fat digestion, in soap systems, in membrane constituents, and in mixed monolayers. Other topics include bile salt micelles, lipid monolayers and membranes, and a definitive review of biological membrane structure.

308 pages with index Cloth (1968) \$10.50

No. 79 Adsorption from Aqueous Solution

Fifteen papers discuss thermodynamic and kinetic aspects of adsorption phenomena and the results of studies on a variety of adsorbate-adsorbent systems.

212 pages with index Cloth (1968) \$10.00

No. 63 Ordered Fluids and Liquid Crystals

Twenty-two studies on characterization, properties, and occurrence of these phenomena in many substances such as tristearin, *p*-azoxyanisole, mono- and di-hydric alcohols, phospholipids, and polypeptides.

332 pages with index Cloth (1967) \$11.50

No. 43 Contact Angle, Wettability, and Adhesion

Surface chemistry studies. Relation of equilibrium contact angle to liquid and solid constitution, contact angle as a thermodynamic property, surface energy estimation from contact angle. Contact angle hysteresis, relationship between wetting and adhesion.

389 pages with index Cloth (1964) \$10.50

No. 33 Solid Surfaces and the Gas-Solid Interface

Thirty-seven papers from the Kendall Award Symposium honoring Stephen Brunauer. Theory and techniques for studying surface phenomena.

381 pages with index Cloth (1961) \$12.00

Order from: **Special Issues Sales**

American Chemical Society, 1155 16th Street, N.W., Washington, D.C. 20036

Solvent Isotope Effects on the Ionization of Hydrofluoric Acid	A. J. Kresge* and Y. Chiang	822
Effect of Various Gases on the pH of Water	Gordon H. Fricke, Rick L. Carpenter, and Rubin Battino*	826
Thermochemistry of the Diels–Alder Reaction. III. Heat of Addition of Cyclopentadiene to Maleic Anhydride	F. E. Rogers* and S. W. Quan	828
Excited State Chemistry of Indigoid Dyes. I. Fluorescence <i>vs.</i> Cis–Trans Isomerization	George M. Wyman* and Bizhan M. Zarnegar	831
Effect of Cholesteryl Alkanoate Structure on Liquid Crystal Transition Thermodynamics. Pure and in Binary Mixtures	Harry W. Gibson* and John M. Pochan	837
Analysis of Potential Difference in Electrically Induced Carrier Transport Systems	J. Bdzil, C. C. Carlier, H. L. Frisch, W. J. Ward, III,* and M. W. Breiter	846
Diffusion of Hydrogen in Gold–Palladium Alloys	S. Maestas and Ted B. Flanagan*	850
A Nuclear Magnetic Resonance Line Broadening Study of Dimethyl Sulfoxide in Tris(ethylenediamine)chromium(III)–Dimethyl Sulfoxide Solution	Charles L. Watkins, Gerald S. Vigeo,* and M. E. Harris	855

COMMUNICATIONS TO THE EDITOR

Photoinduced Molecular Aggregation and Precipitation	E. Fischer	859
Extended Hückel Molecular Orbital Calculation on 4-Methylumbelliferone and Its Tautomer	J. R. Huber, M. Nakashima,* and J. A. Sousa	860
Quenching of the Ru(dipy) ₃ ²⁺ Phosphorescence by Cr(CN) ₆ ³⁻ . Evidence for a Diffusion-Controlled Mechanism	F. Bolletta, M. Maestri, and L. Moggi*	861

AUTHOR INDEX

- Amaro, A. A., 805
Andrews, L., 801
Armstrong, D. A., 734
Arthur, N. L., 772
Asmus, K.-D., 749

Barat, F., 742
Battino, R., 826
Bdzil, J., 846
Behar, D., 777
Bolletta, F., 861
Breiter, M. W., 846

Carlier, C. C., 846
Carpenter, R. L., 826
Chawla, O. P., 772
Chiang, Y., 822
Chiou, C. C. T., 809
Christian, S. D., 813

Dees, K., 759
Draganić, I. G., 765
Draganić, Z. D., 765

Fessenden, R. W., 772, 777
Fischer, E., 859
Flanagan, T. B., 850
Frech, R., 813
Fricke, G. H., 826
Frisch, H. L., 846
Fujisaki, N., 755

Gibson, H. W., 837
Gilles, L., 742

Hall, W. K., 791
Harris, M. E., 855
Hatano, Y., 755
Hickel, B., 742
Holmes, B. E., 725
Huber, J. R., 860

Jung, K. H., 734

Kim, K. C., 725
Koob, R. D., 759
Köster, R., 749

Kresge, A. J., 822

Lesigne, B., 742
Lunsford, J. H., 780

MacFadden, K. O., 734
Maestas, S., 850
Maestri, M., 861
Manes, M., 809
Mialocq, J. C., 742
Misono, M., 791
Miyoshi, K., 819
Moggi, L., 861

Nakashima, M., 860

Pochan, J. M., 837

Quan, S. W., 828

Rogers, F. E., 828
Rupert, J. P., 784

Samuni, A., 777
Seff, K., 805
Setser, D. W., 725
Shida, S., 755
Smardzewski, R. R., 801
Sousa, J. A., 860

Taarit, Y. B., 780
Tominaga, T., 819
Tschuikow-Roux, E., 734

Vigee, G. S., 855

Wada, T., 755
Ward, W. J., III, 846
Watkins, C. L., 855
Wyman, G. M., 831

Yanagida, R. Y., 805
Yeo, K. O., 813

Zarnegar, B. M., 831

In papers with more than one author the name of the author to whom inquiries about the paper should be addressed is marked with an asterisk in the by-line.

ANNOUNCEMENT

On the last two pages of this issue you will find reproduced the table of contents of the January 1973 issue of the *Journal of Chemical and Engineering Data*.

Hydrogen Fluoride and Deuterium Fluoride Elimination Reactions of Chemically Activated 1,1,1-Trideuterio-2,2-difluoroethane, 1,1-Difluoroethane, and 1,1,1-Trideuterio-2-fluoroethane

K. C. Kim, D. W. Setser,* and B. E. Holmes

Department of Chemistry, Kansas State University, Manhattan, Kansas 66506 (Received August 16, 1972)

Vibrationally excited CD_3CHF_2 and CH_3CHF_2 were produced from radical combination reactions initiated by cophotolysis of acetone- d_6 and acetone- d_0 with 1,1,3,3-tetrafluoroacetone in order to study the α,α and α,β HF or DF elimination reactions. The decomposition of chemically activated $\text{CD}_3\text{CH}_2\text{F}$ produced from cophotolysis of acetone- d_6 and 1,3-difluoroacetone was studied as a reference for the α,β process. The half-quenching pressures for HF or DF eliminations of CH_3CHF_2 , CD_3CHF_2 , and $\text{CD}_3\text{CH}_2\text{F}$ were 110 ± 5 , 41 ± 2 , and 65 ± 5 Torr, respectively, at 358°K . These chemical activation rate constants and the thermal activation fall-off data were interpreted by RRKM theoretical calculations and the threshold energies for the α,α and α,β processes for CD_3CHF_2 were assigned as 64 and 62 kcal/mol, respectively. The α,α elimination channel comprised 18% of the total rate; the removal of the intramolecular isotope effects was estimated to lower the α,α contribution for CH_3CHF_2 to 10%. The previously reported variation of the α,α and α,β reaction rate ratio with pressure, which we observed only at higher temperatures, was shown not to be a consequence of the change in the average energy of reacting molecules. This and other problems, such as the origin of the CH_2CF_2 product, which presumably are associated with the photochemistry of $(\text{CHF}_2)_2\text{CO}$ are discussed.

Introduction

The competition between α,α and α,β HF elimination was first demonstrated by Pritchard and coworkers for the chemically activated CD_3CHF_2 molecule.¹ An unusual temperature and pressure dependence of the intramolecular rate constant ratio was observed, and the variation of the average energy of the reacting molecules with pressure and temperature was invoked as an explanation. For a number of chemically activated fluoroalkanes^{2,3} it has been shown that the energy distribution is rather narrow and the variation of the average energy of reacting molecules, or the chemical activation rate constant, with pressure is small. This point and a recent estimation of the threshold energy for the α,α process in $\text{CHCl}_2\text{CD}_2\text{Cl}$ ⁴ argue against any significant variation in the α,α and α,β rate ratio with change of pressure. Since CD_3CHF_2 should be a simple example of chemically activated unimolecular reaction, we decided to reinvestigate this system and to apply RRKM calculations to try to resolve some of the secondary questions raised by the important work of Pritchard and coworkers.¹

Thermal pyrolysis studies⁵ provide Arrhenius parameters for decomposition of CH_3CHF_2 . Since the α,α process

accounts for a minor fraction of the reaction, the Arrhenius parameters are a close estimate for the α,β process. Since $D_0(\text{CH}_3\text{-CHF}_2)$ is fairly well known, the chemical activation experimental data can be matched to RRKM calculations to establish threshold energies for both reaction channels. The four-center transition model that was developed for $\text{CH}_3\text{CH}_2\text{F}$ ^{2,3} was extended to $\text{CD}_3\text{CH}_2\text{F}$, CH_3CHF_2 , and CD_3CHF_2 , and a three-center transition state model⁴ was developed for the α,α process by specifying the bond order of the major bonds undergoing rearrangement. The resulting models were used to calculate a thermal fall-off curve, which was compared to recently published data.^{5d}

- (1) M. J. Perona, J. T. Bryant, and G. O. Pritchard, *J. Amer. Chem. Soc.*, **90**, 4782 (1968).
- (2) H. W. Chang and D. W. Setser, *J. Amer. Chem. Soc.*, **91**, 7648 (1969).
- (3) H. W. Chang, N. L. Craig, and D. W. Setser, *J. Phys. Chem.*, **76**, 954 (1972).
- (4) K. C. Kim and D. W. Setser, *J. Phys. Chem.*, **76**, 283 (1972).
- (5) (a) D. Sianesi, G. Nelli, and R. Fontanelli, *Chim. Ind. (Milan)*, **50**, 619 (1968); (b) P. Cadman, M. Day, and A. F. Trotman-Dickenson, *J. Chem. Soc. A*, 1356 (1971); (c) E. Tschuikow-Roux, W. J. Quiring, and J. M. Simmie, *J. Phys. Chem.*, **74**, 2449 (1970); (d) B. Noble, H. Carmichael, and C. L. Baumgardner, *ibid.*, **76**, 1680 (1972).

Vibrationally excited CD_3CHF_2 and CH_3CHF_2 were produced by cophotolysis of acetone- d_6 and acetone- d_0 with $(\text{CHF}_2)_2\text{CO}$ from room temperature to 573°K; however, most experiments were done at 358°K. For comparison, a parallel experiment was carried out for vibrationally excited $\text{CD}_3\text{CH}_2\text{F}$, which was produced by cophotolysis of acetone- d_6 and $(\text{CH}_2\text{F})_2\text{CO}$. Major effort was centered on the rate constants for the α,α and α,β channels of CD_3CHF_2 . Following HF α,α elimination, the carbene intermediate rearranges to form vinyl fluoride and analysis for $\text{CD}_2=\text{CDF}$ vs. $\text{CD}_2=\text{CHF}$ gives the ratio of reaction channels. Recently Quick and Whittle⁶ demonstrated that $\text{CH}_2=\text{CF}_2$ was formed from photosensitization of $\text{CH}_3\text{CF}_2\text{Br}$ by hexafluoroacetone and the possibility of sensitized elimination of HF from CH_3CHF_2 by $(\text{CHF}_2)_2\text{CO}$ was tested in the present study. Experiments also were done to test the reaction mechanism for formation of the 1,1-difluoroethene product, which Perona, Bryant, and Pritchard tentatively attributed to the elimination of molecular hydrogen from chemically activated difluoroethane.

The unimolecular reactions of fluoroethanes activated by hot atom substitution reactions^{7,8} have received considerable study, and Krohn, Manning, and Root⁷ have used these unimolecular reactions to make fundamental deductions about the behavior of the activated fluoroethanes. Bunker⁹ has called attention to the significance of angular momentum for the fluoroethane molecules formed by hot atom substitution. For this reason it is desirable to understand the behavior of CD_3CHF_2 activated to high energies, but not in high angular momentum states. This constitutes another reason for reinvestigating the anomalous pressure and temperature dependence of the ratio of reaction rates previously found¹ for CD_3CHF_2 .

Experimental Section

The acetones were analyzed and, when necessary, purified by gas chromatography to give better than 98% purity. For establishing retention times and mass spectral cracking patterns, research grade Matheson and Peninsular Chemical Research Inc. chemicals were used without further purification.

For most runs about 2 cc of reactant gas mixtures were measured, transferred into various sizes of vessels to attain the desired pressure, and photolyzed using the unfiltered light of a General Electric AH-6 high-pressure mercury arc for about 1 hr. The effective wavelength was 3200 ± 200 Å. The samples were placed inside an oven for 10–15 min at the desired temperature before being photolyzed at that temperature. After the photolysis the condensable products were recovered by pumping the photolyzed sample through a glass wool packed trap kept at liquid nitrogen temperature. The products were then separated by gas chromatography. For a few runs the trap was cooled to solid N_2 temperature to check for possible loss of ethene, which has slight vapor pressure at 77°K.

Two analytical columns were used for the analyses. A silver nitrate-saturated ethylene glycol column in series with a short Porapak-S column at room temperature was used for the separation of ethylene and ethyl fluoride from the photolysis of acetone- d_6 and $(\text{CH}_2\text{F})_2\text{CO}$. Products from the photolysis of $(\text{CHF}_2)_2\text{CO}$ with acetone- d_0 and acetone- d_6 were analyzed by a 9-ft Porapak-S column with appropriate oven temperature programming. Products were identified by their retention times on the above-mentioned columns and mass spectral patterns of the

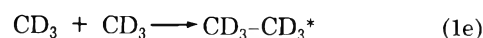
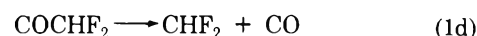
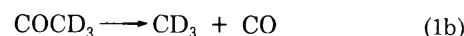
fractions trapped from the He effluent. Gas chromatographic calibrations for the deuterated products were made with their nondeuterated analogs. Neither of the difluoroethane isomers gave a detectable parent ion for 70-eV electron energy; the highest masses were m/e 68 and 65 corresponding to α hydrogen rupture from CD_3CHF_2 and CH_3CHF_2 , respectively. The most abundant ion, m/e 51 (CHF_2^+), was common to the mass spectra of both CD_3CHF_2 and CH_3CHF_2 . Other major peaks in the mass spectrum of CD_3CHF_2 were approximately the same as the results of Perona, Bryant, and Pritchard¹ except for discrepancies in the assignment of the highest mass to the parent ions.

The temperature effect upon the α,α and α,β rate ratio for CD_3CHF_2 was studied from 300 to 570°K. The temperature of the reaction vessel was monitored using a thermocouple attached to the vessel. After photolyzing the sample consisting of $(\text{CD}_3)_2\text{CO}$ and $(\text{CHF}_2)_2\text{CO}$ in the ratio of 3:1, the condensable products were analyzed as already described. Vinyl fluoride was collected from the helium effluent and the ratio of vinyl- d_3 and - d_2 fluoride was determined from the 49/48 mass ratio obtained from 15-eV electron energy spectra with a EAI Quad 250 mass spectrometer.

Several diagnostic type experiments were done using the apparatus and procedures described above. These experiments are described in the section of the text concerned with the reaction mechanism.

Experimental Results

Photochemical and High-Pressure Reaction Mechanisms. General features of photodecomposition reactions of acetone and fluoroacetones¹⁰ are well established. The following reaction sequence is pertinent to forming chemically activated molecules.



All three products, 1e–1g, were observed, although only CD_3CHF_2 and its decomposition products were measured as a function of temperature and pressure. The only significant disproportionation reaction is self-disproportionation of CF_2H radical.¹ Reactions 1b and 1d are enhanced by high temperature which results in increased overall quantum yields. Methane, CF_2H_2 , and CF_2HD , which are formed by abstraction, and several higher boiling components were observed (see later section).

(6) (a) L. M. Quick and E. Whittle, *Can. J. Chem.*, **45**, 1902 (1967); (b) *Trans. Faraday Soc.*, **67**, 1727 (1971); **68**, 878 (1972).

(7) (a) N. J. Parks, K. A. Krohn, and J. W. Root, *J. Chem. Phys.*, **55**, 5785 (1972); (b) K. A. Krohn, R. G. Manning, and J. W. Root, private communication, 1972.

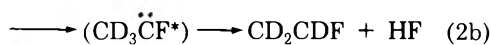
(8) C. T. Ting and F. S. Rowland, *J. Phys. Chem.*, **74**, 480 (1970).

(9) D. L. Bunker, *J. Chem. Phys.*, **57**, 332 (1972).

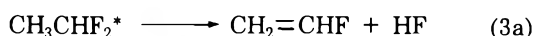
(10) (a) G. O. Pritchard and R. L. Thommarson, *J. Phys. Chem.*, **71**, 1674 (1967); (b) A. M. Tarr, J. W. Coomber, and E. Whittle, *Trans. Faraday Soc.*, **61**, 1182 (1965).

Except for various isotope effects, the $\text{CH}_3\text{COCH}_3 + (\text{CHF}_2)_2\text{CO}$ photolysis system is identical and an equivalent set of reactions exist. The reactions describing the photolysis of $(\text{CD}_3)_2\text{CO}$ and $(\text{CH}_2\text{F})_2\text{CO}$ also are very similar and need not be repeated. For the latter case only $\text{CD}_3\text{CH}_2\text{F}$ and $\text{CD}_2=\text{CH}_2$ were measured at various pressures.

Unimolecular Reactions and Rate Constants. The molecules formed by the binary radical combination reaction (reaction 1f) contain internal energy equal to the potential energy released by the C-C bond formation plus thermal energy carried by the radicals. These excited molecules may eliminate HF and DF or be collisionally stabilized.



For the α,α process HF elimination is followed by D atom migration to give $\text{CD}_2=\text{CDF}$. It is not possible to separate out the α,α and α,β processes for excited CH_3CHF_2 although both presumably exist



Analysis of the ethene showed that ethene- d_2 was the only decomposition product from $\text{CD}_3\text{CH}_2\text{F}$



This observation is consistent with the results of others for fluoroethane^{1,11} and chloroethane.^{12b} Apparently the α,α process competes with the α,β process only if two halogens are attached to the same carbon.^{1,4,13,14}

The apparent chemical activation rate constants can be defined as¹⁵

$$k_{ai} = k_M[M](D_i/S_i)$$

where D_i and S_i denote the measured decomposed and stabilized product yields, respectively, and $k_M[M]$ is the collision frequency. For unit deactivation, which should be a good approximation for acetone bath molecules,^{2,3} and for $D/S \leq 2$, k_a may be obtained from the usual plot of D/S vs. $1/P$ (see Figure 1). The rate constants in pressure units can be converted to sec^{-1} units by assuming collision cross sections for the computation of k_M .

Table I summarizes the product yields from photolysis of $(\text{CD}_3)_2\text{CO} + (\text{CHF}_2)_2\text{CO}$ at $\sim 358^\circ\text{K}$. Figure 1 includes the D/S data for all the molecules. Below $D/S \leq 2$ a linear relationship exists and from the slopes of the lines, k_{ai} values were obtained. From least-squares analyses of the data points with $D/S < 2.0$, the rate constants were 41 ± 2 (CD_3CHF_2), 110 ± 5 (CH_3CHF_2), and 65 ± 5 ($\text{CD}_3\text{CH}_2\text{F}$) Torr. Taking a medium value for the 49/48 mass ratio of vinyl- d_3 fluoride and - d_2 as 0.22 at 358°K (see Table II), the rate constant ratio for 2a and 2b is 34:7 in Torr units.

Converting the rate constants from pressure units to sec^{-1} units gave 3.8×10^8 , 1.0×10^9 , and $6.6 \times 10^8 \text{ sec}^{-1}$ for CD_3CHF_2 , CH_3CHF_2 , and $\text{CD}_3\text{CH}_2\text{F}$ for a temperature-independent collision diameter of 5.0 Å. Small variations in reactant gas mixtures were ignored and the bath

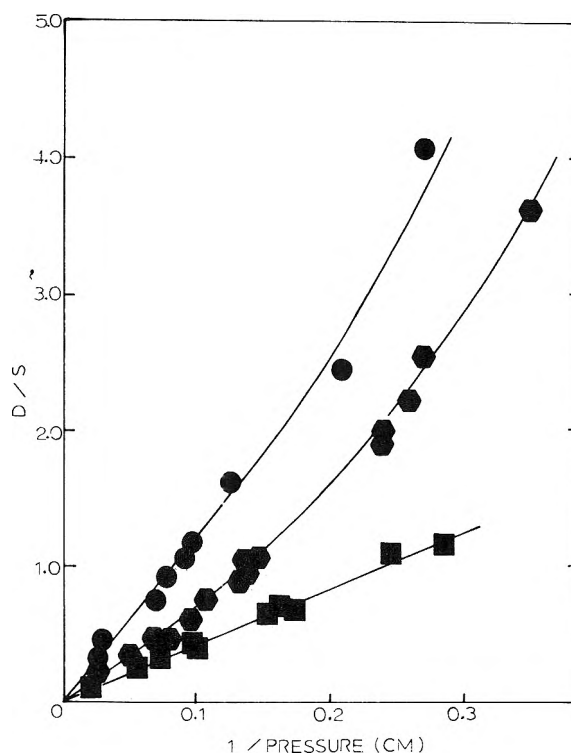


Figure 1. Decomposition product yields—stabilized product yields vs. $1/P$ (cm) for CD_3CHF_2 (■), CH_3CHF_2 (●), and $\text{CD}_3\text{CH}_2\text{F}$ (▲). Photolysis temperatures were 358°K for 1,1-difluoroethanes and 343°K for fluoroethane- d_3 .

gas was treated as a mixture of $1/3$ fluorinated acetone + $2/3$ acetone- d_6 or acetone- d_0 . If the $\Omega^{(2,2)*}$ integrals¹⁶ with $\epsilon/K = 475^\circ$ are included in the collision diameter the rate constants in sec^{-1} increase by a factor of 1.8 at 358°K . Since good σ and ϵ/K values are not available, the rate constants from the 5.0-Å collision diameter will be used.

Since some curvature is evident for the lower pressures of Figure 1, cascade deactivation is occurring and the high-pressure rate constants are not unit deactivation rate constants. Previous studies of fluoroethanes³ suggest that reduction of the rate constants obtained from the linear part of a D/S vs. $1/P$ plot by ~ 0.8 yields unit deactivation rate constants for gases as efficient as the acetones. Since this factor is comparable to the uncertainty in collision cross sections, no change was made from the least-squares values.

Temperature and Pressure Effects on the Ratio of the α,α and α,β Processes. Table II summarizes mass spectral analyses of the vinyl- d_3 and - d_2 fluoride; both electron energies gave the same ratio. Data were obtained from 24 to 148 Torr at virtually constant temperature and from room temperature to 553°K at virtually constant pressure, ~ 35 Torr. The following points should be noted: (1) at the lower temperatures the 49/48 ratio did not vary signif-

(11) Y. N. Tang and F. S. Rowland, *J. Amer. Chem. Soc.*, **90**, 570 (1968).

(12) (a) K. Dees and D. W. Setser, *J. Chem. Phys.*, **49**, 1193 (1968); (b) W. G. Clark, D. W. Setser, and K. Dees, *J. Amer. Chem. Soc.*, **93**, 5328 (1971).

(13) E. Tschuikow-Roux and J. E. Marte, *J. Chem. Phys.*, **42**, 2049 (1965).

(14) H. W. Chang, D. W. Setser, and M. J. Perona, *J. Phys. Chem.*, **75**, 2070 (1971).

(15) B. S. Rabinovitch and D. W. Setser, *Advan. Photochem.*, **3**, 1 (1964).

(16) J. O. Hirshfelder, C. F. Curtiss, and R. B. Bird, "Molecular Theory of Gases and Liquids," Wiley, New York, N. Y., 1965.

TABLE I: Product Analyses from Photolysis of $(\text{CD}_3)_2\text{CO} + (\text{CH}_2)_2\text{CO}^{a,b}$ at 358°K

Sample composition (STP), cc	Pressure, Torr	$\text{CD}_2=\text{CHF} + \text{CD}_2=\text{CDF}$ (D)	CD_3CHF_2 (S) ^b	D/S	k_a, sec^{-1}
0.4	24	140.0	86.0	1.50	3.97×10^8
1.3					
0.9	31	182.5	161.6	1.15	3.98×10^8
1.3					
0.4	35	222.0	180.0	1.13	3.99×10^8
1.3					
0.4	40	128.0	108.0	1.09	4.00×10^8
1.3					
0.4	55	111.0	148.0	0.69	4.03×10^8
1.3					
0.4	61	24.0	32.0	0.69	4.04×10^8
1.3					
0.9	63	48.6	68.8	0.65	4.05×10^8
1.5					
0.9	94	232.0	601.5	0.39	4.08×10^8
1.4					
0.4	97	19.2	42.4	0.41	4.08×10^8
1.3					
0.4	132	49.6	147.2	0.31	4.12×10^8
1.3					
0.8	147	91.2	470.0	0.20	4.13×10^8
1.3					
0.4	164	47.2	168.0	0.25	4.14×10^8
1.3					
0.9	387	12.0	155.2	0.08	4.24×10^8
1.3					

^a Product yields are in units of gc peak areas. ^b D/S values were obtained from the ratio of peak areas after correcting for the sensitivity of the thermal conductivity detector for CH_2CHF and CH_3CHF_2 , which varied between 0.92 and 1.02.

icantly with pressure, which correspond to $D/S = 0.2$ to 1.5; (2) from room temperature to 423°K the variation in the ratio of vinyl- d_3 fluoride/vinyl- d_2 fluoride was no larger than experimental error. However, as the temperature was increased from 423 to 553°K the ratio increased markedly and nearly doubled at the highest temperature. The observations in Table II parallel the results of Perona, Bryant, and Pritchard,¹ although we did not observe the pressure dependence of the ratio that they reported. However, our study of the pressure effect was at a lower temperature.

Calculated Results

RRKM Calculated Rate Constants for CD_3CHF_2 and CH_3CHF_2 . The microscopic unimolecular rate constants were calculated from the expression

$$k_E = \frac{\sigma P_1^\dagger}{h P_1^*} \sum_{E_v \leq E} P^\dagger(E_v - E_0) / N^*(E) \quad (\text{I})$$

The dagger and the asterisk superscripts denote complex and energized molecule, respectively. The details regarding the computations have been discussed elsewhere.^{2,3,15} All internal degrees of freedom of the fluoroethanes were active and the overall rotations are adiabatic for both molecule and complex (P_1 is the partition function for overall rotation). Harmonic oscillator sums, $\Sigma P^\dagger(E_v)$, and densities, $N^*(E)$, were used.

For unit deactivation, the experimental unimolecular rate constants for CD_3CHF_2 are related to the microscopic

TABLE II: Summary^a of Mass Spectral Analyses of Vinyl Fluorides

Sample composition (STP), cc	Pressure, Torr	Temp, °K	49/48 (15 eV)	49/48 (70 eV)	D/S ^b
0.4	24	368	0.22	0.24	1.5
1.3					
0.9	31	351	0.21	0.21	1.1
1.3					
0.8	63	358	0.21	0.19	0.6
1.5					
0.9	94	358	0.19	0.20	0.4
1.4					
0.8	148	378	0.20	0.21	0.2
1.3					
0.9	25	298	0.20	0.25	
1.4					
1.0	37	298	0.24	0.25	
1.3					
1.2	29	298	0.19	0.20	
1.3					
0.9	56	403	0.25	0.24	0.9
1.3					
0.9	37	423	0.26	0.26	
1.4					
0.9	39	441	0.25	0.30	2.5
1.4					
0.9	37	463	0.31	0.32	
0.2					
1.3	36	493	0.33	0.38	
1.5					
0.9	30	553	0.46	0.50	
1.2					

^a The first five runs are arranged in order of increasing pressure and the rest are in order of increasing temperature. ^b D/S represents the ratio of the decomposition to stabilized product yields; for some cases the stabilization product was not measured.

rate constants for CD_3CHF_2 and distribution function, $f(E)$, by the following expression

$$k_a(\alpha, \beta) = \frac{\int_{E_0(\alpha, \beta)}^{\infty} \frac{k_E(\alpha, \beta)}{k_M[\text{M}] + k_E(\alpha, \beta) + k_E(\alpha, \alpha)} f(E) dE}{\int_{E_0(\alpha, \beta)}^{\infty} \frac{k_M[\text{M}]}{k_M[\text{M}] + k_E(\alpha, \beta) + k_E(\alpha, \alpha)} f(E) dE} \quad (\text{II})$$

The experimental rate constant for the α, α process is obtained in a similar manner with $k_E(\alpha, \alpha)$ interchanged for $k_E(\alpha, \beta)$. For activation by simple bimolecular combination reactions, the distribution function takes the form

$$f(E) dE = k_E' K(E) dE / \int_{E_{\min}}^{\infty} k_E' K(E) dE$$

k_E' is the rate constant for dissociation of CD_3CHF_2 into two radicals, and $K(E)$ is the Boltzmann distribution. E_{\min} , the on-set of the distribution function, is determined by $D^\circ(\text{CD}_3\text{-CHF}_2)$ plus any activation energy for the radical combination reaction. The chemical activation distribution function at 358°K along with the specific rate constants are shown in Figure 2.

For unit deactivation, the calculated ratio, $k_a(\alpha, \alpha) / k_a(\alpha, \beta)$, corresponds to the experimentally measured value. For inefficient bath gas molecules cascade deactivation should be explicitly included¹⁷ in the calculations

(17) C. W. Larson and B. S. Rabinovitch, *J. Chem. Phys.*, 51, 2293 (1969).

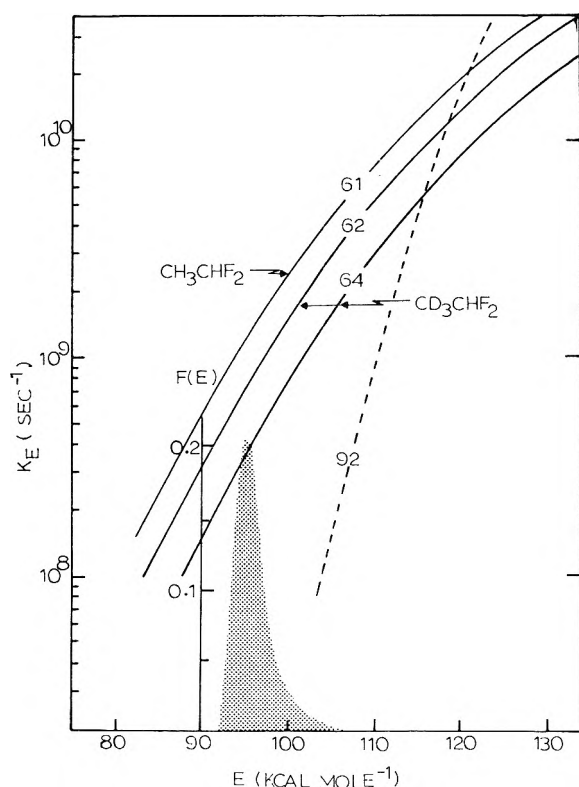


Figure 2. RRKM calculated rate constants and energy distribution function. The two solid lines with $E_0 = 62$ and 64 kcal are the α, α and α, β reaction channels, respectively, of CH_3CHF_2 . The dotted line is for the dissociation channel for CD_3CHF_2 . The distribution function is for CD_3CHF_2 formed by radical combination at 358°K . The solid line with $E_0 = 61$ is the α, β process for CH_3CHF_2 .

for comparison with experimental data. For the present case with $E_0(\alpha, \alpha) \approx E_0(\alpha, \beta)$ and for relatively efficient bath gases, this effect can be neglected.

Models for Difluoroethane- d_0 and - d_3 , and the Elimination Transition States. The frequencies and moments of inertia for CH_3CHF_2 are known.¹⁸ Frequencies for CD_3CHF_2 were obtained from vibrational frequencies of CH_3CHF_2 , CD_3CF_3 ,¹⁹ and by Wilson's F - G matrix treatment with a modified valence force field, which was assigned from the results of normal mode analysis of typical hydrocarbons²⁰ and fluoroalkanes.²¹ The force constants used for the CH_3CHF_2 molecule are listed in Table III. The four-center complex model was treated by a full F - G matrix calculation for the whole eight-atom complex. Johnston's force constant relationships²² with bond orders of 1.5, 0.9, 0.1, and 0.1 for C-C, C-F, C-H, and H-F bonds, respectively, were used to obtain stretching force constants between ring atoms. A reaction coordinate frequency ($\sim 300 \text{ cm}^{-1}$) was obtained in a similar manner as for linear triatomic complexes²³ by setting the ring interaction force constants $f_{\text{CC-CH}} = (f_{\text{CC}}f_{\text{CH}})^{1/2}$ and $f_{\text{CC-CF}} = (f_{\text{CC}}f_{\text{CF}})^{1/2}$. Except for the torsional mode, the remaining force constants of the transition state were taken to be the same as for the molecule. The torsional force constant was adjusted in order to obtain a frequency which gave a preexponential factor for the thermal unimolecular rate constant of $\sim 10^{13} \text{ sec}^{-1}$ per reaction path. The magnitude of the torsion force constant governs the magnitude of the out-of-plane bending mode of the ring, which in our previous work^{2,3,12} was termed the ring puckering mode and was varied to obtain the best fit with data. The final

TABLE III: Force Constants^a for CH_3CHF_2

$K_{\text{C-H}}$	4.72	$K_{\text{<HCF}}$	0.63
$K_{\text{C-F}}$	4.37	$K_{\text{C-C-<HCC}}$	0.28
$K_{\text{C-C}}$	4.52	$K_{\text{<HCH-<HCH}}$	-0.005
$K_{\text{<FCF}}$	0.66	$K_{\text{<HCC-<HCC}}$	-0.015
$K_{\text{<FCC}}$	0.86	$K_{\text{C-C-<FCC}}$	0.35
$K_{\text{<HCH}}$	0.54	$K_{\text{<FCC-<FCC}}$	-0.020
$K_{\text{<HCC}}$	0.66	torsion	0.024

^a Stretching force constants are in units of $\text{mdyn}/\text{\AA}$, bending force constants in units of $\text{mdyn}/(\text{rad})^2$, and interaction force constants are in unit of mdyn/rad for stretching-bend interaction and $\text{mdyn}/(\text{rad})^2$ for bending-bending interaction

frequencies for the molecule and for the transition states satisfied the Teller-Redlich product rule within 5%. The α, β threshold energy (E_0 value) for CD_3CHF_2 was obtained from the value selected for CH_3CHF_2 and calculated changes in zero-point energies.

Compared to a model² formerly used for 1,2-difluoroethane, the present transition state has three in-plane ring vibrational frequencies that are about 100 cm^{-1} lower than the previous model. The ring puckering frequency was nearly the same as for the previous model. These small differences arise from the coupling of normal modes between in-plane and out-of-plane frequencies in the full Wilson's F - G matrix treatment and from the lowered^{12b} (1.5 vs. 1.9) C-C bond order.

A three-centered complex was constructed in a manner similar to the method used for the four-centered complex. The bonds undergoing major rearrangement were assigned bond orders of 0.9, 0.1, and 0.5 for C-F, C-H, and H-F bonds, respectively; other force constants were the same as for the stable molecule.

Preexponential factors in terms of the partition function ratio at 800°K were 4.6×10^{13} , with a reaction path degeneracy of 4, for the α, β process and 3.9×10^{13} , with a reaction path degeneracy of 2, for the α, α process. The hindered internal rotation of the molecule was treated as a torsion for computing the partition function. The frequencies and moments of inertia are summarized in the Appendix. The agreement between the calculated and experimental⁵ values of the preexponential factor for the α, β process is satisfactory.

Dissociation Rate Constants and Distribution Functions. Since it was necessary to calculate dissociation rate constants to obtain the distribution function of CH_3CHF_2 and CD_3CHF_2 , effort was extended to obtain a realistic model. The model consisted of the frequencies of CD_3 and CHF_2 plus four low bending modes (see Table VI in Appendix), which were varied to obtain the desired preexponential factor.^{3,24} From the consideration of the reversibility of forward and reverse reactions, $k_{\text{uni}} = K_{\text{eq}}k_{\text{bi}}$; k_{bi} is the equilibrium radical combination constant which is typically $\sim 10^{13} \text{ cc mol}^{-1} \text{ sec}^{-1}$. Since the equilibrium constant, K_{eq} , can be calculated, estimation of k_{uni} is

(18) (a) D. C. Smith, R. A. Sanders, and J. R. Nielson, *J. Chem. Phys.*, **20**, 847 (1952); (b) N. Solimene and B. P. Dailey, *ibid.*, **22**, 2042 (1954).

(19) B. Lafon and J. R. Nielson, *J. Mol. Spectrosc.*, **21**, 175 (1966).

(20) J. H. Schachtschneider and R. G. Snyder, *Spectrochim. Acta.*, **19**, 117 (1963).

(21) (a) J. R. Nielson, AEC Accession No. 38312, Rept. No. TID-22063 Avail. CFSTI, 29 (1965); (b) J. R. Nielson, *Nucl. Sci. Abstr.*, **19**, 4782 (1965).

(22) H. S. Johnston, *J. Amer. Chem. Soc.*, **86**, 1643 (1964).

(23) R. A. More O'Ferrall and J. Kouba, *J. Chem. Soc. B*, 985 (1967).

(24) E. V. Waage and B. S. Rabinovitch, *Int. J. Chem. Kinet.*, **3**, 105 (1971).

possible. The model so adjusted had a preexponential factor of $7.23 \times 10^{16} \text{ sec}^{-1}$ at 800°K, which corresponds to a radical combination rate constant of $2.8 \times 10^{13} \text{ cc mol}^{-1} \text{ sec}^{-1}$.

The k_E values were calculated from eq I, which only approximately accounts for centrifugal effects,²⁴ for several values of the threshold energy. The results, which are shown in Figure 2, demonstrate that the dissociation rate constant increases much faster with energy than the HF elimination rate constants and radical dissociation should compete with HF elimination at energies above $\sim 120 \text{ kcal mol}^{-1}$. The CD_3CHF_2 distribution function using this dissociation model and $E_{\text{min}} = 92 \text{ kcal}$ is shown in Figure 2 for 358°K; the average energy of the formed molecules is $95.7 \text{ kcal mol}^{-1}$.

Discussion

Chemical Activation Rate Constants for CH_3CHF_2 , CD_3CHF_2 , and $\text{CD}_3\text{CH}_2\text{F}$. Three sets of data are in the literature^{25,26} for chemically activated CH_3CHF_2 formed by combination of CH_3 and CHF_2 radicals. The rate constants of Bryant and Pritchard²⁵ are in good agreement with those measured in the present study; however, the data of Trotman-Dickenson and coworkers give rate constants which are higher than our values by about a factor of 2. On the other hand, the rate constants of Trotman-Dickenson and coworkers have a more reasonable dependence on temperature, which was the objective of that study, than the more limited results of Bryant and Pritchard. Our rate constant (for the same collision cross sections) for CD_3CHF_2 is in good agreement with that measured by Pritchard and coworkers.¹

There are no previous studies of $\text{CD}_3\text{CH}_2\text{F}$; however, the isotope effect relative to $\text{CH}_3\text{CH}_2\text{F}$ ³ is 2.3, which is similar to the value for $\text{CD}_3\text{CH}_2\text{Cl}-\text{CH}_3\text{CH}_2\text{Cl}$ (2.2). Although the isotope effect for $\text{CD}_3\text{CHF}_2-\text{CH}_3\text{CHF}_2$ (2.7) is distributed over two channels, it appears to be about 20% too large on the basis of comparison with calculations, *vide infra*, and with the other two pairs.

In order to make comparison between various chemically activated fluoroethanes,²⁷ the threshold energies are needed. Four determinations have been made of the activation energy for CH_3CHF_2 : 61.9,^{5a} 64.9,^{5b} 61.9,^{5c} and 63.4^{5d} kcal mol^{-1} . For our models at 800°K the activation energies are converted to threshold energies by subtracting 1.7 kcal mol^{-1} , and we used 61 kcal as the threshold energy for CH_3CHF_2 . The threshold energies^{3,28,29} of $\text{C}_2\text{H}_5\text{F}$ and 1,2- $\text{C}_2\text{H}_4\text{F}_2$ are 57 and 61.5 kcal . Recent results show that increasing fluorine substitution has the effect of increasing the threshold energies for HF elimination.^{3,28,29}

The chemical activation rate constant³ for $\text{C}_2\text{H}_5\text{F}$ is 1.4 times larger than for 1,1- $\text{C}_2\text{H}_4\text{F}_2$ and both are considerably larger than for 1,2- $\text{C}_2\text{H}_4\text{F}_2$ (half-quenching pressure^{2,28b} of 20 Torr at 300°K). The 4-kcal increase in E_0 for 1,1- $\text{C}_2\text{H}_4\text{F}_2$ relative to $\text{C}_2\text{H}_5\text{F}$ has the effect of lowering k_E values by a factor of ~ 3 . This is offset by the 3-4-kcal higher average energy of 1,1- $\text{C}_2\text{H}_4\text{F}_2$, which gives back a factor of 1.5. Thus the frequency patterns play a relatively minor role in determining the relative changes in the rate constants for $\text{C}_2\text{H}_5\text{F}$ and 1,1- $\text{C}_2\text{H}_4\text{F}_2$. This is in direct contrast to the difluoroethane isomers which have nearly the same E_0 values. The higher rate for the 1,1 isomer is a consequence of (1) a slightly higher average energy (the bond energy appears to be about 2 kcal mol^{-1} higher than for 1,2- $\text{C}_2\text{H}_4\text{F}_2$) and (2) the lower density of states for

1,1- $\text{C}_2\text{H}_4\text{F}_2$ because the low-frequency vibrations are higher (240 and 392 *vs.* 196 and 320 cm^{-1}) than for 1,2- $\text{C}_2\text{H}_4\text{F}_2$. This general trend was pointed out before,² however, better thermochemical data now permit a better assignment of the factors. These three molecules emphasize the need for detailed evaluation of all factors pertaining to eq I; casual generalizations do not suffice for explaining even these relatively straightforward elimination reaction rates.

Comparison of the α,α and α,β Processes. One of the goals of the present investigation was to deduce the critical energy for the α,α channel by comparison with the α,β channel which has a critical energy of 61 kcal mol^{-1} . As shown in Table IV, good agreement exists between the calculated (α,β channel only) and the experimental rate constant for CH_3CHF_2 . Based upon the calculations for α,α elimination from CD_3CHF_2 , the α,α channel is estimated to contribute only $\sim 10\%$ to the decomposition rate for CH_3CHF_2 and the use of only the α,β rate constant for Table IV is satisfactory. The critical energy for α,β elimination from CD_3CHF_2 is 62 kcal (obtained from zero-point energy considerations) and the comparison with experimental results is presented in Table IV. The agreement is quite satisfactory and, since the same force constants were used for CD_3CHF_2 and CH_3CHF_2 , there are no adjustable parameters in these calculations. The calculated isotope effect is somewhat smaller than the experimental value, and the latter may contain some systematic error.

The best fit to the experimental rate constant for the α,α elimination from CD_3CHF_2 was with $E_0 = 64 \text{ kcal mol}^{-1}$. Considering all factors the absolute value of E_0 is probably reliable to $\pm 2 \text{ kcal mol}^{-1}$; however, the uncertainty in $E_0(\alpha,\alpha) - E_0(\alpha,\beta)$ is much less and we estimate $\pm 0.4 \text{ kcal mol}^{-1}$. Since the α,α channel has no primary isotope effect, the E_0 for α,α elimination from CH_3CHF_2 will be nearly the same as for CD_3CHF_2 , *i.e.*, the difference in $E_0(\alpha,\beta)$ and $E_0(\alpha,\alpha)$ for CH_3CHF_2 will be 3 kcal mol^{-1} . For $\text{CH}_2\text{Cl}-\text{CDCl}_2$ the $E_0(\alpha,\alpha)$ was found⁴ to be 2 kcal higher than the $E_0(\alpha,\beta)$ and correction for the isotope effect narrowed the difference between channels to 1 kcal for $\text{CH}_3\text{Cl}-\text{CHCl}_2$.

The necessity of double halogen substitution for opening the α,α channel is well established. The explanation⁴ is the much greater thermodynamic stability of the singlet carbene with a halogen rather than a hydrogen atom at a radical site. Since the reaction between the carbene and HF or HCl must have only a small activation energy, the greater thermodynamic stability necessarily means a significant lowering of the critical energy for the elimination reaction yielding a halogen substituted carbene relative to the hydrogen substituted reference. The rearrangement of the halocarbene to the olefin, however, still is exothermic. It would be of interest to try scavenging experiments for the purpose of trapping the more stable halogen-substituted carbene before rearrangement. Such experiments have not been successful for ethylidene.^{7b,30}

(25) J. A. Bryant and G. O. Pritchard, *J. Phys. Chem.*, **74**, 2449 (1970).

(26) J. A. Kerr, D. C. Phillips, and A. F. Trotman-Dickenson, *J. Chem. Soc. A*, 1806 (1968).

(27) D. W. Setser in "Reaction Kinetics," J. C. Polanyi, Ed., MTP-Butterworths Biennial Review of Chemistry, London, 1972.

(28) (a) J. A. Kerr and D. M. Timlin, *Int. J. Chem. Kinet.*, **3**, 427 (1971); (b) *Trans. Faraday Soc.*, **67**, 1376 (1971).

(29) G. E. Millward, R. Hartig, and E. Tschuikow-Roux, *J. Phys. Chem.*, **75**, 3195 (1971).

(30) E. Tschuikow-Roux, J. R. McNesby, W. M. Jackson, and J. L. Faris, *J. Phys. Chem.*, **71**, 1531 (1967).

TABLE IV: RRKM Calculated Rate Constants

Molecule	Temp, °K	Exptl ^a $k_a(\alpha, \alpha + \alpha, \beta)$	Calcd results			
			$k_a^\infty(\alpha, \beta)$	$k_a^0(\alpha, \beta)$	$k_a^\infty(\alpha, \alpha)/k_a^\infty(\alpha, \beta)$	$k_a^0(\alpha, \alpha)/k_a^0(\alpha, \beta)$
CH ₃ CHF ₂	358 ^b	10.3 × 10 ⁸	9.03 × 10 ⁸	8.25 × 10 ⁶		
CD ₃ CHF ₂	300		3.69 × 10 ⁸	3.42 × 10 ⁶	0.19	0.19
	358 ^b	3.83 × 10 ⁸	4.38 × 10 ⁸	3.92 × 10 ⁶	0.21	0.20
	400		4.99 × 10 ⁸	4.34 × 10 ⁶	0.21	0.20
	450		5.80 × 10 ⁸	4.90 × 10 ⁶	0.22	0.21
	500		6.66 × 10 ⁸	5.52 × 10 ⁶	0.22	0.21

^a These are the α, α and α, β combined experimental rate constants in units of sec⁻¹. ^b The average energy of the formed CD₃CHF₂ molecules is 95.7 kcal mol⁻¹; the thermal contribution is 3.7 kcal at 358°K. The average energy of the CH₃CHF₂ is 0.5 kcal mol⁻¹ lower. ^c $k_a(\text{expt}) = 3.83 \times 10^8$ for CD₃CHF₂ was partitioned into 3.14×10^8 sec⁻¹ for the α, β process and 6.89×10^7 for the α, α process based on the experimental $\alpha, \alpha/\alpha, \beta$ ratio of 0.22 at 358°K.

TABLE V: Fall-Off Calculations^a for CH₃CHF₂

Pressure, Torr	k/k^∞		
	800°K	1000°K	1300°K
10 ³	0.997	0.990	0.980
10 ²	0.971	0.922	0.844
10	0.843	0.671	0.476
1	0.561	0.335	0.165
10 ⁻¹	0.256	0.113	0.040

^a The calculated k/k^∞ values at 800°K can be compared with the pyrolysis data in Figure 2 of ref 5d, which indicates $k/k^\infty = 0.85$ and 0.57 at 10 and 1 Torr, respectively.

The calculated ratio of the $\alpha, \alpha/\alpha, \beta$ reaction rates at limiting high and low pressure for temperature up to 500°K are presented in Table IV. Although the calculated ratio does change slightly with temperature and pressure, the effect is too small to explain the reported observations.⁷ The energy of the reacting molecules does increase with increased pressure (0.43 kcal difference between 24 and 380 Torr for 358°K) and temperature as explained by Pritchard, *et al.*; however, the energy change is too small to be experimentally significant. Competitive reactions of chemically activated CH₂ClCH₂Br have been previously examined³¹ and for that case no variation in the rate ratio with pressure was found. This is typical of chemical activation with high E_{min} and relatively narrow distribution functions and contrasts with the large alkyl radicals studied by Rabinovitch and coworkers.³²

The photolysis of (CHF₂)₂CO and (CD₃)₂CO appears to provide a well-behaved chemical activation system for CD₃CHF₂ at temperatures up to ~360°K. However, at higher temperatures a source of CD₂=CDF, other than α, α elimination, seems to be present. A further complication is the presence of the CD₂=CF₂ product, which Pritchard and coworker attributed to HD elimination from CD₃CHF₂. A discussion of these aspects of the reaction system is presented in the last section. For our immediate purpose the important question is; if experimental error of unknown source is affecting the chemical activation data above 423°K, what is the probability that the data at lower temperature are a true measure of the rates of α, β and α, α elimination? Since the pressure dependence of the ratio was as expected at 358°K, we believe that the ratio of 0.2 ± 0.1 is reliable. The general agreement of the CH₃CHF₂ rate constants from four independent studies and with the calculated results from a model which fits results from a whole series of haloethanes²⁷ also lends support to the validity of this ratio.

Comparison of Calculated and Experimental Fall-Off for CH₃CHF₂. In spite of the wealth of knowledge about unimolecular HX (X = F, Cl, Br) elimination reactions of haloalkanes,²⁷ there is not good data for the thermally activated fall-off behavior. The recent pyrolysis work^{5d} with CH₃CHF₂ may be the start toward obtaining such information and for this reason we compared the results from our model to the data, which cover the k/k^∞ region from 1.0 to 0.3; $k/k^\infty = 0.5$ at ~0.6 Torr.

The calculations from our models are straightforward;³² the RRKM form of k/k^∞ for comparison with experiment for thermal systems is given by¹⁵

$$k/k^\infty = \int_{E_0}^{\infty} \frac{k_m[M]}{k_E + k_m[M]} k_E K(E) dE / \int_{E_0}^{\infty} k_E K(E) dE \quad (\text{III})$$

All terms have been previously defined and the calculated fall-off results are summarized in Table V. For the pressure range covered by the 800° thermal data, the calculated results fit the curvature of the data quite well and the absolute pressure fit also is excellent. Our results show that the chemical activation data, the thermal activation preexponential factor, and the thermal fall-off data can be fitted by the same four-centered transition state model.

Effects of Angular Momentum on the Elimination and Dissociation Rate Constants. Bunker⁹ has provided a formulation accounting for angular momentum effects in the secondary unimolecular processes following a hot atom substitution reaction. We used this approach to estimate the effect that the angular momentum from the combination reactions might have upon the HF elimination and radical dissociation rate constants. Rabinovitch and Waage²⁴ have given a similar formulation for estimation of the centrifugal effects on dissociation reactions.

Bunker's formulation was used to assign the average rotational energy in the complex and molecule. This was then used to select the appropriate sums and densities to be used to calculate the rate constant. For our k_E equation the following expression results

$$k(E, E_s, \sigma) = \frac{\sum P^\ddagger \left[E - E_0 - \sigma E_s \left[\frac{1}{I_1^\ddagger} + \frac{1}{I_2^\ddagger} + \frac{1}{I_3^\ddagger} \right] \mu / 4\pi \right]}{h N^* \left[E - \sigma E_s \left[\frac{1}{I_1^*} + \frac{1}{I_2^*} + \frac{1}{I_3^*} \right] \mu / 4\pi \right]} \quad (\text{IV})$$

E is the internal energy of the molecule, $E = E^\ddagger + E_0$; E

(31) R. L. Johnson and D. W. Setser, *J. Phys. Chem.*, **71**, 4366 (1967).

(32) (a) E. A. Hardwidge, C. W. Larson, and B. S. Rabinovitch, *J. Amer. Chem. Soc.*, **92**, 3278 (1970); (b) C. W. Larson and B. S. Rabinovitch, *J. Chem. Phys.*, **52**, 5181 (1970); (c) Numerous other studies referenced in above two papers.

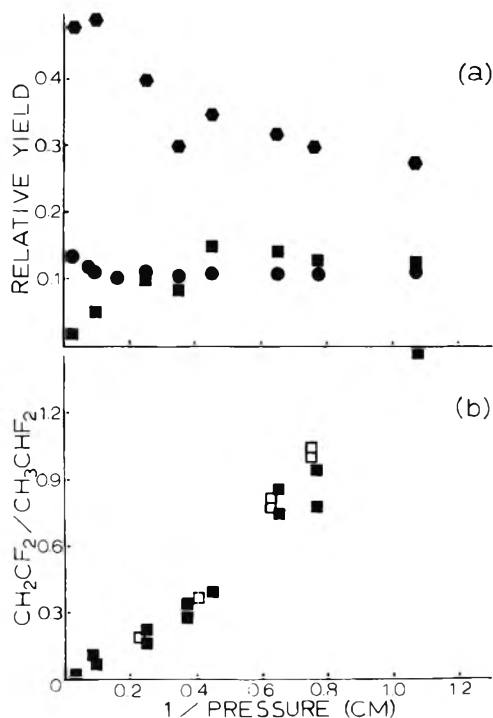


Figure 3. (a) The yields of (i) CH₂F₂ relative to CH₃CHF₂ + CH₂CHF (●), (ii) CH₂F₂ relative to CHF₂CHF₂ + CF₂CHF (●), and (iii) CH₂CF₂ relative to CH₃CHF₂ + CH₂CHF (■) vs. P^{-1} at 298°. (b) The relative yields of CH₂=CF₂ and CH₃CHF₂ vs. pressure⁻¹ at temperatures of 298 (■) and 350°K (□).

itself does not depend on J although E includes the centrifugal energy. E_s is the relative translational energy, μ is reduced mass for two radicals and σ is the cross section (not collision diameter) for the radical combination reaction. For combination of thermal radicals at 360°K, E_s is ~ 2 kcal and a reasonable estimate of σ is 20 \AA^2 .

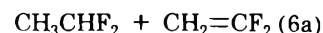
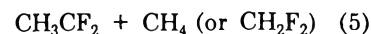
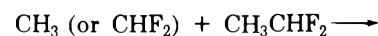
Since the moments of inertia of the dissociation transition state are larger than that for elimination, which virtually are the same as the molecule, eq IV affects the rate constants for dissociation more than for elimination. This was noted by Bunker for CH₃CF₂¹⁸F activated by F for F substitution which yields molecules in high angular momentum states. For our purposes comparison of the results of eq IV and I to k_E for $J = 0$ is of interest. The $J = 0$ result is obtained by dropping the P_1^\dagger/P_1^* of I or by setting $\sigma = 0$ in IV. The $k_E(J = 0)$ curves for dissociation and α, β elimination cross at $123 \text{ kcal mol}^{-1}$. For $E_s = 2 \text{ kcal}$ and $\sigma = 20 \text{ \AA}^2$ the result for the elimination reaction from eq IV is indistinguishable from eq I; the result for the dissociation rate constant is about 20% lower than from eq I, which is about the same result that would be obtained from Rabinovitch and Waage's formulation. This is because the potential energy release by radical combination mainly becomes vibrational energy of CH₃CHF₂, so that the centrifugal effect is virtually insignificant for both channels. We conclude that the centrifugal energy effects upon the rate constants for molecules activated by combination of thermalized radicals is within the experimental uncertainty of the rate constants and/or the uncertainty in assignment of models and use of harmonic oscillator sums and densities.

Mechanistic Consideration for the (CD₃)₂CO-(CHF₂)₂CO System. There are several unresolved problems. One, of course, is the variable CD₂CHF/CD₂CFD

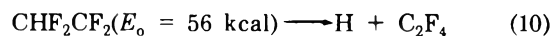
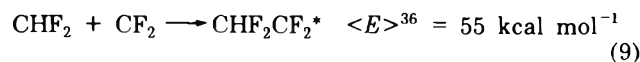
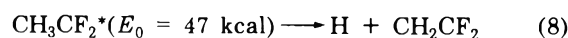
ratio at higher temperatures. A second is the source of the CD₂CF₂ product, which at first glance¹ appears to be a consequence of HD elimination from CD₃CHF₂. A third is the rather large number of minor products which require that reactions other than 1-4 be added to the mechanism. Some diagnostic type experiments, which originally were addressed to the first two problems, are described below.

We first checked for the possibility of sensitized decomposition of CD₃CHF₂ because Whittle and coworkers⁶ have shown that photosensitized decomposition of haloethanes by hexafluoroacetone are not uncommon. However, the photolysis of (CHF₂)₂CO or (CH₃)₂CO with CH₃CHF₂ at ~ 75 Torr for 2 hr produced no CH₂CHF or CH₂CF₂. Apparently sensitization reactions of CH₃CHF₂ by (CHF₂)₂CO or (CH₃)₂CO are insignificant.

Difluoroethylene was observed in the cophotolysis of 1.5 cc of (CH₃)₂CO and 0.5 cc of (CHF₂)₂CO (total pressure = 3-300 Torr), at 298 and 350°K; however, at least ten other unidentified products (with longer retention times than CH₃CHF₂) were present in larger yields. The CH₂CF₂/CH₃CHF₂ product yield ratio vs. P^{-1} , Figure 3b, shows the pressure and temperature dependence characteristic of a chemically activated reaction, which previously was invoked to explain this product.¹ Since elimination of molecular H₂ from ground electronic states of haloethanes is rather unusual, some alternative possibilities are worth considering. Formation of CH₂CF₂ in the pyrolysis^{5d} of CH₃CHF₂ was explained by



Photolyses of 0.5 cc of (CHF₂)₂CO with 0.2 cc of CH₃CHF₂ and 1.5 cc of (CH₃)₂CO with 0.2 cc of CH₃CHF₂ (at pressures of 10-300 Torr) at 298 and 350°K gave no CH₂CF₂. These reactions are, thus, not a viable mechanism for conditions of the photochemical experiment, even though abstraction³³ of H from the α position is highly favored. Since disproportionation, $k_d/k_c = 0.19$, is reported³⁴ for CHF₂ radicals, reactions 7-10 may be considered.³⁵



Since the formation of H + C₂F₄ is virtually thermoneutral, the CHF₂CF₂* radical will not decompose. For reactions 7 and 8 to account for the observed CH₂CF₂ yields,

(33) (a) P. M. Scott and K. R. Jennings, *J. Phys. Chem.*, **73**, 1513 (1969); (b) R. D. Giles, L. M. Quick, and E. Whittle, *Trans. Faraday Soc.*, **63**, 662 (1967).

(34) G. O. Pritchard and J. T. Bryant, *J. Phys. Chem.*, **70**, 1441 (1966).

(35) F. W. Dalby, *J. Chem. Phys.*, **41**, 2297 (1964).

(36) (a) $\Delta H_f^\circ(\text{CF}_2) = -44.5 \text{ kcal mol}^{-1}$ was obtained from G. A. Carlson, *J. Phys. Chem.*, **75**, 1625 (1971); (b) $\Delta H_f^\circ(\text{CHF}_2\text{CF}_2) = -158 \text{ kcal mol}^{-1}$ and $\Delta H_f^\circ(\text{CH}_3\text{CF}_2) = -71 \text{ kcal mol}^{-1}$ were calculated from bond dissociation energies of the ethanes; (c) The ΔH_f° of all other species are from ref 41, or values cited in text.

TABLE VI: Frequencies and Moments of Inertia for Molecules and Complexes^a

CH ₃ CHF ₂	Complex	
	Four center	Three center
	Log A = 13.59 sec ⁻¹ ^e	Log A = 13.54 sec ⁻¹
2988 (4)	2972 (3)	2997 (3)
1413 (5)	1406 (2)	1427 (4)
1146 (3)	1310 (1)	1089 (3)
904 (2)	1083 (3)	840 (2)
521 (2)	876 (4)	607 (2)
392 (1)	615 (3)	432 (2)
240 (1)	450 (1)	300 (1)
54.6; 57.5; 99.7 ^b	56.1; 57.9; 101.2	51.8; 59.9; 104.1

CD ₃ CHF ₂	Complex		
	Four center	Three center	Association ^{c,d}
	Log A = 13.66 sec ⁻¹	Log A = 13.58 sec ⁻¹	Log A = 16.86 sec ⁻¹
2942 (1)	2942 (1)	2209 (3)	3086 (1)
2209 (3)	2175 (2)	1320 (2)	2230 (3)
1320 (2)	1186 (3)	1045 (5)	1135 (4)
1080 (6)	978 (3)	696 (2)	950 (2)
758 (2)	710 (4)	532 (2)	481 (2)
450 (3)	548 (3)	390 (2)	80 (2)
180 (1)	350 (1)	300 (1)	50 (2)
57.7; 68.7; 110.9	62.4; 67.5; 113.1	57.7; 69.8; 116.3	c

^a The last entry of each column is the moments of inertia in amu Å². ^b D. C. Smith, R. A. Saunders, J. R. Nielsen, and F. E. Ferguson, *J. Chem. Phys.*, **20**, 847 (1952). ^c The product of three moments of inertia for the association complex was taken as 1.607×10^6 in comparison with 4.20×10^5 for the stable molecule. ^d Reference 24 discusses some basic questions concerning the formulation of transition state models for dissociation type reactions. ^e Preexponential factors are given in terms of the partition function ratio at 800°K.

competition between (8) and collisional stabilization must exist above 50 Torr. RRKM³⁷ calculations for CH₃CF₂* gave $k_E \sim 10^{12}$ sec⁻¹ for $E = 60$ kcal mol⁻¹, indicating that collisional stabilization will compete with (8) only at pressures much greater than 1 atm. Reactions 7 and 8, thus, cannot be responsible for the observed pressure dependent yield of CH₂CF₂. We have no evidence that CH₂CF₂ is not formed by the unimolecular decomposition of CH₃CHF₂*. However, the actual yield of CH₂CF₂ is small, about 1/10 of the CHF=CH₂ yield, and it is premature to assign a unimolecular mechanism until the photochemical mechanism for some of the more major products is better known, *vide infra*.

During the consideration of reactions 7 and 8, a search was made for C₂F₄ in order to check for the presence of CF₂. Only trace quantities were found from the photolysis of 0.5 cc of (CHF₂)₂CO at 5–200 Torr and 298°. However, in this photolysis we found a minimum of five products (in addition to CHF₂CHF₂, CH₂F₂, C₂F₄, and CHF₂CF₂) which, from mass spectral data, were tentatively assigned as fluorinated propanes, butanes, or propenes, but specific identification was not possible. All of these products, two of which showed a strong pressure dependence, exceeded the CH₂CF₂ yield (relative to CHF₂CHF₂ in both systems) in the cophotolysis of (CH₃)₂CO and (CHF₂)₂CO by factors of 2–10.

In an effort to find independent, positive evidence for the presence of CF₂, experiments at 300° were done with 10% added ethene and propene. No change in product distribution and no new products were observed, which is not surprising considering the slow reaction rates of CF₂ with olefins.^{35,38} Nevertheless all of these observations led to the suspicion that CF₂ radicals may not be formed in significant amounts. This somewhat startling possibility led to a check

of the importance of H atom abstraction, presumably from the acetones, as the source of CH₄ and CH₂F₂. Consequently, the noncondensable (77°K) products from room temperature cophotolysis of (CH₃)₂CO and (CHF₂)₂CO were analyzed by mass spectrometry. At an ionization voltage of 25 eV, the observed ions were m/e 28, 16, and 15. At total acetone pressures of 12.5, 20, 25, and 60 Torr the m/e 15 to 28 ratios were 0.07, 0.08, 0.12, and 0.12 and correction for mass spectrometer sensitivity (obtained from prepared calibration mixtures) gave CH₄/CO = 0.08, 0.09, 0.13, and 0.13, respectively. Without doubt CH₄ was formed, presumably by H-atom abstraction. The relative yield of CH₂F₂ to (CH₃CHF₂ + CH₂CHF) and (CHF₂CHF₂ + CF₂CHF) *vs.* P^{-1} , Figure 3a, is virtually constant at 0.3 and 0.11 respectively. Since H atom abstraction seems to be occurring, 0.11 must be an extreme upper limit for the disproportionation-combination ratio of CF₂ and it must, in fact, be considerably lower than this. These H atom abstraction reactions also must be partly responsible for the unidentified products with long retention times.

In summary, we have not identified the reaction mechanisms which are responsible for the complications in the cophotolysis of (CH₃)₂CO and (CHF₂)₂CO. In fact, we have added a new question about the reliability of the CHF₂ disproportionation-combination ratio. In our opinion H abstraction from (CHF₂)₂CO cannot be ignored and we suspect that either the CF₂COCHF₂ radical or long-lived excited states of the ketone are involved seriously in the mechanism. Much careful work clearly remains to be done.

(37) The models for ethyl radical type decomposition reactions are discussed in ref 15.

(38) W. J. R. Tyerman, *Trans. Faraday Soc.*, **65**, 1188 (1969).

Acknowledgments. This work was supported by the National Science Foundation (G.P.-27536X) and by the Kansas State University Computing Center.

Appendix

The frequencies and moments of inertia used for the molecular and transition states are summarized in Table VI. In order to obtain E_{min} for $\text{CH}_3 + \text{CHF} \rightarrow \text{CH}_3\text{CHF}_2$, the ΔH_f° for CH_3CHF_2 , CH_3 , and CHF_2 are needed. We used the -117.3 kcal value (298°) of Kolesov and coworkers³⁹ for $\Delta H_f^\circ(\text{CH}_3\text{CHF}_2)$, which agrees closely with Lacher⁴⁰ and Skinner's value of -118 kcal. Conversion to 0°K gives $\Delta H_f^\circ = -115.1$ kcal. The well-known⁴¹ $\Delta H_f^\circ(\text{CH}_3) = 34.9$ kcal value was used. The $\Delta H_f^\circ(\text{CHF}_2)$

was obtained from Tarr, Coomber, and Whittle's value^{10b} of 101.0 kcal for $D_{473}^\circ(\text{CHF}_2\text{-H})$. Conversion to 0°K ($D_0^\circ(\text{CHF}_2\text{-H}) = 98.7$ kcal) and using $\Delta H_f^\circ(\text{CH}_2\text{F}_2) = -106.4$ kcal gives $\Delta H_f^\circ(\text{CHF}_2) = -59.3$ kcal. This is well within the error limits of the value (-58.5 kcal) recommended by Kerr and Timlin.²⁸ Combining these values and using a 1.0 kcal activation energy for the radical combination gives $E_{\text{min}} = 91.7$ kcal mol⁻¹. The E_{min} value for CD_3CHF_2 of 92.2 kcal was obtained from 91.7 kcal and the zero-point energy changes for CD_3CHF_2 and CD_3 vs. CH_3CHF_2 and CH_3 .

(39) V. P. Kolesov, S. N. Shtekher, A. M. Martynov, and S. M. Skuratov, *Zh. Fiz. Khim.*, **42**, 3033 (1968).

(40) J. R. Lacher and H. A. Skinner, *J. Chem. Soc. A*, 1034 (1968).

(41) "JANAF Thermochemical Tables," The Dow Chemical Company, Midland, Mich., 1965.

Kinetics of the Thermal Dissociation of Tetrafluorohydrazine^{1a}

E. Tschuikow-Roux,* K. O. MacFadden,^{1b} K. H. Jung,^{1c} and D. A. Armstrong

Department of Chemistry, University of Calgary, Calgary, Alberta T2N 1N4, Canada (Received November 14, 1972)

The shock initiated thermal dissociation of tetrafluorohydrazine, $\text{N}_2\text{F}_4 \rightleftharpoons 2\text{NF}_2$, in excess argon and nitrogen has been investigated over the temperature range $351\text{--}453^\circ\text{K}$, at total pressures $1.0\text{--}9.4$ atm in Ar and $0.69\text{--}12.0$ atm in N_2 . The progress of the reaction behind incident shock waves was followed by monitoring the NF_2 radical concentration in absorption at 260 nm using a time-resolved spectrophotometric technique. The rate of dissociation in both systems was found to be pressure dependent, characteristic of a unimolecular reaction in the fall-off region and approaching the high- and low-pressure limiting values at the extremes of the pressure range. Assuming that the activation energy in the high-pressure limit may be approximated by the enthalpy of reaction, the high-pressure limiting rate constant is given by $k_{\text{Ar}} (\text{sec}^{-1}) = 10^{15.37} \exp(-19,800/RT)$. A similar value was obtained from the $\text{N}_2\text{F}_4\text{-N}_2$ data. At pressures below 2 atm the rate is essentially in the second-order region and the bimolecular rate constants for the $\text{N}_2\text{F}_4\text{-Ar}$ data were found to be in good agreement with literature values. The combined data may be represented by $k_{\text{bi}}^0 (M^{-1} \text{sec}^{-1}) = 10^{13.56 \pm 0.1} \exp[-(15,300 \pm 600)/RT]$. The results are discussed in terms of the RRKM theory of unimolecular reactions and it is shown that a loose activated complex structure in which the NF_2 radicals are bound by a London attractive potential is adequate to describe the observed fall-off behavior. However, computed second-order rate constants in the low-pressure limit were found to be higher than those observed. The discrepancy can be removed if allowance is made for nonequilibrium effects at low pressure.

Introduction

Tetrafluorohydrazine presents an interesting chemical system by virtue of the elementary character of its molecule-stable radical equilibrium, $\text{N}_2\text{F}_4 \rightleftharpoons 2\text{NF}_2$. In the temperature range $300\text{--}500^\circ\text{K}$ recombination is the only reaction of NF_2 radicals and the equilibrium is completely reversible. The concentration of NF_2 radicals has been determined by electron paramagnetic resonance,^{2a} ultraviolet,^{2b} and infrared^{3,4} spectroscopy, as well as mass spectroscopy.⁵ Equilibrium constants and ΔH values for the reaction determined by these methods are in reasonable agreement with $(\Delta P/\Delta T)_v$ data,^{2b} and these results have recently been reviewed.⁶ From a practical point of view an

understanding of the chemistry and reaction kinetics of the $\text{N}_2\text{F}_4\text{-NF}_2$ system at elevated temperatures is of interest in rocket propellant technology, and more recently in

(1) (a) Work supported by the Defence Research Board of Canada under D. R. B. Grant No. 9530-107. (b) Postdoctoral Fellow, 1971-1973. (c) Predoctoral Fellow, 1969-1972.

(2) (a) L. H. Piette, F. A. Johnson, K. A. Booman, and C. B. Colburn, *J. Chem. Phys.*, **35**, 1481 (1961); (b) F. A. Johnson and C. B. Colburn, *J. Amer. Chem. Soc.*, **83**, 3043 (1961).

(3) (a) M. D. Harmony, R. J. Myers, L. J. Schoen, D. R. Lide, Jr., and D. E. Mann, *J. Chem. Phys.*, **35**, 1129 (1961); (b) M. D. Harmony and R. J. Myers, *ibid.*, **37**, 636 (1962).

(4) J. R. Durig and R. C. Lord, *Spectrochim. Acta*, **19**, 1877 (1963).

(5) J. T. Herron and V. H. Dibeler, *J. Chem. Phys.*, **35**, 747 (1961).

(6) D. A. Armstrong and J. L. Holmes, *Compr. Chem. Kinet.*, **4**, 143 (1972).

the field of chemical lasers where HF vibrational-rotational stimulated emission has been observed in the flash photolysis of N_2F_4 with suitable hydrogen sources.⁷

The kinetics of the thermal dissociation of N_2F_4 in the presence of excess inert gas has been reported by two groups of investigators.^{8,9} Both studies were carried out behind incident shock waves and the reaction was followed by optical density measurements of the NF_2 absorption band at about 260 nm. Modica and Hornig⁸ used primarily excess argon as diluent at total pressures of 0.6–3.3 atm and temperatures 350–450°K. Over the pressure range 0.6–2.7 atm the rate was found to be first order in N_2F_4 and 0.9 order in argon concentration. It was concluded that well within the experimental error the reaction was in the second-order, low-pressure region. Brown and Darwent⁹ studied the reaction by essentially the same technique using 1% N_2F_4 mixtures in nitrogen and argon in the temperature range 344–410°K. The dissociation with N_2 as diluent was carried out over a tenfold pressure range from 0.6 to 6 atm, and that with argon over a more limited range from 1.4 to 2.1 atm. The kinetic data from the nitrogen mixture indicated that the dissociation of N_2F_4 was quasi-unimolecular throughout the experimental pressure range, attaining the first-order limit just above 6 atm and the second-order region below 0.6 atm. It has been pointed out⁶ that the difference in the pressure dependence of the $N_2F_4-N_2$ and N_2F_4-Ar data cannot be solely explained on the basis of collision rates alone, and nitrogen must be more efficient than argon in transferring energy. Nevertheless, the difference in behavior with these two gases is greater than would normally be expected¹⁰ and thus a reinvestigation of this system, coupled with a theoretical treatment, would appear in order. Since structural studies on N_2F_4 ^{11–13} and NF_2 ³ are quite complete the dissociation of tetrafluorohydrazine lends itself to a fairly detailed analysis in terms of the quantum statistical RRKM theory¹⁴ of unimolecular reactions and this forms another objective of the present study.

Experimental Section

Apparatus. The shock tube was constructed from seven sections of cylindrical aluminum tubing (80 mm i.d., 10 mm wall) with flanged ends to allow for versatility in shock tube geometry. In the present study the driver and channel sections were 305 and 417 cm, respectively. The tube was designed for cold driver operation, and aluminum diaphragms of various gauge thickness were used to give the desired temperature and density behind the incident shock wave. The test section was provided with two fabricated aluminum valves which were machined to fit flush with the internal wall of the tube to minimize disturbances in the flow.

The incident shock velocity was measured by three pressure transducers of 1- μ sec rise time (Kistler, Model 603A/623F) located 40, 60, and 80 cm from the end plate. The signals from the transducers were amplified (Kistler, Model 566 Charge Amplifiers) and fed to two universal counters (Hewlett-Packard, Model 5325A) which provided a direct readout of the transit times of the shock wave.

The spectrophotometric detection station was located downstream from the last pressure transducer, 36 cm from the end plate. It consisted of a rectangular section milled from an aluminum block and bored out to the shock tube diameter. The windows were made from polished sapphire in the shape of truncated cones (base, 10 mm). The inner surface was ground to a curvature of radius 40 mm to pro-

vide a flush fit with the shock tube wall. The light source was a 900-W xenon arc lamp (Hanovia, No. 538C-1). The light was spatially defined by a slit and quartz lens arrangement. The 260-nm wavelength was isolated on the opposite side of the shock tube by a 0.3-m plane grating monochromator (McPherson, Model 218). The intensity of the transmitted light was monitored by a high-gain photomultiplier (EMI = 9635 QB) powered by a regulated dc power supply (Kepco, Model 750). The photomultiplier output was fed through an adjustable load resistor to a Tektronix oscilloscope (Model 535A). The load resistor was adjusted so that the signal-to-noise ratio (S/N) was approximately 40 and the rise time less than the transit time of the shock through the light beam. The response of the optical system was calibrated before every experiment with a light chopper which provided a reference signal corresponding to 0 and 100% light transmittance.

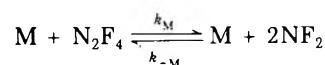
Pressures in the range 0–800 Torr and 0–1000 psi were measured with Heise gauges (Models 5027 and 5028, respectively). Pressures below 1 Torr were measured with thermocouple and cold cathode gauges. Typical pressure readings in the shock tube prior to an experiment were $<10^{-4}$ Torr.

Materials. The tetrafluorohydrazine from the Air Products Co. was 99.8% pure and was used without further purification. Matheson research grade argon and nitrogen of better than 99.995% stated purity were used as diluent gases, while helium was used as the driver gas. Reaction mixtures of 0.1 and 1.0% N_2F_4 -diluent composition were prepared in an all metal vacuum-pressure line and stored in stainless steel tanks.

Data Reduction

Gasdynamic Considerations. The temperature and density across the incident shock were evaluated from measured shock velocities using an iterative procedure which takes explicit account of the effects of chemical relaxation and dissociation processes. The details of this procedure are outlined in Appendix A-1.

Kinetic Analysis. The expression for the thermal dissociation of N_2F_4 in the general pressure region may be written



where M is a collision partner. For dilute mixtures of N_2F_4 in argon or nitrogen, [M] is simply the concentration of the inert gas. The rate of disappearance of N_2F_4 is then given by

$$-d[N_2F_4]/dt_p = k_M[M][N_2F_4] - k_{-M}[M][NF_2]^2 \quad (1)$$

where the concentrations refer to the region behind the incident shock, and t_p is the particle time which is related

- (7) (a) R. K. Pearson, D. W. Gregg, E. B. Huss, S. J. Thomas, R. E. Niver, and J. R. Creighton, *Chem. Phys. Lett.*, **8**, 609 (1971); (b) T. D. Padrick and G. C. Pimentel, *J. Chem. Phys.*, **54**, 720 (1971); (c) L. E. Brus and M. C. Lin, *J. Phys. Chem.*, **75**, 2546 (1971).
- (8) A. P. Modica and D. F. Hornig, *J. Chem. Phys.*, **49**, 629 (1968).
- (9) L. M. Brown and B. de B. Darwent, *J. Chem. Phys.*, **42**, 2158 (1965).
- (10) H. S. Johnston, "Gas Phase Reaction Rate Theory," Ronald Press, New York, N. Y., 1966.
- (11) D. R. Lide, Jr., and D. E. Mann, *J. Chem. Phys.*, **31**, 1129 (1959).
- (12) J. R. Durig and J. W. Clark, *J. Chem. Phys.*, **48**, 3216 (1968), and earlier references quoted therein.
- (13) M. M. Gilbert, G. Gundersen, and K. Hedberg, *J. Chem. Phys.*, **56**, 1691 (1972).
- (14) (a) R. A. Marcus, *J. Chem. Phys.*, **20**, 359 (1952); (b) G. M. Wiedner and R. A. Marcus, *ibid.*, **37**, 1835 (1962); (c) R. A. Marcus, *ibid.*, **43**, 2658 (1965).

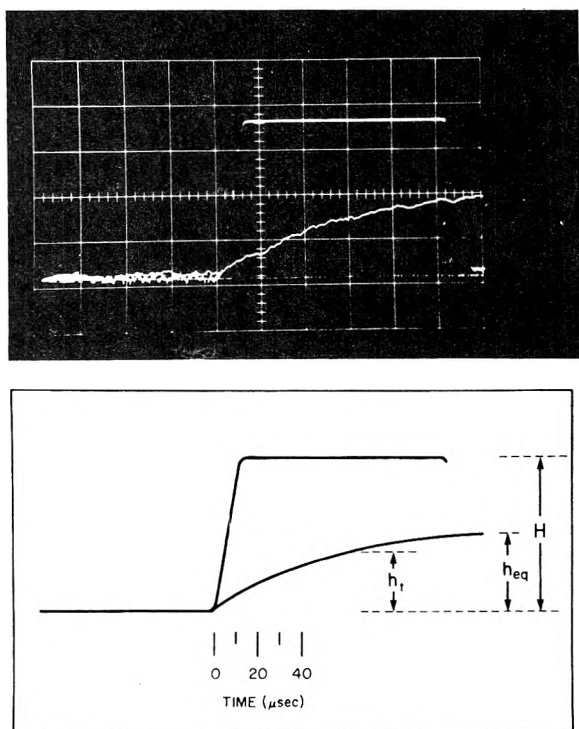


Figure 1. Typical oscillogram of NF_2 absorption at 260 nm for 1% N_2F_4 - N_2 mixture. Writing speed 20 $\mu\text{sec}/\text{cm}$.

to the laboratory time, t_1 , by $t_p = \rho_{21}t_1$ where $\rho_{21} = \rho_2/\rho_1$ is the density ratio across the shock front. If α is defined as the fraction of N_2F_4 molecules dissociated, $\alpha = [\text{N}_2\text{F}_4]_{\text{diss}}/[\text{N}_2\text{F}_4]_0$, we have the mass balance equations

$$\begin{aligned} [\text{NF}_2] &= 2\alpha[\text{N}_2\text{F}_4]_0 \\ &= 2\alpha\rho_{21}[\text{N}_2\text{F}_4]_{01} \end{aligned} \quad (2)$$

$$\begin{aligned} [\text{N}_2\text{F}_4] &= (1 - \alpha)[\text{N}_2\text{F}_4]_0 \\ &= (1 - \alpha)\rho_{21}[\text{N}_2\text{F}_4]_{01} \end{aligned} \quad (3)$$

where $[\text{N}_2\text{F}_4]_{01}$ refers to the initial N_2F_4 concentration in zone 1, the undisturbed gas in front of the shock. Substitution of eq 2 and 3 in 1 yields

$$d\alpha/dt_1 = k_M\rho_{21}^2[M]_1(1 - \alpha) - 4k_{-M}\rho_{21}^3[M]_1[\text{N}_2\text{F}_4]_{01}\alpha^2 \quad (4)$$

where $[M]_1 = [M]/\rho_{21}$ now refers to the concentration of M in zone 1. Integration of eq 4 subject to the boundary condition $\alpha = 0$ at $t_1 = 0$ yields

$$\ln [(\psi + \alpha)/(\phi - \alpha)] = \ln(\psi) + 2BCt_1 \quad (5)$$

where

$$\psi = C + \frac{1}{2}b \quad (6)$$

$$\phi = C - \frac{1}{2}b \quad (7)$$

$$b = K_c/4\rho_{21}[\text{N}_2\text{F}_4]_{01} \quad (8)$$

$$C = (1 + 4/b)^{1/2}b/2 \quad (9)$$

$$B = 4k_M\rho_{21}^3[M]_1[\text{N}_2\text{F}_4]_{01}/K_c \quad (10)$$

and $K_c = k_M/k_{-M}$ is the equilibrium constant. The plot of $(2C)^{-1} \ln [(\psi + \alpha)/(\phi - \alpha)]$ vs. t_1 is linear with positive slope B from which k_M , or the apparent first-order rate constant, $k_{\text{uni}} = k_M[M] = k_M\rho_{21}[M]_1$, can be determined

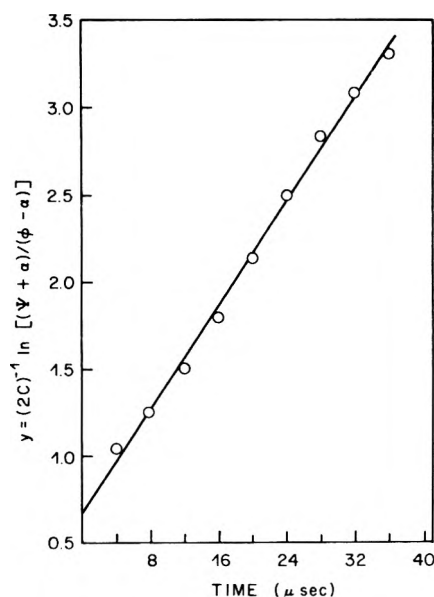


Figure 2. Plot of the integrated rate expression, eq 5.

for each experiment. The equilibrium constant was evaluated at the appropriate temperature from the equation

$$\log K_c = (-19.1 \text{ kcal}/2.303RT) + 6.67 \quad (11)$$

obtained from $(\Delta p/\Delta T)_v$ data.^{2b}

The degree of dissociation α is found from the experimentally determined concentration of NF_2 using the Beer-Lambert law

$$\begin{aligned} I/I_0 &= \exp(-\epsilon L[\text{NF}_2]) \\ &= \exp(-2\epsilon L\rho_{21}[\text{N}_2\text{F}_4]_{01}\alpha) \end{aligned} \quad (12)$$

where I_0 and I are the incident and transmitted light intensity; $L = 8.0$ cm is the optical path length (*i.e.*, the shock tube diameter), and ϵ is the absorption coefficient of NF_2 .

A typical oscilloscope trace of the NF_2 radical absorption and a reference signal are shown in Figure 1a and an idealized version is redrawn in Figure 1b. Deflection for 100% absorption is the height H of the signal generated by the light chopper. The absorption due to NF_2 radicals during the dissociation process is shown as h_t at time t , and at chemical equilibrium as h_{eq} . The difference $(H - h_t)$ is the light transmitted and hence $I/I_0 = (H - h_t)/H$. The value of α is therefore given by

$$\alpha = \ln [H/(H - h_t)]/2\epsilon L\rho_{21}[\text{N}_2\text{F}_4]_{01} \quad (13)$$

A plot of eq 5 for a typical run is shown in Figure 2.

Results

Absorption Coefficient of NF_2 . The absorption coefficient of NF_2 at 260 nm was determined for 0.1% N_2F_4 -Ar mixtures in 14 experiments in which the temperature exceeded 600°K and total concentrations ranged from 3×10^{-5} to 6×10^{-5} M. At these temperatures the N_2F_4 dissociation is virtually complete ($\alpha \approx 1.0$) and since in the concentration range used the optical density was linear with NF_2 concentration the absorption coefficient is given by

$$\epsilon = \ln [H/(H - h_{\text{eq}})]/2L\rho_{21}[\text{N}_2\text{F}_4]_{01} \quad (14)$$

The mean value obtained, $\epsilon = 615 \pm 25 \text{ M}^{-1} \text{ cm}^{-1}$, was

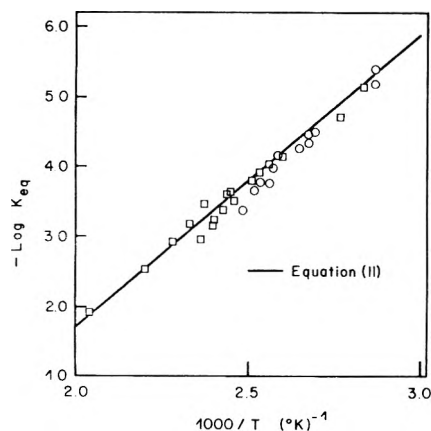


Figure 3. Temperature dependence of the equilibrium constant for $\text{N}_2\text{F}_4 \rightleftharpoons 2\text{NF}_2$: squares, 0.1% N_2F_4 -Ar mixture; circles, 0.1% N_2F_4 - N_2 mixture.

TABLE I: Experimental Results for the Dissociation of N_2F_4 in Argon

P_1 , atm	W_1	P_2 , atm	T_2 , °K	$10^2[M]$, M	ρ_{21}	$10^{-5}k_M$, $M^{-1} \text{sec}^{-1}$
0.98 ^a	1.34	1.82	393	5.65	1.41	0.76
0.49 ^a	1.38	1.03	405	3.10	1.54	1.64
0.73 ^a	1.39	1.58	411	4.68	1.56	1.47
0.73	1.44	1.72	424	4.94	1.63	2.89
0.46 ^a	1.45	1.08	428	3.09	1.65	3.88
3.06	1.32	5.86	390	18.33	1.47	0.39
2.72	1.32	5.23	391	16.32	1.47	0.41
1.23 ^a	1.35	2.61	399	7.97	1.59	0.79
1.23 ^a	1.38	2.66	408	7.96	1.59	0.95
2.38	1.39	5.15	412	15.22	1.57	1.58
2.04	1.41	4.58	416	13.43	1.60	2.17
2.04	1.41	4.57	417	13.39	1.60	1.34
2.04	1.44	4.72	422	13.65	1.62	1.81
1.23	1.45	2.91	430	8.27	1.65	3.57
1.70	1.47	4.15	432	11.71	1.67	3.27
1.70	1.48	4.18	438	11.63	1.68	4.40
1.70	1.49	4.25	439	11.80	1.69	3.22
1.36	1.53	3.64	453	9.77	1.76	8.24
6.19	1.19	9.41	351	32.69	1.28	0.029
5.10	1.22	8.18	359	27.80	1.32	0.057
3.40	1.44	6.34	384	20.12	1.44	0.030

^a 1% N_2F_4 -argon mixtures, all other 0.1%.

found to be temperature independent in agreement with earlier observations.^{8,9} This value of ϵ is in reasonable agreement with the value of $550 M^{-1} \text{cm}^{-1}$ reported by Johnson and Colburn,^{2b} and may be taken as a system and apparatus constant.

Equilibrium Constant. As a check of our system the equilibrium constant for N_2F_4 dissociation $K_c = 4\alpha^2\rho_{21}[\text{N}_2\text{F}_4]_{01}/(1-\alpha)$, was determined in 0.1% N_2F_4 -Ar and N_2F_4 - N_2 mixtures shocked to temperatures between 351 and 489°K and compared with previous studies. The results are shown in Figure 3 and are in good agreement with the $(\Delta P/\Delta T)_v$ data.^{2b}

Rate Constants. The results of the kinetics of N_2F_4 dissociation in argon at total concentrations between 0.03 and 0.33 M are summarized in Table I. The column headings denote the initial pressure of the mixture in the tube, P_1 ; the measured shock Mach number, W_1 ; the pressure,

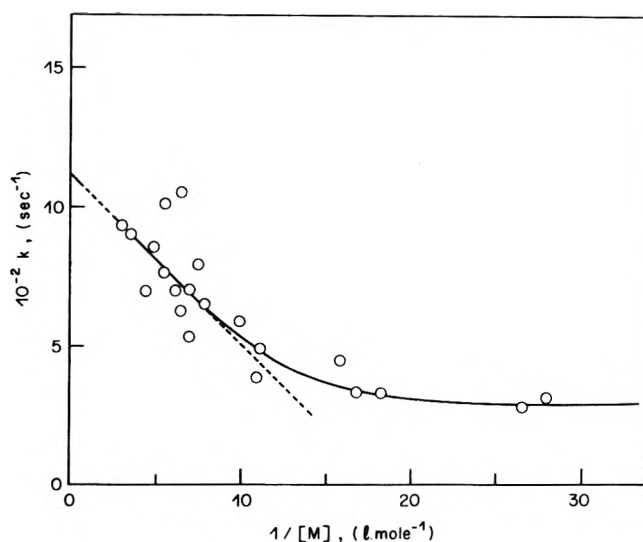


Figure 4. Extrapolation of the first-order rate constants to the high-pressure limit, N_2F_4 -Ar at 351°K.

P_2 ; temperature, T_2 ; and total concentration $[M]$ behind the incident shock; and the corresponding density ratio across the shock front, ρ_{21} . The rate coefficients are given as bimolecular rate constants, k_M . The data are grouped in three concentration ranges and are listed in order of increasing temperature within each group.

The dissociation of N_2F_4 in the pressure and temperature range of this investigation exhibits the characteristics of a quasi-unimolecular reaction. The dependence of the rate on total concentration is shown in Figure 4, where first-order rate constants are plotted as a function of the reciprocal of the concentration, $[M]$, at a fixed temperature. Such a plot¹⁵ has negative slope and positive curvature and extrapolation to $[M]^{-1} = 0$ yields the high-pressure limit first-order rate constant, k^∞ , while in the limit of very low concentrations, *i.e.*, the second-order region, a zero slope is predicted. For the purpose of constructing Figure 4, the bimolecular rate constants in Table I were first reduced to a common reference temperature (351°K) and then converted to first-order rate constants by multiplying by total concentrations evaluated at the reference temperature at constant pressure, P_2 . The temperature correction was carried out using apparent activation energies derived from Arrhenius plots for each of the concentration ranges ($E_{app} = 15.2, 15.6,$ and $18.1 \text{ kcal mol}^{-1}$, respectively). The reference temperature chosen corresponds to the experiment at highest total pressure of $\sim 9.4 \text{ atm}$ which provides an anchor point for extrapolation to $1/[M] = 0$. The best straight line drawn through the data points at concentrations greater than $0.15 M$ gives $k_{351}^\infty = 1.13 \times 10^3 \text{ sec}^{-1}$ as the intercept. Assuming the activation energy at the high-pressure limit is roughly equal to the enthalpy of dissociation, $E^\infty = \Delta H = 19.8 \text{ kcal mol}^{-1}$, the Arrhenius equation for k is given by

$$k_{Ar}^\infty (\text{sec}^{-1}) = 2.36 \times 10^{15} \exp(19,800/RT) \quad (15)$$

This expression is in good agreement with

$$k_{N_2}^\infty (\text{sec}^{-1}) = 2 \times 10^{15} \exp(-19,800/RT) \quad (16)$$

derived by Brown and Darwent⁹ by extrapolation to 400°K of their N_2F_4 - N_2 data.

(15) H. S. Johnston, *J. Chem. Phys.*, **20**, 1103 (1952).

TABLE II: Experimental Results for the Dissociation of N₂F₄ in Nitrogen

P_1 , atm	W_1	P_2 , atm	T_2 , °K	$10^2[M]$, M	ρ_{21}	$10^{-3}k_{\text{uni}}$, sec^{-1}
0.33 ^a	1.49	0.79	381	2.49	1.83	1.60
0.39 ^a	1.51	0.95	383	3.02	1.84	1.86
0.49	1.53	1.18	385	3.76	1.86	4.38
0.26	1.59	0.69	402	2.19	2.01	3.51
1.31 ^a	1.31	2.62	351	8.33	1.54	0.29
1.19 ^a	1.46	2.22	375	7.02	1.74	3.11
0.98	1.47	2.76	375	8.73	1.77	1.39
1.14	1.48	2.78	375	8.82	1.79	2.34
1.16	1.47	2.66	377	8.44	1.77	3.87
1.02	1.54	2.47	389	7.84	1.87	7.01
1.02	1.58	2.58	394	8.18	1.95	7.84
0.95	1.59	2.43	397	7.69	1.97	8.74
0.82	1.63	2.14	403	6.76	2.01	10.62
1.77	1.54	4.35	389	13.78	1.89	5.68
2.45	1.53	5.90	387	18.69	1.86	6.38
4.90	1.53	12.00	387	37.90	1.88	5.31
2.45	1.57	6.15	392	19.50	1.93	6.42
3.68	1.58	9.40	396	29.69	1.96	8.41

^a 1% N₂F₄-N₂ mixtures, all other 0.1%.

The results of the kinetics of N₂F₄ dissociation in nitrogen at total concentrations between 0.02 and 0.37 *M* are summarized in Table II. The column headings are similar to those in Table I with the exception that the rate coefficients are given as first-order rate constants, k_{uni} . The data are shown in this form since the apparent activation energy for runs near 0.07 *M* was 19.6 kcal mol⁻¹ implying these data are close to the unimolecular region. The data are grouped in three concentration ranges and are listed in order of increasing temperature within each group.

The high-pressure, first-order rate constant, k^{∞} , was found using a similar procedure as that used in the argon data. In this case the unimolecular rate constants in Table II for experiments at concentration between 0.06 and 0.10 *M* were reduced to a common reference temperature (385°K) using an apparent activation energy of 19.6 kcal mol⁻¹ derived from an Arrhenius plot in this concentration range. In those experiments where the concentration was above 0.13 *M* an activation energy of 19.8 kcal mol⁻¹ was used. For experiments in the concentration range below 0.06 *M* the data were reduced by the same method as employed for the argon data using an apparent activation energy at 15.4 kcal mol⁻¹. The reference temperature chosen is close to the experiment at the highest total pressure of ~12 atm. The best straight line drawn through the data points at concentrations greater than 0.08 *M* gave $k_{385}^{\infty} = 6.87 \times 10^3 \text{ sec}^{-1}$, or a preexponential factor of $A^{\infty} = 1.15 \times 10^{15} \text{ sec}^{-1}$ (with $E^{\infty} \approx 19.8 \text{ kcal mol}^{-1}$) which is a factor of 2 lower than the *A* factor for the N₂F₄-Ar data. We cannot offer a satisfactory explanation for this lower value except that the N₂F₄-N₂ data showed in general more scatter.¹⁶

Error Analysis. The sources of error in determining the activation energy and the rate constants were the inaccuracies in measuring the shock velocity, the absorption signal on the oscilloscope, and errors due to the dynamic nature of the shock wave.

The precision of the velocity measurement was 0.8% the distance between pressure transducers being $200 \pm 1 \text{ mm}$

and the shock transit time being of the order to 400 μsec. Hence the uncertainty in the temperature change across the shock front was 2% producing an error of approximately 10% in the activation energy. The measured standard deviation in the activation energy was 10% in agreement with that predicted from the error calculation.

Discussion

Over the pressure and temperature range of this investigation, the thermal dissociation of N₂F₄ in argon and nitrogen is characteristic of a unimolecular reaction in the fall-off region with $p_{1/2} \approx 4.0 \text{ atm}$ (pressure at which $k/k^{\infty} = 1/2$) and approaching the second-order region at pressures below 2 atm. The Arrhenius preexponential factor for the high-pressure limiting rate constant of the more accurate argon data [$\log(A^{\infty}/\text{sec}) \approx 15.4$] is in the range commonly found for simple bond fission reactions. This value of A^{∞} leads to a high positive entropy of activation of $\Delta S_{\text{expt}}^{\ddagger} = 9.73 \text{ gibbs mol}^{-1}$ at 351°K, which suggests a relatively loose activated complex structure.

In previous investigations^{8,9} the dissociation of N₂F₄ was interpreted in terms of the RRK theory of unimolecular reactions in the fall-off region, while classical collision theory was invoked in the low-pressure, second-order region. In the present study the combined results are compared with RRKM theory predictions. For the purpose of this comparison two activated complex models were considered.¹⁷ In the first case (model C-I), a variational approach was adopted to establish the value of the N-N bond distance, d_{NN} , whereby agreement was sought between the potential energy difference based on binding energy calculations and the observed N-N bond dissociation energy. Other geometrical parameters in this model were unaltered from the reactant. Binding energy calculations for molecule and complex were carried out using the INDO method,¹⁸ and this procedure gave $d_{\text{NN}} = 1.52 \text{ \AA}$, corresponding to a fractional bond order of $n = 0.83$ using Pauling's rule. The plausibility of this model was checked by comparing the experimental entropy of activation with that calculated from molecular structure. The vibrational entropy contribution was evaluated from a self-consistent set of vibrational frequencies¹⁷ derived from the normal coordinate analysis of the activated complex using a set of transferred force constants from the molecule, and making use of the force constant-bond order relations of Johnston.^{10,19a} The entropy of activation determined in this manner was found to be too low ($\Delta S_{\text{calcd}}^{\ddagger} \approx 0.3 \text{ eu}$ at 351°K); hence a proper meshing with the observed preexponential factor and energy of activation could not be achieved and this activated complex model was rejected.

The second activated complex model (C-II) was arbitrarily chosen as planar, with the NF₂ radicals loosely bound ($d_{\text{NN}}^{\ddagger} = 4.3 \text{ \AA}$) by a London attractive potential,^{19b} and the N-N normal mode of vibration was again assigned as the reaction coordinate. Since this model consists essentially of two separate NF₂ entities, the evaluation of vibrational frequencies by applying the small amplitude oscillation concept is no longer possible; instead the vibrational frequencies were assigned as follows: the

(16) In this treatment the nitrogen vibration was assumed frozen during the period of observation (30–50) μsec which appears to be a reasonable assumption.⁹

(17) K. H. Jung, Ph.D. Thesis, University of Calgary, 1972.

(18) J. A. Pople and D. L. Beveridge, "Approximate Molecular Orbital Theory," McGraw-Hill, New York, N. Y., 1970.

(19) (a) H. S. Johnston and P. Goldfinger, *J. Chem. Phys.*, **37**, 700 (1962); (b) E. Tschuikow-Roux, *J. Phys. Chem.*, **72**, 1009 (1968).

TABLE III: Molecular Parameters for N₂F₄ and Activated Complex

	Molecule	Complex C-II
Frequencies, cm ⁻¹ ^a		
	1031	1069 (2) ^b
	1023	931 (2) ^b
	738	573 (2) ^b
	586 ^c	95 (4) ^d
	423	
	295	
	116 ^e	
	958	
	933	
	519	
	284	
	242	
Geometrical Parameters ^f		
<i>d</i> _{N-N} , Å	1.47	4.12 ^g
<i>d</i> _{N-F} , Å	1.37	1.37
∠ FNF, deg	108	108
∠ NNF, deg	104	128
τ, deg	65 ^h	
Moments of Inertia, 10 ⁻³⁹ g cm ²		
<i>I</i> _a	15.0 ⁱ	14.7
<i>I</i> _b	26.2 ⁱ	134.5 ⁱ
<i>I</i> _c	29.8 ⁱ	147.2 ⁱ
<i>I</i> _m		3.7 ^j

^a Molecular frequencies taken from ref 12. ^b Frequencies of two independent NF₂ radicals, ref 3. ^c N-N stretch, taken as reaction coordinate in complex. ^d Low bending vibrations deduced from experimental entropy of activation. ^e Torsional mode, becomes internal rotation in complex. ^f Reference 11. ^g Calculated from $\langle R \rangle = 1.309_2(2a_L/kT)^{1/6}$ in Å units, where *a_L* is the London attractive constant evaluated from polarizability data, ref 19b. ^h Dihedral angle. ⁱ For the calculation of *I_b*[†] and *I_c*[†], the apparent square of the distance, $\langle (R^2) \rangle = 1.354(2a_L/kT)^{1/3}$, was used, ref 21b. ^j Reduced moment of inertia.

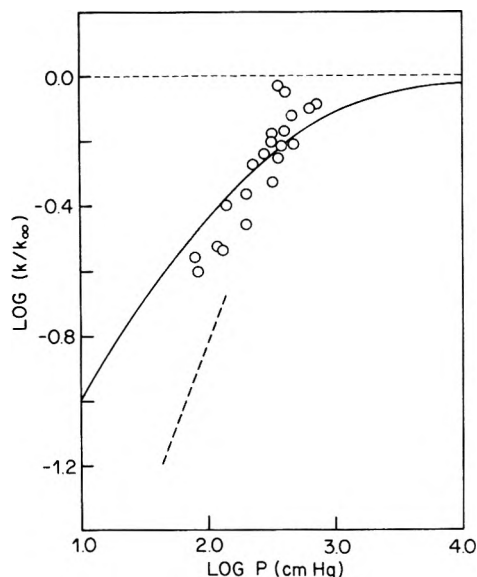


Figure 5. Pressure dependence of the reduced rate constant ratio for N₂F₄-Ar mixture at 351°K: solid line, RRKM theory prediction, Model C-II; dashed line, second-order limiting slope.

torsional mode in the molecule was treated as a free internal rotation in the complex; six vibrations were taken to be the same as those of two independent NF₂ radicals;³ and four degenerate low frequencies were deduced from

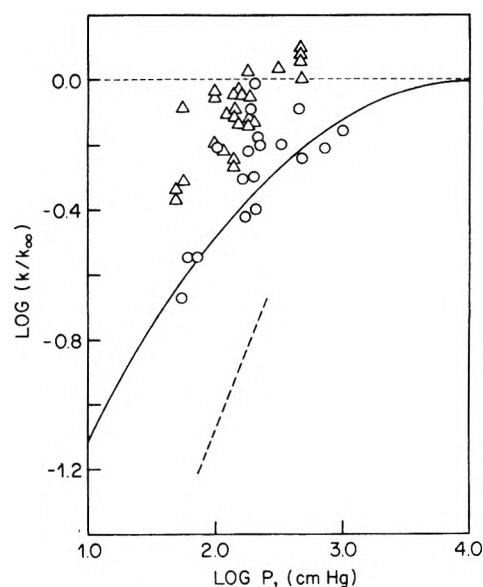


Figure 6. Pressure dependence of the reduced rate constant ratio for N₂F₄-N₂ mixture at 385°K: circles, this study; triangles, ref 9 and 20; solid line, RRKM theory prediction, Model C-II; dashed line, second-order limiting slope.

the experimental entropy of activation. The frequency assignment and other molecular parameters for N₂F₄ and complex C-II are listed in Table III.

The predicted fall-off behavior for this model is compared with experimental results in Figures 5 and 6, and a summary of the formalism is given in Appendix A-2. Although the data show a high degree of scatter, the theory supports the observation that both systems are in the general fall-off region, approaching the high- and low-pressure limiting values at the extremes of the pressure range of this investigation. Also shown in Figure 6 are the data of Brown and Darwent which were reduced for the purpose of comparison to 385°K using appropriate activation energies derived from their data.^{9,20} Their rate constants are generally higher than those determined in the present study or predicted by the RRKM theory.

The temperature dependence of the bimolecular rate constants for the N₂F₄-Ar system at pressures below 2 atm (denoted by *k_{bi}*⁰) is shown in Figure 7 and compared with the extensive data near the second-order region of Modica and Hornig, and also that of Brown and Darwent. Our rate constants are slightly lower, but the combined data are adequately represented by the Arrhenius equation

$$k_{bi}^0 (M^{-1} \text{ sec}^{-1}) = 10^{13.56 \pm 0.1} \exp[-(15,300 \pm 600)/RT] \quad (17)$$

This equation is compared with the RRKM theory expression for the quantum statistical second-order rate constant, $k_{bi}^q = k_{uni,p} - o/p$, which, including recent refinements, is given by^{14,21}

$$k_{bi}^q = k_2 (Z_v^c / Z_v^q) (D^\ddagger / D)^{1/2} F_w \Lambda e^{-E_a/RT} / \Gamma(n+1) \quad (18)$$

where $k_2 = \omega/p$ is the gas kinetic collision number; D^\ddagger / D is the ratio of the product of the principal moments of inertia of the complex and molecule; Z_v^c / Z_v^q is the classical

(20) L. M. Brown, Ph.D. Thesis, Catholic University of America, 1967.

(21) (a) E. V. Waage and B. S. Rabinovitch, *J. Chem. Phys.*, **52**, 5581 (1970); (b) E. V. Waage and B. S. Rabinovitch, *Chem. Rev.*, **70**, 377 (1970).

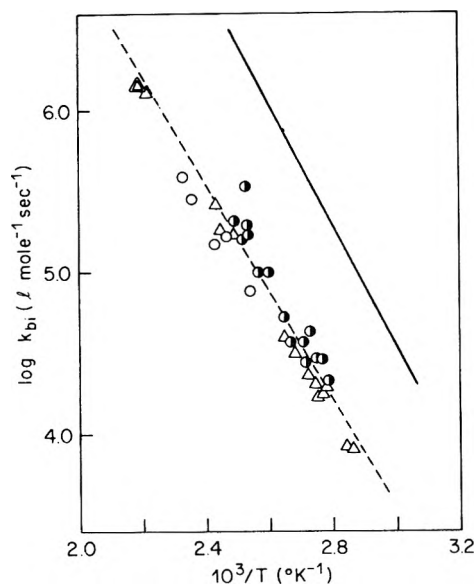


Figure 7. Temperature dependence of second-order rate constants for dissociation of N_2F_4 in argon at total concentrations $\leq 0.056 M$: triangles, ref 8; shaded circles, ref 20; open circles, this study; solid line, RRKM theory prediction, eq 18.

to quantum vibrational partition function ratio for the molecule

$$Z_v^c/Z_v^q = \exp(-E_z/RT) \prod_{i=1}^s \sinh(u_i/2)/(u_i/2); \quad u_i = hc\omega_i/kT \quad (19)$$

and

$$\Lambda = \sum_{l=0}^n n! W^{n-l} / (n-l)!; \quad (n = \text{integer}) \quad (20)$$

$$W = (E_c + aE_z)/RT \quad (21)$$

$$n = s - 1 \quad (22)$$

where $E_z (= \frac{1}{2}\sum hc\omega_i)$ is the zero-point energy, a is a quantum correction factor,^{21,22} s is the total number of vibrational degrees of freedom, and E_c is the critical energy for reaction. The factor F_w is a centrifugal correction factor which takes proper cognizance of the contribution of adiabatic rotations to the reaction rate, and which has been the subject of several recent modifications and refinements. A convenient and accurate form has been given by Waage and Rabinovitch²¹

$$F_w^{-1} = 1 + (s-1)[(I^{\dagger}/I) - 1]RT/(E_c + aE_z) \quad (23)$$

where I^{\dagger}/I is the ratio of the principal moments of inertia for adiabatic rotations if molecule and complex are treated as quasidiatomic species (for the purpose of evaluating F_w , only).

The critical energy was evaluated from the known enthalpy change for reaction at 298°K using the relation

$$E_c = \Delta H^{\circ} - 4RT - 2\langle E_v \rangle_{NF_2} + \langle E_v \rangle_{N_2F_4} \quad (24)$$

$$\approx 19.1 \text{ kcal mol}^{-1}$$

where $\langle E_v \rangle$ denotes average vibrational energy. The input parameters for the evaluation of k_{bi}^q at three temperatures are given in Table IV, and the results of the calculation are shown in Figure 7. The theoretical rate constants exhibit approximately a parallel temperature dependence but are uniformly higher (a factor of ≈ 13.5) than the experimental values of the three independent research

TABLE IV: Input Parameters for the Calculation of k_{bi}^q for N_2F_4 in Argon

	351°K	3E5°K	400°K
$10^{-11}k_2,^a M^{-1} \text{ sec}^{-1}$	1.918	2.009	2.048
β^b	1.178	1.178	1.178
$E_z, \text{ kcal/mol}$	10.22	10.22	10.22
$(D^{\dagger}/D)^{1/2}$	4.98	4.98	4.98
ρ^c	5.37	5.22	5.14
$10^5(Z_v^c/Z_v^q)$	1.417	2.990	4.032
a^d	0.931	0.931	0.931
$10^{-7}\Gamma(n+1)$	3.99168	3.99168	3.99168
F_w	0.409	0.394	0.389
W	41.02	37.40	35.997
$10^{11} \exp(-E_c/RT)$	0.128	1.438	3.668
$10^{-17} \Lambda^e$	7.3844	2.7493	1.8289
$10^{-5}k_{bi}^q, M^{-1} \text{ sec}^{-1}$	1.32	11.69	26.88
$10^{-5}k_{bi}^0,^f M^{-1} \text{ sec}^{-1}$	0.103	0.796	1.910

^a The collision diameter for N_2F_4 -Ar was taken as 4.7 Å. ^b Frequency dispersion parameter^{22a} defined as $\beta = (s-1)(s+r/2)\sum\omega_i^2/s(\sum\omega_i)^2$. For the N_2F_4 molecule, $r = 0$, $s = 12$. ^c $\rho = (I^{\dagger}/I) - 1$, see text. ^d Quantum correction factor to the zero point energy²² which was evaluated by an iterative procedure from $a = 1 - \beta \exp[-2.419\{(E_c + \Delta E_j + E^{\dagger})/E_z\}^{1/4}]$ where $\Delta E_j = -n\rho RT/(W + n\rho)$. ^e Evaluation of this factor was truncated after the third term since higher terms contribute less than 3%. ^f Experimental value from eq 17.

groups. Here, it may be noted that k_{bi}^q depends only weakly on the properties of the activated complex since the factors (D^{\dagger}/D) and F_w in eq 18 will tend to compensate each other, and in the case of tight complexes, k_{bi}^q becomes virtually model independent. This, then suggests that eq 18 requires further refinement.

Before proceeding with further discussion it is helpful to recall some of the earlier postulates of the RRKM theory formulation. The first postulate is the strong collision assumption according to which collisional activation processes are described by means of the principle of microscopic reversibility in terms of the deactivation processes, which, in turn, are assumed to occur in every gas-kinetic collision. According to this model, then, a molecule with a total energy $E > E_c$ will eventually undergo decomposition unless it suffers a deactivating collision beforehand. The second postulate involves the equilibrium assumption which states that the steady-state population of energized molecules with energies less than the critical threshold, E_c , is given by the equilibrium Boltzmann distribution at all pressures. This assumption is closely related to the first assumption and both usually prevail in laboratory experiments for larger molecules. However, in the case of small molecules at low pressure, the rate of collision-induced transitions between various energy levels of the molecules is low, *i.e.*, the intramolecular vibrational relaxation time is considerably faster than the time between collisional activation-deactivation. Under these conditions the high rate of dissociation of the energized molecules will deplete the equilibrium population and the equilibrium assumption breaks down. Hence a correction factor for the deviation from the equilibrium assumption must be included in the rate expression at low pressures.

Troe and Wagner²³ have developed a nonequilibrium theory of unimolecular reactions in the low-pressure re-

(22) (a) G. Z. Whitten and B. S. Rabinovitch, *J. Chem. Phys.*, **38**, 2466 (1963); **41**, 1883 (1964); (b) D. C. Tardy, B. S. Rabinovitch, and G. Z. Whitten, *ibid.*, **48**, 1427 (1968).

(23) V. J. Troe and H. G. Wagner, *Ber. Bunsenges. Phys. Chem.*, **71**, 937 (1967).

gion, which contains, in part, the original RRKM expression as a limiting case. In their formulation the nonequilibrium effect appears as a correction factor. By comparing Troe and Wagner's expression with k_0^a of the RRKM theory, the correction factor $\Omega(T)$ may be expressed as

$$\Omega(T) = [1 + \sqrt{2RT/(\langle \Delta E \rangle)}]^{-2} \quad (25)$$

where $\langle \Delta E \rangle$ is the mean energy transfer per collision. Assuming that the discrepancy between experiment and theory may be ascribed entirely to the nonequilibrium effect (to the exclusion, for example, of small anharmonicity corrections or, more importantly, failure of the random lifetime assumption) agreement can be forced by multiplying eq 18 by $\Omega(T) \simeq 13.5$, i.e., $k_{bi}^a \simeq 13.5k_{bi}^0$, over the temperature range of this study. From eq 25, the mean energy transfer per collision is found to be 0.4 kcal mol⁻¹ at 385°K (average temperature), which is to be compared with $RT \simeq 0.76$ kcal mol⁻¹. From the uncertainty principle in the form $\tau_c \langle \Delta E \rangle \simeq \hbar$, one finds the collision duration $\tau_c \simeq 0.4 \times 10^{-13}$ sec, not an unreasonable value.

Acknowledgment. We are indebted to Dr. R. Hartig for his contribution in the construction of the apparatus at an early stage of this project.

Appendix A-1²⁴

The properties of the fluid across a stationary shock front are related by the equations of conservation of mass, momentum, and energy

$$\rho_1 u_1 = \rho_2 u_2 \quad (A1)$$

$$P_1 + \rho_1 u_1^2 = P_2 + \rho_2 u_2^2 \quad (A2)$$

$$h_1 + \frac{1}{2} u_1^2 = h_2 + \frac{1}{2} u_2^2 \quad (A3)$$

where h is the enthalpy per unit mass. An additional relation is provided by the ideal gas equation of state which may be written in the form

$$P = \rho RT\mu \quad (A4)$$

where R is the gas constant per mole, and for a pure inert gas μ is simply the inverse of the molecular weight, $\mu = 1/M$, while for a mixture of two gases, A and B

$$\mu = f_m/M_A + (1 - f_m)/M_B \quad (A5)$$

where $f_m = M_A/(M_A + M_B)$ is the weight fraction of A. For a two component mixture in which gas B is inert (argon diluent) while gas A undergoes symmetric dissociation, i.e., $N_2F_4 \rightarrow 2NF_2$, we have, at equilibrium

$$\mu = (1 + \alpha)f_m/M_A + (1 - f_m)/M_B \quad (A6)$$

which can be derived from Dalton's law of partial pressures.

From eq A1, A2, and A4 the pressure difference across the shock front is

$$P_2 - P_1 = \rho_1 u_1^2 (1 - \rho_{21}^{-1}) \\ = \rho_1 R (\rho_{21} T_2 \mu_2 - T_1 \mu_1)$$

and hence

$$u_1^2 = R(\rho_{21} T_2 \mu_2 - T_1 \mu_1) / (1 - \rho_{21}^{-1}) \quad (A7)$$

where μ_1 and μ_2 are given by eq A5 and A6, respectively. We note that for a shock propagating into a gas at rest, $u_1 = W_s - v_1 = W_s$, the measured shock velocity relative to the tube. Equation A7 may therefore be solved for T_2 to provide a first approximation for the temperature behind the shock front.

A second relation for u_1 can be obtained by combining eq A1 and A3 to give

$$u_1^2 = 2(h_2 - h_1) / [1 - (\rho_{21}^{-1})^2] \quad (A8)$$

where the enthalpy change can be considered as the sum of two terms, due to relaxation and chemical reaction

$$\Delta h = h_2 - h_1 = \Delta h_{\text{therm}} + \Delta h_{\text{react}} \quad (A9)$$

If ΔH_{T_2} is the molar enthalpy change due to chemical reaction, the heat absorbed per unit mass of mixture is simply

$$\Delta h_{\text{react}} = f_m \alpha \Delta H_{T_2} / M_A \quad (A10)$$

Noting that in the temperature range of interest the molar heat capacity of N_2F_4 is approximately two times that of NF_2 , it can be readily shown that the heat capacity per gram of mixture is given by

$$C_{p,\text{mix}} = C_{p,\text{mix}}' / \bar{M} \\ = f_m C_{p,A} / M_A + (1 - f_m) C_{p,B} / M_B$$

and hence

$$\Delta h_{\text{therm}} = \int_{T_1}^{T_2} C_{p,\text{mix}} dT \\ = \xi (T_2 - T_1) \quad (A11)$$

where

$$\xi = f_m \bar{C}_{p,A} / M_A + (1 - f_m)(5/2)R / M_B \quad (A12)$$

and $\bar{C}_{p,A}$ is the mean molar heat capacity of N_2F_4 in the temperature interval. Introducing eq A10 and A11 in eq A8 leads to the second relationship for u_1

$$u_1 = 2[\xi(T_2 - T_1) + \alpha f_m \Delta H_{T_2} / M_A] / (1 - \rho_{21}^{-2}) \quad (A13)$$

or the shock Mach number $W_1 = W_s/a_1 = u_1/a_1$ where a_1 is the velocity of sound in the undisturbed gas ahead of the shock.

The evaluation of the ambient temperature behind the incident shock of a dilute reactive mixture can now be carried out by an iterative procedure. As a starting point ρ_{21} is evaluated from the relation

$$\rho_{21} = (\gamma + 1) W_1^2 / [(\gamma - 1) W_1^2 + 2] \quad (A14)$$

which can be readily derived from eq A1-A3 and the calorific equation for an ideal gas

$$h = [\gamma/(\gamma - 1)] R' T \quad (A15)$$

where R' is the gas constant per unit mass, and $\gamma = C_p/C_v$ is the specific heat capacity ratio. With this value of ρ_{21} , the degree of dissociation α is obtained from eq 13. Next, a first approximation to T_2 is obtained from eq A7 and this temperature value is used in eq A13 to compute a Mach number W_1' which is compared with the measured value, W_1 . The iterative cycle was repeated by adjusting ρ_{21} in increments of ± 0.001 until $|W_1'^{i+1} - W_1^i| \leq 0.01$ was achieved, and the corresponding value of T_2 was taken as the reaction temperature.

Appendix A-2

The evaluation of the pressure-dependent fractional rate, k/k^∞ , within the framework of the RRKM theory is greatly simplified by making use of the accurate rotation-vibration energy level sums approximation developed by

(24) The derivation here follows closely that of ref 8 but is given in more detail since ref 8 contains what appears to be typographical errors which may lead to some confusion.

Whitten and Rabinovitch.²² With this approximation the rate constant ratio may be cast conveniently into the form^{25,26}

$$\frac{k_{\text{uni}}}{k^{\infty}} = A_1 \sum_{l=1}^3 \int \frac{G_l(x) e^{-(E_z^\ddagger + l x)/kT} dx}{1 + (A_2/P)[G_l(x)/H(x)]F_w} \quad (\text{A2.1})$$

where the integral is partitioned into three ranges of integration to take proper account of quantum restrictions and the functional form of the quantum correction factor to the semiclassical energy density expression. The variable of integration is the reduced energy, $x = E^\ddagger/E_z^\ddagger$, where E^\ddagger is the energy of the active modes of the activated complex in excess of its zero-point energy, E_z^\ddagger . In the absence of free internal rotations in the molecule and r^\ddagger such rotations in the complex, the functions in eq A2.1 and limits of integration are given by

$$G_1(x) = \left[\Gamma(n^\ddagger + 1) \prod \omega_i^\ddagger / \Gamma(1 + r^\ddagger/2) (E_z^\ddagger)^{s^\ddagger} \right] x^{r^\ddagger/2} \quad 0 \leq x < \theta$$

$$G_2(x) = [x + 1 - \beta^\ddagger / (b_3 x + b_4 x^{b_5} + b_6)]^{n^\ddagger} \quad \theta \leq x \leq 1.0$$

$$G_3(x) = [x + 1 - \beta^\ddagger \exp(-b_1 x^{b_2})]^{n^\ddagger} \quad 1.0 \leq x \leq 8.0$$

$$H(x) \approx [x + (E_c/E_z^\ddagger)] \times (E_z/E_z^\ddagger) [1 - \beta \exp(-b_1[(E_c + E_z^\ddagger x)/E_z]^{b_2})]^{n^\ddagger} \\ \approx [x + (E_c + E_z)/E_z^\ddagger]^{n^\ddagger} \quad E_c > E_z$$

$$A_2 = (\sigma_1/\sigma_1^\ddagger) Z_r^\ddagger [\Gamma(n + 1)/\Gamma(n^\ddagger + 1)] \times [(E_z^\ddagger)^{n^\ddagger - n} / k_2 h (RT)^{r^\ddagger/2}] \left(\prod \omega_i / \prod \omega_i^\ddagger \right)$$

$$A_1 = (E_z^\ddagger)^{n^\ddagger + 1} / Z_v^\ddagger (RT)^{1 + r^\ddagger/2} \Gamma(n^\ddagger + 1) \prod \omega_i^\ddagger$$

where the dagger (\ddagger) refers to the activated complex, and n, n^\ddagger are defined as

$$n = s - 1 \quad (r = 0)$$

$$n^\ddagger = s^\ddagger + \frac{1}{2} r^\ddagger$$

The upper limit of integration of the first range, θ , is taken here for convenience as $\theta < \omega_{\text{min}}^\ddagger/E_z^\ddagger$, where $\omega_{\text{min}}^\ddagger$ is the lowest vibrational frequency in the complex. Other quantities not previously defined are Γ , the gamma function; ω_i , vibrational frequencies in energy units (cm^{-1}); $\sigma_1, \sigma_1^\ddagger$, symmetry numbers for adiabatic rotations; Z_r^\ddagger , partition function for active (internal) rotations; Z_v^\ddagger , quantum vibrational partition function; h , Planck's constant. The quantities b_i are empirical constants relating to the quantum correction factor to the zero point energy:²² $b_1 = 2.419$; $b_2 = 0.25$; $b_3 = 5.00$; $b_4 = 2.73$; $b_5 = 0.5$; $b_6 = 3.510$.

(25) E. Tschuikow-Roux, *J. Chem. Phys.*, **49**, 3115 (1968).

(26) In ref 25 the interpretation of the effect of the centrifugal correction on the trend of $k_{\text{uni}}/k^{\infty}$ with pressure is incorrect as a result of a typographical error in the sign of the F factor in the original formulation.^{14c} Inclusion of the centrifugal correction shifts the fall-off region toward higher pressures. Also, the following typographical errors should be noted: eq 18, replace $\sum \omega_i^\ddagger$ by $\prod \omega_i^\ddagger$; eq 19, change $(E_z)^{n^\ddagger - n}$ to $(E_z^\ddagger)^{n^\ddagger - n}$. Expression for ΔE_J should read: $\Delta E_J = -RT[(l^\ddagger/l) - 1]/2$.

Flash Photolysis of Chlorine Dioxide in Aqueous Solution

J. C. Mialocq, F. Barat,* L. Gilles, B. Hicckel, and B. Lesigne

Département de Recherche et Analyse. Cen-Saclay. B.P. N°2 91190. Gif S/Yvette. France (Received April 18, 1972)

Publication costs assisted by the Commissariat à l'Énergie Atomique

The flash photolysis of chlorine dioxide in aqueous solution leads to little O(³P) oxygen atom production (little O₃ production in oxygenated media) with respect to the amount of ClO₂ decomposed; at the same time, no spectrum ascribable to the ClO radical can be detected. However, the spectrum of a transitory species whose maximum lies at 310 nm is observed just after the photolytic flash. Working on the reasonable hypothesis that the primary act of photodissociation is O-Cl-O + $h\nu$ → ClO(2π) + O(³P), these experimental results are explained in terms of a cage recombination of the photolysis fragments leading to the formation of chlorine atoms and molecular oxygen and a rapid bulk reaction between ClO and ClO₂ leading to the species Cl₂O₃. The reaction between Cl (or Cl₂⁻) and ClO₂ gives Cl₂O₂, which has an absorption maximum at 310 nm.

Introduction

Many studies have been devoted to the thermal¹ or photochemical² decomposition of gaseous chlorine dioxide. The oxide Cl₂O₃ was prepared for the first time by Kantzer.³ Mc Hale and von Elbe⁴ showed that it is a product of the equilibrium



and that its most probable structure is (O)₂-Cl-Cl-O. These authors suggest that Cl₂O₃, by a chain reaction

(1) E. T. Mc Hale and G. von Elbe, *J. Phys. Chem.*, **72**, 1849 (1968).

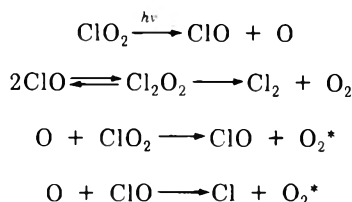
(2) For a complete literature survey see N. Basco and S. K. Dogra, *Proc. Roy. Soc., Ser. A*, **323**, 29 (1971).

(3) M. Kantzer, *C. R. Acad. Sci. (Paris)*, **202** (1936).

(4) E. T. Mc Hale and G. von Elbe, *J. Amer. Chem. Soc.*, **89**, 2795 (1967).

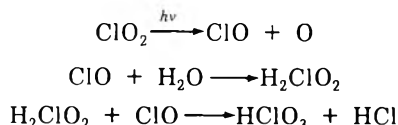
mechanism, reduces the induction time of the chlorine dioxide explosion.

Basco and Dogra² have continued the earlier investigations on the isothermal flash photolysis of gaseous chlorine dioxide and proposed a mechanism involving an intermediate species Cl_2O_2



where O_2^* refers to a vibrationally excited oxygen molecule.

Little work has been published however on the continuous photolysis of chlorine dioxide in aqueous solutions.^{5,6} Bowen and Cheung⁵ proposed the following mechanism for wavelengths between 300 and 436 nm



At shorter wavelength (254 nm), Taube⁶ obtains a stoichiometry slightly different from that proposed by Bowen and Cheung. This is probably due to the formation of electronically excited oxygen atoms $\text{O}({}^1\text{D})$, which insert into a water molecule



thus changing the subsequent reactions.

The absorption spectrum of ClO_2 ^{7,8} has been interpreted as follows: for wavelengths between 260 (point of convergence) and 375 nm (theoretical predissociation wavelength), the molecule dissociates into two fragments, $\text{ClO}({}^2\pi)$ and $\text{O}({}^3\text{P})$; below 260 nm it dissociates to form $\text{ClO}({}^2\pi)$ and $\text{O}({}^1\text{D})$.

The aim of this work was to find out whether ClO_2 photolyzed in the appropriate wavelength region could generate oxygen atoms $\text{O}({}^3\text{P})$, to study the reactions of these oxygen atoms, and to determine the absorption spectra and the appearance and disappearance kinetics of any transitory species formed.

Experimental Section

Most of the present work was carried out using a coaxial flash photolysis lamp filled with oxygen (10 Torr) giving a flash duration of 4 μsec at half-intensity for an energy of 1300 J. The interelectrode distance was 13 cm. The tail of the emission precluded oscillographic measurements at times shorter than 30–40 μsec after the triggering of the flash. The continuous analytical light source was a xenon arc (OSRAM XBO 450 W). Mc Pherson Model 218 and Huet M25 monochromators were used. The photomultipliers were RCA 1P28 tubes and only the first six dynodes were used in order to improve the signal-to-noise ratio. The absorption cell (Pursil 453, Quartz et Silice) was 18 cm long and 1.5 cm in diameter.

With this apparatus, partly described in a previous publication,⁹ it was not possible to demonstrate the formation of ClO which is thought to be one of the principal photolytic fragments. We therefore modified the photolytic flash lamp in order to reduce the tail and so permit mea-

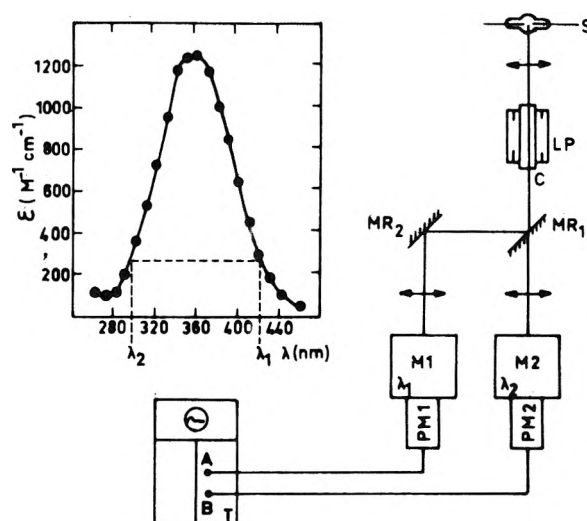


Figure 1. Experimental set up. Inset, chlorine dioxide absorption spectrum in aqueous solution: S, analytical light source; C, absorption cell; LP, photolysis lamp; MR₁, MR₂, mirrors; PM₁, PM₂, photomultipliers; M₁, M₂, monochromators; T, differential amplifier.

surements to be made at shorter times after the flash. This was done by increasing the plasma quenching area thus reducing to 3 μsec the flash half-intensity width and to 9 μsec the time for the intensity to reach 1% of its maximum value (for a dissipated energy of 770 J).¹⁰ Under these conditions the interelectrode distance was 23 cm, the cell length 36 cm, and the cell diameter 1 cm. Using this system and a pulsed xenon arc analytical light source¹¹ it was possible to observe transitory species during the photolytic flash, the first significant points for their disappearance being obtained 8 μsec after the triggering of this flash.

A method was developed to determine the absorption spectrum of transitory species absorbing in the same wavelength region as ClO_2 . Two conditions are taken into account: (1) symmetry of the ClO_2 absorption band with respect to its maximum centred at 360 nm and (2) absence of any absorption spectrum attributable to a transitory or stable species for wavelengths above 350 nm. It should be remarked that the presence of a low concentration of Cl^- in the ClO_2 solutions could give rise to the production of Cl_2^- absorbing at 350 nm. However, experiments have shown (*vide infra*) that the rate of reaction of Cl_2^- with ClO_2 is so great that direct observation of its absorption is impossible except at low ClO_2 concentrations, when its half-life becomes sufficiently long.

The spectrum of transitory or stable species absorbing at wavelengths below 350 nm is then measured by choosing pairs of wavelength values λ_1 and λ_2 (Figure 1). The signal A given for λ_1 represents the gain in transmission due to the decomposition of ClO_2 ; signal B, given for λ_2 , is the sum of the same gain in transmission and the absorption of the transitory or stable species. These two sig-

- (5) E. J. Bowen and W. M. Cheung, *J. Chem. Soc.*, 1200 (1932).
- (6) H. Taube, *Trans. Faraday Soc.*, 53, 656 (1957).
- (7) W. Finkelnburg and H. D. Schumacher, *Z. Phys. Chem., Bodenst. Festband*, 704 (1931).
- (8) J. B. Coon and E. Ortiz, *J. Mol. Spectrosc.*, 1, 81 (1957).
- (9) F. Barat, L. Gilles, B. Hickel, and J. Sutton, *J. Chem. Soc. A*, 1982 (1970).
- (10) F. Barat, L. Gilles, B. Hickel, and B. Lesigne, CEA-N-1438, p 22, April 1971.
- (11) B. D. Michael, private communication.

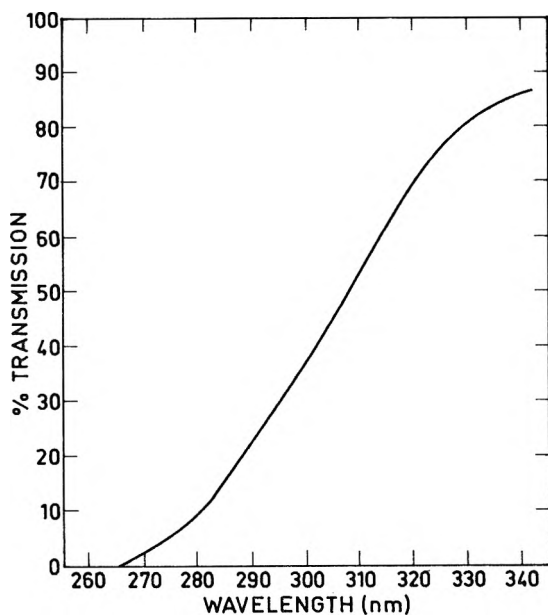


Figure 2. Transmission curve for a Heliosil II filter (1 mm width, corrected for reflexion losses).

nals are sent to a differential amplifier (type Tektronix 1A5) of a Tektronix 556 oscilloscope and the recorded trace measures the absorption due to the transitory or stable species alone. In this way it is unnecessary to correct the optical density for ClO_2 decomposed in the flash. It is also possible to keep λ_1 constant and to record the signal A on one oscilloscope beam. The optical density of the photolysis transient species at the wavelength λ_2 is then obtained from the signal B after correction for the gain in transmission due to the ClO_2 decomposed, the concentration of this latter being obtained from the signal A. Whichever method is employed the error in the values of the absorption optical density is about 10%.

Photolysis wavelengths below 270 nm are eliminated by an optical filter (Quartz et Silice, Heliosil II tube) surrounding the absorption cell. The transmission curve of this filter is shown in Figure 2. A shutter, placed on the optical path and not opened until a few seconds before the flash, prevents decomposition of ClO_2 by the analytical light.

ClO_2 is prepared by Bray's method,¹² working at reduced pressure. ClO_2 , CO_2 , and Cl_2 are dried over calcium chloride; ClO_2 is trapped at Dry Ice temperature and purified by trap-to-trap distillations. It is then transferred in a current of nitrogen into triply distilled water. The stock solution ($\text{ClO}_2 = 10^{-2} M$) kept at low temperature in the dark is diluted, just prior to use, to the desired concentration which is determined exactly by spectrophotometry. The pH of a $10^{-4} M$ solution of ClO_2 is 5.0. For example, the concentrations of Cl^- and ClO_3^- produced by hydrolysis and photochemical decomposition during preliminary manipulations, taking into account the photolytic decomposition by the analytical source during the few seconds before the flash and determined respectively by nephelometry and by reduction with Fe^{2+} and subsequent spectrophotometric measurement of Fe^{3+} at 302 nm, are of the order of $10^{-5} M$. The absorption spectra of these decomposition products of ClO_2 are situated at wavelengths below 220 nm. They are therefore not photolyzed under our experimental conditions. We will see later the effect of chloride ions on the results obtained.

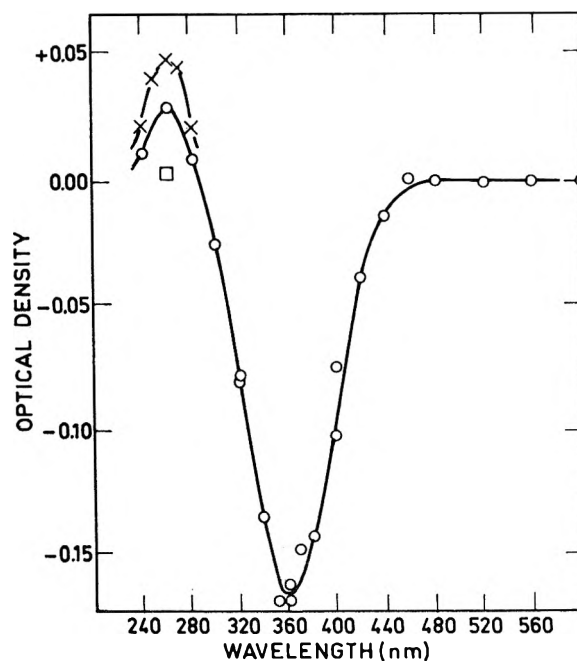


Figure 3. Flash photolysis of ClO_2 ($3 \times 10^{-5} M$) in aqueous solution showing variation of the optical density of the solution 400 μsec after the photolytic flash: O, aerated solution; X, oxygenated solution; \square , deaerated solution.

The products used are supplied by Merck and employed without further purification.

The absorption curve for ClO_2 (Figure 1) was obtained using a Cary 14 spectrophotometer.

Results

Two sets of experiments were carried out (a) with and (b) without a Heliosil II filter.

(a) *Photolysis at Wavelength above 200 nm.* Whether or not the solution is degassed, the chlorine dioxide decomposition yield for an initial concentration of $3 \times 10^{-5} M$ is equal to $33 \pm 4\%$ for a 1300-J flash. At wavelengths below 350 nm a weak absorption due to a transitory species is observed, superimposed on the gain in transmission caused by the disappearance of ClO_2 . As the oxygen concentration of the solution is increased from 10^{-6} (degassed solution) to $10^{-3} M$ (oxygen-saturated solution) the absorption spectrum characteristic of ozone, centred at 260 nm,¹³ appears. In oxygenated solution only $12 \pm 2\%$ of the ClO_2 destroyed leads to the formation of ozone (taking $\epsilon(\text{O}_3)$ at 260 nm $2900 M^{-1} \text{cm}^{-1}$).¹³ Figure 3 gives the optical density variation of the solution, 400 μsec after the photolytic flash.

(b) *Photolysis at Wavelength above 270 nm.* Whatever the oxygen concentration between 10^{-6} and $10^{-3} M$ the chlorine dioxide decomposition yield ($3 \times 10^{-5} M < [\text{ClO}_2] < 3 \times 10^{-4} M$) is $12 \pm 2\%$ for a 1300-J flash. The difference between this value and that found in experiment a is mainly due to the decrease in the intensity of the incident radiation caused by inserting the filter. Figure 4 shows the absorption spectrum of a transitory species X with a maximum at 310 nm, traced by the differential photometry method described above (see Experi-

(12) W. C. Bray, *Z. Phys. Chem.*, **54**, 575 (1904).

(13) J. W. Boyle, J. A. Ghormley, and C. J. Hochenadel, *Chem. Div. Ann. Rept.*, May 20, 1969; ORNL 4437, p 48.

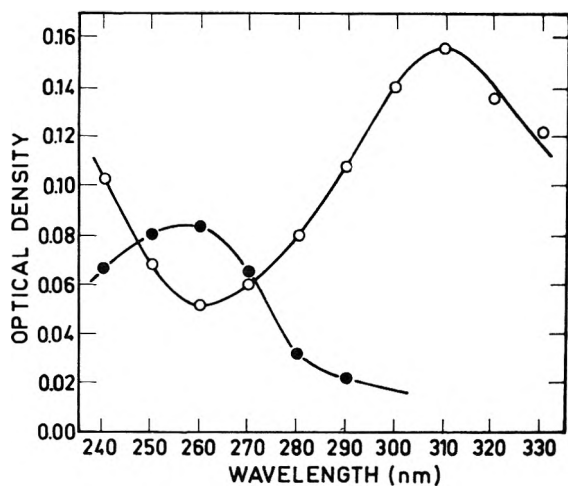


Figure 4. Flash photolysis of ClO_2 ($2 \times 10^{-4} M$) in aqueous solution (with 270 nm optical filter): O, optical density 50 μsec after the photolytic flash; ●, optical density 500 μsec after the photolytic flash.

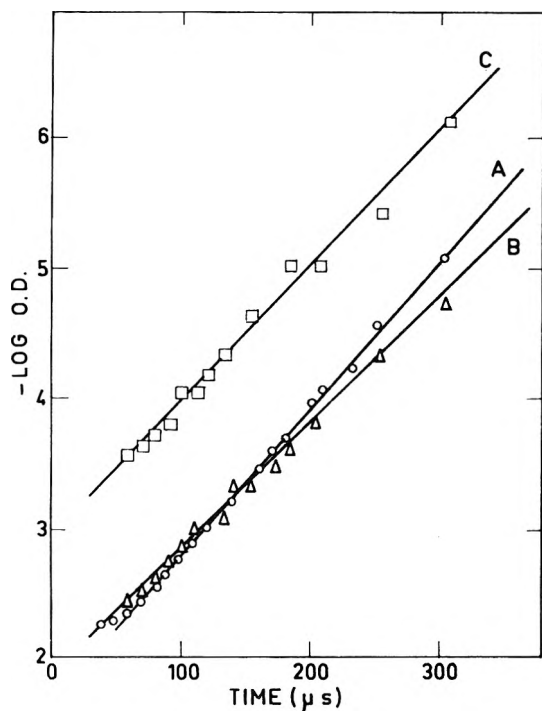


Figure 5. First-order decay for transient X in aerated solution: O, λ 290 nm, $[\text{ClO}_2] = 2.5 \times 10^{-4} M$; Δ , λ 310 nm, $[\text{ClO}_2] = 10^{-4} M$; \square , λ 290 nm, $[\text{ClO}_2] = 2.5 \times 10^{-4} M$, $[\text{iPrOH}] = 10^{-3} M$.

mental Section). This species disappears with a first-order rate constant equal to $(1.0 \pm 0.1) \times 10^4 \text{ sec}^{-1}$. No effect was observed, within the limits of experimental error, on its disappearance as a function of the ClO_2 concentration between 10^{-4} and $2.5 \times 10^{-4} M$ (Figure 5, curves A and B). The spectrum recorded 500 μsec after the flash shows a maximum around 260 nm (Figure 4) which we believe is due to a combination of the ClO_3 and O_3 spectra. Indeed if the ClO_2 concentration is reduced and the oxygen concentration increased the well-known spectrum of ozone appears (Figure 6, curve A). For the same concentration of chlorine dioxide, but in deoxygenated solution, this spectrum is replaced by an absorption band center at 250–260 nm which we attribute to ClO_3 (Figure 6, curve

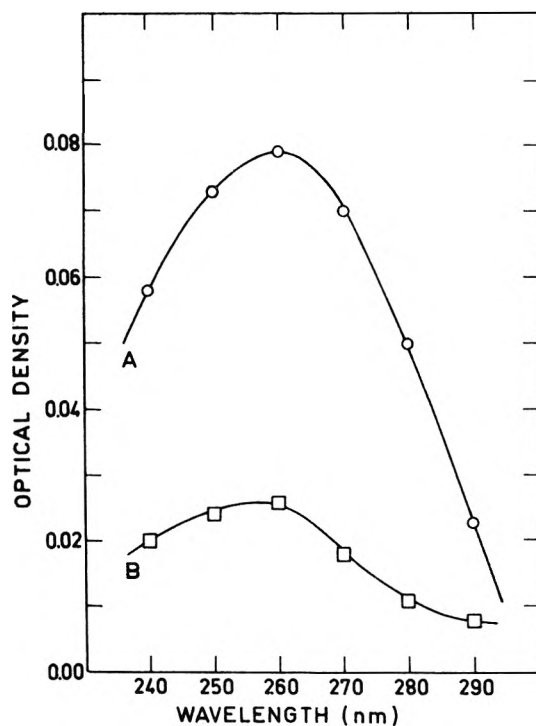


Figure 6. Flash photolysis of ClO_2 ($10^{-4} M$) in aqueous solution showing optical density 500 μsec after the photolytic flash: O, oxygenated solution; \square , deoxygenated solution.

B). From the optical densities observed in oxygenated solution it can be estimated that $14 \pm 2\%$ of the ClO_2 destroyed leads to the formation of ozone (for a $2.5 \times 10^{-4} M$ ClO_2). The disappearance kinetics for O_3 ($t_{1/2} = 80 \text{ msec}$) and ClO_3 ($t_{1/2} = 4 \text{ msec}$) are complex and correspond to no simple order.

pH Effect. No experiments were carried out in basic solution, where chlorine dioxide is rapidly hydrolyzed. The acidity of the solutions was increased (using HClO_4) to pH 2.2 and no effect was observed, either on the ClO_2 decomposition yield or on the appearance and decay of the species X.

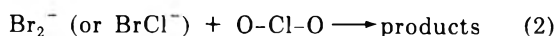
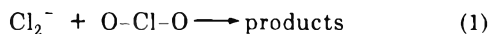
Effect of Alcohol (Methanol, Ethanol, Isopropyl Alcohol, tert-Butyl Alcohol). For alcohol concentrations between 10^{-4} and $10^{-2} M$ and in aerated solution a slight decrease in the ClO_2 decomposition yield is observed ($8 \pm 2\%$ for $10^{-2} M$ isopropyl alcohol), together with the gradual disappearance of X which maintains the same decay kinetics as those observed in pure water (Figure 5, curve C). This implies that alcohol acts on the precursor of X. New transitory species appear in the flash; the spectra obtained, in the presence of isopropyl alcohol ($t_{1/2} = 2.3 \text{ msec}$) and in the presence of tert-butyl alcohol ($t_{1/2} = 1.5 \text{ msec}$) show maxima at 250 and 260 nm, respectively (Figure 7). While the intensities of these spectra increase in oxygenated solution they decrease sharply, without entirely disappearing, in deoxygenated solution. The mode of disappearance is different for these two species. The disappearance of the species obtained in the presence of isopropyl alcohol follows pseudo-first-order kinetics with $k_{\text{obsd}} = 300 \pm 50 \text{ sec}^{-1}$ and is accompanied by the simultaneous disappearance of a new ClO_2 fraction. That of the species obtained in the presence of tert-butyl alcohol obeys second-order kinetics such that $2k/\epsilon$ at 260 nm is equal to $3.2 \pm 0.2 \times 10^5 \text{ cm sec}^{-1}$, and no simultaneous disappearance of a new ClO_2 fraction is observed.

TABLE I

Rate constant	ClO ₂ , M		
	1.0 × 10 ⁻⁵	2.5 × 10 ⁻⁵	2.7 × 10 ⁻⁵
k(Cl ₂ ⁻ + ClO ₂), sec ⁻¹	(0.9 ± 0.1) × 10 ⁴	(2.6 ± 0.2) × 10 ⁴	
k(Br ₂ ⁻ + ClO ₂), sec ⁻¹	(1.2 ± 0.1) × 10 ⁴		(3.4 ± 0.2) × 10 ⁴

Effect of Isobutane ($5.8 \times 10^{-3} M$), Ethylene ($4.7 \times 10^{-3} M$), Propylene ($2.0 \times 10^{-2} M$), and Oxygen (up to $10^{-3} M$). The isobutane, ethylene, and propylene concentrations quoted lead to the disappearance of the species X. An increase in the oxygen content of the solution raises the ozone concentration and has no effect on either the ClO₂ decomposition yield or the formation of the species X was observed.

Effect of Cl⁻ (10^{-5} – $10^{-2} M$) and Br⁻ (10^{-5} – $10^{-2} M$). The addition of Cl⁻ or Br⁻ ions gives rise to the formation of transitory species absorbing in the 340–360-nm region. The spectra observed overlap that of chlorine dioxide. From the signal obtained, which combines a gain in transmission due to the dissociation of ClO₂ in the flash and a decrease in transmission due to these absorbing species disappearing very quickly (in less than 100 μsec), it is not possible to trace the absorption spectra with precision, but we conclude that they are those of Cl₂⁻ and Br₂⁻.¹⁴ We must note that a transient with low absorption is observed in the 340–360-nm region (Cl₂⁻) even in the absence of any additive. This may be explained by the presence of Cl⁻ ions coming from the decomposition of ClO₂ before photolysis. The Cl₂⁻ and Br₂⁻ species disappear with first-order kinetics depending upon the chlorine dioxide concentration. The values of the rate constants observed for the decay of Cl₂⁻ and Br₂⁻ in the presence of ClO₂ are given in Table I. We obtain $k_1 = (1.0 \pm 0.1) \times 10^9 M^{-1} sec^{-1}$ and $k_2 = (1.2 \pm 0.1) \times 10^9 M^{-1} sec^{-1}$ for reactions 1 and 2, respectively. The absorption spectra of Cl₂⁻ or Br₂⁻ do not appear in the presence of alcohols ($10^{-2} M$), isobutane ($5.8 \times 10^{-3} M$), ethylene ($4.7 \times 10^{-3} M$), or propylene ($2.0 \times 10^{-2} M$). The formation of X is totally suppressed by a $10^{-4} M$ concentration of Br⁻ ions, whereas in the presence of Cl⁻ ions ($10^{-4} M$) it increases by a factor of 3.



Discussion

The most striking results obtained by flash photolysis of ClO₂ in aqueous solution are the following.

(1) The small production of O(³P) atoms (small ozone production in oxygenated media) with respect to the quantity of chlorine dioxide decomposed. Since no rapid disappearance of the O₃ species was observed during the 50 μsec following the flash the quantity of ozone produced may be reasonably considered as a measure of the concentration of these oxygen atoms which, after their production, diffuse into the bulk of the solution. Reaction 3 is rapid and probably has a rate constant greater than $10^9 M^{-1} sec^{-1}$ (according to gas-phase studies).¹⁵



(2) The absence of any spectrum attributable to the ClO radical. This spectrum is well known in the gas² and solid¹⁶ phases and according to the very recent results of

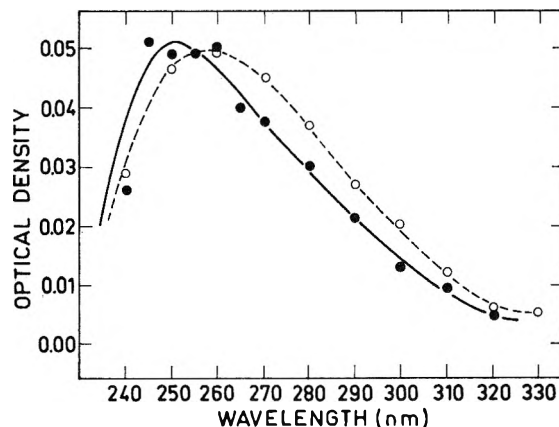


Figure 7. Flash photolysis of ClO₂ ($10^{-4} M$) in aerated solution and in the presence of alcohols showing optical density 50 μsec after the photolytic flash: ●, isopropyl alcohol ($10^{-2} M$); ○, *tert*-butyl alcohol ($10^{-4} M$).

Buxton and Subhani¹⁷ on the pulse radiolysis of aqueous solutions of hypochlorite and chlorite ions it should be expected to appear in the region 270–300 nm where they found $\epsilon_{\max 280 \text{ nm}} = 900 M^{-1} cm^{-1}$ for this species. However, the second-order decay of ClO in aqueous solution is rapid ($2k = 1.3 \times 10^9 M^{-1} sec^{-1}$ in the absence of chlorite ions) and leads to the species Cl₂O₂ which rapidly hydrolyses.

If in the present experiments the amount of ClO produced is comparable to the amount of ClO₂ photolyzed and if its only mode of disappearance is the bimolecular process referred to above then its spectrum should have been observed during several tens of microseconds after the flash. This was not the case.

Even if the concentrations of ClO formed is only of the same order as that of the ozone produced in oxygenated media (a few μmol/l.) the sensitivity of our detection system is such that its spectrum should still lead to a deformation in the 280-nm region of the absorption spectrum presented in Figure 6 (curve B). This also is not the case even in deaerated solution where a possible reaction between ClO and O₂ (to give ClO₃) would be eliminated.

It appears then that the most probable explanation for this absence of a ClO spectrum is that this species reacts very rapidly with the solvent, the solute, ClO₂, or one of the photolytic products. The reaction with water may be eliminated immediately; Buxton and Subhani observed the spectrum and a second-order decay in aqueous media.

With regard to possible reactions with O₃ or ClO₃, a corresponding rapid decrease of the absorption in the region 250–300 nm, and during a very short interval after

(14) L. I. Grossweiner and M. S. Matheson, *J. Phys. Chem.*, **61**, 1089 (1957).

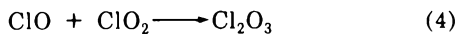
(15) F. Kaufmann, *Progr. React. Kinet.*, **1**, 1 (1961).

(16) I. Norman and G. Porter, *Proc. Roy. Soc., Ser. A*, **230**, 399 (1955).

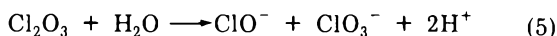
(17) G. V. Buxton and M. S. Subhani, *J. Chem. Soc., Faraday Trans. 1*, **68**, 947 (1972).

triggering the flash (5 μsec), was looked for but not observed which appears to rule out the intervention of such processes. The only transient species disappearing in less than 30 μsec in a 10^{-4} M solution of ClO_2 has been identified as Cl_2^- of which the extinction coefficient is still of the order of $500\text{--}1000 M^{-1} \text{cm}^{-1}$ in this wavelength range.

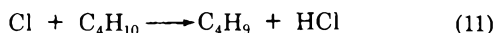
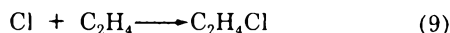
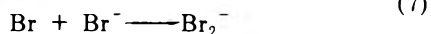
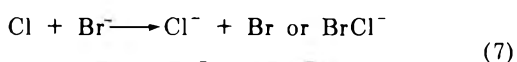
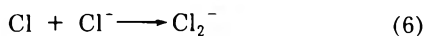
The most probable explanation of the failure to observe the radical ClO is the intervention of the addition reaction with ClO_2



Mc Hale and von Elbe¹⁸ have clearly demonstrated the occurrence of this reaction in their study of the explosive decomposition of gaseous ClO_2 in which the induction period is a function of the Cl_2O_3 concentration. These same authors have also isolated Cl_2O_3 .⁴ If our explanation is valid, either the extinction coefficient of Cl_2O_3 between 440 and 240 nm must be low ($<500 M^{-1} \text{cm}^{-1}$) or the lifetime of the species must be short ($<20 \mu\text{sec}$), its disappearance probably being by hydrolysis



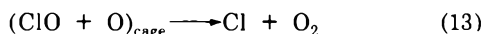
Formation of Chlorine Atoms and Molecular Oxygen in the Photolysis. The identification of Cl_2^- as a photolysis product of ClO_2 in the presence of chloride ions, or of Br_2^- (or BrCl^-) in the presence of bromide ions, and the fact that these species disappear on addition of alcohol, isobutane, ethylene, or propylene, clearly indicates that chlorine atoms figure among the photolysis products and that the following reactions take place^{19,20}



Since the most probable primary decomposition mechanism under our experimental condition is

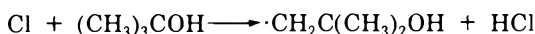
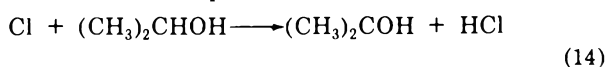


the low $\text{O}(^3\text{P})$ oxygen atom production and the chlorine atom production are explained by assuming considerable cage recombination of the ClO and O fragments as follows

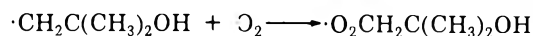
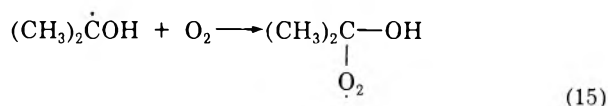


This fast reaction has been studied in the gas phase ($k = 7 \times 10^9 M^{-1} \text{sec}^{-1}$)² and found to be responsible for the initial rapid decay of ClO observed at high flash energies in the flash photolysis of chlorine dioxide.

The absorption spectra of the transitory species observed by flash photolysis of ClO_2 in aerated solution and in the presence of isopropyl alcohol or *tert*-butyl alcohol (Figure 7) correspond to those of the peroxyalkoxyl radicals given by Hayon, *et al.*,²¹ and show that reactions 14 and 15 occur. These spectra cannot be confused with those



of isopropyl hypochlorite or *tert*-butyl hypochlorite, which



lie in the same wavelength region but are much less intense (the extinction coefficients at 260 nm are about $50\text{--}100 M^{-1} \text{cm}^{-1}$).²²

The concentration of chlorine atoms formed in the photolysis of a 2.5×10^{-4} M solution of ClO_2 containing 10^{-2} M isopropyl alcohol and 1.2×10^{-3} M oxygen has been determined. Under these conditions reactions 14 and 15 go to completion and the optical density of the absorption of the radical $(\text{CH}_3)_2\text{C}(\text{O}_2)\text{OH}$ at 260 nm, where its extinction coefficient is $1100 M^{-1} \text{cm}^{-1}$,²¹ was measured. The result showed that $55 \pm 7\%$ of the chlorine dioxide decomposed gave rise to chlorine atoms. It should be noted that in the presence of this concentration of alcohol the overall photolytic decomposition of ClO_2 is 8% whereas in the absence of alcohol the value is 12%. This point will be taken up later in the discussion.

The fact that the spectra attributed to the radicals $\dot{\text{O}}_2\text{ROH}$ appear even in initially deaerated solution may be taken as a proof of the formation of molecular oxygen (reaction 13). In fact, when a 2.5×10^{-4} M chlorine dioxide solution is photolyzed in the presence of isopropyl alcohol, it is found that the intensity of the absorption band centered at 250 nm is 4.4 ± 0.7 times greater in an oxygen-saturated solution than in an initially deaerated solution. Reaction 15 has a rate constant of $6 \times 10^9 M^{-1} \text{sec}^{-1}$ ²³ and competes with the reaction



which is analogous to the recombination of the OH and ClO_2 species formed in the flash photolysis of ClO_3^- .²⁴ From the equation

$$1/D_1 = 1/D_2(1 + k_{16}[\text{ClO}_2]/k_{15}[\text{O}_2])$$

where D_1 and D_2 represent respectively the optical density of the $(\text{CH}_3)_2\text{C}(\text{O}_2)\text{OH}$ radical in a initially deaerated and in an oxygen saturated solution, we may write

$$k_{16}[\text{ClO}_2]/k_{15}[\text{O}_2] = 3.4 \pm 0.7$$

The order of magnitude of k_{16} was determined by flash photolysis of ClO_3^- (2×10^{-3} M deaerated solution) in the presence of isopropyl alcohol (10^{-3} M). The oscillograms obtained (Figure 8) show that k_{16} is about $10^9 M^{-1} \text{sec}^{-1}$, assuming the following reaction scheme where $k_{17} = 1.4 \times 10^9 M^{-1} \text{sec}^{-1}$.²¹



(18) E. T. Mc Hale and G. von Elbe, *J. Phys. Chem.*, **72**, 1849 (1968).

(19) H. Schmitz, H. J. Schurracher, and A. Jager, *Z. Phys. Chem.*, **B51**, 281 (1952).

(20) J. Knox and R. Nelson, *Trans. Faraday Soc.*, **55**, 937 (1959).

(21) M. Simic, P. Neta, and E. Hayon, *J. Phys. Chem.*, **73**, 3794 (1969).

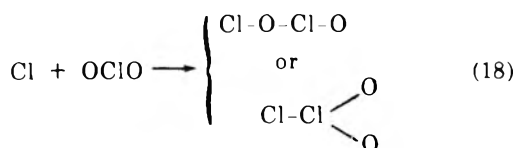
(22) M. Anbar and I. Dostrovsky, *J. Chem. Soc.*, 1105 (1954).

(23) G. E. Adams, B. D. Michael, and R. L. Willson, *Advan. Chem. Ser.*, **No. 81**, 289 (1968).

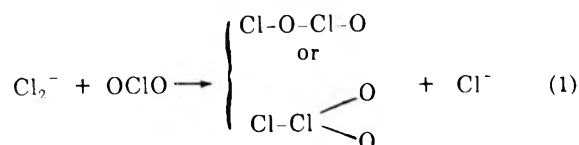
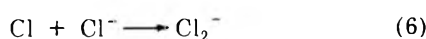
(24) F. Barat, B. Hickel, L. Gilles, and B. Lesigne, *J. Phys. Chem.*, **75**, 2177 (1971).

We obtain $[O_2] = 12.2 \pm 2.5 \times 10^{-6} M$. This value must be corrected for the molecular oxygen introduced in the preparation of the solution by a 100-fold dilution of an aerated $2.5 \times 10^{-2} M$ solution of ClO_2 . Thus the initial oxygen concentration before photolysis was $2.5 \times 10^{-6} M$ leading to a value of $(9.7 \pm 2.5) \times 10^{-6} M$ for the concentration of photolytically produced oxygen. This value is close to that observed for the production of chlorine atoms and may be explained by the occurrence of reaction 13.

Identification of Cl_2O_2 . One of the main reactions observed would involve the chlorine atom which is highly reactive toward chlorine dioxide

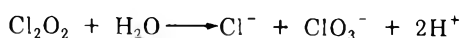


and toward chloride ion



with $k_1 = (1.0 \pm 0.1) \times 10^9 M^{-1} sec^{-1}$ (*vide supra*). Reaction 18 was found to occur in the gas phase ($k = 5 \times 10^9 M^{-1} sec^{-1}$) leading to the formation of two ClO radicals.² This formation is excluded in the aqueous phase if reaction 4 occurs; we have not observed any difference in the decomposition yield of ClO_2 , in the presence or in the absence of Cl^- ions. Reactions 18, 6, and 1 are suppressed in the presence of alcohols in aerated solution and this explains the decrease observed in the decomposition yield of ClO_2 (8% compared to 12% in the absence of alcohols for a $2.5 \times 10^{-4} M$ ClO_2 solution). In the absence of alcohols and following this reaction scheme, only $37 \pm 5\%$ of the ClO_2 decomposed leads to the formation of chlorine atoms.

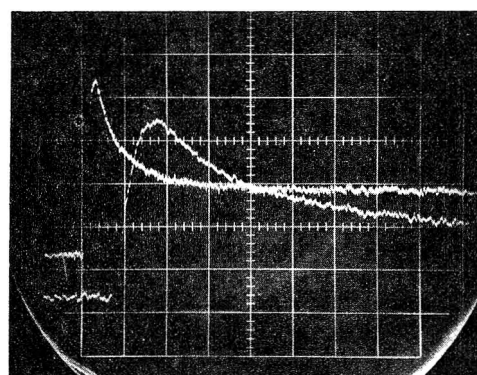
The fact that the intensity of the spectrum observed at 310 nm is sensitive to the addition of chlorine atom scavengers (reactions 7-11) enables us to suggest that X is Cl_2O_2 . This species has been suggested by Porter and Wright,²⁵ Kiryushin and Poluektov²⁶ in the gas-phase bimolecular decay mechanism of ClO and by Taube and Dodgen²⁷ in a study of the mechanisms of reactions involving changes in the oxidation state of chlorine. The first-order decay observed for Cl_2O_2 may be explained by a rapid hydrolysis of the product ($k_{obsd} = (1.0 \pm 0.1) \times 10^4 sec^{-1}$) to form Cl^- and ClO_3^- in equal quantities



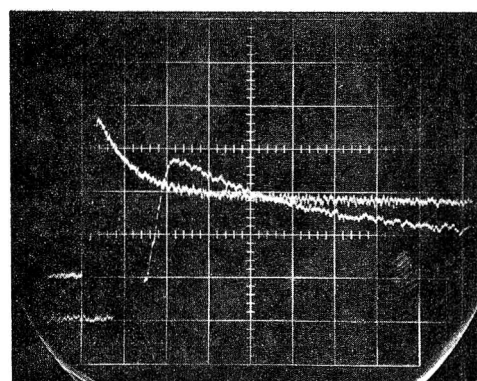
Although this agrees with the observation of Bowen and Cheung,⁵ the mechanism proposed by these authors is quite different (see Introduction).

Reactions 6 and 1 account for an increase in the Cl_2O_2 formation (by a factor of 3 in the presence of $10^{-3} M$ chloride ions) if the latter is assumed to lead preferentially (compared to reaction 19) to the form $Cl-O-Cl-O$ or $Cl-Cl-(O)_2$ which absorbs at 310 nm.

The hypothesis that the spectrum observed around 310 nm is due to Cl_2O_2 finds support in the work of Rochkind and Pimentel,²⁸ the photolysis of Cl_2O in solid nitrogen at 20°K gives rise to the formation of infrared bands (C



a



b

Figure 8. Flash photolysis of ClO_3^- ($2 \times 10^{-3} M$) in deaerated aqueous solution in the presence of isopropyl alcohol ($10^{-3} M$): (a) λ 360 nm, 50 and 200 μsec per large division, 5% transmission per large division, oscillogram showing the disappearance of ClO_2 ; (b) λ 260 nm, 50 and 200 μsec per large division, 5% transmission per large division, oscillogram showing the disappearance of the $(CH_3)_2COH$ radical.

bands) attributed to $(ClO)_2$. The intensity of these bands increases with time for photolysis wavelengths about 334 nm and an equilibrium is set up between formation and disappearance for wavelengths above 316 nm, while a distinct decrease is observed for wavelengths above 270 nm. These experimental results suggest that the $(ClO)_2$ molecule has a uv absorption in the region of 310 nm.

Formation of O_3 and Tentative Assignment of the ClO_3 Spectrum. The spectra observed 500 μsec after the flash in oxygenated and deoxygenated solution (Figure 6, curves A and B) are due respectively to O_3 and probably ClO_3 , although in the latter case the absorption maximum observed (255 nm) differs from that found by Goodeve and Richardson²⁹ (278 nm) in the gas phase. On the other hand, if we assume that all the oxygen atoms produced are scavenged by ClO_2 to give ClO_3 (in deoxygenated solution) and by O_2 to give O_3 (in oxygenated solution) we can calculate, by comparison of the two spectra obtained, a value $\epsilon(ClO_3)$ (255 nm) $920 M^{-1} cm^{-1}$ which is close to

(25) G. Porter and F. J. Wright, *Discuss. Faraday Soc.*, **14**, 23 (1953).

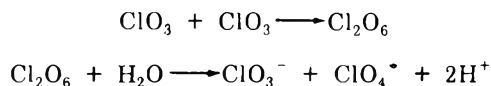
(26) A. Kiryushin and F. A. Poluektov, *Khim. Vys. Energ.*, **3**, 316 (1969).

(27) H. Taube and H. Dodgen, *J. Amer. Chem. Soc.*, **71**, 3330 (1949).

(28) M. M. Rochkind and G. C. Pimentel, *J. Chem. Phys.*, **46**, 4481 (1967).

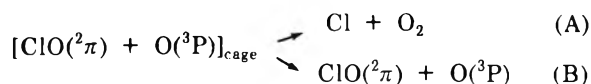
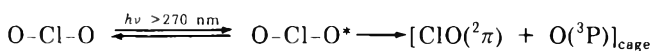
(29) C. F. Goodeve and F. D. Richardson, *Trans. Faraday Soc.*, **33**, 453 (1937).

the maximum extinction coefficient given by these authors, $\epsilon(\text{ClO}_3)$ (278 nm) $1100 \text{ M}^{-1} \text{ cm}^{-1}$. Under our experimental conditions the half-life of ClO_3 is 4 msec. The disappearance kinetics are not studied in the present work because the optical densities obtained are so low that any interpretation is hazardous, besides which they are probably perturbed by the appearance and subsequent hydrolysis of Cl_2O_6 which absorbs in the same wavelength region as ClO_3 .²⁷ In fact the most probable ClO_3 disappearance mechanism is as follows



Conclusion

On the basis of this discussion, we propose the following primary photolytic decomposition mechanism for chlorine dioxide in aqueous solution



The determination of the chlorine atom concentration (or that of O_2) indicates that process A accounts for $37 \pm 5\%$ of the chlorine dioxide disappearing in the flash and the subsequent fast reactions of chlorine atom (reactions 18, 6, and 1) accounts for an identical amount. Process B accounts for $14 \pm 2\%$ of the chlorine dioxide disappearing in the flash (determination of O_3 concentration in oxygenated solution) and the subsequent fast reaction of the ClO radical with ClO_2 accounts for an identical amount. The reaction of atomic chlorine (or Cl_2^-) with ClO_2 leads to the formation of Cl_2O_2 and we suggest that the absorption spectrum observed at 310 nm could be attributed to one of the two forms $\text{Cl}-\text{O}-\text{Cl}-\text{O}$ or $\text{Cl}-\text{Cl}-(\text{O})_2$. Finally, our failure to detect ClO by its absorption spectrum may be explained on two ways, a low production of this species in process B or a fast reaction with ClO_2 to form Cl_2O_3 .

Acknowledgment. We wish to thank Mr. Sutton for helpful discussion.

Reactions of Fluorinated Benzenes with Hydrated Electrons and Hydroxyl Radicals in Aqueous Solutions

R. Köster and K.-D. Asmus*

Hahn-Meitner-Institut für Kernforschung Berlin GmbH, Sektor Strahlenchemie, 1 Berlin 39, West Germany
(Received September 28, 1972)

Publication cost assisted by Hahn-Meitner-Institut für Kernforschung

The reactions of fluorinated benzenes with hydrated electrons and hydroxyl radicals in aqueous solutions have been investigated by pulse radiolysis and γ -irradiation experiments. One fluoride ion per attacking e_{aq}^- is eliminated from the higher fluorinated compounds *via* a dissociative electron capture process. The yields of F^- ions are lower in the reaction of e_{aq}^- with mono-, *o*-di-, and *p*-difluorobenzene. The majority of electrons here interact with the aromatic ring, and the molecular anions thus formed are neutralized to yield fluorocyclohexadienyl radicals. The oxidation of fluorinated benzenes by hydroxyl radicals occurs *via* addition of the $\text{OH}\cdot$ to any of the six carbon atoms with almost equal probability. If the attacked carbon atom carries a hydrogen atom a fluorohydroxycyclohexadienyl radical is produced. The addition to a carbon atom carrying a fluorine atom leads to the elimination of hydrogen fluoride. Rate constants have been determined for the reactions of the fluorinated benzenes with e_{aq}^- and $\text{OH}\cdot$ and for the reactions of transient species produced from these processes. Radicals and stable products have also been characterized by their optical absorption spectra. Mechanistic details of the reduction and oxidation reactions are discussed.

Introduction

Mechanistic studies on the reduction and oxidation of halogenated organic compounds recently became a subject of considerable interest. A combined optical and conductivity pulse radiolysis method, in particular, has proven to be very useful for the investigation of elementary reac-

tions initiated by hydrated electrons, hydrogen atoms, and hydroxyl radicals in aqueous solutions.¹⁻³ The reactions of these species with chlorinated and fluorinated

- (1) K.-D. Asmus, G. Beck, A. Henglein, and A. Wigger, *Ber. Bunsenges. Phys. Chem.*, **70**, 869 (1966).
- (2) G. Beck, *Int. J. Radiat. Phys. Chem.*, **1**, 361 (1969).
- (3) K.-D. Asmus, *Int. J. Radiat. Phys. Chem.*, **4**, 417 (1972).

methanes⁴⁻⁹ and chlorinated ethylenes¹⁰ have already been examined in detail. In the present investigation the reactions of fluorinated benzenes, as an example of aromatic systems, were studied. Little data have so far been available on the radiation chemical reduction and oxidation of these compounds. The rate constant had been determined for the reaction of hydrated electrons with monofluorobenzene,¹¹ and fluoride ions had been detected though no specific yield had been given.¹² Gas-phase experiments on the reaction of C₆H₅F with hydrogen atoms demonstrated the formation of fluorocyclohexadienyl radicals.¹³ Similarly OH· radicals were found to add to the aromatic ring of monofluorobenzene.¹⁴ Our experiments include not only reactions of monofluorobenzene but also of higher fluorinated compounds. They are particularly concerned with mechanistic aspects of the interaction of electrons with the aromatic ring and the fluorine substituent, and the addition of a hydroxyl group to a carbon atom carrying either a hydrogen or a fluorine atom.

Experimental Section

Solutions. The solutions were prepared from triply distilled water. Commercially available fluorinated benzenes (mono-, o-di-, p-di-, 1,2,3,4-tetra-, penta-, and hexafluorobenzene) of gas chromatography grade (≥98%) and the other chemicals of analytical quantity were used without further purification. The water was deoxygenated by bubbling through either argon or nitrous oxide prior to the addition of the solutes which were also degassed separately. Since most of the fluorinated benzenes dissolve very slowly in water the solutions were stirred for ca. 1-2 hr in the dark to reduce photolytic processes.

For the γ -irradiation experiments 20-ml solutions were sealed off in a ca. 25-ml glass vessel. These solutions generally were buffered with 2×10^{-4} M phosphate (KH₂PO₄ + K₂HPO₄) to pH \approx 6.5 to avoid competition of hydrated electrons for the H_{aq}⁻ ions produced during the irradiation.

Irradiation Conditions. The experimental details of the optical and conductivity pulse radiolysis setup have already been described.^{2,15} Pulses of 1.5-MeV electrons were generated by a Van de Graaff generator (10 mA). The pulse length was 0.5-5.0 μ sec, and the absorbed dose rate ca. 700 rads/ μ sec of the pulse. The absorbed dose was monitored with a secondary emission foil. Absolute dosimetry was based on simultaneous optical and conductivity measurements of C(NO₂)₃⁻ ions which are formed with $G = 6.0$ in irradiated aqueous solutions of 10^{-3} M C(NO₂)₄ and 10^{-1} M 2-propanol^{2,3} (maximum absorption of C(NO₂)₃⁻ at 350 nm with ϵ 1.5×10^4 M⁻¹ cm⁻¹, and equivalent conductivity of a C(NO₂)₃⁻/H_{aq}⁺ ion pair $\Lambda = 360$ Ω^{-1} cm² equiv⁻¹).

The analyzing light was filtered through a 2-cm thick cell filled with CHCl₃ located between light source and irradiation cell. Without this filter, which cut off the light below 260 nm, slight photolysis of the fluorine-containing compounds was observed, indicated by an increasing background conductivity.

The γ -radiolysis experiments were carried out in a ⁶⁰Co source of ca. 1500 Ci and an absorbed dose rate of ca. 3 \times 10⁴ rads/hr (determined with a Fricke dosimeter).

Yields and Analysis. Radiation chemical yields were based on the generally accepted yields of reducing and oxidizing species from the radiolysis of aqueous solutions: $G(e_{aq}^-) = 2.7$; $G(OH\cdot) = 2.8$; $G(H\cdot) = 0.6$ ($G \equiv$ number of species produced per 100-eV absorbed energy).^{16,17}

Quantitative analysis of the conductivity data is based on²

$$\Delta V_s = \frac{V_b R_a}{10^3 k_z} \Delta \sum_i c_i |z_i| \Lambda_i$$

ΔV_s is the observed voltage signal due to the conductivity changes in the pulsed solution; V_b is the voltage between the electrodes in the cell (30 V); R_a is an operating resistance (1 k Ω); k_z is the cell constant (0.7 cm⁻¹); c_i is the concentration of the i th charged species produced as a result of the pulse; z_i is the charge number; and Λ_i is the equivalent conductivity in Ω^{-1} cm² equiv⁻¹.

Fluoride ion yields were determined directly in the irradiated solutions by an Orion fluoride ion activity electrode (94-09) in conjunction with an Orion single-junction reference electrode (90-01). The electrode potential differences were measured by the Orion Model 801 digital pH meter. Calibration of the electrodes was done for each set of experiments with standard NaF solutions of the same ionic strength as the irradiated samples.

Error limits are estimated to $\pm 10\%$ for all data derived from optical measurements, and $\pm 5\%$ for conductivity data and fluoride ion yields. All experiments were done at room temperature.

Results and Discussion

Reduction of Fluorinated Benzenes by Hydrated Electrons. Rate Constants and Fluoride Ion Yields. The rate constants for the reactions of fluorinated benzenes with hydrated electrons were measured pulse radiolytically from the effect of the solutes on the lifetime of hydrated electrons, i.e., $k(S + e_{aq}^-)$ was obtained from the half-lives of the e_{aq}^- absorption at various solute concentrations. (The decay of the e_{aq}^- absorption was of pseudo first order since $c(\text{solute}) \gg c(e_{aq}^-)$.) The solutions also contained alcohol (5×10^{-1} M *tert*-butyl alcohol or 2×10^{-1} M CH₃OH) to remove OH radicals and H atoms which are produced simultaneously with the hydrated electrons.¹⁸ The bimolecular rate constants for the reaction of e_{aq}^- with fluorinated benzenes in neutral (pH \approx 6.5) solutions are listed in the second column of Table I. Reaction with hexa-, penta-, and 1,2,3,4-tetrafluorobenzene is essentially diffusion controlled. Much lower rate constants are obtained for o-di-, p-di-, and monofluorobenzene. Our result for the reaction $e_{aq}^- + C_6H_5F$ of $k = 7 \times 10^7$ M⁻¹ sec⁻¹ agrees well with that previously obtained for solutions at pH 11.¹¹

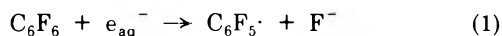
- (4) J. Těplý and A. Habersbergerová, *Collect. Czech. Chem. Commun.*, **30**(3), 785 (1965).
- (5) T. I. Balkas, J. H. Fendler, and R. H. Schuler, *J. Phys. Chem.*, **74**, 4497 (1970).
- (6) T. I. Balkas, J. H. Fendler, and R. H. Schuler, *J. Phys. Chem.*, **75**, 455 (1971).
- (7) R. Köster and K.-D. Asmus, *Z. Naturforsch. B*, **26**, 1104 (1971).
- (8) J. Lillie, D. Behar, R. J. Sujdak, and R. H. Schuler, *J. Phys. Chem.*, **76**, 2517 (1972).
- (9) T. I. Balkas, *Int. J. Radiat. Phys. Chem.*, **4**, 199 (1972).
- (10) R. Köster and K.-D. Asmus, *Z. Naturforsch. B*, **26**, 1108 (1971).
- (11) M. Anbar and E. J. Hart, *J. Am. Chem. Soc.*, **86**, 5633 (1964).
- (12) E. J. Fendler and J. H. Fendler, *Prog. Phys. Org. Chem.*, **7**, 229 (1970).
- (13) M. C. Sauer, Jr., and I. Mani, *J. Phys. Chem.*, **74**, 59 (1970).
- (14) C. R. E. Jefcoate and R. O. C. Norman, *J. Chem. Soc. B*, **48** (1968).
- (15) A. Henglein, *Allg. Prakt. Chem.*, **17**, 296 (1966).
- (16) M. S. Matheson and L. M. Dorfman, "Pulse Radiolysis," The M.I.T. Press, Cambridge, Mass., 1969, and references cited therein.
- (17) E. J. Hart and M. Anbar, "The Hydrated Electron," Wiley-Interscience, New York, N. Y., 1970, and references cited therein.
- (18) Hydroxyl radicals and hydrogen atoms are removed from the solution by alcohols via $OH\cdot/H\cdot + ROH \rightarrow H_2O/H_2 + ROH$.

TABLE I: Rate Constants and Fluoride Ion Yields for the Reaction of Fluorinated Benzenes with Hydrated Electrons in Neutral Aqueous Solutions^a

Solute S	$k(e_{aq}^- + S)$, $M^{-1} \text{sec}^{-1}$	$G(F^-)$	
		Pulse experiments	γ -Irradiation
C_6H_5F	7×10^7	0.55	1.8
<i>o</i> - $C_6H_4F_2$	1.2×10^9	1.0	2.5
<i>p</i> - $C_6H_4F_2$	2.0×10^9	0.4	0.6
1,2,3,4- $C_6H_2F_4$	2.6×10^{10}	2.7	5.0
C_6HF_5	1.6×10^{10}	2.7	5.6
C_6F_6	2.0×10^{10}	2.7	4.8

^a The γ -irradiation experiments were carried out in buffered solutions (pH \approx 6.5 by $2 \times 10^{-4} M$ $KH_2PO_4 + K_2HPO_4$) containing $2 \times 10^{-1} M$ CH_3OH . Solute concentration for $G(F^-)$ determination: 1×10^{-3} – $1 \times 10^{-2} M$ (depending on solubility).

Fluoride ions were identified as a reaction product in γ -irradiation experiments. In the pulse radiolysis investigations fluoride ion yields were calculated from the permanent change in conductivity after the pulse using the known values for the specific conductance of fluoride ions ($\Lambda(F^-) = 46 \Omega^{-1} \text{cm}^2 \text{equiv}^{-1}$)¹⁹ and its positive counter ion, the hydrated proton ($\Lambda(H_{aq}^+) = 315 \Omega^{-1} \text{cm}^2 \text{equiv}^{-1}$).¹⁹ $G(F^-)$ was generally measured at high solute concentrations (5×10^{-3} – $1 \times 10^{-2} M$); *i.e.*, they represent limiting yields, when all hydrated electrons are scavenged by the fluorinated benzenes. The results are listed in the third column of Table I. The fluoride ion yield is seen to equal $G(e_{aq}^-)$ for the higher fluorinated compounds, *i.e.*, the reduction of hexafluorobenzene, for example, occurs quantitatively *via*



Much lower yields, however, are found for the reaction of hydrated electrons with mono- and the two difluorobenzenes indicating that scavenging of an electron by these compounds does not necessarily lead to the elimination of a fluoride ion.

Comparable results were obtained for γ -irradiated solutions of fluorinated benzenes (containing also high concentrations of alcohol to remove $OH\cdot$ and $H\cdot$) (Table I). Again much lower fluoride ion yields are found for the reaction of e_{aq}^- with mono-, *o*-di, and *p*-difluorobenzene than for the higher fluorinated compounds. The absolute yields are generally higher compared with the pulse experiments which means, at least for the higher fluorinated benzenes, that more than one F^- ion is eliminated per reacting electron. This can be attributed, for example, to secondary reactions of any intermediate on a time scale greater than 10 msec (limit of the pulse radiolysis dc conductivity method). Owing to the much lower dose rate, *i.e.*, lower steady-state concentration, compared with the pulse experiments, the lifetime of radicals with respect to radical-radical reactions is increased by several orders of magnitude thereby leaving open the possibility of other reactions such as hydrolysis, etc. Quite similar results, *i.e.*, halide ion yields which are higher for γ -irradiation than for pulse experiments, have also been found for the reduction of chlorinated methanes,^{4,7,9} ethylenes,¹⁰ and mixed fluorochloromethanes.⁶

Formation of Fluorocyclohexadienyl Radicals. Figure 1 shows the optical absorption of the hydrated electron traced at 700 nm and the conductivity signal as a function

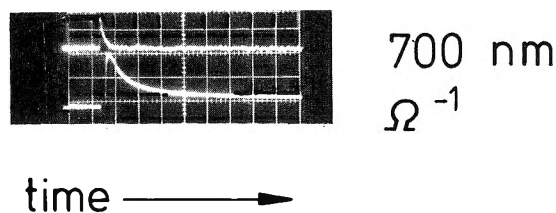
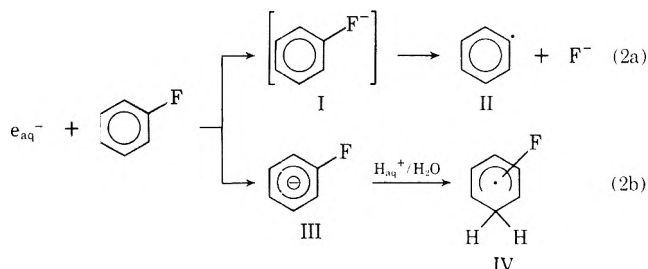


Figure 1. Upper curve shows optical absorption–time curve at 700 nm in a pulsed solution of $2.5 \times 10^{-3} M$ C_6H_5F and $2 \times 10^{-1} M$ CH_3OH ; time scale: 20 μsec /large division. Lower curve shows conductivity–time curve for the same solution: time scale, 20 μsec /large division.

of time obtained for a pulsed, argon-saturated, neutral solution of $2.5 \times 10^{-3} M$ monofluorobenzene. In addition, $2 \times 10^{-1} M$ CH_3OH was present to remove $OH\cdot$ radicals and $H\cdot$ atoms, so that hydrated electrons were the only species to react with C_6H_5F . The e_{aq}^- absorption in the upper curve is seen to decay very fast with a half-life of 4 μsec . The conductivity signal shown in the lower curve decays much more slowly with a first half-life of 12 μsec . At long times, *i.e.*, after ca. 50 μsec , it reaches a constant value corresponding to a change in conductivity of $\Delta\Lambda = 72 \Omega^{-1} \text{cm}^2$ which is equivalent to the formation of fluoride ions with $G(F^-) = 0.52$ (see also Table I). The maximum conductivity value immediately after the pulse corresponds to $\Delta\Lambda = 380 \Omega^{-1} \text{cm}^2$ which indicates the initial formation of one H_{aq}^+ /anion pair per reacting electron.¹⁹ (The conductivity signal of e_{aq}^- itself cannot be seen on account of the short lifetime of e_{aq}^- under the present conditions and the fact that the signal is distorted during the first few microseconds for instrumental reasons.)² Optical measurements carried out simultaneously in the uv region showed a transient absorption below 340 nm. Part of it arises from the $\cdot CH_2OH$ radical which is produced *via* the reaction of CH_3OH with $OH\cdot$ and $H\cdot$. If its well-known spectrum^{20,21} is subtracted from the overall absorption, a spectrum remains with a maximum at 300 nm, *i.e.*, a second transient species besides the $\cdot CH_2OH$ is formed. Quite similar observations have also been made for the other less highly fluorinated benzenes. The uv spectra of the transients are shown in Figure 2. The species resulting from *o*- and *p*-difluorobenzene have maximum absorption at 300 and 320 nm, respectively. No such absorptions were observed for reactions of e_{aq}^- with the higher fluorinated benzenes, which lead only to F^- ions and phenyl radicals.

The results presented above are compatible with the mechanism shown in Scheme I as is formulated for

Scheme I



(19) Landolt-Börnstein, "Zahlenwerte und Funktionen," Vol. 11/7, Springer-Verlag, Berlin-Heidelberg, 1960.

(20) (a) I. A. Taub and L. M. Dorfman, *J. Amer. Chem. Soc.*, **84**, 4053 (1962); (b) M. Simic, P. Neta, and E. Hayon, *J. Phys. Chem.*, **73**, 3794 (1969).

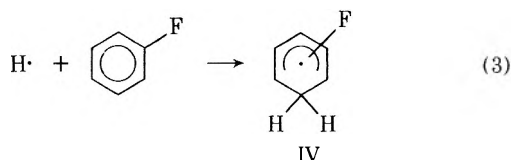
(21) K.-D. Asmus, A. Henglein, A. Wigger, and G. Beck, *Ber. Bunsenges. Phys. Chem.*, **70**, 756 (1966).

monofluorobenzene. The addition of an electron to an aromatic system preferably occurs *via* interaction with the π orbital system of the ring.¹² In our case this leads to the formation of the molecular anion III which will subsequently be neutralized by H_{aq}^+ and H_2O to form the fluorocyclohexadienyl radical IV.

A reaction path similar to that of 2b has, in fact, been observed for the reaction of benzene with electrons. Studier and Hart in their γ -radiolysis study of the reaction $C_6H_6 + e_{aq}^-$ postulate a $C_6H_6^-$ anion and a $C_6H_7\cdot$ radical as intermediates.²² The existence of these two species has also been confirmed in liquid ammonia²³ (reduction of benzene by sodium atoms) and by esr measurements on electrochemically reduced benzene.²⁴

Interaction of an electron with an aromatic system is also possible at the substituent. If this is a very electronegative group such as $-NO_2$, $-NO$, $-CHO$, $-I$, etc., it is, in fact, the exclusive site of attack.¹² The net electron-withdrawing effect of a fluorine atom at an aromatic ring estimated from the σ_I and σ_M Hammett parameters for the inductive ($-I$) and mesomeric ($+M$) effect, however, is almost equal to that of a hydrogen atom.²⁵ This may explain the low yield of electrons attacking at the fluorine atom in the C_6H_5F *via* reaction path 2a.

The optical absorption spectra of the fluorocyclohexadienyl radicals (type IV) are shown in Figure 2. They were taken from the maximum absorption immediately after a *ca.* 5- μ sec pulse. Such long pulses had to be used because of the relatively low extinction coefficients of these radicals. Owing to the long pulses the yield of H_{aq}^+ was high enough for an almost complete neutralization of the molecular anion (type III) during the pulse. Thus any contribution of these anions to the absorption will be very small. The extinction coefficients have been calculated by taking $G(\text{fluorocyclohexadienyl}) = G(e_{aq}^-) - G(F^-)$ according to the mechanism given in eq 2a and 2b. As to be expected the observed spectra are identical with those obtained for the direct addition of an H atom to the fluorobenzenes, as, for example



These reactions were observed in pulsed acid solutions where e_{aq}^- are converted to $H\cdot$ atoms prior to their reaction with the fluorobenzenes. The spectrum of the monofluorocyclohexadienyl radical also agrees with that obtained during gas-phase experiments on the reactions of C_6H_5F with hydrogen atoms.²⁶

The neutralization of III to IV shown in the conductivity curve of Figure 1 is of mixed order kinetics owing to a pseudo-first-order reaction of the anion with H_2O and a second-order reaction with H_{aq}^+ which in neutral solutions are present at approximately the same concentration as III. Addition of acid ($HClO_4$) to the solution completely removes the transient conductivity signal since the neutralization of III now is too fast to be observable.

Changes in the pH of the solution did not change the fluoride ion yield from the reaction of e_{aq}^- with mono- and the difluorobenzenes. This would indicate that reactions 2a and 2b are independent from each other. The yield of fluoride ions may then be regarded as a measure for the probability of the electrons to attack at the fluorine atom (reaction path 2a) whereas the yield of fluorocy-

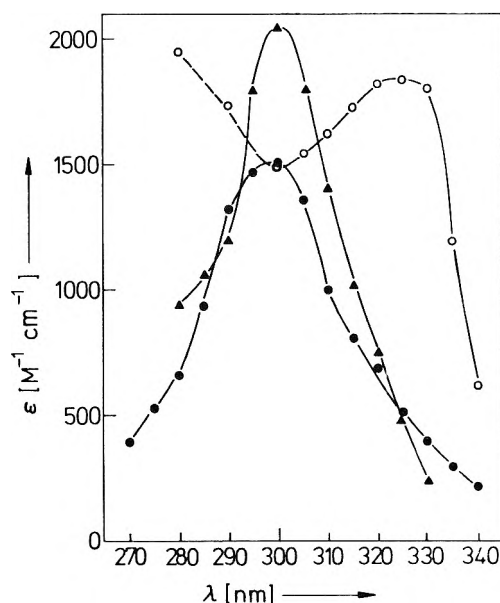


Figure 2. Spectra of monofluorocyclohexadienyl (●), o-difluorocyclohexadienyl (▲), and p-difluorocyclohexadienyl (○) radicals.

clohexadienyl radicals represents the probability of the electron's interaction with the aromatic ring (reaction path 2b).

Oxidation of Fluorinated Benzenes by Hydroxyl Radicals. Rate Constants for OH· Reactions. The rate constants for the reaction of fluorinated benzenes with hydroxyl radicals were measured by the thiocyanate competition method.^{27,28} The results are listed in Table II. The slowest reaction occurs with hexafluorobenzene, the fastest with monofluorobenzene. However, no characteristic trend can be observed since the di-, tetra-, and pentafluorobenzenes react with approximately the same rate constants. For comparison, the same order of magnitude had been found for the rate constant of the reaction of OH· radicals with benzene.²⁹

Monofluorobenzene. The reaction of monofluorobenzene with hydroxyl radicals leads to a transient species which absorbs in the near uv. It can be observed in pulse irradiated, N_2O -saturated solutions of $2 \times 10^{-4} M$ C_6H_5F . In such solutions all hydrated electrons are converted to OH· radicals ($e_{aq}^- + N_2O \rightarrow OH\cdot + OH^- + N_2$) and the monofluorobenzene is oxidized with a total $G(OH\cdot) = 5.5$. The spectrum of the transient is shown in Figure 3. Maximum absorption occurs at 310 nm with an extinction coefficient of $3.1 \times 10^3 M^{-1} cm^{-1}$. The spectrum is attributed to the OH addition product which is formed in

(22) M. H. Studier and E. J. Hart, *J. Amer. Chem. Soc.*, **91**, 4068 (1969).

(23) H. Smith, "Organic Reactions in Liquid Ammonia," Interscience, New York, N. Y., 1963.

(24) R. G. Lawler and G. K. Frankel, *J. Chem. Phys.*, **49**, 1126 (1968).

(25) Autorenkollektiv H. Becker, et al., "Organikum," VEB Deutscher Verlag der Wissenschaften, Berlin, 1965.

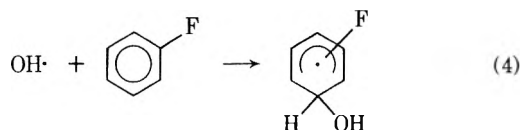
(26) M. C. Sauer, Jr., and B. Ward, *J. Phys. Chem.*, **71**, 3971 (1967).

(27) G. E. Adams, J. W. Boag, J. Currant, and B. D. Michael in "Pulse Radiolysis," by M. Ebert, J. P. Keene, A. J. Swallow, and J. H. Baxendale, Ed., Academic Press, New York, N. Y., 1965.

(28) J. H. Baxendale, P. L. T. Bevan, and D. A. Stott, *Trans. Faraday Soc.*, **64**, 2389 (1968).

(29) (a) L. M. Dorfman, R. E. Buhler, and I. A. Taub, *J. Chem. Phys.*, **36**, 549 (1962); (b) L. M. Dorfman, I. A. Taub, and R. E. Buhler, *ibid.*, **36**, 3051 (1962).

the reaction



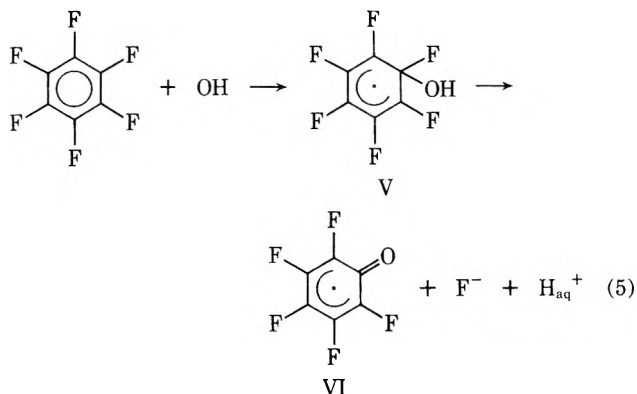
It is almost identical with that of the hydroxycyclohexadienyl radical from the reaction of $\text{OH}\cdot$ with benzene.²⁹

Conductivity measurements carried out simultaneously confirmed this mechanism, since ionic species are formed only to an almost negligible extent in the reaction of $\text{OH}\cdot$ with $\text{C}_6\text{H}_5\text{F}$. The fluorohydroxycyclohexadienyl radical disappears by a pure second-order process presumably *via* disproportionation and combination. From the kinetic analysis of the decay of the optical absorption at 310 nm, the bimolecular rate constant for this process is found to be $2k = 9.0 \times 10^8 \text{ M}^{-1} \text{ sec}^{-1}$.

Hexafluorobenzene. The reaction of hydroxyl radicals with hexafluorobenzene also leads to a transient species. This is seen in Figure 4a where the optical absorption of a pulsed, N_2O -saturated solution of $3 \times 10^{-4} \text{ M C}_6\text{F}_6$ is recorded as a function of time. The spectrum of the transient calculated from the maximum signal after the pulse at various wavelengths is also shown in Figure 3. It has maxima at *ca.* 260 ($\epsilon 4 \times 10^3 \text{ M}^{-1} \text{ cm}^{-1}$) and 400 nm ($\epsilon 1 \times 10^3 \text{ M}^{-1} \text{ cm}^{-1}$), and is seen to be quite different from the $\text{OH}\cdot$ addition product to monofluorobenzene.

Figure 4b shows the formation of the transient in a N_2O -saturated solution of $5.8 \times 10^{-5} \text{ M C}_6\text{F}_6$. The bimolecular rate constant for this process is identical with that obtained for the reaction of $\text{OH}\cdot$ radicals with hexafluorobenzene by the competition method (see Table II).

The oxidation of hexafluorobenzene by hydroxyl radicals leads to the formation of ions. The conductivity signal (Figure 4c) traced simultaneously in the same solution grows in with the same rate as the optical absorption in Figure 4b. In γ -irradiated solutions fluoride ions are identified as a product of the oxidation of hexafluorobenzene. The conductivity signal in the pulse experiment is, therefore, attributed to the formation of $\text{F}^-/\text{H}_{\text{aq}}^+$ ion pairs. The yield calculated from the final conductivity change and using $\Lambda(\text{F}^- + \text{H}_{\text{aq}}^+) = 360 \Omega^{-1} \text{ cm}^2 \text{ equiv}^{-1}$ ¹⁹ amounts to $G(\text{F}^-) = 5.5$; *i.e.*, one F^- ion is eliminated from the C_6F_6 per attacking $\text{OH}\cdot$ radical. On account of the results presented above the following mechanism can be formulated



Accordingly the first step is the addition of the OH radical to the aromatic ring similar to reaction 4. The hexafluorohydroxycyclohexadienyl radical (V) thus formed, however, is unstable because of the location of a halogen atom and a hydroxyl group on the same carbon

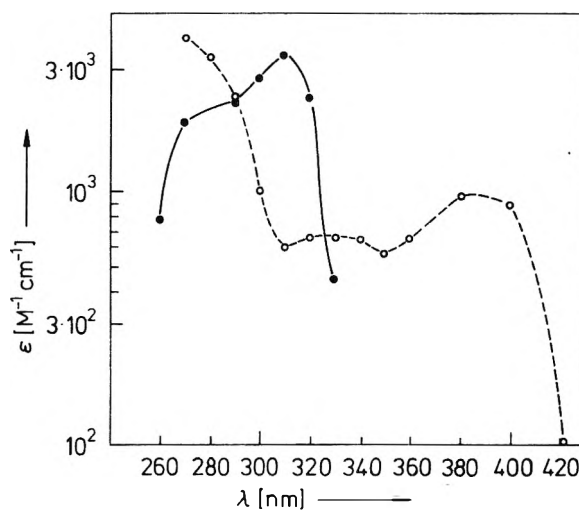


Figure 3. Spectra of the transient products from the reaction of $\text{OH}\cdot$ radicals with $\text{C}_6\text{H}_5\text{F}$ (●) and C_6F_6 (○).

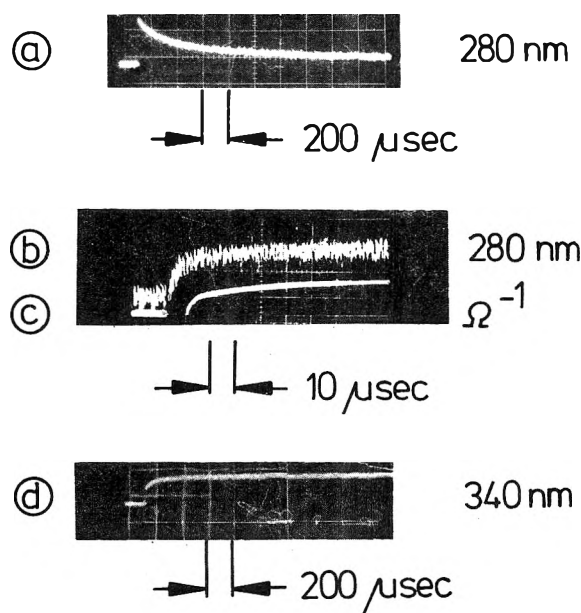
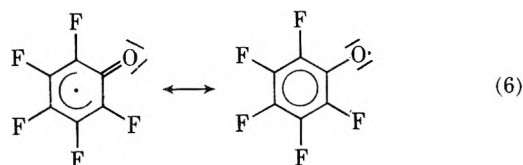


Figure 4. (a) Optical absorption-time curve at 280 nm in a pulsed, N_2O -saturated solution of $3 \times 10^{-4} \text{ M C}_6\text{F}_6$ (time scale, $200 \mu\text{sec}$ /large division); (b) optical absorption-time curve at 280 nm in a pulsed, N_2O -saturated solution of $5.8 \times 10^{-5} \text{ M C}_6\text{F}_6$ (time scale, $10 \mu\text{sec}$ /large division); (c) conductivity-time curve, conditions same as for b; (d) optical absorption-time curve at 340 nm, conditions same as for a.

atom. Such configurations are stabilized by hydrogen halide elimination.^{8,10} In our case this leads to the formation of F^- and H_{aq}^+ ions. The structure given in eq 5 for the radical VI is, of course, only one of the possible mesomeric forms



The rate-determining step for the $\text{F}^-/\text{H}_{\text{aq}}^+$ ion pair formation is the OH radical attack on the C_6F_6 as is indicated from the conductivity experiments. The lifetime of the intermediate radical (V), therefore, must be very short.

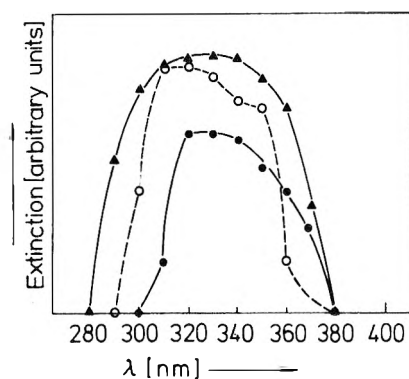


Figure 5. Spectra of the permanent products from the pulse radiolytic oxidation of hexafluoro- (▲); pentafluoro- (○), and 1,2,3,4-tetrafluorobenzene (●).

TABLE II: Rate Constants and Fluoride Ion Yields for the Oxidation of Fluorinated Benzenes by Hydroxyl Radicals in Neutral N_2O -Saturated Aqueous Solutions^a

Solute S	$k(OH + S)$, $M^{-1} sec^{-1}$	$G(F^-)$		
		Pulse ex- periments	b	γ -Irra- diation
C_6H_5F	8×10^9	≈ 0.3	0.9	1.4
<i>o</i> - $C_6H_4F_2$	4.5×10^9	1.2	1.8	2.2
<i>p</i> - $C_6H_4F_2$	6×10^9	1.4	1.8	2.0
1,2,3,4- $C_6H_2F_4$	5×10^9	3.2	3.7	6.0
C_6HF_5	4×10^9	4.6	4.6	7.8
C_6F_6	2×10^9	5.5	5.5	8.0

^a The γ -irradiation experiments were carried out in buffered solutions (pH ≈ 6.5 by $2 \times 10^{-4} M$ $KH_2PO_4 + K_2HPO_4$). ^b One-sixth of $G(F^-)$ from hexafluorobenzene multiplied by the number of fluorine atoms per solute molecule. Solute concentration for $G(F^-)$ determination 1×10^{-3} to $1 \times 10^{-2} M$ (depending on solubility).

No evidence for V by either a delayed formation of conductivity or an optical absorption similar to that of other hydroxycyclohexadienyl radicals could be observed on the experimental time scale limit of $1 \mu sec$ of the pulse radiolysis conductivity method. From this a first-order rate constant $k(V) \rightarrow (VI) > 7 \times 10^5 sec^{-1}$ is derived. The mechanism given in eq 5 is also supported by similar results obtained for the reaction of chlorinated ethylenes with hydroxyl radicals.¹⁰

The optical absorption spectrum accordingly has to be attributed to the radical VI. It is interesting to note that our transient has a very similar spectrum to the phenoxy radical,³⁰ $C_6H_5O\cdot$, and the semiquinone radical,³¹ $HOC_6H_4O\cdot$, which are formed in the reaction of hydroxyl radicals with phenol and hydroquinone, respectively. This certainly indicates a structural similarity to VI.

The radical VI disappears by a second-order process. From the kinetic analysis of the decay of the optical absorption-time curve in Figure 4a, a bimolecular rate constant $2k = 2.5 \times 10^8 M^{-1} sec^{-1}$ is derived.

If the optical absorption is traced at 340 nm (4d), in the same solution which gave the signal at 280 nm (4a), a different picture is obtained. The initial fast increase is due to the formation of VI. The slow second increase leads to a stable absorption. This step occurs simultaneously with the decay of the optical signal at 280 nm, *i.e.*, of VI. The absorption spectrum of the stable product shown in Figure 5, is, therefore, attributed to the dimerization (and possibly disproportionation) products of the $C_6F_5O\cdot$ (VI) radi-

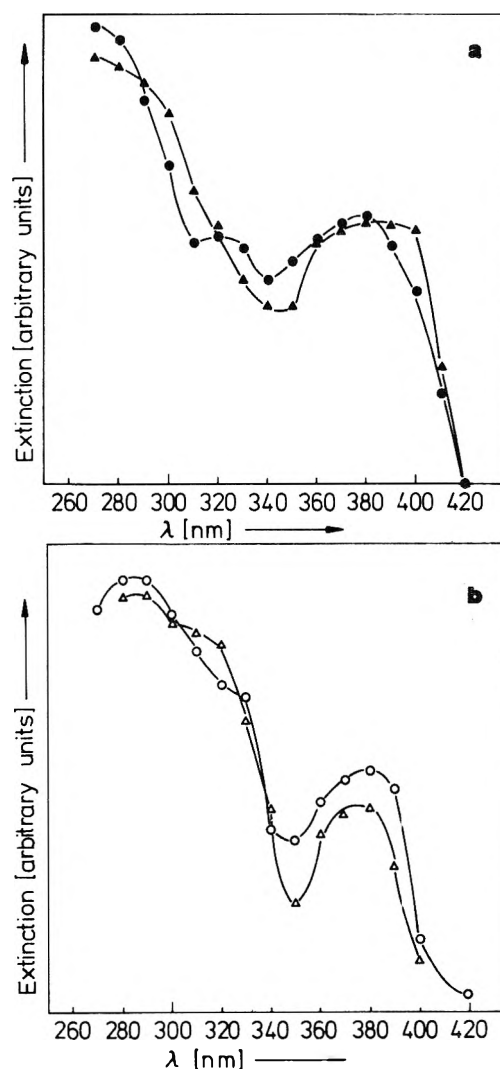


Figure 6. Spectra of the transient products from the reaction of $OH\cdot$ radicals with pentafluorobenzene [(●) a], 1,2,3,4-tetrafluorobenzene [(▲) a], *p*-difluorobenzene [(○) b], and *o*-difluorobenzene [(Δ) b].

cal. Since too many isomers are possible, no extinction coefficients have been evaluated.

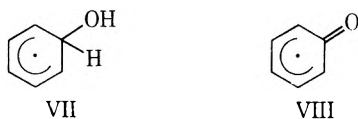
Other Fluorobenzenes. The fluoride ion yields from the oxidation of all fluorobenzenes which have been investigated are listed in the third column of Table II. $G(F^-)$ was calculated from the permanent changes in conductivity obtained for pulsed, N_2O -saturated solutions of $(1-5) \times 10^{-4} M$ solute. Only hexafluorobenzene is found to eliminate fluoride ions with $G = 5.5$, *i.e.*, with a yield which equals the yield of attacking hydroxyl radicals. Lower yields are found for the less highly fluorinated compounds. The ratio $G(F^-)/G(OH\cdot)$ decreases with the number of fluorine atoms per molecule. Fluoride ion elimination can only occur if the OH radical adds to a carbon atom carrying already an F atom. If $OH\cdot$ adds to a C atom carrying an H atom, no fluoride ions will be produced. Our results would indicate, therefore, that the hydroxyl radical attacks all six carbon atoms in the fluorinated benzenes with almost equal probability. This, in fact, can be expected on account of the following considerations; the hydroxyl radi-

(30) E. J. Land and M. Ebert, *Trans. Faraday Soc.*, **63**, 1181 (1967).

(31) G. E. Adams and B. D. Michael, *Trans. Faraday Soc.*, **63**, 1171 (1967).

cal is known to be an electrophilic reagent.¹² Since the net electron-withdrawing effect of F atoms in a C-F bond is essentially the same as that of H atoms in a C-H bond²⁵ only little difference in the electron density between the carbon atoms is expected. Also sterical effects should have only little if any influence on the site of the OH· attack. Only a very slight overall directing effect might be indicated from the comparatively low fluoride ion yields obtained for the oxidation of mono- and difluorobenzene (compare columns 3 and 4 of Table II).

The reaction of fluorinated benzenes with OH· radicals leads to either VII- or VIII-type radicals according to the



mechanisms given in eq 4 and 5. The lifetime of the precursors of VIII, the fluorohydroxycyclohexadienyl radicals, was not long enough for a positive identification of these species. The absorption spectra of the transient species observed immediately after the pulse from the reaction of OH· radicals with *o*-di-, *p*-di-, 1,2,3,4-tetra-, and pentafluorobenzene are shown in Figure 6. The spectra obtained for tetra- and pentafluorobenzene are quite similar to that for hexafluorobenzene since they are mainly given by the VIII-type radical. Extinction coefficients estimated for the maxima at 260 and 400 nm by taking $G(\text{VIII}) = G(\text{F}^-)$ and ignoring any contribution of the VII-type radical at these wavelengths are of the same order of magnitude as for the $\text{C}_6\text{F}_5\text{O}^\cdot$ radical (VI). In the case of mono- and difluorobenzenes the reaction of most of the OH· radicals leads to the formation of a VII-type radical and accordingly a much stronger absorption at *ca.* 310 nm is observed.

All the radicals (VII and VIII) disappear by second-order processes. As has been found for hexafluorobenzene the dimerization of the VIII-type radicals from tetra- and pentafluorobenzene also yields stable absorbing products. The spectra of these compounds obtained from the pulse experiments (as described above for hexafluorobenzene) are shown in Figure 5.

γ Experiments. Fluoride ion yields have also been determined for the reaction of fluorinated benzenes with hydroxyl radicals in buffered (pH \approx 6.5) γ -irradiated solutions. The conditions were the same as for the pulse experiments, *i.e.*, solutions were N_2O saturated so that a total $G(\text{OH}) = 5.5$ was available for the oxidation reactions. The results are listed in the last column of Table II. $G(\text{F}^-)$ is generally found to be higher than the yields from the single-pulse experiments. This is explained on the same grounds as discussed above for the reaction of fluorinated benzenes with hydrated electrons; *i.e.*, owing to the longer lifetime of the radicals under γ -radiolysis conditions additional reactions become possible which could lead to higher F^- ion yields. Stable products with absorptions below 400 nm have also been identified in the γ -radiolysis of the higher fluorinated benzenes. In the 400 to 300 nm range the spectra are quite similar to those of the stable products from the pulse experiments shown in Figure 5. Additional strong absorptions below 300 nm indicate, however, the formation of other stable products as well. This again is explained by radical reactions which become possible because of the longer lifetime of the radicals in the γ -irradiated system.

Acknowledgment. The authors are very grateful to Mrs. M. Schöner for experimental assistance. This work has been supported by funds made available by the "Verband der Chemischen Industrie."

The Yields of Fragment Ions in the Radiolysis of Liquid *n*-Butane

Noboru Fujisaki, Toshinori Wada, Shoji Shida,* and Yoshihiko Hatano

Laboratory of Physical Chemistry, Tokyo Institute of Technology, Meguro-ku, Tokyo, Japan (Received December 20, 1971)

An attempt to estimate the yields of fragment ions has been made in the radiolysis of liquid *n*-butane. The G values of C_2H_5^+ , C_3H_7^+ , and C_4H_9^+ are estimated by using charge scavengers such as sulfur hexafluoride and ammonia to be at least about 0.25, 0.15, and 0.6, respectively. Their yields are also estimated by measuring the isotopic composition of ethane and propane formed in the radiolysis of equimolar mixtures of *n*- C_4H_{10} -*n*- C_4D_{10} . Although somewhat large errors are involved in the isotopic composition, the yields of fragment ions in both the estimations seem to be in fairly good agreement with each other, except for the yield of butyl ion which could not be estimated by the latter method.

Introduction

It has generally been recognized that the fragmentation of parent ion in the radiolysis of hydrocarbons occurs to a lesser extent in the liquid phase than in the gas phase. So far, however, there have been no investigations in which the yields of fragment ions in the radiolysis of liquid hydrocarbons have been determined unequivocally. For this

purpose the following various attempts have been proposed.

Ward and Hamill¹ estimated the yields of fragment ions by measuring the yields of adducts formed in the liquid-

(1) J. A. Ward and W. H. Hamill, *J. Amer. Chem. Soc.*, **89**, 5116 (1967).

phase radiolysis of hydrocarbon-alcohol mixtures. They explained the adduct formation by the reaction



Since, however, the proton transfer from RH^+ to $R'OH$ may compete with reaction 1, the results might involve some uncertainty. Scala and Ausloos² and later other investigators³ also estimated the yields of fragment ions by analyzing the isotopically mixed products formed in the liquid-phase radiolysis of $C_nH_{2n-2}-C_nD_{2n-2}-O_2$ mixtures and of partly deuterated compounds. The use of the deuterated compounds seems to give some useful informations on fragment ions which undergo $H^-(D^-)$ and $H_2^-(D_2^-)$ transfer reactions. However, it seems to be difficult for this method to distinguish isotopically mixed products produced by ion-molecule reactions from those produced by hydrogen-atom abstraction reactions of hot radicals or radical reactions in spurs. Tanno, Miyazaki, and Shida⁴ estimated the yields of fragment ions in the radiolysis of liquid hydrocarbons using a proton acceptor (NH_3) in the presence of an electron scavenger (SF_6). This method seems to be suitable for measuring the yields of fragment ions (carbonium ions) because ammonia and sulfur hexafluoride have high reactivities toward carbonium ions and electrons, respectively, but the yields of fragment ions which undergo H_2^- transfer reactions cannot be estimated unequivocally. Besides, interpretation of the results obtained by this method is somewhat complicated when a radical scavenger (O_2) is not added to the system.

In the present paper, we have tried to estimate the yields of fragment ions in the radiolysis of liquid *n*-butane by the use of ammonia and sulfur hexafluoride, and the results obtained are compared with those obtained by the use of perdeuterated *n*-butane.

Experimental Section

The purities of materials used in the present investigation are as follows: *n*-butane (>99.998%), perdeuterated *n*-butane (>99.999%),^{3b} sulfur hexafluoride (>98%), oxygen (>99.9%), and ammonia (>99%). Pyrex sample tubes (6 cm long, 0.3 cm i.d.), which were attached to a vacuum line, were filled with about 0.25 ml of *n*-butane. The volume of the vapor phase above the liquid level in these tubes is estimated to be about 0.1 cm³.

The samples were irradiated at 0° by ⁶⁰Co γ rays at a dose rate of 4.33×10^{19} eV/g hr to a total dose of 1.29×10^{20} eV/g. The hydrocarbon products were analyzed with a Shimadzu GC-1C gas chromatograph with a flame ionization detector and a 3-m activated alumina column. When necessary, ethane and propane were separately trapped at -196° for isotopic analysis after emerging from an activated alumina column. The isotopic analyses of ethane and propane were, as before,^{3b} made mass spectrometrically using standard cracking patterns. Other experimental details have been described elsewhere.^{3b}

Results

Figures 1 and 2 show, respectively, the effect of ammonia on the yields of products from *n*-C₄H₁₀-0.5 M SF₆ and *n*-C₄H₁₀-0.5 M SF₆-0.08 M O₂ mixtures. It is seen that in these figures the increases in the yields of ethylene and propylene upon the addition of ammonia are accompanied by decreases in the yields of ethane and propane. It should be noted that in Figure 2 the *G* value of total bu-

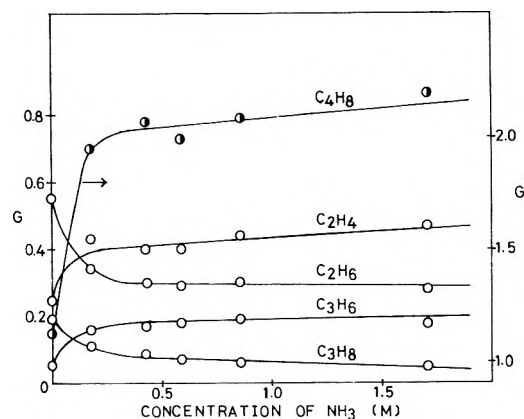


Figure 1. Effect of ammonia on the product yields from liquid *n*-butane containing 0.5 M SF₆.

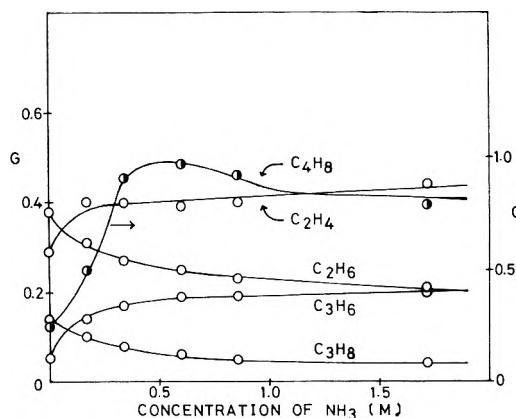


Figure 2. Effect of ammonia on the product yields from liquid *n*-butane containing both 0.5 M SF₆ and 0.08 M O₂.

TABLE I: The *G* Values of Products Formed in the Radiolysis of Liquid *n*-Butane with and without Various Scavengers^{a,b,c}

Product	Additive ^d					
	None	SF ₆	SF ₆ + NH ₃	O ₂	O ₂ + SF ₆	O ₂ + SF ₆ + NH ₃
C ₂ H ₆	1.03	0.55	0.30	0.55	0.38	0.21
C ₂ H ₄	0.86	0.25	0.46	0.70	0.29	0.43
C ₃ H ₈	0.16	0.19	0.04	0.11	0.14	0.04
C ₃ H ₆	0.20	0.05	0.19	0.17	0.05	0.19
C ₄ H ₈	2.63	1.12	2.14	0.92	0.25	0.82

^a Dose: 1.29×10^{20} eV/g. ^b Irradiation temperature: 0°. ^c Probable errors in *G* values: $\pm 5\%$. ^d Concentration: SF₆ 0.5 M, NH₃ 1.7 M, and O₂ 0.08 M in all runs in this table.

tenes from the *n*-C₄H₁₀-SF₆-O₂ mixture attains a maximum value at low ammonia concentration and then decreases gradually with increasing ammonia concentration. The results on the *G* values of products from liquid *n*-butane with and without various scavengers are summarized in Table I. The *G* values for products are determined in this experiment with the probable errors of $\pm 5\%$. The iso-

- (2) A. A. Scala and P. Ausloos, *J. Chem. Phys.*, **47**, 5129 (1967).
 (3) (a) R. D. Koob and L. Kevan, *Trans. Faraday Soc.*, **64**, 706 (1968); (b) N. Fujisaki, S. Shida, Y. Hatano, and K. Tanno, *J. Phys. Chem.*, **75**, 2854 (1971).
 (4) (a) K. Tanno, S. Shida, and T. Miyazaki, *J. Phys. Chem.*, **72**, 3496 (1968); (b) K. Tanno, T. Miyazaki, K. Shinsaka, and S. Shida, *ibid.*, **71**, 4290 (1967); (c) K. Tanno and S. Shida, *Bull. Chem. Soc. Jap.*, **42**, 2128 (1969).

TABLE II: Isotopic Distribution of Ethane^{a,b,c}

System	G(ethane) ^d	Ethane (%)					
		C ₂ D ₆	C ₂ D ₅ H	C ₂ D ₄ H ₂	C ₂ H ₄ D ₂	C ₂ H ₃ D	C ₂ H ₆
C ₄ H ₁₀ -C ₄ D ₁₀ -O ₂ -SF ₆	0.38	24.9	14.2	2.5	4.0	12.2	42.2
C ₄ H ₁₀ -C ₄ D ₁₀ -O ₂ -SF ₆ -NH ₃	0.21	16.1	9.8	1.5	2.0	12.1	58.5

^a The ratio C₄H₁₀/C₄D₁₀ is 1.0. ^b Concentrations of additives: SF₆ 0.5 M, NH₃ 1.7 M, and O₂ 0.08 M in all runs in this table. ^c Probable errors in percentages of ethanes: ±10% for C₂D₆ and C₂D₅H and ±10% to ±15% for other ethanes. ^d The G values of ethane from *n*-C₄H₁₀-O₂-SF₆ and *n*-C₄H₁₀-O₂-SF₆-NH₃ mixtures.

TABLE III: Isotopic Distribution of Propane^{a,b,c}

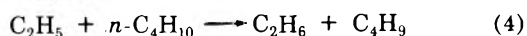
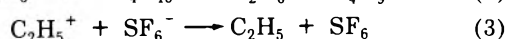
System	G(prop- pane) ^d	Propane (relative intensity)		
		C ₃ D ₈	C ₃ D ₇ H	C ₃ D ₆ H ₂
C ₄ H ₁₀ -C ₄ D ₁₀ -O ₂ -SF ₆	0.14	100	100	10
C ₄ H ₁₀ -C ₄ D ₁₀ -O ₂ -NH ₃ -SF ₆	0.04	100	89	35

^a The ratio C₄H₁₀/C₄D₁₀ is 1.0. ^b Concentration of additives: SF₆ 0.5 M, NH₃ 1.7 M, and O₂ 0.08 M in all runs in this table. ^c Probable errors in relative intensity of C₃D₇H and C₃D₆H₂: ±10%. ^d The G values of propane from *n*-C₄H₁₀-O₂-SF₆ and *n*-C₄H₁₀-O₂-SF₆-NH₃ mixtures.

topic distribution of ethanes and propanes from C₄H₁₀-C₄D₁₀-O₂-SF₆ and C₄H₁₀-C₄D₁₀-O₂-SF₆-NH₃ mixtures are, respectively, tabulated in Table II and III. The values of %C₂D₆ and %C₂D₅H in Table II determined mass spectrometrically include errors probably ±10% of these values, while those of %C₂H₃D and %C₂H₆ include somewhat large errors ±(10–15)% of these values.

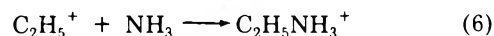
Discussion

The Yield of Ethyl Ion. We will be concerned here with ethane and ethylene produced by processes involving ethyl ion. When sulfur hexafluoride is added as an efficient electron scavenger to liquid *n*-butane, thermal electrons should be converted into sulfur hexafluoride negative ions which are less diffusive than the electron itself. Thus the lifetime of ethyl ion with respect to neutralization with electron should be prolonged in the presence of the electron scavenger so that the ethyl ion undergoes the hydride-ion transfer reaction (2) more efficiently than in the absence of the electron scavenger. In the presence of sulfur hexafluoride, ethyl ion in part undergoes the neutralization reaction (3)^{5,6} to give ethyl radical which then undergoes in part the hydrogen abstraction reaction (4) to give ethane. The fact that the decrement of *G*(C₂H₆) caused by the addition of ammonia is larger in C₄H₁₀-SF₆ mixture than in C₄H₁₀-SF₆-O₂ mixture suggests that the neutralization reaction (3) should be taken into consideration in the radiolysis of the C₄H₁₀-SF₆ mixture, because ethyl radical resulting from reaction 3 should be scavenged by oxygen.

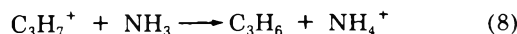
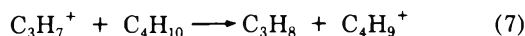


As shown in Figure 1, the yield of ethane from the *n*-C₄H₁₀-SF₆ mixture decreases with increasing ammonia concentration, while the yield of ethylene increases complementarily. From these observations, we can estimate the yield of ethyl ion produced by the fragmentation of *n*-

butane parent ion. Upon the addition of ammonia to the *n*-C₄H₁₀-SF₆ mixture, ethyl ion undergoes the proton transfer reaction (5) prior to the occurrence of the hydride-ion transfer reaction (2) and neutralization reaction (3). Thus, the decrease in the yield of ethane upon the addition of ammonia is ascribed to the suppression of reactions 2 and 3. Taking into consideration that ethyl radical produced by reaction 3 in part undergoes the hydrogen abstraction reaction (4) and that the yield of ethane decreases gradually even at the highest concentration of ammonia, we can estimate the *G* value of the ethyl ion to be more than about 0.25 from the decrement of ethane yield upon the addition of ammonia to the *n*-C₄H₁₀-SF₆ mixture. According to reactions 2–5, the *G* value of ethylene should be increased by more than 0.25 by the addition of ammonia to the C₄H₁₀-SF₆ mixture. However, the *G* value of ethylene increases upon the addition of ammonia by less than 0.25. This may be due to the occurrence of condensation reaction (6) besides the proton transfer reaction (5) between ethyl ion and ammonia.



The Yield of Propyl Ion. The yield of propyl ion can be estimated by a way similar to that for ethyl ion. The decrease in the yield of propane upon the addition of ammonia to the C₄H₁₀-SF₆ mixture is due to the occurrence of the proton transfer reaction (8) prior to the occurrence of the hydride-ion transfer reaction (7). Taking into consideration that the yield of propane decreases gradually even at the highest concentration of ammonia, we can estimate the *G* value of propyl ion to be more than about 0.15 from the decrement of propane yield upon the addition of ammonia to the C₄H₁₀-SF₆ mixture. The difference between the decrement of *G*(C₃H₈) caused by the addition of ammonia in the C₄H₁₀-SF₆ mixture and in the C₄H₁₀-SF₆-O₂ mixture might be referred to the occurrence of the neutralization of C₃H₇⁺ with SF₆⁻ and the hydrogen abstraction by C₃H₇ as mentioned in the case of C₂H₅⁺. In view of the relatively small yield of propyl ion and the experimental errors, however, the contribution of these reactions to the propane formation may be disregarded.



The Yield of Butyl Ion. As seen in Figure 2, the *G* value of total butene from the C₄H₁₀-SF₆-O₂ mixture attains a maximum value at low ammonia concentration and then

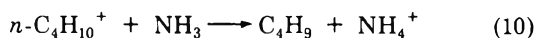
(5) An alternative reaction to (3)
 $\text{C}_2\text{H}_5^+ + \text{SF}_6^- \longrightarrow \text{C}_2\text{H}_4 + \text{HF} + \text{SF}_5$ (3')
 could take some part.⁶

(6) P. T. Holland and J. A. Stone, *Can. J. Chem.*, **48**, 3277 (1970).

decreases gradually with increasing ammonia concentration. At low ammonia concentration, the proton transfer reaction (9) occurs between ammonia and both butyl ion produced by the fragmentation of *n*-butane parent ion and one produced secondarily by the hydride-ion transfer reactions of ethyl and propyl ions, reactions 2 and 7. At high ammonia concentration, however, the ethyl and propyl ions thus produced have already been intercepted by ammonia and do not give butyl ion by hydride-ion transfer reactions. Thus, in the radiolysis of C_4H_{10} - SF_6 - O_2 mixture the *G* value of butyl ion produced by the fragmentation of *n*-butane parent ion can be estimated to be more than 0.6 from the increment of $G(C_4H_8)$ at high ammonia concentration, allowing again for the possible occurrence of the condensation reaction between $C_4H_9^+$ and NH_3 .



As seen in Figure 1, the *G* value of butene from the C_4H_{10} - SF_6 mixture increases gradually with increasing ammonia concentration. In this case, both butyl ion and *n*-butane parent ion undergo the proton transfer reactions (9) and (10) to give, respectively, butene and butyl radical, the latter of which partly gives butene in disproportionation reaction. On the one hand, the *G* value of butene produced by the proton-transfer reaction between ammonia and butyl ion resulting from hydride-ion transfer reactions of fragment ions should decrease with increasing ammonia concentration. On the other hand, the *G* value of butene produced by the disproportionation reaction of butyl radical resulting from the proton transfer reaction (10) should increase with increasing ammonia concentration. Thus, as a resultant of dual effects of ammonia, the *G* value of butene from the C_4H_{10} - SF_6 mixture may increase gradually with the increasing ammonia concentration.



It has been shown that parent-minus-H ion is produced by the fragmentation of parent ion with a fairly large yield in the liquid-phase radiolysis of propane^{4c} and *n*-hexane.⁷ The relatively large yield of parent-minus-H ion compared with the yields of other fragment ions seems to be characteristic of the radiolysis of liquid *n*-alkane. The following is offered as a plausible explanation for this characteristic. That is, even though the parent ion dissociates into a fragment ion and a large neutral fragment, the geminate pair will probably recombine efficiently. On the other hand, when a parent ion dissociates once into a parent-

minus-H ion and a hydrogen atom, the hydrogen atom may disappear from the vicinity of the ion more easily than does other neutral fragment. It should be taken into consideration here that the variation of the initial ion fragment pattern with the phase is also important in determining these yields. Thus the relatively large yield of parent-minus-H ion may be expected in the radiolysis of liquid *n*-alkane.

The Yields of Fragment Ions Obtained by the Use of Perdeuterated n-Butane. In Table II, the formation of isotopically mixed ethanes from the C_4H_{10} - C_4D_{10} - SF_6 - O_2 mixture suggests that the hydride-ion transfer reaction (2) is in part responsible for the formation of ethanes from the mixture. The bimolecular ethanes from the C_4H_{10} - C_4D_{10} - SF_6 - O_2 - NH_3 mixture may be produced by the hydrogen abstraction reaction of hot ethyl radical or by radical reaction in the spur. The *G* value of ethyl ion scavengable by ammonia is given by the difference between $G(C_2D_6 + C_2D_5H + C_2H_5D + C_2H_6)$ found for C_4H_{10} - C_4D_{10} - SF_6 - O_2 and C_4H_{10} - C_4D_{10} - SF_6 - O_2 - NH_3 mixtures. This difference is approximately equal to the decrement of $G(C_2H_6)$, caused by the addition of ammonia to the C_4H_{10} - SF_6 - O_2 mixture. Although the percentages of ethanes obtained do not seem to be sufficiently precise, it may be said that the decrease in yield of ethanes upon the addition of ammonia to the C_4H_{10} - C_4D_{10} - SF_6 - O_2 mixture is accounted for by a decrease in these isotopic species (C_2D_6 , C_2D_5H , C_2H_5D , C_2H_6) expected to result from reaction 2.

A discussion similar to the one above can be made on the isotopic distribution of propanes (Table III). Most of the propanes from the C_4H_{10} - C_4D_{10} - SF_6 - O_2 mixture consist of bimolecular propanes, suggesting that they are produced by the hydride-ion transfer reactions of propyl ions. In fact, the observation that the *G* value of propane from the C_4H_{10} - SF_6 - O_2 mixture decreased from 0.14 to 0.04 upon the addition of ammonia indicates that most of the propane from the mixture is produced by the hydride-ion transfer reaction of propyl ion.

Although the results obtained as above from relatively small *G* values include somewhat large errors, it may be suggested that the yields of fragment ions obtained by the use of ammonia are nearly equal to those obtained by the use of perdeuterated *n*-butane under the corresponding conditions.

(7) K. Shinsaka and S. Shida, *Bull. Chem. Soc. Jap.*, **43**, 3728 (1970).

Methylene Produced by Vacuum-Ultraviolet Photolysis. V. Energy Partitioning in the Reaction *cis*-Dimethylcyclopropane + $h\nu(123.6 \text{ nm}) \rightarrow 2\text{-Butene} + {}^1\text{CH}_2$

K. Dees and R. D. Koob*

Department of Chemistry, North Dakota State University, Fargo, North Dakota 58102 (Received May 18, 1972)

cis-1,2-Dimethylcyclopropane, (CDMC) with small amounts of oxygen added to scavenge free radicals, was photolyzed at 165, 147, and 123.6 nm. Among the primary processes was the reaction $\text{CDMC} = \text{CH}_2 + \text{cis-2-butene}$. The *cis*-2-butene (CB2) thus produced was observed not to isomerize at 165 and 147 nm, but did undergo pressure-dependent isomerization to *trans*-2-butene (TB2) at 123.6 nm. The relative yields of CB2 and TB2 were measured over the pressure range from 0.1 to 105 Torr. The ratio CB2/TB2 remained larger than unity at 0.1 Torr and approached infinity at high pressures. Further, the quantum yield of total 2-butene was observed not to vary over the pressure range investigated. The primary photoprocess at 123.6 nm appears to impart a broad range of energy to CB2. While photolysis at 123.6 nm may give up to 142 kcal mol⁻¹ excess energy in this reaction, no fraction of the CB2 produced has enough energy to cause observable dissociation of CB2 ($E_{\text{act}} = 85 \text{ kcal mol}^{-1}$) at 0.1 Torr. However, a considerable fraction may isomerize ($E_{\text{act}} = 65 \text{ kcal mol}^{-1}$) at this pressure. Nonetheless, it would appear from Figure 1 that even with extrapolation to very low pressures not all CB2 is capable of isomerizing. A detailed analysis of the pressure dependence of the CB2/TB2 ratio using RRKM formalism supports the suggestion that CB2 is produced with a broad range of energies. While a unique distribution function for the energy of CB2 could not be obtained, a family of such functions could be obtained. All were characterized by extreme broadness and tailing below E_0 , the minimum energy necessary for CB2 isomerization. Thus, qualitative agreement with the experimentally observed features was obtained, even though the complexity of the system and the absence of data for similar systems precluded a quantitative interpretation.

Introduction

The experimental investigations of the distribution of energy among the primary products of photochemical reactions have proved helpful in the elucidation of features of the overall reaction mechanisms. Studies of this kind have been possible for several types of complex molecules. One measure of the energy partitioning process is to compare the apparent average internal energy of the product molecules to the average internal energy predicted from a statistical partitioning model in which the total available excess energy is partitioned on a statistical basis among the vibrational modes of the product molecules. Studies of the photolyses of a cyclic ketone¹ and a cyclic ether² have indicated that the excess energy is partitioned such that the most complex product received more than a statistical share. On the other hand, studies of the photolyses of several complex azo compounds³⁻⁵ demonstrated that less than a statistical share of the excess energy was channeled into the most complex product. In these cases the energy distribution appeared to be governed by a rather broad distribution function. A recent study⁶ of energy partitioning on the photolysis of di-*tert*-butyl peroxide indicated that the *tert*-butoxy radical products are formed with a fairly narrow distribution of energy and that they contain less energy than predicted by a statistical model. These studies have clearly shown that energy partitionings for photochemical reactions of relatively complex molecules are complex processes governed by little understood potential hypersurfaces. Of particular help in understanding photochemical systems are the similar chemical activation studies.^{7,8} These systems have the

advantage of simplification in that the activated molecules are formed in the ground electronic state.

Recently,⁹ we reported on the distribution of available excess energy (133 kcal mol⁻¹) between methylene and ethane from the primary photolytic (123.6 nm) decomposition of propane. The methylene was found to contain $\geq 31 \text{ kcal mol}^{-1}$. Only a limit was placed on the average internal energy content of the ethane ($< 70 \text{ kcal mol}^{-1}$) due to its high energy of activation and the inaccessibility of its unimolecular decomposition pressure range. Similarly,¹⁰ methylene from the photolytic (165 nm) decomposition of cyclopropane was found to contain $\geq 31 \text{ kcal mol}^{-1}$. We report in this paper on the way energy is distributed to *cis*-2-butene (CB2) from a primary photolytic reaction of *cis*-dimethylcyclopropane (CDMC). The rela-

- (1) R. J. Campbell and E. W. Schlag, *J. Amer. Chem. Soc.*, **89**, 5103 (1967).
- (2) B. C. Roquette, *J. Amer. Chem. Soc.*, **91**, 7664 (1969).
- (3) T. F. Thomas, C. I. Sutin, and C. Steel, *J. Amer. Chem. Soc.*, **89**, 5107 (1967).
- (4) P. Cadman, H. M. Meunier, and A. F. Trotman-Dickenson, *J. Amer. Chem. Soc.*, **91**, 7640 (1969).
- (5) (a) F. H. Dorer, *J. Phys. Chem.*, **73**, 3109 (1969); (b) *ibid.*, **74**, 1142 (1970); (c) F. H. Dorer, E. Brown, J. Do, and R. Rees, *ibid.*, **75**, 1640 (1971).
- (6) F. H. Dorer and S. N. Johnson, *J. Phys. Chem.*, **75**, 3651 (1971).
- (7) (a) K. C. Kim and D. W. Setser, *J. Phys. Chem.*, **76**, 283 (1972); (b) K. Dees, D. W. Setser, and W. G. Clark, *J. Chem. Phys.*, **75**, 2231 (1971); (c) H. W. Chang, D. W. Setser, and M. J. Perona, *J. Phys. Chem.*, **75**, 2070 (1971).
- (8) P. N. Clough, J. C. Polanyi, and R. T. Taguchi, *Can. J. Chem.*, **48**, 2919 (1970).
- (9) J. H. Vorachek and R. D. Koob, *J. Phys. Chem.*, **76**, 9 (1972).
- (10) (a) A. K. Dhingra, J. H. Vorachek, and R. D. Koob, *Chem. Phys. Lett.*, **9**, 17 (1971); (b) A. K. Dhingra and R. D. Koob, *J. Phys. Chem.*, **74**, 4490 (1970).

tively low energy of activation of *cis*-*trans* isomerization of CB2 allowed the experimental determination of the *cis*-*trans* ratio over three orders of magnitude of pressure. Consequently, the forms of the distribution functions accounting for the energy channeled into CB2 could be investigated for several descriptions of the energetics for the primary photolytic reaction. Since the reverse reaction ($\text{CH}_2 + \text{olefin}$) has little, if any, energy of activation, the decomposition of CDMC does not involve an unknown "rearrangement energy" associated with the energy of activation. This important simplification suggests that the distribution of energy for CB2 is a direct reflection of the molecular absorption and fragmentation process. In contrast to other systems in which energy partitioning studies have been done, CDMC offers no chromophore for the obvious site for electronic excitation.

Experimental Section

CDMC (*cis*-dimethylcyclopropane) was obtained from Chemical Samples Co. and was used without further purification. The compound was listed as 99% pure; gpc indicated the impurities were other than decomposition products from the photolysis of the CDMC. The hydrogen used in some experiments was Air Products ultrahigh purity grade. Oxygen was Linde CP. Both were used without further purification.

A krypton resonance lamp described in detail earlier⁹ was used for the photolyses. The chromatic purity was >98% for the absorption region of CDMC. Several exploratory runs were made with a xenon resonance lamp also described previously.¹⁰

Small amounts of oxygen ranging from 5 to 10% of the total pressure were added to the reaction mixtures. This alleviated complications arising from free radicals and triplet methylene. For the photolyses of CDMC (and oxygen), interchangeable vessels of various sizes were attached to the window of the photolysis lamp in order to obtain pressures from 0.1 to 105 Torr. In several high-pressure experiments (1-10 atm) a specially designed high-pressure reaction vessel made from brass and Pyrex was used. In this case the total pressure was made up of ~3 cm pressure of CDMC, 0.5 cm of oxygen, and the remainder was accounted for by hydrogen.

To guard against the possibility of secondary photolyses of products, photolyses were carried to less than 1% conversion of parent to product in all experiments. This limit was achieved at very low pressures where product analyses became difficult due to the small amounts of starting products. All gas reaction mixtures were prepared on a standard vacuum rack. The analyses were performed by gas chromatography on a 20 ft, 0.25 in. o.d. 25% (w/w) squalane column maintained at ambient temperature. The high-pressure runs with hydrogen were analyzed by the above column and a 16 ft, 0.25 in. o.d. silica gel column maintained at ambient temperature. The silica gel was used to separate hydrogen and methane.

Results

Butenes formed in the photolysis of 1,2-dimethylcyclopropanes do not isomerize when the absorbed photon corresponds to 165¹⁰ and 147 nm, respectively. Isomerization of these products does occur for photolysis at 123.6 nm at low and moderate pressures. The ratio of *cis*-2-butene to *trans*-2-butene in the photolysis of *cis*-1,2-dimethylcyclopropane (CDMC) approaches infinity at high pressures,

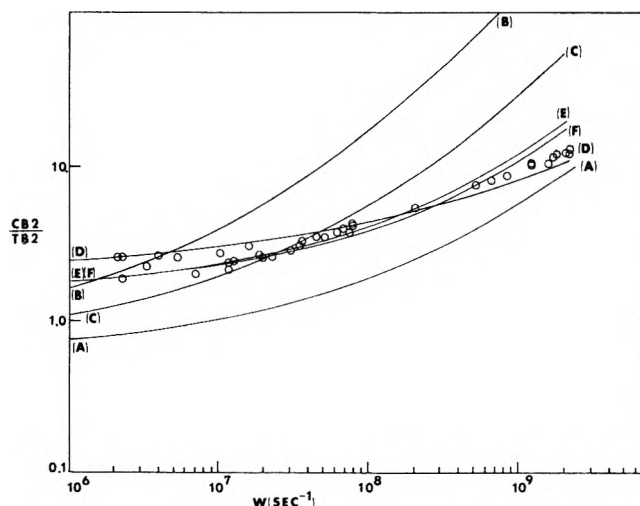
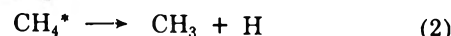


Figure 1. The experimental CB2/TB2 ratios as a function of collision frequency plotted on a log-log axes. The solid lines are the results of model calculations using eq 17. The models and parameters are identified in Table I. CDMC is the deactivation gas in all experiments.

but does not become as small as unity at low pressures.

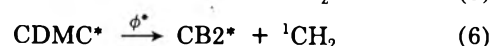
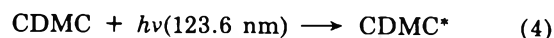
The experimental CB2/TB2 ratios are displayed in Figure 1 as a function of collision frequency (ω). The collision diameters¹¹ of 7.0 Å for CDMC and 6.5 Å for CB2 were used to convert experimental pressures to ω . The presence of the small amounts of oxygen was neglected in the ω calculation. High-pressure runs from 1- to 10-atm total pressure with large excesses of hydrogen added to the CDMC and oxygen mixtures were performed. The reactions of interest are



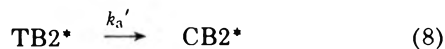
where ${}^1\text{CH}_2$ arises directly from the photolysis of CDMC. No significant increase in CH_4 yield was found even at 10-atm of pressure. A small constant amount of CH_4 from some unidentified source was present. This result may be directly interpreted as indicating that all methylenes formed in the primary photodissociation carry excess internal energy, a conclusion consistent with previous studies.^{9,10}

No detectable decrease in the total quantum yield of CB2 and TB2 was found even at 0.1 Torr. Hence, unimolecular decomposition of CB2^* and TB2^* was unimportant in our system. It is estimated that >15% unimolecular decomposition of CB2^* or TB2^* could be detected based on the scatter of the lowest pressure points.

The following general mechanism is consistent with the experimental results. *cis*-2-Butene is designated as CB2, *trans*-2-butene as TB2, and *cis*-dimethylcyclopropane as CDMC.



(11) D. W. Setser and B. S. Rabinovitch, *Can. J. Chem.*, **40**, 1425 (1962).



The primary photolytic reactions 5 and 6 account for approximately 10% of the total quantum yield for disappearance of CDMC. Any $^3\text{CH}_2$ and all free radicals were scavenged by the addition of small amounts of oxygen. An asterisk was maintained on CB2 and TB2 to indicate sufficient internal energy was retained to allow for possible unimolecular isomerization. Because the ratio of CB2 to TB2 does not appear to reach the thermodynamic value even with extrapolation, Figure 1, reaction 5 was included to account for a source of CB2 that could not undergo unimolecular isomerization. Subsequent analyses (Discussion section) suggest that reaction 5 accounts for a significant fraction of CB2 yield.

That CB2 is produced in a primary process in which methylene is eliminated from CDMC is clear,¹⁰ since there is no alternative reaction channel by which a C_4H_8 fragment may be produced which is consistent with the thermodynamics of the system. Bimolecular reaction modes with the exception of $^1\text{CH}_2$ reactions are eliminated by the presence of the radical inhibitor O_2 . That the CB2 results from the elimination of the unsubstituted CH_2 in the cyclopropane ring is less straightforward. Methylene could conceivably be eliminated also from either of the methyl groups in CDMC. The methylcyclopropane so produced could then isomerize to yield 2-butenes. This isomerization would yield both *cis*- and *trans*-2-butenes, *cis*- and *trans*-1-butene, and isobutene. At 147 and 165 nm, no *trans*-butene was produced. Thus this reaction channel is not competitive at these energies, even though it presumably is energetically available (CH_2 is produced in the 147-nm photolysis of propane, for example¹⁰). The possibility of CH_2 elimination becoming competitive at the larger energies employed in this study exists, but does not appear likely as no isobutene is found among the products of CDMC photolysis at 123.6 nm. Since isobutene to 2-butenes yield ratios vary from 0.3 to 0.5 in the isomerization of methylcyclopropane under a variety of conditions,¹² we conclude that the only source of observable 2-butenes is the primary photoelimination of CH_2 from the unsubstituted ring position in CDMC.

Discussion

A steady-state analysis of reactions 4–10 gives the rate of formation, R , of CB2 and TB2 as

$$R(\text{CB2}) = \phi(\text{CDMC}^*) + \omega(\text{CB2}^*) \quad (11)$$

$$R(\text{TB2}) = \omega(\text{TB2}^*) \quad (12)$$

The steady-state concentrations of CB2^* and TB2^* are

$$(\text{CB2}^*) = \frac{\phi^*(\text{CDMC}^*)(k_a' + \omega)}{\omega(k_a + k_a' + \omega)} \quad (13)$$

$$(\text{TB2}^*) = \frac{\phi^*(\text{CDMC}^*)k_a}{\omega(k_a + k_a' + \omega)} \quad (14)$$

Substitution of eq 13 and 14 into eq 11 and 12 gives the following expression for the CB2/TB2 ratios

$$\frac{(\text{CB2})}{(\text{TB2})} = \frac{R(\text{CB2})}{R(\text{TB2})} = \frac{\phi}{\phi^* k_a} + \left[\frac{(k_a' \omega)}{(k_a + k_a' + \omega)} \right] \left/ \left[\frac{k_a}{(k_a + k_a' + \omega)} \right] \right. \quad (15)$$

Equation 15 shows that the apparent CB2/TB2 ratio is accountable for by two separate and distinct terms. The first term, involving the ratio of ϕ and ϕ^* , features the CB2 from reaction 5 which cannot isomerize. One possibility¹³ is to view this CB2 as merely the CB2 formed below the critical energy, ϵ_0 , for isomerization.

The second term of (15) accounts for the CB2 and TB2 originating from the CB2^* from reaction 6. This can be readily seen by setting $\phi = 0$. For this condition

$$\frac{(\text{CB2})}{(\text{TB2})} = \left[\frac{(k_a' + \omega)}{(k_a + k_a' + \omega)} \right] \left/ \left[\frac{k_a}{(k_a + k_a' + \omega)} \right] \right. \quad (16)$$

The apparent experimental CB2/TB2 ratios can be related to the microscopic rate constants, k_E , in a manner similar to earlier nonequilibrium unimolecular systems.¹⁴ If all excited CB2 were formed above the critical energy for isomerization and could either isomerize or be collisionally stabilized, replacing k_a and k_a' by their respective microscopic rate constants and integrating over a proper internal energy range to account for an internal energy distribution function, $f(E)$, would give

$$\frac{\text{CB2}}{\text{TB2}} = \frac{\int_{E=0}^{E^+} \frac{(k_E' + \omega)}{(k_E + k_E' + \omega)} f(E) dE}{\int_{E=0}^{E^+} \frac{k_E}{(k_E + k_E' + \omega)} f(E) dE} \quad (17)$$

E^+ is the active energy above that required for isomerization. Equation 17 is based on the internal energy distribution function for the steady-state concentration of CB2^* . Calculation of CB2/TB2 is straightforward for an $f(E)$ which is placed totally above ϵ_0 on the energy scale. However, for the case of a $f(E)$ which extends below ϵ_0 , and CB2 (reaction 5) and CB2^* belong to the same electronic state, CB2 in eq 17 represents only the stabilized CB2 from reaction 9. For a properly normalized $f(E)$, the CB2 represented in reaction 5 and the first term in eq 15 is given by

$$\text{CB2}(\phi) = 1.0 - (\text{CB2}[\phi^*] + \text{TB2}) \quad (18)$$

where $\text{CB2}(\phi^*)$ and TB2 are those calculated from eq 17 using the part of the normalized $f(E)$ which extends above ϵ_0 . Hence, for this case, the theoretical ratios to be compared to experiment are $(\text{CB2}[\phi] + \text{CB2}[\phi^*])/\text{TB2}$.

An accurate knowledge of the specific rate constants k_E and k_E' allows the experimental ratios to be fit with an appropriate internal energy distribution function, $f(E)$. Unfortunately, due to the large variation in the reported¹⁵

- (12) (a) See ref 16; (b) A. K. Dhingra, Ph.D. Thesis, North Dakota State University, available University Microfilms, Ann Arbor, 1972; (c) M. G. Topor and R. W. Carr, submitted for publication.
 (13) A. W. Kirk and E. Tschuikow-Roux, *J. Chem. Phys.*, **51**, 2247 (1969).
 (14) D. W. Setser and B. S. Rabinovitch, *Advan. Photochem.*, **3**, 1 (1964).
 (15) (a) G. B. Kistiakowsky and W. R. Smith, *J. Amer. Chem. Soc.*, **58**, 766 (1936); (b) W. F. Anderson, J. A. Bell, J. M. Diamond, and K. R. Wilson, *J. Amer. Chem. Soc.*, **80**, 2384 (1958); (c) B. S. Rabinovitch and K. W. Michel, *ibid.*, **81**, 5065 (1959); (d) R. B. Cundall and T. F. Palmer, *Trans. Faraday Soc.*, **57**, 1936 (1961); (e) A. Lifshitz, S. H. Bauer, and E. L. Resler, Jr., *J. Chem. Phys.*, **38**, 2056 (1963); (f) P. M. Jeffers and W. Shaub, *J. Amer. Chem. Soc.*, **91**, 7706 (1969).

energy of activation, ϵ_a , and the Arrhenius A values, it was not possible to select a unique set of k_E . The preferred values by Benson and O'Neal¹⁶ of $\log k_\infty = 13.78 - 62,800/\theta$, selected from a review of the experimental reportings, were those of Rabinovitch and Michel.^{15c} This choice appears to be consistent with the parameters measured for cis-trans isomerization of similar compounds^{15f,17} and also with a recent shock tube measurement^{15f} for CB2. However, the k_{uni} (RRKM theory) calculated from an activated complex model based on these parameters failed to predict the thermal unimolecular fall-off behavior for cis-trans isomerization of CB2.^{18,19} In fact, the fall-off behavior is predicted well¹⁸ by a model based on the larger Arrhenius parameters measured by Lifshitz, *et al.*,^{15e} of $\log k_\infty = 14.54 - 65,000/\theta$. Due to these considerations we have carried out calculations using two sets of k_E : those calculated from the model of Lin and Laidler¹⁸ (based on $\log k_\infty = 14.54 - 65,000/\theta$) and those calculated from the model of Weider and Marcus¹⁹ (based on $\log k_\infty = 13.78 - 62,800/\theta$). These two sets of k_E are hereafter designated model 1 and 2, respectively. The specific rate constants were calculated (or reproduced) using the RRKM theory²⁰ and we assume the general validity of this formulation for our experimental conditions. In each case the k_E' (trans to cis isomerization) were calculated using exactly the same model as for the k_E (cis to trans isomerization) except ϵ_0 was raised 1.24 kcal mol⁻¹ to account for the difference in ΔH_0° ²¹ for the forward and reverse isomerization. Further details on the models are given in the Appendix.

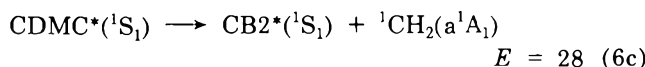
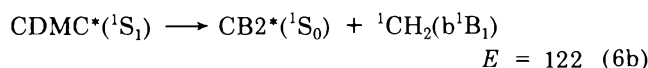
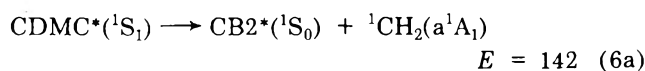
The maximum amount of internal energy that may be distributed between ¹CH₂ and CB2 from CDMC decomposition is given by

$$E = h\nu(123.6 \text{ nm}) + \Delta H_f^\circ(^1\text{CH}_2) + \Delta H_f^\circ(\text{CB}_2) - \Delta H_f^\circ(\text{CDMC}) + (H_{298} - H_0)(\text{CDMC}) = 142 \text{ kcal/mol}^{-1}$$

ΔH_f° refers to the standard state heat of formation at 0°K. The $(H_{298} - H_0)$ term is for the internal modes (vibrations in our case) which are not considered adiabatic for the partitioning process. The following thermodynamic values were selected (all in kcal mol⁻¹): $\Delta H_f^\circ(^1\text{CH}_2) = 91.9$;^{22a} $\Delta H_f^\circ(\text{CDMC}) = 4.7$;¹² $\Delta H_f^\circ(\text{CB}_2) = 3.48$;²¹ and $(H_{298} - H_0)(\text{CB}_2) = 1.61$.^{22b} Although ¹CH₂ is known to be a higher electronic state than ³CH₃, the difference in energy between the electronic states is thought to be small.²³ Due to the present uncertainty in the ΔH_f° value for methylene, we assumed $\Delta H_f^\circ(^3\text{CH}_2) = \Delta H_f^\circ(^1\text{CH}_2)$ and selected the value of Chupka and Lifshitz^{22a} for ³CH₂.

Since the electronic states of products and reactants in the primary process are not well known, a survey approach to the calculation was necessary. Likely descriptions of the energetics for CDMC* decomposition were used as parameters. Reflection on the thermodynamics and separate experimental evidence indicates that the two simplest possibilities generate ¹CH₂ in the ¹A₁ and ¹B₁ states as in reaction 6a and 6b. ¹S₀ and ¹S₁ represents the lowest and first excited singlet states. The CDMC* is most likely decomposing from an excited singlet state. When electronic excitation energy is partitioned, as well as vibrational energy, and when the products are in their lowest singlet states reaction 6a has the maximum E value of 142 kcal mol⁻¹. The ¹CH₂(¹B₁) and ¹CH₂(¹A₁) states are located ~20 and 70 kcal mol⁻¹, respectively,

above the ¹CH₂(¹A₁) electronic state.²⁴ Hence, the maximum E value for reaction 6b must be reduced 20 kcal mol⁻¹ to account for the electronic energy contained in ¹CH₂(¹B₁). The ¹CH₂(¹A₁) case was not considered because the maximum E value would be ~62 kcal mol⁻¹. Since ϵ_0 for CB2* isomerization is 62-63 kcal mol⁻¹, a maximum energy of 62 kcal mol⁻¹ to be distributed allows negligible probability for isomerization. The possibility of the formation of the ¹S₁ electronic state for CB2*, as in reaction 6c, was not considered at this time for the following reasons. The energy associated with the ¹S₁ state of CB2 is estimated by comparison to ethylene^{24,25} as ~114 kcal mol⁻¹ above the ¹S₀ state; the E for reaction 6c would be ~28 kcal mol⁻¹. Earlier work¹⁰ on a similar system (c-C₃H₆ → ¹CH₂ + C₂H₄) indicated that ¹CH₂ carries, on the average ≥31 kcal mol⁻¹ into an insertion product (¹CH₂ + C₃H₈ → C₄H₁₀). Assuming that the average internal energy of ¹CH₂ should be of a similar magnitude for CDMC* decomposition, reaction 6c would be unimportant.



The direct formation of an excited triplet state of CB2 is also unlikely. It seems well established that the triplet state (or states) formed in Hg photosensitization of CB2²⁶ eventually stabilizes to nearly a 50-50 mixture of CB2 and TB2 (experiments run at 60-81 Torr). Since nearly negligible TB2 is found at pressures >105 Torr in our work, it is unlikely that there is any direct formation of the triplet state of CB2 in our system. Existing evidence thus argues that CB2* is a vibrationally excited ground electronic state species.

Several important facts can be inferred about the $f(E)$ for the vibrationally excited CB2 from CDMC* decomposition. First; the lack of significant cis-trans isomerization in 147-nm photolyses indicates that nearly the total $f(E)$ lies below ϵ_0 under these conditions. The thermodynamics predicts a maximum internal energy, E , to be distributed of ~105 kcal mol⁻¹. Use of the higher-energy 123.6-nm line increases the maximum E and apparently shifts the

(16) S. W. Benson and H. E. O'Neal, *Nat. Bur. Stand. (U. S.), Ref. Data System*, NBS-21, (1970).

(17) M. C. Flowers and N. Jonathon, *J. Chem. Phys.*, **50**, 2805 (1969).

(18) M. C. Lin and K. J. Laidler, *Trans. Faraday Soc.*, **64**, 94 (1968).

(19) G. M. Weider and R. A. Marcus, *J. Chem. Phys.*, **37**, 1835 (1962).

(20) (a) R. A. Marcus and O. K. Rice, *J. Phys. Colloid Chem.*, **55**, 894 (1951); (b) R. A. Marcus, *J. Chem. Phys.*, **20**, 352, 359 (1952); (c) *ibid.*, **43**, 2658 (1965).

(21) F. D. Rossini, "Selected Values of Physical and Thermochemical Properties of Hydrocarbons and Related Compounds," Carnegie Press, Pittsburgh, Pa., 1953.

(22) (a) W. A. Chupka and C. Lifshitz, *J. Chem. Phys.*, **48**, 1109 (1968). (b) Calculated using statistical mechanical equations. The torsions were considered low-frequency vibrations.

(23) (a) W. Braun, A. M. Bass, and M. Pilling, *J. Chem. Phys.*, **52**, 5131 (1970); (b) R. W. Carr, Jr., T. W. Eder, and M. G. Topor, *ibid.*, **53**, 4716 (1970).

(24) G. Herzberg, "Electronic Spectra of Polyatomic Molecules," Van Nostrand, Princeton, N. J. 1967.

(25) J. T. Gary and L. W. Pickett, *J. Chem. Phys.*, **22**, 599 (1954).

(26) R. J. Cvetanovic, *Prog. React. Kinet.*, **2**, 73 (1964).

$f(E)$ such that a large portion lies above ϵ_0 since isomerization is found.

A second restraint on the $f(E)$ is the limitation on total energy imposed by the unimolecular decomposition of CB2*. Vibrationally excited CB2 can undergo hydrogen atom rupture²⁷ as depicted in reaction 19. The ϵ_{act} for this reaction is ~ 85 kcal mol⁻¹.²⁷ Our experiments showed that no decrease in the quantum yields of CB2 and TB2 was evident even at 0.1 Torr. Since an experimental decrease in the yield of the butene could be detected for >15% unimolecular decomposition, the shape of the $f(E)$ must be such that the total area which extends above 85 kcal mol⁻¹ must predict <15% unimolecular decomposition by H atom rupture. It is apparent that an estimate of the unimolecular decomposition for each trial $f(E)$ is needed. The predicted percentages of decomposition were calculated in a manner similar to the calculations using eq 19. The k_E values for CB2 unimolecular decomposition were based on the best models presented for the similar reaction of H atom rupture from propene²⁸ (see Appendix). These predicted decomposition values are of an approximate nature due to this estimation procedure.



The RRKM based energy partitioning model of Lin and Rabinovitch²⁹ was first employed for the $f(E)$. For this model

$$f(E) = \frac{N(E) \sum_{E=0}^{E^*-E} P_R(E^* - E)}{\sum_{E=0}^{E^*} P^+(E^*)} \quad (20)$$

For an activated complex for CDMC decomposition, $N(E)$ is the density of states for the internal degrees of freedom that will become CB2 and ΣP_R is the sum of states (between the designated energies) for the remainder of the internal degrees of freedom of the complex. ΣP^+ (normalization factor) is the sum of states for the internal degrees of freedom of the complex having excess energy E^+ . The CDMC activated complex was assumed to be identical with the molecule³⁰ with the 890-cm⁻¹ frequency chosen as a reaction coordinate. This choice for the complex and the reaction coordinate is not critical since the $f(E)$ are rather insensitive to the complex chosen. The sums and densities were computed with the same computer programs used to compute the k_E in (17). Equation 20 is often used⁶ to discern whether the total excess energy (including electronic energy) is statistically partitioned to the products. The statistical model $f(E)$ for reaction 6a ($E = 142$ kcal mol⁻¹) and 6b ($E = 122$ kcal mol⁻¹) are displayed as curve A and curve B in Figure 2. Curve B satisfies the unimolecular decomposition restraint since <10% decomposition is expected at 0.1 Torr. On the other hand, the validity of curve A is marginal since 21% unimolecular decomposition is predicted at 0.1 Torr. Using eq 17 and statistical curve B the predicted CB2/TB2 ratios, as a function of ω are displayed in Figure 1 as curves A and B for the model 1 and 2 sets of k_E . Curve C is the predicted ratios for statistical curve A and the model 1 set of k_E . The use of the model 2 set of k_E with curve A gives a similar curve to the others in that too small cis-trans ratios are predicted at 0.1 Torr and too large of ratios are predicted at 100 Torr. It is apparent that the statistical $f(E)$

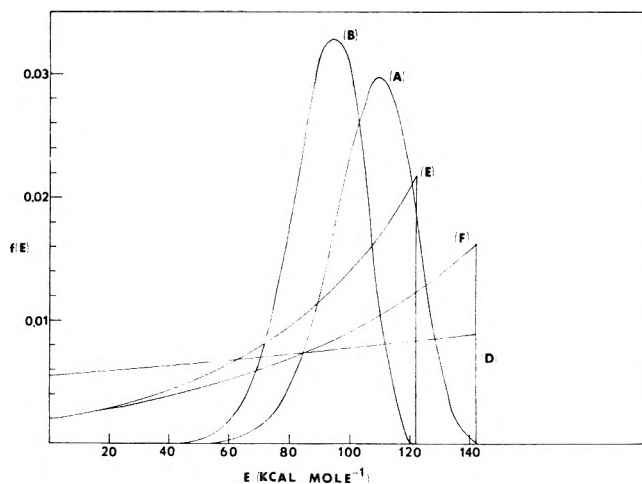


Figure 2. Calculated distribution functions for the excess internal energy partitioned to CB2. Curve A and B are statistical distribution functions calculated from eq 20 with a total available internal energy of 142 and 122 kcal mol⁻¹, respectively. The remainder of the curves are exponential distribution functions calculated from eq 21 and the parameters listed in Table I.

fails badly for all cases. One possibility is that not all internal energies are available for partitioning. Computation wise, this occurrence can be approximated by allowing less total excess energy to be statistically distributed. Merely shifting the statistical $f(E)$ such that the maxima occur at even lower energies still fails to predict the experimental ratios.

The forms of the $f(E)$ needed to predict the experimental cis-trans ratios were determined by an iterative computer procedure in which two selected functions were varied in effective width. The gaussian and exponential were chosen as representative of expected type functions. It will be shown that, within the theoretical framework presented here, the two constraints of predicting the experimental cis-trans ratios and accounting for the lack of unimolecular decomposition of CB2 puts quite severe limitations on the $f(E)$. The mathematical form of the exponential and gaussian $f(E)$ are given as

$$f(E) = \frac{\exp(E/\sigma)}{\sum \exp(E/\sigma)} \quad (21)$$

$$f(E) = \frac{\exp\left(-1/2\left[\frac{E_{mp} - E_i}{\sigma}\right]^2\right)}{\sum \exp\left(-1/2\left[\frac{E_{mp} - E_i}{\sigma}\right]^2\right)} \quad (22)$$

σ is a constant governing the effective width of the functions.

The exponential $f(E)$ that best predicted the experimental ratios (without regard to unimolecular decomposition) are displayed in Figure 2. Curves D and E are the $f(E)$ for a total internal energy of 142 (reaction 6a) and 122 kcal mol⁻¹ (reaction 6b) using the model 1 set of k_E . Curve F is the $f(E)$ for a total internal energy of 142 kcal mol⁻¹ (reaction 6a) and using the model 2 set of k_E . With a constraint of 122 kcal mol⁻¹ (reaction 6b), the experi-

(27) E. Jakubowski, H. S. Sandhu, and O. P. Strausz, *J. Amer. Chem. Soc.*, **93**, 2610 (1971).

(28) J. W. Simons, B. S. Rabinovitch, and F. H. Dorer, *J. Phys. Chem.*, **70**, 1076 (1966).

(29) Y. N. Lin and B. S. Rabinovitch, *J. Phys. Chem.*, **74**, 1769 (1970)

(30) C. M. Richards and J. Rud Nielsen, *J. Opt. Soc. Amer.*, **40**, 442 (1950).

Table I: Calculation Parameters

Reaction	k_{ϵ} model	a	E^b	Figure 1 designation	Figure 2 designation	Average ^c energy	$E(<\epsilon_0)^d$
3a	1	280	142	D	D	77.5	0.37
3a	2	70	142	F	F	94.0	0.22
3b	1	50	122	E	E	84.0	0.23
3a	1	e	142	A	A	107.0	0.0
3b	2	e	122	B	B	91.5	0.02
3b	1	e	122	C	B	91.5	0.02

^a The σ value is for eq 21. ^b E = excess internal energy to be distributed (kcal mol⁻¹). ^c The mathematical values of the average energy are listed, although much of the practical meaning is lost for broad distribution functions. ^d This value represents the fraction (relative to unity) of the distribution function which was below ϵ_0 on the energy scale. ^e Equation 20 was used for the $f(\epsilon)$.

mental ratios could not be predicted with the model 2 set of k_E . The predicted theoretical curves using curves D, E, and F of Figure 2 are shown as curves D, E, and F, respectively, in Figure 1. Table I lists all important parameters and thermodynamic values. The predicted percentages of decomposition of H rupture were as follows: curve D, 19%; curve E, 9%; and curve F, 35%. Hence, curve F must be eliminated and curve D is of questionable validity. It is apparent from the elimination of curve F that the model 2 set of k_E cannot predict the experimental ratios with the exponential $f(E)$.

If the model 1 set of k_E are accepted, the most significant features of the corresponding curves D and E are their extreme broadness. It should be noted from Table I that 20–40% of the total area extends below the critical energy for isomerization. This was the most dominant feature of the calculations. Since the fraction of $f(E)$ below ϵ_0 represents CB2* which cannot isomerize, the gross effect of increasing or decreasing this fraction was to raise or lower the CB2/TB2 ratio scale. Enough area of the $f(E)$ must lie below ϵ_0 to raise the theoretical CB2/TB2 ratio to fit the experimental ratios at 0.1 Torr. The use of the statistical $f(E)$ is an example of the theoretical fit if no percentage of the $f(E)$ lies below ϵ_0 . The inclusion of area of the $f(E)$ below ϵ_0 resulted in a dampening effect on the sensitivity of the calculations to the exact form of the $f(E)$. The exponential $f(E)$ proved to be of more general use. The gaussian $f(E)$ worked as well as the exponential $f(E)$ at high energies (~ 142 kcal mol⁻¹) but failed at lower energies. At these high energies an $f(E)$ which is nearly a constant function of energy, for example, curve D, is needed and the difference between a broad gaussian and a broad exponential is minimal. For example, curve D of Figure 1 is nearly exactly reproduced by an extremely broad gaussian with an E_{mp} of 110 kcal mol⁻¹ and a σ value of 105. It should be noted that curves D and E are based on the maximum internal energy available for reaction 6a or 6b. If the decomposition process channels energy into translation or overall rotations of the products, the E values would be less than the maximum available. In this case curves D and E of Figure 2 would merely represent the form of the $f(E)$. This interesting feature originates from the fact that the experimental ratios are not predicted by a unique exponential $f(E)$. In fact, a set of adequate exponential $f(E)$ can be generated, as a function of total energy E , from approximately $E = 110$ – 140 kcal mol⁻¹. The $E = 140$ value is an extreme upper limit due

to the unimolecular decomposition arguments presented earlier. A more exact theoretical fit of the experimental CB2/TB2 ratios than shown would require a more elaborate $f(E)$ than the simple exponential forms used here. Since E_{max} is not uniquely known, it is pointless to pursue a "better" distribution function using the present data alone.

The analyses and calculations are based on the unit deactivation assumption inherent in eq 17. In an effort to estimate the error incorporated by this assumption, a simple stepladder deactivation model³¹ was employed with only reactions 7 and 9 considered. The model has been described previously³¹ and basically allows each collision to remove from an excited molecule a specified constant amount of energy. The results showed that for the broad $f(E)$ such as curves D and F of Figure 2, the predicted CB2/TB2 ratios are almost totally dominated by the breadth of the $f(E)$ function and collisional deactivation (>4 kcal per collision) has little effect.

From an RRKM treatment of the CB2/TB2 pressure dependence using a moderately loose model and the assumption that 2-butene is produced in a vibrationally excited electronic ground state, it may be concluded that about 20% of the butenes are formed with less than 62 kcal mol⁻¹, 30% with energies between 62 and 85 kcal mol⁻¹, and the remaining 50% with energies greater than 85 kcal mol⁻¹. The exact shape of the distribution function of the energy of the butenes, however, cannot be determined from our data.

Summary

CB2 produced from CDMC at 165 and 147 nm does not isomerize and undergoes incomplete isomerization at 123.6 nm in spite of potentially large energies in excess of the activation energy at each wavelength. The CB2 produced at all three wavelengths undergoes no observable dissociation at pressures as low as 0.1 Torr. These features are coupled with a RRKM treatment of the pressure dependence of CB2 isomerization at 123.6 nm to provide a qualitative picture of the energy carried by the CB2 as it is produced in the photolysis of CDMC. A quantitative interpretation is precluded by the complexity of the system and the distribution of energy to CB2 may only be estimated.

Acknowledgment. The support of this work by the National Science Foundation is gratefully acknowledged. We wish to thank Professor D. W. Setser of Kansas State University for the generous loan of computer programs.

Appendix

The grouped molecular CB2 frequencies³⁰ were 2976(8), 1670(1), 1433(7), 1196(2), 980(6), 622(2), 396(1), and 279(3). The Lin and Laidler¹⁸ CB2 cis–trans isomerization complex frequencies were 2980(8), 1672(1), 1452(5), 1340(3), 1000(7), 304(3), and 131(2). The Weider and Marcus¹⁹ CB2 cis–trans isomerization complex frequencies were 3000(8), 1385(7), 1154(5), 924(3), and 230(3). These frequencies predict¹⁸ an ϵ_0 factor of 62.6 and 61.8 kcal mol⁻¹ for the former model 1 and latter model 2, respectively. Harmonic oscillator models¹⁴ were used to evaluate the sums and densities of states for the RRKM equations.

(31) (a) D. W. Setser and J. C. Hassler, *J. Phys. Chem.*, **71**, 1364 (1967); (b) G. H. Kohlmaier and B. S. Rabinovitch, *J. Chem. Phys.*, **38**, 1962 (1963).

The RRKM calculations were performed using an exact count calculation for the sum of states at low E^+ . The Haarhoff approximation³² was used for the density of states of the molecule and the sum of states at high E^+ values. The moments of inertia for the complex and molecule were assumed identical. All overall rotations were assumed adiabatic. A reaction path degeneracy of 2 was employed.

The model for unimolecular decomposition of CB2 by hydrogen atom rupture was approximated by adding identical frequencies characteristic of a methyl group to both the complex and molecule for propene unimolecular decomposition by hydrogen rupture.²⁸ The ϵ_0 was taken as 85 kcal mol⁻¹ and a reaction path degeneracy of 6 was used.

(32) P. C. Haarhoff, *J. Mol. Phys.*, **6**, 337 (1963); **7**, 101 (1963).

Studies on the Formation of Primary Yields of Hydroxyl Radical and Hydrated Electron in the γ -Radiolysis of Water

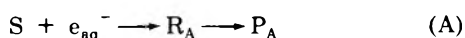
Z. D. Draganić and I. G. Draganić*

Boris Kidrič Institute of Nuclear Sciences, Belgrade, Yugoslavia (Received August 21, 1972)

The formation of G_{OH} and $G_{e_{aq}^-}$ was studied in γ -irradiated aqueous solutions containing selected mixtures of scavengers for both oxidizing and reducing primary radical products of water decomposition. Various assumptions based on the free-radical model of water radiolysis were experimentally tested. It has been shown that efficient scavenging of e_{aq}^- increases not only $G_{e_{aq}^-}$ but also G_{OH} , by reducing the extent of water re-formation and leaving more OH radicals for other reactions. Similarly, the removal of OH leads not only to an increase in G_{OH} but also in $G_{e_{aq}^-}$. Unifying curves were obtained for the dependence of observed fractional changes, G/G^0 , on reactivities. The results obtained for solutions containing simultaneously larger amounts of scavengers for both the hydroxyl radical and hydrated electron fit the unifying curves well and point out that the secondary spur reactions are exceptions even at reactivities up to about 10^{10} sec⁻¹. It has been found that the yield of water decomposition increases with reactivity. The values of $G(-H_2O)$, calculated according to the equation of material balance both from the primary oxidizing and reducing yields, agree well up to the reactivity of 10^9 sec⁻¹. At larger reactivities the water decomposition yields calculated from the yields of primary reducing species are lower and possible reasons for this are considered. A summary of the reactivity influence on all primary free-radical and molecular yields of water γ -radiolysis is given.

Introduction

The use of higher solute concentrations, *e.g.*, in studying early events in the radiolysis of water or aqueous solutions, requires the knowledge of primary free-radical yields ($G(R)$) at higher reactivities, $\nu_R = k_{R+S}[S]$, in reciprocal seconds. Here, R is H, OH, or e_{aq}^- , S is the scavenger concentration in M and k_{R+S} the corresponding rate constant in M⁻¹ sec⁻¹. Our present knowledge of $G(R)$ is, however, mainly based on experiments with dilute solutions.¹ Theoretical considerations of the spur model²⁻⁴ predict an increase of $G(R)$ with increasing reactivity toward R because of radical removal from the places of localized energy depositions. Experimental verification can be based on the measurement of the free-radical or stable product yields at increasing scavenger concentrations in the reactions



where S and RH are the appropriate scavengers, R_A and

R_B the short-lived intermediates, and P_A and P_B the corresponding stable products. However, only scarce information can be found in the literature; the radiolysis of concentrated solutions⁵⁻⁷ provides some data; relative values of $G_{e_{aq}^-}$, observed at nano- and picosecond scale in pulsed electron beam experiments, have recently been reported for various scavengers at larger concentrations.^{8,9} Also, some systematic studies in a relatively limited range of reactivities were reported concerning the dependence of

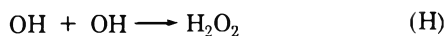
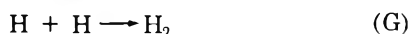
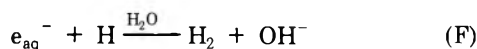
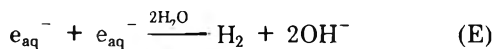
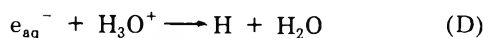
- (1) I. G. Draganić and Z. D. Draganić, "The Radiation Chemistry of Water," Academic Press, New York, N. Y., 1971.
- (2) A. H. Samuel and J. L. Magee, *J. Chem. Phys.*, **21**, 1080 (1953).
- (3) A. Kuppermann in "Radiation Research 1966," G. Silini, Ed., North-Holland Publishing Co., Amsterdam, 1967, p 212.
- (4) H. A. Schwarz, *J. Phys. Chem.*, **73**, 1928 (1969).
- (5) M. F. Hecquet, J. C. Roux, G. N. Simonoff, and J. Sutton, *Int. J. Radiat. Phys. Chem.*, **1**, 529 (1969).
- (6) Ch. Baquey, J. C. Roux, and J. Sutton, *J. Phys. Chem.*, **74**, 4210 (1970).
- (7) B. Hickel, Report No. CEA-R-4046, 1970.
- (8) (a) E. Peled and G. Czapski, *J. Phys. Chem.*, **75**, 3626 (1971); (b) G. W. Buxton, *Proc. Roy. Soc., Ser. A*, **328**, 9 (1972).
- (9) R. K. Wolff, M. J. Brncskill, and J. W. Hunt, *J. Chem. Phys.*, **53**, 4211 (1970); J. E. Aldrich, M. J. Brncskill, R. K. Wolff, and J. W. Hunt, *ibid.*, **55**, 530 (1971).

G_{OH} on the reactivity toward OH^{10} and of $G_{e_{aq}^-}$ on the reactivity toward e_{aq}^- .^{8,11-15}

Another aspect of the $G(R)$ dependence on reactivity is even neglected in the current experimental approaches. According to the free-radical model of water radiolysis, an efficient removal of e_{aq}^- (eq A) should not only increase $G(P_A) = G_{e_{aq}^-}$ but also $G(P_B) = G_{OH}$ (eq B). The reason is that more OH species should remain for reaction B because of the depression of water re-formation



and the consequences on other primary reactions



Similarly, an efficient removal of OH (eq B) should not only increase $G(P_B) = G_{OH}$ but also $G(P_A) = G_{e_{aq}^-}$ (eq A). At present, we are lacking direct experimental evidence that the primary yields of e_{aq}^- and OH actually depend on the concentrations of both e_{aq}^- and OH scavengers. An indirect proof is given in our previous studies on the formation of primary hydrogen atom yield (eq D)¹⁶ and on the origin of the primary molecular product yields (eq E-H).^{17,18} These results show that the primary molecular yields depend on the presence of scavengers for both primary reducing and oxidizing radicals, as assumed above. The purpose of the present work is a direct experimental verification by measuring the products formed in reactions A and B. Sodium formate, ethanol, 2-propanol, nitrate, cadmium, and perchloric acid were used as RH and S; their radiation behavior is well established^{5,10,11,19-21} and the radiolytic products, CO_2 , $(CH_3)_2CO$, NO_2^- , and H_2 , can be determined with good accuracy. In choosing the scavengers of e_{aq}^- we also took into account Hamill's²² and Hunt and coworkers⁹ observations on their possible reactions with the precursor of the hydrated electron. We have used the nitrate and cadmium ions, which apparently react efficiently with both species, and perchloric acid where the hydrogen ion reacts with e_{aq}^- only. Also some measurements were made on solutions containing various amounts of glycine or alanine, substances known as poor e_{aq}^- scavengers but, apparently, efficient in reacting with its precursor.^{8a,9}

As in our preceding experiments on the formation of primary yields, in studying reactions A and B we often had the simultaneous presence of larger amounts of scavengers for both primary oxidizing and reducing species. This made the working conditions deliberately more complex than those in other studies on the formation of $G_{e_{aq}^-}$ and G_{OH} ; the reason was to check our previous finding that the secondary spur reactions of radicals with products of radical-solute scavenging reactions are rather exceptions even at reactivities up to about 10^{10} sec^{-1} .

One would expect that the use of higher solute concentrations, and the depression of water re-forming reactions (eq C and I), should lead to an increase in water decomposition yield, $G(-H_2O)$, with increasing reactivities. The data presented here confirm this assumption.

Experimental Section

All the chemicals used were BDH or Merck products of the highest purity available. They were not subjected to additional purification except for the sodium formate, which was recrystallized before use. The purification of water and sample preparation were carried out by standard procedures previously described.¹⁶⁻¹⁸ Deaerated solutions were used in the $G(P_A)$ measurements. Oxygen was present, $1 \times 10^{-4} M$, in solutions where $G(P_B)$ was determined.

Irradiations were carried out using a 3000 Ci (nominal) radioactive cobalt source. Absorbed doses varied from 2×10^{17} to $7 \times 10^{17} \text{ eV g}^{-1}$. Where necessary, the corrections were applied for the electron density of the solution studied.

Gas chromatography was used for CO_2 and H_2 determinations;²³ the accuracy of yield measurements was higher than to ± 3 and $\pm 2\%$, respectively. Special attention was paid to the blank corrections in CO_2 measurements. To minimize the blanks, the pH of the solutions was adjusted to about 6 with perchloric acid. In general, eight ampoules were prepared as a series but three of them were not irradiated and their CO_2 content was plotted at the zero dose of the dosage curve.

Nitrite was determined spectrophotometrically by the method described by Rider and Mellon;²⁴ the molar extinction coefficient was $53,000 M^{-1} \text{ cm}^{-1}$ at 540 nm and 24° . After a modification, the stability of colored compound was improved and the presence of other solutes did not interfere even in molar concentrations. The accuracy was higher than $\pm 3\%$.

Acetone was determined spectrophotometrically.²⁵ The molar extinction coefficient was found to be $17,700 M^{-1} \text{ cm}^{-1}$ at 474 nm and 24° . Special attention had to be paid to the blanks; the accuracy of measurements was higher than $\pm 5\%$. The presence of 0.25 M sodium nitrate and/or 1 M 2-propanol did not interfere.

Results

Table I summarizes the yields of the nitrite ion measured in irradiated neutral solutions containing various concentrations of sodium nitrate as e_{aq}^- scavenger and different RH ($HCOONa$, CH_3CH_2OH , or $(CH_3)_2CHOH$) as hydroxyl radical scavengers. The formation of nitrite is attributed to the following reactions.^{5-7,11,19-21}



- (10) I. Draganić, M. Nenadović, and Z. Draganić, *J. Phys. Chem.*, **73**, 2564 (1969).
- (11) J. T. Allan, *J. Phys. Chem.*, **68**, 2697 (1964).
- (12) J. C. Russell and G. R. Freeman, *J. Chem. Phys.*, **48**, 90 (1968).
- (13) F. S. Dainton and S. R. Logan, *Trans. Faraday Soc.*, **61**, 715 (1965).
- (14) T. I. Balkas, J. H. Fendler, and R. H. Schuler, *J. Phys. Chem.*, **74**, 4497 (1970).
- (15) J. T. Allan and C. M. Beck, *J. Amer. Chem. Soc.*, **86**, 1483 (1964).
- (16) Z. Draganić and I. Draganić, *J. Phys. Chem.*, **76**, 2733 (1972).
- (17) Z. Draganić and I. Draganić, *J. Phys. Chem.*, **73**, 2571 (1969).
- (18) Z. Draganić and I. Draganić, *J. Phys. Chem.*, **75**, 3950 (1971).
- (19) M. Daniels and E. E. Wigg, *J. Phys. Chem.*, **73**, 3703 (1969); M. Daniels, *ibid.*, **73**, 3710 (1969).
- (20) M. Ottolenghi and J. Rabani, *J. Phys. Chem.*, **72**, 593 (1968).
- (21) M. Grätzel, A. Henglein, and S. Taniguchi, *Ber. Bunsenges. Phys. Chem.*, **74**, 292 (1970).
- (22) W. H. Hamill, *J. Phys. Chem.*, **73**, 1341 (1969); P. L. T. Bevan and W. H. Hamill, *Trans. Faraday Soc.*, **66**, 2533 (1970); T. Sawai and W. H. Hamill, *J. Chem. Phys.*, **52**, 3843 (1970); **74**, 3914 (1970).
- (23) Lj. Petković, M. Kosanić, and I. Draganić, *Bull. Boris Kidrić Inst. Nucl. Sci.*, **15**, 9 (1964).
- (24) B. Rider and M. G. Mellon, *Ind. Eng. Chem., Anal. Ed.*, **18**, 96 (1946).
- (25) S. Berntsson, *Anal. Chem.*, **28**, 1337 (1956).

TABLE I: Yields of Nitrite Ion Measured in Deaerated, Neutral, Aqueous Solutions Containing Various Concentrations of NaNO_3 and Efficient Scavengers for OH^a

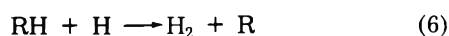
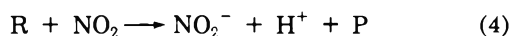
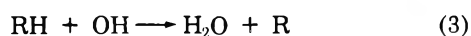
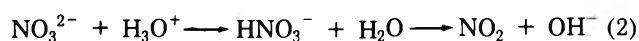
Scavenger for OH, M	$G(\text{NO}_2^-)$ measured in the presence of NaNO_3 , M				
	2.5×10^{-4}	2.5×10^{-3}	2.5×10^{-2}	0.25	1.0
HCOONa					
5×10^{-3}		2.70			
5×10^{-2}	2.60	2.84	3.19	3.76 (0.10)	
0.1		2.89		3.85 (0.05)	
0.2					4.27 (0.10)
0.5		2.94		3.89	
1.0		3.08	3.45	4.10	4.40
$\text{CH}_3\text{CH}_2\text{OH}$					
0.068		2.75			
1.37		2.96		3.91 (0.06)	
$(\text{CH}_3)_2\text{CHOH}$					
0.043			3.12 (0.12)		
0.86			3.30		4.43 (0.11)
0.86					4.50 (0.10) ^b

^a The values in the parentheses concern the contribution of H atoms to the nitrite formation, calculated as $G_{\text{H}}/(1 + k_6[\text{RH}/k_5[\text{NO}_3^-]])$ (see eq 7) and expressed in G units. ^b Concentration of $\text{NaNO}_3 = 2.0 \text{ M}$.

TABLE II: Yields of Nitrite Ions Measured in Deaerated, Neutral, Aqueous Solutions of Sodium Nitrate Containing Various Amounts of Cadmium or Amino Acids

Solute, M	NaNO_3 , ^a M	$G(\text{NO}_2^-)$
	0.025	3.19
	0.25	3.80
	1.0	4.17
Cd^{2+}		
0.01	0.025	3.45
0.1	0.25	4.00
0.4	1.0	4.22
1.0	1.0	4.21
Alanine		
0.1	0.025	3.15
1.0	0.025	2.52
Glycine		
0.1	0.025	3.17
1.0	0.025	2.87
2.0	0.025	2.24
3.0	0.025	2.10
1.0	0.25	3.65
2.0	0.25	3.56
3.0	0.25	3.23

^a All solutions contained sodium formate. The concentrations were 0.05, 0.1, and 0.2 M for 0.025, and 1.0 M NaNO_3 , respectively.



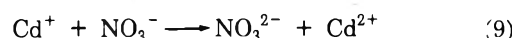
The rate equation for nitrite production

$$G(\text{NO}_2^-) = G_{e_{aq}^-} + \frac{G(\text{H})}{1 + k_6[\text{RH}]/k_5[\text{NO}_3^-]} \quad (7)$$

shows that in certain cases the contribution of H atoms to the nitrite production should be taken into account. The values of k_5 and k_6 are known and these corrections are

reliably calculated; as can be seen from the values given in the parentheses in Table I, they are not significant. Nevertheless, there might be a limitation in using eq 7 in the $G_{e_{aq}^-}$ calculations. According to picosecond pulse radiolysis study,⁹ the observed relative yields of e_{aq}^- decrease with increasing concentration of nitrate. This has been attributed to a reaction of NO_3^- with a precursor of the hydrated electron, apparently a low-energy electron that reacts prior to solvation. Nothing has been reported about the product of this reaction. According to esr studies of irradiated aqueous glasses,²⁶ this could also be the radical ion NO_3^{2-} and the nitrite yield would be then a measure of both hydrated electron and its precursor.

Table II shows how the yields of nitrite formation are affected by the solutes that are assumed to react differently toward e_{aq}^- and its precursor. When cadmium is used at larger concentrations in the presence of nitrate ion, the reaction $\text{Cd}^{2+} + \text{H}$ can be neglected because of the low rate constant ($<10^5 \text{ M}^{-1} \text{ sec}^{-1}$),²⁷ so that we have only



Actually, it can be seen that the measured nitrite yields are increasing with cadmium concentration. In the presence of alanine or glycine they are significantly lowered.

An efficient conversion of the hydrated electron to the hydrogen atom (eq D) takes place in the presence of perchloric acid and H atoms disappear in reaction 6. The yield of molecular hydrogen corresponds to

$$G(\text{H}_2) = G_{e_{aq}^-} + G_{\text{H}} + G_{\text{H}_2} \quad (10)$$

and can be used as a measure of $G_{e_{aq}^-}$. Table III represents $G(\text{H}_2)$ measured in solutions containing various concentrations of perchloric acid as e_{aq}^- scavenger and ethanol as OH and H scavengers. The values in the parentheses refer to the contribution of primary yields of atomic and molecular hydrogen, $G_{\text{H}} + G_{\text{H}_2}$ to the measured yields of H_2 taken from our previous measurements.^{18,18}

(26) P. B. Ayscough and R. G. Collins, *J. Phys. Chem.*, **70**, 3128 (1966).

(27) E. Hayon and M. Moreau, *J. Chim. Phys.*, **62**, 391 (1965).

TABLE III: Yields of Molecular Hydrogen Measured in Deaerated Aqueous Solutions Containing Various Concentrations of Perchloric Acid and Ethanol^a

CH ₃ - CH ₂ - OH, M	G(H ₂) measured in the presence of HClO ₄ , M			
	1 × 10 ⁻³	1 × 10 ⁻²	0.1	1.0
0.068	3.68 (1.03)	4.05 (0.96)	4.15 (0.84)	4.11 (0.71)
0.30	3.91 (1.03)		4.27 (0.84)	
1.37	4.16 (1.05)	4.55 (1.01)	4.68 (0.98)	4.58 (0.83)
^b	0.45	0.41	0.38	0.33

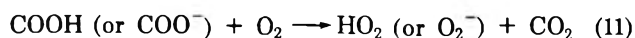
^a The values in the parentheses concern the contribution of G_H + G_{H₂} to the molecular hydrogen measured (see eq 10), and expressed in G units. The G_H and G_{H₂} data were taken from our previous determination of reactivity influence on primary yields.^{16,18} ^b No ethanol, 5 × 10⁻⁴ M NaNO₂ present.

TABLE IV: Yields of CO₂ Measured in Neutral, Oxygenated, Aqueous Solutions Containing Various Concentrations of NaNO₃ and HCOONa^a

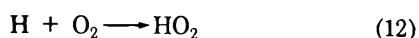
HCOONa, M	G(CO ₂) measured in the presence of NaNO ₃ , M		
	2.5 × 10 ⁻²	0.25	1.0
5 × 10 ⁻³	2.85 (0.20)		
1 × 10 ⁻²	3.27 (0.32)	3.42 (0.17)	3.48 (0.06)
2.5 × 10 ⁻²	3.60 (0.44)		
0.1	4.03 (0.55)	4.31 (0.41)	4.24 (0.24)
0.5	4.50 (0.64)	5.00 (0.54)	
1.0	4.81 (0.70)	5.15 (0.58)	5.29 (0.46)
2.0	5.28 (0.78)		

^a The values in the parentheses concern the contribution of H atoms to the formation of CO₂, calculated as G_H1 + [(k₅[NO₃⁻] + k₁₁[O₂])/k₆[HCOO⁻]]⁻¹ (see eq 13) and expressed in G units.

When sodium formate is used as RH in neutral solutions containing different amounts of sodium nitrate, carbon dioxide is the product P in reaction 4. Experimental results are shown in Table IV. To ensure the conversion of all the carboxyl radicals to carbon dioxide, 1 × 10⁻⁴ M oxygen was present in irradiated solutions



The oxygen presence also leads to the removal of H atoms



in competition with reactions 5 and 6. The rate equation for CO₂ production shows that one also has to take into account reactions 5, 6, and 11.

$$G(\text{CO}_2) = G_{\text{OH}} + G_{\text{H}} \left[1 + \frac{k_5[\text{NO}_3^-] + k_{11}[\text{O}_2]}{k_6[\text{HCOO}^-]} \right]^{-1} \quad (13)$$

The values given in the parentheses in Table IV refer to this contribution. It varies from 2 to 15% of the total CO₂ yield, depending on the concentration ratios of the solutes present.

Table V gives the yields of acetone measured in the solutions containing 2-propanol with RH and sodium nitrate as a hydrated electron scavenger. The usual kinetic treatment for acetone formation gives

$$G((\text{CH}_3)_2\text{CO}) = G_{\text{OH}} + G_{\text{H}} \left[1 + \frac{k_5[\text{NO}_3^-] + k_{11}[\text{O}_2]}{k_6[(\text{CH}_3)_2\text{CHOH}]} \right]^{-1} \quad (14)$$

Here, also, the terms in the parentheses refer to the contribution of hydrogen atoms to the measured yields of the

TABLE V: Yields of Acetone Measured in Neutral, Aqueous Solutions Containing Oxygen and Various Concentrations of 2-Propanol and NaNO₃^a

(CH ₃) ₂ - CHOH, M	G(acetone) measured in the presence of NaNO ₃ , M			
	2.5 × 10 ⁻³	2.5 × 10 ⁻²	0.1	0.25
2.2 × 10 ⁻³		2.60 (0.03)		2.83
8.6 × 10 ⁻³	2.83 (0.11)	2.84 (0.09)	3.00 (0.08)	
2.2 × 10 ⁻²				3.26 (0.08)
8.6 × 10 ⁻²	3.48 (0.41)		3.71 (0.35)	
0.22				4.21 (0.46)
0.86	4.47 (0.70)		4.78 (0.56)	
2.15				5.38 (0.67)

^a The values in the parentheses concern the contribution of H atoms to the formation of acetone, calculated as G_H1 + [(k₅[NO₃⁻] + k₁₁[O₂])/k₆[(CH₃)₂CHOH]]⁻¹ (see eq 14) and expressed in G units.

TABLE VI: Rate Constants Used in the Reactivity Calculation^a

Scavenger	k(OH + S), M ⁻¹ sec ⁻¹	k(e _{aq} ⁻ + S), M ⁻¹ sec ⁻¹	k(H + S), M ⁻¹ sec ⁻¹
HCOO ⁻	2.5 × 10 ⁹	<10 ⁶	2.5 × 10 ⁸
C ₂ H ₅ OH	1.83 × 10 ⁹	<400	1.6 × 10 ⁷
(CH ₃) ₂ CHOH	2.9 × 10 ⁹		5 × 10 ⁷
NO ₃ ⁻	<5 × 10 ⁵	1.05 × 10 ¹⁰	1 × 10 ⁷
0.1 M NO ₃ ⁻		1.3 × 10 ¹⁰	
1.0 M NO ₃ ⁻		1.6 × 10 ¹⁰	
H ₃ O ⁺		2.5 × 10 ¹⁰ ^b	2.6 × 10 ³
0.1 M H ₃ O ⁺		1.7 × 10 ¹⁰ ^b	
0.5–1.0 M H ₃ O ⁺		1.2 × 10 ¹⁰ ^b	
CdSO ₄		6.4 × 10 ¹⁰ ^c	<10 ⁵ ^d
0.1 M CdSO ₄		1.9 × 10 ¹⁰ ^c	
1.0 M CdSO ₄		9.6 × 10 ⁹ ^c	

^a If not otherwise indicated, the rate constants were taken from ref 18. ^b Reference 9. ^c Reference 29. ^d Reference 27.

stable product observed. In using eq 14 for G_{OH} calculations we had also to take into account that only 95% of OH radicals attack the α hydrogen atom in the 2-propanol molecule,²⁸ i.e., that the reaction producing acetone gives OH yields apparently lower by 5%.

Discussion

Yield-Reactivity Curves. The data in Tables I–V and eq 7, 10, 13, or 14 were used for the primary yields calculations. The rate constants used in the reactivity calculations are summarized in Table VI.

Figure 1 represents the hydroxyl radical yield dependence on the reactivity toward OH. Primary hydroxyl yields increase with reactivity; also, larger values were observed in the presence of larger amounts of scavengers of e_{aq}⁻ (curves 1 and 2) than in solutions where this concentration was low (curve 3). It should be noted that the trends of curves 1–3 are the same, pointing out that the mechanism of OH scavenging is not disturbed by the presence of larger amounts of sodium nitrate, a solute which is assumed to remove efficiently both e_{aq}⁻ and its precursor. This can be seen also from Figure 2. It shows that the hydroxyl radical yield can be quantitatively correlated also with the reactivity toward e_{aq}⁻. Curve 3 refers to the solution containing RH in a concentration sufficient only to remove the OH species from the bulk.

(28) G. E. Adams and R. L. Willson, *Trans. Faraday Soc.*, **65**, 2981 (1969); G. E. Adams, personal communication, 1972.

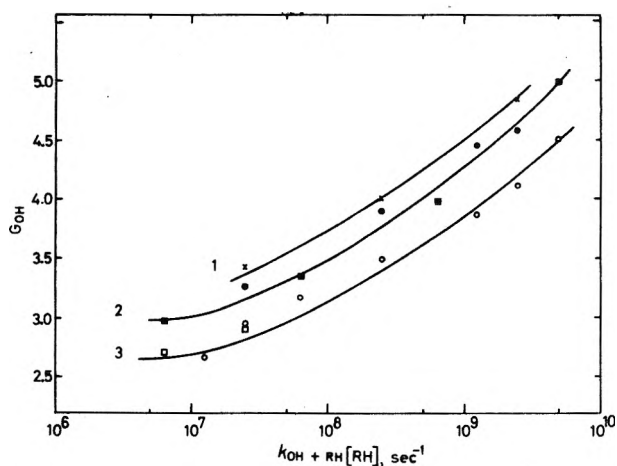


Figure 1. Dependence of experimentally derived hydroxyl radical yield on hydroxyl radical reactivity in solutions containing e_{aq}^- scavengers: Curve 1, X, 1.0 M NaNO₃ + HCOONa; curve 2, ●, 0.25 M NaNO₃ + HCOONa; ■, 0.25 M NaNO₃ + (CH₃)₂CHOH; curve 3, ○, 0.025 M NaNO₃ + HCOONa; □, 0.025 M NaNO₃ + (CH₃)₂CHOH.

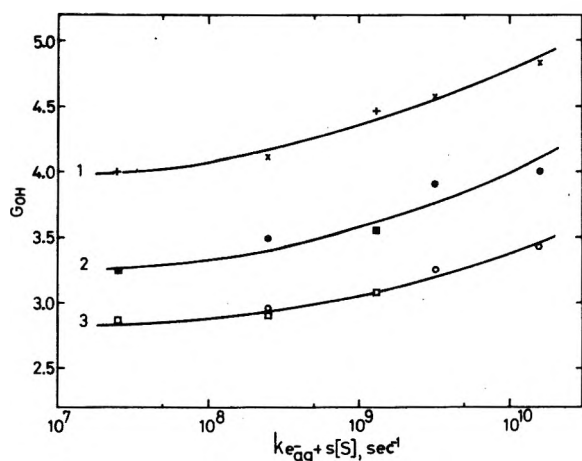


Figure 2. Dependence of experimentally derived hydroxyl radical yield on hydrated electron reactivity in solutions containing OH radical scavengers: curve 1, X, 1.0 M HCOONa + NaNO₃; +, 0.86 M (CH₃)₂CHOH + NaNO₃; curve 2, ●, 0.1 M HCOONa + NaNO₃; ■, 0.086 M (CH₃)₂CHOH + NaNO₃; curve 3, ○, 0.01 M HCOONa + NaNO₃; □, 0.009 M (CH₃)₂CHOH + NaNO₃.

Curves 1 and 2 represent the data for concentrated solutions of OH scavengers.

The results presented in Figure 3 provide experimental evidence that $G_{e_{aq}^-}$ depends on the reactivity toward OH. The increase of primary yield of the hydrated electron takes place also in solutions containing larger amounts of scavengers of e_{aq}^- . In these cases the yields measured are larger (curves 1 and 2) because of the increased e_{aq}^- scavenging from the places of localized energy deposition.

Figure 4 shows how the increased reactivity toward e_{aq}^- leads to the increase in the primary yield of hydrated electron. The absolute values are larger when a larger amount of OH scavenger is present in the solution (curve 1); the lower curve (curve 2) refers to solutions where the concentration was considerably lower. It should be noted that the primary yields derived from solutions containing both cadmium and nitrate agree well with nitrate data; the reactivity was calculated here as the sum of reactivities of Cd²⁺ and NO₃⁻ toward e_{aq}^- . There is also a very

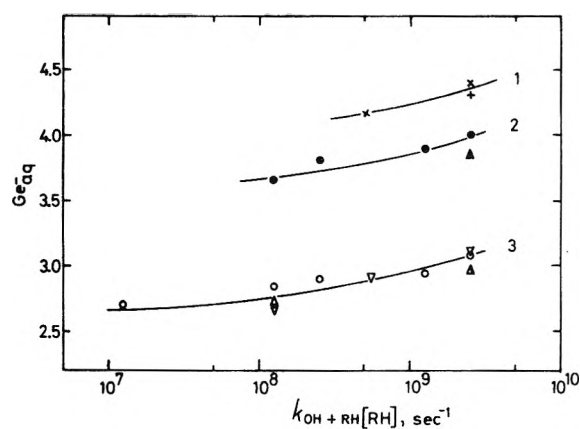


Figure 3. Dependence of experimentally derived hydrated electron yield on OH radical reactivity in solutions containing hydrated electron scavengers: curve 1, X, 1.0 M NaNO₃ + HCOONa; +, 1.0 M NaNO₃ + (CH₃)₂CHOH; curve 2, ●, 0.25 M NaNO₃ + HCOONa; ▲, 0.25 M NaNO₃ + CH₃CH₂OH; curve 3, ○, 2.5 × 10⁻³ M NaNO₃ + HCOONa; Δ, 2.5 × 10⁻³ M NaNO₃ + CH₃CH₂OH; ▽, 1 × 10⁻³ M HClO₄ + CH₃CH₂OH.

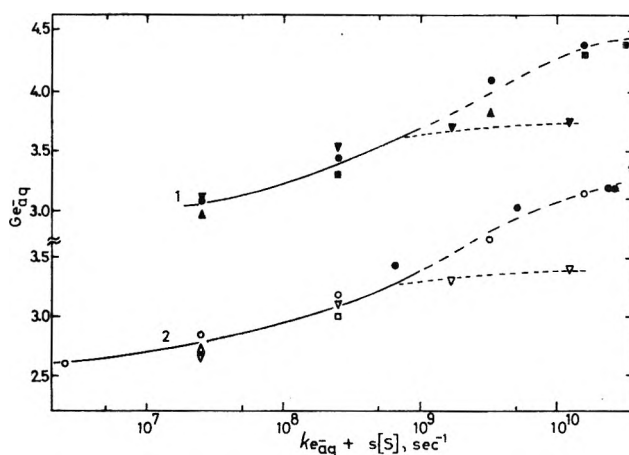


Figure 4. Dependence of experimentally derived hydrated electron yield on hydrated electron reactivity: curve 1, ●, 1.0 M HCOONa + NaNO₃; ▲, 1.37 M CH₃CH₂OH + NaNO₃; ■, 0.86 M (CH₃)₂CHOH + NaNO₃; ▽, 1.37 M CH₃CH₂OH + HClO₄; curve 2, ○, 0.05 M HCOONa + NaNO₃; Δ, 0.068 M CH₃CH₂OH + NaNO₃; □, 0.043 M (CH₃)₂CHOH + NaNO₃; ▽, 0.068 M CH₃CH₂OH + HClO₄; ●, 0.05 M HCOONa + NaNO₃ + CdSO₄. In solutions containing cadmium, in order to normalize the data to 0.05 M HCOONa concentration, the nitrite yields from Table II were corrected by 0.06 and 0.13 G units for the solutions containing respectively 0.1 and 0.2 M of sodium formate.

good agreement between the hydrated electron yields derived from perchloric acid and nitrate data, but only up to a reactivity of about 10⁹ sec⁻¹. The difference observed at larger reactivities could be partially explained by the reactivity calculations, where we have only taken into account the reaction with e_{aq}^- , and its rate constant dependence on ionic strength.²⁹ More studies are required for a better understanding of reactions of e_{aq}^- and its precursor in aqueous solutions containing larger concentrations of H₃O⁺ and nitrate ions. However, it can be seen that $G_{e_{aq}^-}$ derived from our experiments on nitrate solutions agree reasonably with some results obtained, with this and other solutes under working conditions similar to ours, on solutions containing lower amounts of OH scav-

(29) E. Peled and G. Czapski, *J. Phys. Chem.*, **74**, 2903 (1970).

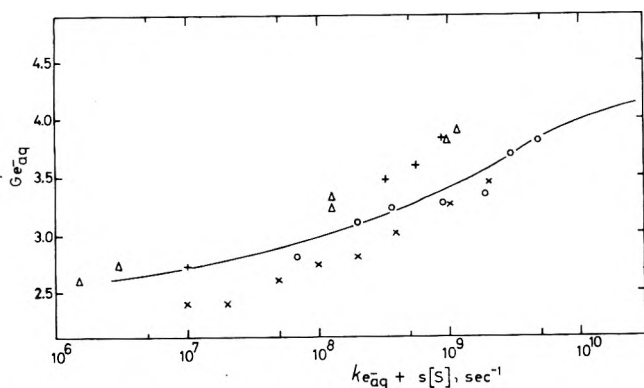


Figure 5. Dependence of $G_{e_{aq}^-}$ on hydrated electron reactivity in solutions containing various e_{aq}^- scavengers and low concentrations of OH radical scavengers: X, $\text{NaNO}_3 + 1 \times 10^{-2} M \text{CH}_3\text{OH}$ (from ref 11); Δ , $\text{N}_2\text{O} + 5-11 \times 10^{-4} M \text{NaNO}_2$ (from ref 13); +, $\text{CH}_3\text{Cl} + 1 \times 10^{-2} M \text{CH}_3\text{OH}$ (from ref 14); O, CdSO_4 (from ref 8a). In the case of CdSO_4 , all yields were normalized to $G_{e_{aq}^-} = 2.8$. Solid line represents the best line through the data on curve 2, in Figure 4.

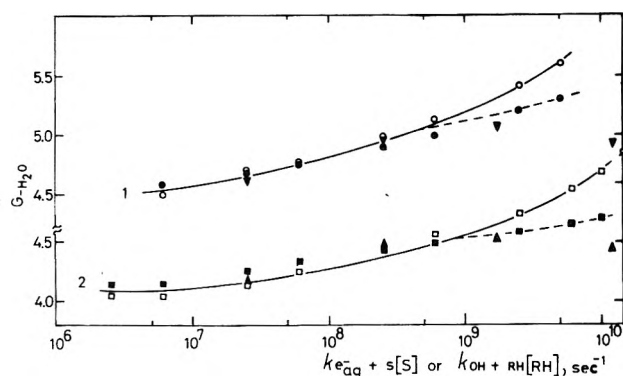


Figure 6. Dependence of water decomposition yield on hydrated electron and hydroxyl radical reactivity: curve 1, O, $0.25 M \text{NaNO}_3 + \text{HCOONa}$ or $(\text{CH}_3)_2\text{CHOH}$; ●, $1 M \text{HCOONa}$ or $0.86 M (\text{CH}_3)_2\text{CHOH} + \text{NaNO}_3$; ▼, $1.37 M \text{C}_2\text{H}_5\text{OH} + \text{HClO}_4$; curve 2, □, $2.5 \times 10^{-2} M \text{NaNO}_3 + \text{HCOONa}$ or $(\text{CH}_3)_2\text{CHOH}$; ■, $5 \times 10^{-2} M \text{HCOONa}$ or $4.3 \times 10^{-2} (\text{CH}_3)_2\text{CHOH} + \text{NaNO}_3$; ▲, $6.8 \times 10^{-2} M \text{C}_2\text{H}_5\text{OH} + \text{HClO}_4$.

engers and cadmium,⁸ nitrate,¹¹ nitrous oxide,¹³ or CH_3Cl .¹⁴ This is shown in Figure 5, where the solid line represents our data (the best line through the values in curve 2 of Figure 4).

The experimental data obtained in this work on G_{OH} and $G_{e_{aq}^-}$, and in previous studies on G_{H} , G_{H_2} , and $G_{\text{H}_2\text{O}_2}$,¹⁶⁻¹⁸ make it possible to calculate water decomposition yield at various reactivities. The equation of material balance

$$G(-\text{H}_2\text{O}) = G_{\text{OH}} + 2G_{\text{H}_2\text{O}_2} = G_{e_{aq}^-} + G_{\text{H}} + 2G_{\text{H}_2} \quad (\text{J})$$

and the mean values of all determinations were used in these calculations. Figure 6 confirms that the increasing scavenging of primary free-radical products of water decomposition leads to an increase in the water decomposition yield. Curve 2 refers to initially dilute solutions and curve 1 refers to the solutions containing initially a larger amount of an efficient scavenger for OH or e_{aq}^- , corresponding to a reactivity of $2.5 \times 10^9 \text{ sec}^{-1}$. The absolute values are larger at larger reactivities but the trends of curves 1 and 2 point out that the decomposition mechanisms are unchanged. It is worth recalling that in the cal-

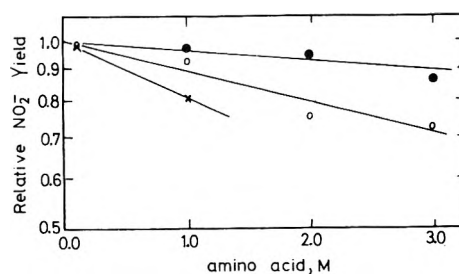


Figure 7. Relative yields of nitrite ion observed in the presence of increasing concentrations of alanine or glycine: ●, $0.25 M \text{NaNO}_3 + \text{glycine}$; O, $2.5 \times 10^{-2} M \text{NaNO}_3 + \text{glycine}$; X, $2.5 \times 10^{-2} M \text{NaNO}_3 + \text{alanine}$.

culations (eq J) we have used the values of primary yields derived from various, independent experiments. It can be seen that, up to a reactivity of 10^9 sec^{-1} , good agreement exists between $G(-\text{H}_2\text{O})$ calculated from primary oxidizing species (open symbols) and those derived from primary reducing yields (solid symbols). However, the values of $G(-\text{H}_2\text{O})$ derived from reducing species yields are considerably lower at larger reactivities; there is even a difference between the nitrate and perchloric data, the latter being lower. The reason for this is not clear for the present. The removal of e_{aq}^- precursor might influence the sequence of reactions given by eq A to I, so that the observed discrepancy might be real. However, at larger concentrations of solutes the mechanisms of nitrite and molecular hydrogen formation could also be more complex than it was assumed in deriving eq 7 and 10. In such a case the expressions used in $G_{e_{aq}^-}$ calculations may turn out to be inadequate and give rise to the observed difference.

Figure 7 shows how alanine and glycine affect the measured nitrite yields. The experimentally obtained nitrite yields from the Table II were corrected before use, because of some e_{aq}^- loss in reactions with molar concentrations of the amino acids considered. It can be seen that increasing the concentration of amino acid leads to a decrease in $G(\text{NO}_2^-)$; glycine is, in this respect, less effective than alanine. Also, the depression of nitrite yield depends on the ratio of NaNO_3 to glycine; for a given amount of glycine it is less significant at larger nitrate concentrations. These data are not sufficient to conclude that a simple competition between the solutes takes place for a precursor of the hydrated electron. Nevertheless, they show clearly that these two substances differently affect the formation of e_{aq}^- yields; the conclusion drawn from nanosecond experiments with both amino acids was somewhat ambiguous.^{8a} The ability of glycine to depress $G_{e_{aq}^-}$ was reported in picosecond experiments⁹ as well as in a recent steady-state γ -radiolysis study.³⁰

Unifying Curves for Reactivity Dependence of Fractional Changes of Primary Yields. In order to normalize the data for comparison, we have calculated unifying curves for the reactivity influence on the fractional yields, G/G^0 . Here, G^0 is the yield measured in the solution where the presence of the scavenger has no effect on the measured yield and G is the primary yield derived at a given reactivity. Figure 8 shows these data for the primary yields of hydroxyl radical and hydrated electron. It can be seen that the yield of a primary free radical depends both on the reactivity toward OH and e_{aq}^- , as assumed in the free-radical model of water radiolysis. The correlation be-

(30) O. Mičić, V. Marković, and D. Nikolić, in press.

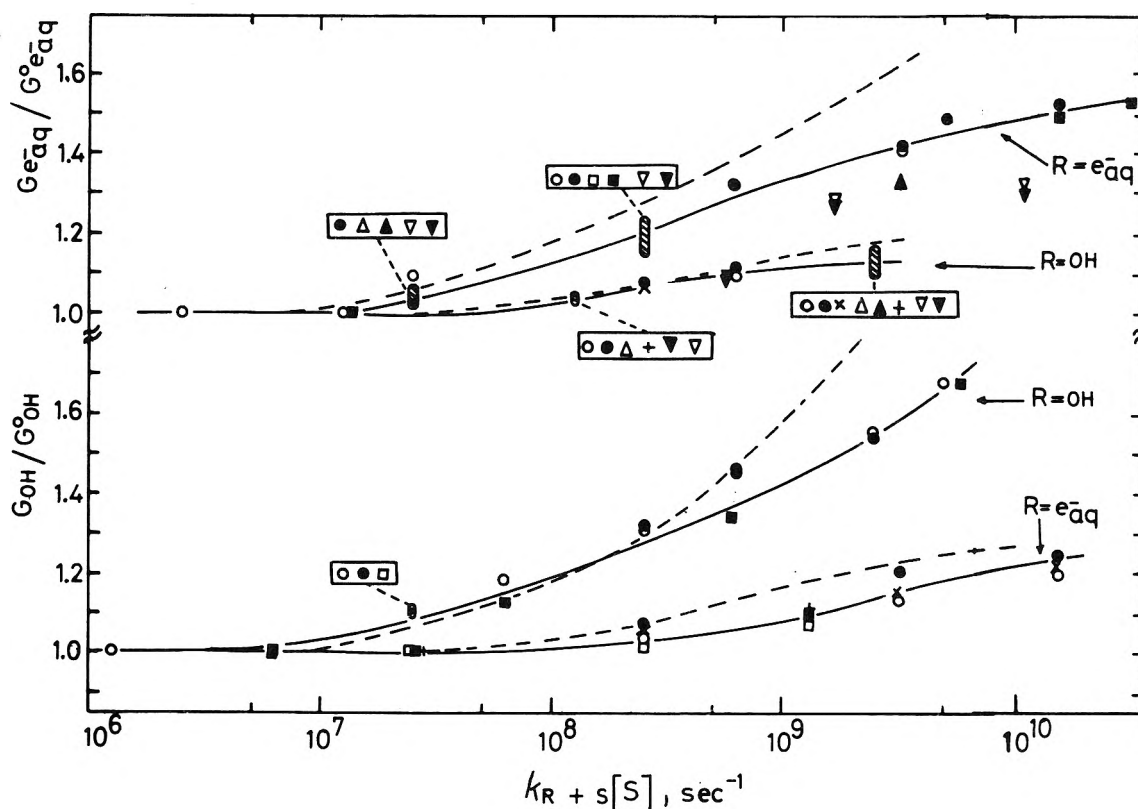


Figure 8. Unifying curves for the reactivity influence on $G_{e_{aq}^-}/G_{e_{aq}^-^0}$: upper curve, O, X 0.05 M HCOONa + NaNO₃; ●, 1.0 M HCOONa + NaNO₃; Δ, 0.068 M C₂H₅OH + NaNO₃; ▲, 1.37 M C₂H₅OH + NaNO₃; □, 0.043 M (CH₃)₂CHOH + NaNO₃; ■, 0.86 M (CH₃)₂CHOH + NaNO₃; ▽, 0.068 M C₂H₅OH + HClO₄; ▾, 1.37 M C₂H₅OH + HClO₄; lower curve, O, 2.5 × 10⁻³ M NaNO₃ + HCOONa; ●, 0.25 M NaNO₃ + HCOONa; X, 1.0 M NaNO₃ + HCOONa; Δ, 2.5 × 10⁻³ M NaNO₃ + C₂H₅OH; ▲, 0.25 M NaNO₃ + C₂H₅OH; +, 1 M NaNO₃ + (CH₃)₂CHOH; ▽, 1 × 10⁻³ M HClO₄ + C₂H₅OH; ▾, 1.0 M HClO₄ + C₂H₅OH. Unifying curves for the reactivity influence on G_{OH}/G_{OH}^0 : upper curve, ●, 0.025 M NaNO₃ + HCOONa; O, 0.25 M NaNO₃ + HCOONa; □, 0.025 M NaNO₃ + (CH₃)₂CHOH; ■, 0.25 M NaNO₃ + (CH₃)₂CHOH; lower curve: O, 0.01 M HCOONa + NaNO₃; ●, 0.1 M HCOONa + NaNO₃; X, 1.0 M HCOONa + NaNO₃; □, 8.6 × 10⁻³ M (CH₃)₂CHOH + NaNO₃; ■, 0.086 M (CH₃)₂CHOH + NaNO₃; +, 0.86 M (CH₃)₂CHOH + NaNO₃. The dotted lines are the diffusion kinetic theoretical curves calculated after Kuppermann.³

tween the fractional yield changes and reactivities is valid even in solutions containing simultaneously larger amounts of scavengers for both primary radicals. This could be a confirmation of our previous finding on the formation of other primary yields in water radiolysis,^{16,18} that in the γ -radiolysis, no significant secondary free-radical or charge transfer reactions take place in the spurs.

This can also be seen from a comparison with theoretical curves, represented by dotted lines in Figure 8. They were derived from a diffusion spur model of water radiolysis³ which essentially consisted of reactions represented by eq A-I; however, the calculations were made for simpler conditions, initial reactivities of $6 \times 10^6 \text{ sec}^{-1}$ only, where the secondary spur reactions of radicals with products of radical-solute scavenging reactions are not expected to occur. At larger reactivities good agreement exists between experimentally derived and calculated values for the e_{aq}^- yield dependence on the reactivity toward hydroxyl radical and the OH yield dependence on the reactivity toward hydrated electron. This is not the case with G_{OH} and $G_{e_{aq}^-}$ dependence on the reactivities toward OH and e_{aq}^- , respectively; here, the experiments point out to a slower yield increase with reactivity.

Remarks on the Reactivity Influence on Primary Yields of Water Radiolysis

The results obtained in this work, and in our previous studies on the primary yields of water radiolysis, provide a

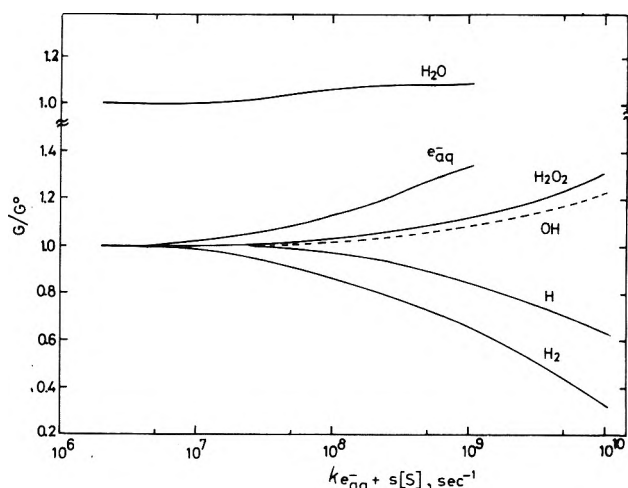


Figure 9. Fractional yield (G/G^0) dependence of primary products of water radiolysis on the reactivity toward e_{aq}^- . Best lines through experimentally derived values: OH and e_{aq}^- , Figure 8 this work; H atom, ref 16 Figure 2; H₂, ref 18 Figure 5; H₂O₂, ref 18 Figure 6 and ref 17 Figure 1.

general picture of the reactivity influence on the yields of primary free-radical and molecular products of water decomposition. It should be mentioned that our experimental testing of the free-radical model was deliberately limited to moderate concentrations and reactivities up to about 10^{10}

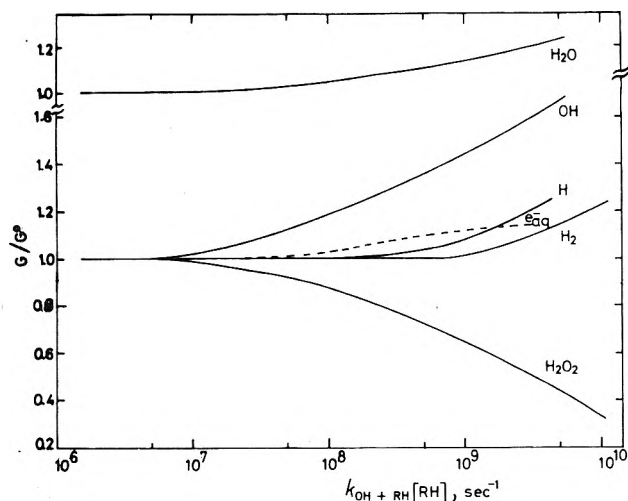


Figure 10. Fractional yield (G/G^0) dependence of primary products of water radiolysis on the reactivity toward hydroxyl radical. Best lines through the experimentally derived values: OH and e_{aq}^- , Figure 8 this work; H atom, ref 16 Figure 2; H₂, ref 18 Figure 6; H₂O₂, ref 18 Figure 5 and ref 17 Figure 1.

sec^{-1} . The reason for this was various technical obstacles because of larger amounts of solutes. Quantitative determination of microgram amounts of radiolytic products not only lacks in accuracy but often becomes impracticable in

the presence of molar concentrations of substances. The direct effect of radiation can not be always neglected, and its contribution is often difficult to evaluate accurately. At larger reactivities also the formation of primary molecular products might be so strongly suppressed that their reliable determination is made difficult if not impossible.

Figure 9 summarizes the effect of reactivity toward hydrated electron on the primary free-radical and molecular yields. Because of the uncertainty considered above, the yield reactivity curves for the yields of e_{aq}^- and for the water decomposition were limited to the reactivity up to about 10^9 sec^{-1} ; more work is required concerning the precursor to the hydrated electron and its eventual importance in the radiation-induced chemical changes in aqueous solutions. Figure 10 summarizes the dependence of primary yields on the reactivity toward hydroxyl radical. As can be seen, experimental evidence confirms the basic assumptions of the free-radical model of water radiolysis. The primary products yield depend indeed on the presence of scavengers for both primary reducing and oxidizing free radicals; this is the case with the yield of water decomposition. The data in Figures 9 and 10 also show that the reactivity effect might be more complex than it is usually assumed.

Acknowledgment. The authors wish to thank Mr. M. Borovičani and Mr. N. Stančić for the technical assistance.

An Electron Spin Resonance Study of the Photolysis of Aqueous Sulfite Solutions¹

Om P. Chawla, N. L. Arthur, and Richard W. Fessenden*

Radiation Research Laboratories, Center for Special Studies and Department of Chemistry, Mellon Institute of Science, Carnegie-Mellon University, Pittsburgh, Pennsylvania 15213 (Received September 6, 1972)

Publication costs assisted by the Carnegie-Mellon University and the U. S. Atomic Energy Commission

Esr experiments are used to confirm that the direct photolysis of aqueous solutions of sulfite yields $\dot{\text{S}}\text{O}_3^-$ and e_{aq}^- . The esr spectrum of SO_3^- is a single line of 70 mG width centered at $g = 2.00307$. The formation of the e_{aq}^- is demonstrated by its reaction with $\text{ClCH}_2\text{CO}_2^-$ to yield CH_2CO_2^- and by radical trapping with $\text{CH}_2=\text{NO}_2^-$ to give CH_3NO_2^- . Photosensitization with a number of ketones, including acetone, has also been shown to give the same decomposition reaction including production of e_{aq}^- . The quenching of excited acetone by SO_3^{2-} is found to be ~ 500 times more rapid than by isopropyl alcohol and occurs at a rate approaching that of a diffusion-controlled process. Quenching of excited acetone by SO_3^{2-} yields $\dot{\text{S}}\text{O}_3^-$ and e_{aq}^- with the same efficiency as quenching by isopropyl alcohol yields two $(\text{CH}_3)_2\dot{\text{C}}\text{OH}$ radicals. The photolysis of SO_3^{2-} is proposed as a source for studies of the reactions of the important intermediate e_{aq}^- .

Introduction

A number of esr studies of radicals in photolytic systems have been made following the initial work of Livingston and Zeldes.² Although some emphasis has been put upon the details of the radical generation process most of

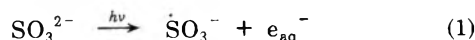
the early papers have emphasized the discussion of the spectral parameters and the structural details derived therefrom. Some of the more recent works^{3,4} have begun

(1) Supported in part by the U. S. Atomic Energy Commission.

(2) R. Livingston and H. Zeldes, *J. Chem. Phys.*, **44**, 1245 (1966).

to emphasize the details of radical formation and reaction. Emphasis has also been upon organic radical species. In the work to be described here we wish to present some studies of the mechanisms in the photolysis of the inorganic sulfite system. The work is restricted to aqueous solutions because of our interest in making the greatest use of the results of somewhat parallel *in situ* radiolysis experiments.⁵⁻⁷

Dogliotti and Hayon⁸ and Hayon, Treinin, and Wilf⁹ have reviewed the photochemistry of SO_3^{2-} and have studied its flash photolysis. The various studies are consistent with the reaction



Absorption spectra of $\dot{\text{SO}}_3^-$ and e_{aq}^- were observed and in the latter paper the identification of the second radical as e_{aq}^- was confirmed. As will be seen below the esr results are consistent with reaction 1.

Experimental Section

The esr spectrometer used for the photolytic studies was the laboratory-built unit described previously.¹⁰ Field modulation was at 10 kHz with synchronous detection at 10 or 20 kHz to provide first- or second-derivative presentation. A flat cell of the usual design with a 0.5 mm spacing was used in a Varian V-4531 cavity. The slotted end plate of the cavity was replaced by a water-cooled brass block (12.5 mm thick) with a ~ 1 cm hole to admit the light. Photolysis was done with a 1-kW Hanovia 977B1 compact arc mercury-xenon lamp in a Schoeffel Instrument Co. LH151N housing. Fused silica lenses of ~ 5 cm diameter and focal length were used to focus the light on the esr cell. The sample was deoxygenated in a 1-l. container by bubbling with N_2 and made to flow through the cell by evacuating the waste jug with an aspirator.

All chemicals with the exception of the organic sensitizers were Baker analyzed reagents. The sensitizers were from various sources and were used without further purification. The pH was adjusted with NaOH or KOH. Doubly distilled water was used throughout.

Results and Discussion

Direct Photolysis. The uv absorption spectrum of aqueous SO_3^{2-} (Na_2SO_3 , pH ~ 9) shows a rapid increase of absorption at wavelengths below 260 nm (for 10 mM solution, 1-cm pathlength). Photolysis of solutions of SO_3^{2-} at concentrations of 2×10^{-4} – 3×10^{-2} M (at the natural pH ~ 9) gives a single narrow esr line at $g = 2.00307$ (width = 70 mG) with a signal-to-noise ratio of about 30. The same esr line is observed from pH 2.2 to 12.5 with somewhat lower signal heights in the acid region. It will be shown below that this line is produced by the radical SO_3^- .

The dependence of the intensity of the esr signal of SO_3^- upon concentration of SO_3^{2-} is given in Figure 1. Above a concentration of about 40 mM little further increase in signal height is observed. The most obvious reason for such behavior is that the solution becomes black at the active wavelengths. However, for wavelengths of 250–260 nm where the lamp output is at a local maximum the absorbance in the cell path length of 0.05 cm is only ~ 0.07 for 30 mM concentration. Only for wavelengths ~ 230 nm is the absorbance near unity. Apparently only these short wavelengths are effective in causing the dissociation (reaction 1). This conclusion is confirmed by ex-

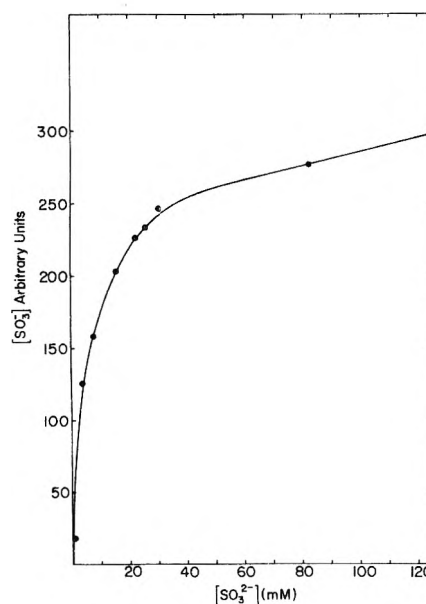


Figure 1. Dependence of the amplitude of the esr line ascribed to SO_3^- upon concentration of SO_3^{2-} . The solution pH was at the natural value (~ 9) for solutions of Na_2SO_3 . (No dependence of signal height on pH is found in this region.)

periments with a filter of 2 cm of 5% $\text{CH}_3\text{CO}_2\text{H}$ in water which absorbs strongly below 245 nm. With such a filter a factor of 2 reduction in the $\dot{\text{SO}}_3^-$ esr signal was found for concentrations of 3–30 mM SO_3^{2-} as compared with pure water in the filter cell. In the case of HSO_3^- (33 mM, pH 4.6) a filter of pure $\text{CH}_3\text{CO}_2\text{H}$ had little effect on signal intensity.

The behavior described above of the SO_3^{2-} photolysis can be discussed with respect to the comments given by Hayon, Treinin, and Wilf⁹ on the nature of the absorption by SO_3^{2-} . They argue that while the absorption of HSO_3^- shows the characteristics of a charge-transfer-to-solvent (CTTS) band that of SO_3^{2-} does not indicating some other overlying absorption. They acknowledged that types of excitation other than CTTS could lead to production of e_{aq}^- . The present conclusions that only the shorter wavelengths are effective in producing e_{aq}^- do not require another type of excitation and are consistent with photolysis in an underlying CTTS band. The low total signal produced is also consistent with this picture in that an efficient utilization of light at 250–260 nm would lead to much higher total signals as is observed in other systems. In the case of HSO_3^- the lack of any effect by the $\text{CH}_3\text{CO}_2\text{H}$ filter shows that photolysis is in the band at ~ 260 nm which is attributed to a dimeric species, $\text{S}_2\text{O}_5^{2-}$.⁹

This esr line with $g = 2.00307$ can be attributed to the SO_3^- radical on the basis of several pieces of evidence. The previous photochemical work has assumed its formation and the g factor matches that found for radicals in

- (3) P. B. Ayscough, R. C. Sealy, and D. E. Woods, *J. Phys. Chem.*, **75**, 3454 (1971).
- (4) S. A. Weiner and G. S. Hammond, *J. Amer. Chem. Soc.*, **90**, 1659 (1968); *ibid.*, **91**, 986 (1969); S. A. Weiner, E. J. Hamilton, Jr., and B. M. Monroe, *ibid.*, **91**, 6350 (1969).
- (5) K. Eiben and R. W. Fessenden, *J. Phys. Chem.*, **75**, 1186 (1971).
- (6) D. Behar and R. W. Fessenden, *J. Phys. Chem.*, **76**, 1706 (1972).
- (7) D. Behar and R. W. Fessenden, *J. Phys. Chem.*, **76**, 1710 (1972).
- (8) L. Dogliotti and E. Hayon, *J. Phys. Chem.*, **72**, 1800 (1968).
- (9) E. Hayon, A. Treinin, and J. Wilf, *J. Amer. Chem. Soc.*, **94**, 47 (1972).
- (10) R. W. Fessenden, *J. Chem. Phys.*, **48**, 3725 (1968).

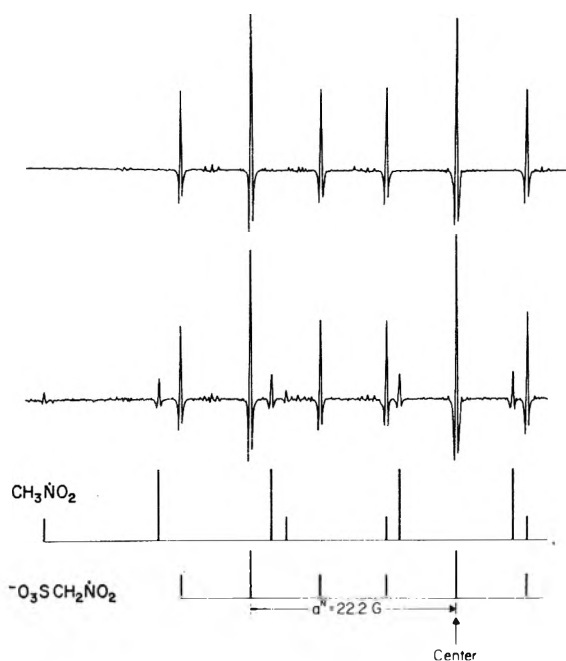
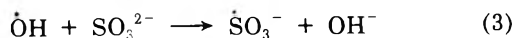
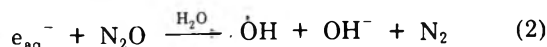


Figure 2. Portions of the second-derivative esr spectra obtained upon photolysis of a solution of 13 mM SO_3^{2-} and 0.9 mM CH_3NO_2 at pH 12.1 with (upper trace) and without (lower trace) N_2O . The complete absence of the signal of CH_3NO_2^- in the N_2O -saturated solution is evident.

the solid^{11,12} which are identified as SO_3^- . A radical with the same g factor is also produced⁶ by OH reaction with sulfite in irradiated aqueous solutions⁷ and in flow systems starting with $\text{Ti}^{3+}-\text{H}_2\text{O}_2$.¹³ The reaction in these latter cases is assumed to be $\text{SO}_3^{2-} + \text{OH} \rightarrow \dot{\text{S}}\text{O}_3^- + \text{OH}^-$.

The photochemical experiments on pure sulfite solutions give no evidence for the partner of $\dot{\text{S}}\text{O}_3^-$, namely, e_{aq}^- , but its formation is suggested by experiments with N_2O . When the solution (7 mM SO_3^{2-}) was saturated with N_2O the $\dot{\text{S}}\text{O}_3^-$ signal increased by a factor of ~ 1.8 . The increase is the result of the reactions



together with the possible effect of eliminating the reaction of $e_{\text{aq}}^- + \text{SO}_3^{2-}$.

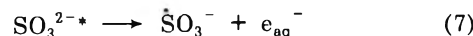
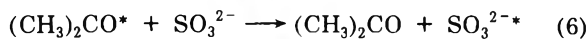
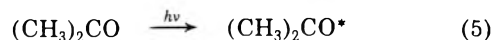
The radicals formed in the photochemical reaction can also be investigated by radical trapping with nitromethane.⁷ Photolysis of a solution 13 mM in SO_3^{2-} and 0.9 mM in CH_3NO_2 at pH 12.1 gave esr signals of the radicals CH_3NO_2^- and $-\text{O}_3\text{SCH}_2\text{NO}_2^-$ as shown in Figure 2. The parameters $a^{\text{N}} = 25.96$, $a^{\text{H}} = 12.12$ G, $g = 2.00502$ and $a^{\text{N}} = 22.21$, $a^{\text{H}} = 7.52$ G, $g = 2.00499$, respectively, are equal within experimental error to those found by Behar and Fessenden⁷ for the same two species. (The $\dot{\text{S}}\text{O}_3^-$ adduct has also been reported by Norman and Storey.¹³) Addition of N_2O to this solution caused the disappearance of the signals of CH_3NO_2^- (see Figure 2) showing that this radical comes from e_{aq}^- .

The formation of e_{aq}^- in the photolysis of SO_3^{2-} suggests the use of SO_3^{2-} as a convenient source of this important species. The potential for such general studies is shown by the formation of CH_2CO_2^- when 7 mM SO_3^{2-} at pH 12.3 is photolyzed in the presence of 8.4×10^{-2} M $\text{ClCH}_2\text{CO}_2^-$.

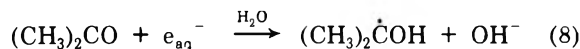


(No signal of CH_2CO_2^- is obtained in the absence of SO_3^{2-}). Before the photolysis of SO_3^{2-} can be proposed as a general source of e_{aq}^- it is important to establish the absence of by-products of the photolysis which could compete for e_{aq}^- . One product which has been identified¹⁴ (in small yield) is dithionate ($\text{S}_2\text{O}_6^{2-}$) formed by coupling of two SO_3^- radicals. However, *in situ* radiolysis experiments with dithionate showed that neither e_{aq}^- nor $(\text{CH}_3)_2\dot{\text{C}}\text{OH}$ react to produce $\dot{\text{S}}\text{O}_3^-$. The other major product,¹⁴ SO_4^{2-} , will not react with e_{aq}^- . We conclude therefore that reaction with photolysis by-products should not be a problem.

Photosensitization. Because of the esr work using excited acetone as an initiator¹⁵ one of the early motivations of this work was to determine if excited acetone can react by other than H atom abstraction. In particular it seemed possible that it could remove an electron from SO_3^{2-} in the same way as OH does. Initial experiments showed that acetone added to solutions of SO_3^{2-} did indeed increase the signal amplitude of $\dot{\text{S}}\text{O}_3^-$ by up a factor of 10 (depending upon sulfite concentration). Typical concentrations of acetone were 0.1–0.5 M but at this concentration the main optical absorption at 265 nm did not significantly overlap that of SO_3^{2-} . An alternative to the mechanism proposed above for the effect of acetone is the transfer of triplet energy from excited acetone to SO_3^{2-} followed by dissociation of the excited SO_3^{2-} .



With these high concentrations of acetone, scavenging of e_{aq}^- is expected



Experiments carried out under proper pH conditions showed the superimposed spectra of $(\text{CH}_3)_2\dot{\text{C}}\text{OH}$ and $\dot{\text{S}}\text{O}_3^-$. (Some care with the pH is necessary in observing $(\text{CH}_3)_2\dot{\text{C}}\text{OH}$ because base-catalyzed exchange⁵ of the hydroxyl proton broadens the lines, beginning at pH ~ 10 .) Relative concentrations of $\dot{\text{S}}\text{O}_3^-$ and $(\text{CH}_3)_2\dot{\text{C}}\text{OH}$ were determined by doubly integrating a first-derivative spectrum taken for 1.6 mM SO_3^{2-} , 0.68 M acetone, and 1 mM $\text{Na}_2\text{B}_4\text{O}_7$ as buffer. The relative concentrations were found to be $[\dot{\text{S}}\text{O}_3^-]:[(\text{CH}_3)_2\dot{\text{C}}\text{OH}] = 1.0:0.61$. The lower concentration of $(\text{CH}_3)_2\dot{\text{C}}\text{OH}$ implies a faster recombination for this radical than for $\dot{\text{S}}\text{O}_3^-$. With equal production rates for $\dot{\text{S}}\text{O}_3^-$ and $(\text{CH}_3)_2\dot{\text{C}}\text{OH}$ it is possible to determine the ratio of the recombination rates for the two species without considering the cross-combination reaction. Taking the rate constant for $(\text{CH}_3)_2\dot{\text{C}}\text{OH}$ ¹⁶ as $1.4 \times 10^9 \text{ M}^{-1} \text{ sec}^{-1}$ gives a value of $2k = 5.4 \times 10^8 \text{ M}^{-1} \text{ sec}^{-1}$ for $\dot{\text{S}}\text{O}_3^-$. This value is significantly less than the value of 1.9×10^9 found by Behar and Fessenden⁶ but is closer to that of 1.1×10^9 given by Hayon, *et al.*,⁹ for zero ionic strength.

(11) G. W. Chantry, A. Horstfield, J. R. Morton, J. R. Rowlands, and D. H. Whiffen, *Mol. Phys.*, **5**, 233 (1962).

(12) V. V. Gromov and J. R. Morton, *Can. J. Chem.*, **44**, 527 (1966).

(13) R. O. C. Norman and P. M. Storey, *J. Chem. Soc. B*, 1009 (1971).

(14) F. Haber and O. H. Wansbrough-Jones, *Z. Phys. Chem.*, **18B**, 103 (1932).

(15) H. Zeldes and R. Livingston, *J. Chem. Phys.*, **45**, 1946 (1966).

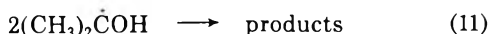
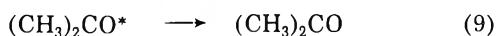
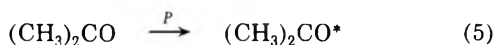
(16) M. Simic, P. Neta, and E. Hayon, *J. Phys. Chem.*, **73**, 3794 (1969).

A number of other sensitizers were also found to affect the $\dot{S}O_3^-$ signal as shown in Table I.¹⁷ While most sensitizers increased the $\dot{S}O_3^-$ signal, the two molecules of lowest triplet energy, biacetyl and anthracene-9-carboxylic acid, decreased it. With acetophenone and benzophenone which absorb strongly at wavelengths >300 nm it was possible to get a significant signal of $\dot{S}O_3^-$ by photolysis with a Pyrex filter (which passes $\lambda >310$ nm where SO_3^{2-} itself does not absorb). Unfortunately (because of solubility limitations) all of the sensitizers which were found to increase the signal of $\dot{S}O_3^-$ are the same type, namely, ketones, so that it is not possible on this basis alone to choose whether the mechanism involves triplet energy transfer to or electron abstraction from the sulfite.

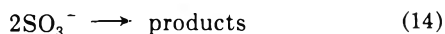
Fortunately, it was possible to demonstrate the triplet energy transfer by detecting the e_{aq}^- formed in the acetone photosensitized decomposition of SO_3^{2-} . In this experiment a solution of 0.19 M acetone and 7.0 mM SO_3^{2-} was photolyzed in the presence of 8.4×10^{-2} M $ClCH_2CO_2^-$. The resulting spectrum contained the lines of $\dot{C}H_2CO_2^-$ and $\dot{S}O_3^-$ at an intensity much larger than obtained in the absence of the acetone. Because $(CH_3)_2\dot{C}OH$ does not react¹⁸ with $ClCH_2CO_2^-$ it must be concluded that e_{aq}^- is formed in the sensitized decomposition and is scavenged by the $ClCH_2CO_2^-$ (reaction 4). A similar reaction was observed for $BrCH_2CO_2^-$.

Quenching Rate Determination. An attempt was made to measure the rate of quenching of triplet acetone by SO_3^{2-} in experiments where this quenching was competitive with the reaction of the triplet with isopropyl alcohol. The relative importance of the two paths was determined by the height of the esr signal of $(CH_3)_2\dot{C}OH$. Rates relative to that of the natural decay of triplet acetone are found and if a value for this rate is available then absolute rate constants for the other processes can be determined.

The reactions with isopropyl alcohol alone are



and in the presence of sulfite one has to add



Use of these equations assumes that e_{aq}^- always reacts with acetone (which is reasonable because of the high concentration of acetone) and that every quenching of $(CH_3)_2CO^*$ by SO_3^{2-} causes decomposition by reaction 12. Before going further we wish to describe experiments relevant to the latter point.

A solution of 0.68 M acetone and 1.3 M isopropyl alcohol was photolyzed first without and then with 5.4 mM SO_3^{2-} under otherwise identical conditions (pH 9.4, buffered with ~ 1 mM $Na_2B_4O_7$). In the first experiment all excited acetone molecules are quenched to produce two $(CH_3)_2\dot{C}OH$ radicals while in the second case one $(CH_3)_2\dot{C}OH$ and one $\dot{S}O_3^-$ should be formed for 100% ef-

TABLE I: Effect of Various Sensitizers on the Height of the SO_3^{2-} Esr Signal in the Photolysis of SO_3^{2-}

Sensitizer	Triplet energy, ^a kcal mol ⁻¹	Concn, M	Effect
Acetone	78.0	0.05–0.7	Increase
Acetophenone	76.3	4×10^{-4}	Increase
Benzophenone	69.2		Increase
β -Acetonaphthone	59.5	$<9 \times 10^{-5}$	Increase
α -Acetonaphthone	58	3×10^{-4}	Increase
Benzil	57.3	3.5×10^{-5}	Increase
Biacetyl	57.2	5.7×10^{-4}	Decrease
Anthracene-9-carboxylic acid		$<10^{-5}$	Decrease

^a Values taken from J. G. Calvert and J. N. Pitts, Jr., "Photochemistry," Wiley, New York, N. Y., 1966, p 298.

iciency upon quenching. If it is assumed that the rate constant for the cross-combination reaction (13) is the geometric mean of those for self-recombinations then the relative (integrated) intensities of the $(CH_3)_2\dot{C}OH$ signals in the two cases can immediately be used to calculate the ratio of production rates (reactions 10 and 12); the value so found is 1 to 0.52. (The differing stoichiometry in the two reactions has been included.) Strictly interpreted this result means that every quenching by SO_3^{2-} yields $\dot{S}O_3^-$ (and an equivalent amount of $(CH_3)_2\dot{C}OH$) only one-half the time but this ratio is probably within experimental error of unity. The possible inefficiency in production of radicals must be considered in the competitive experiments with acetone and SO_3^{2-} both present.

In carrying out the competitive quenching experiments a solution 0.68 M in acetone and 1.3 M in isopropyl alcohol was photolyzed with no sulfite present. Analysis of the kinetics of the appropriate reactions (5, 9, 10, and 11) shows that a plot of $1/[R]^2$ against $1/[RH]$ should be linear with a ratio of slope to intercept of k_9/k_{10} (here $R = (CH_3)_2\dot{C}OH$ and $RH = (CH_3)_2CHOH$). This plot is given in Figure 3 with $[R]$ measured by the height of the largest component of the central line. The value of k_9/k_{10} from this plot is 0.17 M.

When SO_3^{2-} is added the kinetic expressions become much more complex. In order to solve them it was necessary to assume that all of the radical combination reactions have the same rate constants. Although the recombination of $\dot{S}O_3^-$ was seen above to be somewhat slower than for $(CH_3)_2\dot{C}OH$ this assumption is not considered to be a serious problem because attention will be focussed on the intensity of the signals of $(CH_3)_2\dot{C}OH$ only and the other recombinations will be small perturbations. The kinetic expression (reactions 5 and 8–14) is

$$\frac{1}{[R]^2} = \frac{k_{11}}{P} \left[\left(1 + \frac{f k_{12}[S]}{k_{10}[RH]} \right) / \left(1 + \frac{f k_{12}[S]}{2k_{10}[RH]} \right) \right] \times \left[1 + \frac{k_9}{k_{10}[RH]} + \frac{k_{12}[S]}{k_{10}[RH]} \right] \quad (A)$$

where $S = SO_3^{2-}$ and f is the fraction of the quenching

(17) Interestingly, J. Weiss very early [*Naturwissenschaften*, 23, 61 (1935)] described the quenching by sulfite of the fluorescence of several dyes such as eosin.

(18) M. Anbar and P. Neta, *J. Chem. Soc. A*, 837 (1967). A blank with acetone and $ClCH_2CO_2^-$ showed no signals from $\dot{C}H_2CO_2^-$ but weak lines were observed when isopropyl alcohol was also added. Apparently $(CH_3)_2\dot{C}OH$ reacts slowly with $ClCH_2CO_2^-$ but not to an extent which significantly affects the conclusion given in the text.

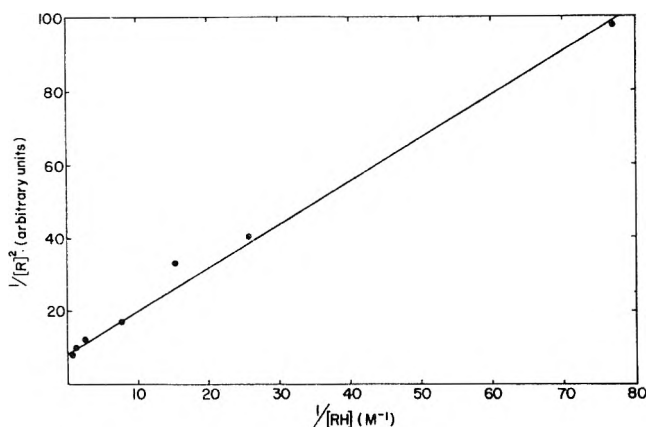


Figure 3. Dependence of $[(\text{CH}_3)_2\dot{\text{C}}\text{OH}]^2$ upon reciprocal concentration of $(\text{CH}_3)_2\text{CHOH}$ in an aqueous solution of 0.68 M acetone.

reaction (12) which leads to radical products. For $fk_{12}[\text{S}] < k_{10}[\text{RH}]$ the first bracketed term is near unity so that $1/[\text{R}]^2$ should be linear in $[\text{SO}_3^{2-}]$. The plot of $[\text{R}]_0^2/[\text{R}]^2$, where $[\text{R}]_0$ is the signal height in the absence of SO_3^{2-} , is given in Figure 4. On the basis of the kinetic expression it is expected that the actual points should fall below the line defined by the low concentration points. In practice the data fall above this line. This departure from the kinetic expression may be the result of the various approximations or of the neglect of the direct photolysis of SO_3^{2-} . The data for $[\text{R}]_0^2/[\text{R}]^2 < 2.5$ lead to the value of $k_{12}/k_{10} = 0.49 \times 10^3$ or $k_{12}/k_9 = 2.9 \times 10^3 \text{ M}^{-1}$. The lifetime of triplet acetone in water has been reported to be 22 μsec .¹⁹ If this value is used to evaluate k_9 then k_{10} and k_{12} become 1.9×10^5 and $9 \times 10^7 \text{ M}^{-1} \text{ sec}^{-1}$, respectively. This value for k_{12} , although indicative of a rapid reaction, is more than an order of magnitude less than that expected for a diffusion-controlled reaction. Some other factor, such as the difference in triplet energy between acetone and sulfite, then appears to be important in determining the rate constant. The fact that triplets of lower energy also seem to transfer to sulfite is against this idea. An alternative explanation of the low value of k_{12} is that the reference lifetime of triplet acetone is greater than the value pertaining under our conditions (0.68 M acetone).²⁰ If so, then the values of k_{10} and k_{12} should be regarded as lower limits. It should be noted that the value of k_{10} is much less than that for $\dot{\text{O}}\text{H}$ reaction with isopropyl alcohol (10^9).²¹

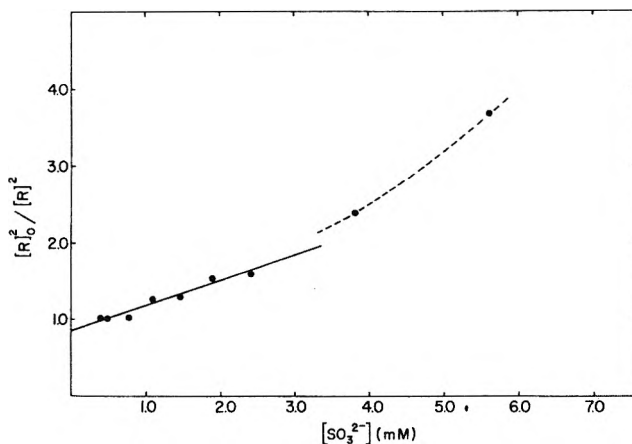


Figure 4. Plot of normalized concentration of $(\text{CH}_3)_2\dot{\text{C}}\text{OH}$ as a function of $[\text{SO}_3^{2-}]$ as appropriate to kinetic eq A for quenching by SO_3^{2-} (see text). Solution contains 0.68 M acetone and 1.3 M $(\text{CH}_3)_2\text{CHOH}$ together with added SO_3^{2-} .

Conclusions

The present results confirm by esr that the photolysis of dilute aqueous solutions of sulfite leads to the production of $\dot{\text{S}}\text{O}_3^-$ and e_{aq}^- and that this decomposition can be sensitized by a number of ketones of triplet energy $>57 \text{ kcal mol}^{-1}$. The sensitization has been specifically shown to result in production of e_{aq}^- . Each quenching reaction leads to dissociation of the SO_3^{2-} with near unit efficiency if it can be assumed that each quenching of excited acetone by isopropyl alcohol leads to reaction producing two $(\text{CH}_3)_2\dot{\text{C}}\text{OH}$ radicals.

Photolysis of SO_3^{2-} is proposed as a source of e_{aq}^- for studies of the reactions of this radical in the absence of an *in situ* radiolysis set up (which is the only other source to date of e_{aq}^-). Although the light absorption by SO_3^{2-} is mainly of shorter wavelengths where the lamp output is small the absence of "back reactions" of products of the photolysis is an advantage.

- (19) G. Porter, R. W. Yip, J. M. Dunston, A. J. Cessna, and S. E. Suga-mori, *Trans. Faraday Soc.*, **67**, 3149 (1971). It should be noted that this value is for an acetone concentration of 10^{-2} M so that under our conditions of 0.68 M a shorter lifetime is possible.
- (20) The reaction of triplet acetone with another acetone molecule cannot be a major source of this proposed lifetime shortening because one should then see strong esr lines of $(\text{CH}_3)_2\dot{\text{C}}\text{OH}$ in solutions of acetone alone. No such signals are seen.
- (21) See M. Anbar and P. Neta, *Int. J. Radiat. Isotopes*, **18**, 493 (1967).

An Electron Spin Resonance Study of Radicals Produced in the Photolysis of α -Keto Acids and Esters¹

A. Samuni, D. Behar, and R. W. Fessenden*

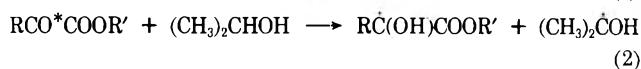
Radiation Research Laboratories, Center for Special Studies and Department of Chemistry, Mellon Institute of Science, Carnegie-Mellon University, Pittsburgh, Pennsylvania 15213 (Received October 16, 1972)

Publication costs assisted by the Carnegie-Mellon University and the U. S. Atomic Energy Commission

Radicals of the type $\text{RC}(\text{OH})\text{COOR}'$, produced by photoreduction of α -keto acids and esters in 2-propanol solutions, have been studied by esr. In each of the five systems, glyoxylic acid, pyruvic acid, ketobutyric acid, methyl pyruvate, and ethyl pyruvate, the esr spectrum gave evidence for the existence of comparable concentrations of two different species interpreted as cis and trans isomers of the $\text{RC}(\text{OH})\text{COOR}'$ radicals. Accurate hyperfine constants are given for the pairs of isomers in all but the first case where resolution of the individual spectra was not possible.

Introduction

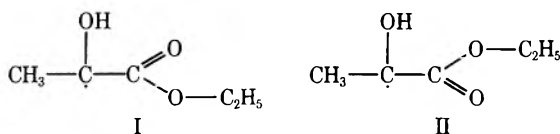
Radicals of the type $\text{RC}(\text{OH})\text{COOR}'$ have been detected in the reduction of the appropriate 2-keto organic acids or esters²⁻⁴ and in the oxidation of the 2-hydroxy compounds.^{5,6} The reduction of the carbonyl-containing compounds was carried out by either photoexcitation^{2,4} of the carbonyl molecule which then abstracts hydrogen from the solvent



or chemically³ via one electron reducing agent such as $\dot{\text{C}}\text{O}_2\text{H}$.



The esr spectra of the resulting α -hydroxyalkyl radicals were observed in both aqueous and nonaqueous solutions. Although in most cases the experimental findings and the spectral assignments agreed, in some cases conflicting results were reported as well as differing interpretations of the spectra. For instance, various characterizations were suggested for the radicals formed from ethyl pyruvate. Fujisawa, *et al.*,² generated the radical by photoreduction of the ester in 2-propanol. They measured values of 16.48, 0.82, and 2.14 G for the coupling constants of the α -methyl, $-\text{CH}_2-$, and OH protons, respectively, and identified the free radical as $\text{CH}_3\dot{\text{C}}(\text{OH})\text{COOC}_2\text{H}_5$. On the other hand, Anderson, *et al.*,³ on reacting the ester with $\dot{\text{C}}\text{O}_2\text{H}$, using a rapid mixing technique, reported the observation of the cis and trans isomers I and II. The splittings of the



methylene and hydroxyl protons measured by them were found to be fortuitously equivalent ($a(\text{CH}_3) = 17.0$ G, $a(\text{CH}_2) = a(\text{OH}) = 1.7$ G for one isomer and $a(\text{CH}_3) = 16.5$ G, $a(\text{CH}_2) = a(\text{OH}) = 1.5$ G for the second isomer). However, not all the features of the spectrum were fitted by these parameters, suggesting either the presence of some other radicals or misinterpretation of the observed

spectra. It has also been found⁷ that the esr spectra derived from the acids themselves ($\text{RC}(\text{OH})\text{COOH}$ where $\text{R} = \text{H}, \text{CH}_3,$ or C_2H_5) exhibit anomalous intensity ratios among the hyperfine lines. Although the most obvious explanation for this phenomenon is some form of exchange of the hydroxyl and carboxyl protons no mechanism is apparent which would account for the observed pattern of line broadening. In the present paper we wish to present some results which help considerably in answering the questions raised by these previous papers.

Experimental Section

The photolysis system and the esr apparatus was as previously described.⁸ Magnetic field measurements were made with a field-tracking nmr unit and frequency counter. The g factors were determined from measurements of field and microwave frequency (also by frequency counting) with account taken of the magnetic field difference between the esr sample and nmr probe positions. Photolysis was performed under flow conditions with a flow rate of about 1 ml/min. Pyruvic acid, methyl pyruvate, ethyl pyruvate, and 2-ketobutyric acid from Aldrich and glyoxylic acid from Pfaltz and Bauer were used without further purification. All solutions were deoxygenated by bubbling with nitrogen prior and during the photolysis. Second-derivative spectra were taken to provide somewhat better resolution than obtainable in the first-derivative mode. This fact accounts in part for the observation of more structure than found by previous workers.²⁻⁴

Results and Discussion

Pyruvic Acid. The esr spectrum observed during the photolysis of a 5% pyruvic acid solution in 2 propanol is shown at the top of Figure 1. This spectrum is in accord with previous findings where the $\text{CH}_3\dot{\text{C}}(\text{OH})\text{COOH}$ radi-

- (1) Supported in part by the U. S. Atomic Energy Commission.
- (2) T. Fujisawa, B. M. Monroe, and G. S. Hammond, *J. Amer. Chem. Soc.*, **92**, 542 (1970).
- (3) N. H. Anderson, A. J. Dobbs, D. J. Edge, R. O. C. Norman, and P. R. West, *J. Chem. Soc. B*, 1004 (1971).
- (4) P. B. Ayscough and M. C. Brice, *J. Chem. Soc. B*, 491 (1971).
- (5) W. T. Dixon, R. O. C. Norman, and A. L. Buley, *J. Chem. Soc.*, 3625 (1964).
- (6) M. Simic, P. Neta, and E. Hayon, *J. Phys. Chem.*, **73**, 4214 (1969).
- (7) N. L. Arthur and R. W. Fessenden, unpublished results.
- (8) D. Behar and R. W. Fessenden, *J. Phys. Chem.*, **75**, 2752 (1971).

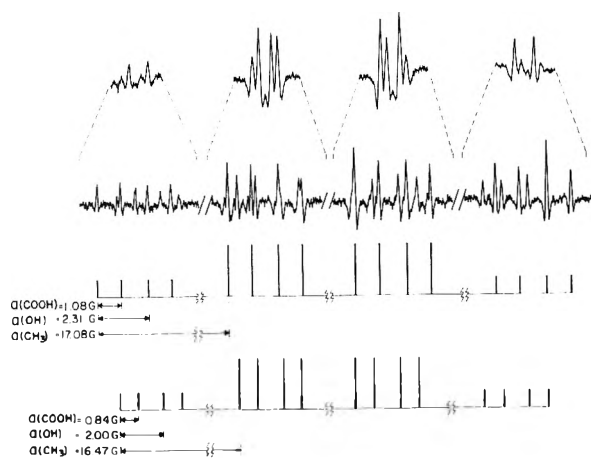


Figure 1. Portions of second-derivative esr spectra observed during the photolysis of pyruvic acid in 2-propanol: upper trace, 5% acid; lower trace, 0.2% acid. Superimposed lines from two isomeric radicals are resolved in the lower trace. Each of the lines of first-order intensity three (i.e., with $I_z = \pm 1/2$) shows a partial resolution into the second-order components of intensity ratio 1:2. Signal enhancement can be seen by comparing corresponding lines in the end groups. The lines in the high-field group are more intense.

cal was produced photochemically² (reactions 1 and 2) or through redox reactions of lactic acid⁵ and pyruvic acid³ in rapid-mixing experiments. In the above-mentioned cases^{2,3,5} the coupling with the carboxyl proton was not observed so that the anomalous intensity pattern, seen at the top of Figure 1, was not detected. Ayscough and Brice⁴ improved the resolution by reducing the acid concentration and were able to observe the splitting by the acid proton. The reason for this improvement is the reduction in the rate of exchange of the acid proton which affects the line widths. They⁴ do not, however, report any unusual broadening of the signals or irregular intensity ratios. In our experiment the splitting by the carboxyl proton was observable even at 10% pyruvic acid. When the concentration of the acid was lowered to 0.2% further resolution was achieved (see the lower trace in Figure 1). Lines from two different radicals, rather than only one, are identified by the stick spectra shown in Figure 1. Each spectrum can be described by three coupling constants ($a(\text{CH}_3)$, $a(\text{OH})$, and $a(\text{COOH})$) as given in Table I. On the addition of 50% water and an increase in pH from 2 to 4 the spectra remained essentially unchanged. The close similarity between the magnetic parameters of these two radicals suggests the presence of two rotational isomers, cis and trans. A lack of free rotation about the $\text{CH}_3\text{C}(\text{OH})\text{-COOH}$ bond as a consequence of partial double bond character would obviously account for the discrete spectra. The finding of two isomers in the case of pyruvic acid is in accord with the recent suggestion³ of cis and trans isomers for the radicals derived from ethyl pyruvate.

Only very weak lines attributable to radicals of the type discussed above were found in experiments on neutral or basic solutions and no interpretation of these lines was possible. However, a more intense set of lines which consists of a 6.89-G septet ($g = 2.00455$) did appear. The intensity of this spectrum was independent of the flow rate suggesting that this radical is not a result of some secondary reactions. The intensity distribution of the lines is very close to 1:6:15:20:15:6:1 which would be found for a radical with six equivalent protons. These magnetic

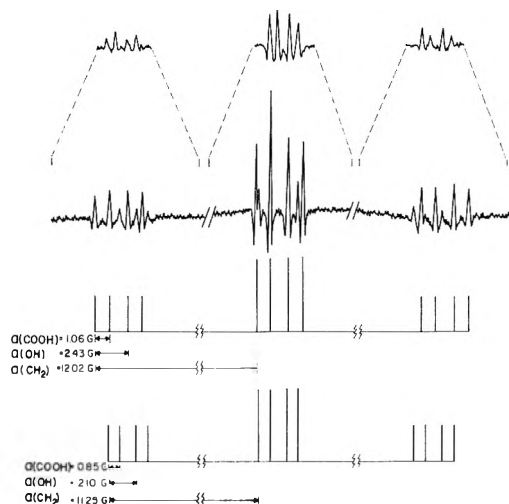


Figure 2. ESR spectra observed during the photolysis of keto-butyric acid in 2-propanol: upper trace, 10% acid; lower trace, 0.2% acid.

parameters fit well with the 6.84-G hyperfine constant ($g = 2.00470$) found by Zeldes and Livingston⁹ for the biacetyl radical anion. In their work⁹ they showed that very low concentrations of biacetyl present as impurities could be responsible for the appearance of the biacetyl radical spectrum. The biacetyl could be present as an impurity in the pyruvic acid or could be produced photolytically in some way.

Similar results were obtained in the photolysis of 2-ketobutyric acid. The unresolved spectrum of $\text{CH}_3\text{CH}_2\dot{\text{C}}(\text{OH})\text{COOH}$ with 10% solute is compared in Figure 2 with the resolved one obtained with 0.2% solute. The measured magnetic parameters are summarized in Table I. The spectra are attributed to the two isomers of $\text{C}_2\text{H}_5\dot{\text{C}}(\text{OH})\text{COOH}$.

When glyoxylic acid was photolyzed, the esr spectrum exhibited the same type of unsymmetrical intensity pattern as was found with the above mentioned acids at high solute concentrations. In this case attempts to achieve better resolution by decreasing the acid concentration were not successful. Nevertheless, it would be reasonable to assume that the rotational isomerism exists also in the case of the glyoxylic acid.

Ethyl and Methyl Pyruvate. Anderson, *et al.*,³ produced $\text{CH}_3\dot{\text{C}}(\text{OH})\text{COOC}_2\text{H}_5$ from ethyl pyruvate by reacting CO_2H radical with the ester. They claim that the spectrum obtained in the pH region 1–5 contains two quartets of quartets which can be attributed to the radicals I and II. As mentioned before, they interpreted their spectra by assuming that in both isomers $a^{\text{H}}(\text{OH}) = a^{\text{H}}(\text{CH}_2)$. Above pH 6 these spectra disappeared and were replaced by two 1:3:3:1 quartets further split into 1:2:1 triplets. They attributed the latter spectra to the dissociated forms of the two isomers given above and estimated a pK of ~ 6 for the dissociation constant of the hydroxyl group.

In our experiments $\text{CH}_3\dot{\text{C}}(\text{OH})\text{COOC}_2\text{H}_5$ was produced by photolyzing the ester in 2-propanol. Again two isomers were found. The spectrum is given in Figure 3 and the hyperfine constants and g value in Table I. As seen in the figure, no equivalence was found between the hyperfine constants of the OH and the CH_2 protons. Anderson, *et*

(9) H. Zeldes and R. Livingston, *J. Chem. Phys.*, **47**, 1465 (1967).

TABLE I: Hyperfine Constants of Radicals Produced in the Photolysis of α -Keto Acids and Esters in 2-Propanol^{a,b}

Source	Radical		$a^H(\beta)$	$a^H(\text{OH})$	$a^H(\text{COOH})$	$a^H(\text{OCH})$	g
CH ₃ COCOOH	CH ₃ $\dot{\text{C}}$ (OH)COOH	Cis	17.08	2.31	1.08		2.00369
		Trans	16.47	2.00	0.84		2.00374
CH ₃ CH ₂ COCOOH	CH ₃ CH ₂ $\dot{\text{C}}$ (OH)COOH	Cis	12.02	2.43	1.06		2.00370
		Trans	11.25	2.10	0.85		2.00375
CH ₃ COCOOC ₂ H ₅	CH ₃ $\dot{\text{C}}$ (OH)COOC ₂ H ₅	Cis	16.74	2.23		1.51 (CH ₂)	2.00384
		Trans	16.41	1.92		1.17 (CH ₂)	2.00387
CH ₃ CH(OH)COOC ₂ H ₅	CH ₃ $\dot{\text{C}}$ (O ⁻)COOC ₂ H ₅	c	11.17			1.61 (CH ₂)	2.00433
		c	10.88			1.43 (CH ₂)	2.00428
CH ₃ COCOCH ₃	CH ₃ $\dot{\text{C}}$ (OH)COOCH ₃	Cis	16.70	2.22		1.57 (CH ₃)	2.00384
		Trans	16.37	1.95		1.31 (CH ₃)	2.00387

^a Hyperfine constants in gauss are accurate to ± 0.03 . Absolute g factors are accurate to ± 0.00003 but relative g factors for the pairs of radicals are known to ± 0.00001 . ^b Tentative assignment of parameters to cis and trans isomers (see text). ^c Because of a different correlation of g factor and methyl group splitting than observed for the other pairs no assignment to cis and trans isomers is made (see text).

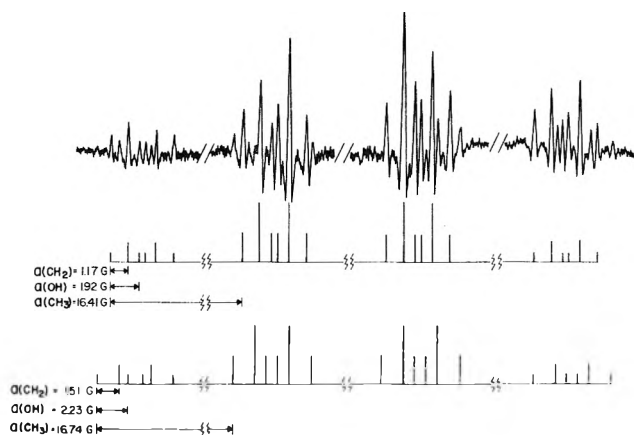


Figure 3. ESR spectrum observed during the photolysis of 5% ethyl pyruvate in 2-propanol.

al.,³ found considerably different coupling constant for the methylene group than did Fujisawa, *et al.*,² and attributed that difference to the solvent used. To check on this effect the solvent was changed from 100% 2-propanol to 50% water-50% 2-propanol (pH 2.1). The spectra obtained in both cases were essentially the same.

It is clear that the previous interpretations^{2,3} represent attempts to fit the incompletely resolved spectra and, on the basis of the present results, must be regarded as incorrect as to the finer detail. Fujisawa, *et al.*,² who did not think in terms of two isomers, reported values which represent averages for the two isomers. These values are not greatly different from the present ones. Anderson, *et al.*,³ who did invoke two isomers, nevertheless arrived at splittings for the OH and CH₂ groups which are not in accord with those given here. Their somewhat poorer resolution seems to be responsible.

We were not successful in producing enough signal intensity to study the dissociated form (CH₃ $\dot{\text{C}}$ (O⁻)-COOC₂H₅) in photolytic experiments. Instead this radical was produced radiolytically¹⁰ by hydrogen abstraction from ethyl lactate. Two isomers with hyperfine constants as given in Table I were present at pH 9.0 and 7.1 with only weak lines at pH 6.2. These hyperfine constants are in excellent agreement with those reported by Anderson, *et al.*³ The observation of these dissociated forms at pH 7.1 supports the suggestion that the pK of the OH proton in CH₃ $\dot{\text{C}}$ (OH)COOC₂H₅ is approximately 6.

The photolysis of methyl pyruvate in 2-propanol and in a 1:1 mixture of 2-propanol and water also yielded spec-

tra of two geometrical isomers. The hyperfine constants and g values are given in Table I. Under slightly basic conditions the spectra of the CH₃ $\dot{\text{C}}$ (OH)COOCH₃ radicals almost disappeared and spectra of two other radicals appeared. One of these radicals was easily identified as the biacetyl radical anion also obtained when pyruvic acid was photolyzed under similar conditions. The spectrum of the other radical consists of four 1:3:3:1 quartets and is described by the parameters $a^H = 19.68$, $a^H = 19.00$, $a^H = 0.11$ G (three protons), and $g = 2.00452$. Interestingly, an experimentally identical spectrum was obtained with ethyl pyruvate. A very similar spectrum was also obtained with pyruvic acid in radiolytic experiments ($a^H = 21.00$, $a^H = 19.09$, $a^H = 0.15$ G (three protons), and $g = 2.00448$). The fact that very similar spectra were obtained from all three compounds shows that the small quartet splitting must arise from the methyl group of the pyruvate portion of the molecule. To have radicals with the proper number of protons all derived from pyruvate group it is necessary to suggest some dimeric species. This species could be formed either by a polymerization reaction of an initially formed radical with an enol of the pyruvate or directly from some condensation product formed prior to irradiation. The similarity of the two large hyperfine constants and the g factor to those of the radical $\cdot\text{CH}_2\text{COCH}_3$ ($a^H = 19.95$, $a^H = 19.48$ G, and $g = 2.00443$)¹¹ suggests that perhaps the present radical has this type of structure (CH₂COR) with the methyl group responsible for the small quartet in a γ or δ position.

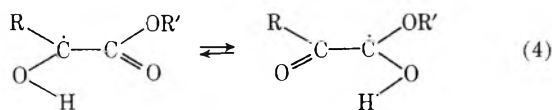
The differences of the methyl group hyperfine constants and g factors between the pairs of isomers in Table I can be used to provide tentative assignments of values to the cis or trans forms. It is generally agreed that the cis isomer of semidiones¹² exhibits the higher β position coupling constant and the lower g factor. A similar correlation exists for anion radicals of oxalate esters.¹³ All of the neutral radical pairs in Table I show this same correlation of hyperfine constant and g factor so it is tempting to identify the isomers accordingly. (Note, however, that for CH₃ $\dot{\text{C}}$ (O⁻)COOC₂H₅ the correlation is in the opposite sense.) A difficulty with this assignment is the possibility of a rapid intramolecular proton exchange for the cis isomer as is observed for the oxalate esters (eq 4).¹³ Such an exchange would reduce the average R group hyperfine

(10) K. Eiben and R. W. Fessenden, *J. Phys. Chem.*, **75**, 1186 (1971).

(11) H. Zeldes and R. Livingston, *J. Chem. Phys.*, **45**, 1946 (1966).

(12) Glen A. Russell, *Science*, **161**, 423 (1968).

(13) H. Zeldes and R. Livingston, *J. Phys. Chem.*, **74**, 3336 (1970).



constant because of the low value in the form on the right. The trans isomer has no comparable exchange possible and the observation of the OH proton splitting shows that no intermolecular exchange is occurring. Because of the very large difference in hyperfine constants between the two forms in eq 4 (16 G *vs.* an estimated 1–2 G where R = CH₃) the exchange would have to be extremely rapid (10¹⁰–10¹¹ sec⁻¹) to give a spectrum with narrow lines. Such a rapid exchange is thought to be unlikely so that assignment as given in Table I is made by analogy with the semidiones.

Conclusions

All α hydroxy radicals of the type RC(OH)COOR' investigated by us showed the existence of comparable concentrations of two cis-trans isomers which differ slightly in their magnetic parameters. The existence of discrete spectra for the pairs of isomers, as is established by this work, shows that internal rotation must be slow. In addition the existence of pairs of isomers clearly shows that the finer details of previous interpretations^{2,3} of the spectrum obtained with ethyl pyruvate must be incorrect. The anomalous intensity distribution of the lines in the spectra previously observed has been shown to arise from poor resolution of the overlapping lines from the pairs of isomers. The improved resolution obtained by decreased acid concentrations and the use of second-derivative spectra has allowed most of the lines to be resolved.

Electron Paramagnetic Resonance Evidence for a Peroxy Type Superoxide Ion on Surfaces

Y. Ben Taarit¹ and J. H. Lunsford*

Department of Chemistry, Texas A & M University, College Station, Texas 77843 (Received October 2, 1972)

Publication costs assisted by the National Science Foundation

The oxygen-17 hyperfine structure for the superoxide ion formed on a decationated zeolite and molybdenum(VI) supported on silica gel confirms that the two oxygen atoms are unequal. Two sets of hyperfine lines were observed for each surface. These are characterized by $a_{yy}(1) = 63 \pm 1$ G and $a_{yy}(2) = 82 \pm 1$ G for the zeolite and $a_{yy}(1) = 69 \pm 1$ G and $a_{yy}(2) = 82 \pm 1$ G for the supported molybdenum. The related sextets responded in exactly the same manner with respect to the rate of formation, thermal stability, and response to variations in the microwave power. The ¹⁷O¹⁷O⁻ pattern was also consistent with the peroxy type structure. The surface-to-ion bond shows from 95 to 100% ionic character, which is considerably different from organic peroxy radicals.

Introduction

A one-electron transfer from a solid surface to molecular oxygen results in the formation of the superoxide ion. This ion has been extensively studied by electron paramagnetic resonance (epr) spectroscopy and the resulting spectra have been recently reviewed.² The spectra were first identified on the basis of the *g* tensor; however, Tench and coworkers³⁻⁵ have used oxygen-17 to verify the assignments on several solids. Their work on MgO, ZnO, TiO₂, and SnO₂ showed that the two oxygen atoms are equivalent and must be in a plane which is parallel to the surface. The 11-line spectrum for two equivalent oxygen-17 atoms is clearly seen for the ion on MgO, ZnO, and SnO₂. On TiO₂ (rutile) the situation is more complex because the superoxide ion is formed at two types of sites; yet, it is possible to resolve the spectra since the species exhibit different stabilities. Here too, it was concluded that the oxygen atoms are equivalent.

Miller and Haneman⁶ analyzed the *g* tensor and the ²⁷Al hyperfine spectrum for O₂⁻ on a clean AlSb surface. They demonstrated that the superoxide ion was not parallel to the surface. Symons⁷ has also suggested that the superoxide ion bound to aluminum in decationated zeolites may be more like a peroxy radical; *i.e.*, the two oxygens are not equivalent. His conclusions were based on the

- (1) On leave from Institut de Recherches sur la Catalyse, C.N.R.S., Villeurbanne, France.
- (2) J. H. Lunsford, *Catal. Rev.*, **8**, 135 (1973).
- (3) A. J. Tench and P. J. Holroyd, *Chem. Commun.*, 471 (1968); A. J. Tench and T. Lawson, *Chem. Phys. Lett.*, **7**, 459 (1970); A. J. Tench, T. Lawson, and J. F. J. Kibblewhite, *J. Chem. Soc., Faraday Trans. 1*, **68**, 1169 (1972).
- (4) C. Naccache, P. Meriaudeau, M. Che, and A. J. Tench, *Trans. Faraday Soc.*, **67**, 506 (1971).
- (5) P. Meriaudeau, C. Naccache, and A. J. Tench, *J. Catal.*, **21**, 208 (1971).
- (6) D. J. Miller and D. Haneman, *Phys. Rev.*, **3**, 2918 (1971).
- (7) M. C. R. Symons, *J. Phys. Chem.*, **76**, 3095 (1972).

similarities between the magnetic parameters of O_2^- and those of other radicals which may have a peroxy type structure.⁸⁻¹¹

Experiments utilizing oxygen-17 were carried out in order to test the proposition that the two oxygen atoms are not equivalent for the superoxide ion formed in deca- tionated zeolites. The work was also extended to a study of O_2^- on molybdenum oxide supported on silica gel.

Experimental Section

The NH_4Y zeolite was prepared by a conventional ion-exchange technique using an NH_4NO_3 solution and a Linde NaY powder. The residual sodium content was about 1% by weight.

Samples of the dry zeolite were activated in a quartz cell which had a 4-mm diameter side arm. The dehydrox- ylation process was carried out at 600° *in vacuo* for 8 hr. Further reduction in hydrogen and a final evacuation were carried out at the same temperature.

Oxygen-16 or oxygen-18 enriched to 44.5% in ^{17}O were adsorbed at room temperature at a pressure of 18 Torr. The powder was then transferred to the side arm which was sealed and pulled off from the main cell.

The samples were γ -irradiated at a dose rate of 500 rads/sec with a ^{60}Co γ source for 15 min to 1 hr at either room temperature or at $77^\circ K$. Prior to recording the epr spectra, color centers were removed by heating the quartz tube while the catalyst was maintained at $77^\circ K$.

The supported molybdenum oxide was prepared by stir- ring silica gel in a suitable volume of ammonium paramo- lybdate solution to obtain 2% of Mo by weight. The acti- vation and reduction processes are similar to those re- ported earlier.¹² The sample was then equilibrated at room temperature with 2 Torr of either $^{16}O_2$ or $^{18}O^{17}O$.

In all cases the epr spectra were recorded at $77^\circ K$ using a Varian E-6 Model spectrometer. The g values were determined by using DPPH ($g = 2.0039$) as a reference. There is an estimated error of ± 0.001 in the reported values.

Results

γ -Irradiated Zeolite. The spectrum of the dehydrated zeolite observed upon γ irradiation at room temperature in the presence of oxygen $^{16}O_2$ is in agreement with that reported previously by Wang and Lunsford.¹³ In the pres- ence of oxygen enriched in ^{17}O , new lines result from the hyperfine coupling of the unpaired electron with the $I = 5/2$ spin of the ^{17}O nucleus. Despite a partial overlap of the lines, two sets of six equally spaced lines appear clearly in the spectrum of Figure 1. Both of these sextets are centered on the same g_{yy} component. Their respective hy- perfine splittings are $a_{yy}(1) = 63 \pm 1$ G and $a_{yy}(2) = 82 \pm 1$ G. Weaker lines also appear as part of the hyperfine pattern. The more widely split sextet appears somewhat weaker, but loss in intensity for hyperfine lines more dis- tant from the field corresponding to g_{yy} is characteristic of such polycrystalline spectra. This sextet may also have a slightly greater line width. The ratio of the two sextets remained unaffected upon changing the microwave power as shown in Figure 2a-2c.

The O_2^- ion is known to be rather stable at room tem- perature, but over a long period of time an appreciable decrease in its intensity occurred. During the decay in amplitude the ratio of the two sextets remained constant. When the zeolite was irradiated for successive increments of time, the two sextets grew at the same rate.



Figure 1. Epr spectrum of O_2^- on a deca- tionated Y type zeolite produced by γ -irradiation at -196° . The hyperfine structure from two nonequivalent oxygen atoms is depicted in the figure. The principal g values are those reported previously for the spectrum observed after heating the sample to 150° ;¹³ $g_{xx} = 2.009$, $g_{yy} = 2.002$, and $g_{zz} = 2.038$.

Upon γ -irradiation at $77^\circ K$ two sharp symmetric lines were observed, one on each side of the O_2^- spectrum. They were centered at $g \sim g_e$ and their separation was equal to 500 G. These lines disappeared as soon as the sample was warmed to room temperature. Simultaneous- ly, the O_2^- signal, including the two sextets, underwent a sharp decrease in intensity. The intensity of the resulting spectrum was similar to that obtained when the sample was irradiated at room temperature. It is also important to note that through this evolution of the spectrum the ratio of the two sextets was unaffected (Figure 2d and 2e).

It is likely that the two symmetric lines characterized by a g value close to the free electron g value and a split- ting of 500 G indicate the formation of hydrogen atoms trapped in the zeolite. Similar results have been reported by several workers.^{14,15} Upon warming the sample to room temperature one would expect that the reactive hy- drogen atoms would combine with O_2^- ions, resulting in the observed decrease in the intensity of the signal due to the latter species.

- (8) R. C. Catton and M. C. R. Symons, *J. Chem. Soc. A*, 1393 (1969).
- (9) S. J. Wyard, R. C. Smith, and F. J. Adrian, *J. Chem. Phys.*, **49**, 2780 (1968).
- (10) R. W. Brandon and C. S. Elliot, *Tetrahedron Lett.*, 4375 (1967).
- (11) M. C. R. Symons, *J. Chem. Soc. A*, 1889 (1970).
- (12) Y. Ben Taarit and J. H. Lunsford, *in press*.
- (13) K. M. Wang and J. H. Lunsford, *J. Phys. Chem.*, **73**, 2069 (1969).
- (14) A. Abou-Kais, J. C. Ved'ine, J. Massardier, G. Dalmay-Imelik, and B. Imelik, *C. R. Acad. Sci., Ser. C*, **272**, 883 (1971).
- (15) A. Abou-Kais, J. C. Ved'ine, J. Massardier, G. Dalmay-Imelik, and B. Imelik, *J. Chim. Phys.*, **69**, 561 (1972).

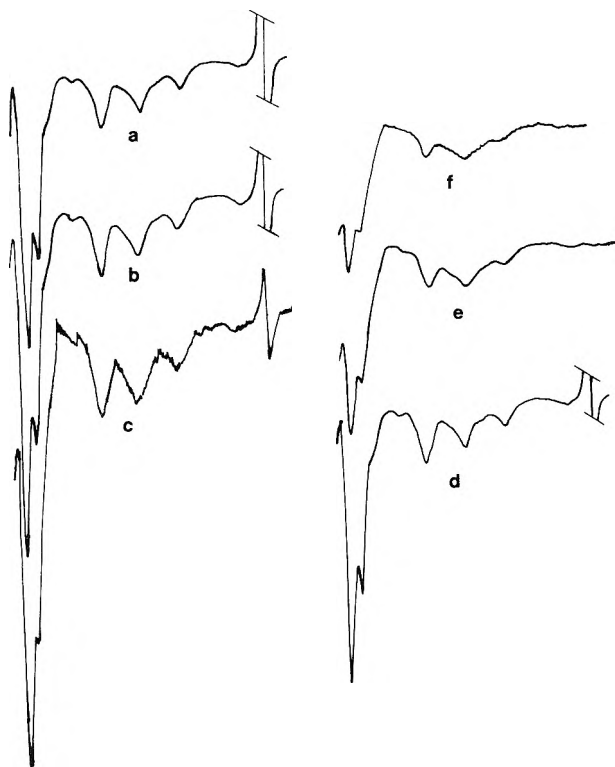


Figure 2. Variations in the high-field region of the epr spectrum of O_2^- on a decationated Y type zeolite as a function of changes in microwave power and warming the sample to room temperature: (a) 0.5 mW, (b) 7 mW, and (c) 100 mW, (d) sample maintained at 77°K, (e) sample warmed 15 min at 25°, and (f) sample warmed 105 min at 25°. All spectra were recorded with the sample at 77°K.

Another independent signal was observed at $g \approx 2.007$. The paramagnetic species responsible for this spectrum was favored by a lower pressure of oxygen and it seems to be more stable than the O_2^- radical upon warming the sample from 77°K to room temperature.

Reduced MoO_3 Supported on Silica Gel. Upon adsorption of $^{16}O_2$ on suitably reduced supported molybdenum oxide, an epr signal similar to the one reported by Kazanskii and Shvets¹⁶ and by Naccache and coworkers¹⁷ developed immediately. The g values are $g_{zz} = 2.018$, $g_{xx} = 2.010$, and $g_{yy} = 2.004$.

When oxygen enriched to (44.5%) in ^{17}O was used, two sets of four equally spaced lines were observed in addition to the main signal due to $^{18}O_2^-$ and the large signal due to Mo^{5+} (Figure 3). These lines are obviously part of two sextets centered around the g_{yy} component. They must also arise from the interaction of the odd electron with the $I = 5/2$ spin nuclei of the $^{17}O^{18}O$ molecules along the yy direction. The respective hyperfine splitting of the two sextets were found to be equal to $a_{yy}(1) = 69 \pm 1$ G and $a_{yy}(2) = 82 \pm 1$ G. The high-field portion of these sextets is hidden by the Mo^{5+} signal. Additional lines which may be attributed to molecules containing two oxygen-17 nuclei were observed at higher amplification. This hyperfine pattern will be discussed in the next section.

Again it appears that the two sextets have the same intensity and the same stability. No variation of this ratio was observed at different levels of microwave power.

Discussion

A singly labeled superoxide ion having two equivalent oxygens would yield $2I + 1$ or six lines of approximately

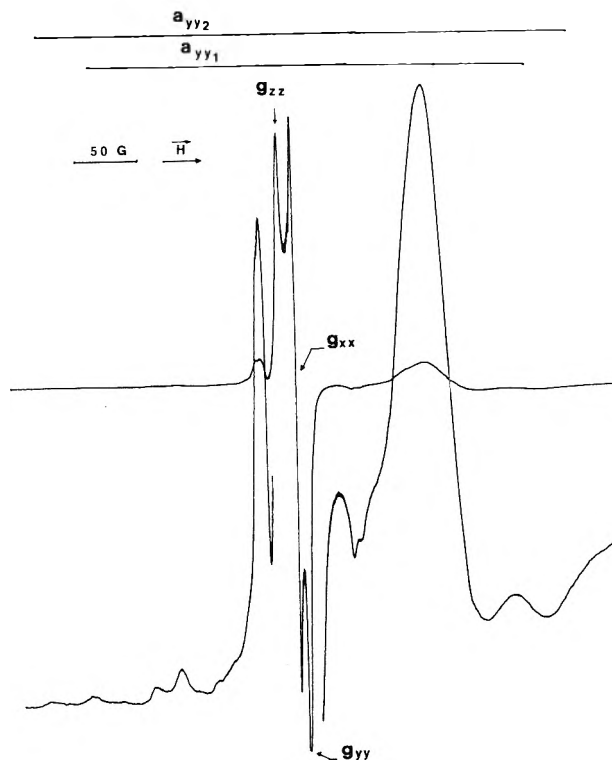


Figure 3. Epr spectrum of O_2^- formed on molybdenum supported on silica gel. Hyperfine splitting for the two types of oxygen is depicted by a_{yy1} and a_{yy2} .

equal intensity for each principal direction. A doubly labeled ion with equivalent atoms would be characterized by $2(2I) + 1$ or 11 lines with an amplitude ratio of 1:2:3:4:5:6:5:4:3:2:1 for each principal direction.

In contrast the peroxy type radical has two nonequivalent oxygens, resulting in a different distribution of the unpaired electron on each of the oxygen atoms. Therefore, an ensemble of ions containing one ^{17}O atom per molecule would yield two sets of six equally spaced lines for each principal direction. These sets characterize the inner and outer oxygen atoms relative to the surface. Since the chances are statistically equal (assuming no isotope effect) for the ^{17}O to be located at either position, the two sextets are expected to have equal intensities. Similar species containing two ^{17}O atoms would provide a still more complicated hyperfine pattern. Each line of a sextet from one oxygen atom would be split into another sextet by the second atom. Such multiple splitting would result in a total of 36 lines for each principal direction.

A detailed analysis of the data presented here provides convincing evidence that the paramagnetic oxygen ions contain two nonequivalent atoms on both the zeolite and the supported molybdenum oxide surfaces. Moreover, it is inconsistent with the experimental data to attribute the hyperfine structure to two different superoxide ions on each surface.

The observation of only one set of g values strongly suggests that the hyperfine lines arise from a single species which is unique to each material. Furthermore, if two different species did exist, it is probable that differences in their relaxation times, rate of formation, reactivity with hydrogen atoms, or thermal stability would be ev-

(16) V. A. Shvets and V. B. Kazanskii, *J. Catal.*, **25**, 123 (1972).

(17) M. Dufaux, M. Che, and C. Naccache, *C. R. Acad. Sci., Ser. C*, **268**, 2255 (1969).

ident in the hyperfine spectra. To the contrary, the experimental results confirm that the related sextets responded in exactly the same manner to each of these factors.

Strong evidence supporting a peroxy type model is provided by an examination of the $^{17}\text{O}^{17}\text{O}^-$ hyperfine pattern as described in Figure 1. This pattern does not fit the two sets of 11 lines each which would be expected for two different superoxide ions containing equivalent oxygen atoms. The rather weak intensity of the central lines from the doubly labeled ions is in sharp contrast with the spectra obtained for equivalent oxygens.³ On the other hand, the pattern of these lines is in agreement with the model of nonequivalent oxygen atoms.

A quantitative treatment of the ^{17}O hyperfine splitting also favors a peroxy type radical. Hyperfine splitting in the x and z directions is unresolved in the polycrystalline spectra; however, it is known from the single crystal data of Känzig and Zeller¹⁸ for O_2^- in alkali halides that the values of a_{xx} and a_{zz} are small. For the discussion here a_{xx} and a_{zz} will be taken as zero. The squares of the coefficients of the hydrogenic wave functions in the molecular orbital which contains the unpaired electron are given by¹⁹

$$c_{s1}^2 + c_{s2}^2 + c_{p1}^2 + c_{p2}^2 = \frac{28}{1660} + \frac{21}{1660} + \frac{54}{104} + \frac{42}{104} = 0.95 \quad (1)$$

assuming a peroxy type structure on the decationated zeolite. It is important to note that if the largest hyperfine splitting were ascribed to the equivalent oxygen atoms, the resulting value for the spin density, upon neglecting the partial delocalization of the electron on the Al orbitals, is $2c_{s1}^2 + 2c_{p1}^2 = 1.08$.² This value is significantly larger than unity, which is physically impossible.

By contrast, the value for the spin density as calculated in eq 1 appears satisfactory, especially if one takes into account the partial delocalization of the electron on the Al orbitals. This delocalization has been estimated to be about 5% from the ^{27}Al hyperfine splitting on AlSb observed by Miller and Hanemann.⁶ A very similar hyperfine splitting has also been observed for O_2^- on the decationated zeolite.¹³

In the case of supported molybdenum oxide

$$c_{s1}^2 + c_{s2}^2 + c_{p1}^2 + c_{p2}^2 = \frac{27.7}{1660} + \frac{22.7}{1660} + \frac{54.3}{104} + \frac{45.3}{104} = 0.99 \quad (2)$$

The bonding appears to be more ionic on this surface since no Mo hyperfine structure was observed. This is in contrast with the results for O^- on the same surface where some covalency has been detected.¹²

The total s character of the superoxide ion on these surfaces has been compared, in Table I, with that obtained for other peroxy type molecules where the isotropic hyperfine splitting from oxygen-17 has been evaluated. The larger values for the radical on the surfaces probably reflect the more ionic character of the bond between the

TABLE I: ^{17}O Hyperfine Constants for Peroxy Radicals

Radical	$A_{0(1)}$	$A_{0(2)}$	Ref
FOO	22.17 ± 0.05	14.50 ± 0.05	a
CF_3OOO	23.2 ± 0.1	14.0 ± 0.01	b
ROO	23.0	18.0	c
$(\text{CH}_3)_3\text{COO}$	21.8 ± 0.1	16.4 ± 0.1	d
$\text{C}_6\text{H}_5(\text{CH}_3)_2\text{COO}$	21.8 ± 0.1	16.4 ± 0.1	d
Decationated YOO	28	21	This work
MoO_3OO	28	23	This work

^a F. J. Adrian, *J. Chem. Phys.*, **46**, 1543 (1967). ^b R. W. Fessenden, *J. Chem. Phys.*, **48**, 3725 (1968). ^c R. W. Fessenden and R. H. Schuler, *J. Chem. Phys.*, **44**, 434 (1966). ^d K. Adamic, K. U. Ingold, and J. R. Morton, *J. Amer. Chem. Soc.*, **92**, 922 (1970).

TABLE II: Principal g Values for O_2^- with Two Equivalent Oxygens

Solid	g_1	g_2	g_3	Ref
MgO	2.077	2.007	2.001	3, a
TiO_2 anatase I	2.025	2.009	2.003	4
TiO_2 anatase II	2.024	2.009	2.003	4
TiO_2 rutile I	2.030	2.008	2.004	4
TiO_2 rutile II	2.020	2.009	2.003	4
SnO_2	2.025	2.009	2.004	5, d
SnO_2	2.028	2.009	2.002	c
ZnO	2.049– 2.051	2.009	2.002	3

^a N. B. Wong and J. H. Lunsford, *J. Chem. Phys.*, **56**, 2664 (1972). ^b M. Che, C. Naccache, and B. Imelik, *Bull. Soc. Chim. Fr.*, 4791 (1968). ^c J. H. C. Van Hooff, *J. Catal.*, **11**, 277 (1968).

surface and the oxygen ion, although it should also be noted that the value of A_{iso} would be somewhat less if nonzero values of a_{xx} and a_{zz} had been chosen.

The peroxy type radical is expected to be characterized by a g tensor similar to that observed for HO_2 ^{8,9} and other peroxy compounds,^{10,11} and it is slightly different from the one predicted by Känzig and Cohen²⁰ for the superoxide ion in orthorhombic symmetry. However, the g values of the superoxide ions for which equivalent oxygen atoms have been confirmed by the use of $^{17}\text{O}_2$ fall into such a wide range (Table II) that it is hardly possible to rely on the g tensor to determine the structure of the ion. Furthermore, Miller and Hanemann⁶ have reported that for triclinic symmetry all three principal g values may be greater than g_e . The use of oxygen-17 still remains the most reliable method to discriminate between the two structures of the superoxide ion.

Acknowledgment. The authors wish to acknowledge the support of this work by the National Science Foundation under Grant No. GP-35662X.

(18) H. R. Zeller and W. Känzig, *Helv. Phys. Acta.*, **40**, 845 (1967).

(19) J. H. Lunsford, *Advan. Catal.*, **22**, 267 (1972).

(20) W. Känzig and M. H. Cohen, *Phys. Rev. Lett.*, **3**, 509 (1959).

Electron Spin Resonance Spectra of Interlamellar Copper(II)-Arene Complexes on Montmorillonite

J. Paul Rupert

The Division of Sponsored Research, Mellon Institute, Carnegie-Mellon University, Pittsburgh, Pennsylvania 15213
(Received October 6, 1972),^a

Publication costs assisted by Baroid Division, NL Industries, Inc.

The esr absorption of interlamellar complexes formed between arene molecules and Cu(II) montmorillonite has been studied. Complexes of the sort termed "type II" by Mortland and Pinnavaia were formed with benzene, biphenyl, naphthalene, and anthracene by azeotropic dehydration. It is shown that the type II complex is characterized by a narrow esr band which has a g factor of 2.0024, very close to the value of 2.0023 for a "free-spinning" electron, as well as by a characteristic infrared spectrum. The latter displays a broad absorption above 1700 cm^{-1} and several broad bands in the $1300\text{--}1600\text{ cm}^{-1}$ region which are not characteristic of the particular arene. The data are interpreted in terms of the d^9 Cu(II) ion functioning as an electron acceptor for the transfer of a π electron from the arene. Electron exchange may then occur between radical cations or between radical and neutral, diamagnetic species resulting in the single, exchange-narrowed esr band.

Introduction

Montmorillonite belongs to the group of expanding layer-lattice silicate minerals known as smectites. Dioctahedral smectites are characterized structurally by an octahedral layer of alumina between two tetrahedral layers of silica. These 2:1 layers are continuous in the a and b directions and are stacked one above the other in the c direction. In montmorillonite, isomorphous substitution of Mg^{2+} for Al^{3+} in the octahedral layer results in the formation of fixed negative charges on the lattice which are balanced by exchangeable cations in the interlamellar space. This interlayer space is also normally occupied by water or organic molecules. The c axis spacing is, therefore, not fixed, but varies according to the nature of the exchange cation, the degree of hydration, and/or the size and geometry of the organic molecule.

If the exchange cation is a transition metal ion, the possibility of complex formation with electron-donating ligands exists. The coordination chemistry of the metal ion is often similar to that of the ion in solution, but frequently is strongly influenced in its behavior by the charged silicate surface. More specifically, Mortland and Pinnavaia^{1,2} have recently shown that copper(II)-arene complexes may be formed in the adsorption of benzene and methyl-substituted benzenes on partially dehydrated, oriented films of copper(II)-exchanged montmorillonite. They reported, in the case of benzene adsorption, the formation of two types of complexes. Under conditions of mild dehydration, a yellow complex is formed. This complex, designated type I, is a π -type complex. Spectroscopic studies by Mortland and Pinnavaia showed that the benzene ring is planar and retains its aromaticity. Similar type I complexes were observed in the adsorption of toluene, xylenes, and mesitylene on copper(II) montmorillonite and for the adsorption of benzene and methyl-substituted benzenes on silver(I)-exchanged montmorillonite.³

Mortland and Pinnavaia reported that films of copper(II) montmorillonite formed a deeply colored red complex under conditions of extreme dehydration with concurrent adsorption of benzene. This complex, designated type II, showed distortion of the benzene ring and a loss of aroma-

ticity. No type II complexes were observed except for the case of benzene-copper(II) montmorillonite.

In the present study, the electron spin resonance (esr) spectra of the type I and type II benzene complexes have been investigated. Further, type II complexes of biphenyl, naphthalene, and anthracene with Cu(II) on montmorillonite have been prepared and their esr and infrared spectra are presented.

Experimental Section

Materials and Complex Formation. The montmorillonite used in these experiments was beneficiated Wyoming bentonite which was provided by the Baroid Division of NL Industries, Inc. The clay was sodium exchanged, centrifuged, and spray-dried before use. The ideal unit cell composition of this clay is $[(\text{Al}_{3.33}\text{Mg}_{0.67})^{\text{VI}}(\text{Si}_8)^{\text{IV}}\text{O}_{20}(\text{OH})_4 \cdot \text{Na}_{0.67}]$. Based on this formula, the cation exchange capacity is calculated to be 91.2 mequiv/100 g. In practice, however, exchange capacity determinations on samples of beneficiated Wyoming bentonite are close to 100 mequiv/100 g. The increase over the calculated value is caused by a small amount of isomorphous aluminum substitution in the tetrahedral layer. There may also be small amounts of ferric (for aluminum) and ferrous (for magnesium) substitution in the octahedral layer which do not result in the creation of lattice charge.

Copper(II) exchange of this clay was effected by treating the clay with a quantity of 0.3 N CuCl_2 -methanol solution such that a threefold excess of equivalents of Cu(II) in solution to total exchange capacity was obtained. The sodium clay was dispersed in the Cu(II) solution and was stirred for 18 hr. The Cu(II)-exchanged clay was then filtered, washed with methanol until the filtrate showed a negative AgNO_3 test for Cl^- , and then air dried. The exchange reaction was carried out in methanol because,

- (1) M. M. Mortland and T. J. Pinnavaia, *Nature (London), Phys. Sci.*, **229**, 75 (1971).
- (2) T. J. Pinnavaia and M. M. Mortland, *J. Phys. Chem.*, **75**, 3957 (1971).
- (3) D. Clementz and M. M. Mortland, *Clays Clay Min.*, **20**, 181 (1972).

while an efficient exchange may be effected, swelling of the clay is slight, thus permitting rapid filtration and washing.

The degree of Cu(II) exchange was determined by X-ray fluorescence analysis using a Cu calibration curve constructed from intensity measurements made on standard samples of CuO in gibbsite. Multiple determinations on the clay samples indicated 3.3% Cu by weight, which corresponds to 104 mequiv of Cu(II)/100 g of clay. Thus, complete replacement by Cu(II) is indicated.

The complexes were formed in the following manner. A quantity of the Cu(II) clay was dispersed in reagent grade benzene (typically, 1 g of clay/50 ml of benzene) in a round-bottomed flask which was fitted with a Dean-Stark trap and a reflux condenser. This mixture was heated to reflux, whereupon it rapidly changed from its original pale green color to pale yellow, then to a deep burgundy. The purpose of the Dean-Stark trap was to trap water which was removed from the clay by azeotropic distillation. If a small quantity of water was added to the red mixture, it immediately turned pale yellow, which it remained until all of this water was distilled and trapped, whereupon the mixture again became deep red in color. After about 1 hr at reflux, the mixture was cooled and filtered in a drybox kept anhydrous with P₂O₅. The benzene-copper montmorillonite complex was then dried *in vacuo* at room temperature. The final product was a brick-red powder which rapidly (<1 min) turned pale yellow upon exposure to moist air.

Another sample of the red benzene complex was prepared at room temperature by the technique previously reported by Mortland which involved placing several grams of the copper-exchanged clay and an open beaker of benzene in a desiccator over P₂O₅. As the clay was allowed to dehydrate and adsorb benzene, it changed to yellow and gradually to a brick red color. Like the previous sample, it turned yellow upon exposure to moist air, but could be stored without change in dry air.

The biphenyl, naphthalene, and anthracene complexes were prepared by refluxing the Cu(II) montmorillonite in cyclohexane solutions of the arene. The biphenyl complex is dark orange-brown and turns blue-gray upon exposure to moist air; the naphthalene complex is purple and turns gray; the anthracene complex is deep blue and did not change upon exposure to moisture. Type I complexes of substituted arenes were prepared by refluxing Cu(II) montmorillonite in toluene and in a solution of polystyrene in cyclohexane.

Oriented films of these complexes were prepared for infrared spectra in the following manner. A quantity of a 4% (w/w) aqueous gel of Na⁺ montmorillonite was spread evenly on a glass plate covered with Teflon laminate (CRC Labtop) using a glass rod. The gel thickness was determined by a single thickness ring of 0.007-in. thick vinyl electrical tape at each end of the glass rod. The gel film was then immersed in 0.01 N CuCl₂ aqueous solution where it remained for 18 hr. It was then immersed in successive water baths to remove excess cupric ions from the gel and was then air dried. A mechanically stable, oriented film (*ca.* 0.8 mg/cm² of Cu(II)-exchanged montmorillonite) resulted which could easily be stripped from the Teflon laminate. Sections of this film were then used to form the desired complex. The film was supported on a plate and frame device, submerged in the proper solvent or solution, and refluxed for several hours. It was then vacuum dried and stored.

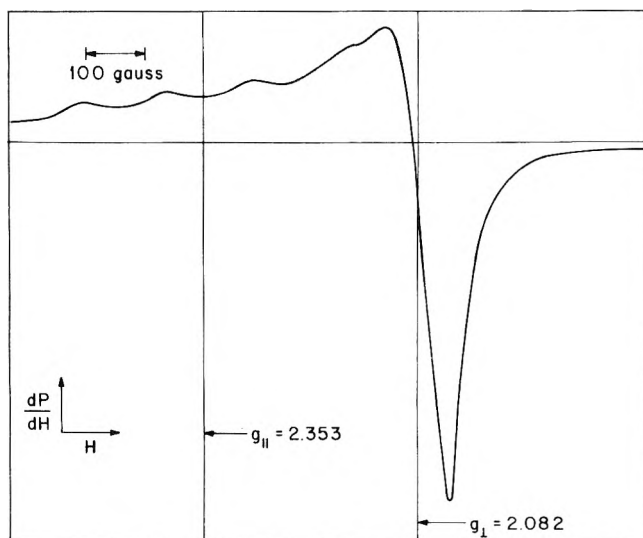


Figure 1. ESR spectrum of Cu(II) exchanged montmorillonite.

Electron Spin Resonance Spectra. The ESR experiments were carried out at room temperature using an X-band spectrometer equipped with a 10-kHz field modulation unit. This spectrometer has been described by Fessenden.⁴ Absolute values of the *g* factor were obtained directly from measurements of the microwave frequency and the proton resonance frequency with appropriate corrections being applied for the difference in field which occurs between the sample and the nmr probe. The possible error in field is estimated to be ~0.1 G. Thus, the *g* factors are accurate to at least one part in 20,000. For details of the field and frequency measurements, the paper by Fessenden and Schuler⁵ should be consulted.

Infrared Spectra. Spectra in the region 300–4000-cm⁻¹ were obtained using a dry-air purged Beckman IR-12 spectrophotometer. The oriented film samples were mounted in an evacuable cell equipped with NaCl windows. All manipulations of the samples were carried out in a drybox.

Results

Esr Spectra. The first derivative ESR spectrum of the Cu(II) montmorillonite is shown in Figure 1. In the spectrum, four hyperfine lines were resolved on the low-field side while on the high-field side a single strong band results. There is no trace of the hyperfine splitting which has been shown⁶ to exist on this band under certain conditions for Cu(II) ions exchanged into synthetic zeolites. The spectroscopic splitting (*g*) factors calculated from the Figure 1 spectrum are *g*_⊥ = 2.082 and *g*_{||} = 2.353 with a hyperfine constant *A* of -0.016 cm⁻¹. These data are in excellent agreement with those of Nicula, Stamires, and Turkevich⁶ for Cu(II)-exchanged synthetic faujasites and with the data taken by Clementz, Pinnavaia, and Mortland⁷ in their study of the stereochemistry of hydrated Cu(II) ions on the interlamellar surfaces of layer silicates. Differences between these data and the *g* factors

(4) R. W. Fessenden, *J. Chem. Phys.*, **48**, 3725 (1968).

(5) R. W. Fessenden and R. H. Schuler, *J. Chem. Phys.*, **39**, 2147 (1963).

(6) A. Nicula, D. Stamires, and J. Turkevich, *J. Chem. Phys.*, **42**, 3684 (1965).

(7) D. M. Clementz, T. J. Pinnavaia, and M. M. Mortland, *J. Phys. Chem.*, **77**, 196 (1973).

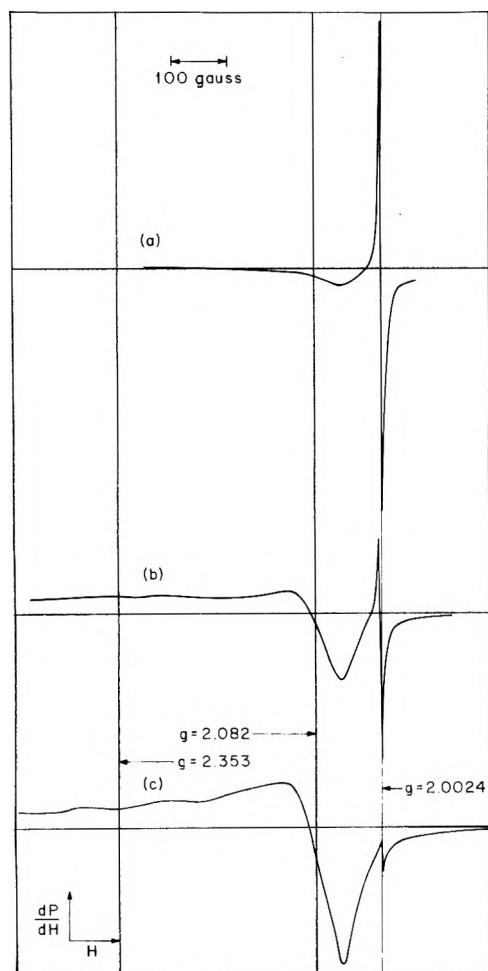


Figure 2. ESR spectra of benzene-Cu(II) montmorillonite complexes: (a) type II prepared at room temperature via P_2O_5 ; (b) type II prepared at 80° via azeotropic dehydration; and (c) type I prepared by the rehydration of b.

measured for solutions of Cu(II) complexes⁸ are attributed to the environmental effect of the silicate lattice.

The ESR spectrum of the unexchanged montmorillonite was also recorded. There was no evidence of the single, asymmetric peak near the region of free-electron spin reported by Friedlander, *et al.*,⁹ and substantiated by Wauchope and Haque.¹⁰ At high gain, a weak spectrum was observed in the region of $g = 2$ which is attributed to Fe(III) exchange ions in the native clay. This was verified by comparison with the spectrum of Fe(III)-exchanged montmorillonite. No signals were obtained following azeotropic dehydration of the unexchanged montmorillonite in cyclohexane, benzene, or cyclohexane solutions of the solid arenes.

The Cu(II)-exchanged montmorillonite whose spectrum is shown in Figure 1 was equilibrated with air at 50% relative humidity. This spectrum is essentially unchanged following azeotropic dehydration in cyclohexane provided that an appropriate correction is made for the change in density of the sample.

In Figure 2, spectra a and b are for the type II (red) benzene complexes prepared by dehydration over P_2O_5 and by azeotropic dehydration, respectively. In both cases, the low-field hyperfine splitting is gone and the high-field band shows a considerable loss in intensity compared to the Cu(II) clay spectrum of Figure 1. In ad-

dition, a new high-field band is obtained. This extremely narrow band has a width of 3 G between points of extreme slope and a g factor of 2.0024. No hyperfine structure is resolved. Spectrum c in Figure 2 is for a portion of the material used for spectrum b which was exposed to air (relative humidity 50%) for 30 min. There are three significant features: (1) the low-field Cu(II) hyperfine structure returns; (2) the high-field Cu(II) band has increased in intensity; and (3) the narrow high-field band has significantly decreased in intensity.

The ESR spectra of the complexes formed from biphenyl, naphthalene, and anthracene are presented in Figure 3. In each case, a 70 to 80% decrease in the intensity of the high-field Cu(II) band has occurred, accompanied by the appearance of a high-field, narrow band with no hyperfine structure. Consideration of the indicated gain factors shows that the narrow band becomes increasingly more intense for biphenyl and anthracene. In each case, the g factor is 2.0024. Figure 4 shows the expanded narrow band for the biphenyl complex. A nearly perfect Lorentzian first-derivative curve results.

The ESR spectrum of a toluene-Cu(II) montmorillonite complex is shown in Figure 5. This spectrum is comparable to that of the type I (yellow) benzene complex. The high-field Cu(II) band is decreased relative to uncomplexed clay and a very small high-field narrow band is resolved. Also shown in Figure 5 is the ESR spectrum of a polystyrene complex with Cu(II) montmorillonite. This complex is type I and shows only a small high-field narrow band.

Table I contains a summary of the positional and intensity data for the ESR spectra. $R(\text{Cu(II)}/\text{Cu(II)}_0)$ and $R(\text{N.B.}/\text{Cu(II)}_0)$ represent the ratios of the integrated intensities of the Cu(II) band for the complex and the narrow band, respectively, to the Cu(II) signal for the uncomplexed clay. ΔH is the width in gauss between points of extreme slope. The column headed Arene/Cu presents molar ratios determined by extracting the complex with methanol and performing quantitative UV analysis on the methanol-arene solution. The last column in Table I contains estimates of the number of arene molecules per free electron spin calculated from columns 2 and 7 assuming one spin per Cu(II).

Infrared Spectra. The infrared spectra of oriented films of the various complexes are presented in Figure 6. The spectrum of uncomplexed Cu(II) montmorillonite which has had loosely bound water removed by evacuation is shown in Figure 6a. Peaks characteristic of clay hydroxyl occur at 3630 (stretch) and 800, 850, 890, and 920 cm^{-1} (libration or "wag"). Water closely associated with Cu(II) is seen to have an -OH bending band at 1615 cm^{-1} . The intense band at 1050 cm^{-1} has been assigned to the Si-O stretch.¹¹ A small amount of carbonate impurity (commonly associated with Wyoming bentonite) is indicated by the band at 1455 cm^{-1} . This band appears to have the same intensity in all spectra.

Figure 6b shows the spectrum of a type II benzene complex formed by azeotropic dehydration. This spectrum is in agreement with the one presented by Mortland and Pinnavaia for a type II benzene complex formed over

(8) B. G. Malmstrom and T. Vanngard, *J. Mol. Biol.*, **2**, 118 (1960).

(9) H. Z. Friedlander, J. Saldick, and C. R. Frink, *Nature (London)*, **199**, 61 (1963).

(10) R. D. Wauchope and R. Haque, *Nature (London), Phys. Sci.*, **233**, 141 (1971).

(11) V. C. Farmer and J. D. Russell, *Spectrochim. Acta*, **20**, 1149 (1964).

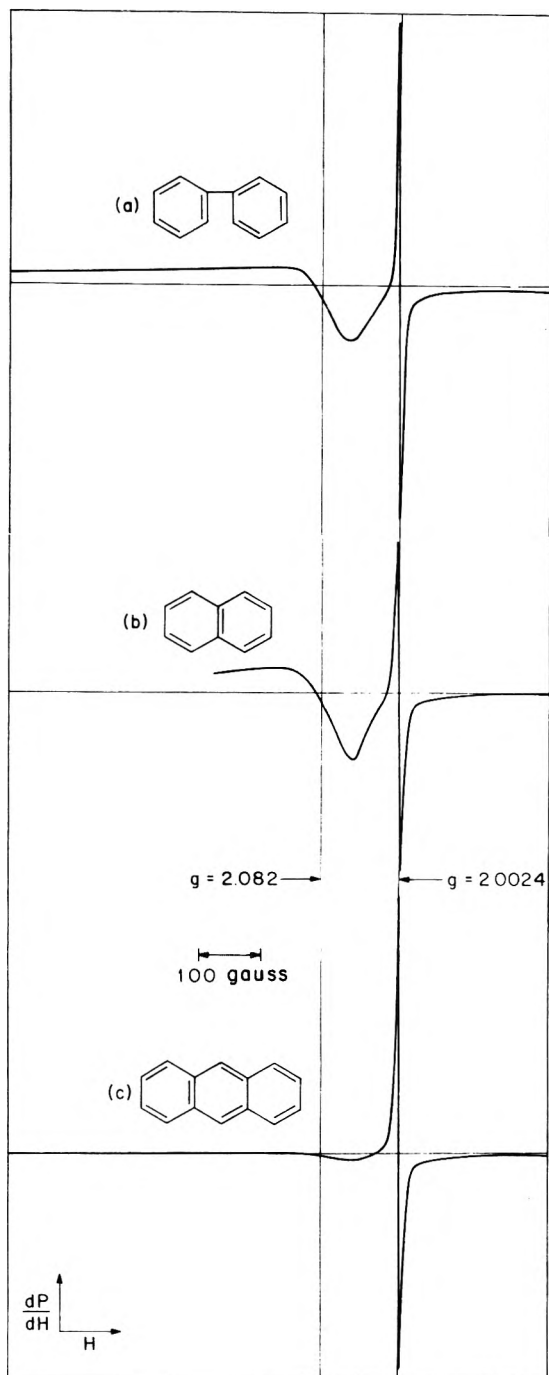


Figure 3. ESR spectra of type II complexes of Cu(II) montmorillonite with (a) biphenyl, (b) naphthalene, and (c) anthracene. Spectrum c has been attenuated by a relative factor of 16.

P_2O_5 . They have assigned the broad, intense bands at 1540 and 1480 cm^{-1} to C-C stretching vibrations and the band at 800 cm^{-1} to C-H out-of-plane deformation. They tentatively assigned the bands at 1280 and 1200 cm^{-1} to C-C stretching and C-H in-plane deformation, respectively. A striking feature of this spectrum is the broad absorption which occurs throughout the infrared region. Mortland and Pinnavaia attributed this absorption, which is particularly strong above *ca.* 1700 cm^{-1} , to a very low-energy electronic transition. In the actual spectrum of Figure 6b, transmission never exceeded 30%. The spectrum of this type II complex of benzene with Cu(II) mont-

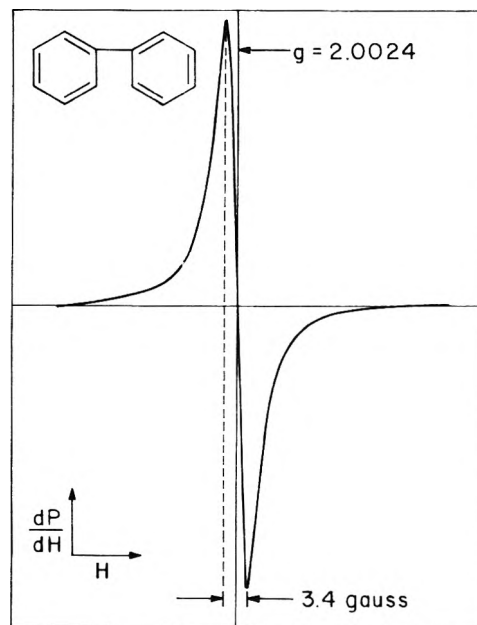


Figure 4. Expanded ESR spectrum of the narrow band portion of the type II complex of biphenyl with Cu(II) montmorillonite.

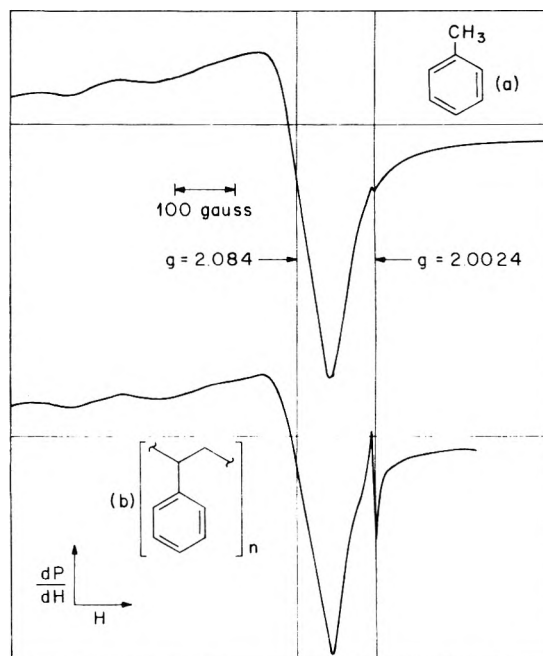
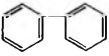
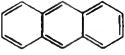


Figure 5. ESR spectra of type I complexes of Cu(II) montmorillonite with (a) toluene and (b) polystyrene.

morillonite bears no resemblance to that of benzene. However, a benzene-on-clay spectrum is generated by rehydration of the complex.

The spectrum of the type II complex of biphenyl with Cu(II) montmorillonite is shown in Figure 6c. It is characterized by a moderately strong electronic absorption above *ca.* 1700 cm^{-1} . In the region 1200-1600 cm^{-1} the spectrum shows bands close to but not identical with the type II benzene complex plus bands at 1577 and 1595 cm^{-1} . No nonclay peak occurs at 800 cm^{-1} . Figure 6d shows the spectrum of this same film after 2 hr of exposure to room air during which time the film turned from brown-orange

TABLE I: Esr and Analytical Data for Arene Complexes with Cu(II) Montmorillonite

Arene	Arene/Cu	Cu(II) spectrum		Narrow band spectrum			Arene/free spin	
		g_{\perp}	$R(\text{Cu(II)}/\text{Cu(II)}_0)$	g	$\Delta H, \text{G}$	$R(\text{N.B.}/\text{Cu(II)}_0)$		
None	0	2.082	1.0					
	over P ₂ O ₅ azeotroped type I	3.8	2.082	0.05	2.0024	2.9	0.015	250
		2.4	2.083	0.23	2.0024	3.6	0.007	340
			2.084	0.45			~0	
	1.4	2.082	0.22	2.0024	3.4	0.013	110	
	1.8	2.081	0.30	2.0024	6.1	0.010	180	
	0.9	2.082	0.27	2.0024	4.2	0.190	5	
		2.084	0.55			~0		
		2.083	0.42			0.002		

to blue-gray. The only nonclay bands present are at 745 and 1483 cm^{-1} . These are the two strongest bands in the infrared spectrum of biphenyl.¹² Loosely bound water has been adsorbed, as evidenced by the shift of the -OH bending band from 1618 to 1630 cm^{-1} .

There is a small amount of the broad electronic absorption present in Figure 6d. Examination of the sample following the scan revealed that the portion exposed to the beam had turned slightly orange. Immediate rescan of the 1300-1600- cm^{-1} region revealed the presence of type II bands. The conclusion is that the type I to type II conversion was effected by beam heating during the scan.

While colored films could be formed from solutions of naphthalene and anthracene in cyclohexane, the infrared spectra revealed only minor differences compared with Cu(II) montmorillonite, indicating that only very small amounts of arene were sorbed. This suggests that it is difficult for large, planar fused-ring aromatic hydrocarbons to work their way into the interlamellar space when the clay minerals crystals are oriented in the a - b plane. Figure 6e shows the spectrum of the anthracene-complexed film. The broad absorption is present (although it is relatively weak) and only very weak nonclay bands are in evidence.

Discussion

It has been shown by Mortland and coworkers that arenes adsorbed in the interlamellar space of montmorillonites can be of three types: (1) physically adsorbed; (2) type I in which the arene retains its aromatic character and is coordinated to either a Cu(II) or Ag(I) exchange ion by a π interaction; and (3) type II in which the ring is distorted and aromaticity is lost. The infrared spectrum of the type II complex is unlike that of the arene and exhibits a broad absorption throughout most of the infrared region. This work has shown that the type II complex is also characterized by the presence of a narrow band in the esr spectrum.

The following summarizes what is known about the type II complex. It can apparently be formed only with Cu(II) as the exchange cation in a 2:1 layer silicate. Experiments in this laboratory and elsewhere have shown that the type II complex may be formed using both synthetic¹³ and natural hectorite,¹⁴ using a synthetic inter-

stratified mica-montmorillonite,¹³ and using nontronite³ while no complex is formed from Cu(II) exchanged synthetic saponite or synthetic faujasite. Transition metal ions tried without success in the complexation of benzene were Fe(II)[d⁶], Co(II)[d⁷], and Ni(II)[d⁸] and the d¹⁰ ions Zn(II), Cu(I), and Hg(II). A type II complex can be formed from the symmetrical aromatic hydrocarbons benzene, biphenyl, naphthalene, and anthracene; alkyl ring substitution on benzene prohibits the type II formation. It may be formed under conditions of extreme dehydration either at room temperature (over P₂O₅) or at the reflux temperature of benzene or cyclohexane (80°). However, in either case, the arene must be present during the dehydration. The infrared spectra of type II complexes contain a broad absorption, especially above 1700 cm^{-1} , and bands which are not characteristic of the arene. Rehydration restores bands from the infrared spectrum of the arene and the arene may be reclaimed unchanged from the type II complex by extraction with methanol (as evidenced by the uv spectrum of the MeOH solution).

The esr spectra of the type II complexes exhibit a narrow band (<5 G wide) with a g factor very close to that for a free-electron spin (2.0024 compared to 2.0023 for a free electron). The narrow band has no hyperfine structure. Cu(II) spins are lost when the type II complex is formed. However, the number of spins obtained in the narrow band does not compensate the number of copper spins lost. Conversion to the type I complex results in the loss of the narrow band signal and an increase in Cu(II) spins. The Cu(II) signal does not, however, regain its original intensity. In the case of formation of the type I complex with toluene, ca. 50% of the Cu(II) spins are lost while no narrow band is obtained.

Considering the preceding, the following physical interpretation is suggested. As the Cu(II) montmorillonite is dehydrated in the presence of arene, physically adsorbed water is lost first. Concurrently, as water is removed from the interlamellar space, adsorption of arene molecules oc-

(12) G. Zerbi and S. Sandroni, *Spectrochim. Acta. Part A*, **24**, 483 (1968).

(13) J. P. Rupert, unpublished data.

(14) G. Stridde, private communication.

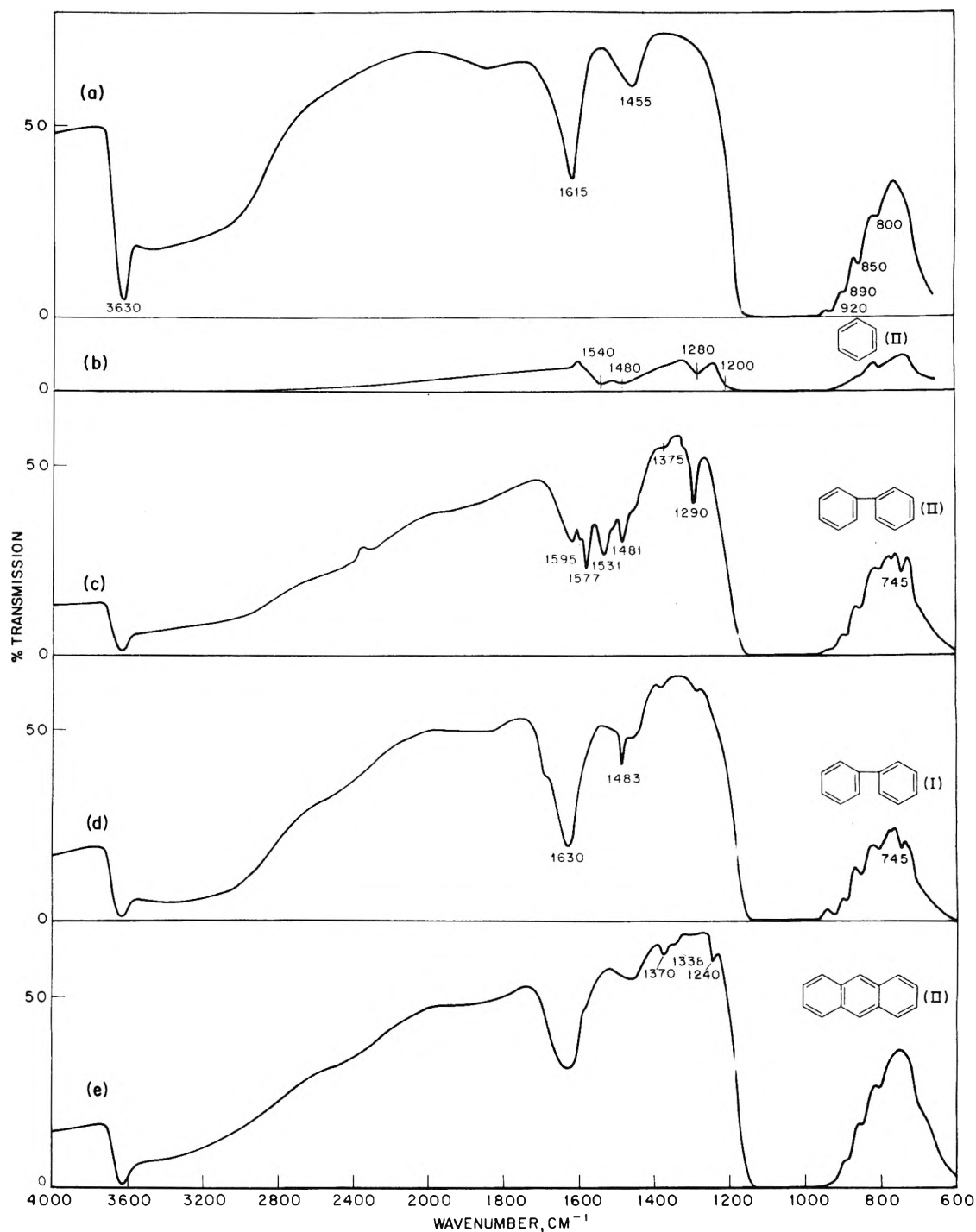


Figure 6. Infrared spectra for (a) Cu(II) montmorillonite and its complexes with (b) benzene (type II), (c) biphenyl (type II), (d) biphenyl (type I), and (e) anthracene (type II).

curs. Further dehydration results in the removal of those water molecules which are loosely bound to the Cu(II) ion. As the Cu(II) is uncovered, electron donation from the π system of the arene to unfilled Cu(II) orbitals can occur, resulting in the formation of the type I complex. Clementz and Mortland³ have suggested that the type I complex is an outer orbital complex with π electron donation into unfilled p orbitals of either Cu(II) or Ag(I).

Under conditions of extreme dehydration, the Cu(II) is bared to the extent that the full influence of its d^9 electronic configuration is felt by the arene. Transfer of one or two π -electrons occurs resulting in the formation of the

more favorable d^{10} configuration of Cu(I) and a radical cation of the type



(only one of several resonance forms which can be drawn) or a dication. It is known that π -electron transfer does occur for polycyclic aromatic hydrocarbons in the presence of electron acceptors resulting in the formation of radical cations.¹⁵ Specifically, Muha^{16,17} has shown that

(15) See, for example, D. Bethell and V. Gold, "Carbonium Ions: An Introduction," Academic Press, New York, N. Y., 1967, p 299.

radical cations may be formed from a series of polynuclear aromatic compounds adsorbed on the electrophilic surfaces of activated silica-alumina gels.

However, the esr spectrum of discrete radical cations would display hyperfine splitting resulting from the interaction of the unpaired electron with the ring protons. It is suggested that the observed single narrow band is the result of electron-exchange narrowing. This is consistent with the observed Lorentzian line shape of the narrow band.

Muha¹⁷ showed that, as the space between anthracene radical cations on a silica-alumina surface was filled with diamagnetic species, the hyperfine spectrum was narrowed to a single line of *ca.* 4 G width between extremes of slope. This narrowing was attributed to an electron-exchange process. Muha assumed saturation of a fixed number of electrophilic sites on the catalyst with paramagnetic radical cations. He calculated the intersite distance to be ~ 400 Å, too great for electron exchange to occur. As the space between sites was filled with diamagnetic species, the intermolecular distance decreased until, at a ratio of diamagnetic/paramagnetic species of 5×10^3 , exchange narrowing was observed. Crude calculations indicated that this corresponds to an intermolecular distance of ~ 26 Å.

The *a* and *b* unit cell dimensions for montmorillonite are 5.3 and 9.2 Å,¹⁸ respectively. Thus, the total face area of a unit cell is 97.5 Å². Fully exchanged sodium clay contains $\frac{2}{3}$ Na⁺ per unit cell. This corresponds to an average interionic distance of approximately 12 Å. The clay used in these studies was completely exchanged with Cu(II) such that each unit cell contained $\frac{1}{3}$ of a Cu(II) ion. A crude calculation, assuming even distribution of the exchange ions, predicts a Cu(II)-Cu(II) interionic distance of 17 Å. Even though it is argued that exchanged ionic species in clays tend to segregate,¹⁹ this calculation is useful for predicting the average interionic distance. Since there are approximately one to four arene molecules per Cu(II) (see Table I), the inter-arene distances are certainly within that suggested by Muha as the distance required for the occurrence of exchange narrowing.

An examination of the Arene/free spin column in Table I shows that the highest proportion of radical spins is generated for anthracene while the lowest is generated for benzene. Naphthalene and biphenyl are intermediate. This is in qualitative agreement with the aromatic oxidation potentials tabulated by Lund.²⁰ However, steric effects are probably also of importance since toluene, which does not form a type II complex, has an oxidation potential very close to that of benzene. The ratios of the integrated signal intensities for type II arene complexes with Cu(II) montmorillonite reveal that only a small fraction of the Cu(II) spins lost are recovered as free electron spins. This could be caused either by the initial formation of diamagnetic dication species or by electron exchange between two radical species to produce a neutral arene and a dication. Another possible explanation is the formation of a complex whose relaxation time is such as to prohibit observation of the spectrum at room temperature.

The interlamellar space of the type II complex is thus visualized as containing arene molecules, radical cations, and possibly dications with rapid electron exchange occurring between radicals or between radicals and neutral

species. The unpaired electrons are considered to be essentially free to move in the collective π system. X-Ray diffraction data indicate that the aromatic molecules are oriented with their planes parallel to the *a-b* plane ($\Delta d_{001} = 2.1$ Å for the anthracene complex compared to Cu(II) montmorillonite). A similar electron transfer mechanism was postulated by Garnett and Rainis²¹ to explain esr data obtained in a study of the reaction of polynuclear aromatic hydrocarbons with platinum chlorides. They also observed a single, narrow esr band with no hyperfine structure which they attributed to "radical cations formed by the transfer of an electron from the aromatic donor to an electron-accepting site on the surface." They also showed that the extent of radical formation was much greater for anthracene than for naphthalene.

The effect of rehydration on the type II complex is not surprising. Rooney and Pink²² showed that the addition of water to a system composed of anthracene radical cations formed by electron transfer to activated silica-alumina resulted in a rapid decay of the esr signal. They attributed this effect, which was found to be reversible, to a competition between the arene and the water molecule for the Lewis acid site. The present case is consistent with this interpretation since the rehydration results in a loss of the narrow band and an increase in the Cu(II) signal.

An interesting comparison may be made between the type II complexes and graphite. The infrared spectrum of ground graphite consists of a broad absorption above 1700 cm⁻¹ and several wide bands in the 1300-1600 cm⁻¹ region.²³ Further, Singer and Wagoner²⁴ have shown that the esr spectrum for a sample of randomly oriented graphite crystals not in electrical contact consists of a symmetrical narrow band whose *g* factor is 2.0026. They also showed that a finely ground sample of graphite produces a narrow esr band with a width of *ca.* 3 G between points of extreme slope. This analogy implies that oriented films of type II complexes could exhibit high electrical conductivity in the plane of the film if there is a means for conduction between crystals. Further, conduction in the *c* direction should be relatively small.

Acknowledgments. The author thanks the Baroid Division, NL Industries, Inc., for sponsorship of this Research Project and permission to publish this work, Professor Richard Fessenden and Mr. Naresh Verma of CMU for providing instrument time and assistance with the esr measurements, Mr. Alan Wright of Baroid for the infrared spectra, Ms. B. J. Jahnke of Baroid for the X-ray fluorescence analysis, and Professors M. M. Mortland and T. J. Pinnavaia of Michigan State University for helpful discussion.

(16) G. M. Muha, *J. Phys. Chem.*, **71**, 633 (1967); *ibid.*, **71**, 640 (1967).

(17) G. M. Muha, *J. Phys. Chem.*, **74**, 787 (1970).

(18) D. M. C. MacEwan, "The X-ray Identification and Crystal Structure of Clay Minerals," G. Brown, Ed., 2nd ed. Mineral. Soc. London, 1961.

(19) J. L. McAtee, *Clays Clay Min.*, **5**, 279 (1958).

(20) H. Lund, *Acta Chem. Scand.*, **11**, 1323 (1957).

(21) J. L. Garnett and A. Rainis, *J. Catal.*, **26**, 141 (1972).

(22) J. J. Rooney and R. C. Pink, *Trans. Faraday Soc.*, **58**, 1632 (1962).

(23) R. A. Friedel and G. L. Carlson, *J. Phys. Chem.*, **75**, 1149 (1971).

(24) L. S. Singer and G. Wagoner, *Proc. Conf. Carbon*, **5th**, 2, 65 (1961).

Oxidation-Reduction Properties of Copper- and Nickel-Substituted Hydroxyapatites

Makoto Misono and W. Keith Hall*¹

Carnegie-Mellon University, Mellon Institute, Pittsburgh, Pennsylvania, 15213 (Received July 26, 1972)

Publication costs assisted by the Gulf Research and Development Company

Epr spectra from Cu^{2+} in the lattice of several crystalline hydroxyapatite samples were determined after treatment with H_2 or O_2 at various temperatures. The extent of the reduction of Cu^{2+} to Cu^+ or Cu^0 (or the reverse processes) was assessed by measuring the consumption of H_2 (or O_2) volumetrically. The stoichiometry of the process was judged by comparing these data with changes in epr signal intensity. The intensities decreased as Cu^{2+} was converted to Cu^+ or Cu^0 and the extent of the change increased with both the temperature of the reduction and the Cu^{2+} loading of the crystals. Under mild conditions and at low Cu^{2+} content, Cu^{2+} was reduced mainly to Cu^+ and this process was readily reversible on treatment with O_2 . Under more severe conditions, the reduction proceeded to Cu^0 and this change was less easily reversible. In this case, the Cu apparently was expelled from the lattice and crystallized as metal; thus, it exhibited no epr signal. Support for this view was found in related experiments in which Cu^{2+} was replaced by Ni^{2+} . Here, ferromagnetic resonance (fmr) was observed on reduction to metal. Experiments where the surface layers of the crystals were removed by dissolution in acid in the presence of chelating agents led to the same conclusion. It was found that the residues of the crystals were greatly diluted in Cu when they had been reduced completely before the treatment, whereas this was not the case when the reduction was only to Cu^+ . The intracrystalline chemistry of the oxidation-reduction cycle is discussed and evidence is advanced suggesting that Cu^+ is the active center for the H_2 - D_2 exchange reaction.

Introduction

Profound changes in catalytic behavior when small amounts of transition metal ions are substituted for Ca^{2+} in the lattice of hydroxyapatite, $\text{Ca}_{10}(\text{PO}_4)_6(\text{OH})_2$. The activity for the hydrolysis of chlorobenzene to phenol was greatly enhanced by 0.5–1% Cu^{2+} .^{2a} Similarly, a large increase in activity for dehydrogenation of alcohols to aldehydes or ketones was effected by substitution of Cu^{2+} or Ni^{2+} , while the dehydration function of these same catalysts was little affected.^{2,3} Nevertheless, the change was so pronounced that the relatively low rate of dehydration was virtually drowned by the greatly enhanced rate of dehydrogenation. Similar catalysts are used for the commercial production of 1,3-butadiene from butenes.

Unlike the dehydration reaction, which can be explained in terms of acid catalysis, dehydrogenation with H_2 evolution does not usually occur in homogeneous chemical systems. Hence, the present work was carried out to shed light on this subject. Because dehydrogenation activity appeared to be related to the presence of a reducible ion, and because this process includes the recombination of 2H and the desorption of H_2 , it was felt that studies of the interaction of H_2 with the catalyst and of the H_2 - D_2 exchange might be helpful. The idea was to assess the valence state of Cu or Ni under reaction conditions and to see if the dehydrogenation function could be related to a particular valence state, or to the ability to switch between two valence states. A variable valence state has frequently been advanced as an important catalytic property, e.g., with chromia catalysts, the ability to form Cr^{2+} was judged to be important for dehydrogenation of olefins,⁴ whereas polymerization has been related to the presence of Cr^{5+} ;⁵ Cu^+ has been postulated as active for chemisorption of H_2 ⁶ and the H_2 - D_2 equilibration.⁷

Earlier studies of the dispersion and oxidation state of supported Cu have been made. Selwood and coworkers^{8,9} studied Cu^{2+} on alumina by means of magnetic susceptibility, before and after reduction or reoxidation. Clusters of the supported ion were found to decrease in size with diminishing Cu loading until at infinite dilution the full atomic magnetic moment of 1.7 BM was attained. The magnetic susceptibility, which became negative upon reduction, was completely restored by reoxidation and all Cu^{2+} contributed to the susceptibility. The disappearance of paramagnetism on reduction was attributed to a tendency for copper atoms to aggregate. These results were extended and amplified by Berger and Roth¹⁰ using the epr technique. Part of the Cu^{2+} ions were found to be imbedded in the alumina surface; upon reduction with H_2 or CO, oxygen was removed from the surface and the Cu atoms expelled from the interstitial positions; the latter migrated to form diamagnetic clusters. Upon reoxidation, the epr signal was slowly recovered (up to 90%) showing the dispersed state to be more stable than the CuO crys-

- (1) To whom correspondence should be addressed: Gulf Research and Development Co., P. O. Drawer 2038, Pittsburgh, Pa, 15230.
- (2) (a) W. T. Reichle, *J. Catal.*, **17**, 297 (1970); (b) C. L. Kibby and W. K. Hall, "Biosurfaces," Vol. 2, Marcel Dekker, New York, N. Y., 1972.
- (3) J. A. S. Bett, F. R. Dollish, and W. K. Hall, to be submitted for publication.
- (4) L. L. VanReigen, W. M. H. Sachtler, P. Cossee, and D. M. Brouwer, *Proc. Int. Congr. Catal.*, **3rd**, 829 (1965).
- (5) P. A. Bukanawa, Y. I. Pecherskaya, V. B. Kazansky, and V. A. Dzisko, *Kinet. Katal.*, **3**, 358 (1962).
- (6) D. O. Hayward and B. M. W. Trapnell, "Chemisorption," Butterworths, London, 1964.
- (7) J. E. Benson, A. B. Walters, and M. Boudart, *J. Phys. Chem.*, **72**, 4587 (1968).
- (8) P. W. Selwood and N. S. Dallas, *J. Amer. Chem. Soc.*, **70**, 2145 (1948).
- (9) P. E. Jacobson and P. W. Selwood, *J. Amer. Chem. Soc.*, **76**, 2641 (1954).
- (10) P. E. Berger and F. Roth, *J. Phys. Chem.*, **71**, 4307 (1967).

tals. The data of Lumbeck and Voitlander¹¹ were in general agreement with these findings. In both these epr studies, only a portion of the Cu²⁺ contributed to the epr signal intensity, viz., about 30% in the former¹⁰ and 2% in the latter.¹¹

With hydroxyapatite, all of the substituted Cu²⁺ are detectable by epr provided that Cu/Ca \leq 0.03, and under this constraint the Cu²⁺ has been shown to be uniformly distributed throughout the crystals.³ Moreover, the material studied is comprised of individual cylindrical crystals about 200 Å in diameter and 700 Å long, having a BET area of about 70 m²/g.¹² The advantages afforded by this system over Cu²⁺-alumina are twofold. With the latter, all of the Cu²⁺ cannot be seen by epr, possibly because of clustering or symmetry considerations; the Cu²⁺-Cu²⁺ distances are much shorter because the ions are distributed over a two-dimensional surface. Secondly, as a consequence of the three-dimensional distribution, it was possible to work with much higher spin concentrations with the hydroxyapatite crystals than was possible in the earlier work. The catalytic activity associated with different valence states of copper was also examined.

Experimental Section

Copper and Nickel Hydroxyapatites. The preparation and characterization of the parent hydroxyapatite has been described elsewhere.¹² Copper or nickel hydroxyapatites were made in a similar manner except that before titrating H₃PO₄ into Ca(OH)₂, either CuO or NiO was dissolved in the acid in the required amounts. The resulting catalysts had the overall stoichiometric ratio of cations to phosphorous, i.e., M²⁺/P = 1.67, but the Cu/Ca ratios were 0.0025, 0.005, 0.0063, 0.0146, and 0.025 and the Ni/Ca ratios were 0.005 and 0.039. These transition metal ion containing catalysts all gave the same X-ray patterns as the parent hydroxyapatite, although line broadening increased with the extent of substitution.³

Gases. H₂ used for reduction and for sorption experiments was purified by passage through a DEOXO purifier followed by two traps containing calcined molecular sieves. H₂ and D₂ used for equilibration were passed through separate Pd thimbles. O₂ was dried by passage over molecular sieves. He, used for the calibration of the volume of the system, was passed through a trap containing molecular sieves kept at liquid nitrogen temperature.

Equipment. The O₂ or H₂ uptakes (or sorptions) were measured with a conventional BET system modified so that the gases could be circulated over the sample by an all glass pump and the H₂O evolved collected in a trap kept at liquid nitrogen temperature. The quartz sample tube which fitted the epr cavity had a coaxial tube so that gas could pass through the sample.

The equipment and procedure used in the H₂-D₂ equilibration experiments has been described elsewhere.¹³ It involved measuring the time of half conversion in a similar circulating system fitted with a thermal conductivity detector.

Epr spectra were determined using a Varian spectrometer (Model V4500; 9-in. magnet) equipped with PAR variable modulation frequency lock-in amplifier.

Procedures. The stoichiometry of the H₂ or O₂ uptakes was estimated by comparing the consumption of one of these gases with the change in the epr signal intensity. From 0.5 to 1.0 g of catalyst was evacuated, first at 25°, then at 100–200°, and finally at 450° for 2 hr. The epr sig-

nal was recorded at room temperature after each step and its intensity determined from the first moment of the absorption derivative. The reference standard was a sample of the same material, which had been calibrated previously³ against CuSO₄·5H₂O and was shown to have one unpaired spin for each Cu²⁺. Sometimes a small decrease in epr intensity accompanied the first evacuation at 450°, but the intensity recovered completely on reexposure to O₂ at the same temperature.

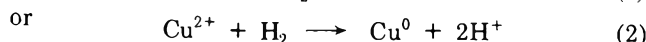
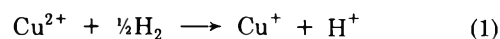
After the dead volume of the system was calibrated with He, a known volume of H₂ was introduced and the pressure change was measured at constant volume as the gas was circulated. After a given time, when the pressure drift was extremely slow, the sample was evacuated and another epr measurement was made. Then, the amount of water collected was measured by expanding it into the BET system. The same procedure was followed for O₂ sorption, following the H₂ uptake measurement.

In some cases the copper content (or its epr spectra) was determined before and after dissolving away the external layers of the crystals. In these cases, about 250 mg of catalyst was treated in a flask at 25° with 30 ml of dilute HCl (10⁻³–10⁻⁴ M) containing acetylacetone (15%) and Ca(NO₃)₂·4H₂O (1%); the mixture was stirred occasionally. Acetylacetone was added to prevent the readorption of Cu²⁺ onto the surfaces of the crystal remnants and Ca²⁺ ion was added to replace any Cu²⁺ ion removed therefrom. After 2 to 20 hr, the sample was washed several times with a similar solution in which the HCl was omitted. In each case, it was treated for about 1 hr with occasional stirring. Finally the sample was washed with distilled H₂O and dried at 120° before weighing and redetermining the epr spectrum. Prior to the epr measurement, samples with reduced copper were reoxidized at 550° for 20 hr. This treatment was sufficient to restore the epr signal of all copper ions, *vide infra*.

Following some treatments, samples fluoresced under the irradiation of uv light of wavelength 2537 or 3660 Å (13 or 9 W). These cases were recorded for comparison with the sorption and epr data. Colors of various preparations were also noted.

Results

Stoichiometry of Reduction and Oxidation. The sorption of H₂ on reduction and of O₂ on reoxidation of the copper contained in catalysts having different Cu/Ca ratios (0.0063, 0.0146, and 0.025) was measured at several temperatures. The results are given in Tables I, II, and III together with the amounts of H₂O collected during these measurements. The epr intensities after each experiment relative to the initial preparation are also given in these tables. The amount of O₂ consumed during reoxidation was always nearly half the H₂ taken up in the preceding step, satisfying the stoichiometry: H₂ + ½O₂ → H₂O. The per cent reduction of Cu²⁺ by H₂ was calculated from the H₂ uptakes assuming either



The stoichiometry may be judged by comparing these re-

(11) H. Lumbeck and J. Voitlander, *J. Catal.*, **13**, 117 (1969).

(12) J. A. S. Bett, L. G. Christner, and W. Keith Hall, *J. Amer. Chem. Soc.*, **89**, 5535 (1967).

(13) W. K. Hall, F. E. Lutinski, and J. A. Hassell, *Trans. Faraday Soc.*, **60**, 1823 (1964).

TABLE I: Reduction and Oxidation of Copper Hydroxyapatite (Cu/Ca = 0.0063)^a

Experimental conditions				% reduction ^c		% oxidation ^d		H ₂ O collected cc(NTP)/g	Relative epr intensity
Temp, °C	Time, hr	Gas	Gas uptake cc(NTP)/g ^b	Cu ²⁺ → Cu ⁺	Cu ²⁺ → Cu ⁰	Cu ⁺ → Cu ²⁺	Cu ⁰ → Cu ²⁺		
25	0.5	Evacuation						7.2 ^e	1.0
150–300	2	Evacuation						20.3 ^e	1.0
450	2	Evacuation						5.6 ^e	0.90
150	0.5	O ₂	0.0			0	0		1.0
150	3.5	H ₂	0.0	0	0				1.0
150	13.5	O ₂	0.04			7	3		1.0
300	2	H ₂	0.14	19	9			0.0	0.70
300	3.5	O ₂	0.10			28	14	0.0	1.0
450	1	H ₂	0.49	70	35			0.17	0.17
450	1.3	O ₂	0.26			73	37	0.20	0.91
450	14	Evacuation						1.26 ^e	1.00
550	17	H ₂	1.44	202	101			1.81 ^e	0.0
550	1	O ₂	0.68			194	97	0.0	0.47
550	+16	O ₂	0.76			217	109	0.04	0.94

^a Weight of sample = 1.016 g. ^b The estimated error is ±0.03 cc(NTP)/g. ^c Per cent reduction was calculated from H₂ uptake by means of (1) Cu²⁺ + ½H₂ → Cu⁺ + H⁺; and (2) Cu²⁺ + H₂ → Cu⁰ + 2H⁺. ^d Per cent oxidation was calculated from the amount of O₂ uptake by means of (1) Cu⁺ + ¼O₂ → Cu²⁺ + ½O²⁻; and (2) Cu⁰ + ½O₂ → Cu²⁺ + O²⁻. ^e Water collected at low temperature was due to the desorption of physisorbed water. Water collected at high temperature includes the water produced by dehydroxylation of parent hydroxyapatite.¹²

TABLE II: Reduction and Oxidation of Copper Hydroxyapatite^a (Cu/Ca = 0.0146)

Experimental conditions				% reduction ^c		% oxidation ^d		H ₂ O collected ^e cc(NTP)/g	Relative epr intensity
Temp, °C	Time, hr	Gas	Gas uptake cc(NTP)/g ^b	Cu ²⁺ → Cu ⁺	Cu ²⁺ → Cu ⁰	Cu ⁺ → Cu ²⁺	Cu ⁰ → Cu ²⁺		
25	0.5	Evacuation							1.0
450	2	Evacuation							0.74 ^f
450	2	O ₂	0.32			19	10		0.95
300	1.5	H ₂	0.66	40	20			0.0	0.48
300	1.5	O ₂	0.31			38	19	0.01	0.94
450	1	O ₂							1.0
450	1	H ₂	1.25	77	39			0.62	0.15
450	2	O ₂	0.66			81	40	0.17	0.98
150	3	H ₂	0.21	13	7			0.0	0.82
150	1	O ₂	0.10			12	6	0.0	0.95
375	1	H ₂	1.08	66	33				0.28
376–450	2	O ₂							0.95
450	2.6	H ₂	1.75	107	54			1.59	0.01
450	5	O ₂							
550	26	H ₂	2.74	170	85			3.15 ^e	0.0

^a Weight of sample = 0.804 g. ^{b–e} See corresponding footnotes to Table I. ^f Sample was reduced partially during evacuation, mainly to Cu⁺ as shown by the following oxidation.

sults with the decrease in epr intensity (last column), *i.e.*, with 100 (one minus relative intensity).

The epr signal from Cu²⁺ in hydroxyapatite is shown in Figure 1. Neither Cu⁺ nor Cu⁰ clusters are paramagnetic; CuO is probably paramagnetic, but its signal is not detected by epr because of rapid relaxation.¹⁰ An epr signal has been reported¹⁴ for isolated Cu⁰ atoms, but this was not observed in the present work nor in the related study of Berger and Roth.¹⁰

It is convenient to adopt the following notation to indicate catalyst composition. Let CuHAP-0.0146 represent the copper hydroxyapatite catalyst having Cu/Ca = 0.0146, etc. With CuHAP-0.0063 and CuHAP-0.0146 treated with H₂ at and below 450°, the per cent reduction calculated by eq 1 was in best agreement with the decreased in epr signal intensity (Tables I and II). With CuHAP-0.025 (Table III), however, the value calculated by eq 2

instead of eq 1 was in better agreement with the epr change. With long reduction times at 550°, however, the H₂ uptakes of all samples corresponded to 85–100% reduction to Cu⁰, eq 2, and no epr signal was observed (Tables I, II, and III).

Generally the O₂ uptakes were in agreement with the stoichiometry of the valence change observed in the preceding reduction step, *i.e.*, the epr change on reoxidation agreed best with the per cent oxidation calculated for oxidation of Cu⁰ or Cu⁺ back to Cu²⁺, whichever was expected. With CuHAP-0.025, however, the epr recovery was sometimes incomplete.

Typical plots of H₂ or O₂ uptake *vs.* time are given in Figure 2. The reproducibility is demonstrated by showing

(14) R. A. Zhitnikov and N. V. Kolosnikov, *Sov. Phys. Solid State*, 6, 2645 (1965).

TABLE III: Reduction and Oxidation of Copper Hydroxyapatite^a (Cu/Ca = 0.025)

Experimental conditions				% reduction ^c		% oxidation ^d		H ₂ O collected ^e cc(NTP)/g	Relative epr intensity
Temp, °C	Time, hr	Gas	Gas uptake cc(NTP)/g ^b	Cu ²⁺ → Cu ⁺	Cu ²⁺ → Cu ⁰	Cu ⁺ → Cu ²⁺	Cu ⁰ → Cu ²⁺		
25	2	Evacuation							1.0
450	2	Evacuation						11.6	1.0
150	9	H ₂	0.48	18	9			0.0	0.94
150	10	O ₂	0.27			20	10	0.0	0.98
300	2	H ₂	2.48	88	44			0.11	0.48
300-450	5	O ₂	1.16			82	41	1.25	1.0
450	1	H ₂	3.55	128	64			1.62	0.15
450-550	22	O ₂	1.87			134	67	2.65 ^f	0.83
550 ^g	22	H ₂	5.30	190	95			4.68 ^f	0.0
550 ^g	24	O ₂	2.65			190	95	0.03	0.69

^a Weight of sample = 583 mg, except for the last two experiments (593 mg). ^{b-e} See corresponding footnote to Table I. ^f The estimated error is ± 0.05 cc(NTP)/g. ^g These two experiments were made with copper hydroxyapatite which had been completely dehydroxylated.

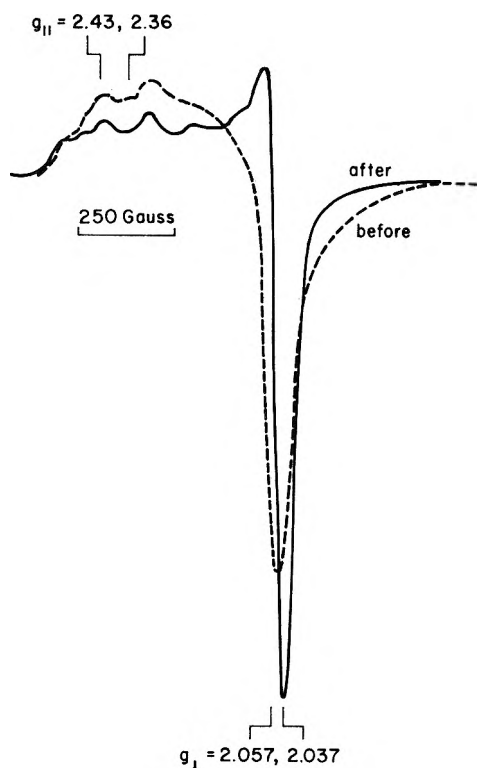


Figure 1. Epr absorption derivatives from copper hydroxyapatite (Cu/Ca = 0.0025) taken at -160° before and after evacuation at 450° .

results of two successive runs. Note that the O₂ uptake was completed faster than the H₂ uptake.

The changes in the epr intensity upon reduction of CuHAP-0.0063, and its recovery upon reoxidation are compared in Figures 3a and 3b, respectively, for experiments at 550° , together with plots of the H₂ and O₂ uptakes *vs.* time. The epr signal disappeared within 10 min on reduction, although the sorption continued for several hours (Figure 3a). (Note that the H₂ uptake after 10 min was about half its final value.) On the other hand, the O₂ uptake was completed within 10 min whereas the epr recovery took a much longer time (Figure 3b). Apparently, at this temperature there are two steps in each process: a rapid reduction step in which the epr signal is eliminated and a slow step in which the consumption of hydrogen is

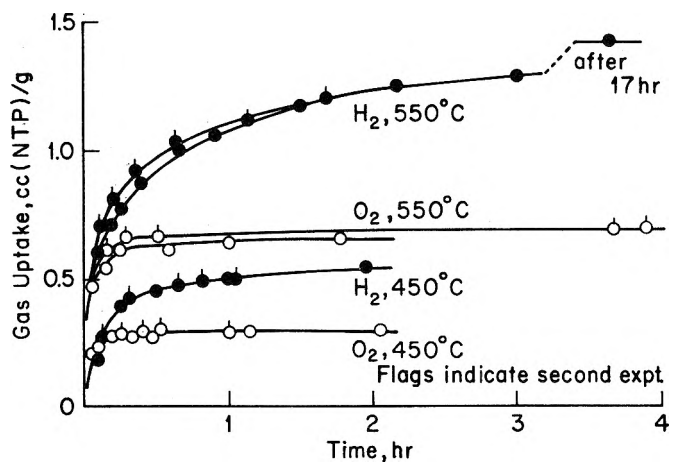


Figure 2. Rates of H₂ and O₂ uptakes by copper hydroxyapatite (Cu/Ca = 0.0063) at 450 and 550° .

about doubled, and a rapid oxidation process in which Cu⁰ is converted to Cu²⁺ followed by a slow recovery of the epr signal. At lower temperatures where partial reduction took place, there was no indication of two steps in either process as is seen from the agreement between H₂ or O₂ uptakes and the epr changes shown in Tables I and II.

The recovery of the epr signal was slow with CuHAP-0.025 at 450 and 500° (Table III). Although the O₂ uptake was sufficient to completely reoxidize the copper reduced in the preceding step, the epr intensity recovered to only 70-85% its initial value after a long reoxidation. In general, the recovery of the epr intensity became slower as the reduction temperature or the copper concentration increased. For example, with CuHAP-0.0063, the recovery was completed by the reoxidation at 300° for 3.5 hr after the reduction at this temperature, but it took about 10 hr when both processes took place at 550° . With CuHAP-0.025, it took 5 hr at 450° after the reduction at only 300° . In all cases, the O₂ uptake was finished long before the epr intensity had completely recovered.

Water collected during the first heat treatment at 450° was the result of dehydroxylation of the hydroxyapatite. Most of the H₂ consumed at 550° was collected as H₂O, and no H₂O was collected during reoxidation. At or below 300° , little H₂O was desorbed during reduction or reoxidation; evidently, it rehydroxylated the catalyst. At 450° , H₂O was collected in both processes, *i.e.*, it was not clean-

TABLE IV: Epr Parameters of Copper Hydroxyapatite^a (Cu/Ca = 0.0025) after Various Pretreatments

Step no.	Pretreatment conditions			Relative epr intensity	<i>g</i> and <i>A</i> ^a						<i>g</i> _± ^{a, b}	
	Temp. °C	Time, hr	Gas		Signal I		Signal II		Signal III		Signal I	Signal II and/or III ^c
					<i>g</i>	<i>A</i> , G	<i>g</i>	<i>A</i> , G	<i>g</i>	<i>A</i> , G		
1	25	0.5	Evacuation	1.0	2.43	102	2.37	115				
5	450	2	Evacuation + O ₂	1.0	2.43	98	2.36	130			2.057	
7	300	1	H ₂	0.7	2.42	99	2.36	130			2.037	
8	300	1	O ₂	1.0	2.42	99	2.36	130			2.035	
9	450	1	H ₂	0.25	2.44	90	2.36	130			2.056	
12	300	10	O ₂	0.70	2.42	93	2.36	130			2.039	
13	450	0.16	O ₂	0.95	2.42	93	2.36	130			2.035	
14	450	2	O ₂	1.0	2.43	90	2.36	120			2.035	
15	450	0.5	H ₂	0.20	2.43	90	2.36	120			2.056	
17	450	1	O ₂	1.0	2.43	90	2.36	125			2.036	
22	540	22	H ₂	0.0								
23	450	1	O ₂	0.15			2.36	140			2.047~2.033	
27	550	15	O ₂	1.0			2.34	150			2.035	

^a Signals I, II, and III are defined in Figures 4 and 5. ^b No hfs was resolved. ^c Signals II and III had about the same *g*_± values.

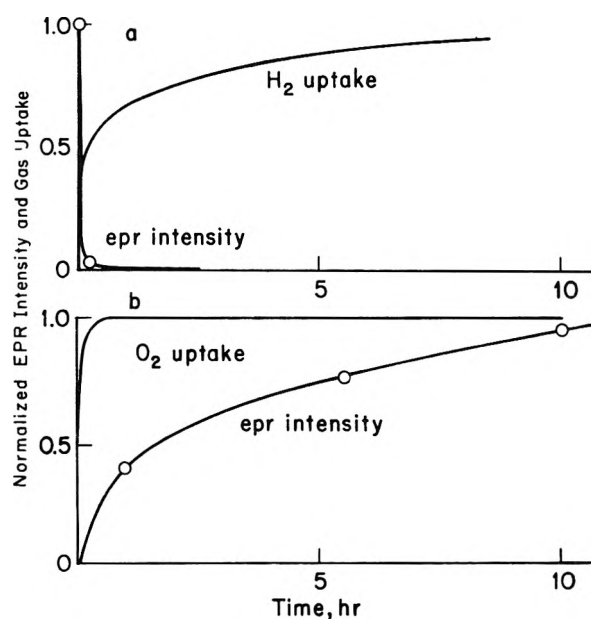


Figure 3. Rates of H₂ and O₂ uptakes and epr intensity change at 550° (Cu/Ca = 0.0063) (ordinate for gas uptake was normalized to unity for complete reduction or oxidation).

ly removed in either the one or the other. The surface area did not change during a series of reduction and oxidation cycles.

Changes in Epr Line Shape upon Reduction and Reoxidation. As found by Berger and Roth¹⁰ for Cu²⁺ supported on alumina, signal resolution increased as the copper concentration decreased. Data for CuHAP-0.0025, which had the best resolved signal, are given in Table IV and typical spectra are shown in Figure 1. The lower field signal (*g*) changed upon reduction and reoxidation as shown in Figures 4 and 5. Complete interpretation of these spectra was not attempted; our interest was in how fast the changes occurred and whether or not they were reversible. The spectral parameters are listed, however, in Table IV.

Untreated copper hydroxyapatite (evacuated at 25°) had at least two sets of hyperfine lines (curve 1 in Figure 4; the corresponding parameters are listed in Table IV) which possibly corresponded to Cu²⁺ substituted in the

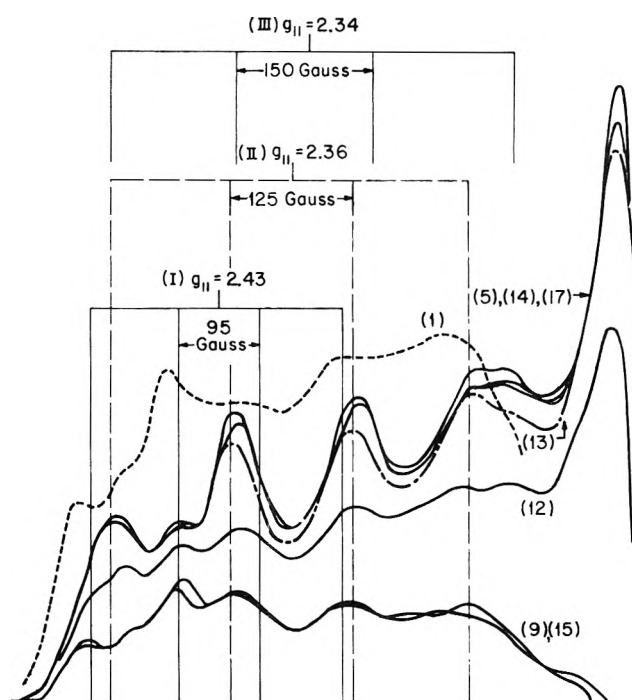


Figure 4. Epr absorption derivatives (lower field) from copper hydroxyapatite (Cu/Ca = 0.0025) taken at -160° after the reduction at 450° and reoxidation. Curve numbers refer to experiments listed in Table IV.

two different Ca²⁺ positions of hydroxyapatite.^{2,15} Heat treatment of CuHAP-0.0025 caused considerable line narrowing and gave better resolved signals. The intensity did not change, but there was a small shift in the spectral parameters (see Figure 1 and curve 5 of Figure 4). Similar line narrowing was observed with other compositions, but to a lesser extent.

When CuHAP-0.0025 was treated at 450° in circulating H₂ for 1 hr, the signal intensity decreased by 75% (75% of the Cu²⁺ was presumably reduced to Cu⁺). The ratio of the intensities of the signals from the two Cu²⁺ species

(15) M. I. Kay, R. A. Young, and A. S. Posner *Nature (London)*, **204**, 1050 (1964).

TABLE V: Fluorescence of Copper Hydroxyapatite

Sample. Cu/Ca ratio	Pretreatment	Valence state of copper ^a	Visible color of sample	Existence of fluorescence ^b
0	None		White	None
0	Evacuated at 450°		White	None
0.0025	Evacuated at 450°		Greenish-blue ^c	None
0.0025	H ₂ at 450°, 0.5 hr	+1 and +2	Pinkish white	Yellow
0.0025	H ₂ at 450°, 1 hr	+1	Pinkish white	Deep yellow
0.0025	O ₂ at 450°, 5 min	+1 and +2	Greenish-blue ^c	None
0.0025	H ₂ at 550°, 4 hr	0	Purple ^d	None
		+1	White ^d	Deep yellow
0.005	None	+2	Light blue	None
0.0063	H ₂ at 450°, 1 hr	+1	Slightly blue	Deep yellow
0.0146	H ₂ at 450°, 1.5 hr	0 and +1	Blue-purple	None
0.025	H ₂ at 300°, 1 hr	0 and +2	Purple	None
0.025	H ₂ at 550°, 24 hr	0	Purple	None

^a Expected from H₂ uptake and epr intensity; see text. ^b Fluorescence was yellow in all observed cases and was stronger with 2540- than with 3660-Å irradiation. ^c Greenish-blue color of the original sample. ^d Some particles were white and others purple.

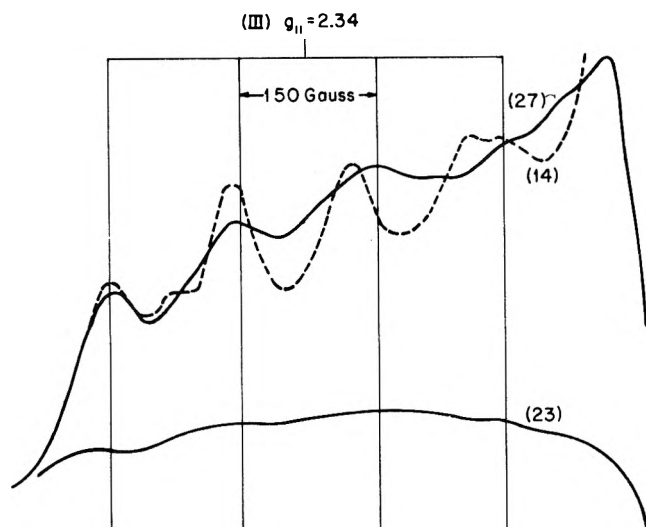


Figure 5. Epr absorption derivatives (lower field) from copper hydroxyapatite (Cu/Ca = 0.0025) taken at -160° after the reduction at 550° and reoxidation. Curve numbers refer to experiments listed in Table IV.

was not the same, however, after reduction as before (see curve 9 in Figure 4 and Table IV). The Cu²⁺ responsible for signal II, which was apparently the majority species, was the most sensitive to reduction. Oxidation at 450° for 10 min effected recovery of 95% of the intensity and the line shape was the same as before reduction (curve 13 in Figure 4 and Table IV), and after 2 hr the recovery was completed (curve 14). This reduction-oxidation process was fairly rapidly reversible (curves 5 \rightarrow 9 \rightarrow 14 \rightarrow 15 \rightarrow 17 in Figure 4 and Table IV).

The epr signal completely disappeared after reduction at 550° for 20 hr. Reoxidation at 450° for 1 hr after the reduction led to the recovery of only 15% of the intensity and the signal was very broad (curve 23 in Figure 5 and Table IV). Compare this with the 95% recovery after 10 min of reoxidation after the reduction at 450° (curve 13). The intensity recovered completely, however, after treatment with O₂ at 550° for 15 hr, but the lines were less resolved and had slightly different parameters (curve 27 in Figure 5 and Table IV).

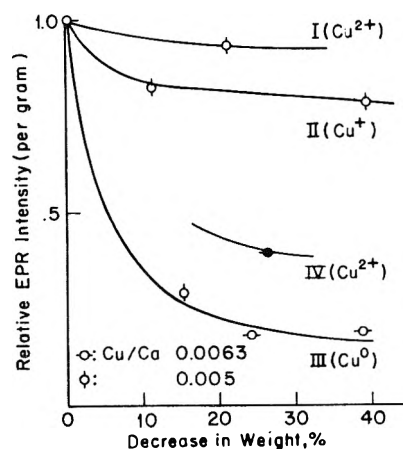


Figure 6. Decrease of copper content as measured by epr after partial dissolution. Pretreatments prior to dissolution were evacuation at 25° (I), reduction by H₂ at 440° for 1 hr (II), reduction at 550° for 17 hr (III), and reduction by H₂ at 550° plus reoxidation by O₂ at 550° for 18 hr (IV).

For comparison, the epr of copper impregnated on Ca₁₀(PO₄)₆(OH)₂ was measured with two copper concentrations, about 0.2% and about 0.05% (*cf.* 0.17% for CuHAP-0.0025). The signals were very broad and the hyperfine splittings were very poorly resolved, even after heat treatment at 450° .

Change in Cu²⁺ Concentration upon Partial Dissolution. Experiments were carried out to determine whether or not copper had migrated from the bulk onto the surface upon reduction. The epr intensity *per gram* was corrected for the filling factor and these data are plotted against the fractional weight loss on acid treatment in Figure 6. The specific epr intensity of the untreated sample decreased by 6% when the outer coat comprising 25% of the mass was dissolved away, *i.e.*, it was unchanged within the experimental error (curve 1 of Figure 6). It decreased by 15–20% following reduction at 440° (curve 2); calculation showed that this decrease in copper concentration agreed very well with that in the surface unit cells of the crystal residues. Exchange may have taken place between the Cu²⁺ in these cells and the Ca²⁺ in the buffer solution. The intensity from the sample which was reduced at 550° ,

TABLE VI: Color Changes of Copper Hydroxyapatite with Different Cu/Ca Ratios after Reduction and Reoxidation

Pretreatment		Cu/Ca Ratio				
Temp, °C	Gas	0.0025	0.005	0.0063	0.0146	0.025
150	H ₂	Light blue ^a	Light blue	Light blue	Light green	Greenish blue
	O ₂	Light blue	Light blue	Light blue	Light blue	Greenish blue
300	H ₂	Light blue	Light blue	Light blue	Bluish purple	Deep purple
	O ₂	Light blue	Light blue	Light blue	Light blue	Grey
450	H ₂	White (slightly pink)	White	Blue	Blue	Deep purple
	O ₂	Light blue	Light blue	Light blue	Slightly greyish green	Grey
550	H ₂	Purple	Purple	Purple	Deep purple	Deep purple
	O ₂	Green	Green	Green	Green	Green

^a Original color of copper hydroxyapatite is slightly greenish blue.

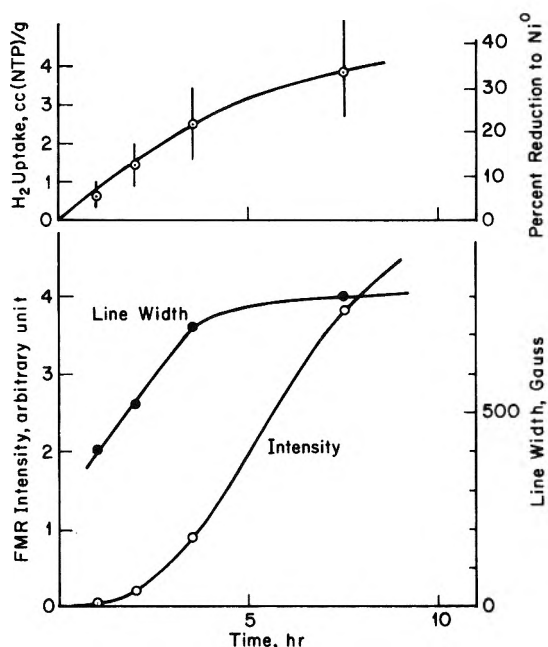


Figure 7. H₂ uptake and ferromagnetic resonance of nickel hydroxyapatite (Ni/Ca = 0.0051) at 550°.

however, showed a significant decrease with increasing weight loss, suggesting that much of the reduced copper had indeed migrated to the surface. An aliquot of the same reduced sample was reoxidized before dissolution. The corresponding result (curve 4) fell in between those of curves 1 and 3.

Fluorescence and Color Changes. A characteristic yellow fluorescence appeared when the preparations shown herein to contain Cu⁺ were exposed to uv light. The effects of various pretreatments are summarized in Table V. In the case where fluorescence was expected but not observed, it is probable that no Cu⁺ was present near the surface. The fluorescence was quenched on exposure to O₂ at 25 or 150°, but was usually restored upon the evacuation at 25° (<10⁻³ Torr). With CuHAP-0.025, reduction at neither 300 nor 500° produced fluorescence.

The color changes (Table VI) upon reduction and oxidation gave further qualitative information concerning the state of the copper. Untreated CuHAP was greenish blue, and the color became greener upon heating (on complete dehydroxylation the color became green). Different colors developed upon reduction, depending on the copper con-

centration and the reduction temperature. With low copper concentration, the samples became colorless or slightly pink upon reduction to Cu⁺. As the copper concentration increased the sample became bluish when the copper in the bulk was presumably Cu⁺, and it became a deep purple as the copper concentration and the reduction temperature was further increased. The color became grey when the reduced samples was reoxidized and epr recovery was not complete. These colors, after some experience, were fair indicators of catalytic properties. Related color changes were reported by Dimitrov and Leach¹⁶ for Cu-X zeolites.

Reduction of Nickel Hydroxyapatite. The consumption of H₂ was determined at 450 and 550° for NiHAP-0.0051 and spectra were recorded after the reductions (Table VII). No signal was observed for Ni²⁺, Ni⁺, or Ni⁰ (atoms). However, the ferromagnetic resonance absorption (fmr) due to nickel clusters was detected. Minimal H₂ uptake was detectable at 450°, but at 550° the uptake after 23 hr was sufficient to account for complete reduction to Ni⁰. The fmr developed at a rate comparable with that of the H₂ uptake (Figure 7). The line width increased at first and then leveled off; the *g* value increased with extent of reduction from 2.21 to 2.25.

The number of nickel atoms per cluster was calculated according to the method of Loy and Noddings¹⁷ using for the total number of nickel atoms, values calculated from the H₂ uptakes assuming that Ni²⁺ was reduced to Ni⁰. Values of about 150 atoms/cluster were estimated for short reduction times and a constant value of 1200 to 1300 atoms/cluster for longer times.

Similar results (Table VII) were obtained with NiHAP-0.039, but at 450°. The average number of atoms per cluster was about 1000 after a 3-hr reduction at 450°.

H₂-D₂ Equilibration over Copper Hydroxyapatite Catalysts. Using the information given in previous sections, it was possible to study catalytic reactions on preparations where most of the copper was initially present as Cu²⁺, Cu⁺, or Cu⁰. Data for the H₂-D₂ equilibration are collected in Table VIII. Since reduction of Cu²⁺ to Cu⁺ occurred at 200°, it was not possible to discriminate between the relative activities of these two ions. The data show clearly, however, that the catalyst in the Cu⁺ form is much more active than when Cu⁰ clusters are present. The rate

(16) C. Dimitrov and H. F. Leach, *J. Catal.*, **14**, 336 (1969).

(17) B. A. Loy and C. R. Noddings, *J. Catal.*, **3**, 1 (1964).

TABLE VII: Reduction of Nickel Hydroxyapatites

Ni/Ca ratio	Experimental conditions			H ₂ uptake, ^b cc(NTP)/g	Ferromagnetic resonance				Color
	Temp, °C	Time, hr	Gas		Intensity ^c	g	Line width, gauss	No. of atoms per cluster ^d	
0.0051 ^a	450	2	H ₂	0.03	0				Yellow
	450	1	H ₂	0.03/0.06	0				Yellow
	450	0.5	O ₂		0				Yellow
	550	1	H ₂	0.06	0.23	2.21	400	130	Darker yellow
	550	1	H ₂	0.08/0.14	0.92	2.22	520	160	Dark yellow
	550	1.5	H ₂	0.11/0.25	4.2	2.25	720	410	Dark yellow
	550	4	H ₂	0.13/0.38	20.0	2.25	780	1300	Gray
	550	16	H ₂	0.62/1.00 ± 0.15	54.0	2.25	880	1200	Black
0.039 ^e	450	1.5	H ₂	0.43	2.2	2.21	380	200	Dark yellow
	450	18	O ₂		0				
	450	1.5	H ₂	0.90	6.1	2.21	380	280	Gray
	450	1.5	H ₂	1.09/2.99 ± 0.12	58	2.22	700		Gray
	450	0.2	Evacuation		73	2.22	880	990	Gray

^a Weight of sample = 910 mg. ^b Where two figures are given, the first is the uptake in that step and the second (following slash) is the sum of this and the amount from previous steps. ^c Intensity is normalized to CuHAP-0.0146. ^d See text. These figures are no more accurate than the H₂ uptake measurements. ^e Weight of sample = 460 mg.

TABLE VIII: H₂-D₂ Equilibration over Copper Hydroxyapatite (Cu/Ca = 0.005) at 202°

Pretreatment conditions			Valence state of copper	Rate constant, 10 ² k, min ⁻¹
Temp, °C	Gas	Time, hr		
500	Dry air	1	+2	
300	H ₂	1.5	+1	8.8
350-410	H ₂	0.5	+1,0	3.9
440	H ₂	0.5	+1,0	1.3
500	Dry air	2		
300	H ₂	0.5	+1	11.3
530	H ₂	0.5	0	<0.3
(Temperature was lowered in H ₂) ^a				
530	Dry air	4.5	+2	7.0
After previous experiment			+1	10.1
530	H ₂	14	0	1.3
(Temperature was lowered in vacuum after evacuation) ^a				

^a Refers to pretreatment in the step above.

was near its maximum value for an initial reduction temperature of 300° (8.8 min⁻¹). When the reduction temperature was raised into the critical region where the formation of Cu⁰ starts (about 400°) the rate fell, but on reoxidation followed by reduction at 300° the rate increased to its maximum value (11.3 min⁻¹). Reduction at 530°, where conversion to Cu⁰ was complete, yielded the minimum value (≤0.3 min⁻¹). The activity was restored by reoxidation at 530°.

The reduction at 530° for 13 hr (to Cu⁰) led to a very low activity if the temperature was lowered in H₂. A higher activity was obtained when the catalyst was evacuated after reduction, before the temperature was lowered in vacuum (1.3 vs. ≤0.3 min⁻¹). However, the activity was still much lower than when the catalyst contained mainly Cu⁺.

The activation energy was 3 kcal/mol over the sample reduced at 300° and 15 kcal/mol over the sample which was reduced at 525° and then evacuated at the same temperature (Figure 8). The rate on the parent stoichiometric hydroxyapatite was still lower by a factor of 10²-10³ and had an activation energy of 24 kcal/mol.¹⁸

Discussion

There are two different Ca²⁺ positions in hydroxyapatite. One is between the *ab* planes containing the phosphate groups and in columns parallel to the *c* axis and the other is in the *ab* planes and centered at the unit cell corners.^{2,15} The Cu²⁺ may have been substituted in either or both of these sites. The X-ray pattern of the Cu-substituted preparations did not differ significantly from that of the parent hydroxyapatite, but the two sets of hfs found for CuHAP-0.0025 suggest that both sites were substituted (Figure 4 and Table IV).

The detectability of all of the copper as Cu²⁺ by epr, and its uniform dispersion, made it possible to study the reduction-reoxidation properties of the catalyst by comparing the stoichiometry of the H₂ and O₂ uptakes with the epr intensity changes. Bulk properties of the crystals were measured in these experiments and one cannot be sure that the valence states of the ions on the surface were the same as those in the bulk. The H₂-D₂ exchange results suggest, however, that the bulk property measurements were fairly accurately reflected by the surface.

The H₂ uptakes after several hours at 550° corresponded to 85-100% of complete reduction of all of the Cu²⁺ present. In these cases, the epr signal disappeared. Since an epr signal is expected for isolated Cu atoms,¹⁴ metallic copper or clusters of atoms must have been present in these circumstances. This explanation was advanced by Berger and Roth¹⁰ for similar observations with their Cu-alumina system and has been implied from earlier paramagnetic susceptibility results.^{8,9} Metal crystal formation upon reduction was evidenced by the appearance of fmr in the case of nickel hydroxyapatite at this temperature. It should be noted that to accomplish this, the nickel must have migrated a considerable distance, both as ions (intracrystalline) and as atoms (extracrystalline).

With low Cu²⁺ concentrations (CuAP-0.0063 and -0.0146), the H₂ uptakes at or below 450° and the corresponding epr intensity decreases, agreed with the assumption that the reduction was mainly from Cu²⁺ to Cu⁺. The O₂ uptakes on reoxidation, which were always about

(18) G. R. Wilson and W. K. Hall, unpublished work.

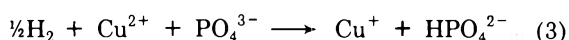
half the H₂ uptakes, and the corresponding epr intensity recoveries were consistent with the reoxidation of Cu⁺ to Cu²⁺. With higher concentrations (Cu/Ca > 0.025), the Cu²⁺ was reduced to Cu⁰ at all temperatures investigated. The larger than expected decreases in epr intensity observed at 450° for CuHAP-0.025 suggest, however, that part of the ions were reduced only to Cu⁺, *e.g.*, Cu⁺ = 40%; Cu⁰ = 45%, and Cu²⁺ = 15%. Longer reduction time undoubtedly would have led to complete reduction.

The results shown in Figure 3a suggest a stepwise reduction process, the first step being a rapid reduction of Cu²⁺ to Cu⁺ and the second a slow conversion of Cu⁺ to Cu⁰. The latter process may be rate limited by the required migration of copper from the interstitial positions to the surface. Thus, only the first step took place with samples containing low concentrations of Cu at or below 450°. At 550°, the second step became faster, but was still slower than the first step in which the epr signal disappeared. After several hours, the epr decrease and H₂ uptake agreed quite well, and corresponded to complete reduction. Reoxidation was also a two-step process (see Figure 3b). The oxygen uptake was completed in the first step, possibly by formation of CuO on the surface. The epr signal recovered slowly in the second step as both Cu²⁺ and O²⁻ migrated back into the lattice.

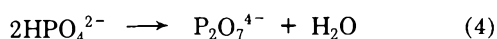
The fmr measurements of NiHAP-0.0051 provided information about cluster formation. No signal was observed after treatment with H₂ at 450°, but one developed rapidly at 550°. This shows clearly that crystallization occurred at this temperature. The chief difference between the Ni²⁺ and Cu²⁺ catalysts was that the former ion resisted reduction to the monovalent state. Hence, the H₂ uptakes became significant only at 550° where the cations have sufficient mobility to migrate to the surface at an appreciable rate. If this is so, the Ni²⁺ adjacent to the surface may have reduced at much lower temperatures and could function effectively as reversible oxidation-reduction centers.

The reason why the catalysts containing high concentrations of Cu²⁺ were reduced completely at low temperatures is not understood. Presumably, the reduction is still a two-step process, as evidenced by changes in epr intensity larger than expected for the corresponding H₂ uptakes required for a one-step reduction to Cu⁰ (Table III). Probably also, the second step of the reduction takes place only at the surface and its rate is limited by the redistribution of the remaining ions in the lattice. The latter step may be concentration dependent, increasing concentration favoring intracrystalline mobility at lower temperatures. Whatever the cause, the NiHAP system behaved similarly. NiHAP-0.0051 showed fmr only after treatment with H₂ at 550°, but NiHAP-0.039 developed a signal after similar treatment at 450°.

Our results may be plausibly described by the following chemistry, which satisfies the condition that the charge balance on the lattice is maintained at all times. The primary reduction step is

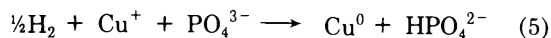


This may be followed by



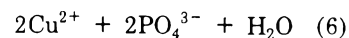
depending upon the temperature, the reaction proceeding to a greater extent as the temperature increases. About half the H₂O was removed in this step at 450° in our ex-

periments and most of it at 550°. Also at 550°, the second step of the reduction always occurs, *i.e.*

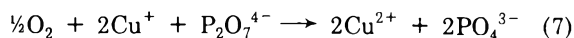


and the resulting HPO₄²⁻ undergoes reaction 4.

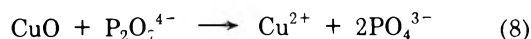
Reoxidation is dependent upon the system existing following reduction. When only Cu⁺ is present, two processes must occur, *viz.*



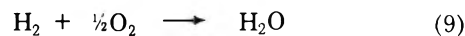
and



When Cu⁰ clusters are present, reoxidation probably results in the formation of CuO which is not detectable by epr. This is then slowly decomposed as it migrates back into the bulk, satisfying the relation



This picture is consistent with the observed overall result that



The epr signal of Cu²⁺ in hydroxyapatite was not well resolved. The broadened signal was caused partly by Cu₂²⁺-Cu²⁺ dipolar interactions (as evidenced by better resolution with the decreasing Cu²⁺ concentration) and partly by the existence of two Cu²⁺ sites in hydroxyapatite. Another contributing factor may have been a shortened relaxation time, T₁, due to the close lying excited state which exists often for Cu²⁺ in near octahedral symmetry.¹⁹ Better resolution when measured at lower temperatures supports this possibility. Line broadening may also have been caused partly by protons present as HPO₄²⁻ or as structural OH⁻ because the resolution of the signal improved substantially when preparations were heated to temperatures where dehydroxylation occurred (Figure 1). A slight distortion of the symmetry around the Cu²⁺ accompanying the formation of P₂O₇⁴⁻ units also may have contributed to this line narrowing. Similar behavior on heat treatment of Cu²⁺-exchanged zeolites has been reported.^{20,21} Starting with the better resolved signal obtained after heat treatment, rapid and reversible changes in epr line shape and intensity upon reduction and reoxidation at 450° were observed (Figure 4). Following reduction at 550°, the reoxidation was very slow and gave a different line shape, although the recovery of intensity was complete. These facts support the picture presented above.

The measurements of the decrease in Cu²⁺ concentration upon partial dissolution of the preparations given in Figure 6 provides good evidence of the migration of copper out of and back into the bulk. Had nearly all of the copper migrated to the surface, the Cu²⁺ resonance intensity (measured after reoxidation of the remaining copper to Cu²⁺) should decrease rapidly when the surface layers of the crystals are removed. On the other hand, the epr intensity (per gram) should remain constant if the reduced

(19) B. R. McGarvey in "Transition Metal Chemistry," R. L. Carlin, Ed., Vol. 3, Marcel Dekker, New York, N. Y., 1966, p 90.

(20) A. Nicula, D. Stamires, and J. Turkevich, *J. Chem. Phys.*, **42**, 3684 (1965).

(21) J. T. Richardson, *J. Catal.*, **9**, 178 (1969).

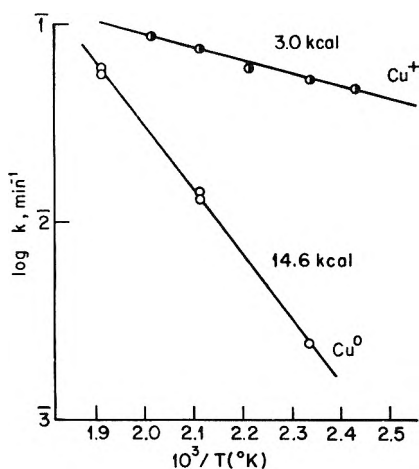


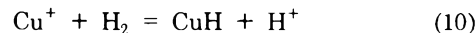
Figure 8. Arrhenius plot for $\text{H}_2\text{-D}_2$ equilibration over copper hydroxyapatite ($\text{Cu}/\text{Ca} = 0.005$).

copper remained uniformly dispersed throughout the bulk. There was, indeed, little change with the untreated sample (curve 1, Figure 6), showing again that Cu^{2+} was initially uniformly distributed throughout the crystal. On the other hand, the data for the sample reduced at 550° show clearly that copper had migrated to the surface in this case. The decrease in the specific epr intensity was relatively small with the sample where copper was reduced only to Cu^+ , supporting the conclusion that significant migration does not occur when only the first step of the reduction is accomplished. On reoxidation of the completely reduced sample before dissolution, copper was shown to have migrated back into the bulk to some extent, although it may have stayed near the surface, *i.e.*, curve 4 fell between curves 1 and 3.

A close correspondence between the expected valence state of Cu^+ and the fluorescence was demonstrated in Table V. Apatites are widely used as phosphors with Mn^{2+} or rare earth ions as activators.²² ZnS activated by Cu^+ has a blue fluorescence which is attributed to the

emission accompanying the process of trapping a positive hole by Cu^+ .²³ Some oxides and phosphates are also phosphors with copper as activator.²⁴ The emission ranges from the blue through the yellow region depending upon the composition.²⁴ Therefore, the identification of the fluorescence in copper hydroxyapatite with Cu^+ is quite reasonable. The results presented in Table V, although qualitative, support the conclusions reached from the combined epr and gas uptake data.

The active valence state of copper for the activation of hydrogen (or dehydrogenation) has been suggested by several authors^{6,7} to be +1. The results of the $\text{H}_2\text{-D}_2$ equilibration experiments presented herein support this view. Stated in the simplest terms, the catalyst was much more active when the catalyst was prerduced to the Cu^+ state than when it was completely reduced to Cu^0 . Its activity was little different when it was initially in the Cu^{2+} state, but the reduction to Cu^+ took place under reaction conditions. That the mechanisms of the exchange over supported copper clusters and the Cu^+ hydroxyapatite were not the same is indicated by the different activation energies derived from Figure 8. In the latter case, it seems likely that the Cu^+ centers function reversibly as hydride acceptors in the heterolytic cleavage of H_2 , *i.e.*, by the reaction



From the data presented herein, it is not at all certain that the $\text{H}_2\text{-D}_2$ catalysis is confined to the surface. It would appear that the entire crystal may function both as a reservoir and as a mixing pot.

Acknowledgment. This work was supported by the Gulf Research and Development Co. as part of its research program on the Fellowship on Petroleum.

- (22) J. S. Prener and W. W. Piper, paper presented at International Symposium on Structural Properties of Hydroxyapatite, Maryland, 1968.
 (23) C. Kittel, "Introduction to Solid State Physics," 2nd ed, Wiley, New York, N. Y., 1956.
 (24) E. W. Claffy and J. H. Schulman, *J. Electrochem. Soc.*, **98**, 409 (1951).

Raman Spectra of the Products of Rubidium and Cesium Atom Argon Matrix Reactions with Oxygen Molecules

Richard R. Smardzewski and L. Andrews*

Chemistry Department, University of Virginia, Charlottesville, Virginia 22901 (Received October 20, 1972)

Raman spectra of the RbO_2 and CsO_2 molecules have been observed from samples of rubidium and cesium atoms codeposited at 16°K with oxygen molecules at high dilution in argon. The strong bands observed at frequency shifts of 1110 and 1114 cm^{-1} , respectively, are assigned to the superoxide fundamentals in the Rb^+O_2^- and Cs^+O_2^- molecules. The splitting of these features into triplets in the $^{16}\text{O}_2$ - $^{16}\text{O}^{18}\text{O}$ - $^{18}\text{O}_2$ experiments indicates isosceles triangular structures while the absence of $\text{M}^+ \cdots \text{O}_2^-$ interionic modes is consistent with the ionic model for the alkali metal superoxide molecules. Strong bands were observed at 298 and 287 cm^{-1} , respectively, in the Rb and Cs oxygen systems; these frequencies are attributed to the intermolecular oxygen-oxygen ($\text{O}_2 \leftrightarrow \text{O}_2$) $^-$ stretching mode in the Rb^+O_4^- and Cs^+O_4^- species.

Introduction

Recent infrared investigation of the argon matrix reaction of alkali metal atoms with O_2 molecules have supported the existence of molecules of the general formula MO_2 where $\text{M} = \text{Li},^1 \text{Na},^2 \text{K}$, and $\text{Rb}.$ ³ Experiments involving mixed oxygen isotopic substitution have indicated the presence of two equivalent oxygen atoms in these molecules. The close agreement of the O-O stretching force constants of MO_2 and O_2^- suggests that the bonding in MO_2 is predominantly ionic and may be more simply described as M^+O_2^- . Additional evidence for ionic bonding is indicated by the observation in the infrared of intense metal-oxygen modes while the intramolecular stretch of the O_2^- anion occurs as a very weak feature.

Recent studies in this laboratory of the Raman spectra of the products of $\text{Li},^4 \text{Na}$, and K^6 atom argon matrix reactions with O_2 molecules have established the viability of this approach to the examination of the intramolecular modes of homonuclear diatomics. As expected, such modes are strong Raman scatterers while, because of the much smaller polarizability changes involved, the interionic metal-oxygen vibrations are not. The precise value of the O_2^- vibrational frequency is directly affected by the charge distribution in the M^+O_2^- molecule. In the previous Raman investigation of the matrix reactions involving Na and K atoms with O_2 molecules,⁵ the amount of ionic character in the MO_2 species appeared to decrease slightly proceeding from Na to K as determined by an increase in the O_2^- vibrational frequency. This was accounted for by the increased polarizability of the potassium cation. In order to determine the generality of this trend, it was considered essential to investigate the analogous argon matrix reactions of the heavier alkali metals. We report here a Raman spectral examination of the matrix reactions of Rb and Cs atoms with O_2 at high dilution in argon. Complementary infrared studies are reported in a following paper.⁷

Experimental Section

The 15°K refrigeration system, vacuum vessel, alkali metal atom source, and infrared spectrometer have been described earlier.^{1,4} Argon (Air Products, 99.995%), oxy-

gen gas (Air Products, U.S.P., therapy), $^{18}\text{O}_2$ (Oak Ridge National Laboratory, 99.3%), and 55% ^{18}O enriched O_2 gas (20% $^{16}\text{O}_2$, 50% $^{16}\text{O}^{18}\text{O}$, 30% $^{18}\text{O}_2$, Miles Laboratories, Inc.) were used without further purification.

Rubidium and cesium atom production were accomplished through the metathetical reactions of lithium metal with RbCl and CsCl , respectively. A fresh 5-mm cube of lithium metal was cut and washed with dry hexane under an argon atmosphere and placed into a Knudsen cell along with an appropriate amount of anhydrous alkali metal chloride. The Knudsen cell was then heated *in vacuo* to a temperature necessary to initiate reaction (*ca.* 350°). Following such a procedure, the Knudsen cell was then placed inside the vacuum vessel for matrix deposition. In the Raman experiments, oxygen gas diluted in argon was deposited through 0.25-in. copper tubing at the rate of 2 mmol/hr for 4-6 hr onto a steeply pitched copper wedge held near 16°K. A simultaneous beam of rubidium or cesium atoms was achieved by heating the Knudsen cell to that temperature necessary to effuse an adequate amount of heavy alkali metal atoms (300°, Rb; 310°, Cs). Values for these temperatures were determined experimentally and correspond approximately to an effective metal atom pressure of 1 μ inside the Knudsen cell. A sliding metal shield inside the vacuum vessel served to contain the metal atom beam prior to deposition.

Raman spectra of deposited samples were recorded using the laser excitation of a Coherent Radiation Model 52G argon ion laser (5145 and 4880 Å) in combination with a Spex 1401 double monochromator. Experimental details have been presented elsewhere.⁶ Through the use of a visual alignment technique it was possible to record the spectra of various segments of the deposited matrix. In this manner unwanted background scatter was reduced

- (1) L. Andrews, *J. Chem. Phys.*, **50**, 4288 (1969).
- (2) L. Andrews, *J. Phys. Chem.*, **73**, 3922 (1969).
- (3) L. Andrews, *J. Chem. Phys.*, **54**, 4935 (1971).
- (4) D. A. Hatzenbuehler and L. Andrews, *J. Chem. Phys.*, **56**, 3398 (1972).
- (5) L. Andrews and R. R. Smardzewski, *J. Chem. Phys.*, in press.
- (6) R. R. Smardzewski and L. Andrews, *J. Chem. Phys.*, **57**, 1327 (1972).
- (7) L. Andrews, J. T. Hwang, and C. Trindle, *J. Phys. Chem.*, to be submitted for publication.

to a minimum while Raman signals were maximized. In the spectral regions above 1000 cm^{-1} Raman shifted, dielectric long wavelength pass filters (4880 and 5145 Å; Corion Instrument Corp.) were used to suppress the intense Rayleigh line and thus minimize the intensity of grating ghosts. Raman frequencies were determined to an accuracy of $\pm 1\text{ cm}^{-1}$ by employing several argon fluorescence lines as a source of calibration.

Results

Raman spectra were recorded from argon samples containing 1% O_2 and similar samples codeposited with Rb and Cs atoms.

Oxygen in an Argon Matrix. The Raman spectrum of a blank matrix was initially determined in order to establish the clarity of the spectral regions of interest prior to the start of metal atom reactions. A blank matrix sample of 8 mmol of $^{16}\text{O}_2$ diluted in argon (M/R = 100) was deposited and its Raman spectrum recorded using both 4880 and 5145 Å laser excitation. With the instrumental slits set at $250\ \mu$ (5-cm^{-1} resolution at 5145 Å) and an amplification range of $0.3 \times 10^{-9}\text{ A}$ (no suppression), no Raman signals were detected in the region from 160 to 1500 cm^{-1} above a 5% noise level. The very intense 1552-cm^{-1} fundamental of $^{16}\text{O}_2$ was the only observable feature in the matrix sample.

Rubidium Atom Reactions. Laser excited Raman spectra recorded after deposition of rubidium atoms with three isotopic samples of oxygen molecules in argon matrices are depicted in Figure 1. Frequency values are listed in Table I. The isotopic frequencies of the oxygen molecule are contained in the $1400\text{--}1600\text{-cm}^{-1}$ region. Several rubidium atom experiments were run to determine the opti-

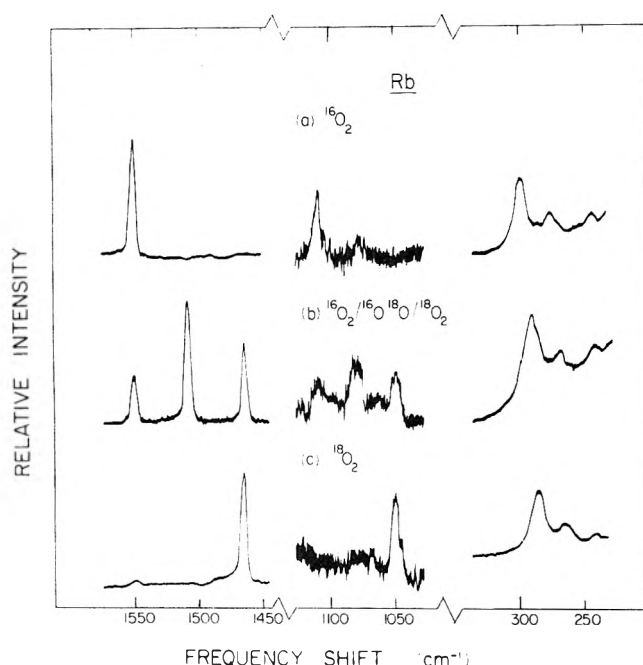


Figure 1. Raman spectra of rubidium atom-oxygen molecule argon matrix reaction products condensed at 15°K : approximately 500 mW of 4880 Å excitation, 5 Å band pass filter, 5-cm^{-1} resolution, $5\text{-cm}^{-1}/\text{min}$ scan speed, 10-sec rise time, little or no suppression. Amplification ranges were $1 \times 10^{-9}\text{ A}$ at $1450\text{--}1550\text{ cm}^{-1}$, $0.3 \times 10^{-9}\text{ A}$ at $1020\text{--}1120\text{ cm}^{-1}$ using dielectric long wavelength pass filter, and $1 \times 10^{-9}\text{ A}$ at $250\text{--}300\text{ cm}^{-1}$: spectrum a $^{16}\text{O}_2$, Ar/O₂ = 100; spectrum b $^{16}\text{O}_2\text{--}^{16}\text{O}^{18}\text{O}\text{--}^{18}\text{O}_2$, Ar/O₂ = 50; spectrum c $^{18}\text{O}_2$, Ar/O₂ = 100.

TABLE I: Raman Spectra (Frequency Shifts, cm^{-1}) Observed from Argon-Oxygen Matrix Samples (Ar/O₂ = 100) Codeposited with Rubidium Atoms at 15°K

$^{16}\text{O}_2$	$^{18}\text{O}_2$	$^{16}\text{O}_2\text{--}^{16}\text{O}^{18}\text{O}\text{--}^{18}\text{O}_2^a$
1552		1552
		1509
	1465	1464
1110		1108
		1076
	1046	1044
298	286	291
275	264	269
244 ^b	244	244

^a Ar/O₂ = 50. ^b Grating ghost.

imum reaction conditions. In the $^{16}\text{O}_2$ experiment the only Raman signal detected in the $300\text{--}1500\text{-cm}^{-1}$ region occurred at 1110 cm^{-1} . Its oxygen-18 counterpart was observed at 1046 cm^{-1} in similar experiments using $^{18}\text{O}_2$. Upon mixed oxygen isotopic substitution the 1110-cm^{-1} band was split into a triplet with a relative intensity pattern similar to that of the parent molecules. In these experiments using the scrambled oxygen isotopes an M/R = 50 was found necessary in order to observe all isotopic bands. The oxygen-16 feature of the triplet appeared weak and broad owing to the low relative abundance of the $^{16}\text{O}_2$ isotope, as seen from the Raman spectra of the parent molecules. The Raman signals in these experiments were not strong enough to make meaningful depolarization measurements.

Two additional Raman bands were observed in the lower frequency region of $200\text{--}300\text{ cm}^{-1}$. In the $^{16}\text{O}_2$ experiment these were observed at 298 and 275 cm^{-1} . As seen in Figure 1, the 298- and the 275-cm^{-1} bands have oxygen-18 counterparts at 286 and 265 cm^{-1} , respectively. The weak 244-cm^{-1} band is due to a grating ghost. The intensity of the 298-cm^{-1} band is approximately 3–5 times that of 1110-cm^{-1} feature. An isotopic splitting pattern was not resolved in the scrambled oxygen isotopic studies due to the large spectral bandwidth of each isotopic feature; the two bands were observed at 291 and 269 cm^{-1} , positions intermediate between the pure isotopic bands.

The Rb-O₂ matrix samples were warmed to approximately 36°K and recooled to 16°K . The lowest frequency bands grew markedly in intensity while the O₂ fundamental and the $1046\text{--}1110\text{-cm}^{-1}$ signals remained essentially unchanged.

Cesium Atom Reactions. Similar matrix reactions were studied with cesium atoms and oxygen molecules in argon matrices. The Raman spectra are exhibited in Figure 2 where three isotopic samples of oxygen in argon matrices were codeposited with a beam of cesium atoms. The observed frequencies are listed in Table II. As was the case with rubidium, a single Raman band was detected in the region of $300\text{--}1500\text{ cm}^{-1}$ for the $^{16}\text{O}_2$ experiment. Several accurate frequency determinations placed this band at 1114 cm^{-1} . On proceeding to the analogous $^{18}\text{O}_2$ experiment this same band shifted downward to 1050 cm^{-1} . The scrambled oxygen isotopic experiments produced weaker bands owing to reduced concentrations of each isotopic species. The 1114-cm^{-1} band does, however, appear to split into a triplet. The low scattering intensities encoun-

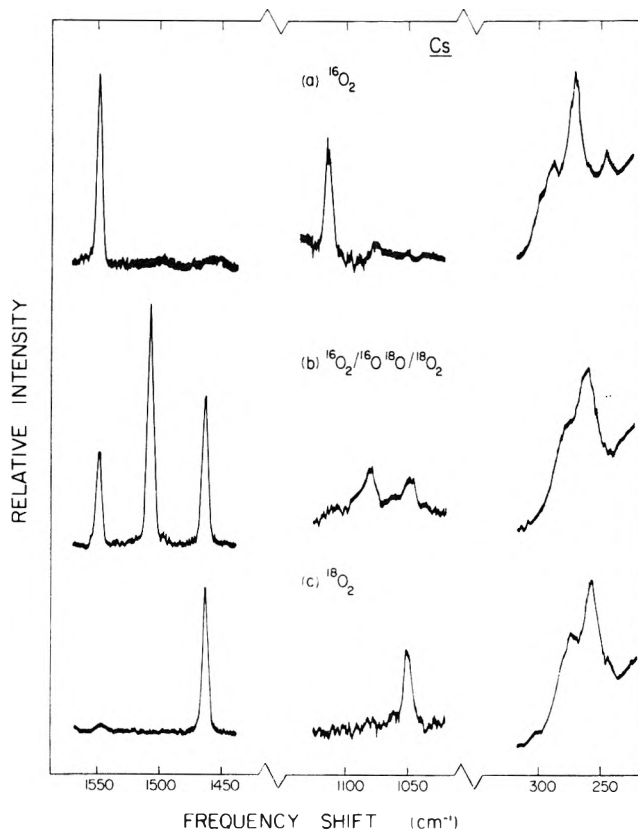


Figure 2. Raman spectra of cesium atom-oxygen molecule argon matrix reaction products isolated at 15°K. Same instrumental conditions and isotopic samples as used in Figure 1.

tered in the $^{16,18}\text{O}_2$ experiment precluded accurate frequency determinations.

Again, as was the case with rubidium, two lower frequency Raman signals were observed in the 200–300- cm^{-1} region. For the case of the $^{16}\text{O}_2$ experiments careful frequency determinations placed these bands at 287 and 270 cm^{-1} . The 287- and 270- cm^{-1} bands shifted downward to 274 and 258 cm^{-1} on proceeding to the $^{18}\text{O}_2$ experiments, while the 244- cm^{-1} band due to a grating ghost remained unchanged. Here again because of the broad spectral features of the bands involved, no splitting could be detected in the scrambled oxygen isotopic experiments; the bands were observed at 278 and 262 cm^{-1} .

The relative intensity pattern of the lower frequency Raman bands is worth mentioning. Unlike the case with rubidium, the higher frequency band is not the most intense component. This is exhibited in a comparison of Figures 1 and 2. The intensity of the 270- cm^{-1} band is approximately 3–5 times that of the 1114- cm^{-1} feature. No signal was detected at 237 cm^{-1} in the $^{16}\text{O}_2$ experiment or 226 cm^{-1} in the $^{18}\text{O}_2$ experiment, where the interionic modes were observed in the infrared.⁷

Discussion

Rb^+O_2^- . Previous infrared experiments in this laboratory involving the reactions of lithium¹ and sodium² with oxygen molecules in argon matrices have established that the major product species contained a single metal atom. Similar conclusions were reached from the infrared experiments relating to the argon matrix reactions of potassium and rubidium atoms with oxygen molecules.³ These results have been supported by a complementary Raman

study of the reactions of lithium atoms in an oxygen matrix.⁴ Additional evidence for this view was provided from a recent Raman spectral investigation of the reactions of lithium, sodium, and potassium atoms with oxygen molecules in argon matrices.^{5,6} In the present investigation therefore, it is reasonable to expect a single metal atom species to predominate.

The Raman band observed at 1110 cm^{-1} in the $^{16}\text{O}_2$ experiments is assigned to the symmetric O–O stretch, ν_1 , of a monomeric Rb^{16}O_2 species. The more probable MO_2 species would be expected in a matrix comprised of 1% O_2 in argon rather than its dimer (MO_2)₂. The assignment is confirmed by an appropriate $^{18}\text{O}_2$ shift for a stretching mode involving a pure O–O motion. The scrambled oxygen isotopic experiments show this band to be split into a triplet and thus establish the presence of *two equivalent* oxygen atoms in the RbO_2 molecule. A similar triplet band was observed for the interionic ν_2 mode of RbO_2 in the infrared spectrum.³ Hence the molecular configuration of RbO_2 is that of an isosceles triangle of C_{2v} symmetry.

The symmetric interionic stretching mode of RbO_2 was observed in the infrared at 255.0 and 244.7 cm^{-1} , respectively, for the $^{16}\text{O}_2$ and $^{18}\text{O}_2$ experiments.³ The absence of this mode in the Raman spectrum adds further support for the ionic model of Rb^+O_2^- . The valence electron of rubidium is transferred into a π -antibonding molecular orbital on O_2 . The resultant decrease in bond order is accompanied by a subsequent decrease in the O–O frequency, which is near the fundamental for O_2^- .

Cs^+O_2^- . In an analogous manner, the Raman signal observed at 1114 cm^{-1} in the reactions involving cesium atoms and $^{16}\text{O}_2$ in argon is assigned to the symmetric O–O stretch in the Cs^{16}O_2 monomer. An isotopic frequency shift of 64 cm^{-1} on proceeding to the $^{18}\text{O}_2$ experiments indicates this vibration to be almost solely comprised of oxygen atom motions. Unfortunately, the scrambled oxygen isotopic experiments were not as well defined as the rubidium analogs. There is, however, the appearance of a triplet in the 1050–1115- cm^{-1} region with the 16–16 component occurring as a broad weak band. Again, a well-resolved triplet feature was observed for the interionic ν_2 mode of CsO_2 in similar $^{16,18}\text{O}_2$ isotopic infrared experiments.⁷ As mentioned earlier, the presence of this triplet establishes the existence of *two equivalent*⁸ oxygen atoms and a symmetrical CsO_2 molecule.

The shift to higher frequency of the O–O stretch of M^+O_2^- in the case of cesium is accounted for by the increased polarizability of a cesium cation as compared to rubidium. Stated more simply, cesium contributes a smaller portion of its valence electron to an antibonding π molecular orbital on O_2 than a corresponding rubidium atom owing to the greater induced dipole moment of opposite polarity on the cesium ion. An increase in the net bonding electron density of O_2^- results in the case of cesi-

(8) The spectroscopic equivalence of the two oxygen atoms in Cs^+O_2^- is best determined from the sharp infrared spectrum of the $^{16}\text{O}_2$ – $^{18}\text{O}^{18}\text{O}$ – $^{18}\text{O}_2$ sample. The ν_1 mode of $\text{Cs}^+^{16,18}\text{O}_2^-$ was observed as a very sharp triplet; the half-widths of all three lines were 1.0 cm^{-1} . How much inequivalence in O atoms can be contained in a 1.0- cm^{-1} wide band for the $\text{Cs}^+^{16}\text{O}^{18}\text{O}$ species when the $\text{Cs}^+^{16}\text{O}_2^-$ species also produced a 1.0- cm^{-1} bandwidth? We suggest that 0.2 cm^{-1} is the upper limit to nonequivalence for the O atoms in Cs^+O_2^- . In marked contrast, the O–O stretching modes in the free radicals $\text{H}^{16}\text{O}^{18}\text{O}$ and $\text{H}^{18}\text{O}^{16}\text{O}$ were separated by 2.6 cm^{-1} (D. W. Smith and L. Andrews, *J. Chem. Phys.* to be published); the HO_2 species contains two nonequivalent oxygen atoms.

TABLE II: Raman Spectra (Frequency Shifts, cm^{-1}) Observed from Argon-Oxygen Matrix Samples ($\text{Ar}/\text{O}_2 = 100$) Codeposited with Cesium Atoms at 15°K

$^{16}\text{O}_2$	$^{18}\text{O}_2$	$^{16}\text{O}_2$ - $^{16}\text{O}^{18}\text{O}$ - $^{18}\text{O}_2^a$
1552		1552
		1508
	1465	1464
1114		1112
		1081
	1050	1050
287	274	278
270	258	262
244 ^b		

^a $\text{Ar}/\text{O}_2 = 50$. ^b Grating ghost.

um, accompanied by a shift to higher frequencies of the O_2^- fundamental.

As was the case with rubidium, no interionic modes of CsO_2 were detected in the Raman thus providing additional evidence for an ionic model of Cs^+O_2^- .

M^+O_4^- . The earlier infrared study of the reactions of potassium and rubidium atoms with O_2 molecules in argon matrices³ has postulated the existence of an MO_4 species which was formed through further reaction of an O_2 with the metal superoxide. Scrambled oxygen isotopic studies have suggested that this species contains two equivalent oxygen molecules. A more recent investigation involving the simultaneous reaction of Na and K atoms from different Knudsen cells with O_2 confirmed the fact that this species contains a single metal atom since only the NaO_4 and KO_4 bands were observed as in the single metal experiments.⁶

In the recent Raman study of $\text{K} + \text{O}_2$ reactions,⁶ an intense band at 305 cm^{-1} was attributed to the KO_4 species. This band will be discussed along with the 298- and 287-cm^{-1} RbO_4 and CsO_4 features since these three bands likely have similar origins. The large oxygen isotopic shifts observed for these features are indicative of predominantly oxygen motions, but their proximity to interionic modes of the M^+O_2^- species invites consideration of possible assignment to interionic modes in the M^+O_4^- species.

The important data here are that the strong Raman MO_4 features near 300 cm^{-1} exhibit large $^{18}\text{O}_2$ isotopic shifts and relatively small alkali metal shifts. On the other hand, the interionic $\text{M}^+ \leftrightarrow \text{O}_2^-$ modes of the K, Rb, and Cs species at 307, 255, and 236 cm^{-1} show larger alkali metal shifts and smaller $^{18}\text{O}_2$ isotopic shifts.^{3,7} For the potassium case, the oxygen isotopic shift difference between the KO_2 and KO_4 modes under discussion is clear cut; the 15-cm^{-1} shift observed for KO_4 clearly exceeds the 10-cm^{-1} $^{18}\text{O}_2$ shift for KO_2 . As was discussed earlier, this comparison suggests that the observed normal mode in KO_4 is primarily an oxygen motion and not an interionic $\text{K}^+ \leftrightarrow \text{O}_2^-$ mode. Unfortunately, the case for RbO_4 and CsO_4 is not as straightforward; the observed $12\text{-}13\text{-cm}^{-1}$ shifts for the MO_4 mode exceed the 10-cm^{-1} shifts for the interionic MO_2 modes, but the MO_4 mode is 20% higher in frequency.

We believe that the 298- and 287-cm^{-1} RbO_4 and CsO_4 Raman bands are best explained as predominantly inter-

molecular oxygen-oxygen stretching modes ($\text{O}_2 \leftrightarrow \text{O}_2$)⁻ in the O_4^- ion bound to Rb^+ and Cs^+ , respectively, rather than to interionic $\text{M}^+ \leftrightarrow \text{O}_4^-$ modes. The relatively small alkali metal shift and relatively large $^{18}\text{O}_2$ shifts are consistent with this argument. Furthermore, we would not expect interionic $\text{M}^+ \leftrightarrow \text{O}_4^-$ modes to occur at higher frequencies than their $\text{M}^+ \leftrightarrow \text{O}_2^-$ analogs nor would we expect the Raman intensity of the former interionic mode to be observable since the latter was not detected. Of course, the Raman modes near 300 cm^{-1} are not pure oxygen motions; the alkali metal shift indicates some metal participation in this normal coordinate. It appears, however, that this vibration is largely an intermolecular oxygen motion within the O_4^- species.

The symmetric stretching within the two O_2 units in O_4^- should produce an intense Raman mode near 1000 cm^{-1} , the position of the antisymmetric infrared counterpart. No such mode was observed in the Raman, presumably due to insufficient Raman intensity as compared to the 300-cm^{-1} feature.

Jacox and Milligan⁹ have recently suggested that the KO_4 species observed earlier³ exists as K^+O_4^- containing a similar O_4^- ion to that observed in gaseous ion molecule reactions. Conway¹⁰ has predicted a trans O_4^- ion with a long (2.1 Å) intermolecular $\text{O}_2\text{-O}_2$ bond based upon molecular orbital calculations. The observation of an intense Raman band near 300 cm^{-1} in heavy alkali metal oxygen matrix systems which is appropriate for the MO_4 species adds support for a M^+O_4^- structure with a weak intermolecular oxygen bond. A vibrational frequency near 300 cm^{-1} for this weak $\text{O}_2\text{-O}_2$ bond is reasonable. Accordingly, the previous assignment⁶ of the 305-cm^{-1} Raman band to a symmetric oxygen motion in K^+O_4^- is supported by the present data; however, the characterization of KO_4 as a D_{2d} species, while required from explicit interpretation of the infrared spectra,³ must give way to the $\text{M}^+(\text{O}_2\text{-O}_2)^-$ model in order to satisfactorily explain the observed infrared and Raman oxygen frequencies and bonding inferred from these frequency positions.

Present information suggests that the M^+O_4^- species consists of a "puckered five-membered ring" with the M^+ ion coulombically bonded to the O_4^- anion, which contains two strong O-O bonds and a weak $\text{O}_2\text{-O}_2$ bond. Structure and bonding in the M^+O_4^- species will be discussed in more detail in a following paper.⁷

Conclusions

Raman spectra of samples of O_2 codeposited with Cs and Rb atoms in argon at 15°K reveal signals arising from the M^+O_2^- and M^+O_4^- species which were the major product absorptions in analogous infrared experiments. The Raman bands at 1110 and 1114 cm^{-1} , respectively, are assigned to intraionic O-O modes in Rb^+O_2^- and Cs^+O_2^- whereas Raman signals at 298 and 287 cm^{-1} are assigned to the intermolecular ($\text{O}_2\text{-O}_2$)⁻ modes in Rb^+O_4^- and Cs^+O_4^- .

Acknowledgment. The authors gratefully acknowledge financial support for this research by the National Science Foundation under Grant No. GP-28582 and matching funds for the laser Raman instrument under Grant No. GP-18251.

(9) M. E. Jacox and D. E. Milligan, *Chem. Phys. Lett.*, **14**, 518 (1972).
 (10) D. C. Conway, *J. Chem. Phys.*, **50**, 3864 (1969).

A Redetermination of the Crystal Structure of Dehydrated Zeolite 4A

Russell Y. Yanagida, Allen A. Amaro, and Karl Seff*

Chemistry Department, University of Hawaii, Honolulu, Hawaii 96822 (Received August 19, 1972)

The crystal structure of vacuum-dehydrated (activated) zeolite A of apparent composition $\text{Na}_{12}\text{Al}_{12}\text{Si}_{12}\text{O}_{48}$ has been determined by single-crystal X-ray diffraction techniques. Least-square refinement in the space group $Pm\bar{3}m$ ($a = 12.263 \text{ \AA}$) has led to a conventional R index of 0.069. Sodium ions are distributed among three equipoints in the structure: eight of the twelve ions occupy threefold axis positions 0.20 \AA from the plane of three nearest neighbors in the six-oxygen ring; three more lie in the planes of the eight-oxygen rings, displaced from the center by 1.23 \AA along a diagonal mirror line; and the twelfth ion is found on a twofold axis opposite a four-oxygen window in the large cavity. The shortest approach distances to framework oxygen atoms are 2.32 , 2.4 , and 2.5 \AA respectively. Small changes in cation positions and in the zeolite framework are observed upon dehydration. The changes due to dehydration in framework angles at the three nonequivalent oxygen atoms, corresponding to rotations of aluminosilicate tetrahedra, are much less than those observed for the Tl-exchanged form of zeolite A. An attempt to sorb C_2Cl_4 , although unsuccessful, yielded a structure in which the twelfth sodium ion is about 1.1 \AA further from its nearest neighbors in the zeolite framework, presumably because an impurity or decomposition product which associates with that sodium ion was sorbed to a small extent.

Introduction

As a test of the suitability of conventional crystallographic procedures applied to the small X-ray diffraction data sets which are currently available for the determination of the structures of organic complexes of zeolite A, the structure of fully dehydrated (activated) zeolite 4A was redetermined with greater precision than had been done before.^{1,2} In such occlusion complexes the sorbed molecules are usually comparatively weak scatterers and the adverse effects of disorder and thermal motion are both expected to be great. In this test, the three-dimensional Fourier synthesis was studied and refinements were attempted on many small peaks. For the procedures³ to be substantiated, no successful least-squares refinement of positions, other than those which could reasonably be ascribed to cations and framework atoms, must occur, even at occupancies corresponding to as few as one or two carbon atoms per unit cell, whose general equipoint is 48-fold.

Meaningful comparisons can be made between this structure and those of hydrated 4A⁴ and dehydrated Tl(I)-exchanged zeolite A⁵ in which the structural changes upon dehydration or ion exchange can be discussed. Similar comparisons with other variously ion-exchanged, dehydrated, or complexed zeolite A structures should logically be made as these latter structures are determined. Presently available² results are inadequate for detailed comparisons.

Description of the Structure

The structure of zeolite A has been previously described when it was determined^{6,7} and in more recent work.⁴ A stereodrawing of eight unit cells, clearly illustrating how a cubic arrangement of eight sodalite units generates the large cavity, is available.⁸

Zeolite A can be considered to be composed of three distinct components. The aluminosilicate framework is anionic, possesses the full symmetry of a cube if the Al^{3+} and Si^{4+} ions are disordered, has large channels of two kinds and two kinds of approximately spherical voids, and

is relatively rigid. The principal channels have eight-oxygen (sixteen-membered) rings as their minimum constriction; these eight-oxygen rings are shared by the large cavities and allow material to pass to the interior of a zeolite crystal. The minor cavity (the sodalite unit) can be accessed only through the minor (six-oxygen or twelve-membered) channels. If a simple cubic arrangement of equivalent hollow spheres (ping-pong balls) were assembled, the symmetry would be precisely that of zeolite A; the sphere cavities would correspond to the large zeolite cavities; the smaller cavity at the center of each cube of eight spheres would be the sodalite cavity at the center of the sodalite unit, and a six-oxygen window would face into each large cavity; the eight-oxygen windows would exist at each point two spheres touched, normal to their line of centers and connecting them.

The cations which balance the framework charge are exchangeable and occupy sites within the zeolite cavities and channels. They coordinate to the zeolite framework and/or to sorbed molecules. The number of ions will, in general, not be equal to the number of equivalent positions available at the most favored site; accordingly, as some equipoints are filled, other less favorable sites will accept ions until all ions are placed. For this reason zeolitic sodium ions, for example, may be nonequivalent and some many-fold sets of equivalent positions may be only partially (statistically) occupied. Often a site, meaning a set of equivalent positions, cannot be more than $\frac{1}{2}$ or $\frac{1}{4}$ filled because a greater filling would require sterically unreasonable approaches.

- (1) P. A. Howell, *Acta Crystallogr.*, **13**, 737 (1960).
- (2) J. V. Smith and L. G. Dowell, *Z. Kristallogr.*, **126**, 135 (1968).
- (3) K. Seff and D. P. Shoemaker, *Acta Crystallogr.*, **22**, 162 (1967).
- (4) V. Gramlich and W. M. Meier, *Z. Kristallogr.*, **133**, 134 (1971).
- (5) P. E. Riley, K. Seff, and D. P. Shoemaker, *J. Phys. Chem.*, **76**, 2593 (1972).
- (6) T. B. Reed and D. W. Breck, *J. Amer. Chem. Soc.*, **78**, 5972 (1956).
- (7) L. Broussard and D. P. Shoemaker, *J. Amer. Chem. Soc.*, **82**, 1041 (1960).
- (8) W. M. Meier and D. H. Olson, *Advan. Chem. Ser.*, No. 101, 166 (1971).

Sorbed molecules are appropriately considered last. They may interact with the zeolite framework, with the cations, and/or with each other. Usually they may be reversibly sorbed and desorbed by varying the temperature and pressure of the system. The sites available to the sorbed molecules are more complex than those found by ions for several reasons. The symmetry of the zeolite before sorption is much lower, usually, than it is before the ions are placed because of the partially occupied cation sites. Also small molecules cannot have the O_h symmetry that monatomic ions have; accordingly, their symmetry may be incompatible with that of the most favored sorption site, and a substantial degree of disorder may be introduced. Furthermore, nonequivalent ions may associate with sorbed molecules, making the latter nonequivalent also. Usually atoms in sorbed molecules occupy sites of low symmetry with, due to the finite sorption volumes of the zeolite, small occupancy parameters, leading to greater crystallographic indeterminacies. Also sorbed molecules are likely to have smaller scattering factors and larger thermal parameters. Usually, then, sorbed molecules are more difficult to locate than ions within the zeolite framework.

Experimental Section

Crystals of zeolite 4A were prepared by Charnell's⁹ method, modified to include a second crystallization using seed crystals from the first preparation. This sample was found by repeated wet chemical analysis to have an approximate framework formula of $Al_{11.3}Si_{12.7}O_{48}^{11.3-}$ per unit cell. Although the values in this stoichiometric formula have been rounded further to the nearest integer in previous reports,^{5,10,11} the precision of the analysis does not exclude the possibility that the correct framework formula might be $Al_{12}Si_{12}O_{48}^{12-}$, which is more ideal and which has been used extensively in previous investigations. Such inconsistencies have been noted previously.⁶

One crystal, a cube approximately 67 μ on an edge, was cautiously dehydrated by slowly raising its temperature to 200° over the course of a few hours at atmospheric pressure, and then maintaining it at 350° and 10^{-5} Torr for 24 hr. The capillary tube containing this crystal was then sealed off under vacuum and mounted on a goniometer head. Diffraction intensities were collected at 19.5° for $0 < 2\theta < 70^\circ$. A Syntex four-circle computer-controlled diffractometer with graphite-monochromatized Mo $K\alpha$ radiation ($K\alpha_1$, λ 0.70926 Å; $K\alpha_2$, λ 0.71354 Å) and a pulse-height analyzer was used throughout for preliminary experiments and for the collection of diffraction intensities. The space group $Pm\bar{3}m$ (no systematic absences) was used instead of $Fm\bar{3}c$ because no significant counts could be observed for expected major superstructure ("b") reflections,⁴ and because Gramlich and Meier⁴ have shown that framework deviations from the former space group are small even when appropriate. Still, $Pm\bar{3}m$ has only one tetrahedral framework site and accordingly treats Al and Si atoms and their immediate environments as entirely equivalent. Therefore some minor but extensive disorder is implicit in this choice of space group. The crystals synthesized here appear not to have long-range Si,Al ordering. The cubic cell constant for the $Pm\bar{3}m$ unit cell ($a = 12.263(2)$ Å) was determined by a least-squares treatment of 15 intense reflections with 2θ values between 20 and 24°.

The θ - 2θ scan technique was employed at a scan rate which varied from 0.5 (in 2θ) to 24°/min in such a way

that more time was spent on weaker reflections to improve their standard deviations. Most reflections were observed at the slowest scan rate. The scan range varied from 2.0° at $2\theta = 3^\circ$ to 2.5° at $2\theta = 70^\circ$. All 881 unique reciprocal lattice points below the maximum 2θ value (70°) were examined. (This high upper limit was chosen for 2θ to maximize the size of the data set, even though few reflections with large 2θ values showed significant intensity.) A time equal to one-half of the scan time for each reflection was spent counting background at each end of the scan range. Two check reflections which were measured periodically during the collection of each data set showed no significant trend in intensity. The effects of Renninger reflection were assumed to be absent because the previous examination⁵ of a related material showed these to be entirely absent.

Standard deviations were assigned according to the formula

$$\sigma(I) = [CT + 0.25(t_c/t_b)^2(B_1 + B_2) + (pI)^2]^{1/2}$$

where CT is the total integrated count obtained in a scan time of t_c , B_1 and B_2 are the background counts each obtained in time t_b , and $I = CT - 0.5(t_c/t_b)(B_1 + B_2)$. A value of 0.02 was assigned to the empirical parameter p to account for instrument instability. The net counts were then corrected for Lorentz and polarization effects; an absorption correction ($\mu R = 0.017$) was unnecessary. All 154 unique reflections for which the net intensity exceeded three times its standard deviation were used throughout.

Structure Determination

Initial full-matrix, least-squares refinement of the structure was carried out using parameters for the framework and Na(1) and Na(2) positions which had been determined and refined¹⁰ for the 32 NH_3 complex of zeolite 4A. Only the Na(1) position, near center of the six-oxygen window, was allowed to refine with anisotropic thermal parameters. This model, which allowed for eleven sodium ions and which put the three Na(2) ions at positions different by symmetry from those previously reported,² refined to an R_1 index, $(\sum|F_o - |F_c||)/\sum F_o$, of 0.069 and a weighted R_2 index, $(\sum w(F_o - |F_c|)^2/\sum wF_o^2)^{1/2}$, of 0.088.

A three-dimensional difference Fourier function was prepared using structure factors calculated from the just-refined parameters. From this synthesis, seven small but predominant peaks were selected for least-squares refinement. None were unreasonably close to the atomic positions already included in the calculations. Six of the new positions would not refine with convergent thermal parameters at or near their observed coordinates. The seventh position refined quickly to the fractional coordinates 0.204, 0.204, 0.500 with an isotropic thermal parameter of 1.6 Å², and the error indices decreased slightly to $R_1 = 0.069$ and $R_2 = 0.086$. This position was judged to be appropriate for a sodium ion, but less so for one or more water molecules, which might be expected to be closer to either the Na(1) or the Na(2) position. The occupancy was limited to one ion per unit cell at this, the Na(3), position because eleven ions had been previously placed and because Loewenstein's rule¹² indicates that the maximum number of aluminum atoms, and therefore of sodium ions,

(9) J. F. Charnell, *J. Cryst. Growth*, **8**, 291 (1971).

(10) R. Y. Yanagida and K. Seff, *J. Phys. Chem.*, **76**, 2597 (1972).

(11) K. Seff, *J. Phys. Chem.*, **76**, 2601 (1972).

(12) W. Loewenstein, *Amer. Mineral.*, **39**, 92 (1954).

TABLE I: Positional, Thermal and Occupancy Parameters^a

	Wyckoff position	x	y	z	B, Å ² or anisotropic b's	Occupancy factor
(Si,Al)	24(k)	0	0.185(1)	0.372(1)	1.4(6)	1
O(1)	12(h)	0	0.225(1)	1/2	2.3(4)	1
O(2)	12(i)	0	0.290(1)	0.290(1)	2.6(4)	1
O(3)	24(m)	0.114(1)	0.114(1)	0.345(1)	2.7(3)	1
Na(1)	8(g)	0.200(1)	0.200(1)	0.200(1)	0.007(1) ^b	1
					0.002(1)	
Na(2)	12(i)	0	0.429(3)	0.429(3)	0.012(6) ^c	1/4
					0.005(3)	
Na(3)	12(j)	0.204(7)	0.204(7)	1/2	2(2)	1/2(0.03)

^a Standard deviations are in the units of the least significant digit given for the corresponding parameter. See Figures 1 and 2 for the identities of the atoms. ^b For Na(1), the anisotropic temperature factor = $\exp[-b_{11}(h^2 + k^2 + l^2) - b_{12}(hk + hl + kl)]$. ^c For Na(2), it is $\exp[-b_{11}(h^2) - b_{22}(k^2 + l^2)]$.

per unit cell is twelve. A refinement of the occupancy parameter of Na(3) converged at 0.8 ions per unit cell, a value insignificantly different from 1.0. When Na(2) was allowed to refine anisotropically, the error indices remained the same. Decreasing the occupancy of this Na(2) position to 2.0 ions per unit cell caused one of these thermal parameters to become significantly negative. Restoring the Na(2) occupancy parameter and decreasing the occupancy of Na(1) to 7.0 ions per unit cell caused each error index, R_1 and R_2 , to increase by 0.002 at convergence. Accordingly the sodium ion at Na(3) appears to be the twelfth ion in the unit cell, and the best integral representation of the formula of the unit cell is $\text{Na}_{12}\text{Al}_{12}\text{Si}_{12}\text{O}_{48}$. The goodness-of-fit, $(\sum w(F_o - |F_c|)^2 / (m - s))^{1/2}$, is 1.14, where m is the number of observations (154), and s (19) is the number of variables in the least-squares refinement. A table of observed and calculated structure factors is available;¹³ the final structural parameters are presented in Table I.

The full-matrix, least-squares program used¹⁴ minimizes $\sum w(\Delta|F|)^2$; the weights were the reciprocal squares of σ , the standard deviation of each observation. Atomic scattering factors¹⁵ for Na^+ , Si^{2+} , $\text{Al}^{1.5+}$, and O^- were used. In the last cycle of least-squares refinement all shifts were less than 1% of their corresponding esd's except those involving the anisotropic thermal parameters of Na(2), whose shifts were less than 10% of their esd's.

Discussion

The test of the adequacy of data sets as small as those reported here for the determination of the positions of small atoms such as carbon, oxygen, or sodium even at low occupancies, has been successful. Of the seven positions which were as much as weakly suggested by a Fourier difference function, six were entirely divergent in least-squares refinement; the seventh converged quickly; no ambiguity was encountered. This indicates that acceptable refinement, when it occurs, successfully describes the positions of previously unlocated atoms. The inverse is not considered demonstrated; unacceptable refinement does not necessarily indicate that the atoms under consideration are absent.

The aluminosilicate framework of the zeolite is quite similar to that found by other workers,^{1-7,10,11} and is presented in Tables II and III. The most meaningful comparisons, within structures of comparable or greater precision, are with hydrated zeolite 4A,⁴ and with hydrated and dehydrated Tl(I)-exchanged zeolite A.⁵ Surprisingly, since changes in framework angles of up to 17° occurred upon

TABLE II: Interatomic Distances(Å) and Angles (degrees)^a

(Si,Al)-O(1)	1.65(1)	O(1)-(Si,Al)-O(2)	110.4 (8)
(Si,Al)-O(2)	1.63(1)	O(1)-(Si,Al)-O(3)	110.3 (8)
(Si,Al)-O(3)	1.68(1)	O(2)-(Si,Al)-O(3)	106.8 (9)
Na(1)-O(3)	2.32(1)	O(3)-(Si,Al)-O(3)	112.1 (9)
Na(1)-O(2)	2.90(1)	(Si,Al)-O(1)-(Si,Al)	145.1 (7)
Na(2)-O(2)	2.40(6)	(Si,Al)-O(2)-(Si,Al)	165.6 (15)
Na(2)-O(1)	2.64(3)	(Si,Al)-O(3)-(Si,Al)	145.5 (10)
Na(3)-O(1)	2.51(7)	Na(3)-O(1)-(Si,Al)	88.2 (4)
Na(3)-O(3)	2.47(7)	Na(3)-O(3)-(Si,Al)	89 (2)
Na(3)-Na(1)	3.68(7)	O(1)-Na(3)-O(1)	102 (2)
		O(3)-Na(3)-O(3)	101 (2)
		Na(1)-Na(3)-Na(1)	178 (2)

^a Standard deviations are in the units of the least significant digit given for the corresponding parameter.

TABLE III: Aluminosilicate Framework Angles (degrees)^a

	4A hydrated ^b	4A dehydrated	Tl-exchanged A hydrated ^c	Tl-exchanged A dehydrated ^c
O(1)-(Si,Al)-O(2)	108(1)	110(1)	110(1)	108(1)
O(1)-(Si,Al)-O(3)	111(1)	110(1)	110(1)	110(2)
O(2)-(Si,Al)-O(3)	108(1)	107(1)	107(1)	109(1)
O(3)-(Si,Al)-O(3)	111(1)	112(1)	111(1)	111(2)
(Si,Al)-O(1)-(Si,Al)	146(0.5)	145(1)	148(1)	162(2)
(Si,Al)-O(2)-(Si,Al)	160(0.5)	166(1.5)	161(2)	144(2)
(Si,Al)-O(3)-(Si,Al)	144(0.5)	146(1)	144(2)	138(2)

^a Standard deviations have the units of degrees. ^b Reference 4. The approximate standard deviations given here are larger than those reported in ref 4 because averages over Si and Al positions have been taken. ^c Reference 5.

dehydration in the Tl(I)-exchanged material, the only significant change in the sodium form is at O(2) and is only +6° (see Table III). In fact, the sign of the change at O(2)

(13) Listings of the observed and calculated structure factors for the dehydrated structure and the corresponding structure factor table for the second structure (nearly dehydrated) discussed above, as well as tables of its structural parameters, bond lengths and angles, will appear following these pages in the microfilm edition of this volume of the journal. Single copies may be obtained from the Business Operations Office, Books and Journals Division, American Chemical Society, 1155 Sixteenth St., N.W., Washington, D.C. 20036. Remit check or money order for \$3.00 for photocopy or \$2.00 for microfiche, referring to code number JPC-73-805.

(14) P. K. Gantzel, R. A. Sparks, and K. N. Trueblood, UCLALS4, American Crystallographic Association Program Library (old) No. 317, modified.

(15) "International Tables for X-Ray Crystallography," Vol. III, Kynoch Press, Birmingham, England, 1962, p. 212.

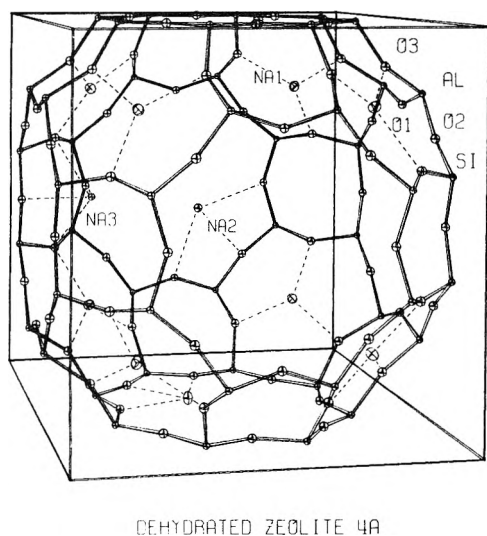


Figure 1. The dehydrated zeolite 4A unit cell¹⁶ is shown with sodium ions placed statistically within each of the three kinds of sites. Positions of partial occupancy are represented so as to maximize the approach distances between sodium ions. Closest ionic approaches to framework oxygens are indicated. Ellipsoids of 10% probability are shown.

was negative in the former structure, indicating that the framework distortions are qualitatively different. (The framework angles in the hydrated form appear to be independent of the state of ion exchange.) As an internal check, it may be noted that in all four of these structures the angles at the aluminum and silicon ions are all very close to tetrahedral and show internal consistency in their deviations from that angle. The change in the cell constant upon dehydration is also correspondingly less for the sodium form of zeolite A (-0.04 Å compared to -0.15 Å).

Eight Na⁺ ions, at Na(1), are located on threefold axis positions (Figures 1 and 2)¹⁶ near the centers of the six-oxygen windows. Each Na(1) is displaced into the large cavity from the plane of its three nearest neighbors (O(3)) at 2.32 Å by 0.20 Å (see Table IV). The sum of the ionic radii¹⁷ of Na⁺ and O²⁻ is 2.35 (Pauling) or 2.30 Å (Goldschmidt), in agreement with the observed distance. Since moving Na(1) into the plane of its O(3) neighbors would decrease this distance by only 0.009 Å and since the zeolite framework has been shown to be somewhat flexible in other structures,⁵ it is likely that interionic Na(1)-Na(1) repulsive forces are predominantly responsible for the displacement of these ions out of the sodalite unit. (Each Na(1) "sees" seven others through the sodalite unit.) The anisotropic thermal parameters indicate that the principle axis of thermal motion (111) for Na(1) is, quite reasonably, normal to the plane of its closest approaches, the six-oxygen window (see Figures 1 and 2).

Three Na⁺ ions, at Na(2), are distributed over a 12-fold equipoint near the centers of the eight-oxygen windows. The number of ions in this position is limited to three because a fourth ion would be required to be too close (2.45 Å) to another Na(2) ion. Although the distances of these ions from Na(1) would be greatest were they to choose the position $0, x, \frac{1}{2}$, this does not occur; Na(2) ions lie on diagonal mirror planes at $0, x, x$ nearest to O(2). In this position irregular but more reasonable approaches can be made to two O(1) atoms, which protrude more into the eight-oxygen window (Table II, angle at O(1)), and to one O(2) atom. In this way the angle subtended by the three nearest neighbors of Na(2) is somewhat greater and the

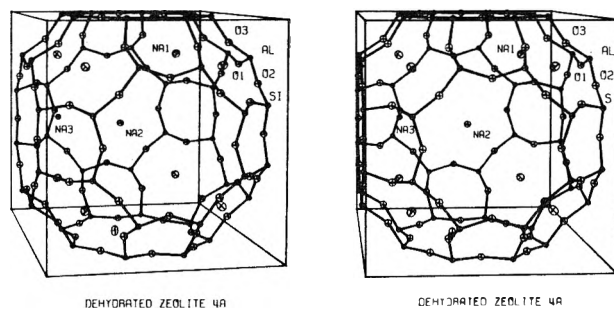


Figure 2. Stereoview¹⁶ of dehydrated zeolite 4A. Ellipsoids of 20% probability are shown.

TABLE IV: Deviations^a of Atoms From Least-Squares Planes at 0(3) (Å)

	Plane	
	111	110
O(1)		-0.02
O(2)	0.06	
O(3)	0	0
Na(1)	0.20	
Na(3)		1.56

^a A negative deviation indicates that the atom lies on the same side of the plane as the origin.

three closest approaches (2.64, 2.40, and 2.64 Å) are more nearly equal. This site does not appear to be as energetically favorable as the Na(1) position because of the longer and less symmetrical approaches to the framework. As was true for Na(1), the principal axis of anisotropic thermal motion (100) for Na(2) is normal to the plane of its closest approaches, in this case the eight-oxygen window (see Figures 1 and 2).

The twelfth Na⁺ ion, Na(3), is statistically distributed over a 12-fold equipoint. This position is in the large cavity and lies on a twofold axis which is normal to a four-oxygen window. The Na(3) ion has four nearest neighbors, all at distances of 2.5 Å, and lies approximately 1.57 Å from their least-squares (110) plane. Na(3) is 3.68 Å from two Na(1) ions, which is appreciably less than the Na(2)-Na(1) distance of at least 4.67 Å. The Na(3) position, then, appears to be the least favorable energetically because its attractive approaches are long and its repulsive ones are short. The twelfth ion is found at such a site because the two more favorable ones are filled.

The following changes have occurred in the sodium ion positions upon dehydration. Na(1) has moved insignificantly closer to its nearest neighbor, O(3), by 0.04 Å (2.36(4) to 2.32(1) Å) and it has moved much closer to the O(3) plane (0.52 to 0.20 Å); that is, further from the more tetrahedral position it occupied, with the aid of a threefold axis water molecule, in the hydrated structure. Position IV,⁴ which can be identified with Na(2) in the present structure, has moved 1.0 Å into the plane of the eight-oxygen window, and has moved closer to O(2) by 0.46 Å (2.86(8) to 2.40(6) Å). It has maintained its distance from O(1) (2.63(4) to 2.64(3) Å). In the hydrated structure, a position analogous to the Na(3) position cannot be found,

(16) C. K. Johnson, ORTEP, Report No. ORNL-3794, Oak Ridge National Laboratory, Oak Ridge, Tenn., 1965.

(17) L. Pauling, "The Nature of the Chemical Bond," 3rd ed. Cornell University Press, Ithaca, N. Y., 1960, p 518.

presumably because this twelfth ion becomes entirely hydrated and is found near the center of the large cavity.⁴ In general, upon dehydration, the Na⁺ ions have moved closer to their framework oxygen nearest neighbors.

It has been suggested that the lengths of Si-O and Al-O bonds in hygroscopic aluminosilicates should increase upon hydration because, due to the formation of hydrogen bonds (to which a small amount of bond order is assigned), the valency of oxygen with respect to Si or Al would be somewhat reduced.¹⁸ This reasoning has been successfully used to locate hydrogen bonds within hydrated aluminosilicates.¹⁸ The average (Si,Al)-O distance (1.67 Å) in hydrated 4A is longer than the average found here (1.65 Å); the corresponding values for Tl(I)-exchanged zeolite A are 1.67 and 1.66 Å. Both pairs of structures, then, demonstrate this effect in a general manner.

An Attempted C₂Cl₄ Complex

An attempt was made to sorb tetrachloroethylene (Aldrich Chem. Co., 99% purity) at 28° onto zeolite 4A, even though calculations indicated that C₂Cl₄ would be too large to fit into the zeolite. Intensity data were collected (171 significant reflections) using a single crystal 81 μ on an edge, and were reduced and refined as described for the principal structure reported here. All framework and sodium ion positions and thermal parameters refined to values insignificantly different from those of the former structure except for those involving Na(3), whose positions and standard deviations are $x = y = 0.27(2)$, $z = \frac{1}{2}$. The final error indices are $R_1 = 0.058$, $R_2 = 0.067$, and

the goodness of fit = 0.99. These low values, for such work, suggest that little material has been sorbed, surely much less than a single molecule of C₂Cl₄. Tables of structure factors, of refined atomic coordinates, and of the corresponding distances and angles are available.¹⁰

These results do indicate, however, that some sorption has occurred and that only Na(3) is affected. Its x coordinate (equivalent to y) has increased from 0.204(7) for the dehydrated structure to 0.27(2), the same value found in the acetylene sorption complex¹⁹ of zeolite 4A. The Na(3) ion has increased its distance from the plane of the four-oxygen ring from 1.56 to 2.7 Å. Evidently, a site near the Na(3) position is the first to be occupied upon sorption. Although the C₂Cl₄ to be sorbed was first passed through a bed of dehydrated zeolite 4A, an impurity or a decomposition product might have been sorbed instead. A single water molecule per unit cell distributed over a low symmetry equipoint and with a large apparent thermal parameter is plausible, would be consistent with our observations, and would be unlocatable by our methods.

Acknowledgment. This work was supported by the U. S. Army Research Office—Durham. We are also indebted to the NSF for their assistance (Grant No. GP-18213) in the purchase of the diffractometer, and to the University of Hawaii Computing Center.

(18) G. Donnay and R. Allmann, *Amer. Mineral.*, **55**, 1003 (1970).

(19) A. A. Amaro and K. Seif, submitted for publication in *J. Phys. Chem.*

Application of the Polanyi Adsorption Potential Theory to Adsorption from Solution on Activated Carbon. IV. Steric Factors, as Illustrated by the Adsorption of Planar and Octahedral Metal Acetylacetonates¹

Cary C. T. Chiou and Milton Manes*

Department of Chemistry, Kent State University, Kent, Ohio 44242 (Received October 25, 1972)

Publication costs assisted by the Research Office, Kent State University

Adsorption isotherms at 25° from methanol solution on a previously studied activated carbon have been determined for the following acetylacetonate (AA) complexes: Co(III)(AA)₃, Fe(III)(AA)₃, Al(AA)₃, Cu(II)(AA)₂, Pt(AA)₂, and Pd(AA)₂. The adsorption isotherms of the platinum, palladium, and cobalt complexes have in addition been determined on a graphitized carbon black. Analysis of the results by application of the Polanyi theory indicates a striking weakening of the adsorption of the octahedral complexes relative to that of the planar complexes; the effect is ascribed to the pronounced steric inability of the octahedral complexes to achieve close approach to the presumably planar adsorbent surfaces. The similarity of the results on both the activated carbon and on the graphitized carbon black demonstrates that the effect is to be distinguished from molecular sieving.

Introduction

The Polanyi adsorption potential theory² leads to the expectation that the physical adsorption of a given solid adsorbate from solution onto a given adsorbent will tend to be weakest (assuming comparable solubilities) in those

solvents that compete most strongly for the limited available adsorption space. Manes and Hofer³ noted that if the

(1) Based on a thesis submitted by C. C. T. Chiou to Kent State University in partial fulfillment of the requirements for the M.S. degree.

adsorption potentials of solvent and solute molecules are approximately proportional to their molar polarizabilities, then the competitive tendency of a solvent should be determined by its polarizability per unit volume, which in turn is a monotonic function of its refractive index. The consequent expectation that the adsorption of a single solid adsorbate onto an activated carbon should decrease with increasing solvent refractive index was experimentally verified for a variety of solvents, with the striking exception of carbon tetrachloride and of cyclohexane; adsorption from these two was anomalously high. Since these solvents were the only ones for which the carbon skeletons of molecular models could not be made to assume a planar configuration, and since the adsorption force field may be expected to be strongly dependent on distance from the surface, the anomalous behavior was attributed to steric inability of a significant part of the solvent molecule to achieve close approach to the (presumed planar) adsorbent surface. Hofer and Manes⁴ suggested subsequently that predictions of solute adsorption isotherms from the comparative polarizabilities per unit volume of solvent and solute would be most accurate when they were of comparable molecular thickness. If the presumed steric effect is real, and if solvent nonplanarity strengthens solute adsorption, then solute nonplanarity may be expected to weaken its adsorption. This nonplanarity should be particularly severe in octahedral complexes of organic ligands. Moreover, a comparison of the adsorption of planar and octahedral complexes of the same ligand should provide a convenient means of assaying the magnitude of the steric effect on adsorption.

This article deals with the effect of steric factors on the adsorption of solid solutes, as exemplified by the adsorption behavior, from methanol solution onto an activated carbon, of a series of metal acetylacetonates that included both planar and octahedral structures. Although some complications turned up, the adsorption of the octahedral acetylacetonates was indeed considerably weaker than one would expect for planar complexes of comparable molecular volume. For example, at low concentrations the adsorption potentials per unit volume of the (planar) platinum and palladium complexes on the activated carbon were comparable to each other and approximately 160% of the corresponding values for the octahedral cobalt complex. Finally, a short series of experiments with a graphitized carbon black as the adsorbent verified that the observed differences between the planar and the octahedral complexes were similarly manifested on an essentially nonporous carbon, and therefore not ascribable to molecular sieving of the octahedral complexes in small pores.

Theoretical Considerations

The underlying theory for the adsorption of solutes from solution, which is summarized below, is an adaptation of the Polanyi adsorption potential theory;² it is given in further detail by Manes and Hofer.³

In the Polanyi theory the driving force for physical adsorption on any part of the energetically heterogeneous adsorption surface (or "adsorption space") is measured by the adsorption potential, which for a given adsorbent and adsorbate is a function of the distance from the surface. Physical adsorption consists of the condensation from vapor (or solution) of liquid (or solid) in those portions of the adsorption space in which the adsorption potential equals or exceeds the work required to concentrate the adsorbate to saturation concentration. At the postulated in-

terface between the bulk phase and the (condensed) adsorbed phase at equilibrium, the adsorption potential is given as

$$\epsilon = RT \ln (p_s/p) \quad (1)$$

in vapor-phase adsorption and as

$$\epsilon_{sl} = RT \ln (c_s/c) \quad (2)$$

in solute adsorption, where p_s and c_s are the saturation pressure and concentration and p and c are the equilibrium pressure and concentration in the vapor or supernatant liquid, as the case may be. A plot of the (liquid or solid) adsorbate volume against ϵ/V (where V is the molar volume of the adsorbate) is called a "correlation curve." The vapor-phase adsorption data for the normal paraffins from methane to *n*-hexane on activated carbon fit a single correlation curve.⁵ In the absence of molecular sieving or other geometric effects, a plot of solute adsorption volume against $(\gamma_{sl}\epsilon_{sl})/V$ (where γ_{sl} is a constant to be determined for each solute-solvent combination, and the subscript in ϵ_{sl} denotes that the adsorption potential of the solute has been corrected for the competition of the solvent) should coincide with the (gas-phase) hydrocarbon correlation curve if the Polanyi theory holds exactly. Manes and Hofer estimated the magnitude of γ_{sl} as

$$\gamma_{sl} = (p_s - p_l)/p_h \quad (3)$$

where

$$p_i = [R]/V = (n_i^2 - 1)(n_i^2 + 2) \quad (4)$$

n_i is the refractive index of the *i*th component, R is the molar refractivity, and s, l, and h refer respectively to the solid, solvent, and heptane (the last being typical of the hydrocarbon correlation curve). For the solid, p_s may be estimated from $[R]$, which in turn may be calculated from a table of bond refractivities. To the extent that the theory and the approximations hold true, one can estimate the adsorption isotherm of a given solid solute in a given solvent on a given adsorbent (*e.g.*, on a given activated carbon) from the hydrocarbon correlation curve (or, more recently, from a correlation curve determined from adsorption of selected organic adsorbates from water solution),⁶ together with the p_i of the solute and solvent and the solubility of the solute. The extent to which the approximation holds is illustrated by the results of Manes and Hofer;³ their adsorption data on two solid dyes showed significant differences between the gas-phase and the solute correlation curves, particularly at the highest capacities. These deviations are presumably due to inefficient packing of the adsorption space with solids. They did not turn up in the work of Wohleber and Manes⁶ on the adsorption of partially miscible liquids from water.

If the attractive forces are primarily London forces, and if two solutes have about the same value of p_s , then the modified Polanyi theory (without consideration of steric effects) leads to the expectation that their experimental correlation curves from the same solvent should exhibit the same values of γ_{sl} . However, if one of the solutes has a severe nonplanar constraint, we would expect this con-

(2) (a) M. Polanyi, *Verh. Deut. Phys. Ges.*, **16**, 1012 (1914); **18**, 55 (1916); *Z. Elektrochem.*, **26**, 370 (1920); (b) M. Polanyi, *Z. Phys.*, **2**, 111 (1920).

(3) M. Manes and L. J. E. Hofer, *J. Phys. Chem.*, **73**, 584 (1969).

(4) L. J. E. Hofer and M. Manes, *Chem. Eng. Progr.*, **65**, 84 (1969).

(5) R. J. Grant, M. Manes, and S. B. Smith, *AIChE J.*, **8**, 403 (1962).

(6) D. A. Wohleber and M. Manes, *J. Phys. Chem.*, **75**, 61 (1971).

straint to manifest itself as a reduced value of γ_{sl} . The experiments carried out in this work consisted essentially of determining the adsorption isotherms of the various acetylacetonates and plotting their correlation curves. To the extent that steric factors are significant one would expect the adsorption of the planar complexes to fit one correlation curve and that of the octahedral complexes to fit another correlation curve with a significantly reduced value of γ_{sl} . Moreover, if the planar complexes are assumed to be sterically unhindered, one should be able to use eq 3 to predict the value of γ_{sl} for the planar complexes. However, bond refractivities were not available for the metal-ligand bonds. In the absence of this information the molar refractivities were estimated by assuming that these bonds make a negligible contribution to the overall polarizability of the complex.

Experimental Section

The activated carbon (Pittsburgh Activated Carbon Div., Calgon Co. grade CAL activated carbon), apparatus, and experimental techniques were the same as described in previous articles in this series,^{4,6,7} except that the supernatant liquids were analyzed (after appropriate dilution when necessary) by ultraviolet spectrophotometry. The carbon black was a graphitized carbon black designated Vulcan-6 that came as a gift from the Godfrey Cabot Corp., Billerica, Mass.

Methanol was the solvent in all of the experiments. Its adsorption on activated carbons is relatively weak; all of the acetylacetonates investigated are conveniently soluble in it; and it is a suitable solvent for the determination of the acetylacetonates by ultraviolet spectrophotometry. Reagent grade absolute methanol was used as received.

The metal acetylacetonates were all purchased from commercial sources and recrystallized to a minimum purity of 99% as determined by comparison of the molar absorptivities with values from the literature.⁸

The solubilities (c_s) of the acetylacetonates at 25° were determined by saturation of methanol solutions in the shaker bath, followed by spectrophotometric determination of the concentrations of the saturated solutions. The densities of the platinum and palladium acetylacetonates were determined by a float-and-sink method on individual crystals. The densities of the other compounds were available in the literature.⁹ The solubilities, in g/100 ml of methanol, and the molar volumes, in cc/mole, were as follows (where (AA) represents the acetylacetonate group, $C_5H_7O_2$): Co(III)(AA)₃, 3.21, 249; Fe(III)(AA)₃, 10.2, 263; Al(AA)₃, 10.5, 269; Pt(AA)₂, 0.273, 179; Pd(AA)₂, 0.141, 173; Cu(II)(AA)₂, 0.270, 166.5.

Results and Discussion

All of the adsorption data on the activated carbon are shown in Figure 1, where the ordinate is the adsorbate volume in cc/100 g of carbon, and the abscissa is $\epsilon_{sl}/4.6\bar{V}$. (The factor of 4.6 is to conform with the notation of earlier publications²). The original isotherms may be calculated from the data of Figure 1 by use of the solubility and molar volume data given earlier. Figure 1 also contains the (vapor-phase) hydrocarbon correlation line for the carbon, taken from earlier work² and plotted against the abscissa on the upper scale. The adsorption data for the carbon black are shown in Figure 2, plotted in the same manner as in Figure 1.

As Figure 1 shows, the correlation curves for the two stable planar complexes (of Pt and Pd) are quite similar

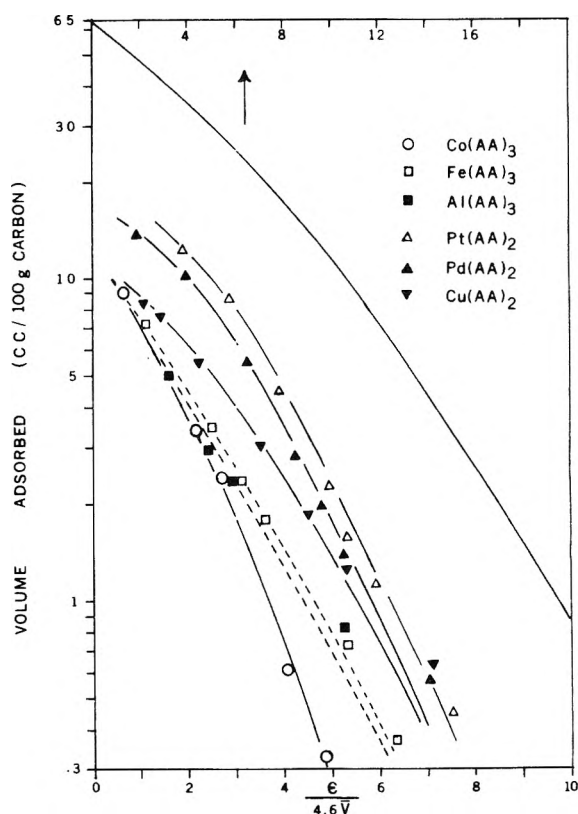


Figure 1. Volume adsorbed as a function of $\epsilon_{sl}/4.6\bar{V}$ ($= T/\bar{V} \log c_s/c$) for six metal acetylacetonates on activated carbon. The solid line with no data points is the hydrocarbon correlation line (note the upper abscissa scale).

to each other, and differ quite sharply from all the others. The upper limits for the volume adsorbed (approximately 20 cc/100 g of carbon) are of the same magnitude as those previously reported by Manes and Hofer² for the planar dyes, Butter Yellow and Sudan III, although they are somewhat lower. The correlation curve for the stable cobalt complex is strikingly lower than those of the platinum and palladium complexes, which is in keeping with our original expectations. The difference is equally striking on the graphitized carbon black (Figure 2), where only the adsorption of the platinum, palladium, and cobalt complexes were determined. Although the capacities on the carbon black are lower by about an order of magnitude relative to the activated carbon, the slightly stronger adsorption of the platinum relative to the palladium complex still persists. The investigation was originally planned for the activated carbon alone, on the assumption that its pore structure was sufficiently open to accommodate both the planar and the octahedral complexes, and therefore to preclude complication of the interpretation of the results by the possibility of molecular sieving. The results were reasoned to be thus uncomplicated, because the correlation curves for the octahedral complexes should have shown a much steeper descent in the presence of molecular sieving than they in fact did. Nevertheless, it seemed better to resolve this question by carrying out some additional experiments with a graphitized carbon black of low porosity, where molecular sieving could not

(7) D. A. Wohleber and M. Manes, *J. Phys. Chem.*, **75**, 3720 (1971).

(8) R. H. Holm and F. A. Cotton, *J. Amer. Chem. Soc.*, **80**, 5658 (1958).

(9) "Inorganic Syntheses," Vol. 2 and 5, McGraw-Hill, New York, N. Y.

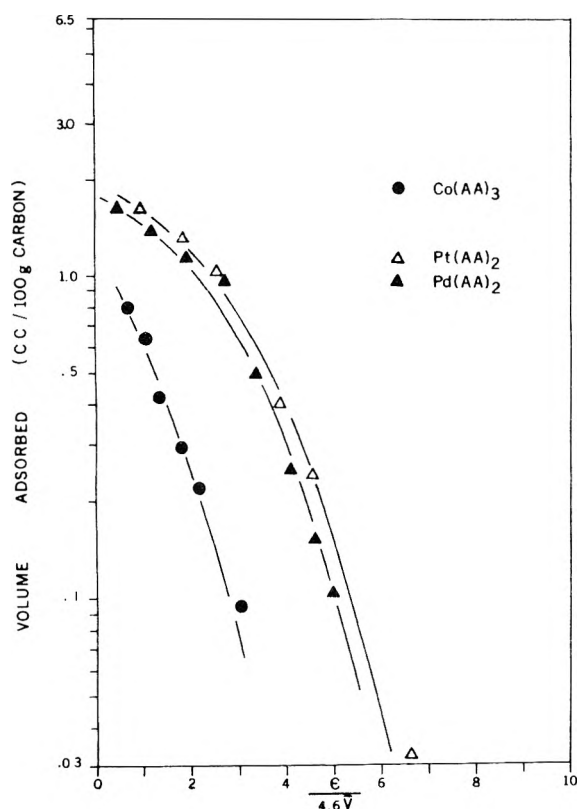


Figure 2. Volume adsorbed as a function of $\epsilon/4.6V (= T/\bar{V} \log c_s/c)$ for the acetylacetonates of cobalt, platinum, and palladium on graphitized carbon black.

be significant. The results came out, if anything, somewhat neater than the original results on the activated carbon. (On a finer-pored carbon, of course, the results could have been quite different.)

Although the distinction between the correlation curve of cobalt and those of platinum and palladium was about as expected (and, in fact, the effect we were looking for), the behavior of the correlation curves for the complexes of iron and aluminum was somewhat puzzling, in that they were rather close to the cobalt correlation curve at the low adsorption potentials (higher loadings), but deviated significantly at decreasing loadings in the direction of higher adsorption potentials than expected. A search of the literature showed that these complexes are of relatively low stability as compared with the stability of the cobalt complex,^{10,11} and that they could be expected to dissociate relatively easily. Although their absorption spectra in methanol solution did not show evidence of significant dissociation, it is reasonable to expect that under the forces of adsorptive attraction the complex may break one of the six metal-oxygen links, which would then allow the entire ligand to assume a position of lower potential energy, closer to the surface. An approximate calculation using the dissociation constants K_3 for the ferric and aluminum acetylacetonates, and assuming that the heat of detachment of one of the bonds would be about half of the heat of dissociation of one ligand, suggests that the energies of adsorption would suffice to bring about the breaking of one bond and the subsequent realignment of the otherwise distant ligand. It is of further interest that the adsorption isotherms for the iron and the aluminum complexes were strongly time dependent and not complete within the 16 hr that sufficed for the others (the correlation curves are

dotted to indicate that equilibrium was not well established). This would suggest that the postulated breaking of one of the attachments is associated with an activation energy.

The other anomaly is in the copper complex, which has been reported as being planar.¹² However, it may also be expected to solvate in methanol solution,¹³ in which case the solvated methanol would interfere with close approach to the surface. One would expect the solvation to approach the bulk solution value at low adsorption potentials; at the higher adsorption potentials one would expect the solvated methanol to be forced out from between the complex and the carbon surface. This would cause the correlation curve to lean more toward the octahedral correlation curve at low adsorption potentials and to approach the planar correlation curve at high adsorption potentials, and this is what is observed.

Finally, having considered the comparison between the adsorption of the square and the octahedral complexes, let us now see whether or not the adsorption of the presumably unhindered planar complexes on the activated carbon is consistent with the earlier work of Manes and Hofer³ on the adsorption of two planar dyes from a number of solvents, including one dye (Butter Yellow) from methanol, on the same activated carbon that was used here. Manes and Hofer reported (a) that the correlation curves for the solid adsorbates could be made to coincide with the (vapor-phase) hydrocarbon correlation curve in the low-capacity region by application of an empirical abscissa scale factor; and (b) that the empirical scale factor could be estimated from the molar refractivities of the solute, solvent, and heptane standard. The results shown in Figure 1 on the complexes of platinum and palladium are reasonably in agreement with both of these findings. The correlation curve can be made to coincide reasonably well with the hydrocarbon correlation curve by application of the empirical γ_{sl} value of 0.31 to the hydrocarbon curve (*i.e.*, the adsorption potential for the complex adsorbing from methanol solution is 0.31 times the adsorption potential of a hydrocarbon of the same molar volume adsorbing from the gas phase). If, as noted earlier, one makes the assumption that the metal ion makes a negligible contribution to the overall molar polarizability, then the estimated scale factor γ_{sl} is essentially what one would calculate for a solid dimer of acetylacetonate (minus two of its hydrogens) with a molar volume equal to the molar volume of the complex. The scale factor thus calculated comes out to 0.29, which is in quite good agreement with the empirical value. The agreement is probably better than one has any right to expect, and one should not assume that it is typical, particularly since the agreement is better than Manes and Hofer found between the calculated and observed values for Butter Yellow from methanol. Nevertheless, the planar compounds become additional solids that can be approximately treated by the methods reported in the earlier work. As noted earlier, the limiting adsorption capacity is somewhat lower than was found for the dyes. We do not yet have enough experience to judge whether or not this difference is typical of what one might expect when investigating the adsorption of a

(10) F. Basolo and R. G. Pearson, "Mechanisms of Inorganic Reactions," Wiley, New York, N.Y., 1958, p 16.

(11) J. Bjerrum, *et al.*, "Stability Constants of Metal-Ion Complexes," Part I, The Chemical Society, London, 1957.

(12) E. G. Cox and K. C. Webster, *J. Chem. Soc.*, 731 (1935).

(13) W. Partenheimer and R. S. Drago, *Inorg. Chem.*, **9**, 47 (1970).

large number of solid solutes. Nevertheless, the rather rough agreement does indicate that the modified Polanyi theory is capable of predicting the adsorption, at least approximately, when there are no complications from steric effects. As we have seen, however, severe steric hindrance in the solute can make a considerable difference in the adsorption potential, and one should therefore exercise caution in applying the Polanyi treatment to the adsorption of solutes that show severe steric hindrance to achieving planarity.

Conclusion

Solutes that have steric hindrance to assuming a planar configuration may be expected to show anomalously weak adsorption (by the criteria of the modified Polanyi adsorp-

tion potential theory). When the steric factor is severe, the difference in adsorption can be quite striking. That the effect shown here is a true steric effect of the solute and not simply one of molecular sieving is shown by the essentially similar results on the activated carbon and on an essentially nonporous graphitized carbon black.

Acknowledgments. We wish to acknowledge the technical assistance of Mr. Jack P. Mann, who carried out some of the measurements on the carbon black, and the benefit of helpful discussions with Professors E. S. Gould, W. G. Movius, and N. V. Duffy on the chemistry of the acetylacetonates. We thank the Calgon Corp. for the gift of the activated carbon, and the Godfrey Cabot Corp. for the gift of the graphitized carbon black.

Use of the Nonpolar Analog Model in Predicting the Effects of Solvents on Molecular Complex Formation Equilibria

Sherril D. Christian,* Roger Frech, and Kwang Ok Yeo

Department of Chemistry, The University of Oklahoma, Norman, Oklahoma 73069 (Received March 6, 1972)

Publication costs assisted by The Petroleum Research Fund

The nonpolar analog (NPA) model is examined theoretically and methods are developed for using it to predict thermodynamic properties of the transfer of donor, acceptor, and complex molecules from the gas phase into dilute solutions in nonpolar solvents. The general problem of inferring free energies of transfer of polar solutes from experimental values of internal energies of transfer is considered. Thermodynamic results calculated by using the NPA model, in conjunction with solubility parameter theory and with the Prigogine refined average-potential cell model theory, are compared with experimental results for polar components involved in several molecular complex formation equilibria. For individual solutes, including complexes, calculated and experimental free energies of transfer into hexadecane and diphenylmethane generally agree to within 0.1–0.7 kcal/mol.

Introduction

As extensive thermodynamic and spectral information about molecular complexes has become available, numerous investigators have noted the important role played by solvents in modifying the physical and chemical properties of complexes.^{1–5} This knowledge has provided the incentive for attempts to obtain accurate experimental results for electron donor–acceptor (EDA) complexes in the vapor phase,^{2,3,5} where the complicating effects of solvents are absent, and for which theoretical treatments of the structure and energy of complexes are becoming feasible. Unfortunately, limitations on the volatility and stability of EDA complexes and the unique experimental problems connected with investigations of associating gases have restricted the number and reliability of studies of gaseous complexes.^{1–6}

There are two primary reasons, therefore, why methods for predicting the effects of media on complex formation reactions are potentially valuable: (1) comparison with theory will be facilitated if reliable techniques evolve for

converting thermodynamic information about complex formation in condensed phases into information about the corresponding gaseous systems; and (2) an understanding of the role of solvents in altering properties of complexes will be essential in future attempts to provide a molecular explanation of biological and industrial systems in which EDA complexes are important.

Attempts to treat the influence of solvents on the energetics of complex formation have generally fallen into two

- (1) W. B. Person and R. S. Mulliken, "Molecular Complexes. A Lecture and Reprint Volume," Wiley, New York, N. Y., 1969, Chapter 7.
- (2) R. Foster, "Organic Charge-Transfer Complexes," Academic Press, New York, N. Y., 1970, Chapter 7.
- (3) M. Tamres and J. M. Gcodenow, *J. Phys. Chem.*, **71**, 1982 (1967); W. K. Duerksen and M. Tamres, *J. Amer. Chem. Soc.*, **90**, 1379 (1968).
- (4) R. L. Scott and D. V. Fenby, *Annu. Rev. Phys. Chem.*, **20**, 126 (1969).
- (5) S. D. Christian, A. A. Taha, and B. W. Gash, *Quart. Revs. Chem. Soc.*, **24**, 20 (1970).
- (6) (a) M. Tamres and J. Grundnes, *J. Amer. Chem. Soc.*, **93**, 801 (1971), and reports cited therein; (b) J. Grundnes, S. D. Christian, V. Cheam, and S. B. Farnham, *ibid.*, **93**, 20 (1971).

classes: methods in which the solvent is treated as a chemical reactant, which forms discrete complexes with donor (D), acceptor (A), or the adduct (DA);⁷ and techniques for inferring the effects of non-specific solvent-solute interactions.^{5,8} Although it is clear that specific complexes between solvent and solute can be important in condensed phase systems of associating solutes, there appears to be no unique way to determine stoichiometries and specific thermodynamic constants for the solvent-solute complexes which are presumed to exist in dilute solution.^{5,8d} Progress has been made in predicting energies and free energies of transfer reactions of the type

X(ideal gas at unit molarity) =

X(ideal dilute solution in solvent S at unit molarity) (1)

for polar solutes involved in representative molecular complex formation reactions.^{5,9} It has been observed that the energies and free energies of transfer of a series of polar solutes into a given nonpolar solvent ($\Delta E^\circ_{X^v \rightarrow s}$ and $\Delta G^\circ_{X^v \rightarrow s}$) are linearly related; empirical correlations and semiempirical lattice or cell model calculations provide a convenient basis for predicting changes which occur in the equilibrium constants (K_c) and energies (ΔE) of complex formation reactions as various nonpolar and slightly polar solvents are employed.^{9a,10}

The general problem of developing a theory of nonelectrolyte solutions involving polar components remains unsolved.¹¹ Attempts have been made to compare properties of solutions of polar solutes with those of homomorphic nonpolar solutes, *i.e.*, with nonpolar molecules similar in molecular size and structure to the polar solutes.¹¹⁻¹³ The homomorphs have frequently been chosen to have the same molecular volume and polarizability as the polar molecules of interest. Differences between properties of mixtures including a polar component and analogous mixtures in which the polar species is replaced by its homomorph are ascribed to inductive interactions or the formation of molecular complexes involving the polar solute.¹³ Estimates have been made of the separate contributions of dispersive and inductive interactions to the solubility parameters of polar liquids, and these parameters have found some utility in treatments of binary mixtures of polar and nonpolar compounds.¹⁴ However, it is apparent that the total effect of interactions between polar and nonpolar molecules, throughout a wide range of concentrations, cannot be rigorously accounted for in terms of a single induction energy density parameter which is concentration independent.¹¹

The transfer reactions (eq 1) for the components participating in a molecular complex formation reaction pertain to the formation of infinitely dilute solutions of polar solutes in a given solvent, S. For purposes of the present discussion, S will be taken to be nonpolar. Solute molecules are in contact only with solvent molecules, and the solvent-solute interactions involve only nonspecific dispersion and induction forces. Therefore, it should be much simpler to develop adequate theories for predicting transfer energies and free energies of polar solutes than to formulate theories of pure polar liquids and of concentrated solutions of polar and nonpolar molecules, in which orientation energy and entropy effects must be considered.

A previous article^{9b} introduced a general model for dilute solutions of polar compounds dissolved in nonpolar media. The model involves use of a nonpolar analog (NPA) of the polar solute (P) in place of the polar solute in calculating properties of the solutions; the NPA mole-

cule is chosen to have the same molecular volume and the same total interaction energy with the surrounding solvent molecules as does P. In this model, the NPA molecule must have a value of molecular polarizability, α , large enough to interact as strongly with the solvent as does P, for which both dispersion and inductive interactions are important. It is assumed that not only $\Delta E^\circ_{P^v \rightarrow s}$, but also $\Delta G^\circ_{P^v \rightarrow s}$, $\Delta S^\circ_{P^v \rightarrow s}$, and other thermodynamic constants for the transfer reactions 1 will be the same as the corresponding transfer quantities for the NPA molecule. No attempt is made to utilize or predict properties of the pure polar component in this treatment. The theoretical basis for the NPA model and methods for applying it to predict the effects of solvents on molecular complex formation equilibria are presented here.

Justification for the Nonpolar Analog Model

An isolated polar molecule dissolved in a nonpolar medium may interact with the solvent through several types of forces, including short-range repulsive forces and van der Waals attractive forces of the dipole-induced dipole and dispersive types.¹⁵ The potential energy of interaction between the polar molecule P and the solvent molecules S resulting from dipole-induced dipole forces is

$$V_{ps}(\text{dip}) = -\frac{1}{2} \hat{\mu}_p \cdot \hat{\mu}_{ps} R_{ps} \quad (2)$$

Here \hat{R}_{ps} is the reaction field at the polar molecule resulting from the polarization of the solvent molecules by the electric moment of the solute molecule, $\hat{\mu}_p$. If one adopts the dielectric cavity model of a solution (in which the solute molecule is at the center of a cavity whose walls consist of a continuum with dielectric properties identical with the bulk solvent) the reaction field is taken to be proportional to the electric moment; the coefficient of proportionality is given in several standard texts on dielectric theory.¹⁵ The reaction field may be written as a summation over the contributions of each solvent-solute pair

$$V_{ps}(\text{dip}) = \frac{1}{2} \hat{\mu}_p^2 \sum_s \frac{\alpha_s f_{ps}}{|r_{ps}|^6} \quad (3)$$

where $|r_{ps}|$ is the magnitude of the vector distance between a solvent molecule and the polar molecule, α_s is the molecular polarizability of a solvent molecule, and f_{ps} is an orientation factor which accounts for the anisotropy of

- (7) (a) R. S. Drago, T. F. Bolles, and R. J. Niedzielski, *J. Amer. Chem. Soc.*, **88**, 2717 (1966); (b) P. J. Trotter and M. W. Hanna, *ibid.*, **88**, 3724 (1966); (c) S. Carter, J. N. Murrell, and E. S. Rosch, *J. Chem. Soc.*, 2048 (1965); (d) T. F. Hunter, N. C. Cutress, K. M. Mitchins, G. N. Rowley, and M. Stillman, *Spectrochim. Acta, Part A*, **27**, 1207 (1971).
- (8) (a) H. Buchowski, J. Devaure, P. V. Huong, and J. Lascombe, *Bull. Soc. Chim. Fr.*, 2532 (1966); (b) S. D. Christian, J. R. Johnson, H. E. Aifsprung, and P. J. Kilpatrick, *J. Phys. Chem.*, **70**, 3376 (1966); (c) P. V. Huong, N. Platzer, and M. L. Josien, *J. Amer. Chem. Soc.*, **91**, 6514 (1969); (d) S. D. Christian and E. E. Tucker, *J. Phys. Chem.*, **74**, 214 (1970).
- (9) (a) J. Grundnes and S. D. Christian, *Acta Chem. Scand.*, **23**, 3583 (1969); (b) S. D. Christian, K. O. Yeo, and E. E. Tucker, *J. Phys. Chem.*, **75**, 2413 (1971).
- (10) S. D. Christian, Office of Saline Water Research and Development Progress Report, No. 706, July 1971.
- (11) J. H. Hildebrand, J. M. Prausnitz, and R. L. Scott, "Regular and Related Solutions," Van Nostrand, New York, N. Y., 1970, Chapter 7.
- (12) A. Bondi and D. J. Simkin, *J. Chem. Phys.*, **25**, 1073 (1956).
- (13) D. E. Martire and P. Riedl, *J. Phys. Chem.*, **72**, 3478 (1968).
- (14) R. F. Weimer and J. M. Prausnitz, *Hydrocarbon Process.*, **44**, 237 (1965); R. Anderson and J. M. Prausnitz, *AIChE J.*, **7**, 96 (1961).
- (15) C. J. F. Böttcher, "Theory of Electric Polarisation," Elsevier, Amsterdam, 1952; B. Chu, "Molecular Forces," Interscience, New York, N. Y., 1967.

the interactions.^{15,16} The dispersive interaction may be written as

$$V_{ps}(\text{disp}) = - \frac{3}{2} I_p \alpha_p \sum_s \frac{I_s \alpha_s}{I_p + I_s} \frac{1}{|\hat{r}_{ps}|^6} \quad (4)$$

where I_p and I_s are the ionization potentials of the solute and solvent, respectively, and α_p is the molecular polarizability of the solute.

The NPA molecule has no permanent dipole moment; it interacts with the solvent molecules solely through dispersive forces.^{9b} However, the magnitude of this interaction must be large enough so that the total energy of interaction of the NPA molecule with the solvent equals the total energy of interaction of the original polar molecule with the solvent (the sum of eq 3 and 4)

$$V_{NPA} = V_{ps}(\text{dip}) + V_{ps}(\text{disp}) \quad (5)$$

Since the vector distances between the polar solute and the solvent molecules are the same as those between NPA and S, and since all of the terms in eq 5 have the same distance dependence, the energy compensation required by eq 5 will be achieved whenever

$$- \frac{3}{2} I_{NPA} \alpha_{NPA} \frac{I_s \alpha_s}{I_{NPA} + I_s} = - \frac{1}{2} \mu_p^2 \alpha_s f_{ps} - \frac{3}{2} I_p \alpha_p \frac{I_s \alpha_s}{I_p + I_s} \quad (6)$$

for each solute-solvent interaction. For example, if the solvent polarizability is spherical, eq 6 may be satisfied by varying only the molecular polarizability of the solute, while leaving the ionization potential invariant. Any other combination of values of I_{NPA} and α_{NPA} satisfying eq 6 may be chosen for the hypothetical solute molecule NPA.

Equation 6 indicates the molecular requirements for equality of $\Delta E_{P \rightarrow S}^{\circ}$ and $\Delta E_{NPA \rightarrow S}^{\circ}$ for homomorphic P and NPA molecules. It can be shown that various cell theories of liquids lead to the result that $\Delta S_{P \rightarrow S}^{\circ} = \Delta S_{NPA \rightarrow S}^{\circ}$ and $\Delta G_{P \rightarrow S}^{\circ} = \Delta G_{NPA \rightarrow S}^{\circ}$ provided the energy compensation required by eq 6 is achieved.¹⁷ Hence the use of the NPA model under quite general conditions appears warranted.

Application of the Nonpolar Analog Model in Predicting Thermodynamic Properties of Polar Solutes

The NPA model does not by itself provide a basis for predicting thermodynamic properties for the transfer reactions (eq 1) for polar solutes. However, to the extent that the model applies it permits the use of theories and properties of nonpolar liquids and liquid mixtures in predicting properties of dilute solutions of polar solutes in nonpolar solvents.^{9b} The model is based on the assumption that $\Delta G_{P \rightarrow S}^{\circ}$ is uniquely determined by $\Delta E_{P \rightarrow S}^{\circ}$ and the molecular volume (more correctly, the molecular geometry) of P. Using the nonpolar analog concept

$$\Delta G_{P \rightarrow S}^{\circ}(\Delta E_{P \rightarrow S}^{\circ}, \bar{V}_P) = \Delta G_{NPA \rightarrow S}^{\circ}(\Delta E_{NPA \rightarrow S}^{\circ}, \bar{V}_{NPA}) \quad (7)$$

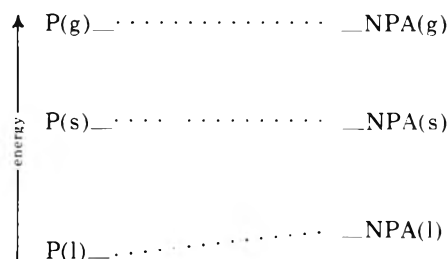
where $\Delta E_{P \rightarrow S}^{\circ} \equiv \Delta E_{NPA \rightarrow S}^{\circ}$ and $\bar{V}_P \equiv \bar{V}_{NPA}$.

The NPA model may be most simply tested by comparing experimental values of $\Delta G_{X \rightarrow S}^{\circ}$ and $\Delta E_{X \rightarrow S}^{\circ}$ for various solutes X (polar and nonpolar) of comparable molecular volume dissolved in a given solvent. Previously,^{9,10} we observed that the empirical relation

$$\Delta G_{X \rightarrow S}^{\circ} = \beta_S \Delta E_{X \rightarrow S}^{\circ} + 300 \text{ cal/mol} \quad (8)$$

provides a good correlation of results for both polar and nonpolar solutes (without regard for molecular volume) in a given solvent S at 298°K.¹⁸ The parameter β_S is characteristic of the solvent only, and has a value of about 0.6 for many common nonpolar solvents. Correlations of this type demonstrate the feasibility of replacing P by its nonpolar analog in thermodynamic calculations; they also show that moderate variation in molecular volume does not strongly influence the magnitude of $\Delta G_{X \rightarrow S}^{\circ}$ corresponding to a given value of $\Delta E_{X \rightarrow S}^{\circ}$. (Actually, there is a reasonably close correlation between $\Delta E_{X \rightarrow S}^{\circ}$ and the molecular volume of related solutes; hence, the effect of variation in solute volume is largely hidden in the $\Delta G_{X \rightarrow S}^{\circ}$ vs. $\Delta E_{X \rightarrow S}^{\circ}$ correlations.)

At a more fundamental level, it would be desirable to develop theories for predicting $\Delta E_{P \rightarrow S}^{\circ}$ and $\Delta G_{P \rightarrow S}^{\circ}$ from molecular parameters of the P, S, and NPA molecules. In this development, it is convenient to refer to the following conceptual diagram of the energy of P and NPA in various states



The states P(g) and NPA(g) refer to ideal gaseous states; P(s) and NPA(s) refer to dilute solution states in the nonpolar solvent;¹⁹ and P(l) and NPA(l) represent pure liquid P and NPA. Note that the energy of P(l) will ordinarily be considerably lower than that of NPA(l) and that the energy change for the transfer P(l) → P(s) will be correspondingly greater than that for the transfer NPA(l) → NPA(s); the reason for this is that in the pure liquid state, P molecules interact relatively strongly with each other through orientation forces, which are absent in liquid NPA and in the states P(s) and NPA(s). The model forces P(g) and NPA(g) to be at the same level of energy (and by assumption, free energy); similarly, P(s) and NPA(s) have the same energy (and, presumably, free energy).

Given the energy level diagram (above) the NPA model requires that

(16) Ordinarily in systems consisting of a polar solute and a nonpolar solvent, orientation effects will not play an important role, and f_{ps} may realistically be taken to be unity. However, interactions between polar molecules capable of donating n electrons and neutral acceptor molecules (e.g., halogens or aromatic hydrocarbons) may be highly specific.^{1,2} Donor-acceptor interaction may therefore produce retardation effects even in systems where the solvent has no permanent dipole moment.

(17) A discussion of the relation between the NPA model and various cell theories of liquids will appear following these pages in the microfilm edition of this volume of the journal. Single copies may be obtained from the Business Operations Office, Books and Journals Division, American Chemical Society, 1155 Sixteenth St., N.W., Washington, D. C. 20036. Remit check or money order for \$3.00 for photocopy or \$2.00 for microfiche, referring to code number JPC-73-813.

(18) In ref 9a the constant term in eq 15 was given erroneously as 450 cal/mol. Incorrect terms were utilized to account for the thermal expansion of the solvent, and the reported $\Delta E_{X \rightarrow S}^{\circ}$ values are all too small (algebraically) by 200–250 cal/mol.

(19) Gaseous standard states are taken to be the unit molarity ideal gas; the infinitely dilute, unit molarity state is used for all solutes in condensed phases.

$$\Delta E_{\text{P}}^{\circ \text{v} \rightarrow \text{s}} = \Delta E_{\text{NPA}}^{\circ \text{v} \rightarrow \text{s}} = E_{\text{NPA(s)}}^{\circ} - E_{\text{NPA(g)}}^{\circ}$$

or

$$\Delta E_{\text{P}}^{\circ \text{v} \rightarrow \text{s}} = (E_{\text{NPA(s)}}^{\circ} - E_{\text{NPA(l)}}^{\circ}) - (E_{\text{NPA(g)}}^{\circ} - E_{\text{NPA(l)}}^{\circ}) \quad (9)$$

and similarly

$$\Delta G_{\text{P}}^{\circ \text{v} \rightarrow \text{s}} = (G_{\text{NPA(s)}}^{\circ} - G_{\text{NPA(l)}}^{\circ}) - (G_{\text{NPA(g)}}^{\circ} - G_{\text{NPA(l)}}^{\circ}) \quad (10)$$

Equations 9 and 10 may be rewritten

$$\Delta E_{\text{P}}^{\circ \text{v} \rightarrow \text{s}} = \Delta E_{\text{NPA}}^{\circ \text{dil}} - \Delta E_{\text{NPA}}^{\circ \text{vap}} \dots \quad (11)$$

and

$$\Delta G_{\text{P}}^{\circ \text{v} \rightarrow \text{s}} = \Delta G_{\text{NPA}}^{\circ \text{dil}} - \Delta G_{\text{NPA}}^{\circ \text{vap}} \dots \quad (12)$$

where $\Delta E_{\text{NPA}}^{\circ \text{dil}}$ and $\Delta E_{\text{NPA}}^{\circ \text{vap}}$ are, respectively, the energy of transfer of NPA from pure liquid NPA into the infinitely dilute solution state in solvent S and the energy of vaporization of liquid NPA, and $\Delta G_{\text{NPA}}^{\circ \text{dil}}$ and $\Delta G_{\text{NPA}}^{\circ \text{vap}}$ are the corresponding free energy changes.

Several current theories of solution provide means for relating $\Delta E_{\text{NPA}}^{\circ \text{dil}}$ and $\Delta E_{\text{NPA}}^{\circ \text{vap}}$ to parameters characteristic of the NPA and S molecules. For example, solubility parameter theory¹¹ predicts that

$$\Delta E_{\text{NPA}}^{\circ \text{dil}} = \bar{V}_{\text{P}}(\delta_{\text{S}} - \delta_{\text{NPA}})^2 \quad (13)$$

and

$$\Delta E_{\text{NPA}}^{\circ \text{vap}} = \delta_{\text{NPA}}^2 \bar{V}_{\text{P}} \quad (14)$$

where δ_{S} and δ_{NPA} are the solubility parameters of S and NPA, respectively, and where for convenience we neglect volume changes on mixing NPA with S. The expressions for $\Delta E_{\text{NPA}}^{\circ \text{dil}}$ and $\Delta E_{\text{NPA}}^{\circ \text{vap}}$ may be substituted into eq 13, which may be rearranged to give

$$\delta_{\text{NPA}} = \frac{1}{2}(\delta_{\text{S}} - \Delta E_{\text{P}}^{\circ \text{v} \rightarrow \text{s}} / \delta_{\text{S}} \bar{V}_{\text{P}}) \quad (15)$$

Thus, it is possible to infer the solubility parameter of the nonpolar analog of a given polar solute from the solubility parameter of the solvent and the energy of transfer of P from the ideal gaseous state into the infinitely dilute state in S. The free energy of transfer of NPA from vapor to the infinitely dilute state in solvent S may then be related to δ_{NPA} and the vapor pressure of pure liquid NPA (P_{NPA}°). Equation 12 may be rewritten

$$\Delta G_{\text{P}}^{\circ \text{v} \rightarrow \text{s}} = RT \ln (P_{\text{NPA}}^{\circ} / RT) + \bar{V}_{\text{P}}(\delta_{\text{S}} - \delta_{\text{NPA}})^2 + RT \ln \bar{V}_{\text{S}} \quad (16)$$

where the first term on the right represents the free energy change for converting NPA vapor at unit molarity into pure liquid NPA under its own vapor pressure; the second term is the free energy of transfer of NPA from the pure liquid state to the ideal dilute solution in S (using the unit mole fraction standard state) and the last term is the free energy change for converting from the mole fraction standard state for the solute to the unit molarity standard state.^{9b}

In order to apply eq 16 to calculate $\Delta G_{\text{P}}^{\circ \text{v} \rightarrow \text{s}}$ it is necessary to obtain the vapor pressure of pure liquid NPA, either from a theory of pure liquids or from experimental measurements on actual nonpolar liquids having approximately the required heat of vaporization and molecular geometry. Fortunately, the vapor pressures of pure low

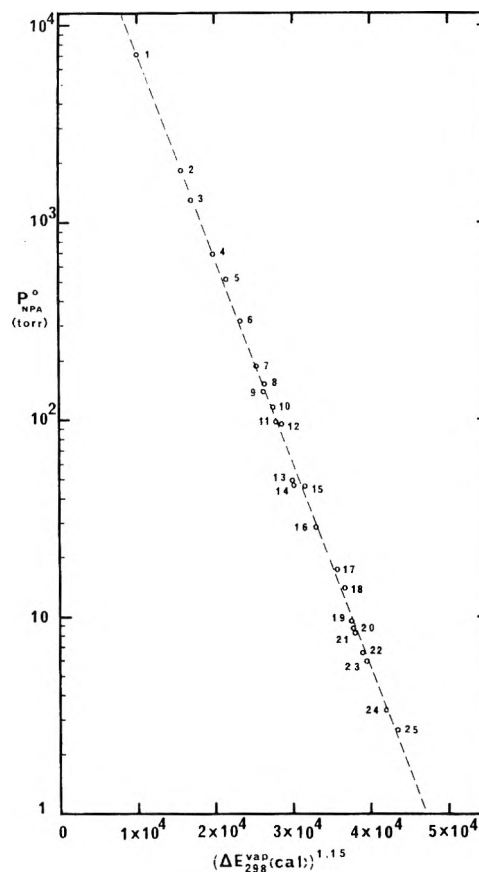


Figure 1. Correlation between vapor pressure and energy of vaporization of nonpolar organic liquids at 25°. All $\Delta E_{298}^{\text{vap}}$ values were taken from J. H. Hildebrand, J. M. Prausnitz, and R. L. Scott, "Regular and Related Solutions," Van Nostrand-Reinhold, New York, N. Y., 1970, except for propane, butane, and methylcyclopentane, for which $\Delta E_{298}^{\text{vap}}$ values were found in "Physical Properties of Chemical Substances," The Dow Chemical Company, Midland, Mich., 1952. Vapor pressures were obtained from the latter publication. Numbers refer to compounds as follows: (1) propane, (2) butane, (3) neopentane, (4) isopentane, (5) pentane, (6) cyclopentane, (7) 1-hexene, (8) hexane, (9) methylcyclopentane, (10) carbon tetrachloride, (11) cyclohexane, (12) benzene, (13) isooctane, (14) methylcyclohexane, (15) heptane, (16) toluene, (17) 1-octene, (18) octane, (19) ethylbenzene, (20) *p*-xylene, (21) *m*-xylene, (22) *o*-xylene, (23) styrene, (24) propylbenzene, (25) mesitylene.

molecular weight nonpolar liquids at 25° vary systematically with their energies of vaporization.²⁰ Figure 1 is a plot of the logarithm of vapor pressure against $\Delta E_{298}^{\text{vap}}$ for a number of common nonpolar liquids (excluding fluorocarbons); the solid curve represents the least-squares equation

$$\log P^{\circ}(\text{Torr}, 298^{\circ}\text{K}) = -1.038 \times 10^{-4}(\Delta E_{298}^{\text{vap}})^{1.15} + 4.889 \quad (17)$$

which may be used to calculate vapor pressures of these liquids, with a standard error of about 9%. By employing $\Delta E_{\text{NPA}}^{\text{vap}} = \delta_{\text{NPA}}^2 \bar{V}_{\text{P}}$ and eq 17 it is possible to obtain a reliable value of P_{NPA}° to use in eq 16.

Another theory of solutions which may be melded with the NPA model is the average-potential cell model theory of Prigogine,²¹ which extends the theorem of correspond-

(20) E. A. Guggenheim, "Thermodynamics," North-Holland, Amsterdam, 1950, pp 142 and 143; ref 11, pp 40 and 41.

(21) I. Prigogine, "Molecular Theory of Solutions," North-Holland, Amsterdam, 1957, Chapters 9 and 10.

ing states to mixtures. In the Prigogine refined average-potential cell model, excess thermodynamic functions for binary mixtures are expressed in terms of parameters σ and ρ defined as

$$\sigma = (\epsilon_B^* - \epsilon_A^*)/\epsilon_A^* \quad (18)$$

and

$$\rho = (r_B^* - r_A^*)/r_A^* \quad (19)$$

where r^* and ϵ^* are the distance of separation and internal energy scale factors in the universal potential function, respectively, and the subscripts A and B denote pure components A and B, respectively. Here, A is taken to be the reference component and B is the solute (either P or NPA). When only dispersion forces operate between the two components (*e.g.*, when the solute is the NPA molecule), $\Delta E^{\circ \text{dil}}$ and $\Delta G^{\circ \text{dil}}$ may be expressed in terms of σ , ρ , and the configurational enthalpies and heat capacities of the nonpolar solvent (see ref 21). Then, by using the relations

$$\Delta H^{\circ \text{vap}} = 0.67\delta Z \epsilon_A^*/RT \quad (20)$$

and

$$\epsilon_B^* = \epsilon_A^*(1 + \sigma) \quad (21)$$

where Z is the number of the nearest neighbors surrounding a cell, one may derive expressions for $\Delta G^{\circ \text{v}\rightarrow\text{s}}$ and $\Delta E^{\circ \text{v}\rightarrow\text{s}}$ for NPA; by the assumptions of the NPA model, these relations will apply as well to P at infinite dilution in S.

To relate $\Delta E^{\circ \text{p}\rightarrow\text{s}}$ and $\Delta G^{\circ \text{p}\rightarrow\text{s}}$, σ_{NPA} may be calculated explicitly for a given value of $\Delta E^{\circ \text{p}\rightarrow\text{s}}$ and a chosen value of ρ , whereupon σ_{NPA} and ρ may be used to calculate $\Delta G^{\circ \text{p}\rightarrow\text{s}}$. The parameter ρ may be evaluated from molecular volumes of the solute and the solvent.²² Alternatively, it is convenient to construct plots of $\Delta G^{\circ \text{p}\rightarrow\text{s}}$ vs. $\Delta E^{\circ \text{p}\rightarrow\text{s}}$ by using arbitrarily chosen σ values and a fixed value of ρ . Knowing ρ , for a given solute and solvent, $\Delta G^{\circ \text{p}\rightarrow\text{s}}$ is estimated from $\Delta E^{\circ \text{p}\rightarrow\text{s}}$ by using the curve corresponding most nearly to the correct ρ value. Figure 2 shows standard $\Delta G^{\circ \text{p}\rightarrow\text{s}}$ vs. $\Delta E^{\circ \text{p}\rightarrow\text{s}}$ curves constructed for ρ values of zero and ± 0.2 ; it may be noted that the plots are not very sensitive to variation in ρ . The predictions based on the theory of Prigogine are seen to be nearly the same as those derived from solubility parameter theory; moreover, the results in Figure 2 are in reasonable agreement with transfer free energy value calculated from empirical eq 8, using a value of β_s equal to 0.60. The calculated intercept ($\Delta G^{\circ \text{p}\rightarrow\text{s}}$ corresponding to $\Delta E^{\circ \text{p}\rightarrow\text{s}} = 0$) equals 241 cal based on solubility parameter calculations (eq 16) and 284 cal using Prigogine's theory with $\rho = -0.27$ and physical properties of heptane at 298°K. (The value $\rho = -0.27$ is computed for a hypothetical solute having a molar volume intermediate between those of Ar and Kr, for which $\Delta E^{\circ \text{v}\rightarrow\text{HPT}}$ is nearly zero at 298°K.)

Table I illustrates a test of eq 14-17, which are based on the NPA model and solubility parameter theory. Values of $-\Delta E^{\circ \text{p}\rightarrow\text{s}}$ given in column 3 are the experimental ones, and column 4 lists $-\Delta E^{\circ \text{p}\rightarrow\text{s}}$ values calculated with the quasi-lattice model of Stevens, *et al.*,^{10,23} which utilizes energy parameters characteristic of interactions between specific atomic and submolecular groups of the solute and solvent molecules. In the fifth and sixth columns are listed values of $-\Delta G^{\circ \text{p}\rightarrow\text{s}}$ computed from eq 13-17, using the values of $\Delta E^{\circ \text{p}\rightarrow\text{s}}$ listed in columns 3 and 4, respectively. Both sets of calculated $\Delta G^{\circ \text{p}\rightarrow\text{s}}$ values are in reasonable agreement with the experimental results, and

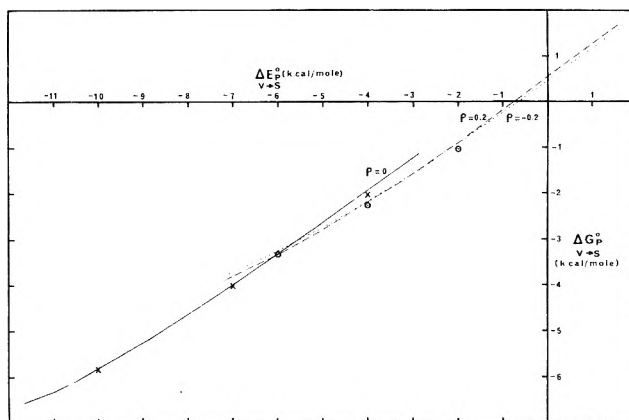


Figure 2. Correlation of transfer free energies and internal energies for the solvent heptane. Calculated curves ($\Delta E^{\circ \text{p}\rightarrow\text{s}}$ vs. $\Delta G^{\circ \text{p}\rightarrow\text{s}}$) are obtained using the Prigogine refined average-potential cell model theory. Points (X) are calculated from the Hildebrand-Scott solubility parameter theory for the solvent heptane, using $\rho = 0$; points (O) are calculated in the same way using $\rho = -0.2$.

there is apparently nearly random deviation on the order of several tenths kcal between the experimental and calculated free energy values. Similar calculations based on Prigogine's cell model lead to results which are nearly equivalent to those in Table I.

A related useful application of the nonpolar analog model is the calculation of limiting activity coefficients of polar solutes (P) in nonpolar solvents, based on the pure liquid P standard state. $\Delta G^{\circ \text{p}\rightarrow\text{s}}$ for the unit molarity solute state in S may be calculated for polar solutes from the value of $\Delta E^{\circ \text{p}\rightarrow\text{s}}$ for a given solute (*vide supra*). But the mole fraction of P (in S) in equilibrium with P vapor at the vapor pressure of pure liquid P may be calculated from the equation

$$X_P^{(s)} = (P_P^{\circ} \bar{V}_s / RT) \exp(-\Delta G^{\circ \text{p}\rightarrow\text{s}} / RT) \quad (22)$$

provided P_P° (the vapor pressure of pure liquid P) is known. Since the activity of P is unity under these conditions, the limiting activity coefficient of P in S can be calculated from

$$\gamma_P^{\infty} = 1/X_P^{(s)} = (RT/P_P^{\circ} \bar{V}_s) \exp(\Delta G^{\circ \text{p}\rightarrow\text{s}} / RT) \quad (23)$$

By using the calculated value $\Delta G^{\circ}(\text{H}_2\text{O})^{\text{v}\rightarrow\text{s}} = -1890$ cal for water dissolved in diphenylmethane (see Table I) and the known vapor pressure of H_2O at 25° (23.7 Torr) one may calculate the value $\gamma(\text{H}_2\text{O})^{\infty} = 192$, whereas the experimental value is $\gamma(\text{H}_2\text{O})^{\infty} = 227$.

Other, more elaborate theories of nonpolar binary mixtures (such as the recent theory of Flory,²⁴ which employs a reduced partition function, formulated in terms of segment volumes and segment interaction energies) may be utilized to calculate $\Delta E^{\circ \text{dil}}$ and $\Delta G^{\circ \text{dil}}$ in terms of mo-

(22) The expressions used here in obtaining transfer energies and free energies apply, strictly speaking, only at zero pressure, however, in applications involving pressures not greater than 1 atm, the pressure dependence of energy or free energy may ordinarily be ignored. The parameter ρ should be evaluated from the critical volumes of A and the solute, but for the present calculations it is satisfactory to estimate from the molar volumes of the pure components at 298°K.

(23) T. L. Stevens, Ph.D. Dissertation, The University of Oklahoma, 1968; J. R. Johnson, P. J. Kilpatrick, S. D. Christian, and H. E. Afsprung, *J. Phys. Chem.*, **72**, 3223 (1968).

(24) P. J. Flory, R. A. Orwoll, and A. Vrij, *J. Amer. Chem. Soc.*, **86**, 3507, 3515 (1964); P. J. Flory, *ibid.*, **87**, 1833 (1965); P. J. Flory, *Disc. Faraday Soc.*, **49**, 7 (1970), and references cited therein.

TABLE I: Experimental and Calculated Transfer Energies and Free Energies of Polar Solutes from Vapor into Nonpolar Solvents

System		$-\Delta E^{\circ}_{P^{v \rightarrow s}}$	$-\Delta E^{\circ}_{P^{v \rightarrow s}}$	$-\Delta G^{\circ}_{P^{v \rightarrow s}}$	$-\Delta G^{\circ}_{P^{v \rightarrow s}}$	$-\Delta G^{\circ}_{P^{v \rightarrow s}}$
Solute	Solvent ^a	kcal/mol (exptl)	kcal/mol ^b (calcd)	kcal/mol ^c (calcd)	kcal/mol ^d (calcd)	kcal/mol (exptl)
H ₂ O	HXD	1.98 ^f	2.60	0.72	0.87	0.45 ^f
CH ₃ OH	HXD	2.75 ^f	2.80	1.16	1.19	1.25 ^f
(C ₂ H ₅) ₂ NH	HXD	5.45 ^f	(5.45) ^e	2.66	(2.66)	3.16 ^f
(C ₂ H ₅) ₂ NH·H ₂ O	HXD	7.50 ^f	6.80	3.93	3.49	3.80 ^f
(C ₂ H ₅) ₂ NH·CH ₃ OH	HXD	5.98 ^f	7.00	2.89	3.57	4.15 ^f
H ₂ O	DPM	4.02 ^f	5.57	1.89	2.19	1.79 ^f
CH ₃ OH	DPM	5.11 ^f	4.78	2.79	2.62	2.34 ^f
(C ₂ H ₅) ₂ NH	DPM	6.14 ^f	(6.14) ^e	3.27	(3.27)	3.36 ^f
(C ₂ H ₅) ₂ NH·H ₂ O	DPM	8.62 ^f	8.26	4.88	4.63	5.20 ^f
(C ₂ H ₅) ₂ NH·CH ₃ OH	DPM	8.11 ^f	7.46	4.40	4.38	5.08 ^f
(CH ₃) ₃ N	HPT	4.60 ^g		2.60		2.57 ^g
SO ₂	HPT	3.60 ^g		1.98		1.40 ^g
(CH ₃) ₃ N·SO ₂	HPT	10.10 ^g		5.92		5.15 ^g

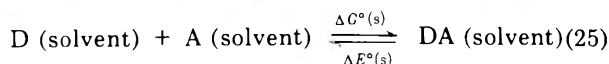
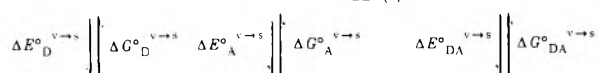
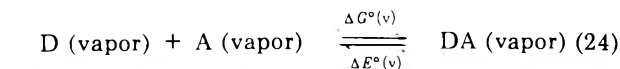
^aHXD = hexadecane, DPM = diphenylmethane, HPT = heptane. ^bCalculated from the lattice model of Stevens, *et al.*²³ ^cCalculated from experimental $\Delta E^{\circ}_{P^{v \rightarrow s}}$ values, using the NPA model and solubility parameter theory. ^dCalculated from $\Delta E^{\circ}_{P^{v \rightarrow s}}$ values derived from the lattice model, using the NPA method in conjunction with solubility parameter theory. ^eExperimental $\Delta E^{\circ}_{P^{v \rightarrow s}}$ for diethylamine used in calculating lattice parameters for N···HXD and N···DPM interaction energy. ^fData from E. E. Tucker, Ph.D. Dissertation, the University of Oklahoma, 1969. ^gData from J. Grundnes and S. D. Christian, *J. Amer. Chem. Soc.*, **90**, 2239 (1968).

lecular parameters of the solvent and the nonpolar analog of P. However, since the differences between $\Delta E^{\circ \text{dill}}$ and $\Delta G^{\circ \text{dill}}$ obtained from various statistical theories are small compared with uncertainties in these quantities for most polar solutes, the equations which can be derived for utilizing these theories with the NPA model are not given here.

Prediction of the Effects of Solvents on Free Energies of Formation of Molecular Complexes

Applications of the nonpolar analog model method for calculating $\Delta G^{\circ v \rightarrow s}$ from $\Delta E^{\circ v \rightarrow s}$ for components which participate in complex formation reactions should be useful in predicting solvent effects on the complex formation constants. Consider the equilibrium cycle shown in scheme I where D is an electron donor molecule, A is an

Scheme I



electron acceptor molecule, and DA is an EDA complex. The changes in standard free energies (ΔG°) and internal energies (ΔE°) for the steps in the cycle are interrelated by the equations

$$\Delta E^{\circ}(s) = \Delta E^{\circ}(v) + \Delta E^{\circ}_{DA}{}^{v \rightarrow s} - \Delta E^{\circ}_D{}^{v \rightarrow s} - \Delta E^{\circ}_A{}^{v \rightarrow s} \quad (26)$$

and

$$\Delta G^{\circ}(s) = \Delta G^{\circ}(v) + \Delta G^{\circ}_{DA}{}^{v \rightarrow s} - \Delta G^{\circ}_D{}^{v \rightarrow s} - \Delta G^{\circ}_A{}^{v \rightarrow s} \quad (27)$$

However, the values $\Delta G^{\circ}(s)$ and $\Delta G^{\circ}(v)$ may be related to the complex formation equilibrium constants in s and v by $\Delta G^{\circ} = -RT \ln K_c$ so that eq 27 may be rearranged to give

$$K_c(v)/K_c(s) = \exp[(\Delta G^{\circ}_{DA}{}^{v \rightarrow s} - \Delta G^{\circ}_D{}^{v \rightarrow s} - \Delta G^{\circ}_A{}^{v \rightarrow s})/RT]$$

TABLE II: Effects of Media on Molecular Complex Formation Equilibria (Comparison of Experimental and Calculated Gibbs Free Energy Values for Formation of Complexes from Monomers)

Complex	$-\Delta G^{\circ}$, kcal/mol	Medium		
		Vapor	Hexa- decane	Di- phenyl- meth- ane
(C ₂ H ₅) ₂ NH·H ₂ O	Calcd ^a		1.77	0.94
	Calcd ^b		1.18	0.39
	Exptl ^c	1.22	1.41	1.27
CH ₃ OH·H ₂ O	Calcd ^a		0.61	-0.12
	Calcd ^b		1.26	0.03
	Exptl ^c	1.54	1.28	0.92
(CH ₃) ₃ N·SO ₂	Calcd ^a			4.74
	Exptl ^d	3.40		4.58

^aFree energy of formation of complex predicted from experimental $\Delta E^{\circ v \rightarrow s}$ values. ^bFree energy of formation predicted from values of $\Delta E^{\circ v \rightarrow s}$ obtained from the lattice model. ^cTable I, footnote f. ^dTable I, footnote g.

The ratio of K_c values may therefore be predicted by using methods described in the preceding section to calculate $\Delta G^{\circ v \rightarrow s}$ for D, A, and DA individually.

The results of application of the nonpolar analog model method to actual EDA complex formation reactions are given in the Table II. The predicted values of changes in ΔG° for complex formation reactions generally agree with experimental values to within a few hundred calories, although for the MeOH·DEA formation reaction in DPM, the discrepancy is about 1 kcal. The agreement is probably satisfactory, considering the fact that several experimental $\Delta E^{\circ v \rightarrow s}$ values, each of which is uncertain by several tenths of a kilocalorie, are involved in calculating a single $\Delta G^{\circ}(s)$ value. When the quasi-lattice model method is employed for calculation of ΔE° for the complex DA, no energy of stabilization is introduced to account for the interaction between the excess dipole moment of the complex and the solvent. This effect has been discussed in rationalizing the abnormally large (negative) value of the energy and free energy of solvation of (CH₃)₃N·SO₂. One

would, therefore, expect the lattice model to lead to values of ΔG° smaller than experimental values because of the complex dipole-solvent interaction; the effect is apparently most important in the case of methanol-diethylamine in diphenylmethane, where the calculated ΔG° is about 1 kcal less than the observed value. It is known that complexes of aliphatic amines with water and alcohols possess dipole moments which are significantly greater than the vector sums of the dipole moments of the monomers. Also, the possibility exist that retardation effects are not insignificant in systems where highly polar molecules, with exposed n -electron pairs, interact with an aromatic solvent.^{1,2}

Conclusion

The nonpolar analog model, combined with various theories of nonpolar liquids, may be used to calculate thermodynamic properties of polar solutes in nonpolar solvents. Theoretically, the NPA model should apply under a

wide range of conditions. The methods developed here permit mapping of the thermodynamic properties of the relatively simple nonpolar solute-nonpolar solvent systems into those of the inherently more complicated polar solute-nonpolar solvent systems. By knowing the energy of transfer of a polar solute, it is possible to make a reliable estimate of the free energy of transfer. An important application of the NPA model is the prediction of solvent effects on molecular complex formation equilibria; such effects are not well understood, and the techniques presented here should be quite generally applicable in predicting them.

Acknowledgment. Financial aid from the National Science Foundation, under Grants No. GP-23278 and GP-33519X, is greatly appreciated. Acknowledgment is also made to the Donors of The Petroleum Research Fund, administered by the American Chemical Society, for partial support of this research.

Conductance and Ion Pair Formation of Bis(2,9-dimethyl-1,10-phenanthroline)copper(I) Perchlorate. III. In Acetonitrile-Carbon Tetrachloride and Water-Dioxane Mixtures

Katsuhiko Miyoshi* and Toshihiro Tominaga

Department of Chemistry, Faculty of Science, Hiroshima University, Hiroshima, Japan (Received August 25, 1972)

Conductance of bis(2,9-dimethyl-1,10-phenanthroline)Cu(I) perchlorate was measured at 25° in CH₃CN-CCl₄ (11 ≤ D ≤ 36) and water-dioxane (10 ≤ D ≤ 19) mixtures. The conductance parameters derived from the analysis with the Fuoss-Onsager-Skinner 1965 conductance theory indicated that the chelate salt is more dissociated in the former mixtures than in the latter and that the plot of log K_A vs. $1/D$ shows a concave-downward curvature in water-dioxane mixtures. These association behaviors were discussed in terms of the interaction of the chelate salt with polar solvent components.

Introduction

In a series of our conductance studies on the bulky and symmetrical electrolyte, bis(2,9-dimethyl-1,10-phenanthroline)Cu(I) perchlorate in nonaqueous and binary mixed solvents, it was found that the chelate salt is more dissociated in these solvents than the tetrabutylammonium perchlorate and bromide,¹ the cation of which was confirmed to be hydrodynamically equivalent to the chelate cation from the comparison of the Walden products in several alcohols.² Two factors were assumed that gave rise to smaller association constants for the chelate salt. The first is the stabilization of the chelate cation by dipolar aprotic solvents such as nitrobenzene,¹ acetone, and methyl ethyl ketone.² The second is the decrease in charge density on the chelate cation arising from the coordination bond between Cu(I) and the aromatic ligands. In order to further ascertain the above assumptions, conductance of the chelate salt was measured at 25° in CH₃CN-CCl₄ and water-dioxane mixtures. The former mixtures are composed of dipolar aprotic and nonpolar solvents and

the latter of dipolar protic and nonpolar solvents. Therefore these mixtures correspond to PhNO₂-CCl₄ and MeOH-CCl₄ mixtures examined previously,¹ respectively.

Experimental Section

Materials. Bis(2,9-dimethyl-1,10-phenanthroline)Cu(I) perchlorate (Dojin Chemicals Ltd.) was recrystallized from acetone solution and its analytical data were as follows: found(%): H, 4.11; C, 58.05; N, 9.67 (calcd(%): H, 4.17; C, 58.03; N, 9.67). Acetonitrile and dioxane were purified by the Berns and Fuoss³ and Lind and Fuoss⁴ methods, respectively. Specific conductance was 3.3×10^{-8} mho cm⁻¹ for the former and was negligible for the latter. Conductivity water was prepared by passing distilled water through mixed-bed ion exchange resin just before use and its specific conductance was usually less than $8 \times$

(1) K. Miyoshi and T. Tominaga, *J. Phys. Chem.*, in press.

(2) K. Miyoshi, *J. Phys. Chem.*, **76**, 3029 (1972).

(3) D. S. Berns and R. M. Fuoss, *J. Amer. Chem. Soc.*, **82**, 5585 (1960).

(4) J. E. Lind and R. M. Fuoss, *J. Phys. Chem.*, **65**, 999 (1961).

TABLE I: Derived Parameters

No.	Λ_0	$a, \text{\AA}$	K_A	L	$\sigma\Lambda$
1 ^a	159.43 ± 0.04	4.22 ± 0.04	0	1247 ± 16	0.046
2	142.46 ± 0.03	4.36 ± 0.06	0	1433 ± 27	0.036
3	117.48 ± 0.05	5.27 ± 0.05	0	2234 ± 42	0.059
4	107.54 ± 0.05	5.58 ± 0.04	0	2517 ± 45	0.055
5	96.29 ± 0.03	5.87 ± 0.03	0	2569 ± 33	0.029
6	89.68 ± 0.09	6.25 ± 0.15	41 ± 11	2600 ± 240	0.009
7	87.18 ± 0.04	6.12 ± 0.05	59 ± 5	2030 ± 100	0.006
8	83.33 ± 0.16	6.71 ± 0.28	165 ± 29	2480 ± 570	0.017
9	83.23 ± 0.02	6.75 ± 0.06	190 ± 7	2330 ± 140	0.009
10	80.42 ± 0.07	7.16 ± 0.15	332 ± 19	2640 ± 340	0.035
11	36.36 ± 0.04	6.21 ± 0.31	63 ± 7	3220 ± 90	0.009
12	36.58 ± 0.06	6.48 ± 0.36	82 ± 10	3640 ± 120	0.008
13	36.68 ± 0.08	6.85 ± 0.40	149 ± 19	1300 ± 190	0.015
14	36.61 ± 0.01	6.83 ± 0.21	303 ± 23	12400 ± 180	0.012
15	34.99 ± 0.08	6.48 ± 0.10	453 ± 22	19710 ± 120	0.008

^a Parameters in mixture no. 1 are quoted from the paper by K. Miyoshi, *Bull. Chem. Soc. Jap.*, in press.

10⁻⁷ mho cm⁻¹. Carbon tetrachloride was washed with conductivity water and was kept over anhydrous calcium chloride for several days. The filtrate was distilled through a 50-cm column packed with glass beads. Its specific conductance was negligibly small. Water content was found to be less than 0.01 and 0.005 wt % for CH₃CN and CCl₄, respectively, by titration with Karl Fischer reagent. Solvent mixtures were prepared individually by weight just before the measurements. Densities of the mixtures were determined in a 50-ml, single-neck capillary tube pycnometer by calibration with water at 25°. Observed values were in good agreement with those interpolated from the data by Berns and Fuoss³ for CH₃CN-CCl₄ mixtures and by Lind and Fuoss,⁴ Fabry and Fuoss,⁵ and Accascina, *et al.*,⁶ for water-dioxane mixtures. Thus other physical constants were interpolated from their values.

Apparatus and Procedure. All the equipment, cells, and general techniques used for conductance measurements were the same as those described previously.² Cell solutions were thermostated to 25 ± 0.01° in a double water bath with a mercury-in-glass thermoregulator. Dilution technique similar to that used by Pistoia and Pecci⁷ was applied to vary the salt concentration. However, in the cases of CH₃CN-CCl₄ mixtures with lower dielectric constant, solution addition technique¹ was used because measurements must be made at low salt concentrations owing to the limitation of the applicability of the conductance theory and because the value of resistance was changed slightly with time, probably due to the slight decomposition of the chelate cation. For example, in mixture no. 10 with the lowest D value, the increase was at the rate of 0.045%/hr. Therefore a small correction for resistance was made by extrapolating the observed resistances to $t = 0$.

Results and Discussion

Physical constants of the solvent mixtures (weight per cent of nonpolar components w , dielectric constant D , viscosity in centipoise η , and density d) are given in the microfilm edition of this journal.⁸ Code numbers are added for the identification of the mixtures. The observed equivalent conductance Λ and the corresponding concentration C in equivalents per liter are also given in the microfilm edition.⁸ These data were analyzed with the Fuoss-Onsager-Skinner 1965 conductance theory.⁹ No viscosity cor-

rection was made. All calculations were performed on a TOSBAC 3400 electronic computer using the least-squares method proposed by Kay.¹⁰

In Table I are summarized the derived conductance parameters where $\sigma\Lambda$ is a standard deviation. Figure 1 shows the dependence of K_A on D of the medium. It is clearly seen in the figure that the chelate salt is more dissociated in CH₃CN-CCl₄ mixtures than in water-dioxane mixtures at a given D when D is relatively high. However, the plot of $\log K_A$ vs. $1/D$ shows a concave-downward curvature in water-dioxane mixtures. A similar curvature is observed for the chelate salt in dipolar protic solvents such as normal alcohols and MeOH-CCl₄ mixtures as seen in the figure where the data of the chelate salt in MEK, normal alcohols,² and MeOH-CCl₄ and PhNO₂-CCl₄ mixtures¹ are included for comparison. Recomputation of the conductance data of Bu₄NBr in water-dioxane mixtures obtained by Mercier and Kraus¹¹ with the 1965 theory indicated that Bu₄NBr has about the same magnitude of K_A as that of the chelate salt in these mixtures despite the facts that Br⁻ ion is much smaller than ClO₄⁻ ion in size and that the tendency of cations to form ion pairs with anions is expected to be stronger for Bu₄N⁺ ion than for the chelate cation owing to the difference in charge density on the two cations. Thus it is assumed that solvation of water molecules to Br⁻ ion decreases the ionic association of Bu₄NBr in water-dioxane mixtures. This solvation phenomenon is quite similar to that observed for Bu₄NBr in MeOH-CCl₄ mixtures.¹ That is, in these mixtures the solvation of methanol to Br⁻ ion is assumed to decrease the extent of ionic association of Bu₄NBr to that of the chelate salt. However, in PhNO₂-CCl₄ mixtures, Bu₄NBr has much larger association constant than the chelate salt

(5) T. L. Fabry and R. M. Fuoss, *J. Phys. Chem.*, **68**, 971 (1964).

(6) F. Accascina, A. D'Aprano, and R. Triolo, *J. Phys. Chem.*, **71**, 3469 (1967).

(7) G. Pistoia and G. Pecci, *J. Phys. Chem.*, **74**, 1450 (1970).

(8) The data will appear following these pages in the microfilm edition of this volume of the journal. Single copies may be obtained from the Business Operations Office, Books and Journals Division, American Chemical Society, 1155 Sixteenth St., N.W., Washington, D. C. 20036. Remit check or money order for \$3.00 for photocopy or \$2.00 for microfiche, referring to code number JPC-73-819.

(9) R. M. Fuoss, L. Onsager, and J. F. Skinner, *J. Phys. Chem.*, **69**, 2581 (1965).

(10) R. L. Kay, *J. Amer. Chem. Soc.*, **82**, 2099 (1960).

(11) P. L. Mercier and C. A. Kraus, *Proc. Nat. Acad. Sci., U. S. A.*, **41**, 1033 (1955).

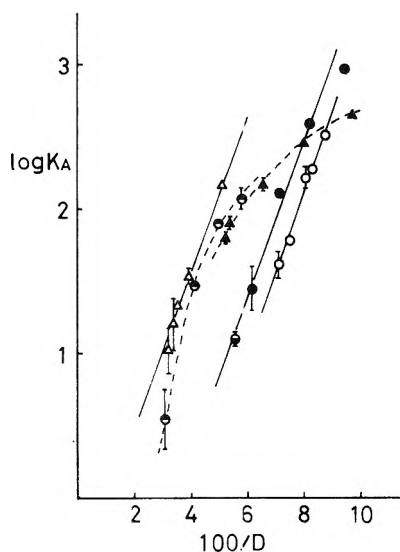


Figure 1. The dependence of association constant on D : O, in $\text{CH}_3\text{CN}-\text{CCl}_4$; ●, in $\text{PhNO}_2-\text{CCl}_4$; ●, in MEK; ●, in normal alcohols; ▲, in water-dioxane; Δ, in $\text{MeOH}-\text{CCl}_4$.

TABLE II: Derived Distances in Å and Values of E_s/kT

	$\text{MeOH}-\text{CCl}_4$	$\text{PhNO}_2-\text{CCl}_4$	$\text{CH}_3\text{CN}-\text{CCl}_4$
a_k	4.4	(4.4)	4.2
R_{∞}^+	3.3	3.2	4.0 ^a
R_{∞}^-	1.7	1.7	2.1 ^a
$R = R_{\infty}^+ + R_{\infty}^-$	5.0	4.9	6.1
a	3.5-5.5	4.3-6.3	4.2-6.7
E_s/kT	+0.09	+3.1	+4.2

^a Limiting equivalent conductances were split according to the transport numbers obtained by Kay, *et al.*, *J. Phys. Chem.*, **73**, 471 (1969).

owing to the complete lack of solvation to Br^- ion and to the difference of anion size and of charge density on the cations. In addition, the chelate cation seems to be stabilized by ion-dipole interactions in $\text{PhNO}_2-\text{CCl}_4$ mixtures.

The derived distances from several sources are given in Table II together with those obtained previously.¹ In addition, the values of the Gilkerson's term¹² calculated with the corresponding a_k values are included.

$$\ln K_A = \ln K_A^{\circ} + e^2/a_k D k T - E_s/k T$$

The corresponding values in water-dioxane mixtures could not be obtained because of extremely low solubility of the chelate salt in both water and dioxane and of the marked concave-downward curvature in the plot of $\log K_A$ vs. $1/D$. It is seen in the table that a_k from the slope in Figure 1 is nearly equal in $\text{MeOH}-\text{CCl}_4$, $\text{PhNO}_2-\text{CCl}_4$, and $\text{CH}_3\text{CN}-\text{CCl}_4$ mixtures, whereas R_{∞}^+ , the hydrodynamic radius of the cation corrected for the dipole relaxation¹³ of the polar components, and the E_s/kT value are the largest in $\text{CH}_3\text{CN}-\text{CCl}_4$ mixtures. Therefore the chelate salt seems to be more dissociated in $\text{CH}_3\text{CN}-\text{CCl}_4$ mixtures than in dipolar protic-nonpolar solvent mixtures such as $\text{MeOH}-\text{CCl}_4$ and water-dioxane mixtures, by the solvation of CH_3CN molecules to the chelate cation (R_{∞}^+) and by ion-dipole interactions (E_s/kT) between the chelate cation and CH_3CN molecules. On the other hand, in $\text{PhNO}_2-\text{CCl}_4$ mixtures, the chelate cation is stabilized chiefly by ion-dipole interactions since R_{∞}^+ in these mixtures is nearly equal to that obtained in $\text{MeOH}-$

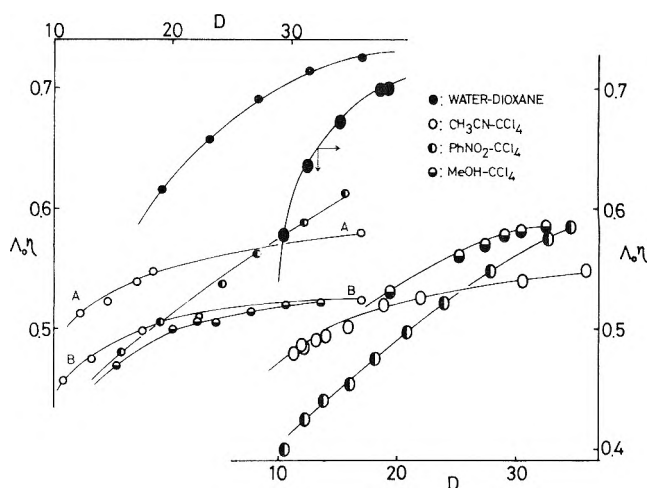


Figure 2. The dependence of the Walden products on D : large circles, lower abscissa scale; small circles, upper abscissa scale.

CCl_4 mixtures in which the chelate salt is thought to form a contact ion pair.^{1,2}

Since the conductance data of Bu_4NClO_4 and Bu_4NBr in $\text{CH}_3\text{CN}-\text{CCl}_4$ mixtures are not available in literature, the direct comparison with the chelate cation with regard to ionic association is impossible. Instead, Berns and Fuoss³ measured the conductance of Me_4NBPh_4 in these mixtures and estimated the a_k and R values to be 6.96 and 6.21, respectively, which are a little larger than the corresponding values of the chelate salt. The association constant is, however, larger by the order of 0.5 for Me_4NBPh_4 than for the chelate salt. This difference in K_A may be responsible largely for the difference in the Gilkerson's term between the two salts with approximately equal-size hydrodynamic diameter (the E_s/kT value is estimated to be zero for Me_4NBPh_4 in these mixtures). It should be noted that the E_s/kT term for the chelate salt represents not only the ion-dipole interactions but also the contribution from the decrease in charge density on the chelate cation arising from the coordination bond between Cu(I) and the aromatic ligands.

In Figure 2, the Walden products in several solvent mixtures are plotted against D . Large circles refer to the chelate salt and small to Bu_4NBr except in $\text{CH}_3\text{CN}-\text{CCl}_4$ mixtures, in which A represents the plot of Bu_4NNO_3 ¹⁴ and B, of Me_4NBPh_4 . It is seen in Figure 2 that these salts show a similar dependence of the Walden product on D in $\text{CH}_3\text{CN}-\text{CCl}_4$ and $\text{PhNO}_2-\text{CCl}_4$ mixtures. On the other hand, in water-dioxane and $\text{MeOH}-\text{CCl}_4$ mixtures, the plot has larger concave-downward curvature for the chelate salt than for Bu_4NBr . Thus it is assumed that solvation of water and methanol molecules to Br^- ion increases the hydrodynamic radius of the Br^- ion and thereby weakens the effect of the dipole relaxation of the polar components on the Walden product.

It may be concluded that the considerations described above account satisfactorily for the difference of the ion-ion interactions and ion-solvent interactions between the chelate salt and Bu_4NBr in dipolar protic-nonpolar and dipolar aprotic-nonpolar solvent mixtures.

(12) W. Gilkerson, *J. Chem. Phys.*, **25**, 1199 (1956); H. Sadek and R. M. Fuoss, *J. Amer. Chem. Soc.*, **81**, 4507 (1959).

(13) R. M. Fuoss, *Proc. Nat. Acad. Sci. U. S. A.*, **45**, 807 (1959).

(14) D. S. Berns and R. M. Fuoss, *J. Amer. Chem. Soc.*, **83**, 1321 (1961).

Solvent Isotope Effects on the Ionization of Hydrofluoric Acid¹

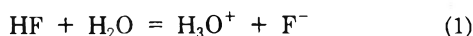
A. J. Kresge* and Y. Chiang

Department of Chemistry, Illinois Institute of Technology, Chicago, Illinois 60616 (Received October 6, 1972)

Measurements of fluoride ion activities using a selective-ion electrode and hydrogen ion activities using a quinhydrone electrode were performed on dilute hydrofluoric acid and hydrogen fluoride-sodium fluoride buffer solutions in H₂O and D₂O. These determinations lead to $pK(\text{H}_2\text{O}) = 3.165 \pm 0.007$, $K(\text{H}_2\text{O})/K(\text{D}_2\text{O}) = 2.05 \pm 0.04$ for $\text{HF} = \text{H}^+ + \text{F}^-$, and $pK(\text{H}_2\text{O}) = -0.598 \pm 0.010$, $K(\text{H}_2\text{O})/K(\text{D}_2\text{O}) = 1.13 \pm 0.03$ for $\text{HF} + \text{F}^- = \text{HF}_2^-$. Calculations show that the dominant contribution to each isotope effect comes from the twofold change in the moments of inertia of hydrogen fluoride produced by isotopic substitution; zero-point energy effects are small, principally because hydrogen fluoride, being a diatomic molecule, has no bending vibrations.

Hydrogen fluoride is the only diatomic acid available in aqueous solution with which acid catalysis may be studied conveniently. As such, it presents a number of unique opportunities for investigating acid-base catalysis² and isotope effects.³

In this paper, we determine the solvent isotope effect on the acid ionization of hydrogen fluoride (eq 1) as well as on the other ionization reaction which it undergoes in aqueous solution: association with fluoride ion to give hydrogen bifluoride (eq 2). These are quantities without which accurate evaluation of kinetic isotope effects on proton transfer from hydrofluoric acid is not possible. However, the equilibrium isotope effects are of considerable interest in themselves, for they are controlled by the same factors which make the kinetic isotope effects unusual.



The fact that hydrogen fluoride associates with fluoride ion in addition to ionizing as an acid is a complication which reduces the accuracy with which the equilibrium constant of either reaction may be determined. In order to compensate for this, an additional quantity was measured in the present work; hydrogen ion activities were determined in the usual way with a pH sensitive electrode and fluoride ion activities were measured with a fluoride ion selective-ion electrode. Since hydrogen fluoride attacks glass, a quinhydrone electrode was substituted for the more usual glass electrode in making the pH determinations.

Experimental Section

Stock solutions of hydrogen fluoride (Baker, AR), sodium fluoride (Mallinckrodt, AR, dried at 110° for 24 hr), and hydrogen chloride (Matheson, Reagent) were made from deionized H₂O, purified further by distillation from potassium permanganate and sodium hydroxide, or D₂O (Bio-Rad Laboratories, 99.8 atom % deuterium) as received. All solutions were prepared and diluted by weight, and polyethylene vessels (beakers with fitted caps or screw-cap dropping bottles) were used exclusively for all fluoride solutions. Acid concentrations were verified by titration with standard base, and sodium fluoride solutions were checked potentiometrically against fluoride

standards (Orion Research, Inc.). Fresh hydrogen fluoride and sodium fluoride stock solutions were prepared daily.

Electrode potentials were measured with a Beckman Research pH meter (Model 1019) against an Orion single-junction reference electrode (Model 90-01) which has a fiber tip and plastic body. The selective-ion electrode was a Beckman lanthanum fluoride membrane assembly (Model 39600), and a length of stiff platinum wire served as the quinhydrone electrode; solutions to be measured were saturated with quinhydrone (Fisher, Reagent).

All three electrodes were supported in a snugly fitting Teflon cap specially constructed for the plastic beakers in which the measurements were made. These beakers were clamped in a constant temperature bath operating at 25.0 ± 0.01°, and at least 30 min was allowed for their contents to reach bath temperature. Potentials were measured at least in duplicate and were reproducible to 0.1 mV. Both cells were calibrated against reference sodium fluoride or hydrogen chloride solutions immediately before each series of measurements.

Results

Potentials of the two cells were translated into hydrogen and fluoride ion activities with the aid of relationships between E and $A(\text{H}^+)$ or $A(\text{F}^-)$ obtained from calibration measurements on reference solutions. These calibration curves were determined daily; each was based upon measurements on six to eight solutions of different concentration designed to provide a range of E appropriate to the unknowns being examined at the time. Concentrations of these reference solutions were converted into activities using activity coefficients estimated by the Debye-Hückel formula with an ion-size parameter of 4.5 Å. In all cases, the relationship between E and $\log A$ was accurately linear, and slopes were generally well within 1% of the theoretically expected value. Best values of the slope and intercept parameters were obtained by least-squares analysis, and these were then used to calculate activities from the potentials of the unknown solutions. Reference solu-

- (1) This research was supported by the National Science Foundation through Grants No. GP 6580 and GP 9253 to the Illinois Institute of Technology.
- (2) (a) R. P. Bell, "The Proton in Chemistry," Cornell University Press, Ithaca, N. Y., 1959, p 179; (b) A. J. Kresge and Y. Chiang, *J. Amer. Chem. Soc.*, **90**, 5309 (1968); **94**, 2814 (1972).
- (3) A. J. Kresge and Y. Chiang, *J. Amer. Chem. Soc.*, **91**, 1025 (1969).

TABLE I: Summary of Experimental Results

$10^2[\text{HF}]_s^a$	$10^2[\text{NaF}]_s^a$	No. of solutions measured	$\text{p}K_1^b$	$\text{p}K_2^b$
H ₂ O				
5.4-0.58		8	3.164 ± 0.002	
3.1-0.33		7	3.156 ± 0.003	
8.7-0.78		8	3.166 ± 0.003	
10.9-0.92		8	3.157 ± 0.001	
6.0-0.63		8	3.159 ± 0.003	
2.7-0.30		7	3.161 ± 0.003	
2.1-0.21		7	3.167 ± 0.005	
			Av	
53-22	10	5	3.181 ± 0.004	-0.589 ± 0.011
45-18	8.5	5	3.169 ± 0.004	-0.605 ± 0.003
45-8.7	5.4	7	3.164 ± 0.003	-0.587 ± 0.005
38-12	6.4	6	3.171 ± 0.005	-0.605 ± 0.001
45-10	3.5	6	3.172 ± 0.003	-0.606 ± 0.005
			Av	
			3.171 ± 0.006	-0.598 ± 0.010
$K_1 = (6.85 \pm 0.11) \times 10^{-4}; K_2 = 3.96 \pm 0.09$				
D ₂ O				
44-8.7	7.8-5.3	5	3.474 ± 0.002	-0.541 ± 0.003
47-16	6.5	6	3.475 ± 0.007	-0.540 ± 0.002
50-15	4.6	6	3.475 ± 0.007	-0.547 ± 0.003
49-15	8.4	6	3.476 ± 0.006	-0.548 ± 0.003
49-16	4.5	6	3.480 ± 0.003	-0.545 ± 0.001
			Av	
			3.476 ± 0.006	-0.545 ± 0.004
$K_1 = (3.34 \pm 0.04) \times 10^{-4}; K_2 = 3.50 \pm 0.03$				
$K_1(\text{H}_2\text{O})/K_1(\text{D}_2\text{O}) = 2.05 \pm 0.04; K_2(\text{H}_2\text{O})/K_2(\text{D}_2\text{O}) = 1.13 \pm 0.03$				

^a Stoichiometric concentrations. ^b Error limits are standard deviations.

tions prepared from H₂O were used for the work in D₂O as well as that in H₂O, after it was established that $E^\circ(\text{D}_2\text{O}) - E^\circ(\text{H}_2\text{O})$ is constant for both electrodes; the value of this quantity was 29.65 ± 0.25 mV for the quinhydrone electrode and -0.31 ± 0.04 mV for the fluoride ion electrode.

Hydrogen ion and fluoride ion activities evaluated in this way were used directly in the expressions for $\text{p}K_1$ and $\text{p}K_2$ (eq 3 and 4). They were also converted into hydrogen ion and fluoride ion concentrations, from which, by simple stoichiometry, the concentrations of the other solute species could be calculated; this led to the other activities needed to evaluate $\text{p}K_1$ and $\text{p}K_2$. In these calculations the activity coefficient of HF was taken to be unity, and those for the ionic species were estimated as for the reference solutions, *i.e.*, by the Debye-Hückel formula with an ion-size parameter of 4.5 Å. In this case, however, the ionic strength was not known in advance, and the calculations had to be done in an iterative fashion; they were performed on a programmable desk calculator (Wang Model 362).

$$\text{p}K_1 = -\log A(\text{H}^+)A(\text{F}^-)/A(\text{HF}) \quad (3)$$

$$\text{p}K_2 = -\log A(\text{HF}_2^-)/A(\text{HF})A(\text{F}^-) \quad (4)$$

Measurements in H₂O were made on unbuffered solutions prepared from hydrofluoric acid alone and also on solutions with added fluoride ion (Table I). The unbuffered solutions contained little HF₂⁻ and were thus of little value in determining $\text{p}K_2$; their ionic strengths, however, were very low ($I = 0.0001$ – 0.001 M), and estimates of activity coefficients could therefore be expected to be very good. Since these solutions gave essentially the same

value of $\text{p}K_1$ as the buffers whose ionic strengths were considerably higher ($I = 0.03$ – 0.01 M), it was concluded that activity coefficients were estimated correctly in the latter cases as well. Measurements in D₂O were therefore performed in buffer solutions alone. In no case could consistent trends in $\text{p}K_1$ or $\text{p}K_2$ with ionic strength be detected, and the results were therefore simply averaged rather than extrapolated to $I = 0$. Averages for sets of experiments performed on a single day as well as overall averages are presented in Table I.

The weighted average value of $\text{p}K_1$ obtained here, 3.165 ± 0.007 , is in good agreement with the early potentiometric work of Broene and De Vries,⁴ who report 3.17, as well as that of Ellis,⁵ who used a conductometric method to get 3.18 ± 0.01 . Several more recent investigations have used a fluoride ion electrode similar to the one employed here. Baumann's⁶ result, 3.164 ± 0.010 , is in excellent agreement with ours, and Vanderborgh's⁷ value, as recalculated by Patel, Moreno, and Patel,⁸ 3.21 ± 0.03 , is not significantly different. Patel, Moreno, and Patel themselves report 3.233 ± 0.002 , in poor agreement with the present work. The value of $\text{p}K_1$ obtained here also gives a self-consistent kinetic analysis of rates of hydrolysis of ethyl vinyl ether measured in buffered and unbuffered hydrofluoric acid solutions, and it is in good agreement with the results of indicator experiments carried out in conjunction with that kinetic work.^{2b} The Patel, Moreno, and

- (4) H. H. Broene and T. J. De Vries, *J. Amer. Chem. Soc.*, **69**, 1644 (1947).
- (5) A. J. Ellis, *J. Chem. Soc.*, 4300 (1966).
- (6) E. W. Baumann, *J. Inorg. Nucl. Chem.*, **31**, 3155 (1969).
- (7) N. F. Vanderborgh, *Talanta*, **15**, 1009 (1968).
- (8) P. R. Patel, E. C. Moreno, and J. M. Patel, *J. Res. Natl. Bur. Stand., Sect. A*, **75**, 205 (1971).

TABLE II: Results of Isotope Effect Calculations^a

Reaction	M	MI plus LIBR	EXC	ZPE	$K(\text{H}_2\text{O})/K(\text{D}_2\text{O})$
$\text{HF} + \text{H}_2\text{O} = \text{H}_3\text{O}^+ + \text{F}^-$	1.012	2.009	0.985	0.803	1.607
$\text{HF} + \text{F}^- = \text{HF}_2^-$	1.036	1.903	0.971	0.663	1.268
$Q(\text{HF})/Q(\text{DF}) = 0.04946$			$Q(\text{HF}_2^-)/Q(\text{DF}_2^-) = 0.06273$		

^a $T = 25^\circ$.

Patel value, on the other hand, agrees less well with the indicator determinations and gives an inconsistent kinetic analysis; when the specific rate for catalysis by HF evaluated from the experiments in unbuffered solutions is used to calculate rates for the buffers, values some 10% greater than observed rates are obtained. This discrepancy is well beyond the accuracy of the kinetic method and is, moreover, in a direction opposite to that expected for additional catalysis by the bifluoride ion.

The average value of $\text{p}K_2$ obtained here, -0.598 ± 0.010 , is in good agreement with all previous reports of this quantity: -0.59 ,⁴ -0.53 ± 0.06 ,⁵ and -0.7 ± 0.2 .⁶

Discussion

Isotope Effect on the Acid Dissociation of Hydrogen Fluoride. Solvent isotope effects on acid dissociation constants originate for the most part in zero-point energy differences between reactants and products, and, for acids similar in strength to hydrogen fluoride, generally amount to about a factor of 3 ($K(\text{H}_2\text{O})/K(\text{D}_2\text{O})$).⁹ The effect observed here, 2.05 ± 0.04 , is therefore somewhat weaker than could have been anticipated. It might, moreover, be unusual in another respect, for hydrogen fluoride is a small diatomic molecule and properties other than its zero-point energy could be affected appreciably by isotopic substitution. In order to investigate this point, as well as to attempt to account for its magnitude, we performed a theoretical calculation of this isotope effect.

The calculation was carried out in the usual way by formulating the isotope effect in terms of ratios of partition functions of isotopically substituted molecules (eq 5).¹⁰ The partition function ratios for hydronium ion and water are available from a recent semitheoretical determination.¹¹ That for hydrogen fluoride was evaluated using the vibrational frequency measured for HF in H_2O solution¹² and the theoretically expected isotopic shift, *i.e.*, $\nu(\text{DF}) = \nu(\text{HF}) (\mu(\text{HF})/\mu(\text{DF}))^{1/2}$, where $\mu(\text{HF})$ and $\mu(\text{DF})$ are the reduced masses of HF and DF, respectively.

$$K(\text{H}_2\text{O})/K(\text{D}_2\text{O}) = \frac{(Q(\text{H}_3\text{O}^+)/Q(\text{D}_3\text{O}^+))}{(Q(\text{H}_2\text{O})/Q(\text{D}_2\text{O}))(Q(\text{HF})/Q(\text{DF}))} \quad (5)$$

The result, $K(\text{H}_2\text{O})/K(\text{D}_2\text{O}) = 1.61$, is in reasonably good agreement with the experimental value, considering the ill-defined nature of the vibrational band of hydrogen fluoride in aqueous solution.¹² Use of the gas-phase vibrational frequency, which is known with much greater accuracy,¹³ gives a result ($K(\text{H}_2\text{O})/K(\text{D}_2\text{O}) = 2.25$) in even better agreement with experiment, but this would seem to be unjustified in view of the fact that the experimental value refers to aqueous solution.

These calculations include medium effects on the transfer of hydronium ion and water species from H_2O to D_2O (as librational frequency contributions to $Q(\text{H}_3\text{O}^+)/$

$Q(\text{D}_3\text{O}^+)$ and $Q(\text{H}_2\text{O})/Q(\text{D}_2\text{O})$), but they do not allow for similar effects on hydrogen fluoride or the fluoride ion. Two different estimates of the free energy of transfer of fluoride ion¹⁴ both predict a medium effect for this species which contributes a factor of 0.85 to $K(\text{H}_2\text{O})/K(\text{D}_2\text{O})$. The medium effect on hydrogen fluoride is more difficult to assess; it is, however, likely to be small.

Fortunately, much of the insight which these calculations provide into the nature of this isotope effect does not depend at all strongly upon medium corrections or the choice of vibrational frequency. Table II lists separately the contributions to the overall effect made by the translational (M), rotational (MI plus LIBR), Boltzmann excitation of vibrational levels (EXC), and zero-point energy (ZPE) parts of the partition function ratios. It may be seen that the dominant factor is provided by MI plus LIBR. Much of that, moreover, may be traced to the effect of isotopic substitution on the two principal moments of inertia of hydrogen fluoride; this alone contributes 1.90 to $K(\text{H}_2\text{O})/D(\text{D}_2\text{O})$. The librational motions of water and the hydronium ion, which replace free rotation in these species, add another factor of 1.06 to bring the overall rotational contribution up to 2.01.

In contrast to this, the zero-point energy effect is small and actually inverse. This is a direct consequence of the fact that hydrogen fluoride has no bending vibrations. Even though its single stretching frequency is high, $\nu(\text{HF}) = 3450 \text{ cm}^{-1}$,¹² that alone is not enough to offset the difference between the frequency sums for hydronium ion and water, $\sum \nu(\text{H}_3\text{O}^+) - \sum \nu(\text{H}_2\text{O}) = 12,320 - 8550 = 3770 \text{ cm}^{-1}$.¹¹ As a result, the product of this reaction (H_3O^+) has nearly 0.5 kcal more zero-point energy than the total for both reactants (HF and H_2O), and the zero-point energy factor in the isotope effect is therefore less than unity.

It is of interest to compare this situation with the solvent isotope effect on the acid ionization of a less unusual substrate. A typical carboxylic acid, for example, has one stretching, $\nu(\text{OH}) \approx 3000 \text{ cm}^{-1}$, and two bending vibrations, $\nu(\text{OH}) \approx 1400$ and 900 cm^{-1} ,¹⁵ which are sensitive to isotopic substitution. The sum of these frequencies, 5300 cm^{-1} , is considerably greater than the difference between the sums for hydronium ion and water, 3770 cm^{-1} ,

- (9) P. M. Laughton and R. E. Robertson in "Solute-Solvent Interactions," J. F. Coetzee and C. D. Ritchie, Ed., Marcell Dekker, New York, N. Y., 1969, p 407.
- (10) L. Melander, "Isotope Effects on Reaction Rates," Ronald Press, New York, N. Y., 1960; W. A. Van Hook in "Isotope Effects in Chemical Reactions," C. J. Collins and N. S. Bowman, Ed., Van Nostrand-Reinhold, New York, N. Y., 1970, Chapter 1.
- (11) R. A. More O'Ferrall, G. W. Koepl, and A. J. Kresge, *J. Amer. Chem. Soc.*, **93**, 1, 9 (1971).
- (12) H. H. Hyman, M. Kilpatrick, and J. J. Katz, *J. Amer. Chem. Soc.*, **79**, 3668 (1957).
- (13) K. Nakamoto, "Infrared Spectra of Inorganic and Coordination Compounds," 2nd ed, Wiley-Interscience, New York, N. Y., 1970, p 78.
- (14) C. G. Swain and R. W. Bader, *Tetrahedron*, **10**, 182 (1960); E. M. Arnett and D. R. McKelvey in ref 9, p 407.
- (15) L. J. Bellamy, "The Infrared Spectra of Complex Molecules," Wiley, New York, N. Y., 1960, Chapter 10.

and that makes the isotopically sensitive zero-point energy of the reaction product in this case some 2.2 kcal less than the total for the reactants. This contributes a factor of approximately 3.0 to $K(\text{H}_2\text{O})/K(\text{D}_2\text{O})$. It is likely, moreover, that this will be the only significant contribution to this isotope effect, for the moments of inertia of the carboxylic acid will be relatively insensitive to isotopic substitution, and M and EXC will probably contribute little as well.

Other weak polyatomic acids will behave similarly, *i.e.*, will receive minor to negligible contributions from M, MI plus LIBR, and EXC to solvent isotope effects on their acid ionization equilibria, which leaves zero-point energy effects as the only important factor. The isotope effect on the ionization of hydrogen fluoride is therefore extraordinary in being principally rotational and not vibrational (ZPE) in origin.

Isotope Effect on the Association of Hydrogen Fluoride with Fluoride Ion. The properties of hydrogen fluoride which make the isotope effect on its acid ionization exceptional also influence the effect on its association with fluoride ion. Again, this becomes apparent when a theoretical calculation of the isotope effect is carried out. This calculation was performed on the basis of eq 6 using the value of $Q(\text{HF})/Q(\text{DF})$ obtained as described above from the

$$K(\text{H}_2\text{O})/K(\text{D}_2\text{O}) = (Q(\text{HF}_2^-)/Q(\text{DF}_2^-))/(Q(\text{HF})/Q(\text{DF})) \quad (6)$$

vibrational frequency of HF measured in aqueous solution. Aqueous solution vibrational frequencies were also used to evaluate $Q(\text{HF}_2^-)/Q(\text{DF}_2^-)$. In this case, values for DF_2^- as well as HF_2^- are available,¹⁶ but, for the sake of consistency with the hydrogen fluoride calculation, experimental numbers for HF_2^- only were used. Frequencies for DF_2^- were calculated from these using the theoretically expected isotopic shift, which again was equal to the square root of the ratio of the reduced masses of the two molecules.¹⁷ The DF_2^- frequencies obtained in this way were actually in good agreement with the experimentally observed values, and use of the latter would have raised $K(\text{H}_2\text{O})/K(\text{D}_2\text{O})$ by only 5%.

The calculated isotope effect, $K(\text{H}_2\text{O})/K(\text{D}_2\text{O}) = 1.27$, is in even better agreement with the experimental value, 1.13 ± 0.03 , than was the case for the acid ionization reaction. This time, however, use of the gas-phase frequency for HF shifts the result away from the observed value by a considerable amount, $K(\text{H}_2\text{O})/K(\text{D}_2\text{O}) = 1.78$, and that tends to reinforce the idea that solution frequencies are more appropriate than gas-phase values for calculating solution isotope effects.

No medium effects are included in these calculations. The effect on fluoride ion, evaluated as before, would raise $K(\text{H}_2\text{O})/K(\text{D}_2\text{O})$ by 1/0.85. That on hydrogen bifluoride is much more difficult to estimate, and there is even some

uncertainty about its direction. Halide ions have medium effects which increase with increasing ion size, with fluoride ion being the only member of the series showing an inverse effect; this suggests that the effect on hydrogen bifluoride might be in the normal direction. Methyl fluoride, on the other hand, although also larger than fluoride ion, has an inverse medium effect;¹⁸ this suggests that the effect on hydrogen bifluoride could be inverse.

Here again, however, medium effects do not alter the major conclusions which can be drawn from these calculations. As Table II shows, the rotational parts of the partition function ratios once more make the largest contribution to the isotope effect. This time, moreover, the entire MI plus LIBR factor of 1.90 comes from the moments of inertia of hydrogen fluoride, for the only other isotopically substituted species involved, bifluoride ion, is a linear symmetrical molecule¹⁹ whose principal moments of inertia are not affected by isotopic substitution.

The zero-point energy effect is again inverse and relatively weak, once more because hydrogen fluoride has no bending vibrations. It is interesting that this factor would have been even more strongly inverse, perhaps enough to make the overall isotope effect less than unity, were it not for the fact that one of the four normal vibrations of hydrogen bifluoride (the symmetrical stretch) is not isotopically sensitive. The inverse nature of the ZPE factor is of significance in connection with kinetic isotope effects on proton transfer from hydrogen fluoride, which are also unusually weak, a phenomenon ascribed to strong bending vibrations in the transition state which are uncompensated for in the diatomic proton donor.³ The present reaction is in fact closely analogous to the kinetic situation, for the two degenerate bending vibrations of hydrogen bifluoride, $\nu(\text{HF}) = 1206 \text{ cm}^{-1}$, here provide more than half of the product zero-point energy.

Hindered Rotation of Hydrogen Fluoride Species. Both a referee and Professor R. P. Bell (personal communication) have pointed out that hydrogen fluoride will be hydrogen bonded in aqueous solution, and that its rotations will thus be hindered rather than free. It would therefore be more appropriate to replace the moment of inertia factors in the present calculations by zero-point energy and Boltzmann excitation contributions from librational vibrations. The necessary frequencies, unfortunately, are not known, but our work on water and hydronium ion species¹¹ suggests that such a substitution would, if anything, reinforce the conclusion that the isotope effects reported here are largely rotational (or librational) in origin.

(16) L. H. Jones and R. A. Penneman, *J. Chem. Phys.*, **22**, 281 (1954).

(17) G. Herzberg, "Molecular Spectra and Molecular Structure," Van Nostrand, New York, N. Y., 1945, p 145.

(18) C. G. Swain and E. R. Thornton, *J. Amer. Chem. Soc.*, **84**, 822 (1962).

(19) W. C. Hamilton and J. A. Ibers, "Hydrogen Bonding in Solids," W. A. Benjamin, New York, N. Y., 1968, p 108.

Effect of Various Gases on the pH of Water

Gordon H. Fricke, Rick L. Carpenter, and Rubin Battino*

Department of Chemistry, Wright State University, Dayton, Ohio 45431 (Received September 25, 1972)

Publication costs assisted by The Petroleum Research Fund

Ultrapure water (>15 megohm cm, 25°) was saturated with various "inert" gases: H_2 , O_2 , N_2 , He, Ar, CH_4 , and CO. The pH difference between degassed water and water saturated with a gas was found to be ± 0.06 (t_{90}) for individual measurements and ± 0.01 (t_{90}) for the average of a series of measurements. These differences are considered to be within experimental error at a pH of 7.00. Thus, previously reported "anomalous" pH effects are either due to impurities in materials or artifacts in the experiment.

Introduction

The pH of relatively pure degassed water was found¹ to shift from a value of 7.00 for pure water to values between 7.50 and 8.00 when the water was saturated with supposedly "inert" gases such as He, N_2 , Ar, and Ne. In what follows we report on our investigation of this phenomenon.

Our early experiments seemed to confirm these results, but we found that each improvement in the purification of water, in the purification of the gases, and in the experimental design resulted in a decrease in the difference between the pH observed for degassed water and the pH observed for water saturated with one of the gases.² The result of our most recent experiments using our most refined procedures is that the pH shifts are zero within the experimental error obtainable with our instruments.

If the pH shift had been real, it was proposed that the decrease in the activity of the hydrogen ions may have been due to an altering of the water structure or to the formation of weak coordinate bonds between the gas and hydrogen ions, causing the gas to act like a Lewis base.^{1,2} It has been suggested that cations such as HNe^+ are likely to exist in water owing to the large electronegativity of neon.³ This would cause an effective decrease in the hydrogen ion concentration which would be observed as a shift to a greater pH value. Although this prediction may be valid, apparently the concentration of the cation present at atmospheric pressure is too low to be detected by conventional pH measurements such as those employed in this research.

Experimental Section

Tap distilled water was redistilled in a Corning all Pyrex still and then transferred to a self-contained recirculating "water system." The water system consisted of four mixed-bed ion exchange columns, an activated charcoal column, a submicron Millipore filter, a conductivity cell, and a peristaltic pump. Tygon tubing was used in the peristaltic pump. The four Illinois Water Treatment Co. ion exchange columns were used in the following order: one Universal Grade, two Research Grade, and one Puritan Grade. All columns were wrapped with aluminium foil to retard degradation of the ion exchange material by light. All connections in the system were made by glass (Pyrex) and Teflon. A procedure similar to this was recommended by Hughes, *et al.*,⁴ and Iverson⁵ for the attainment of ultrapure water.

The gases were purified before they were dispersed into the water in the reaction vessel. Each gas was passed through a series of liquid scrubbers which were separated by Kjeldahl traps. The scrubbers were arranged in the following order: base, acid, base, acid, pH 7.00 phosphate buffer, water, and water. The acid was 5% H_2SO_4 and the base was saturated $Ca(OH)_2$. After the scrubbers, the gas passed through three cold traps (maintained at *ca.* -78°) packed with glass beads, molecular sieves, and glass beads, respectively. We used three cold traps in series because we found that the microscopic mist created by the scrubbers was not removed by a single trap.

The all Pyrex glass 1-l. reaction vessel with Rotaflon Teflon stopcocks was designed so that only a Teflon-coated magnetic stirring bar and the gas dispersion tube came in contact with the water after the water entered the vessel. The reaction function was separated from the measuring function. A stopcock located at the bottom of the reaction vessel was opened to allow water to flow from the vessel so that measurements could be made at various times without disturbing the reaction. Water flowed through the conductivity cell, through the pH cell, and was then discarded. The reaction vessel was directly attached by Pyrex tubing to the ultrapure water system and to the vacuum system which was used to degas the water. The reaction vessel had been steamed with about 40 l. of water before it was glass blown into the system. Figure 1 shows the reaction vessel with the location of the flow-through conductivity cell and the flow-through pH cell.

For most of the runs, the pH of the water and the aqueous solutions was measured with a Sargent Model 30070-10 combination electrode which contained a platinum rope junction for the reference electrode. Two nitrogen runs and all of the hydrogen runs were performed with a Fisher Model E-5 combination electrode which contained a ceramic disk junction. The latter electrode was necessary for the hydrogen runs because the platinum rope of the Sargent electrode apparently established a platinum-hydrogen electrode.² The reference potential of the platinum rope electrode was altered greatly. The ceramic disk electrode eliminated this problem.

- (1) E. M. Holleran, J. T. Hennesy, and F. R. LaPietra, *J. Phys. Chem.*, **71**, 3081 (1967).
- (2) R. L. Carpenter, M.S. Thesis, Wright State University, Dayton, Ohio, 1972.
- (3) B. Fung, *J. Phys. Chem.*, **69**, 596 (1965).
- (4) R. C. Hughes, P. C. Müräu, and G. Gundersen, *Anal. Chem.*, **43**, 691 (1971).
- (5) A. Iverson, *J. Phys. Chem.*, **68**, 515 (1964).

The combination electrode was located below the level of the liquid in the reaction vessel (see Figure 1). A tygon tube, which was partially filled with water, was connected to the vent in the electrode. This pressure-compensating tube was raised to the proper level to balance the pressure head of the liquid in the reaction vessel.

The pH readings were obtained with an Orion Ionalyzer Model 801 digital pH/mV meter. Simultaneously, the pH was monitored with a Texas Instruments Servo-Riter II recorder. The pH meter and recorder were adjusted with pH 7.00 and 4.01 buffers before each run. After the buffer adjustment, the electrode was rinsed and soaked in deionized water for a minimum of 20 min before it was placed in the flow-through pH cell. The electrode was checked with the buffers after each run.

At one point, erratic pH readings were observed which seemed to be caused by the magnetic stirring motor used to rotate the stirring bar. The magnet used to turn the magnetic stirring bar in the reaction vessel was then mounted on the end of a 7-in. rod which was driven by a high-torque motor (see Figure 1). No further problems were observed with the motor.

Since the resistance of pure water varies from 31.8 megohm cm at 15° to 11.1 megohm cm at 35°^{5,6} and since possible resistance changes were anticipated, the resistance of the water was monitored whenever pH measurements were made. The resistance was measured with a new design flow-through conductivity cell⁷ and an Industrial Instruments Model RC-16B2 conductivity bridge. The conductivity cell had a cell constant of approximately 0.005 cm⁻¹.

The temperature of the water in the reaction vessel was measured with a copper-constantan thermocouple which was attached to the outside of the reaction vessel. The thermocouple was thermally insulated from the surroundings.

The water in the reaction vessel was degassed by the extraction procedure of Battino, *et al.*⁸ The final residual pressure in all cases was less than about 100 μ . The pressure was measured with a Consolidated Vacuum Corp. thermocouple vacuum gauge Type GTC-100.

Measurements were carried out in the following manner. The reaction vessel was flushed with gas, and with the gas still flowing into the vessel, the pure water was allowed to flow into the vessel through the conductivity cell. The vessel was rinsed twice by this procedure with about 800 ml of water each time before introducing the test water into the vessel. The pH, resistance, and temperature of the final incoming waters were recorded. The water was purged for about 10 min and degassed. The magnetic stirring bar was rotating at a fairly high speed during this procedure. The purging and degassing procedure were repeated. The second time the extraction was continued until the residual pressure was about 100 μ . Then, with the stirrer stopped, gas was allowed to enter the reaction vessel above the water. The bottom stopcock was opened. The resistance, pH, and temperature of the degassed water were measured, after which the water was purged with the stirrer rotating. At various times about 100 ml of water were withdrawn from the vessel and the resistance, pH, and temperature were recorded. All gases were purged for a minimum of 1 hr before the final readings were made. No additional resistance or pH changes were found for water which had been purged for up to 24 hr.

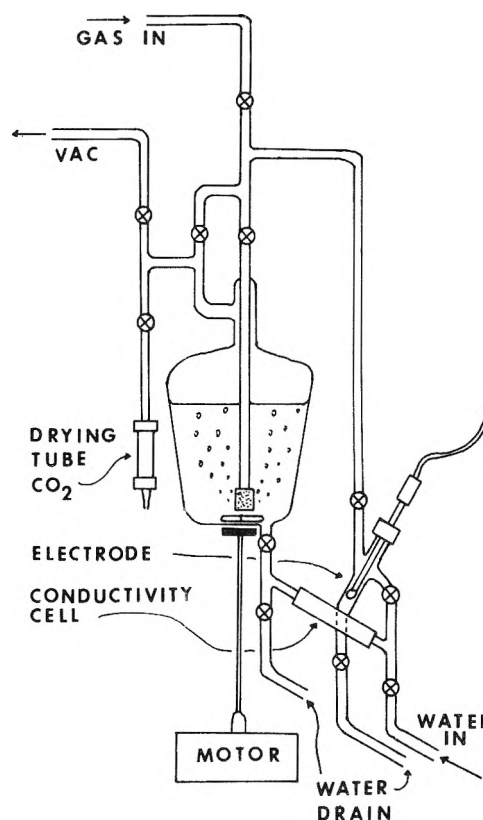


Figure 1. Reaction vessel for measurements showing pH electrode flow-through conductivity cell, stopcocks, gas dispersion tube, stirring apparatus, and flow patterns.

The water was brought into the reaction vessel from the recirculating water system under an atmosphere of the gas in question. From the time the water entered the reaction vessel until the final measurements were made was a maximum 6 hr. There appears to be negligible conductivity changes (less than a few per cent) in the water if it remains in contact with Pyrex glass for less than 24 hr.

The unstable pH response in an unbuffered flowing water system which was reported by Bates⁹ and Quickenden¹⁰ was also observed in this research. The pH differences reported in this paper were for a static condition. The electrode responded with a stable, constant pH value within 1 min of the time the flow was stopped. The reading remained constant for a minimum of 2 min. Occasional drifting was observed for longer time intervals.

Results and Discussion

The result of purging ultrapure water with various gases was measured by a change in pH from degassed water to water saturated with a gas: $\Delta\text{pH} = \text{pH of saturated water} - \text{pH of degassed water}$. The results for the seven gases are presented in Table I. The reported average deviation of ΔpH is for absolute values of the deviations

The reaction vessel was not thermostated. It was observed that, in some cases, the resistance of the water in-

- (6) G. Otten, *Amer. Lab.*, 41, July, 1972.
- (7) G. H. Fricke and R. Battino, to be submitted for publication.
- (8) R. Battino, M. Banzhof, M. Bogan, and E. Wilhelm, *Anal. Chem.*, 43, 806 (1971).
- (9) R. G. Bates, "Determination of pH: Theory and Practice," Wiley, New York, N. Y., 1964.
- (10) T. I. Quickenden, D. M. Betts, B. Cole, and M. Noble, *J. Phys. Chem.*, 75, 2830 (1971).

TABLE I: Temperature Corrected ΔpH Values^a

Gas	No. of runs	Absolute average deviation, ΔpH	Standard deviation, ΔpH
N ₂	7	0.03	0.04
O ₂	4	0.04	0.05
H ₂	2	0.03	0.04
He	2	0.03	0.04
Ar	4	0.03	0.04
CH ₄	2	0.03	0.04
CO	1	0.06	
Total	22	0.030	0.038

^a Confidence interval (f_{90}) mean = 7.00 ± 0.014 . Confidence interval (f_{90}) individual = 7.00 ± 0.065 .

creased during the course of the reaction. This was attributed, in those cases, to a lowering of the temperature of the water by as much as 3°. The water temperature was lowered by the gas which had just gone through three cold traps at -78°. The pH is also temperature dependent by about 0.017 pH/°C at 25°. The pH values in Table I have been corrected for temperature differences between degassed and saturated water.

The value of the pH of pure water was as low as about 6.9 with each run. The buffer which was initially pH 7.00 also showed this low pH value at the end of a run. After a few minutes in the high ionic strength buffer solution the electrode responded properly to the buffer with the original value of pH 7.00. Apparently, the low pH response of the electrode in pure water was due to the great difference in ionic strength between pure water and the buffer system in which it was originally calibrated.

It was shown in a separate study¹¹ with CO₂ that it is extremely difficult to degas water which is known to contain CO₂. In any case, the difference in pH between the initial degassed water and the final gas-saturated water is

the value which shows the effects of saturating water with a gas. It is observed from the confidence interval results that the pH shifts are negligible. These shifts are within experimental error for a pure unbuffered water system.

In conclusion, we found that the pH changes observed in the early stages of this research complement those of Holleran, *et al.*¹ In view of the latest data it appears that, with the proper precautions, ultrapure water may be purged with various gases with no pH shift. Therefore, if a pH shift is observed upon purging water with one of the gases which we have checked, we suggest that the effect is due to impure water, impure gas, or some extrinsic property of the apparatus.

Drost-Hansen¹² found similar anomalous effects in determining the conductivity (to a few parts in 100,000) in dilute solutions of potassium chloride (10^{-3} – 10^{-5} M) or tetraethylammonium bromide (10^{-5} M). Solutions which had been saturated with helium were then saturated with argon or methane with a subsequent increase (several tenths of a per cent) in conductivity. This effect disappeared when the argon or methane was thoroughly scrubbed (three acid washes, three base washes, and three distilled water at the end). Drost-Hansen traced the initial anomalous effect to carbon dioxide contamination of the order of a few parts per billion in the compressed gases.

Acknowledgments. The authors wish to thank Dr. Emerich Wilhelm and Mr. Daniel R. Grove for their assistance at various stages of this research. Acknowledgment is made to the donors of The Petroleum Research Fund, administered by The American Chemical Society, for support of this research.

(11) The average pH of three runs of pure water saturated with CO₂ was 3.94 ± 0.00 at 27.6° and 740 mm.

(12) W. Drost-Hansen, University of Miami, personal communication, 1972. Work done in 1962.

Thermochemistry of the Diels–Alder Reaction. III. Heat of Addition of Cyclopentadiene to Maleic Anhydride¹

F. E. Rogers* and S. W. Quan

Department of Chemistry, University of Dayton, Dayton, Ohio 45469 (Received September 25, 1972)

Publication costs assisted by The University of Dayton

The heat for the Diels–Alder addition of cyclopentadiene to maleic anhydride has been determined by solution calorimetry. Corrections for the heats of solution and vaporization give the heat of the gas-phase reaction at 25°. Implications of these results are discussed.

Introduction

The Diels–Alder (D–A) reaction is an extremely useful reaction for the formation of carbocyclic or heterocyclic compounds of one or more rings.² Over the years, the reaction has received considerable synthetic and theoretic-

cal attention³ and our previous papers^{1,4} have dealt with the thermochemistry of the D–A reaction. We reported the heats of addition of tetracyanoethylene to five acyclic

(1) For Part II of this series see F. E. Rogers, *J. Phys. Chem.*, **76**, 106 (1972).

TABLE I: Heats of Solution, Vaporization, and Reaction (kcal/mol, 25°)

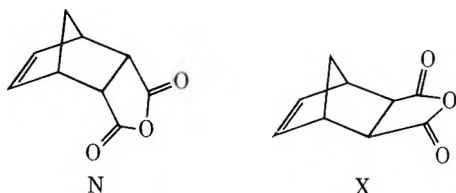
	ΔH_{soln}	ΔH_{v}	$\Delta H_{\text{r}}(\text{exptl})$	$\Delta H_{\text{r}}(\text{soln})$	ΔH_{r}	$\Delta H_{\text{r}}(\text{g})$
Maleic anhydride	3.76 ± 0.08 (0.100) ^a	17.1 ± 1.2 ^c				
Cyclopentadiene	0.1 ^b (0.080) ^a	6.9 ^d				
Endo adduct (N)	3.43 ± 0.05 (0.100) ^a	23.19	-22.45 ± 0.03	-26.21	-25.78	-26.59

^a Average amount of component (grams) used. ^b Reference 1. ^c Reference 16. ^d R. Stull, E. F. Westrum, Jr., and G. C. Sinke, "The Chemical Thermodynamics of Organic Compounds," Wiley, New York, N. Y., 1969.

and cyclic dienes in the solution, standard state, and gas phase. Comparison of these results with the analogous ethylene reactions yielded the empirical equation for the estimation of the heat of any D–A reaction.

$$\Delta H_{\text{r}}^{\text{d}}(\text{g}) - \Delta H_{\text{r}}^{\text{e}}(\text{g}) = \Delta H_{\text{H}}^{\text{d}} + 32.8 \quad (1)$$

To a first approximation, the difference in the gas-phase heat of addition of any diene to dienophile (d) and ethylene is given by the difference in the heat of hydrogenation of dienophile (d) and ethylene (-32.8 kcal/mol). Since values of $\Delta H_{\text{r}}^{\text{e}}(\text{g})$ and ΔH_{H} are readily available from existing literature, $\Delta H_{\text{r}}^{\text{d}}(\text{g})$ can easily be determined. This equation has been tested further and we now wish to report the heat of addition of cyclopentadiene to maleic anhydride to form *endo*-5-norbornene-2,3-dicarboxylic anhydride (N). Corrections for the heats of solution and vaporization gave the heat of the D–A reaction in the solution, standard state, and gas phase. Since the *endo* (N) compound is the major product (~99%) of the reaction⁵ it was necessary to estimate the heat leading to the *exo* product from other data. The kinetic implications of these results are discussed.



Experimental Section

Maleic anhydride (Eastman Organic Chemicals) purified three times by vacuum sublimation at 35° melted at 52° (lit.⁶ mp 52°). The purified compound was stored in a desiccator. Cyclopentadiene was obtained by cracking dicyclopentadiene (Aldrich Chemical Co.) above 164°. The adduct, *endo*-5-norbornene-2,3-dicarboxylic anhydride was prepared by adding an excess of freshly prepared cyclopentadiene to a benzene solution of maleic anhydride at room temperature. The solvent was removed *in vacuo*; the crude product was washed with cold ether and sublimed three times at 88–90°, mp 164–165° (lit. mp 164°, 165°⁸). The nmr spectrum is the same as that reported by Wilder and Gratz.⁹

The addition reaction was run at 25 ± 0.5° in a solution calorimeter by previously described techniques.⁴ The reaction is quantitative and complete in less than 10 min as shown by uv spectroscopy when an excess of cyclopentadiene is used. To compensate for the slow dimerization reaction of cyclopentadiene both reference and reaction calorimeter contained the same amount of the diene. The

reaction was initiated by the injection of about 1 mmol of maleic anhydride into 200 ml of dichloromethane containing a tenfold excess of cyclopentadiene. The results in Table I are the average of five runs.

The heats of vaporization of the reactants are known and the heat of sublimation of the adduct (N) was determined by the McLeod gauge method previously described.^{1,4} The vapor pressure (VP) of the *endo* adduct was measured over the temperature range 74.4–94.2° at 4° intervals. A least-squares slope of a plot of log (VP) against 1/T gave a heat of sublimation at 84.3° of 23.20 kcal/mol. The value corrected to 25° is 23.19 kcal/mol.

The heat of solution of cyclopentadiene is known from our previous work.¹ The heats of solution of maleic anhydride were measured by introducing *ca.* 0.1-g samples of each compound into the calorimeter containing 200 ml of dichloromethane at 25.0 ± 0.5°. The values reported in Table I are the average of at least three runs.

Discussion

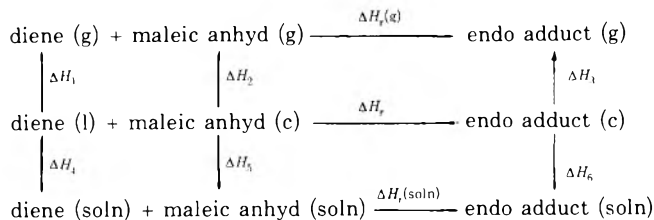
The heat of the Diels–Alder reaction in the solution standard state and gas phase were calculated according to the cycle shown in Scheme I. The values of ΔH_1 , ΔH_2 , and ΔH_4 are already known so that a complete enthalpy description of the cycle comes with a knowledge of ΔH_3 , ΔH_5 , ΔH_6 , and the heat of the reaction in any one phase. When maleic anhydride was added to the diene solution the measured experimental enthalpy is given by the relation, $\Delta H_{\text{r}}(\text{exptl}) = \Delta H_5 + \Delta H_{\text{r}}(\text{soln})$. Subsequent treatment of the data in the manner previously described^{1,4} allows the calculation of ΔH_{r} and $\Delta H_{\text{r}}(\text{g})$. These results are shown with the analogous ethylene reaction in Table I. The data show the heat of the D–A reaction is about the same in any state; the heat of reaction in the gas and solution phase differ by only 0.4 kcal/mol. This difference is given by the expression

$$\Delta H_{\text{r}}(\text{g}) - \Delta H_{\text{r}}(\text{soln}) = \sum \Delta H_{\text{soln}}(\text{reactants}) - \Delta H_{\text{soln}}(\text{adduct})$$

- The following reviews summarize our knowledge of the Diels–Alder reaction: (a) A. Wasserman, "Diels–Alder Reaction," Elsevier, New York, N. Y., 1965; (b) J. Hamer, "1,4-Cycloaddition Reactions; The Diels–Alder Reaction in Heterocyclic Synthesis," Academic Press, New York, N. Y., 1967; (c) J. Sauer, *Angew. Chem., Int. Ed. Engl.*, **5**, 211 (1966); **6**, 16 (1967).
- See W. C. Herndon, *Chem. Rev.*, **72**, 157 (1974), and references therein.
- F. E. Rogers, *J. Phys. Chem.*, **75**, 1734 (1971).
- O. Diels and K. Alder, *Ann.*, **460**, 98 (1928).
- R. C. Weast, "Handbook of Chemistry and Physics," 47th ed., Chemical Rubber Publishing Co., Cleveland, Ohio, 1966.
- R. E. Pincock, K. R. Wilson, and T. E. Klovsky, *J. Amer. Chem. Soc.*, **89**, 6890 (1967).
- D. Craig, *J. Amer. Chem. Soc.*, **73**, 4889 (1951).
- P. Wilder, Jr., and R. F. Gratz, *J. Org. Chem.*, **35**, 3269 (1970).

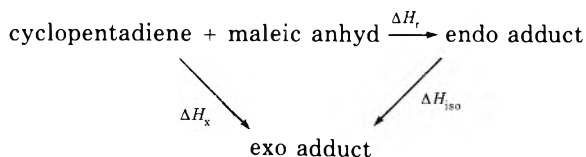
where the heats of solvation are defined as $\Delta H_{\text{solv}}(\text{adduct}) = \Delta H_6 - \Delta H_3$ and $\Sigma \Delta H_{\text{solv}}(\text{reactants}) = \Delta H_4 + \Delta H_5 - (\Delta H_1 + \Delta H_2)$. The near equality of the solution and gas-phase reaction heats requires that the heats of solvation of the reactants and products approximate each other. Since the total molar volume is greater for the reactants than the adduct the solvation possibilities are greater hence $\Delta H_{\text{solv}}(\text{reactant}) \geq \Delta H_{\text{solv}}(\text{adduct})$. These observations would require the solution heat of reaction to be equal to or slightly greater than the value for the gas-phase reaction. The available data, albeit limited, suggests this is so.

Scheme



If the solution heat of reaction is close to the gas-phase reaction heat the next step then is to estimate the latter value using eq 1. The heat of the analogous ethylene reaction, $\Delta H_r^e(\text{g})$, is -23.8 kcal/mol; the heat of hydrogenation of maleic anhydride to succinic anhydride is -33.02 kcal/mol. Substitution gives $\Delta H_r^d(\text{g}) = -24.02$ kcal/mol, which is smaller than the experimental value by 2.57 kcal. Considering the simplicity of the method the agreement must be considered satisfactory.

Experimentally it is only possible to measure the reaction heat leading to the endo adduct (N). From other data it is possible to estimate the reaction heat leading to the exo adduct (X) according to the following cycle



where ΔH_r is our experimental heat; ΔH_{iso} , the heat of isomerization; and ΔH_x , the reaction heat leading to exo. The equilibration of pure N or X at 170° lead to an equilibrium mixture of 55% X and 45% N.⁷ It is reasonable to assume that C_p for isomerization is nearly zero, hence $\Delta H_{\text{iso}}(170^\circ) \approx \Delta H_{\text{iso}}(25^\circ)$. From the equilibrium constant, $K_{\text{iso}} = X/N$ and $\Delta G_{\text{iso}} = -RT \ln K_{\text{iso}}$, we calculate $\Delta G_{\text{iso}} = -0.177$ kcal/mol. From the relationship, $\Delta G_{\text{iso}} = \Delta H_{\text{iso}} - T\Delta S_{\text{iso}}$ where ΔS_{iso} is taken as 2 eu,¹⁰ $\Delta H_{\text{iso}} = 0.709$ kcal/mol or the endo adduct is slightly more stable. Substitution in the equation $\Delta H_x = \Delta H_r + \Delta H_{\text{iso}}$ where $\Delta H_r = -26.21$ gives $\Delta H_x = -25.5$ kcal/mol, or the reaction leading to the exo isomer is less exothermic by 0.7 kcal/mol. This value is in even closer agreement with that predicted by eq 1, -24.0 kcal/mol. Since the equation makes no provision for the development of new stabilizing interactions it is reasonable to assume better agreement for the less stable isomer.

The enhanced stability of the endo isomer is also consistent with some related work. While this reaction has been studied repeatedly and found to yield the endo isomer "exclusively," Wilder and Gratz fractionally crystallized a kinetically determined reaction mixture and found 1.4% exo.⁹ If it is assumed that the formation of endo (N)

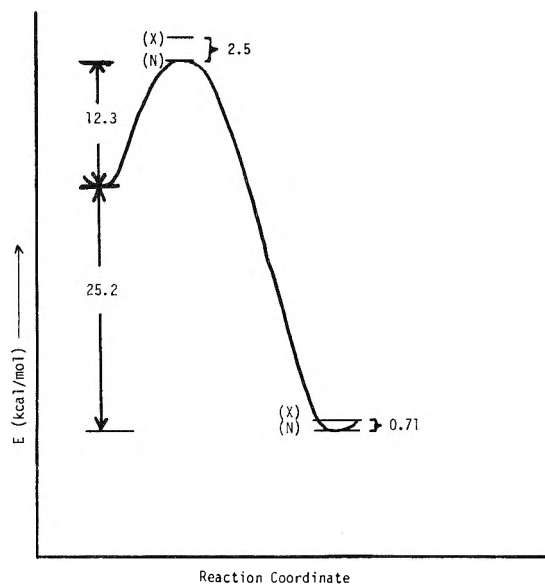


Figure 1. Energy profile for the reaction of cyclopentadiene and maleic anhydride.

and exo (X) adducts follow rate laws of the same form, the product ratio N/X is equal to the ratio of the specific rate coefficients k_N/k_X . Furthermore, the ground-state reactants leading to a pair of endo-exo isomeric transition states are identical, so that $\log(k_N/k_X)$ is directly proportional to the free energy difference between the two transition states. From the Arrhenius equation then, it appears that the endo transition state is 2.5 kcal more stable than the exo transition state. The enhanced stability of the endo transition state depends, according to Stein and Alder,¹¹ on the possibility for the "maximum accumulation of unsaturation." In more recent times this concept has been restated in quantum chemical terms.³ In going from an almost coplanar transition state to product there is an increase in volume¹² which presumably reduces the stabilizing interaction of the endo species from 2.5 to the point where the endo isomer is only 0.7 kcal more stable than the exo isomer. Therefore, the endo transition state and endo isomer are more stable than the exo alternative although the margin of stability is reduced in the products. These results are summarized in the reaction profile shown in Figure 1.

The activation energy of the forward reaction $E_{f\ddagger}$ leading to the endo isomer is solvent dependent, decreasing with increasing solvent polarity.¹³ We have adopted the value for decalin, $E_{f\ddagger} = 12.3$ kcal/mol. The heat and energy of the reaction are related by the expression, $\Delta H = \Delta E - P\Delta V$. Although the volume decrease in a typical D-A reaction¹² is on the order of 30 cc/mol, the $P\Delta V$ term for a solution reaction is nevertheless negligible. Hence we assume that $\Delta H \approx \Delta E$ and the activation energy for the retroreaction, $E_{r\ddagger}$, is 37.5 kcal/mol. Ganter, Scheidegger, and Roberts¹⁴ have shown quite conclusively that the thermal isomerization of the endo to exo isomer occurs by a

(10) M. P. Kozina, L. P. Timofeeva, S. M. Skuratov, N. A. Belikova, E. M. Milvitskaya, and A. F. Plate, *J. Chem. Thermodynam.*, **3**, 563 (1971), give 2 eu for the entropy of isomerization of endo-2-methyl-5-norbornene to the exo isomer.

(11) K. Alder and G. Stein, *Angew. Chem.*, **50**, 510 (1937).

(12) R. A. Grieger and C. A. Eckert, *J. Amer. Chem. Soc.*, **92**, 2918 (1970).

(13) A. Wasserman, "Diels-Alder Reactions," Elsevier, Amsterdam, 1965.

(14) C. Ganter, U. Scheidegger, and J. D. Roberts, *J. Amer. Chem. Soc.*, **87**, 2271 (1965).

dissociation-recombination mechanism rather than a stepwise process. The mechanism appears to be a reverse of the formation of the endo adduct followed by recombination contrary to the Alder rule.¹¹ From the earlier kinetic data of Baldwin and Roberts¹⁵ on the thermal isomerization of endo to exo isomer in decalin we calculate the activation energy for the reverse process, $E_{r\ddagger}$, as 35 kcal/mol. This value is in satisfactory agreement with the activation energy, $E_{r\ddagger}$ (37.5), derived from our thermochemical data.

As the accumulation of thermochemical data lags, it has become necessary to develop empirical methods for the estimation of thermodynamic parameters. While eq 1 is satisfactory in dealing with this particular D-A reaction we have explored another approach for estimation of the gas-phase reaction heat which is somewhat simpler and equally satisfactory. From the gas-phase heats of formation of ethane (-20.24 kcal/mol),¹⁶ and succinic anhydride (-128 kcal/mol) it appears that the replacement of two hydrogens by an anhydride group changes the heat of formation by -108 kcal/mol. Combining this value with the heat of formation of norbornene (20.6 kcal/mol)¹ gives $\Delta H_f(\text{adduct}) = -88$ kcal/mol. With this value and the heats of formation of cyclopentadiene (31.95 kcal/mol) and maleic anhydride (-95.2 kcal/mol), the gas-phase

heat of reaction is calculated as $\Delta H_r(g) = -25$ kcal/mol compared to the experimental value of -26.6 (endo) kcal/mol. Thus, this simple group approach also yields good results.

The heat of formation of the endo adduct calculated from the heats of formation of the reactants and $\Delta H_r(g)$ is -89.8 kcal/mol. The strain energy in a molecule is generally assigned as the difference between this experimental value and the heat of formation predicted on the basis of some empirical scheme. We have adopted the olefinic and carbonyl increments of Benson¹⁷ and the "single conformation" values of the saturated CH and CH₂ groups from Schleyer.¹⁸ The predicted formation heat and strain energy are -113.57 and 23.7 kcal/mol, respectively. The strain energy of norbornene itself is 23 kcal/mol which implies a small contribution from the succinic anhydride moiety. Benson estimates the strain in this ring system at 1.1 kcal/mol.¹⁷

(15) J. E. Baldwin and J. D. Roberts, *J. Amer. Chem. Soc.*, **85**, 115 (1963).

(16) Unless otherwise noted all heat of formation data are from J. D. Cox and G. Pilcher, "Thermochemistry of Organic and Organometallic Compounds," Academic Press, New York, N. Y., 1970.

(17) S. W. Benson, "Thermochemical Kinetics," Wiley, New York, N. Y., 1968.

(18) P. v. R. Schleyer, J. E. Williams, and K. R. Blanchard, *J. Amer. Chem. Soc.*, **92**, 2377 (1970).

Excited State Chemistry of Indigoid Dyes. I. Fluorescence vs. Cis-Trans Isomerization¹

George M. Wyman* and Bizhan M. Zarnegar

U. S. Army Research Office—Durham, Durham, North Carolina 27706 (Received May 30, 1972)

Publication costs assisted by the U. S. Army Research Office—Durham

The absorption spectra of the cis and trans isomers of thioindigo, 6,6'-diethoxythioindigo, selenoindigo, and 3,3'-dioxo-4,4,4',4'-tetramethyl-2,2'-bithiolanylidene were determined by a combination of absorption and fluorescence spectroscopy in the visible region. Quantum yields of fluorescence (for the trans isomers) and for the photochemical cis \rightarrow trans and trans \rightarrow cis isomerizations were measured. The effect of structural parameters on the absorption spectra and on the rates of the excited state processes (fluorescence, twisting, and nonradiative decay) of indigoid dyes is discussed.

Introduction

In conjunction with studies on the quenching of the fluorescence and the photochemical cis-trans isomerization of some indigoid dyes,² it was necessary to determine their absorption spectra accurately in the visible region. Although the existence of cis and trans isomers has been known for some time,³⁻⁶ their facile interconversion had made an accurate measurement of the spectrum of each isomer difficult. Reasonably accurate spectra have been determined for the chromatographically separated isomers of two thioindigo dyes,³ while the spectra of others have been calculated from photostationary mixtures, based on certain reasonable assumptions,^{3,7} the correctness of which may be subject to some doubts.

Recently Blanc and Ross developed an ingenious method for determining accurately the spectral absorption curve of the cis isomer from the composite spectrum of a mixture of cis and trans isomers by a combination of fluo-

(1) Presented at the IVth IUPAC Conference on Photochemistry, Baden-Baden, July 1972.

(2) G. M. Wyman, *Chem. Commun.* 1332 (1971).

(3) G. M. Wyman and W. R. Brode, *J. Amer. Chem. Soc.*, **73**, 1487 (1951).

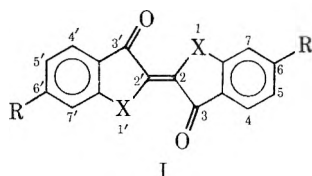
(4) W. R. Brode, E. G. Pearson, and G. M. Wyman, *J. Amer. Chem. Soc.*, **76**, 1034 (1954).

(5) J. Weinstein and G. M. Wyman, *J. Amer. Chem. Soc.*, **78**, 4007 (1956).

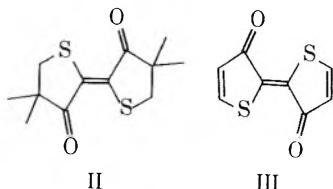
(6) R. Pummerer and G. Marondel, *Chem. Ber.*, **93**, 2834 (1960).

(7) I. Y. Bershtein and Y. L. Kaminskii, *Opt. Spektrosk.*, **15**, 381 (1963).

rescence and absorption spectroscopy, provided that only the trans isomer exhibited fluorescence.⁸ Since thioindigo⁹ and *N,N'*-diacetylindigo satisfy this requirement, they calculated the absorption curves for the cis isomers of these compounds and, in a later communication,¹⁰ extended this to selenoindigo. Unfortunately, due apparently to an instrumental artifact in their fluorescence measurements¹¹ the curves they obtained for the cis compounds were in error. They also calculated the trans absorption curves, extinction coefficients, and quantum yields for photoisomerization based on the computed cis curves.



- Ia, thioindigo: X = S, R = H
 Ib, 6,6'-diethoxythioindigo: X = S, R = OC₂H₅
 Ic, selenoindigo: X = Se, R = H
 Id, oxindigo: X = O, R = H



The visible absorption spectra for both the cis and the trans isomers, the quantum yields of fluorescence, and of cis \rightarrow trans and trans \rightarrow cis photoisomerization were determined for four indigoid dyes (Ia, Ib, Ic, and II) in the present study. The excited state behavior of these compounds was compared with that reported for oxindigo (Id)¹² and, to a limited extent, with thiopheneindigo (III).¹³

Experimental Section

Materials. The 3,3'-dioxo-4,4,4',4'-tetramethyl-2,2'-bi-thioanilidene (II) and thiopheneindigo (III) were research samples provided through the courtesy of Professor W. Luetke of the Organic Chemistry Institute, University of Goettingen; selenoindigo was a research sample kindly provided by Dr. D. L. Ross of RCA Laboratories, Princeton, N. J. Thioindigo (further purified by recrystallization from chloroform) and 6,6'-diethoxythioindigo were research samples kindly furnished by the duPont Co. and Ciba-Geigy S. A. (Basel), respectively. Rhodamine B was purchased from Matheson Coleman and Bell. Phenol was reagent grade from Baker and Adamson. Reagent grade benzene with no further purification was used for all measurements.

Spectroscopic Measurements. Absorption spectra were measured on a Cary Model 17 spectrophotometer and fluorescence intensities determined using a Hitachi Perkin-Elmer MPF-2A fluorescence spectrophotometer on the same solutions (concentration $\sim 10^{-5}$ M) contained in fused quartz cells. The high sensitivity of the Cary instrument permitted accurate measurements of absorption spectra on the weakly absorbing solutions that are required for fluorescence studies.

Irradiation of Dye Solutions. The dye solution contained in a 1-cm absorption cell was preirradiated for 5 min to

obtain a trans- or cis-rich solution in an apparatus described previously, using appropriate Corning glass filters to isolate the required wavelengths.¹⁴ A rectangular water bath was inserted between the lamp and the solutions in order to eliminate heat effects.

Quantum Yield Measurements. The quantum efficiency of fluorescence of thioindigo was determined relative to a corrected fluorescence spectrum of Rhodamine B ($\phi_f = 0.69$)¹⁵ kindly provided by Dr. R. N. Keller of NBS. Undegassed solutions of thioindigo in benzene and Rhodamine B in ethanol were prepared with an optical density of 0.02 at 500 nm. The "cut and weigh" method was used to determine the area of the fluorescence emission and the appropriate correction was made for the difference in the refractive indices of the two solvents.¹⁵ The quantum efficiencies of Ib, Ic, and II in benzene were determined relative to thioindigo. All the determinations for the indigoid dyes were made on trans-rich solutions and normalized to 100% trans concentration.

The quantum yield of trans to cis photoisomerization of thioindigo was determined in a "merry-go-round" apparatus¹⁶ with Corning glass filters used to isolate the 546- and 577-579-nm lines from a 450-W Hanovia medium-pressure lamp. Ferric oxalate actinometry was used to monitor the intensity of the exciting light.¹⁷ The quantum yields of photoisomerization for Ib, Ic, and II were determined using exciting light from a Bausch & Lomb monochromator; elimination of stray light of higher orders was accomplished by the use of appropriate filters. Thioindigo was used as a secondary actinometer in the determination of the $\phi_{t \rightarrow c}$ for Ib and Ic. Since ferric oxalate actinometry is relatively insensitive to visible light¹⁷ and the long irradiation times and concurrent low conversions might introduce large errors in the determination of the lamp intensity, the $\phi_{t \rightarrow c}$ for thioindigo was redetermined using the Bausch & Lomb monochromator and an actinometer developed by Wegner and Adamson.¹⁸ The $\phi_{t \rightarrow c}$ value determined in this manner agreed within experimental error with the $\phi_{t \rightarrow c}$ value obtained using ferric oxalate actinometry. Irradiations were carried out to low conversions (~ 3 -7%). Analysis was by absorption spectroscopy; appropriate corrections from the calculated curves were made to obtain the amounts of cis and trans isomer present.

Flash Photolysis. Flash photolysis experiments were carried out in degassed solutions contained in cylindrical cells. A mercury-xenon flash having a fall time of ca. 10 μ sec was used with Corning glass filters to activate the dye

- (8) J. Blanc and D. L. Ross, *J. Phys. Chem.*, **72**, 2817 (1968).
- (9) D. A. Rogers, J. D. Margerum, and G. M. Wyman, *J. Amer. Chem. Soc.*, **79**, 2464 (1957).
- (10) D. L. Ross, J. Blanc, and F. J. Matticoli, *J. Amer. Chem. Soc.*, **92**, 5750 (1970).
- (11) Their fluorescence spectra showed double emission maxima with the long wavelength peak at ca. 620 nm, the wavelength at which their intensity measurements were made. This second peak appears to have been in error since it had not been observed in the earlier work⁹ nor was it found in this investigation or in a third laboratory (U. Wild, Federal Institute of Technology, Zuerich, private communication), using three different types of instruments.
- (12) H. Guesten, *Chem. Commun.*, 133 (1969).
- (13) H. Herrmann and W. Luetke, *Chem. Ber.*, **101**, 1715 (1968).
- (14) G. M. Wyman and A. F. Zenhausern, *J. Org. Chem.*, **30**, 2348 (1965).
- (15) C. A. Parker and W. T. Rees, *Analyst*, **85**, 587 (1960).
- (16) F. G. Moses, R. S. H. Liu, and B. M. Monroe, *Mol. Photochem.*, **1**, 245 (1969).
- (17) C. G. Hatchard and C. A. Parker, *Proc. Roy. Soc., Ser. A*, **235**, 518 (1956).
- (18) E. E. Wegner and A. W. Adamson, *J. Amer. Chem. Soc.*, **88**, 394 (1966).

visible band. A tungsten steady-state lamp was used to monitor transients over the entire range of the visible spectrum.

Results

Calculation of Cis Absorption Curves. These were calculated by the method of Blanc and Ross and are shown in Figures 1-4; the molecular extinction coefficients at the absorption peaks are listed in Table I. The observed very gradual tapering off of the curves for Ia and Ic at the long-wavelength side is in contrast with curves previously calculated for these compounds.^{3,7,8} The correctness of the curve for *cis*-Ia was verified by (1) separating the *cis* isomer (containing *ca.* 2% *trans*)³ chromatographically and observing that its absorption in the 530-560-nm region was less than that reported by Blanc and Ross⁸ and (2) by observing *cis* → *trans* isomerization upon irradiating a *cis*-rich solution with light of wavelengths >575 nm, as shown in Figure 5.

Calculation of Trans Absorption Curves. Fischer has shown that, if ϵ_c is known as a function of λ , ϵ_t can be calculated based on the assumption that $\phi_{c \rightarrow t} / \phi_{t \rightarrow c}$ is constant and independent of the wavelength used for the photochemical isomerization.¹⁹ In using Fischer's method

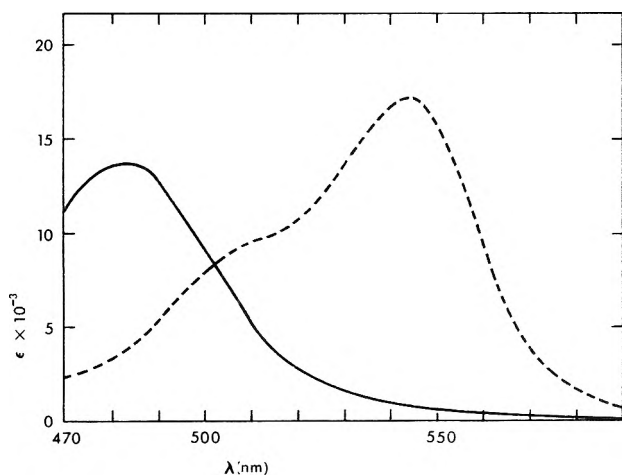


Figure 1. Visible absorption spectra for *cis*- (—) and *trans*- (---) thioindigo (Ia) in benzene.

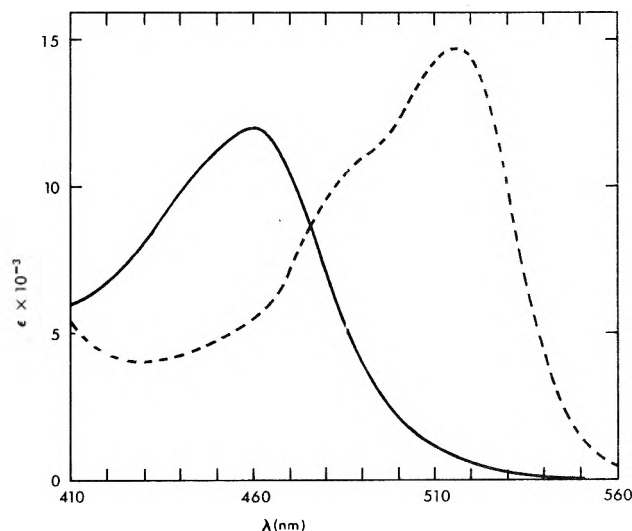


Figure 2. Visible absorption spectra for *cis*- (—) and *trans*- (---) 6,6'-diethoxythioindigo (Ib) in benzene.

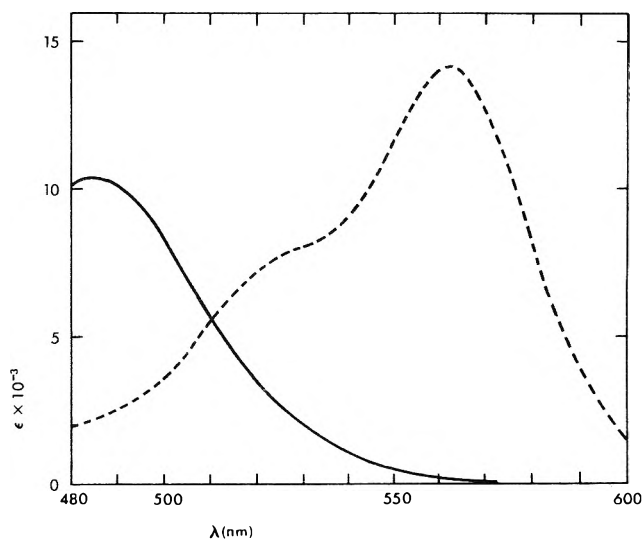


Figure 3. Visible absorption spectra for *cis*- (—) and *trans*- (---) selenoindigo (Ic) in benzene.

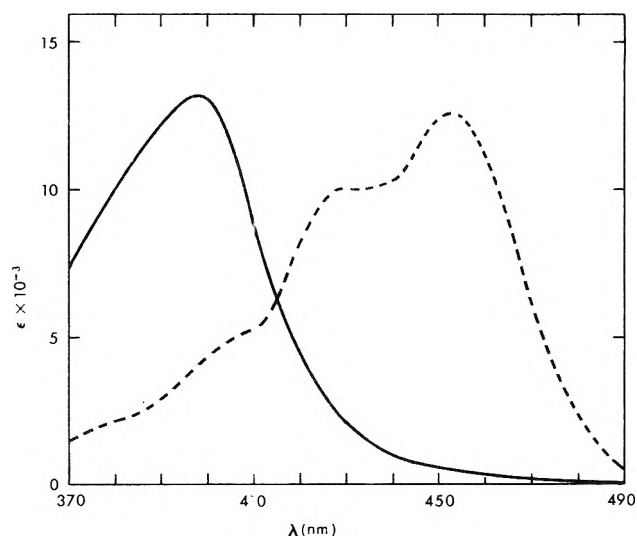


Figure 4. Visible absorption spectra for *cis*- (—) and *trans*- (---) II in benzene.

TABLE I: Molecular Extinction Coefficients at the Wavelengths of the Absorption Maxima (nm)

Compd	λ_{\max}^t	ϵ_t	ϵ_c	λ_{\max}^c	ϵ_c	ϵ_t
Ia	543	17,000	800	484	13,700	4050
Ib	516	14,800	760	460	12,000	5400
Ic	562	14,100	90	485	10,400	2200
II	452	12,700	540	397	13,400	4100

it is necessary to obtain absorption curves characteristic of two different photostationary states by irradiating the same solution at wavelengths, $\lambda(1)$ and $\lambda(2)$. In their paper Blanc and Ross have pointed to the simplification introduced into this type of calculation from knowledge of the ratio of concentrations (R) of the *trans* isomer present in the two photostationary states; unfortunately it appears that the eq A5 they derived is not in the correct form.⁸

Let α_1 and α_2 represent (*trans*)/(total) in the photostationary states resulting from irradiating at $\lambda(1)$ and $\lambda(2)$,

(19) E. Fischer, *J. Phys. Chem.*, **71**, 3704 (1967).

TABLE II: Quantum Yields and Rate Constants for Excited State Processes

Compd	τ , nsec	ϕ_f	$\phi_{t \rightarrow c}$	$\phi_{c \rightarrow t}$	ϕ_c/ϕ_t^e	ϕ_{td}	ϕ_{td}	$k_f(\text{calcd.}) \times 10^7$	$k_f(\text{obsd.}) \times 10^7$	$k_{tp} \times 10^8$	$k_{td} \times 10^8$	Decay ratio cis/trans
Ia	13.4 ^a	0.56 ^c	0.041	0.45 ^f	11	0.075	0.37	3.6	4.1	0.056	0.27	1.22
Ib	0.9 ^a	0.03 ^d	0.19	0.37	2.0	0.30	0.67	3.8	3.3	3.3	7.4	1.70
Ic	1.7 ^b	0.03 ^d	0.032	0.81	25.5	0.17	0.80	2.6	1.8	1.1	4.7	0.24
II	0.7 ^a	0.02 ^d	0.34	0.41	1.2	0.58	0.40	2.8	2.9	8.3	5.7	1.44
Id			0.63	0.35	0.55	0.98	0.02	6.7				1.85

^a Determined through the kindness of Professor W. R. Ware by the single-photon technique. ^b Determined by the Stern-Volmer method using phenol as the quencher. ^c Vs. Rhodamine B as reference ($\phi_f = 0.69$). ^d Vs. Thioindigo (Ia) as reference. ^e From photostationary state concentration measurements. ^f Determined indirectly by applying the factor from quantum yield ratios to $\phi_{t \rightarrow c}$.

respectively, and the (known) molecular extinction coefficients for the cis isomer be $\epsilon_c^{\lambda(1)}$ and $\epsilon_c^{\lambda(2)}$. If the observed optical densities in the two photostationary states are designated as D_1 (measured at $\lambda(1)$) and D_2 (measured at $\lambda(2)$), then

$$R = \alpha_1/\alpha_2; \alpha_1 = R\alpha_2 \quad (1)$$

$$\phi_{c \rightarrow t}/\phi_{t \rightarrow c} = \alpha_1 \epsilon_t^{\lambda(1)} / (1 - \alpha_1) \epsilon_c^{\lambda(1)} = R\alpha_2 \epsilon_t^{\lambda(1)} / (1 - R\alpha_2) \epsilon_c^{\lambda(1)} = \alpha_2 \epsilon_t^{\lambda(2)} / (1 - \alpha_2) \epsilon_c^{\lambda(2)} \quad (2)$$

where eq 2 is eq 1 in ref 19

$$D_1 = \alpha_1 \epsilon_t^{\lambda(1)}(A) + (1 - \alpha_1) \epsilon_c^{\lambda(1)}(A) = R\alpha_2 \epsilon_t^{\lambda(1)}(A) + (1 - R\alpha_2) \epsilon_c^{\lambda(1)}(A) \quad (3)$$

where A = total concentration

$$D_2 = \alpha_2 \epsilon_t^{\lambda(2)}(A) + (1 - \alpha_2) \epsilon_c^{\lambda(2)}(A) \quad (4)$$

where eq 3 and 4 are derived from Beer's law.

By appropriate substitution one obtains the following solutions for the unknown quantities

$$\alpha_2 = (\epsilon_c^{\lambda(1)} D_2 - \epsilon_c^{\lambda(2)} D_1) / (R\epsilon_c^{\lambda(1)} D_2 - \epsilon_c^{\lambda(2)} D_1)$$

and

$$(1 - \alpha_2) = (R - 1) \epsilon_c^{\lambda(1)} D_2 / (R\epsilon_c^{\lambda(1)} D_2 - \epsilon_c^{\lambda(2)} D_1) \quad (5)$$

$$\epsilon_t^{\lambda(1)} = \{D_1 / [(A) - \epsilon_c^{\lambda(1)}] / R\alpha_2\} + \epsilon_c^{\lambda(1)} \quad (6)$$

$$\epsilon_t^{\lambda(2)} = [D_2 / (A) - (1 - \alpha_2) \epsilon_c^{\lambda(2)}] / \alpha_2 \quad (7)$$

(In actual practice eq 6 and 7 are not needed, since once α_1 and α_2 are known, the trans curves can be calculated by subtraction from the composite curves.) In order to test the validity of these equations, calculated values for ϵ_t from photostationary states were compared with measured values for ϵ_t from chromatographically separated all trans thioindigo with excellent agreement.

Solutions containing only the trans isomers can be readily obtained for Ia, Ic, and II by column chromatography of trans-rich solutions of these dyes in benzene in the dark. The separation of the trans isomers of Ia and Ic was also helped by the high $\phi_{c \rightarrow t}/\phi_{t \rightarrow c}$ ratio (*vide infra*), minimizing the effect of stray light during the separation. Unfortunately, column chromatography of Ib requires a more polar solvent mixture for elution.³ Thus, in order to obtain the trans curve for Ib in benzene, it was necessary to calculate it by eq 5. The visible absorption curves for the trans isomers are also shown in Figures 1-4 and the molecular extinction coefficients (ϵ_t) are tabulated in Table I. (It should be noted that our absorption curves for Ib are similar to the curves reported for 6,6'-diisopropoxy-thioindigo by Ross,²⁰ except that *cis*-Ib shows weaker absorption on the long-wavelength side of the absorption peak than Ross reported for his compound.)

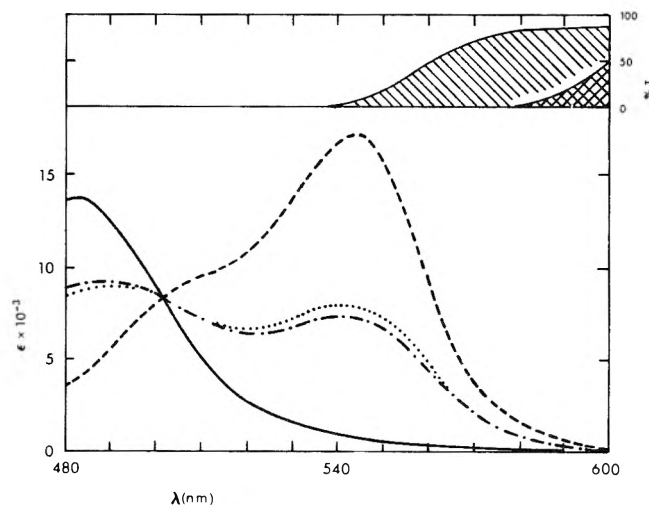


Figure 5. Photochemical activity of *cis*-Ia at long wavelengths: (---) photostationary state obtained by irradiating with Corning filter No. 3-67; (.....) photostationary state obtained by irradiating with Corning filter 2-63. Shaded area in insert shows wavelengths transmitted by filter No. 3-67; cross-hatched area indicates wavelengths transmitted by both filters. Cis (—) and trans (---) curves are included for reference purposes.

Quantum Yields, Excited State Lifetimes, and Reaction Constants. The energy diagram and reaction scheme shown in Figure 6 was devised in order to allow us to analyze and interpret the excited state processes exhibited in these systems. Although the intermediacy of a triplet can not be ruled out altogether, attempts to detect transients ($\tau > 20 \mu\text{sec}$) using flash photolysis techniques were unsuccessful for each of the four dyes studied. Since *cis*-thioindigo in the S_1 state does not fluoresce⁹ and the rate of its *cis*-*trans* isomerization is not affected by quenchers,² it was assumed for all of these dyes that the $c_1^* \rightarrow p^*$ (twisted form) step occurs with 100% efficiency. The various parameters obtained and/or calculated for the four dyes studied in this work (Ia, Ib, Ic, and II) are tabulated in Table II, along with data reported for oxindigo (Id).¹² Since thiopheneindigo (III) does not fluoresce at room temperature, its absorption spectra could not be obtained with any degree of certainty; for this reason we have not obtained quantum yield data on this dye. Excited state lifetimes (τ) for Ia, Ib, and II were determined by the single photon counting technique by Professor W. R. Ware; because of the very short observed lifetimes the values for Ib and II are only approximate ($\pm 35\%$). The excited state lifetime for Ic was obtained by Stern-Volmer treatment of fluorescence quenching results, using phenol

(20) D. L. Ross, *Appl. Opt.*, **10**, 571 (1971).

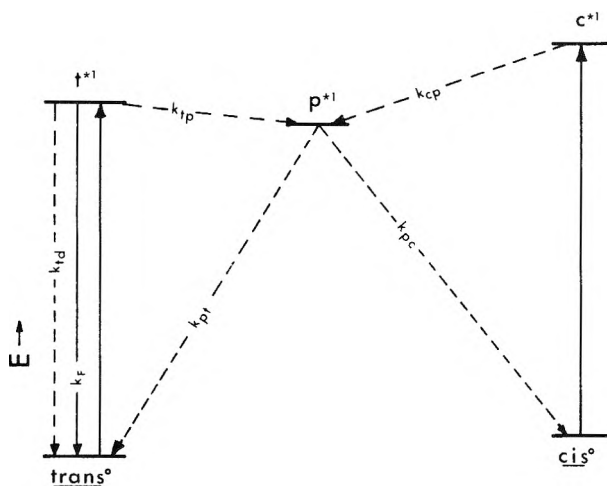


Figure 6. Schematic representation of the photochemical and photophysical processes.

as the quencher, assuming a diffusion-controlled rate.² The calculated rate constant for fluorescence ($k_{f(\text{caicd})}$) was estimated from the absorption spectra by means of eq 8.²¹ The quantum yield of fluorescence (ϕ_f) for *trans*-Ia

$$k_f = 1/\tau_f; \tau_f = (3.5 \times 10^8) / \nu^2 \epsilon_{\text{max}} \Delta \bar{\nu}_{1/2} \quad (8)$$

was determined against Rhodamine B as the reference ($\phi_f = 0.69$) according to Parker's procedure;¹⁵ ϕ_f values for the other compounds were measured against Ia as the secondary standard. In addition to measuring the quantum yields for the *cis*-*trans* isomerizations ($\phi_{c \rightarrow t}$ and $\phi_{t \rightarrow c}$), $\phi_{c \rightarrow t} / \phi_{t \rightarrow c}$ ratios were also determined from photostationary state concentrations, according to eq 2, using exciting light from a Bausch & Lomb monochromator. $\phi_{c \rightarrow t}$ was not determined directly for Ia, because of the unfavorable (7/3) (*cis*)/(*trans*) ratio in the *cis*-rich photostationary state. The rate constants for the various excited state processes were calculated from eq 9.

$$k_x = \phi_x / \tau \quad (9)$$

Discussion

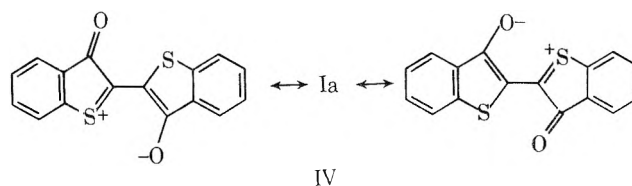
Absorption Spectra. The absorption curves obtained in this work for the *trans* isomers are not significantly different from those that had been observed^{3,7,8,13} with the exception of *trans*-Ib, where the intensity of the absorption peak relative to the isobestic point was found to be considerably lower than had been reported previously.³ This is not surprising, because the *trans*-rich photostationary state that can be obtained for this dye contains a larger fraction of the *cis* isomer than is the case for the others; furthermore its two isomers could not be conveniently separated chromatographically, hence the method of calculation used earlier was subject to error. The absorption curves also agree with the corresponding excitation spectra within the error of the measurement.²²

On the other hand the curves obtained for the *cis* isomers differ in many respects from those reported in the literature. In two of the earlier papers^{3,7} arbitrary assumptions were made with respect to the extinction coefficient of one of the isomers in regions of intense absorption by the other; *e.g.*, Wyman and Brode assumed from the shapes of the absorption curves that $\epsilon_c = 0$ at a wavelength ($\lambda_{\text{max}}^t + 25$) nm. Application of the method of Blanc and Ross⁸ permitted for the first time the calcula-

tion of *cis* absorption curves for such systems without having to resort to any arbitrary assumptions.

As can be seen from Figures 1-4, the calculated absorption curves obtained for the *cis* isomers have one unusual feature in common: the continuous gradual tapering off of absorption in the wavelength region of λ_{max}^t . This is in sharp contrast with the results of Blanc, *et al.*,^{8,10} whose curves had distinct "shoulders" in this region. The existence of this almost imperceptible absorption "tail" was verified by observing *cis* \rightarrow *trans* isomerization upon irradiating a *cis*-rich solution of Ia with light $\lambda > 575$ nm (*cf.* Figure 5); the high $\phi_{c \rightarrow t} / \phi_{t \rightarrow c}$ ratio (*cf.* Table II) suggested this as a diagnostic tool for this purpose. Moreover, it is these weak long-wavelength absorptions that extend through almost the entire length of the *trans* absorption bands (when coupled with high $\phi_{c \rightarrow t} / \phi_{t \rightarrow c}$ ratios!) that make it impossible to obtain high *trans* \rightarrow *cis* conversions by photochemical means.

Based on both spectroscopic³ and quantum mechanical²³ evidence the first excited singlet (S_1) state of indigoid dyes is believed to be a charge transfer state, resulting from the partial transfer of a "lone pair" of electrons from the heteroatom to the carbonyl oxygen, as shown in structures IV. Since the electron transfer occurs between



the two five-membered rings that are connected by the central double bond, the energy level of the S_1 state will be affected not only by electronic, but also by steric factors. This can be readily seen from a comparison of the spectra of the planar *trans* with the noncoplanar *cis* isomers; in every instance the first absorption peaks of the latter are shifted to higher frequencies.^{3,8,10} Further evidence for the noncoplanarity of the *cis* isomers comes from comparing the ν_{max} for the series Id, Ia, and Ic. For the *trans* isomers the order expected on the basis of electronegativity (*viz.*, O > S > Se) is observed, while among the *cis* compounds Ia and Ic absorb at the same frequency.²⁴ This indicates that the additional electron release effect (+M) normally associated with heavier atoms in the same group of the periodic table is effectively blocked from the chromophore by the noncoplanarity of *cis*-Ic. It is also interesting to note that $\Delta \nu_{\text{max}}(\text{cis } vs. \text{ trans})$ increases in the order O < S < Se *viz.*, with increasing size of the heteroatoms.

The noncoplanarity of the *cis* isomers in the ground state and the assumption that in the S_1 state a twisted (p^*) form represents minimum energy suggests two possible explanations for the long-wavelength absorption "tails" seen in their spectra. It is possible that, in view of the differences in the geometry between S_0 and S_1 , these may represent weak nonvertical transitions forbidden by

(21) N. J. Turro, "Molecular Photochemistry," W. A. Benjamin, Amsterdam, 1967, p 48.

(22) This comparison was suggested by one of the referees. Unfortunately the precision obtainable in excitation spectra determinations is not as good as in absorption measurements, hence only a qualitative comparison is possible.

(23) M. Kiessinger, *Tetrahedron*, **22**, 3355 (1966).

(24) M. Kiessinger and W. Luetke, *Chem. Ber.*, **99**, 2136 (1966).

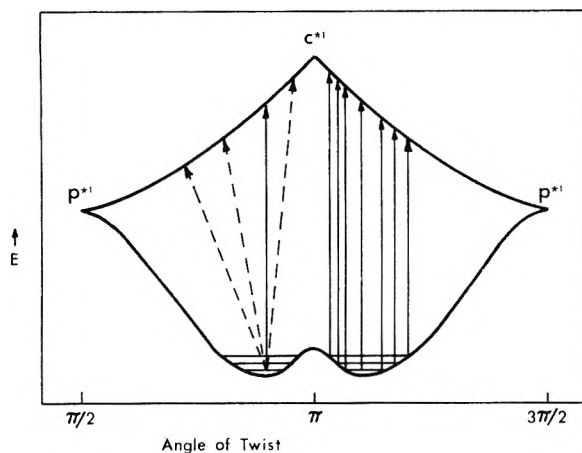


Figure 7. Energy diagram for cis and twisted forms showing possible Franck-Condon forbidden (---) and "hot-band" transitions. The double minimum in the ground state is indicated by the probable noncoplanarity of the cis isomers.

the Franck-Condon principle,²⁵ (as shown by dotted lines in Figure 7). An alternative explanation might involve "hot-band" vertical transitions from an upper vibrational c_0 level; such $c_0 \rightarrow c_1^*$ transitions would occur at a variety of lower frequencies due to the steep downward slope of the energy curve of the S_1 state. (Such transitions are shown by the solid lines in Figure 7.)

Excited State Chemistry. It is known that in the ground state the trans isomers possess the greater stability. The hypsochromic shifts observed in the spectra of the cis isomers indicate that the energy difference between the cis and the trans isomers is even greater in the S_1 state than in the ground state. A consequence of the high potential energy of c_1^* appears to be its short lifetime, as shown by its lack of fluorescence and failure to undergo quenching.² Thus the assumption (see above) that c_1^* undergoes exclusively fast radiationless deactivation to the twisted p^* form should be consistent with these observations.

Since the trans isomer of each of the four dyes studied fluoresces, it is possible to arrive at some correlations (from the data contained in Table II) between their excited state processes and structural parameters. It is immediately apparent from the data that the rates of fluorescence ($k_{f(\text{obsd})}$) differ little from each other for the four dyes; they correspond to a range of radiative lifetimes of 34–55 nsec. In view of the uncertainties involved in the measurement of fluorescent quantum yields¹⁵ and in the determination of the excited state lifetimes of the short-lived Ib and II, it is reasonable to look upon these rate constants as substantially identical. This is not too surprising, since radiative lifetimes are related to absorption spectra by eq 8 and the visible absorption curves of the four dyes are quite similar, except for differences in the frequency of their absorption maxima. The agreement between the observed and calculated values for k_f is also quite satisfactory; this confirms that the long-wavelength absorption bands correspond to the $S_0 \rightarrow S_1$ transitions.²⁶ Since the radiative lifetimes for the four dyes are substantially identical, the large differences seen in their excited state lifetimes (τ) must be attributable to changes in the relative rates of the competing nonradiative processes of twisting and deactivation.

Although a number of theoretical discussions have appeared in the literature recently on the subject of nonradiative transitions,²⁷ the compounds studied in the present

work are too complex to be treated by any of the approaches proposed. However, it is interesting to note that for all of the dyes studied the rates of twisting and of non-radiative decay show a close parallelism when viewed as functions of chemical structure. This tends to support the view of Noyes, *et al.*, who recently suggested that isomerizations may be an important route for radiationless transitions.²⁸

While it is not possible to arrive at quantitative correlations between chemical structure and the rates of the radiationless processes from our data, it is possible to correlate the latter with what may surmised concerning the potential energy of the t_1^* molecule on the basis of electronic and steric considerations. Thus, in assessing the effect of the heteroatom on these rates in the series Id-Ia-Ic, it is clear that thioindigo (Ia) occupies a unique position with the lowest rates for both twisting (k_{tp}) and decay (k_{td}). Substitution of either oxygen or selenium for the sulfur atoms results in a drastic drop in the fluorescence quantum yields due to the enhancement of the rates of the nonradiative processes.²⁹ In oxindigo (Id) the high electronegativity of the oxygen atoms minimizes the resonance interaction between the heteroatoms and the carbonyl groups (*cf.* structure IV), hence the t_1^* state will possess relatively high potential energy; this is also evident from the position of its first long-wavelength band (413 nm).¹² Consequently, in the excited state it appears to behave more like a conjugated olefin (*cf.* stilbene)³⁰ than an indigoid dye. On the other hand, in selenoindigo (Ic) the high degree of charge transfer expected on the basis of the low electronegativity of the selenium atoms appears to be counterbalanced by steric factors; the large size of the selenium atoms makes coplanarity difficult to achieve even in the trans configuration without introducing some ring strain,³¹ hence resonance stabilization of the charge transfer S_1 state is reduced. Further evidence for the steric effects of the selenium atoms may be seen in the decay ratios tabulated in Table II. Ic is the only compound for which the cis isomer is not favored during the decay of the twisted intermediate (p^*). This suggests that for Ic there may well be steric hinderance even in this state and that the intermediate may have a transoid configuration from which it can decay to t_0 approximately four times faster than to c_0 . A direct corollary of this is the exceptionally high value for $\phi_{c \rightarrow t}$.

The high fluorescence quantum yield and the low values for the rates of the two radiationless processes for thioindigo suggest that the heteroatoms in this compound possess the maximum in electron-donating power that is compatible with coplanarity, a combination that is expected to endow t_1^* with greatest stability. Furthermore, X-ray diffraction studies on the crystal have shown evidence of secondary valence forces between the sulfur and oxygen atoms in adjacent rings holding this molecule in a

(25) The authors are indebted to Professor Dr. Th. Foerster for this suggestion.

(26) W. R. Ware in "Creation and Detection of the Excited State," Vol. 1A, A. A. Lamola, Ed., Marcel Dekker, New York, N. Y., 1971, p 215.

(27) For a review *cf.* D. Phillips in "Photochemistry," Vol. 2, D. Bryce-Smith, Senior Reporter, The Chemical Society, London, 1971, pp 18–43.

(28) D. Phillips, J. Lemaire, C. S. Burton, and W. A. Noyes, Jr., *Advan. Photochem.*, 5, 329 (1968).

(29) Since Id is reported not to fluoresce (*ref* 12), our observations concerning this compound can only be qualitative.

(30) *Cf.* D. Gegiou, K. A. Muszkat, and E. Fischer, *J. Amer. Chem. Soc.*, 90, 3907 (1968).

(31) H. v. Eller, *Bull. Soc. Chim. Fr.*, 106, 1444 (1955).

tight coplanar configuration.³¹ It is possible that, if this bonding should persist in solution, it may stabilize the t_1^* state still further and explain the uniquely low values found for twisting and for radiationless decay.

Electronic effects due to the introduction of substituents in the thioindigo framework can also be evaluated to some extent by a comparison of the data on Ia with those on Ib and II. In Ib the "out-of-phase" conjugation of the electron-donating ethoxy groups with the carbonyls would be expected to raise the energy of the S_1 state, leading to an enhancement of the nonradiative processes, low fluorescence quantum yield, and a short lifetime. Compound II differs from Ia by the elimination of the two fused benzene rings and the resonance stabilization associated therewith. Here again the radiationless processes dominate, although a weak fluorescence can still be observed. Further studies on other substituted thioindigo dyes will have to be undertaken to confirm these tentative conclusions.

From a comparison of the chemical behavior (in the ground state), the spectroscopic properties, and quantum mechanical calculations of II with Ia, Herrmann and Luettké concluded that the conjugated system in the former represents the basic chromophore ("Grundchromophor") of indigo¹³ and that it can not be considered to belong to the family of merocyanines, as had been pro-

posed by Leupold and Daehne.³² Our studies support Luettké's contention, since although we were able to observe fluorescence from *trans*-II, we were unable to detect any emission from *trans*-III in benzene solution at room temperature. Based on their MO calculations Herrmann and Luettké concluded that the conjugation between the cyclic double bonds and the carbonyl oxygen atoms actually lessens the indigoid character of III.³³ Such out-of-phase conjugation in the S_1 state would be expected to have an effect similar to that caused by the introduction of the 6,6'-diethoxy groups into the thioindigo structure. Since the quantum yield of fluorescence is only 0.02 for *trans*-II, the lack of fluorescence found for *trans*-III appears to be consistent with their views.

Acknowledgments. The authors are greatly indebted to Professors D. G. Whitten and W. R. Ware for their interest in this research and their many helpful suggestions. Financial support of this work by the U. S. Army Research Office-Durham is gratefully acknowledged. The authors are also deeply appreciative for the facilities provided for carrying out this work by the Chemistry Department, University of North Carolina—Chapel Hill.

(32) D. Leupold and S. Daehne, *Theor. Chim. Acta*, **3**, 1 (1965).

(33) Cf. M. Klessinger and W. Luettké, *Tetrahedron, suppl.* **2**, 19, 315 (1963).

Effect of Cholesteryl Alkanoate Structure on Liquid Crystal Transition Thermodynamics. Pure and in Binary Mixtures

Harry W. Gibson[†] and John M. Pochan

Xerox Corporation, Rochester Research Center, Webster, New York 14580 (Received August 10, 1972)

Publication costs assisted by the Xerox Corporation

The position, number, and length of branches in the alkanoate portion of cholesteryl alkanoates profoundly effect their mesomorphic behavior. Interactions of the carbonyl moieties are believed to be major cohesive forces in the helix of the cholesteric mesophase. We postulate that branching in the neighborhood of the carbonyl alters these bonding forces and thereby leads to smectic behavior. Branching also decreases conformational mobility of the alkanoate chain leading to more organization in the crystalline state; this can to some extent be offset by increasing the branch length. These latter factors control ΔH_f and the melting point. The binary phase diagrams are explicable in terms of mutual disruption of the crystal lattices of the two components. Materials similar in size and shape behave more ideally in admixture than dissimilar materials. Small amounts of a long-chain alkanoate in a short one have a greater disruptive effect on the crystal structure than *vice versa*. In some cases eutectics are observed.

Substituent effects of the aromatic portion of cholesteryl benzoates on the mesomorphic transition temperatures and thermodynamics have been examined.¹⁻³ The effect of altering chain length in cholesteryl *n*-alkanoates has also received a great deal of attention.⁴

In contrast, the effect of alkanoate chain branching (length, degree, and position) on the mesomorphic transition temperatures and thermodynamics of cholesteryl alkanoates has not been reported. In this paper we discuss

the results of such a study. The effect of these structural variations on the behavior of binary mixtures⁵ is also examined.

(1) C. Wiegand, *Z. Naturforsch. B*, **3**, 313 (1954).

(2) C. Earborn and N. H. Hartshorne, *J. Chem. Soc.*, 549 (1955).

(3) E. M. Barrall, II, K. E. Bredfeldt, and M. Vogel, *Mol. Cryst. Liq. Cryst.*, in press.

(4) G. J. Davis, R. S. Porter, and E. M. Barrall, II, *Mol. Cryst. Liquid Cryst.*, **11**, 319 (1970), and references therein.

Experimental Section

Cholesteryl hexanoate and nonanoate were purchased from Eastman Chemical Co. The other cholesteryl alkanates were prepared by esterification of cholesterol (Eastman Chemical Co., primary standard grade) with the requisite acid chlorides, generally in 95–100% yield. All samples were purified by repeated crystallization from 1-pentanol-ethanol and/or ethyl acetate-ethanol. Elemental analyses were consistent with chemical structures. Thin layer chromatography revealed no impurities. Purity analysis by the method of David and Porter⁶ yielded purity of 99.5 mol % or greater.

The calorimetric data and the phase diagrams were primarily generated by use of a Perkin-Elmer DSC-1B differential scanning calorimeter at a scan rate of 10°/min. The observations were augmented by microscopic examination (see below) at a scanning rate of 0.2°/min. Temperature readout was calibrated at 10°/min through use of standards, as was the enthalpic readout, which was obtained by planimetry. Transition temperatures were taken as the maxima in the DSC traces and as the midpoint of the transition range in the microscopic observations. Each sample was examined on heating and cooling; within experimental error all mesophase-mesophase and mesophase-isotropic transitions were in agreement. Generally, at least two independent measurements were made. In cases where the identity of the mesophase was in doubt, optical microscopy (Ortholux Leitz polarizing microscope with calibrated Mettler hot stage, 0.2°/min) was employed.

Binary samples for DSC measurement were prepared by two methods. The first method involved melting the weighed mixture to the fully isotropic liquid and cooling it quickly, allowing recrystallization to take place at the lower temperature. The second method was to evaporate chloroform solutions of the mixtures. The two methods gave the same results for all transitions except in some cases the shape of the melting transitions. The melting technique resulted in phase separation in a few cases and could not be applied to high melting point compounds without causing some decomposition. Microscopic examination with polarized light, while not quantitative, indicated that all samples were crystalline with very little amorphous character prior to measurement.

All mixtures were examined microscopically for gross phase separation as manifested by incomplete crystal melting, *i.e.*, presence of crystals in mesophases or isotropic phases. Except for those mixtures yielding eutectics such behavior was not observed.

For pure materials all transitions are believed to be accurate to better than $\pm 1.0^\circ$. For the binary mixtures crystal melting points are believed to be accurate to $\pm 2^\circ$, the lower precision being due to peak broadness, and the other transitions to $\pm 1^\circ$.

Results

Several distinct structural variations were employed. In series 1 the position of a one carbon fragment was varied along a chain of the alkanate portion of esters of cholesterol. In series 2 the length of the branch at the position adjacent to the carbonyl was varied. The degree of branching in isomeric systems was examined in series 3 and finally the effect of steric bulk was studied in series 4. A total of eleven cholesteryl alkanates were used.

I. Pure Esters. The transition temperatures, enthalpies, and entropies of fusion for the pure esters are listed in Table I according to the structural series designations given above.

A. Position of Branch. In series 1a a one-carbon unit is moved from the terminal position of an alkanate chain to a position adjacent to the carbonyl. In this isomeric pentanoate series as the single carbon unit approaches the carbonyl both ΔH_f and ΔS_f increase. Additionally, introduction of branching causes loss of enantiotropic mesomorphism. Likewise in the analogous isomeric butyrate series 1b, ΔH_f and ΔS_f both increase as the carbon is moved from the end of the chain toward the carbonyl; once more, enantiotropic mesomorphism disappears in the branched ester.

B. Length of Branch. In series 2a the length of a branch at the α position of cholesteryl 2-methylbutyrate is increased from one to two to four. As a result both ΔH_f and ΔS_f decrease, though not markedly. However, the cholesteric mesophase disappears with the addition of the one-carbon branch, there being no observable enantiotropic mesophase in the 2-methylbutyrate. Addition of yet another carbon brings about the appearance of a monotropic smectic phase. Addition of a four-carbon side chain causes the appearance of an enantiotropic smectic phase. In this series there is a progressive lowering of the isotropic transition and the temperature at which the mesophase appears.

Series 2b and 2c show behavior analogous to 2a. Likewise, the data for series 2c are in agreement with those for series 2a and 2b.

C. Degree of Branching. The effect of degree of branching is examined by means of series 3, a set of isomeric pentanoates. As the degree of branching increases ΔH_f and ΔS_f also increase, enantiotropic mesomorphism disappears, and the isotropic transition temperature increases, most markedly on changing from 2-methylbutyrate to pivalate. The expected monotropic transition temperature (Table I) also decreases as the degree of branching increases.

D. Rigidity. Finally, in series 4 two esters containing quaternary carbons adjacent to the carbonyl, pivalate and 1-adamantane carboxylate, are compared. The adamantyl unit is more rigid and larger than the pivalyl group. Neither are enantiotropically mesomorphic but may be monotropic in character. The melting point of the adamantyl derivative is much higher, while ΔH_f is about equal to that of pivalate. Of course ΔS_f reflects the difference in melting point, *i.e.*, ΔS_f for pivalate is higher.

II. Binary Mixture with Cholesteryl Nonanoate. In addition to studies of pure materials, mixtures of the various esters with cholesteryl nonanoate were examined in order to gain insight into the effect of various structural parameters on the interaction of the two constituents as manifested by thermal and calorimetric behavior. Crystalline melting points of the samples are less accurate than usual DSC determinations because of the broad transition peaks. Microscopic examination reveals this peak broadness is due to partial phase separation of the mixtures upon recrystallization. In a few cases, two melting peaks were observed (one usually much larger) and the ΔH list-

(5) A study of crystal nucleation in binary mixtures has been reported: J. M. Pochan and H. W. Gibson, *J. Amer. Chem. Soc.* **93**, 1279 (1971).

(6) G. J. Davis and R. S. Porter, *J. Therm. Anal.*, **1**, 449 (1969).

TABLE I: Thermal Behavior of Cholesteryl Esters

Series	Alkanoate	Structural ^a formula	Transitions, ^b °C	Predicted ^c monotropic transitions, °C	Figure no.	ΔH_f , ^d kcal/mol	ΔS_f , ^e eu
1a	Pentanoate	ChOCO(CH ₂) ₃ CH ₃	K 93 C 97 I ^f		1	4.50	12.4
	Isopentanoate	ChOCOCH ₂ CH(CH ₃) ₂	K 109 I	(C 93)	2	4.90	12.8
	2-Methylbutyrate	ChOCOCH(CH ₃)CH ₂ CH ₃	K 108 I	(S 89)	3	4.98	13.0
1b	Butyrate	ChOCO(CH ₂) ₂ CH ₃	K 97 C 108 I ^g		4	5.07	13.7
	Isobutyrate	ChOCOCH(CH ₃) ₂	K 131 I	(C 95)	5	6.36	15.8
2a	2-Methylbutyrate	ChOCOCH(CH ₃)CH ₂ CH ₃	L 108 I	(S 89)	3	4.98	13.0
	2-Ethylbutyrate	ChOCOCH(CH ₂ CH ₃) ₂	K 89 I (71 S) ^h	(S 66)	6	4.26	11.8
	2-Ethylhexanoate	ChOCOCH(CH ₂ CH ₃)(CH ₂) ₃ CH ₃	K 44 S 50 I		7	3.13	8.22
2b	Isobutyrate	ChOCOCH(CH ₃) ₂	K 131 I	(C 95)	5	6.36	15.8
	2-Methylbutyrate	ChOCOCH(CH ₃)CH ₂ CH ₃	K 108 I	(C 89)	3	4.98	13.0
2c	2-Methylhexanoate	ChOCOCH(CH ₃)(CH ₂) ₃ CH ₃	K 44 S 52 I		8		
	2-Ethylhexanoate	ChOCOCH(CH ₂ CH ₃)(CH ₂) ₃ CH ₃	K 44 S 50 I		7	3.13	8.22
3	Pentanoate	ChOCO(CH ₂) ₃ CH ₃	K 93 C 97 I		1	4.50	12.4
	2-Methylbutyrate	ChOCOCH(CH ₃)CH ₂ CH ₃	K 108 I	(C 89)	3	4.98	13.0
	Pivalate	ChOCOC(CH ₃) ₃	K 164 I			7.80	17.9
4	Pivalate	ChOCOC(CH ₃) ₃	K 164 I			7.80	17.9
	1-Adamantane carboxylate	ChOCOAd ⁱ	K 235 I			7.87	15.5

^a Ch = cholesteryl. ^b Notation of L. Verbit, *Mol. Cryst. Liquid Cryst.*, 15, 89 (1971). ^c By extrapolation of transition lines in phase diagram indicated. ^d Standard deviation less than 0.1 kcal/mol. ^e Standard deviation less than 0.2 eu. ^f $\Delta H_{C/I} = 0.11$ kcal/mol. ^g $\Delta H_{C/I} = 0.155$ kcal/mol. ^h $\Delta H_{I/S} = 0.591$ kcal/mol. ⁱ Ad = adamantane.

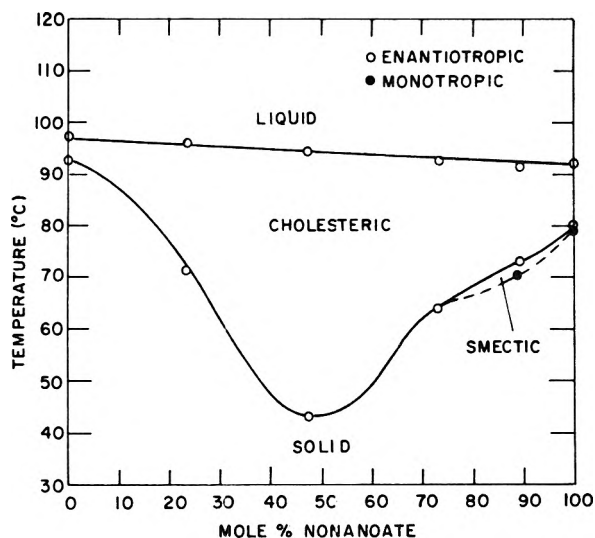


Figure 1. Phase diagram for cholesteryl pentanoate-cholesteryl nonanoate.

ed in Table I is the total of both; the melting temperature is that associated with the larger enthalpy transition. In the cases where two such peaks were observed, both were much lower than either pure component melting points, indicating, as in the microscopic observations, mixed crystalline states. This does not, however, rule out the possibility of solid solutions, though we have no evidence for this. In cases where two DSC peaks were observed, of course, composition changes occur during melting; in other instances this may or may not occur.

Mesomorphic-mesomorphic and mesomorphic-isotropic transitions of the mixtures, however, were as sharp as those in the pure materials. Microscopic examination revealed only one phase (except at transition temperatures).

These results are presented graphically; Figures 1-9 are the phase diagrams for the binary mixtures and Figures

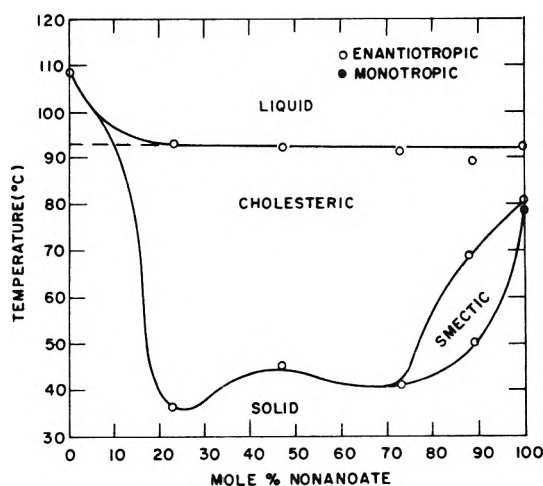


Figure 2. Phase diagram for cholesteryl isopentanoate-cholesteryl nonanoate.

10-17 show ΔH_f as a function of composition for the various mixtures. ΔS_f is not shown but generally parallels ΔH_f . The results will be discussed in terms of the same structural variables and series used above.

A. *Position of Branch.* The binary phase diagrams of series 1a with cholesteryl nonanoate are given in Figures 1-3. Examination of these diagrams reveals that as the carbon fragment is moved from the end of the chain to the carbon adjacent to the carbonyl the total mesomorphic domain decreases and the smectic region expands at the expense of the cholesteric. The melting point (T_m) minimum is about the same for all three systems. Figures 10-12 show the dependence of ΔH_f on composition. Pentanoate and isopentanoate show a broad minimum ΔH from about 20-90 mol % nonanoate, while 2-methylbutyrate has two minima, the lowest at 22% nonanoate, the other at 73% nonanoate. The minimum for isopentanoate is slight-

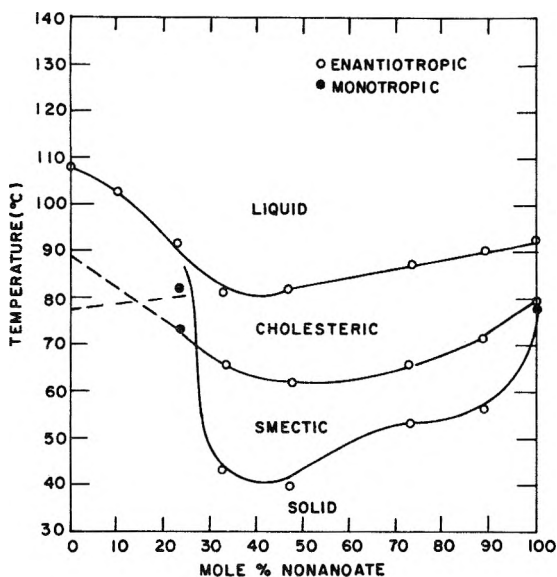


Figure 3. Phase diagram for cholesteryl 2-methylbutyrate-cholesteryl nonanoate.

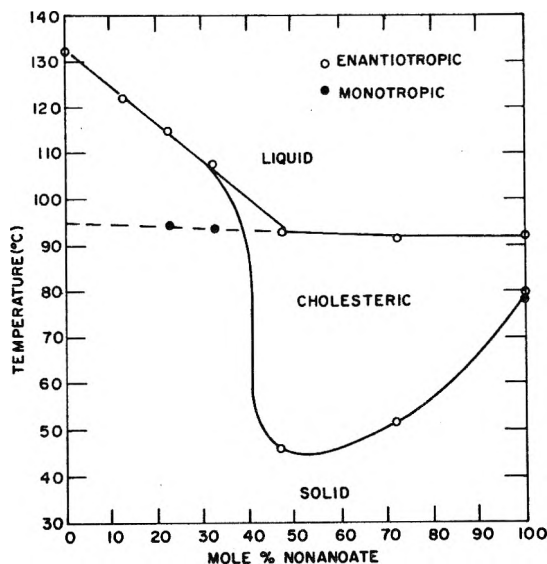


Figure 5. Phase diagram for cholesteryl isobutyrate-cholesteryl nonanoate.

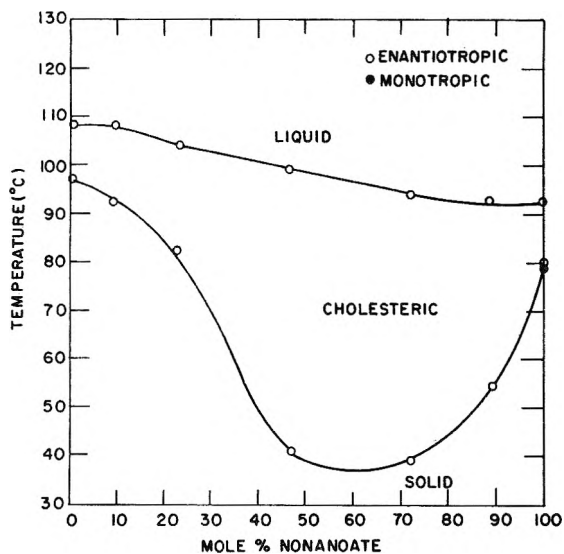


Figure 4. Phase diagram for cholesteryl butyrate-cholesteryl nonanoate.

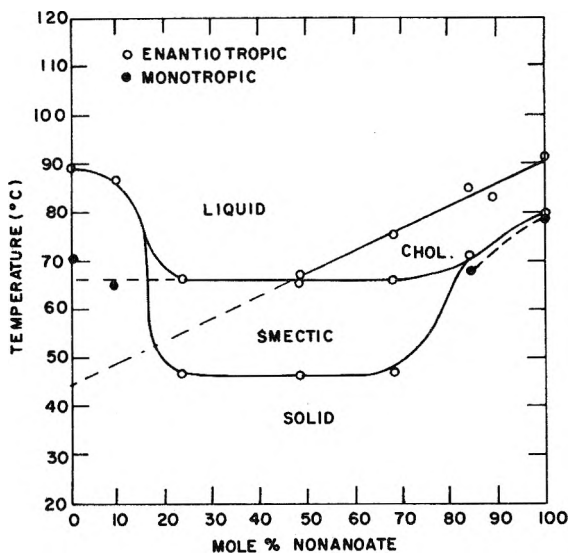


Figure 6. Phase diagram for cholesteryl 2-ethylbutyrate-cholesteryl nonanoate.

ly lower than that of pentanoate, while that for 2-methylbutyrate is substantially lower. That is, as the carbon unit is placed closer to the carbonyl, ΔH_f for a given composition is lowered in contrast to the pure esters (Table I). The change of ΔH_f with composition at the extremes is also in the same order.

In series 1b (Figures 4 and 5) the mesomorphic domain also shrinks as the carbon unit moves from the end of the chain toward the carbonyl; these systems do not exhibit a smectic phase except near 100% nonanoate. The isobutyrate system showed phase separation during melting in the region near 50%; however, the liquid crystal transitions were reversible and took place from homogeneous phases. The T_m minimum is somewhat lower for the straight chain butyrate. ΔH_f varies with composition very similarly for the two systems (Figures 13 and 14), showing minima at 20–25% nonanoate.

B. Length of Branch. The effect of the length of a branch α to the carbonyl on the behavior of binary

mixtures was examined *via* series 2a (Figures 3, 6, and 7, respectively). As the side chain is lengthened the mesomorphic region decreases in size and the smectic mesophase region increases at the expense of the cholesteric region. The T_m minimum decreases somewhat with increasing chain length. In accord with the pure esters (Table I) ΔH_f (Figures 12 and 15, respectively) decreases with increasing branch length. The thermal data for mixtures of nonanoate with members of series 2b (Figures 5, 3, and 8) and series 2c (Figures 8 and 7) support that of series 2a as do the enthalpic data (Figures 14 and 12, respectively). It was not possible to obtain ΔH_f and T_m for many compositions in mixtures of 2-methyl- and 2-ethylhexanoate because the mixtures (Figures 8 and 7) would not crystallize, even at -20° for several months.

C. Degree of Branching. By comparison of Figures 1 and 3 the effect of degree of branching (series 3) on phase diagrams of the binary mixtures is observed. As with the

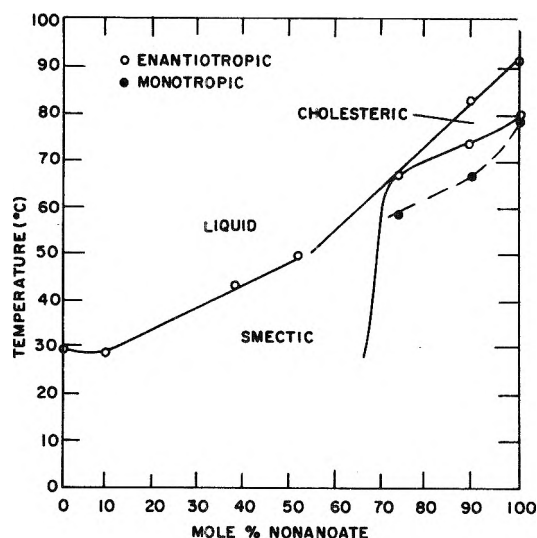


Figure 7. Partial phase diagram for cholesteryl 2-ethylhexanoate-cholesteryl nonanoate.

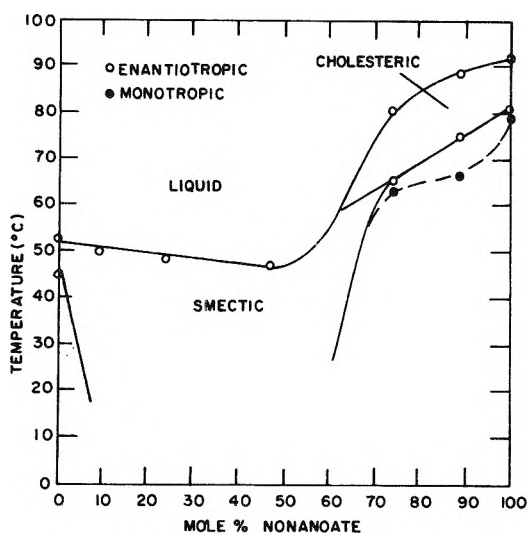


Figure 8. Partial phase diagram for cholesteryl 2-methylhexanoate-cholesteryl nonanoate.

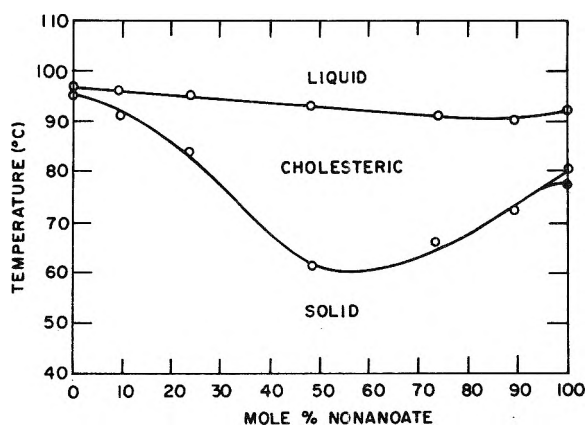


Figure 9. Phase diagram for cholesteryl hexanoate-cholesteryl nonanoate.

pure esters of series 3 the total mesomorphic range decreases with increased degree of branching. In agreement with data for the pure esters of series 3 (Table I) the en-

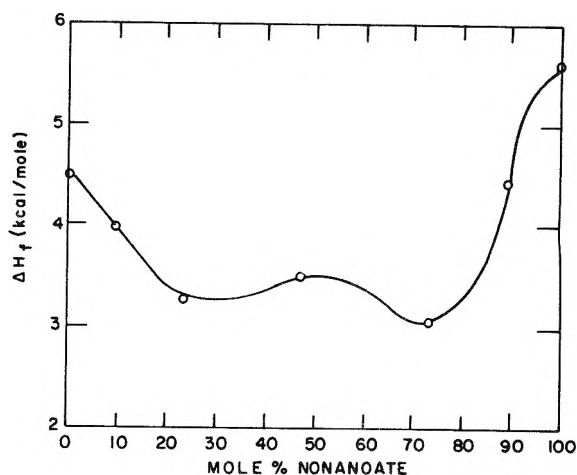


Figure 10. Enthalpy of fusion as a function of composition for cholesteryl pentanoate-cholesteryl nonanoate.

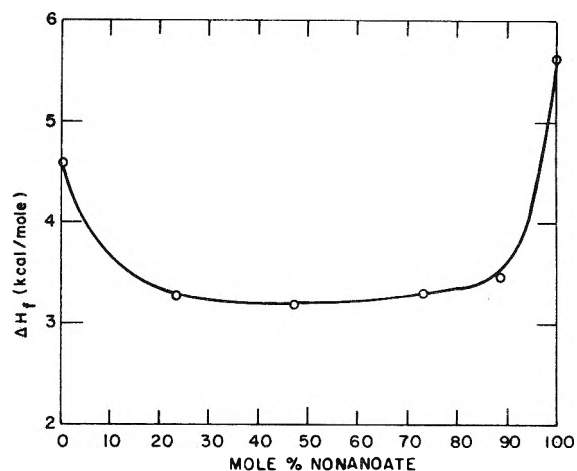


Figure 11. Enthalpy of fusion as a function of composition for cholesteryl isopentanoate-cholesteryl nonanoate.

thalpy of fusion plots (Figures 13 and 12, respectively) show an increase in ΔH as the degree of branching increases.

D. Rigidity. The effect of rigidity and steric bulk of esters having quaternary carbons adjacent to the carbonyl on the binary behavior is to cause so great a mutual disruption of the crystal lattices in admixture with nonanoate that phase separation in the form of eutectics results. Such was the case for both pivalate and 1-adamantane carboxylate.

E. Straight Chain Length. One more structural parameter of the alkoanoate is evaluated in terms of its effect on behavior of binary mixtures with nonanoate: chain length. Straight chain alkoanoates containing four, five, and six carbons⁵ were employed (Figures 4, 1, and 9,⁵ respectively). All are, with the exception of a small region near 100% nonanoate, purely cholesteric across the entire composition range. The salient difference in the phase diagrams is the mesomorphic range; note that as chain length increases, the temperature range decreases (minimum melting points of 37, 43, and 60°, respectively). The ΔH_f curves (Figures 13, 10, and 17, respectively) show that the shorter the chain, the lower is ΔH_f .

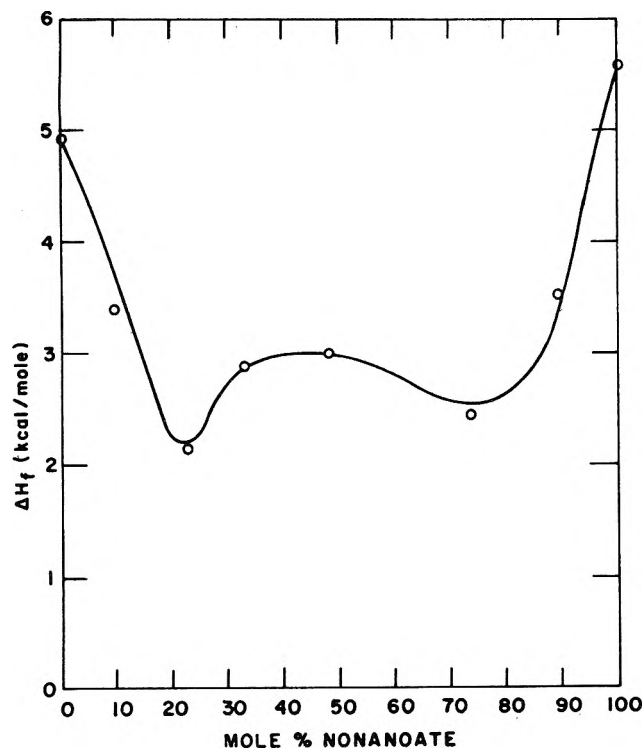


Figure 12. Enthalpy of fusion as a function of composition for cholesteryl 2-methylbutyrate-cholesteryl nonanoate.

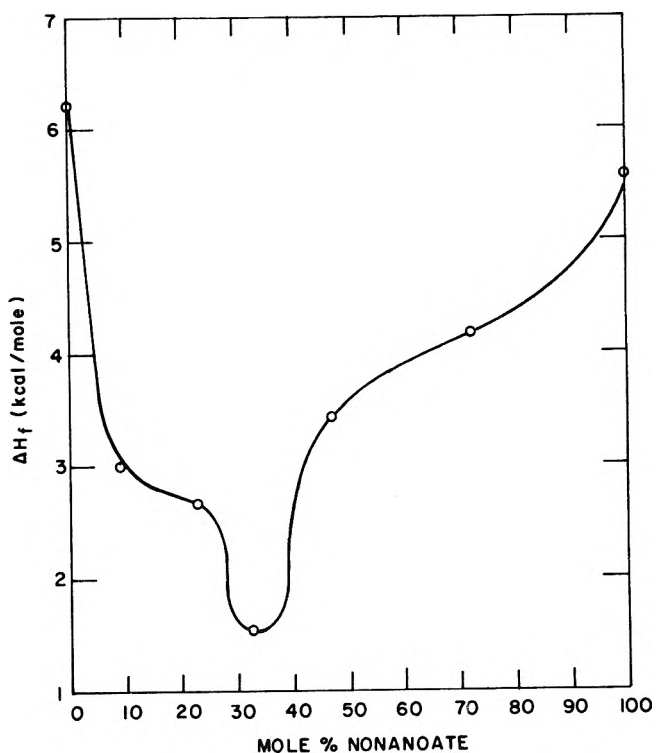


Figure 14. Enthalpy of fusion as a function of composition for cholesteryl isobutyrate-cholesteryl nonanoate.

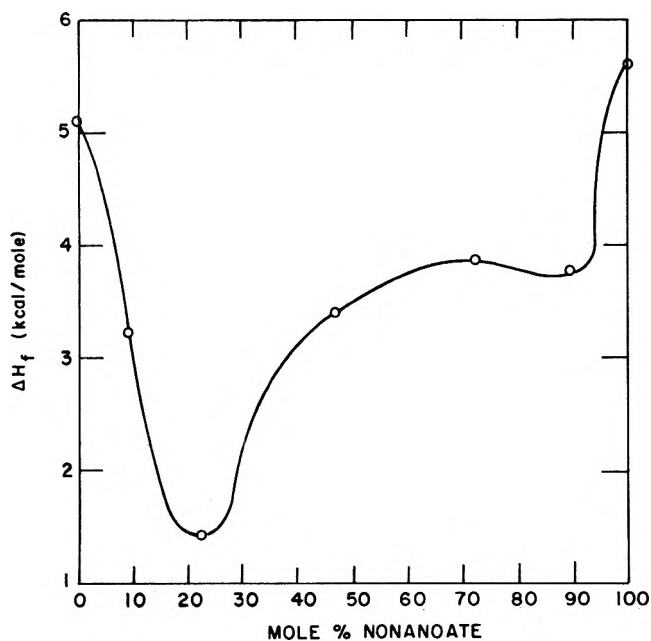


Figure 13. Enthalpy of fusion as a function of composition for cholesteryl butyrate-cholesteryl nonanoate.

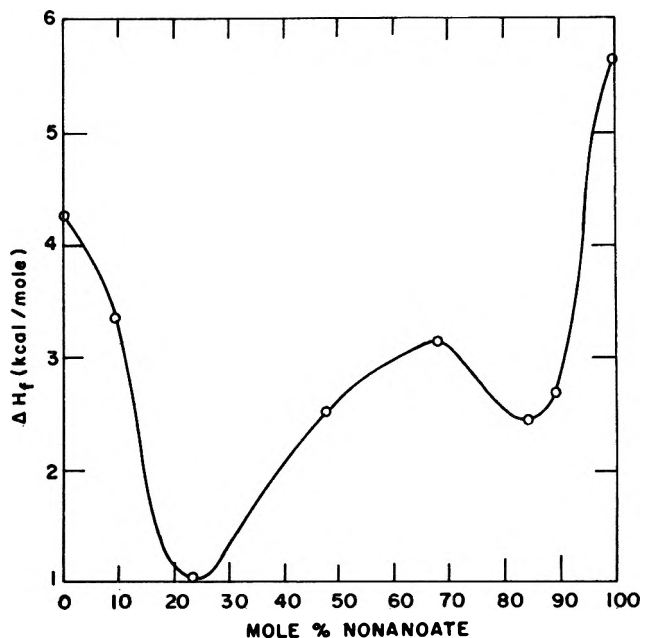


Figure 15. Enthalpy of fusion as a function of composition for cholesteryl 2-ethylbutyrate-cholesteryl nonanoate.

In all phase diagrams where appropriate transition lines were extrapolated in order to predict monotropic mesophases.^{7,8} Such predicted values are included in Table I.

Discussion

The results for the pure esters in light of the results for the binary mixtures suggest several conclusions relating alkanolate structure and mesomorphic behavior for these materials. Introduction of branching tends to cause the

cholesteryl alkanolates to be monotropic (series 1a and 1b); this is due to an increase in the crystal melting point since the extrapolated monotropic mesomorphic transition temperatures decrease as the branch approaches the carbonyl group (see series 1a and 1b, Table I). The slightly increased ΔH_f and ΔS_f support the conclusion deduced

(7) A. Bogojawlensky and N. Winogradoff, *Z. Phys. Chem.*, **60**, 433 (1907).

(8) R. Walter, *Chem. Ber.*, **58**, 2303 (1925).

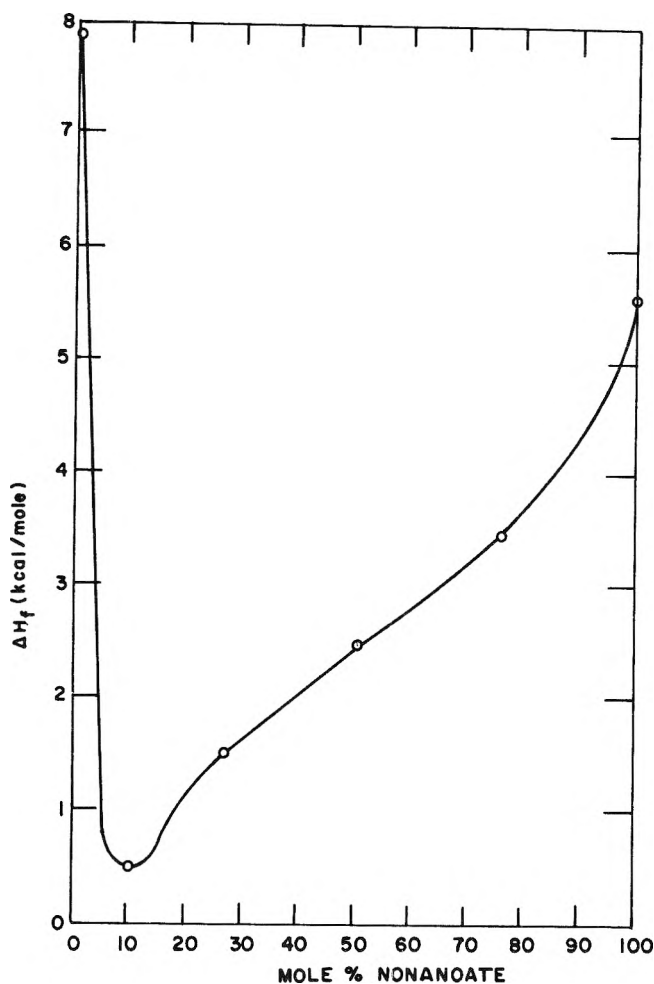


Figure 16. Apparent enthalpy of fusion as a function of composition for cholesteryl 1-adamantane carboxylate-cholesteryl nonanoate.

from the increased melting points, namely, the closer the branch to the carbonyl, the more highly organized the crystal structure. This point is corroborated by comparison of isopentanoate and isobutyrate (Table I), the later being significantly higher in melting point, ΔH_f and ΔS_f . This increased order is readily rationalized in terms of decreased rotation about the carbon-carbon single bonds of the alkanate portion due to steric influences of the branch.⁹

The results for the phase diagrams using series 1a indicate an increasing tendency for smectic behavior as the branch moves closer to the carbonyl in that pentanoate and isopentanoate are both predicted to be cholesteric (observed for pentanoate); 2-methylbutyrate is expected to be smectic rather than cholesteric, since the former extrapolated transition temperature is higher than that for the cholesteric transition. The tendency for alkanates with branches near the carbonyl to be smectic rather than cholesteric may be a steric effect. The carbonyl moiety undoubtedly is a major contributor to the intermolecular cohesive forces (either by dipole-dipole or dipole-induced dipole interactions) in the cholesteric mesophase of these compounds.¹⁰ Proximal branches could easily alter such an interaction to the point where the cholesteric mesophase is less stable than the smectic.

The adverse effect of branching on the tendency to mesomorphism can to some extent be offset by increasing the

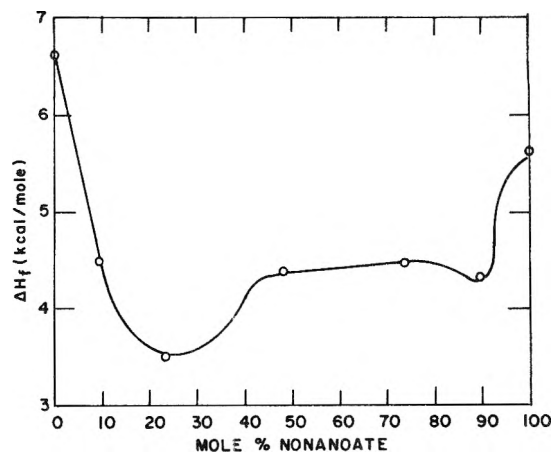


Figure 17. Enthalpy of fusion as a function of composition for cholesteryl hexanoate-cholesteryl nonanoate.

length of the branch. This tends to lower the melting point and ΔH_f and ΔS_f (series 2a and 2b), as a result of lowering the degree of organization in the crystal structure. When the chain length is increased monotropic smectic behavior is first observed, then enantiotropic smectic. However, this effect is not merely one of decreasing the melting point, as evidenced by the decreasing extrapolated and observed mesomorphic transitions of series 2a and 2b (see Table I). Thus, increasing the chain length decreases the thermal stability of both the crystal and mesophase, the former being more pronounced, and brings about smectic, rather than cholesteric behavior. Increased conformational flexibility apparently is the cause of these disorderings. Again, steric interference with the intermolecular bonding between carbonyl moieties in the cholesteric configuration is indicated; as the branch length is increased, disruption of the cholesteric mesophase occurs and a smectic mesophase results (compare Figures 3, 6 and 7; 5, 3, and 8; and 8 and 7, respectively).

Increases in the degree of branching bring about increased organization in the crystal phase as evidenced by increased melting point, ΔH_f and ΔS_f (series 3, Table I). Again this is attributed to decreased flexibility due to restricted rotation. The increased tendency toward smectic *vs.* cholesteric behavior as the degree of branching increases is evident in the phase diagrams (Figures 1, 3, and 9). Again, we attribute this to steric interference with the cohesive forces necessary for existence of the cholesteric mesophase, namely, those involving the ester carbonyl functions.

In series 4, although steric bulk and rigidity increase the melting point markedly, ΔH_f is relatively unaffected. We interpret this again in terms of conformational effects.

The unusual behavior of the 2-ethylhexanoate is noteworthy. The pure recrystallized material shows initial melting to a smectic phase at 47°. At 49.5° the system becomes completely isotropic. Upon cooling to room temperature an isotropic-smectic transition occurs at 28°. Since the isotropic-smectic transition cannot be supercooled, the following rationale is proposed. There are two diastereomers of cholesteryl 2-ethylhexanoate, since the racemic acid chloride was used in its preparation. When recrystallized these phases separate, but when melted they

(9) E. Eliel, N. Allinger, S. A. Anjyal, and G. Morrison, "Conformational Analysis," Wiley, New York, N. Y., 1965, p 5.

(10) H. Baessler and M. M. Labes, *J. Chem. Phys.*, **52**, 631 (1970).

TABLE II: Conclusions Relating Alkanoate Structure to Behavior of Cholesteryl Alkanoate-Cholesteryl Nonanoate Mixtures

Series	Alkanoate parameter	Meso-morphic comp. range	Effect on ^a maximum meso-morphic temp. range	Min T_m	S/C ^b	Min ΔH_f
1a, 1b	Branch closer to C=O	-	0	0	+	-
2a, 2b	Longer branch	+	-	+	+	+
3	Increased branching	-	-	+	+	-
d	Increased chain length	0	-	+	c	+

^a Plus indicate increasing value, minus decreasing, and 0 no meaningful change. ^b S/C = enantiotropic smectic/cholesteric area ratio. ^c No conclusion possible based on data presented here, but undoubtedly is plus generally. ^d Comparison of butyrate, pentanoate, and hexanoate (Figures 4, 1, and 11, respectively).

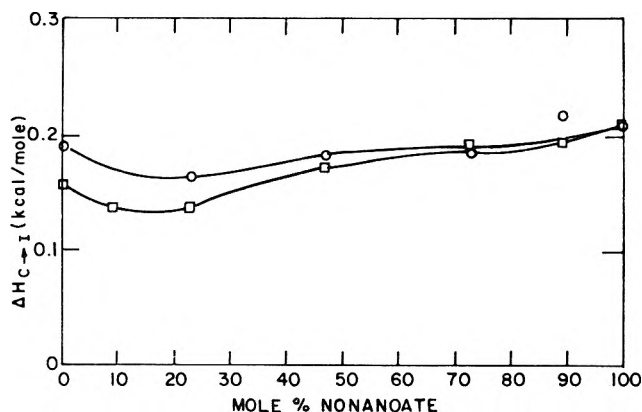


Figure 18. Enthalpy of the cholesteric to isotropic transition as a function of composition for (a) cholesteryl butyrate-cholesteryl nonanoate, \square , and (b) cholesteryl pentanoate-cholesteryl nonanoate, \circ .

form a homogeneous solution. This is why the extrapolated smectic point is in disagreement with that observed on the first heating (Figure 7); the extrapolated point is for homogeneous solid solution. The 2-methylhexanoate and 2-methylbutyrate do not exhibit this behavior even though they, too, were prepared from the racemic acid chlorides. A later paper will describe the effects of the chirality of the alkanoate portion of cholesteryl alkanoates on mesomorphic behavior.

We turn our attention now to the effect of these esters on behavior of binary mixtures with cholesteryl nonanoate. The general conclusions reached from our results are summarized in Table II.

The transition lines leading to the isotropic liquid in all the phase diagrams (Figures 1-9) are well approximated by one or more intersecting straight lines. If the total composition range is cholesteric (Figures 1, 4, and 9), a single straight cholesteric-isotropic transition line is observed. The slope of the isotropic transition line depends upon the alternate phase (*e.g.*, Figure 6). The enthalpic data of course reflect this. In Figure 18 the enthalpy of the

cholesteric to isotropic transition is shown as a function of composition for binary mixtures of the butyrate and valerate esters with nonanoate. An ideal straight line relationship exists within experimental error. All of the foregoing results imply ideality of the transition to the isotropic liquid. Such behavior has been observed in smectic and nematic mixtures.^{7,8,11-13} In fact, such ideal straight line behavior is an implicit assumption in the extrapolation of transition lines for prediction of monotropic mesomorphism.^{7,8} This behavior has been explained on the basis of the phase rule in cases where the transition is from the mesomorphic state to the isotropic liquid.¹⁴ It is indicative of ideal behavior in the isotropic liquid and in the mesomorphic state. In other words, the two materials in the cholesteric state are completely compatible (Figures 1, 4, and 9) as they are in the isotropic liquid. Very nearly straight line behavior is exhibited by the smectic to cholesteric transitions in Figures 3 and 6. Again, the two compounds in the smectic state are behaving nearly ideally.

The phase diagrams show that from 0 to 10% of material added to nonanoate, *i.e.*, >90% nonanoate, the slope, dT/dN , varies with the structure of the second component. Thus, the van't Hoff equation is not obeyed. However, the presence of solid solutions could modify the van't Hoff equation in a manner dependent on the nature of the second component due to distribution between the two phases involved.¹⁵ Thus, all our data at low solute levels could be described in terms of this modified van't Hoff equation. Alternatively nonideal or a combination of solid solution and nonideal behavior could explain the results.

Bearing in mind that these results are for binary mixtures of cholesteryl nonanoate, we believe that the melting point depression and ΔH_f are based upon mutual disruption of the crystal lattices of the two components.¹⁶ Enthalpy and entropy data indicate that the geometrical crystal packing of cholesteryl nonanoate differs from that of its lower homologs.¹⁷ A plot of interfacial (liquid crystal-crystal) surface energy *vs.* chain length of cholesteryl *n*-alkanoates has a minimum at about C₅.¹⁸ This implies a difference in crystal structure, mesomorphic structure, or both. Those molecules most similar to nonanoate in shape (minimal branching, short branches, or branches far away from the carbonyl) and size (length of longest chain) cause minimal change from ideal averaging of T_m 's and ΔH_f 's. The ΔH_f plots indicate that maximum disruption of crystal structure occurs near 25 and 75 mol % levels of nonanoate in most cases. Generally, the minimum ΔH_f occurs at about 25% nonanoate. This, we believe, indicates that nonanoate disrupts the second component more than *vice versa*. Again, this is consistent with the increased order in the branched species due to hindered

- (11) J. S. Dave and K. L. Vasnath, *Ind. J. Chem.*, **7**, 498 (1969).
- (12) J. S. Dave, P. R. Patel, and K. L. Vasnath, *Mol. Cryst. Liquid Cryst.*, **8**, 93 (1969).
- (13) M. J. S. Dewar and R. S. Goldberg, *J. Amer. Chem. Soc.*, **92**, 1582 (1969); *J. Org. Chem.*, **35**, 2711 (1970).
- (14) J. S. Dave and M. J. S. Dewar, *J. Chem. Soc.*, 4616 (1954); 4305 (1955).
- (15) G. N. Lewis and M. Randall, "Thermodynamics," 2nd ed. McGraw-Hill, New York, N. Y., 1961, p 235.
- (16) A. Ubbelohde, "Melting and Crystal Structure," Clarendon Press, Oxford, 1965.
- (17) E. M. Barrall, III, J. F. Johnson, and R. S. Porter, *Mol. Cryst. Liquid Cryst.*, **8**, 27 (1969).
- (18) J. M. Pochan and H. W. Gibson, *J. Amer. Chem. Soc.*, **94**, 5573 (1972).

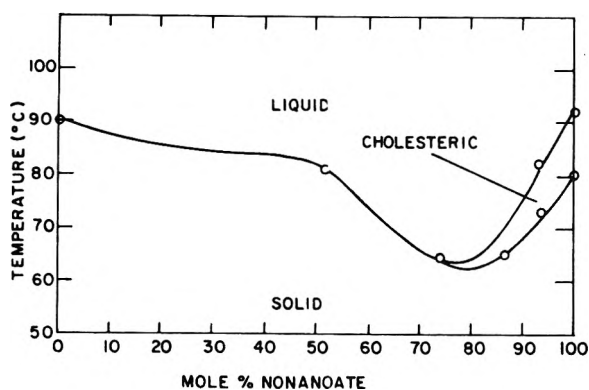


Figure 19. Phase diagram for cholest-5-ene-cholesteryl nonanoate.

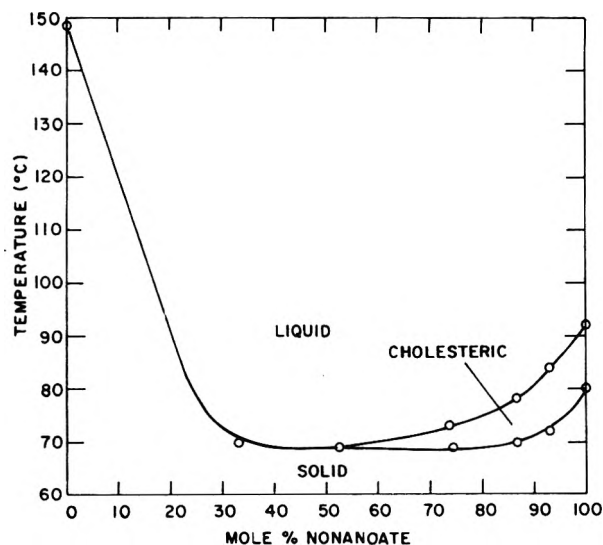


Figure 20. Phase diagram for cholesterol-cholesteryl nonanoate.

rotation about carbon-carbon bonds. Additionally, nonanoate is longer than any of the other materials. Apparently, it is able to accommodate the other alkanates within its crystal structure, leaving some voids, but it cannot be incorporated into the other crystal structures without great disruption. In the cases of pivalate and 1-adamantane carboxylate the crystal structures are not compatible with nonanoate over a wide composition range. For the latter there is a eutectic containing mainly (>90%) nonanoate as deduced from the data (Figure 16). The eutectic

melts at slightly lower temperature (75°) than nonanoate. It is cholesteric up to 90° and is monotropic smectic at 73°. The rest of the crystals melt gradually, up to the melting point of pure 1-adamantane carboxylate in some cases. The latter melting is not observed by DSC; thus, the apparent ΔH_f (Figure 16) increases linearly from 10 to 90% nonanoate as the proportion of the eutectic in the total mixture increases. Similar behavior was observed for pivalate.

The phase diagrams for 2-methylbutyrate, 2-methylhexanoate, and 2-ethylhexanoate with nonanoate, it should be pointed out, are in reality ternary, since each of the three alkanates is a mixture of diastereomers. This effect will be discussed in more detail in a forthcoming publication, but suffice it to say that no changes in the trends discussed here are observed.

It is of interest to note that in several of the esters (*e.g.*, isopentanoate and 2-methylbutyrate) incipient monotropic liquid crystalline behavior was observed near the predicted temperatures (Table I); apparently the ordering due to formation of the mesophase caused rapid recrystallization.

The binary phase diagrams of cholest-5-ene and cholesterol with cholesteryl nonanoate are presented in Figures 19 and 20. Neither of these materials has high mesomorphic tendency since the extrapolated transition temperatures are very low.

In summary then, the position, number, and length of branches in the alkanate portion of cholesteryl alkanates profoundly effect their mesomorphic behavior. Interactions of the carbonyl moieties are believed to be one of the major cohesive forces in the helix of the cholesteric mesophase. We postulate that branching in the neighborhood of the carbonyl interferes with these bonding forces and thereby leads to smectic behavior. Branching also decreases conformational mobility of the alkanate chain leading to more organization in the crystalline state; this can to some extent be offset by increasing the branch length. These latter factors control ΔH_f and melting point. The phase diagrams are explicable in terms of mutual disruption of the crystal lattices of the two components. Materials similar in size and shape behave more ideally in admixture than dissimilar materials. Small amounts of a long chain alkanate in a short one have a greater disruptive effect than *vice versa*.

Acknowledgment. The authors wish to thank Mr. F. C. Bailey for assistance in the synthesis of cholesteryl esters and Drs. Gunther, O'Reilly, and Goldberg for encouragement.

Analysis of Potential Difference in Electrically Induced Carrier Transport Systems

J. Bdzil, C. C. Carlier, H. L. Frisch,

Department of Chemistry, State University of New York, Albany, New York 12203

W. J. Ward, III,* and M. W. Breiter

General Electric Corporate Research and Development Center, Schenectady, New York 12301 (received July 28, 1972)

Publication costs assisted by General Electric Corporate Research and Development Center

Electrically induced carrier transport is a novel transport mechanism which can be operative in certain systems in which facilitated transport occurs. A result of this process is that a partial pressure difference across a liquid membrane causes an electrical potential difference to develop. A mathematical analysis of this potential resulted in a simple expression to calculate its value. The agreement of calculated and experimental potential differences is satisfactory.

1. Introduction

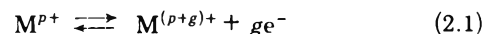
Facilitated transport of a solute across a membrane occurs as a result of a reversible reaction of the solute with a carrier which shuttles between opposite faces of the membrane.¹ The phenomenon is of interest because it is a fundamental process of living systems, and because it may have practical application in the development of new highly efficient separation processes. In an exploratory investigation of facilitated transport by Ward,² it was found that by a process of electrically induced carrier transport it was possible to "pump" a gas through a liquid film across which there was no partial pressure difference in that gas. By a related process, a partial pressure difference across the membrane resulted in an electrical potential difference.

Electrically induced carrier transport has been shown to occur with nitric oxide in a solution containing ferrous and ferric ions, and with carbon monoxide in a solution of cuprous and cupric ions. There are numerous other simple systems in which this type of transport process could be operative. In such systems, electrically induced carrier transport could have practical application for concentrating or detecting a particular gas. In order to evaluate the process for such applications and, in general, to understand it more thoroughly, a quantitative understanding of it is desirable. In this paper an expression is developed for the electrical potential difference, at zero current flow, caused by a partial pressure difference across the membrane.

2. Theory of the Monitoring Cell

A detailed qualitative description of electrically induced carrier transport has been given elsewhere.² When used as a monitoring device in the case of nitric oxide, for example, the system consists of an immobilized film of ferric and ferrous chloride solution with electrodes at each face of the film separating two reservoirs of nitric oxide. Nitric oxide reacts reversibly with ferrous ion, to form FeNO^{2+} , and does not react with ferric ion. When steady state is reached, there is a flux of nitric oxide across the membrane, accompanied by the appearance of an electrical potential across the electrodes. It is the magnitude of this potential that we wish to predict as a function of the system variables.

A generalized monitoring cell of width l with platinum electrodes at $x = 0$ and $x = l$ is shown schematically in Figure 1. The liquid film is contained between membranes permeable to the diffusing gas A, and consists of a solution (in a suitable solvent, e.g., formamide) of salts MX_p and MX_{p+g} where M is a metal, and X a monovalent anion which can be Cl^- . The solvent is to have a sufficiently high dielectric constant (ϵ) so that complete dissociation of the salts into the ions M^{p+} , X^- , and $\text{M}^{(p+g)+}$ occurs. We also shall assume that at the platinum electrodes the electrochemical reaction



has achieved equilibrium. The difference in electric potential ΔV across the electrodes can then be written as a sum of three potential differences (cf. Figure 1)

$$\Delta V = \varphi_1 - \varphi_4 = (\varphi_1 - \varphi_2) + (\varphi_2 - \varphi_3) + (\varphi_3 - \varphi_4)$$

where $\varphi_1 - \varphi_2$ and $\varphi_3 - \varphi_4$ are the galvanic potential differences and $\varphi_2 - \varphi_3$ is the diffusion potential drop inside the cell. The reference points 1 and 4 are on the electrodes and 2 and 3 are inside the cell in the "vicinity of the electrodes," i.e., in the solution just outside the electrical double layer of the electrode-solution interface.

It follows from the equilibrium of the reaction shown in (2.1) that (neglecting, here as elsewhere, activity coefficients)

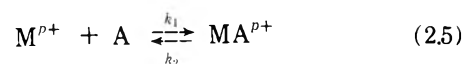
$$\varphi_1 - \varphi_2 = E_0 + (RT/gF) \ln [(M^{(p+g)+})_2 / (M^{p+})_2] \quad (2.3)$$

and

$$\varphi_4 - \varphi_3 = E_0 + (RT/gF) \ln [(M^{(p+g)+})_3 / (M^{p+})_3] \quad (2.4)$$

with E_0 the standard electrode potential and the expressions in parentheses with the subscripts 2 and 3 refer to the concentrations of the indicated ions in the planes 2 and 3, respectively.

Let A be the diffusing gas, and assume that it reacts only with M^{p+} (not $\text{M}^{(p+g)+}$) according to the reversible reactions



(1) W. J. Ward, *AIChE J.*, **16**, 405 (1970).

(2) W. J. Ward, *Nature (London)*, **227**, 162 (1970).

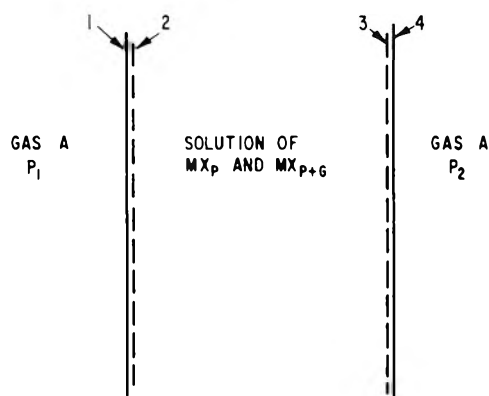


Figure 1. Schematic of monitoring cell.

with k_1 and k_2 the rate constants for the forward and reverse reaction, respectively. The species present in the liquid film are M^{p+} , $M^{(p+g)+}$, MA^{p+} , X^- , and dissolved A. Let the steady-state concentrations and diffusion coefficients of these species be denoted by

$$\begin{aligned} c &= (A) & D_c &= kTB_c \\ u &= (M^{(p+)}) & D_u &= kTB_u \\ v &= (M^{(p+g)+}) & D_v &= kTB_v \\ w &= (MA^{p+}) & D_w &= kTB_w \\ n &= (X^-) & D_n &= kTB_n \end{aligned} \quad (2.6)$$

with the B 's the constant mobilities. The condition of differential mass balance at any point within the film, $0 < x < l$, for each species leads at steady state to the following Nernst-Planck equations

$$B_c kT(d^2c/dx^2) - k_1cu + k_2w = 0 \quad (2.7)$$

$$B_u[kTd^2u/dx^2 + ped/dx(ud\varphi/dx)] - k_1cu + k_2w = 0 \quad (2.8)$$

$$B_v[kTd^2v/dx^2 + (p+g)ed/dx(vd\varphi/dx)] = 0 \quad (2.9)$$

$$B_w[kTd^2w/dx^2 + ped/dx(wd\varphi/dx)] - k_2w + k_1cu = 0 \quad (2.10)$$

$$B_n[kTd^2n/dx^2 - ed/dx(nd\varphi/dx)] = 0 \quad (2.11)$$

where e is the electronic charge and the electric potential $\varphi(x)$ satisfies the Poisson equation

$$d^2\varphi/dx^2 = -(4\pi F/\epsilon)[pu + (p+g)v + pw - n] \quad (2.12)$$

The system (2.7-2.12) has to be solved subject to the following boundary conditions. (a) The film boundaries are impermeable to the ionized species; *viz.*, at $x = 0$ or l

$$kT(du/dx) + peu(d\varphi/dx) = 0 \quad (2.13)$$

$$kT(dv/dx) + (p+g)ev(d\varphi/dx) = 0 \quad (2.14)$$

$$kT(dw/dx) + pew(d\varphi/dx) = 0 \quad (2.15)$$

$$kT(dn/dx) - en(d\varphi/dx) = 0 \quad (2.16)$$

(b) The gas A dissolves at the film surfaces $x = 0, l$ according to the relations

$$c(0) = Sp_1, c(l) = Sp_2 \quad (2.17)$$

where S is the Henry's law solubility and p_1 and p_2 are

the partial pressures of A in the reservoirs adjacent to the film surface $x = 0$ and $x = l$, respectively. (c) There is overall electroneutrality in the liquid film

$$\int_0^l [pu + (p+g)v + pw - n]dx = 0$$

Integrating (2.12) over x from $x = 0$ to $x = l$ and using the above we have

$$(d\varphi/dx)_{x=0} = (d\varphi/dx)_{x=l} \quad (2.18)$$

We also need the initial concentration of MX_p and $MX_{(p+g)}$

$$(MX_p)_0 = C_p^0, (MX_{(p+g)})_0 = C_{p+g}^0 \quad (2.19)$$

Basic simplification of this problem can be achieved if the mobility of MA^{p+} , B_w , can be set equal to the mobility of M^{p+} , B_u

$$B_w = B_u = B \text{ or } D_w = D_u = D \quad (2.20)$$

Ordinarily, for most simple, diatomic gases, $D_c > D_u, D_v$. The diffusion coefficient of the complex MA^{p+} , being first charged and second of larger mass, ought to be of the same order of magnitude as D_u or D_v . While this is not an argument for the identity exhibited in (2.20), it suggests that (2.20) might be taken to be the starting point for a perturbation treatment of this problem. As we shall see in the Appendix, the results of the perturbation substantiate the results of assuming (2.20) to be strictly valid. In the remainder of this section we accept (2.20) and show that as a consequence $\varphi(x)$ is constant everywhere in $0 < x < l$ and that the system of six, coupled, nonlinear differential equations (2.7-2.19) reduces to three, simpler, coupled nonlinear differential equations whose numerical solution has already been obtained.¹ The physical basis of this simplification is straightforward; if $D_u = D_w$, the rate of M^{p+} ion transfer is independent of whether the ion is in the state, local electroneutrality is established everywhere within the film, *i.e.*, the right-hand side of (2.12) vanishes. Thus, $\varphi(x)$ must be constant and in turn (2.9) and (2.11) are decoupled from the remaining system of equations, and by virtue of (2.14) and (2.16) possess constant solutions.

To demonstrate that this is the *unique* solution we note that (2.9) and (2.11) can be immediately integrated subject to (2.14) and (2.16), respectively, to give

$$v(x) = v(0) \exp[-(p+g)e(\varphi(x) - \varphi(0))/kT] \quad (2.21)$$

and

$$n(x) = n(0) \exp[-e(\varphi(x) - \varphi(0))/kT] \quad (2.22)$$

Subject to (2.20) one finds, adding (2.8) and (2.10), as well as (2.13) and (2.15), that $u(x) + w(x)$ is given by

$$u(x) + w(x) = N \exp[-pe(\varphi(x) - \varphi(0))/kT] \quad (2.23)$$

with $N = u(0) + w(0)$. Set

$$y(x) = e[\varphi(x) - \varphi(0)]/kT \quad (2.24)$$

and substituting (2.21-2.24) in (2.12) one obtains

$$d^2y/dx^2 = -(4\pi Fe/\epsilon kT)[pNe^{-py} + (p+g)v(0)e^{-(p+g)y} - n(0)e^y] \quad (2.25)$$

The constants N , $v(0)$, and $n(0)$ can be eliminated from (2.25) by using conservation of species and the given initial concentrations in (2.19), *viz.*, we have from (2.21-2.23)

$$N = \int_0^l [u(x) + w(x)] dx / \int_0^l e^{-py} dx =$$

$$lC_p^0 / \int_0^l e^{-py} dx = C_p^0 / \int_0^1 e^{-py(x')} dx' \quad (2.26)$$

$$v(0) = C_{p+g}^0 / \int_0^1 e^{-(p+g)(x')} dx'$$

$$n(0) = [(p+g)C_{p+g}^0 + pC_p^0] / \int_0^1 e^{y(x')} dx'$$

with $x' = x/l$. Introducing the dimensionless constants

$$Q = (4\pi Fe l^2 / \epsilon k T) [(p+g)C_{p+g}^0 + pC_p^0] \quad (2.27)$$

and

$$\alpha = pC_p^0 / [(p+g)C_{p+g}^0 + pC_p^0]$$

together with (2.26) allows us to rewrite (2.25) as

$$d^2y(x')/dx'^2 = -Q\{\alpha e^{-py}/p \int_0^1 e^{-py} dx' +$$

$$\{(1-\alpha)e^{-(p+g)y} / \int_0^1 e^{-(p+g)y} dx'\} + (e^y / \int_0^1 e^y dx')\} \quad (2.28)$$

Setting $P = dy(x')/dx'$, $d^2y(x')/dx'^2 = dP/dx' = (dP/dy)(dy/dx') = P dP/dy$ we can integrate (2.28) once to obtain

$$P^2/2 = Q\{\alpha e^{-py}/p \int_0^1 e^{-py} dx' +$$

$$[(1-\alpha)e^{-(p+g)y} / (p+g) \int_0^1 e^{-(p+g)y} dx'] +$$

$$(e^y / \int_0^1 e^y dx')\} + (P_0^2/2) \quad (2.29a)$$

with $(dy/dx')_{x'=0} = P_0$. If $z = \exp[-y(x')]$, $\theta = \exp[-y(1)]$, $P_1 = (dy/dx')_{x'=1}$ and using (2.18) we have from (2.29a) that

$$(P_1^2 - P_0^2)/2Q = 0 = \{\alpha(\theta^p - 1)/p \int_0^1 z^p dx' +$$

$$[(1-\alpha)(\theta^{p+g} - 1)/(p+g) \int_0^1 z^{p+g} dx'] +$$

$$[(\theta^{-1} - 1) / \int_0^1 z^{-1} dx']\} \quad (2.29b)$$

Substituting the value of

$$\int_0^1 z^{-1} dx'$$

obtained from (2.29b) in (2.29a) one obtains after some rearrangement

$$P^2 - P_0^2/2Q = -[(1-z)/z] \times$$

$$\alpha \sum_{i=1}^p (z^i - \theta^i) / p \int_0^1 z^p dx' + [(1-\alpha) \times$$

$$\sum_{i=1}^{p+g} (z^i - \theta^i) / (p+g) \int_0^1 z^{p+g} dx'] = F(z, \theta) \quad (2.30)$$

One solution of (2.30) is $y(x') = 0$ subject to $y(0) = 0$ (cf. (2.24)). We now show that this solution is the unique, real, bounded solution of (2.30).

To do this we note that the only finite positive roots of $F(z, \theta)$ are $z = 1$ and $z = \theta$. At $x = 0$, $P = P_0$. At $x = 0 + \epsilon$ we consider the following possibilities. (a) $P > P_0$; then $y > P_0\epsilon$ and must remain so until $(P - P_0)$ can vanish for $y = y(1)$ (not necessarily at the boundary). However, in this interval $P^2 - P_0^2 > 0$ while $F < 0$, a clear contradiction. (b) $P > -P_0$; then $y < -P_0\epsilon$ and must remain so until $(P - P_0)$ can vanish for $y = y(1)$. However, in this interval

$P^2 - P_0^2 > 0$ while $F < 0$, a clear contradiction. (c) $-P_0 < P < P_0$; then P is bounded by the rays, P_0x' and $-P_0x'$, and can never achieve the boundary value at $x' = 1$ which is $P = P_0$. (d) $P = P_0$; whence $P^2 - P_0^2 = 0$. However, F can only vanish if $y = y(0) = 0$ or $y = y(1)$. This can only occur if $y = y(0) = 0$ and $P_0 = 0$.

Thus,

$$\varphi(x) = \varphi(0)$$

a constant, and

$$\varphi_2 - \varphi_3 = 0 \quad (2.31)$$

By virtue of (2.31) we find from (2.21), (2.22), and (2.23) that $v(x) = v(0)$, $n(x) = n(0)$, and $u(x) + w(x) = N$ are all constant within the liquid film. Thus, from (2.2) and (2.3), the desired expression for ΔV is simply

$$\Delta V = (RT/gF) \ln [(M^{p+})_3 / (M^{p+})_2] =$$

$$(RT/gF) \ln [u(l)/u(0)] \quad (2.32)$$

Since $\varphi(x)$ is constant, subject to our basic assumption (2.20), the electrical migration terms vanish in the coupled simplified system of nonlinear equations from which $u(x)$ can be determined. These are obtained from (2.7), (2.8), and (2.10), respectively

$$D_c(d^2c/dx^2) - k_1cu + k_2w = 0 \quad (2.33)$$

$$D(d^2u/dx^2) - k_1cu + k_2w = 0 \quad (2.34)$$

$$D(d^2w/dx^2) - k_2w + k_1cu = 0 \quad (2.35)$$

subject to (2.17) and

$$du/dx = dw/dx = 0 \quad (2.36)$$

at $x = 0, l$. This system of equations can be reduced to a single, second-order, non-linear differential equation in c (for details the reader is referred to ref 1). A numerical procedure for solving this equation, based on Galerkin's method, has been worked out by Roe and is described in ref 1. In particular for nitric oxide transport in ferrous ion solution, numerical data are given in Figure 3 of ref 1 for the flux of nitric oxide as a function of C_2^0 , the total ferrous ion concentration from which $u(l)/u(0) = (Fe^{2+})_3 / (Fe^{2+})_2$ needed in (2.32) can be evaluated.

3. Experimental Verification

The establishment of the equilibrium of the reaction shown in eq 2.1 for Fe^{2+} , Fe^{3+} was verified experimentally on electrodes of smooth and platinized platinum in formamide solutions containing different amounts of $FeCl_2$ and $FeCl_3$. The electrode potential of the test electrode was determined vs. an $Ag|AgCl$ reference electrode as a function of the concentration ratio $(Fe^{3+})/(Fe^{2+})$ in formamide solutions, saturated with pure nitrogen. The potentials of smooth and platinized platinum agreed within 1 mV at a given ratio of $(Fe^{3+})/(Fe^{2+})$. The plot of the electrode potential vs. the logarithm of the concentration ratio yielded a straight line with a slope of 58 mV/decade as to be expected from a one-electron reaction, $Fe^{2+} \rightleftharpoons Fe^{3+} + e^-$.

The liquid film holder, vacuum system, and arrangement of electrodes, shown schematically in Figure 1, employed to make emf and transport measurements of NO across the Fe^{2+}, Fe^{3+} formamide solution film are described in ref 2 and 3.

(3) G. Sansone and J. Gerretsen, "Lectures on the Theory of Functions of Complex Variables," P. Noordhoff, Ltd., Groningen, The Netherlands, 1960, p 458 ff.

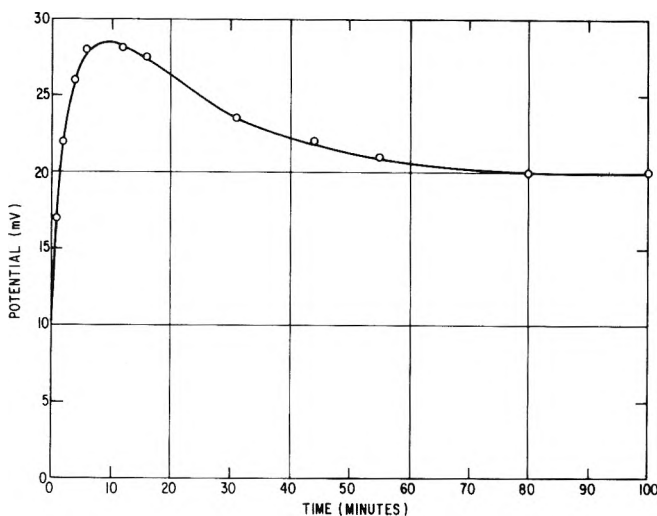


Figure 2. Electrical potential buildup vs. time for nitric oxide permeation through liquid film initially 0.25 M in Fe^{2+} and Fe^{3+} .

Initially with vacuum applied to both sides of the film, ΔV was zero. At time zero, 750-mm of NO was admitted to the high-pressure reservoir and the potential difference was recorded as a function of time. Invariably, the potential rose to a maximum value in several minutes, and then declined to an almost stable value. Typical data are shown in Figure 2 for the case of a film initially 0.25 M in Fe^{2+} and 0.25 M in Fe^{3+} . The reason for the maximum in the curve is not understood. After a nearly steady value is reached, a very slow drop in potential occurs, probably because of a slow oxidation of Fe^{2+} in the system.

The experimental measurements and potential differences calculated from eq 2.32 are shown in Table I. The values of $u(l)$ and $u(0)$ were obtained numerically as described above, using the following system constants previously determined¹

$$\begin{aligned}
 l &= 0.103 \text{ cm} \\
 D_{\text{NO}} &= 1.5 \times 10^{-5} \text{ cm}^2/\text{sec} = D_c \\
 D_{\text{Fe}^{2+}} &= 2 \times 10^{-6} \text{ cm}^2/\text{sec} = D \\
 D_{\text{FeNO}^{2+}} &= 2 \times 10^{-6} \text{ cm}^2/\text{sec} = D \\
 k_1 &= 7.15 \times 10^3 \text{ cc/mol sec} \\
 k_2 &= 9 \times 10^{-3} \text{ sec}^{-1}
 \end{aligned} \tag{3.1}$$

$$C(0) = 2.62 \times 10^{-6} \text{ mol/cc} \quad (p_1 = 750 \text{ mm pressure of NO})$$

$$c(l) = 0 \quad (p_2 = 0 \text{ (vacuum)})$$

The agreement between the experimental and calculated values is reasonably good, and suggests that this analysis is sufficiently realistic to use it in evaluating the application of electrically induced carrier transport as a detection method.

Clearly, substantial theoretical problems remain in developing a quantitative understanding of electrically induced carrier transport. The reason for the observed maximum in the potential difference is not clear, and no analysis exists for nonzero current flow.

Appendix

Perturbation Theory. In this appendix we relax (2.20) and set

$$D = D_u = kTB \tag{A.1}$$

$$D_w = kTB(1 - \sigma), \quad |\sigma| < 1$$

so that σ will be our dimensionless perturbation parameter. We expand c , u , v , w , n , and φ in σ , viz.

$$\begin{aligned}
 c &= c_0 + \sigma c_1 + \dots \\
 u &= u_0 + \sigma u_1 + \dots \\
 v &= v_0 + \sigma v_1 + \dots \\
 w &= w_0 + \sigma w_1 + \dots \\
 n &= n_0 + \sigma n_1 + \dots
 \end{aligned} \tag{A.2}$$

Substituting (A.1) and (A.2) into (2.7-2.19) we find that c_0, \dots, φ_0 is the previously found unperturbed solution, with φ_0 a constant, and c_1, \dots, φ_1 , which satisfy the system of equations

$$D_c(d^2c_1/dx^2) - k_1(c_0u_1 + c_1u_0) + k_2w_1 = 0 \tag{A.3}$$

$$\begin{aligned}
 B\{kTd^2u_1/dx^2 + ped/dx(u_0d\varphi_1/dx)\} - \\
 k_1(c_0u_1 + c_1u_0) + k_2w_1 = 0 \tag{A.4}
 \end{aligned}$$

$$B_0\{kTd^2v_1/dx^2 + (p + g)ed/dx(v_0d\varphi_1/dx)\} = 0 \tag{A.5}$$

$$\begin{aligned}
 B\{kTd^2w_1/dx^2 + ped/dx(w_0d\varphi_1/dx)\} - \\
 k_2w_1 + k_1(c_0u_1 + c_1u_0) - BkTd^2w_0/dx^2 = 0 \tag{A.6}
 \end{aligned}$$

$$B_n\{kTd^2n_1/dx^2 - ed/dx(n_0d\varphi_1/dx)\} = 0 \tag{A.7}$$

$$d^2\varphi_1/dx^2 = (4\pi F/\epsilon)[pu_1 + (p + g)v_1 + pw_1 - n_1] \tag{A.8}$$

with the boundary conditions (2.13)-(2.16) and (2.18) on the dependent variables with subscript one and (2.17) replaced by

$$c_1(0) = c_1(l) = 0 \tag{A.9}$$

Differentiating (A.8) and setting $y_1 = e|\varphi_1(x) - \varphi_1(0)|/kT$ one finds

$$\begin{aligned}
 d^3y_1/dx^3 = -4\pi Fe/\epsilon kT[p(du_1/dx + dw_1/dx) + \\
 (p + g)dv_1/dx - dn_1/dx]
 \end{aligned}$$

Adding (A.4) and (A.6) and integrating this sum as well as (A.5) and (A.7) once, using the boundary conditions, and substituting in the above equation for $d(u_1 + w_1)/dx$, dv_1/dx , and dn_1/dx one obtains

$$\begin{aligned}
 d^3y_1/dx^3 = -4\pi Fe/\epsilon kT[pdw_0/dx - p^2(u_0 + v_0)dy_1/dx - \\
 (p + g)^2v_0dy_1/dx - n_0dy_1/dx] \tag{A.10}
 \end{aligned}$$

Now using (cf. (2.12))

TABLE I: Comparison between Calculated and Measured Values of ΔV

Film composition	Maximum ΔV , mV	ΔV (steady value), mV	ΔV (calculated from eq 2.32 $u(l)/u(0)$ obtained numerically), mV
0.05 M FeCl_2	40	30 ^a	20
0.045 M FeCl_3			
0.05 M FeCl_2	36	20	20.4
0.05 M FeCl_3			
0.25 M FeCl_2	28	20	19.3
0.25 M FeCl_3			

^a Value obtained after 30 min, before $\Delta V(t)$ levels off.

$d^2\varphi_0/dx^2 = -(4\pi F/\epsilon)[pu_0 + (p+g)v_0 + pw_0 - n_0] = 0$
 in (A.10) one can rewrite it, after some algebra, as

$$d^3y_1/dx^3 = -(4\pi Fe/\epsilon kT)\{p(dw_0/dx) - (dy_1/dx)[g(p+g)v_0 + (p+1)n_0]\} \quad (\text{A.11})$$

But $v_0(x) = v_0(0)$ and $n_0(x) = n_0(0)$ (cf. section 2) and introducing the dimensionless variable $x' = x/l$ we can write (A.11) as

$$(d^3y_1/dx'^3) - H^2(dy_1'/dx') = -(H^2/S_0)p(dw_0/dx') \quad (\text{A.12})$$

with

$$S_0 = g(p+g)v_0(0) + (p+1)n_0(0) \\ H^2 = S_0(4\pi Fe l^2/\epsilon kT) \quad (\text{A.13})$$

Adding (2.7) and (2.10) and integrating once one finds that

$$dw_0/dx' = -D_c[dc_0/dx' - (dc_0/dx')_{x=0}]/D_w = S_0f(x')/p \quad (\text{A.14})$$

and that

$$f(x' = 0) = 0 \quad (\text{A.15})$$

Introducing (A.14) into (A.12) and setting $z_1(x') = dy_1/dx'$ we obtain

$$(d^2z_1/dx'^2) - H^2z_1 = H^2f(x') \quad (\text{A.16})$$

whose solution subject to the boundary conditions on dy_1/dx' is

$$z_1(x') = \int_0^x Hf(x) \sinh [H(x' - x)] dx - \\ \sinh (Hx')/\sinh (H) \int_0^1 Hf(x) \sinh [H(1-x)] dx \quad (\text{A.17})$$

Finally the desired difference in potential is

$$e[(\varphi_1)_2 - (\varphi_1)_3]/kT = \sigma \int_0^1 z_1(x') dx' \quad (\text{A.18})$$

Rather than carrying out an explicit evaluation of (A.17) and (A.18) we content ourselves to an order of magnitude estimate. We note that usually $H^2 \gg 1$ ($H^2 \approx 10^{16}$ under the conditions discussed in section 3). Standard asymptotic theory³ of ordinary differential equations thus assures us that subject to (A.15)

$$e[(\varphi_1)_2 - (\varphi_1)_3]/kT \sim \sigma O(H^{-1}) \quad (\text{A.19})$$

which provides the justification for employing the procedure adopted in section 2.

Acknowledgments. This work was supported in part by the National Science Foundation Grants No. GA-27700 and PR I988I00I and the American Chemical Society Petroleum Research Fund Grant No. 35I9C56.

Diffusion of Hydrogen in Gold-Palladium Alloys

S. Maestas and Ted B. Flanagan*

Chemistry Department, University of Vermont, Burlington, Vermont 05401 (Received September 27, 1972)

Diffusion constants for interstitial hydrogen have been determined for a series of randomly substituted face-centered cubic gold-palladium alloys (0-112%) at small hydrogen contents where the dissolved hydrogen behaves ideally. A gold content of approximately 20 atom % has little effect on the diffusion constant, *i.e.*, it is unchanged from that of pure palladium. For gold contents greater than 20%, values of D decline logarithmically with gold content to $D = 7.4 \times 10^{-10} \text{ cm}^2 \text{ sec}^{-1}$ (37°) for the Au(55.7%)-Pd which was the largest gold content investigated here. The energies of activation and the preexponential factors have been measured for two alloys with large gold contents.

Introduction

The diffusion of hydrogen in substitutional face-centered cubic (fcc) palladium alloys offers great scope for the fundamental elucidation of interstitial diffusion. The electronic and geometric (size of the lattice) character of the host palladium matrix can be systematically altered by alloying. With this approach it may be possible to determine what factors influence the magnitude of the diffusion constants.

A variety of conventional, macroscopic techniques employed in different laboratories have recently given nearly

similar results for the diffusion of hydrogen in the α and β phases of the Pd-H₂ system.¹⁻⁵ (By contrast, microscopic techniques such as inelastic neutron scattering give significantly smaller energies of activation;^{6,7} the reason for the difference is not known.)

- (1) G. Bohmholdt and E. Wicke, *Z. Phys. Chem. (Frankfurt am Main)*, **56**, 133 (1967).
- (2) G. Holleck and E. Wicke, *Z. Phys. Chem. (Frankfurt am Main)*, **56**, 155 (1967).
- (3) J. W. Simons and T. B. Flanagan, *J. Phys. Chem.*, **69**, 358 (1965).
- (4) M. von Stackelberg and P. Ludwig, *Z. Naturforsch.*, **19**, 93 (1964).
- (5) H. Zuchner, *Z. Naturforsch. A*, **25**, 1490 (1970).

Hydrogen is known to occupy the octahedral interstitial positions in the α and β phases of the Pd-H₂ system^{8,9} and in several fcc palladium-rich alloys.^{10,11} It seems safe to assume that in all fcc palladium-rich alloys the octahedral sites are occupied by the hydrogen interstitials. Diffusion then involves a migration from one octahedral interstitial position to an adjacent vacant octahedral interstitial position. It has been suggested that this occurs *via* a tetrahedral site.¹²

Most available data for the diffusion of hydrogen in palladium alloys is on the Ag-Pd-H₂ system^{2,5,13-15} because this system is of technological interest for the purification of hydrogen. Surprisingly the addition of substitutional silver up to about 25% has little effect on the diffusion constant. Above 25% silver the value of the diffusion constant declines markedly with silver so that, for example, at 60% silver it is 5×10^{-10} compared to 3×10^{-7} cm²/sec for pure palladium (30°). These constants were measured at very small hydrogen contents where nonideality can be neglected.

The gold-palladium system is of interest with regard to hydrogen diffusion because it has been frequently employed for ascertaining the effect of the filling in of the d band on the catalytic activity of palladium. In addition, since the thermodynamics of absorption have been determined,^{16,17} these data may be used for the interpretation of diffusion data.

Experimental Section

Apparatus and Materials. Most diffusion measurements were performed electrochemically using a time-break-through method. Membranes of gold-palladium of various compositions were mounted with Teflon O-rings in a cell which separated two solutions of 1 N H₂SO₄. The potential on the polarization side was controlled potentiostatically *via* a Luggin capillary which was connected to the potentiostat (Wenking). On the diffusion side of the cell a reference electrode, generally a Au(26.5%)-Pd electrode was inserted, which, together with the diffusion side of the membrane, comprised a cell which monitored changes of the potential on the diffusion side. The gold-palladium electrode was employed rather than, for example, a Pt electrode so that the electrode had a greater amount of stored hydrogen and consequently a greater stability with time when the charging of the membrane was interrupted. A strip chart recorder (Moseley, Model 7101B) was employed to follow potential changes on the diffusion side of the membrane.

The gold-palladium membranes were supplied by Engelhard Industries, Inc., and were about 0.01 cm in thickness. The compositions of the various alloys are quoted in atomic per cent gold. The alloys were prepared by melting under argon. They all exhibit fcc lattices with spacings consistent with literature values. There is no evidence of any long-range order judging from the absence of superlattice reflections in the X-ray patterns.

After the diffusion runs were completed for a given membrane, it was mounted in clear plastic casting resin. The plaster castings were polished and the thickness of the membrane could be accurately determined microscopically. Typical measurements of the thickness gave, *e.g.*, on the Au(40%)-Pd, 0.0101 ± 0.00005 cm. The thickness was determined over at least five portions of the membrane and it was uniform to the thickness noted. The area of the exposed portion of the membrane was approximately 1 cm².

For the gas-phase measurements a large plate of alloy was activated by electrolytic deposition of palladium black onto its surface. It was then placed into a reaction vessel and attached to a Sieverts' type apparatus. The pressure was maintained constant by adjusting a mercury buret during hydrogen uptake. The sample was protected from mercury by gold foil.

Procedure. Data determined here were under the conditions $n \rightarrow 0$, where n = H-to-metal atom ratio. For the electrochemical determinations the membrane and the reference electrode were charged potentiostatically to the same potential, which corresponded to a vanishingly small hydrogen content, *e.g.*, 100 mV with respect to a normal hydrogen electrode for the Au(18.8%)-Pd sample. This potential corresponds to a small hydrogen content, *i.e.*, $n \rightarrow 0$. Electrode potentials were measured with a potentiometer prior to the diffusion runs (Leeds and Northrup, K-3). When the potentiostatic charging was interrupted, the potential difference, ideally zero, between the reference electrode (Au(26.5%)-Pd) and diffusion side of the membrane was recorded. When this potential difference, and its change with time, was small, a diffusion run could be initiated. However, before a diffusion run was started, the diffusion side of the membrane and the reference electrode were connected directly to the high internal impedance recorder; at this stage of the procedure all other components were removed from the circuit. It was generally a time-consuming procedure to equilibrate the membrane and reference electrode to the same potential. It would have been more convenient to employ a different type of reference electrode, *e.g.*, SCE, and to have compensated for the difference between the two electrodes with a potentiometer. However, the inclusion of a potentiometer in the circuit during the diffusion run gave rise to spurious effects. A maximum in the potential-time trace, such as noted by Küssner,¹⁵ was observed when the potentiometer was included in the circuit and this gives rise to difficulties in evaluation of the breakthrough time. Küssner attributed a similar maximum which he had observed (see Figure 7, ref 15) to an elastic deformation of the membrane associated with the introduction of the pulse of hydrogen.¹⁵ It is suggested that it is an effect of experimental origin since it was eliminated here as described above.

The reference electrode, which must have a large surface and be catalytically active, was located as close to the diffusion side of the membrane as possible so that the IR drop between the reference and diffusion side of the membrane was small. A small minimum following the perturbation (Figure 1) could not be eliminated and is probably associated with a capacitance effect on the diffusion side of the membrane resulting from the perturbation on the polarization side. The recovery time for this minimum was rapid compared to the breakthrough times. The

- (6) K. Skold and G. Nelin, *J. Phys. Chem. Solids*, **28**, 2369 (1967).
- (7) M. M. Beg and D. K. Ross, *J. Phys. C*, **3**, 2487 (1970).
- (8) J. E. Worsham, M. K. Wilkinson, and C. G. Shull, *J. Phys. Chem. Solids*, **3**, 303 (1957).
- (9) G. Nelin, *Phys. Status Solidi (b)*, **45**, 527 (1971).
- (10) A. Maeland, *Can. J. Phys.*, **46**, 121 (1968).
- (11) M. R. Chowdhury, Ph.D. Thesis, University of Birmingham, 1971.
- (12) E. Wicke, *Simp. Dynam. Reaz. Chim.*, **265** (1966).
- (13) D. N. Jewett and A. C. Makrides, *Trans. Faraday Soc.*, **61**, 932 (1965).
- (14) G. L. Holleck, *J. Phys. Chem.*, **74**, 503 (1970).
- (15) A. Küssner, *Z. Naturforsch. A*, **21**, 515 (1966).
- (16) K. Allard, A. Maeland, J. Simons, and T. B. Flanagan, *J. Phys. Chem.*, **72**, 136 (1968).
- (17) T. B. Flanagan, to be submitted for publication.

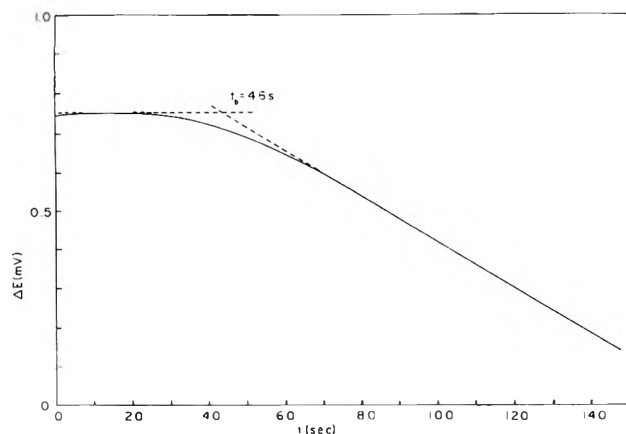


Figure 1. Typical potential-time trace for Au(26.5%)–Pd alloy (37°). Initial potential of membrane 144.3 mV with respect to Pt–H₂. Anodic perturbation applied ~2 mV.

cell was thermostatted in an oil bath to $\pm 0.1^\circ$. The membrane was well grounded.

After the potentials of the reference Au–Pd electrode and membrane were nearly similar and stable, a small anodic or cathodic pulse, generally 2 mV, was applied potentiostatically between the polarization side of the membrane and the working platinum electrode. A potential-time trace was recorded (Figure 1) from which the breakthrough time could be evaluated. The recorder has a 1 megohm input resistance and the resistance of the cell, *i.e.*, the resistance between the diffusion side (activated with palladium black) and the Au–Pd reference electrode, was <10 ohms. When the diffusion side was unactivated, the cell resistance was larger by a factor of about 5. If a microvoltmeter (Keithley, Model 153 of input resistance 10 megohms) was substituted for the recorder, similar breakthrough times were measured for typical gold–palladium alloy membranes.

Evaluation of Potential-Time Traces. Küssner¹⁵ has shown that the breakthrough time is related to the diffusion coefficient, *D*, by

$$t_b = 0.755s^2/\pi^2D$$

where *s* is the thickness of the membrane. The breakthrough time is defined as the time interval from the initiation of the run to the intersection of the extrapolated linear part of the potential-time trace (Figure 1) onto the time axis.

The perturbation Δc must be small in comparison to *c* where *c* is the concentration of H atoms in the metal phase and is related to *n* by $n = V_M c$ where *V_M* is the molar volume of the metal. Small changes in *c* are proportional to small changes in the electrode potential, *E*. This can be shown for the low concentration region studied here where Sieverts' law holds, *i.e.*, $n = cV_M = K_s p^{1/2}$. The relationship between $p(\text{atm})^{1/2}$ and *E* is $p(\text{atm})^{1/2} = \exp(FE/RT)$, therefore

$$c(t) - c(t=0) = (K_s/V_M) \{ \exp[-(\Delta E(t) + E(t=0)) F/RT] - \exp[-(E(t=0) F/RT)] \} \quad (1)$$

For the small perturbations applied here, *e.g.*, $\Delta E = \pm 2$ mV, eq 1 reduces to

$$\Delta c(t) = K_s F \Delta E(t) / V_M RT \exp[-(E(t=0) F/RT)] \quad (2)$$

Gas-Phase Method. The rate of hydrogen uptake by sheets of gold–palladium alloys was followed at constant

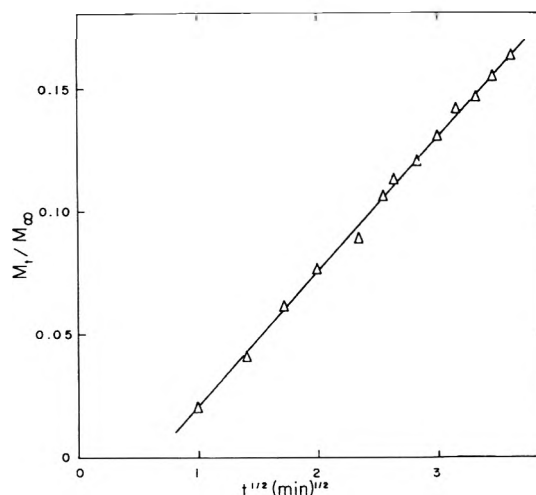


Figure 2. Typical absorption run for Au(55.7%)–Pd alloy at 37° and at constant pressure 5.252 cm of H₂ gas.

pressures of hydrogen in the Sieverts' type apparatus. The uptake was monitored by the changes in the volume of gas which were followed in a gas buret manually. The uptake of hydrogen was so rapid that measurements by this technique were limited to the alloy with the largest gold content, *i.e.*, Au(55.7%)–Pd.

For the boundary condition of $c = \text{constant}$ at $x = 0$ and *s* and the initial condition of $c = 0$ at $t = 0$ for $s > x > 0$, where *s* is the thickness of the plate, the following solution holds at small times

$$M_t/M_\infty = 4(Dt/s^2\pi)^{1/2} \quad (3)$$

where M_t/M_∞ is the fraction of hydrogen absorbed at time *t*, and at $t = \infty$, respectively.¹⁸ The solubility of hydrogen in the Au(55.7%)/Pd alloy is small so that the measured diffusion constants represent the ideal, concentration-independent values. The value of *M_∞* was estimated from absorption isotherms established for this alloy.¹⁷

Results

Typical gas-phase absorption data are shown in Figure 2 plotted according to eq 3. There is a small time-lag corresponding to the initiation of the run, approximately 0.35 min, and thereafter the data follow the $t^{1/2}$ relation admirably. The derived diffusion constants were found to be independent of pressure in the range 2–9 cm. The energy of activation for the Au(55.7%)–Pd alloy was determined in the temperature range 0–112° and the Arrhenius' plot is shown in Figure 3. The results are represented by $D(\text{cm}^2/\text{sec}) = 4.8 \times 10^{-4} \exp(-8680/RT)$.

The time breakthrough method was applicable over the whole range of alloy compositions which were available here, *i.e.*, up to a gold content of 55.7% but it did not work for pure gold. This is presumably due to the extremely small solubility of hydrogen in pure gold. Results at 37° are summarized in Table I and Figure 4 where data for pure gold are included from the higher temperature investigations of Eichenauer and Liebscher.¹⁹ It can be seen that there is an increase in *D* in passing from the highest content gold alloys studied here to pure gold. A similar

(18) J. D. Crank, "Mathematics of Diffusion," Oxford University Press, Fair Lawn, N. J., 1956

(19) W. Eichenauer and D. Liebscher, *Z. Naturforsch. A*, **17**, 355 (1962).

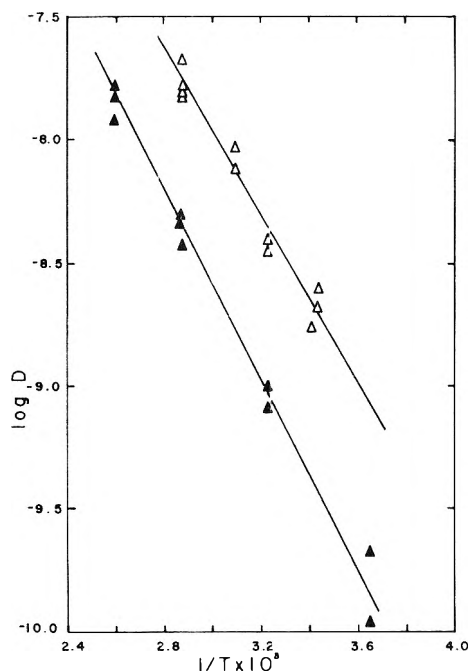


Figure 3. Arrhenius' plot of diffusion constants: ▲, Au(55.7%)–Pd alloy determined by gas phase absorptions; △, Au(44.7%)–Pd alloy determined from electrochemical breakthrough times.

TABLE I: Diffusion Constants for Hydrogen at $n \rightarrow 0$ (37°) for a Series of Gold-Palladium Alloys

Alloy	D , $\text{cm}^2 \text{sec}^{-1}$	D_0 , $\text{cm}^2 \text{sec}^{-1}$	E_{act} , kcal/mol
Pd	3.6×10^{-7} ^a	4.0×10^{-3} ^a	5.75 ^a
Au(18.8%)–Pd	3.5×10^{-7}		
Au(26.5%)–Pd	1.7×10^{-7}		
Au(35.1%)–Pd	2.7×10^{-8}		
Au(44.7%)–Pd	3.7×10^{-9}	6×10^{-4}	7.26
Au(55.7%)–Pd	7.4×10^{-10}		
Au(55.7%)–Pd ^b	9.4×10^{-10}	4.8×10^{-4}	8.68
Au	5.91×10^{-8} ^c	5.6×10^{-4} ^c	5.64 ^c

^a Reference 5. ^b Values determined from gas-phase absorption rates. ^c Reference 19.

phenomenon is noted in the Ag–Pd system.⁵ Other aspects of the D vs. % Au plot are similar to those of Ag–Pd.^{1–5} The diffusion constant is nearly unchanged from that of pure palladium to a gold content of approximately 20%. They then decline in a nearly logarithmic fashion to a quite low value for the Au(55.7%)–Pd alloy. The breakthrough time for this highest content alloy was $\sim 10,000$ sec at 37° . Since this breakthrough time gives a diffusion constant in reasonable agreement with the gas-phase hydrogen uptake method (Table I), it can be concluded that this electrochemical technique is valid up to this gold content. The gas-phase hydrogen uptake method may or may not be valid for alloys where the diffusion constant is greater than in the Au(55.7%)–Pd alloy (it could not be measured because the uptake was too rapid to follow with the samples available here). It is possible that this method was fortuitously successful here for the Au(55.7%)–Pd alloy because the bulk diffusion step was slow compared to surface steps.

Data were taken for both anodic and cathodic perturbations and no systematic differences were noted. Küssner¹⁵

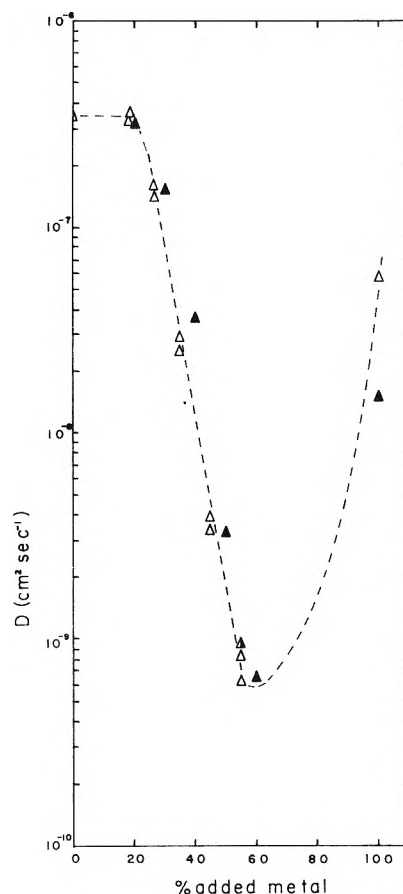


Figure 4. Diffusion constants at 37° for a series of Au–Pd and Ag–Pd alloys: ▲, Ag–Pd data (ref 5) and pure Ag (ref 19); △, Au–Pd data (this work) and pure Au (ref 19); ▲, gas-phase measurement.

has pointed out that the charging of the double layer on the polarization side of the membrane should be rapid, ~ 1 msec, but at small perturbations he noted an effect due to charging of the double layer on the diffusion side. Küssner limited his investigations to the Ag(23%)–Pd alloy where the diffusion constant is relatively great and consequently the breakthrough times are correspondingly small. The time of charging of the double layer would be expected to play a smaller role for alloys with gold contents greater than 20%. In order to experimentally assess the role of double layer charging on the breakthrough times the following experiment was performed. Several runs were made with palladium black deposited only on the polarization side of the membrane. The absence of palladium black on the diffusion side markedly decreases the double layer capacity of this side. A reduction in the breakthrough time was noted for the Au(18.8%)–Pd alloy from 28 to 17 sec (37°) and for the Au(26.5%)–Pd alloy from 57 to 47 sec (37°). On the other hand, there was no effect detected for the Au(35.1%)–Pd alloy where the breakthrough times were 318 and 316 sec (37°) with and without activation by palladium black, respectively. It can be concluded that the breakthrough times are affected by the double layer capacity of the black only for those gold alloys with small breakthrough times, i.e., alloys with less than about 30% gold (37°). Data reported for such alloys in Figure 4 are for membranes palladized only on the polarization side of the membrane.

In order to demonstrate that the alloys were indeed in the low region of hydrogen contents where ideal behavior

prevailed, some breakthrough times were measured at various small hydrogen contents. Typical results are shown in Table II, where it can be seen that the effect of concentration over this small concentration region is small and probably within experimental error.

The temperature dependence of D_{n-0} (0–75°) was determined for a representative alloy of high gold content in order to determine whether the principal influence of the substitutional impurity is on the energy of activation or on the preexponential factor. The Arrhenius' plot for the Au(44.7%)–Pd alloy is shown in Figure 3. Results can be expressed as $D(\text{cm}^2 \text{sec}^{-1}) = 6 \times 10^{-4} \exp(-7260/RT)$ compared to $D(\text{cm}^2 \text{sec}^{-1}) = 4 \times 10^{-3} \exp(-5750/RT)$ for pure palladium.⁵ It can be seen that both D_0 and E_{act} are affected by the presence of a large amount of substitutional gold.

For the Ag–Pd alloys the decrease in D_0 with silver content is somewhat smaller than that reported here but the dependence of E_{act} upon added gold is very similar to that reported for the Ag–Pd alloys.^{5,14} Since the values of D are somewhat smaller for the Au–Pd alloys, the small difference in behavior of the two alloy systems is apparently caused by the smaller values of D_0 for the Au–Pd alloys.

Discussion

It is noteworthy that the magnitude of the diffusion constant is insensitive to the amount of substitutional impurity in the Au- and Ag–Pd alloy systems up to approximately 20% added impurity. The heat of solution of hydrogen at infinite dilution, $-\Delta H_{\text{H}}^\circ$, for both of these systems increases with added metal content, *e.g.*, $-\Delta H_{\text{H}}^\circ$ increases from 2300 (pure palladium) to 4670 cal/mol of H (Ag(20%)–Pd).²⁰ The reason offered for this increase in both of these systems¹⁶ is that the addition of silver or gold increases the size of the interstitial site and the compressibility of its environment thereby making the occupation of the interstitial site energetically more favorable. Züchner⁵ shows evidence of a slight decrease in E_{act} in the low silver region (not covered here for the Au–Pd system). This has been related to the lattice expansion of these alloys⁵ but the effect is small, 0.25 kcal for the Ag(20%)–Pd alloy, compared with the large increases in values of $-\Delta H_{\text{H}}^\circ$ observed for these alloys.

The theory of diffusion in solids gives for D_0

$$D_0 = (a_0^2/12)\kappa z\nu \exp(\Delta S^\ddagger/R) \quad (4)$$

where a_0 is the lattice parameter, κ the transmission coefficient, z the number of neighboring octahedral holes, 12 for palladium and its alloys, ν the vibrational frequency of the hydrogen, and ΔS^\ddagger is the activation entropy.^{5,12,21} There is no specific allowance for the presence of the substitutional impurity save indirectly as values of ν , a_0 , and ΔS^\ddagger are altered by alloying. Aside from a_0 , these quantities are not well characterized for alloys of palladium. Chowdhury and Ross²² have recently suggested that the vibrational frequency (Einstein) depends on the number of electrons per atom and is otherwise independent of the surroundings of the interstitial site. (This conclusion

TABLE II: Breakthrough Times at 37° for the Au(26.5%)–Pd Alloy at Several Small Hydrogen Contents

n	E , mV	t_b , sec	$D \times 10^7$, $\text{cm}^2 \text{sec}^{-1}$
0.001	144.3	46.0	1.67
0.001	143.8	47.6	1.64
0.005	113.8	44.7	1.75
0.010	103.8	44.8	1.74
0.012	96.0	50.0	1.56
0.017	86.1	47.2	1.65

should be examined more thoroughly as it is based only on results from Ag–Pd and pure Pd.) Since the Einstein frequency decreases about 20% in going from α to β phase Pd–H₂,^{23,24} this cannot explain the fourfold decrease in D_0 going from pure palladium to Ag(50%)–Pd⁵ or the approximate sixfold decrease observed here for the Au(44.7%)–Pd alloy. The changes of a_0 are in the wrong direction to account for the changes in D_0 observed for the Au- and Ag–Pd systems.

The changes of E_{act} with added metal are difficult to estimate theoretically. It is interesting that in both the Au- and Ag–Pd systems the magnitude of E_{act} and D itself decrease with added metal and then increase again when the palladium content vanishes. This suggests that a specific effect, hitherto unaccounted for in the theory of diffusion of interstitials in substitutional alloys, may be present. This effect arises from lattice disorder. It would be of interest to examine the diffusion constants in the gold- or silver-rich region. The experimental techniques which were employed here are, however, unsuitable for this region of concentration.

This investigation of the diffusion of interstitial hydrogen represents the second comprehensive study in a substitutional palladium alloy. Results are quite similar to the Ag–Pd system and, therefore, it is difficult to draw any conclusions about the relative roles on interstitial diffusion of the geometric and electronic properties of the metallic matrix. It can be concluded, however, that those properties which do differ between gold and silver do not contribute significantly to values of D for the alloys, *e.g.*, compressibility. Before the relative contributions of the electronic and geometric effects can be evaluated, data on more palladium alloys must be obtained.

Acknowledgments. We are grateful to the U. S. Atomic Energy Commission for financial support of this research. We are also indebted to Engelhard Industries, Inc., for the loan of the gold–palladium alloys.

(20) H. Brodowsky and E. Poeschel, *Z. Phys. Chem. (Frankfurt am Main)*, **44**, 143 (1965).

(21) C. A. Wert and C. Zener, *Phys. Rev.*, **76**, 1169 (1949).

(22) M. R. Chowdhury and D. K. Ross, *Proc. Int. Meet. Hydrogen Metals*, 346 (1972).

(23) G. Verdán, R. Rubin, and W. Kley, "Neutron Inelastic Scattering," Vol. 1, IAEA Vienna, 1968, p 223.

(24) J. Bergsma and J. A. Goedkoop, *Physica*, **26**, 744 (1960).

A Nuclear Magnetic Resonance Line Broadening Study of Dimethyl Sulfoxide in Tris(ethylenediamine)chromium(III)–Dimethyl Sulfoxide Solution

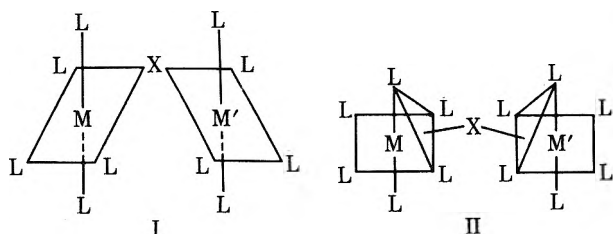
Charles L. Watkins, Gerald S. Vigue,* and M. E. Harris

Department of Chemistry, University of Alabama, Birmingham, Alabama 35294 (Received October 12, 1972)

Proton nmr line broadening studies of DMSO in $\text{Cr}(\text{en})_3^{3+}$ -DMSO solutions were conducted between 20 and 90°. The resulting data were interpreted using the Swift–Connick relationship. The dominant contribution to line broadening in the temperature range 20–50° was a second coordination sphere exchange process. Above 70°, the dominant process was a first coordination sphere exchange process of partially dissociated $\text{Cr}(\text{en})_3^{3+}$. The kinetic parameters for the first and second coordination sphere processes respectively were found to be $\Delta H^\ddagger = 25$ kcal/mol, $k^0 = 1.4$ sec⁻¹ and $\Delta H^\ddagger' = 6.6$ kcal/mol, $k' = 1.2 \times 10^3$ sec⁻¹. A discussion is given of the possibility of electron transfer through second coordination sphere bonding.

Introduction

Eaton¹ has recently made a strong case for elucidating the effects of second coordination sphere ligands about transition metal complexes. The geometry and stability of the second coordination sphere ligands will have a very large influence on the catalytic and enzymatic processes of the complex. Other workers have recognized the importance of studying the chemical and structural makeup of the molecules surrounding a complex in solution.²⁻⁷ The mechanisms by which oxidation–reduction reactions take place are also dependent upon the nature of the molecular structure surrounding the oxidizing and reducing ions.⁸⁻¹⁰ A preferred mechanism^{11,12} for redox reactions involves the bridging of the oxidizing and oxidized metal ions by a common ligand which occupies one of the six positions of the first coordination sphere of each metal ion (structure I). A less cited mechanism which may have an equally important role is a bridging mechanism in which the bridging ligand occupies a second coordination position on one of the eight faces of the octahedrally coordinated metal ions (structure II).



Requirements for this mechanism to occur are that the exchange rate of the bridging ligand X be reasonably fast and the ligand be attached sufficiently to the metal ions to cause a pathway (orbital bridge) for electron transfer to occur. Vigue and Ng^{13a} have demonstrated that DMSO molecules are strongly attached to the eight faces of the $\text{Cr}(\text{DMSO})_6^{3+}$ complex and the exchange rate is reasonably fast. This study suggests that the octahedrally coordinated Cr^{3+} may participate in electron transfer reactions using second coordination sphere bridging similar to model II.

The present work is designed primarily to investigate the solvent structure of DMSO molecules about the kinetically stable $\text{Cr}(\text{en})_3^{3+}$ ion. The study is also expected to lend support to mechanisms which may occur by or may require a second coordination sphere structure.

Experimental Section

Preparation of Solutions. DMSO was dried over molecular sieves and a stock solution of DMSO with 2% benzene was prepared. Three solutions of 0.01, 0.015, and 0.024 M $[\text{Cr}(\text{en})_3]_2(\text{SO}_4)_3$ in DMSO were prepared. A stoichiometric amount of $\text{Ba}(\text{NO}_3)_2$ necessary to precipitate the sulfate ion was added to increase the solubility of $\text{Cr}(\text{en})_3^{3+}$ in DMSO. The sample was filtered prior to use. Analysis of $[\text{Cr}(\text{en})_3]_2(\text{SO}_4)_3(\text{H}_2\text{O})_4$ was performed by Galbraith Lab., Inc. and found to be as follows. Calcd: C, 17.35; H, 7.00. Found: C, 17.38; H, 7.04.

Physical Methods. A Varian HA60-IL nmr spectrometer was used to measure the chemical shift, δ (cps), and half-height line width, $\nu_{1/2}$ (cps), of neat DMSO and DMSO solutions of $\text{Cr}(\text{en})_3^{3+}$ between 20 and 90°. The measurements were made by first increasing the temperature and then by decreasing the temperature over the entire temperature range. The line width and chemical shift data obtained in this way indicate that any chemical changes occurring are reversible. Instrument temperature calibration was accomplished using the relations of Van Geet.^{13b}

Theory

Line Width and Exchange Rate. One of the conditions for obtaining the line width of an nmr contact shift spectrum is that $1/\tau_m \gg A_n$. This condition suggests that the exchange rate of the coordinated ligand with ligands in the bulk solvent, $1/\tau_m$, can be measured. Equations were developed by Swift and Connick¹⁴ to investigate the solvent exchange rate using line broadening techniques. The general relationship of Swift and Connick which has been

- (1) D. R. Eaton, *Advan. Chem. Ser.*, **No. 100**, 175 (1971).
- (2) R. H. Fisher and W. Dew Horrocks, *Inorg. Chem.*, **7**, 2659 (1968).
- (3) M. F. Rettig and R. S. Drago, *J. Amer. Chem. Soc.*, **88**, 2966 (1966).
- (4) G. N. LaMar, R. H. Fischer, and W. Dew Horrocks, *Inorg. Chem.*, **6**, 1798 (1967).
- (5) Z. Luz and R. G. Shulman, *J. Chem. Phys.*, **43**, 3750 (1965).
- (6) S. Frankel, *Inorg. Chem.*, **10**, 814 (1971); (b) *ibid.*, 2360 (1971).
- (7) D. W. Larsen, *Inorg. Chem.*, **5**, 1109 (1966).
- (8) F. Basolo and R. Pearson, "Mechanisms of Inorganic Reactions," 2nd ed, Wiley, New York, N. Y., 1967, Chapter 6.
- (9) J. Halpern, *Quart. Rev. Chem. Soc.*, **15**, 207 (1961).
- (10) R. G. Wilkins, *Quart. Rev. Chem. Soc.*, **16**, 316 (1962).
- (11) T. J. Williams and C. S. Garner, *Inorg. Chem.*, **9**, 2058 (1970).
- (12) H. Taube and E. L. King, *J. Amer. Chem. Soc.*, **76**, 4053 (1954).
- (13) (a) G. S. Vigue and P. Ng, *J. Inorg. Nucl. Chem.*, **13**, 2477 (1971); (b) A. L. Van Geet, *Anal. Chem.*, **42**, 679 (1970).
- (14) T. J. Swift and R. E. Connick, *J. Chem. Phys.*, **37**, 307 (1962).

widely used to examine exchange rates¹⁵⁻¹⁷ is given as

$$T_2^{-1} - T_{2a}^{-1} = \sum_m f(\tau_{am}^{-1}) \left[\frac{T_{2m}^{-2} + T_{2m}^{-1}\tau_{ma}^{-1} + (\Delta\omega_m)^2}{(T_{2m}^{-1} + \tau_{ma}^{-1})^2 + (\Delta\omega_m)^2} \right] \quad (1)$$

where $1/T_2$ is obtained from the half-height line width ($\pi\Delta\nu_{1/2} = 1/T_2$) and f is the fraction of coordinated solvent molecules. $1/T_{2m}$ is the relaxation rate for a coordinated molecule, $\Delta\omega$ is the contact shift of the resonance peak in radians per second, and $1/T_{2a}$ is the relaxation rate of the pure solvent. Hereafter, the quantity $1/T_2 - 1/T_{2a}$ will be represented by $1/T_{2p}$. If second sphere coordination is significant, the Swift and Connick relationship (for equivalent first coordination sites and for equivalent second coordination sites) becomes

$$T_{2p}^{-1} = f^0\tau_m^{-1} \left[\frac{T_{2m}^{0-2} + T_{2m}^{0-1}\tau_{ma}^{-1} + (\Delta\omega_m^0)^2}{(T_{2m}^{0-1} + \tau_{ma}^{-1})^2 + (\Delta\omega_m^0)^2} \right] + f^1\tau_{ma}^{-1} \left[\frac{T_{2m}'^{-2} + T_{2m}'^{-1}\tau_{ma}'^{-1} + (\Delta\omega_m')^2}{(T_{2m}'^{-1} + \tau_{ma}'^{-1})^2 + (\Delta\omega_m')^2} \right] \quad (2)$$

where the superscript zero represents first coordination sphere effects and the prime represents second coordination sphere effects. At low temperatures where exchange is rather slow but still controls the line broadening and either $(\Delta\omega_m)^2 \gg (1/T_{2m})^2$, $(1/\tau_m)^2$, or $(1/T_{2m})^2 \gg (\Delta\omega_m)^2$, $(1/\tau_m)^2$, the Swift-Connick equation reduces to

$$1/T_{2p} = f/\tau_m \quad (3)$$

At higher temperatures where the exchange is more rapid and the conditions $(1/\tau_m)^2 \gg (\Delta\omega)^2 \gg (1/T_{2m}\tau_m)$ exist, the Swift-Connick equation reduces to

$$1/T_{2p} = f\tau_m(\Delta\omega)^2 \quad (4)$$

The mean lifetime of the coordinated ligand, τ_m , is temperature dependent for the regions covered by eq 3 and 4 and can be represented as a first-order rate in the equation taken from transition state theory

$$1/\tau_m = k = kT/h \exp[\Delta S^\ddagger/R - \Delta H^\ddagger/RT] \quad (5)$$

At even higher temperatures where $1/\tau_m$ is not a line broadening factor, exchange is very fast and the conditions $(1/T_{2m}\tau_m) \gg (1/T_{2m})^2$, $(\Delta\omega)^2$ exist, the Swift-Connick relation reduces to

$$1/T_{2p} = f/T_{2m} \quad (6)$$

The line width data are usually reported as a plot of $\log 1/(fT_{2p})$ vs. $1/T$ in which the three temperature regions given by eq 3, 4, and 6 are identified as three different but connecting lines. A fourth temperature region which appears at temperatures below the region in eq 3 also may appear as another line in the plot of $\log 1/(fT_{2p})$ vs. $1/T$. Exchange is too slow in this region to be measured by the nmr technique. Line broadening in this region is caused by outer sphere exchange (dipole-dipole broadening) and is used to correct the exchange data found in eq 5 and 6.

The general quantitative relationship for the total contact shift (Fermi and pseudo) is given by

$$\Delta\nu/\nu = -A_n \frac{\gamma_e g \beta S(S+1)}{\gamma_n 3kT} \quad (7)$$

where $\Delta\nu$ is the chemical (contact) shift relative to the

diamagnetic resonance peak, ν is the operating frequency of the instrument, A_n is the electron spin-nuclear spin coupling constant, β is the Bohr magneton, k is the Boltzmann constant, S is the total electron spin, g is the Landé splitting factor, γ_e is the electron gyromagnetic ratio, γ_n is the nuclear gyromagnetic ratio, and T is the absolute temperature. When the coordinated ligand exchanges rapidly with ligand molecules in the bulk solvent, $\Delta\nu$ is found from the weighted average chemical shift using the relation

$$\Delta\nu \times f = \Delta\nu_{wa} \quad (8)$$

where $\Delta\nu$ is the contact shift, $\Delta\nu_{wa}$ is the weighted average (solution) chemical shift, and f is the fraction of ligand molecules which are coordinated.

Results and Discussion

Figure 1 is a plot of $\log 1/T_{2p}$ vs. $10^3/T$ for the data normalized to 0.01 M Cr(en)₃³⁺ solution. An analysis of the plot indicates the existence of two exchange (line broadening) mechanisms. The first lies above 70° (approximately) and was assigned to first coordination sphere exchange and the second, at temperatures below 50°, was assigned to second coordination sphere exchange. The two processes are mixed between 50 and 70°.

Through the mathematical consideration of eq 2, the experimental data were resolved by curve-fitting processes into the lines shown in Figure 2 using a technique similar to Würthlich and Connick.¹⁸

To begin the curve-fitting process it was necessary to assume that the high-temperature points of the experimental data on Figure 2 represented a pure process. The line generated by this assumption was subtracted from the experimental data, and from the resulting new data the line representing second sphere exchange effects was generated. All other lines were generated as a result of these exchange data.

Line 1. Line broadening $1/(T_{2p})$ results from first coordination sphere exchange of DMSO molecules in the temperature region described by eq 4.

$$1/(T_{2p}) = f^0\tau_m^0(\Delta\omega^0)^2$$

Line 2. Line broadening $1/(T_{2p})$ results from second coordination sphere exchange of DMSO molecules in the temperature region described by eq 4.

$$1/(T_{2p}) = f^1\tau_m^1(\Delta\omega^1)^2$$

Line 3. Line broadening $1/(T_{2p})$ results from first coordination sphere exchange of DMSO molecules in the temperature region described by eq 3.

$$1/(T_{2p}) = f^0/\tau_m^0$$

Line 4. Line broadening $1/(T_{2p})$ results from second coordination sphere exchange of DMSO molecules in the temperature region described by eq 3.

$$1/(T_{2p}) = f^1/\tau_m^1$$

Line 5. Line broadening $1/(T_{2p})$ results from a composite of effects called T_{2Cr} .

Table I lists the kinetic parameters determined or measured for the processes represented by lines 1-5.

(15) Z. Luz and S. Meiboom, *J. Chem. Phys.*, **40**, 2686 (1964).

(16) N. A. Matwiyoff, *Inorg. Chem.*, **5**, 788 (1966).

(17) D. K. Ravage, T. S. Stengle, and C. H. Langford, *Inorg. Chem.*, **6**, 1252 (1967).

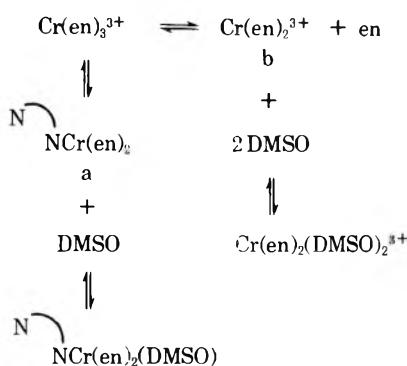
(18) K. Würthlich and R. E. Connick, *Inorg. Chem.*, **7**, 1377 (1968).

TABLE I: Kinetic Parameters

	k_0, sec^{-1}	k', sec^{-1}	$\Delta H\ddagger^\circ, \text{kcal/mol}$	$\Delta S\ddagger^\circ, \text{eu}$	$\Delta H\ddagger', \text{kcal/mol}$	$\Delta S\ddagger', \text{eu}$	$1/T_{2\text{Cr}}, \text{sec}^{-1}$	T_{1e}, sec
f-6 (line 2)		$1.2 \pm 0.2 \times 10^3$			6.6 ± 0.5	-22 ± 2	$1.1 \pm 0.5 \times 10^2$	$1.0 \pm 0.2 \times 10^{-9}$
f-8 (line 2)		$0.90 \pm 0.2 \times 10^3$			6.6 ± 0.5	-23 ± 2	$8.3 \pm 0.5 \times 10^1$	$6.6 \pm 0.2 \times 10^{-9}$
f-2 (line 1)	1.4 ± 0.2		25.0 ± 0.5	$+26 \pm 2$				

From the $\Delta H\ddagger'$ given in the table, for line 1 ($\Delta H\ddagger^\circ = 25$ kcal/mol), it is reasonable to assume this process to be first coordination exchange. Basolo and Pearson⁸ have found the enthalpy of activation for exchange of a number of Cr^{3+} complexes to be about 25 kcal/mol. In addition, the exchange rate was found to be 1.4 sec^{-1} at 25° . This slow exchange rate is in keeping with the well-known, highly stable Cr^{3+} . Similar arguments can be made for the process represented by line 2. Obviously, there is some dissociation of the $\text{Cr}(\text{en})_3^{3+}$ molecule at temperatures above 60° (Scheme I).

Scheme I



The breaking of one N-Cr³⁺ bond may occur (Scheme I-a) or the complete en molecule may dissociate as given in Scheme I-b in order to allow DMSO exchange to occur. Our data fits best the exchange of two DMSO molecules indicating that probably one en molecule dissociates to allow first coordination sphere exchange of DMSO. This exchange mechanism is supported by the work of Vige and Ng^{13a}. Their exchange study of the $\text{Cr}(\text{DMSO})_6^{3+}$ in DMSO indicated a second coordination sphere exchange at 25° of $1.3 \times 10^3 \text{ sec}^{-1}$ which is much greater than the exchange rate shown for line 1. Langford and Chung¹⁹ also found that significant first coordination sphere exchange effects were observed for $\text{Fe}(\text{DMSO})_6^{3+}$ in DMSO above 80° .

From the $\Delta H\ddagger'$ given in Table I for line 2 ($\Delta H\ddagger' = 6.6$ kcal/mol), it is reasonable to assume from the above discussion that this process is a second coordination sphere process, consistent with the previous findings of Vige and Ng for $\text{Cr}(\text{DMSO})_6^{3+}$. The exchange rate at 25° for this process was found to be $1.2 \times 10^3 \text{ sec}^{-1}$ (for f-6) or 0.90×10^3 (for f-8).²⁰ Although eight faces of the octahedral $\text{Cr}(\text{en})_3^{3+}$ are available for coordination, data for six exchanging molecules are also reported because of its agreement with previously reported data.^{13a} It is significant at this time to point out that the second coordination sphere exchange parameters are found to be in the same range as the exchange parameters k and $\Delta H\ddagger'$ found for the first coordination sphere exchange of DMSO in the $\text{Ni}(\text{DMSO})_6^{2+}$, $\text{Cu}(\text{DMSO})_6^{2+}$, and $\text{Co}(\text{DMSO})_6^{2+}$ sys-

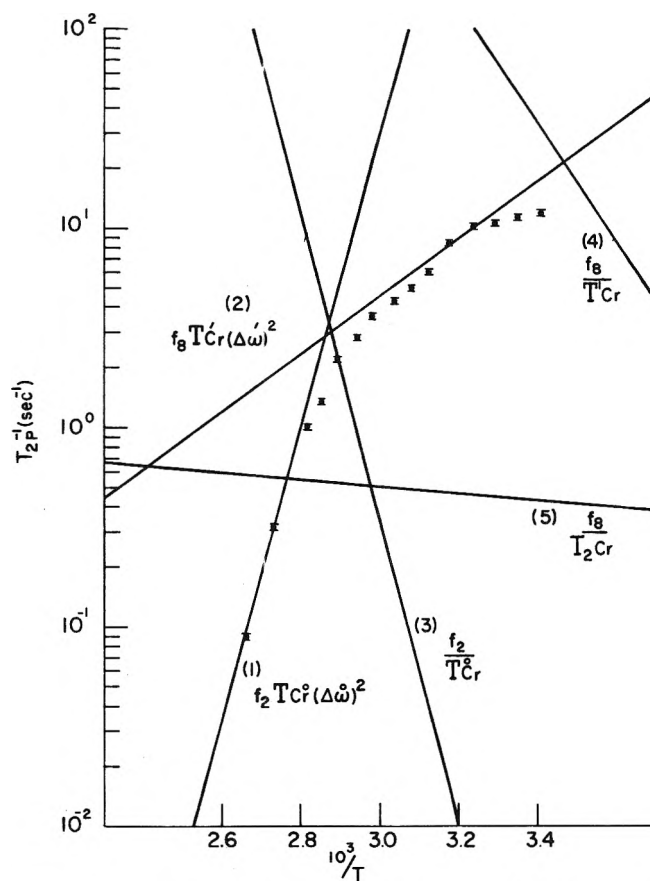


Figure 1. Log $1/T_{2p}$ vs. $1/T$ for the $\text{Cr}(\text{en})_3^{3+}$ -DMSO system. The data are normalized to $0.01 M \text{Cr}(\text{en})_3^{3+}$.

tems.^{13a} Bonding of DMSO to the $\text{Cr}(\text{en})_3^{3+}$ must, therefore, be significantly more than the electrostatic forces usually associated with second sphere coordination. The contact shift (280 cps) and electron spin-nuclear spin coupling constant ($3.0 \times 10^5 \text{ cps}$)²¹ reinforce the proposition of covalent bonding suggested in the second sphere coordination of DMSO to $\text{Cr}(\text{en})_3^{3+}$. Similar arguments can be made for the process represented by line 4.

Line broadening effects on T_{2p} which result from $T_{2\text{Cr}}$ are a composite of effects. $1/T_{2\text{Cr}}$ (dipolar) is a process which depends upon the spatial coupling between the unpaired spin of the Cr^{3+} and the DMSO proton (in this case probably in the second coordination sphere or bulk solvent). Any contribution to τ_c , the correlation time for dipolar relaxation,²² due to tumbling would be minimal because such a mechanism requires pseudocontact cou-

(19) C. Langford and F. M. Chung, *J. Amer. Chem. Soc.*, **90**, 4485 (1968).

(20) f-6 and f-8 indicate second coordination numbers of 6 and 8.

(21) Determined from eq 7 and 8.

(22) R. A. Bernheim, et al., *J. Chem. Phys.*, **30**, 950 (1959).

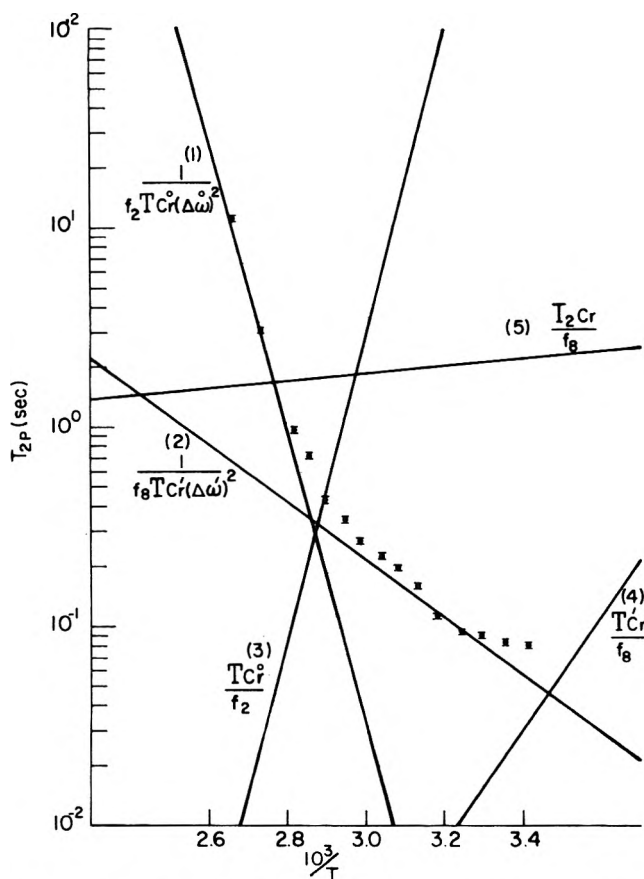


Figure 2. Log T_{2P} vs. $1/T$ for the $\text{Cr}(\text{en})_3^{3+}$ -DMSO system. The data are normalized to 0.01 M $\text{Cr}(\text{en})_3^{3+}$.

pling which presupposes an electronic g factor which is anisotropic. Cr^{3+} , a d^3 electron configuration with octahedral symmetry, is isotropic. If the molecule is attached to the $\text{Cr}(\text{en})_3^{3+}$, the $1/T_{2\text{Cr}}$ (dipolar) may also be affected by electron relaxation if τ_e (electron correlation time) is more rapid than the exchange process, and if the coupling between the DMSO proton of the attached molecule and the unpaired spin of the Cr^{3+} is significant. Such a mechanism is possible in this case since the DMSO proton coordinated to the second coordination sphere is expected to be about 7–9 Å, which would give a reasonable $1/T_{2P}$.²² But again, such a coupling would be consistent only with an anisotropic g factor for the Cr^{3+} .

A more likely mechanism for controlling $1/T_{2\text{Cr}}$ is the scalar coupling between the unpaired electrons of Cr^{3+} and the DMSO protons coordinated in the second coordination (and greater) sphere given by Bernheim, *et al.*²²

$$1/T_{2\text{Cr}}(\text{scalar}) = 4/9I(I+1)S(S+1)(A_n^2/\hbar^2)\tau_e \quad (9)$$

If the electron spin-nuclear spin coupling constant A_n determined from the experimental contact shift using eq 7 is used with the experimental $1/T_{2\text{Cr}}$ in eq 9 to determine τ_e , the value for τ_e is found to be 10^{-9} sec. Assuming that

$$1/\tau_e \approx 1/T_{1e} + 1/\tau_{\text{Cr}} \approx 1/T_{1e} \quad (10)$$

A value of $\tau_e = 1/T_{1e} = 10^{-9}$ is consistent with the esr value of 10^{-9} found for Cr^{3+} in H_2O .⁷ Further support for

a scalar coupling mechanism for $T_{2\text{Cr}}$ is given by work of Hausser and Laukien.²³ A study of Cr^{3+} - H_2O indicated that the ratio of longitudinal (T_1) and transverse (T_2) relaxation times was found to be anomalous, *i.e.*, $T_1/T_2 \neq 1$. Metal ions in water generally cause the ratio T_1/T_2 for the relaxation of the water proton to be about unity over a range of temperatures. The T_1 and T_2 are controlled by a dipole-dipole coupling mechanism between the unpaired electrons on the metal ion and the water protons.^{24,25} It has been shown that if the electron relaxation time, τ_e , is long and the ratio $T_1/T_2 \neq 1$, but rather, is anomalous, as in the case of VO^{2+} ,¹⁸ Cu^{2+} , and Mn^{2+} ,¹⁴ the controlling relaxation mechanism for T_2 is a scalar one as proposed by Bloembergen.²⁴ The work of Hausser and Laukien, which gives $T_1/T_2 \neq 1$ for Cr^{3+} - H_2O system support a scalar coupling for $T_{2\text{Cr}}$ in this work. Thus it would appear that $T_{2\text{Cr}}$ is controlled by a scalar coupling mechanism which is further supported by the fact that the contact shift (determined from the bulk chemical shift) is found to be approximately 300 cps. In any case $1/T_{2\text{Cr}}$ provides only a small correction to $1/T_{2P}$.

Summary and Conclusions

Plots of $\log 1/T_{2P}$ vs. $1/T$ for the $[\text{Cr}(\text{en})_3]^{3+}$ -DMSO system indicate the existence of two exchange mechanisms, these being first and second coordination sphere exchange. Through mathematical analysis of the experimental data the thermodynamic parameters determined for the first and second coordination sphere processes are consistent with previously reported thermodynamic parameters for first and second coordination sphere exchange. Our data indicate that first coordination sphere exchange is the dominant process above 70° where one en molecule is replaced by two DMSO molecules. Also, second coordination sphere exchange seems to be the dominant line broadening process below 50°. Even though eight sites are available on the faces of the $[\text{Cr}(\text{en})_3]^{3+}$ complex ion for second coordination sphere exchange with the bulk solvent, our data are more consistent with six exchanging DMSO molecules.

The contact shift calculations are of a scalar nature. Their values and the second coordination sphere parameters are in the range of the contact shift and exchange parameters for first coordination sphere exchange in M^{2+} -DMSO systems. Bonding of DMSO to the $[\text{Cr}(\text{en})_3]^{3+}$ complex ion must, therefore, be significantly more than the electrostatic forces usually associated with second sphere coordination. Thus, one must consider electron transfer *via* a second coordination sphere mechanism in M^{3+} complexes to be a real possibility.

The line broadening technique provides a good method for investigating the structure and behavior of the first and second coordination sphere of transition metal complexes. Investigations are continuing in our laboratory, using this method, to determine the influence of first and second coordination sphere molecules on reaction rates and mechanisms.

(23) R. Hausser and G. Laukien, *Z. Phys.*, **153**, 394 (1959).

(24) N. Bloembergen, E. M. Purcell, and R. V. Pound, *Phys. Rev.*, **73**, 679 (1948).

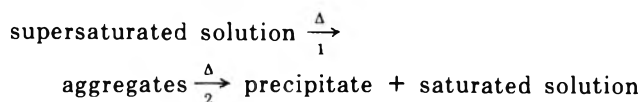
(25) I. Solomon, *Phys. Rev.*, **99**, 559 (1955).

COMMUNICATIONS TO THE EDITOR

Photoinduced Molecular Aggregation and Precipitation

Sir: The importance of aggregation phenomena in solutions is obvious. The present communication outlines a method by which the kinetics of the aggregation process may be followed by static or "fast" methods at appropriate temperatures, in appropriate systems. The method is based on the following points.

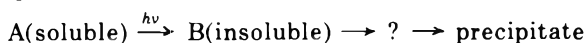
(a) "Precipitation" (*i.e.*, formation of crystals or micro-crystals) out of a supersaturated solution of a compound must pass through a stage of aggregation, *i.e.*, formation of larger units from a number of single molecules



In other words, by creating conditions of supersaturation we force the system to form aggregates, at least as transients.

(b) Aggregation and precipitation are activated processes, necessitating diffusion and probably other steps (crystal growth) which can be impeded by sufficiently low temperatures and high viscosities, in particular if very dilute solutions of sparsely soluble materials are used. On the other hand, the solubility of organic solutes usually has a positive temperature dependence, *i.e.*, the thermodynamic driving force in the direction of the above equation grows on cooling. The result is the well-known observation of an optimal temperature region for crystallization from a solution. It follows that if one creates a supersaturated solution at a sufficiently low temperature, it should be possible to follow the kinetics of the above steps at leisure, *e.g.*, by spectroscopic means. Thermal quenching of saturated solutions, by rapid cooling to low temperatures, is the obvious method to achieve this goal, but is difficult to carry out in practice, in particular for larger volumes of solutions.

(c) Photoinduced conversion of a compound from a "soluble" into an "insoluble" isomeric form suggests itself as a suitable method, provided it can be carried out at low temperature



(d) In many stilbene derivatives, the trans isomer is much less soluble than the cis isomer. However, cis can be converted into trans by irradiation at a suitable wavelength. It is thus possible to produce photochemically a highly supersaturated solution of the trans isomer in a rigid organic glass at low temperature, *i.e.*, under conditions where this unstable system is frozen-in. In fact in an earlier paper we showed that this is the only way in which the absorption and emission spectra of the monomeric trans isomer of certain stilbenes can be obtained.¹

Two such cases are described in Figures 1 and 2. The compounds were 1,2-di(2-naphthyl)ethylene (I) and 4-methoxystilbene (II). The respective supersaturated solutions of the trans isomer, when heated to a somewhat higher temperature, exhibit pronounced spectral changes, with one or more isosbestic points being preserved. The temperature range in which the rates of these changes are observable spectrophotometrically depend on the concentration and the solvent. Lower solubility and higher concentrations push this range toward lower temperatures. Thus, compound I exhibits the absorption changes shown in Figure 1 within about 2 hr at -170° when dissolved in a 2:1 mixture of methylcyclohexane and 2-methylpentane at $10^{-5} M$, and at -180° in 2-methylpentane at $5 \times 10^{-5} M$. Both figures also show the estimated spectral absorption curves 3 of the products of the spontaneous changes, calculated by maximal extrapolation of the *observed* changes, *i.e.*, without running into negative absorptions. The spectra of the newly formed species, assumed to be aggregates, are noteworthy, but do not form the subject of this communication. If the supersaturated solutions are heated to somewhat higher temperatures, the total absorption decreases sharply, indicating formation of precipitate and saturated very dilute solutions. It thus seems that the two steps in the above equation can be separated to a large extent by working at appropriate temperatures.

At still higher temperatures, above about -80° , the normal spectra of the trans isomers are re-formed. Flash

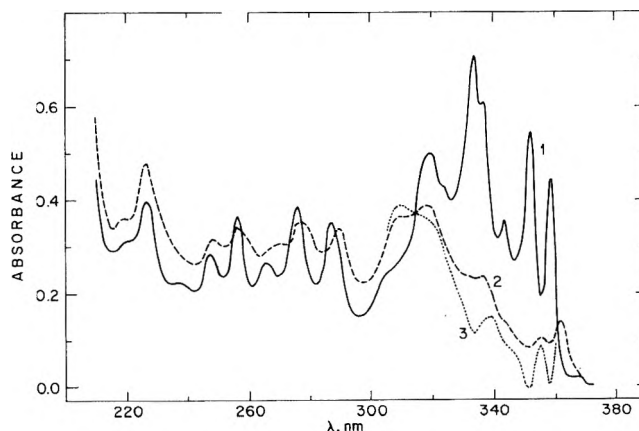


Figure 1. Absorption spectra of a $10^{-5} M$ solution of compound I in MCH-2-MP(2:1). The cis isomer solution was irradiated at -180° with light at 366 nm, to achieve cis \rightarrow trans conversion: curve 1, immediately after heating to -170° ; curve 2, after 2 hr at -170° ; curve 3, extrapolated to 100% conversion into product, assuming that curve 2 corresponds to 80% conversion in going from 1 to 2.

(1) D. Gegiou, K. A. Muszkat, and E. Fischer, *J. Amer. Chem. Soc.*, **90**, 3907 (1968).

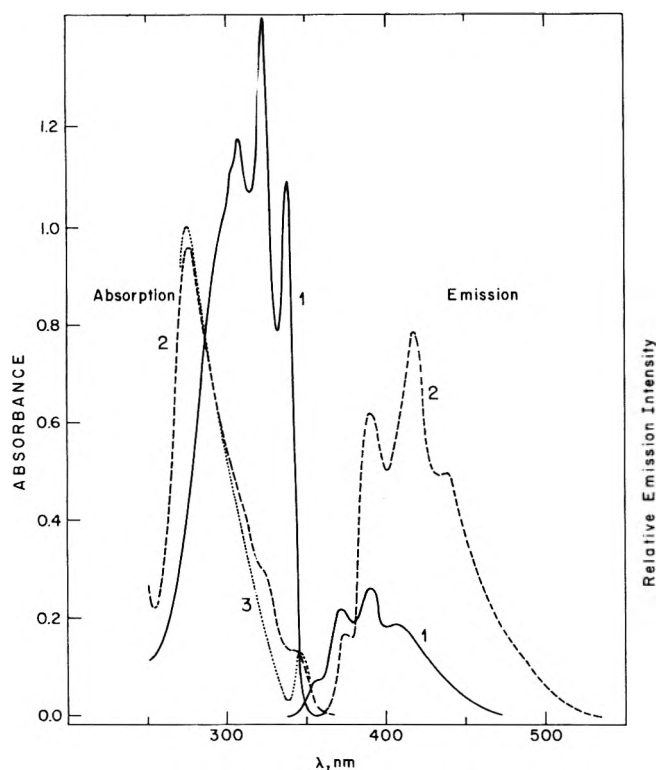


Figure 2. Absorption and emission spectra of a ca. 3×10^{-5} M solution of 4-methoxystilbene (II) in MCH-2-MP(1:3). The cis isomer solution was irradiated at -185° with light at 313 nm, to give the trans isomer (about 80%): curve 1, immediately after irradiation at -185° ; curve 2, after heating to -160° and re-cooling to -185° ; curve 3, extrapolated, assuming 90% conversion in going from 1 to 2. Emission and absorption curves were taken under similar conditions. Excitation was at 275 nm, but qualitatively similar spectra were obtained with 335-nm excitation.

techniques should make it possible to follow the kinetics of the spectral changes at intermediate temperatures, where their rates may be expected to be in the sec^{-1} region.

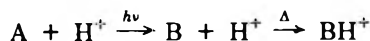
The emission spectra were measured under similar conditions. In compound I the only change observed was a reduction in fluorescence intensity, while in II new emission bands appeared, in parallel with the new long-wavelength absorption band.

Measurements of the spectra of the respective crystalline trans compounds are in progress, in order to compare them with those of the proposed aggregates.

It should be stressed that the suggested method involves freezing-in of nonequilibrium states, or slowing down their changes, rather than measurements of temperature-dependent equilibria as described, *e.g.*, by Katul and Zahlan² for the dimerization of tetracene, or by Goumet, Dupuy, and Nouchi³ for the dimerization of anthracene derivatives.

The above method is only one of many possible applications of photochemical or radiation-chemical methods to transform equilibrium systems into nonequilibrium systems and then to follow the kinetics of the approach to the new equilibrium. An earlier example was our use of certain photochromic spiropyrans to follow the kinetics of spontaneous protonation reactions in a wide temperature range.⁴ There a very weak base A is transformed radiatively, in the presence of an acid, into a fairly strong base

B, which then starts reacting with the surrounding acid.



The formation of BH^+ and the disappearance of B can be followed spectroscopically by both slow and fast techniques.

- (2) J. A. Katul and A. B. Zahlan, *J. Chem. Phys.*, **47**, 1012 (1968).
- (3) G. Goumet, F. Dupuy, and G. Nouchi, *C. R. Acad. Sci., Ser. B*, **267**, 41 (1968).
- (4) T. Bercovici, R. Heiligmann-Rim, and E. Fischer, *Mol. Photochem.*, **1**, 189 (1969).

Department of Structural Chemistry
The Weizmann Institute of Science
Rehovot, Israel

E. Fischer

Received November 3, 1972

Extended Hückel Molecular Orbital Calculation on 4-Methylumbelliferone and Its Tautomer

Publication costs assisted by the U.S. Army Natick Laboratories

Sir: Owing to its wide tunability, the title compound 4-methylumbelliferone (4-MU) is one of the most popular dyes in the field of dye lasers. However, there have been a number of postulates as to the nature of the excited state species which accounts for the longer wavelength end of the tunability.^{1,2} In this communication we would like to address ourselves to the suggested tautomerism of 4-MU, a molecule which is of great interest in photochemistry of proton transfer reactions.

In relating to our dye laser studies, we have reported four fluorescence emission species of 4-methylumbelliferone (4-MU, I).¹ These species appear as a function of ethanol-water ratio and the acidity of the solvent. Since only three ground-state absorbing species (two ionic and one neutral) were observed with the changes in solvent acidity, we have tentatively assigned the fourth emission band to the tautomeric form II (*cf.* Figure 2) which is proposed to arise through an excited state-tautomerism mechanism.² The fluorescence of I ($\lambda_{\text{max}} \sim 26,000 \text{ cm}^{-1}$) and II ($\lambda_{\text{max}} \sim 20,800 \text{ cm}^{-1}$) dominates the emission at pH ~ 1 ; their relative intensities vary from predominantly I to predominantly II as the water content in the ethanol solution is increased.¹

To provide further information about the feasibility of valence-isomeric forms of umbelliferones, we have performed extended Hückel (EHMO) calculations³ on the two structures I and II. With this simple all-valence orbital treatment we expected to obtain a good estimation of the difference in the ground-state energies of the two tautomeric forms, as well as a reasonable prediction of the energy difference of their first excited states. The EHMO program used in this study was Hoffman's original program distributed by the Quantum Chemical Program Ex-

- (1) M. Nakashima, J. A. Sousa, and R. C. Clapp, *Nature (London), Phys. Sci.*, **235**, 16 (1972).
- (2) Just recently, G. J. Yakatan, R. J. Juneau, and S. G. Schulman, *Anal. Chem.*, **44**, 1044 (1972), proposed a very similar mechanism for 4-MU.
- (3) R. Hoffman, *J. Chem. Phys.*, **39**, 1397 (1963).

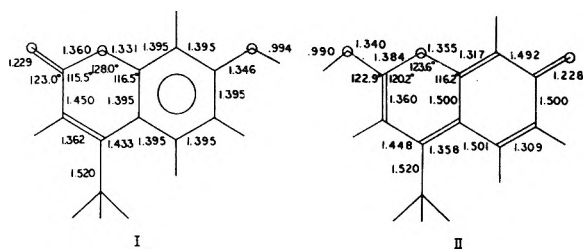


Figure 1. Structures and assumed geometries of 4-methylumbelliferone (I) and its tautomer (II). Terminal atoms are hydrogens. Other atoms are carbons and oxygens. H-C = 109 Å.

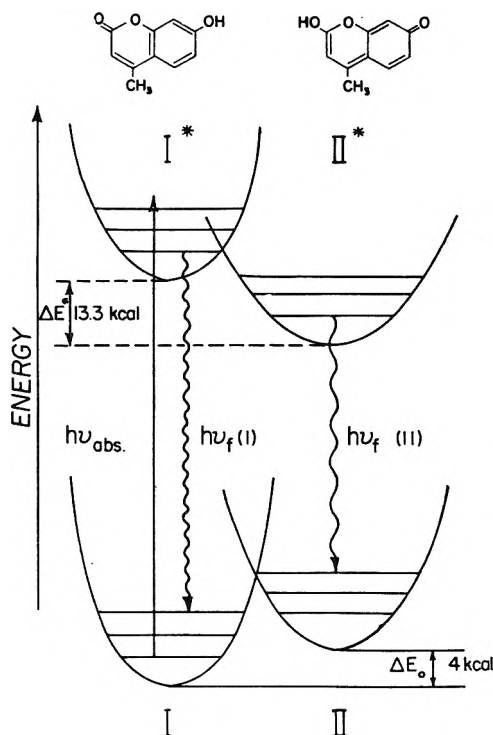


Figure 2. Simplified potential energy diagram for the 4-methylumbelliferone system.

change. For the diagonal elements H_{ii} of the Hamiltonian matrices, the following valence state ionization potentials I [eV] were used:⁴ $I(\text{H})$ -13.6; $I(\text{C})$ -21.40, -11.40; $I(\text{O})$ -35.30, -17.76. These values were also incorporated in the off-diagonal elements $H_{ij} = KS_{ij} (H_{ii} + H_{jj})/2$ with $K = 2.000$. As usual, the orbital exponents were obtained using Slater's rules. Since no X-ray data of umbelliferone were available, the geometries were assumed⁵ as shown in Figure 1. Except for the methyl group, the structures are planar, and the bond angles are 120° unless otherwise indicated.

The results of this calculation in terms of a simplified potential energy diagram are summarized in Figure 2. The ground-state energy of form I is lower than that of II by 4 kcal. As expected, form I is the more stable configuration in the ground state. The first excited states of I and II, on the other hand, are predicted to lie 30,000 cm^{-1} (experimental value $\sim 31,000 \text{ cm}^{-1}$)¹ and 24,000 cm^{-1} above their respective ground states which places the excited state of II 13.3 kcal below that of I (cf. Figure 2). Since form II is not stable in the ground state, the predicted red shift of its longest wavelength absorption band with respect to I is considered in the emission. If we assume similar Stokes

shifts for both forms, a red shift of 6000 cm^{-1} in the fluorescence of II relative to I emerges. This latter value compares favorably with the experimentally observed energy difference between the maximum of the two fluorescences of ca. 5200 cm^{-1} .

The results of the EHMO calculation appear to be consistent with the experimental findings supporting the suggested phototautomerism. For such a process we may, therefore, propose a feasible mechanism, illustrated in some detail in Figure 2. Here, irradiation into the first electronic transition of I produces the excited singlet I^* . Deactivation of this state occurs mainly *via* fluorescence $h\nu_f$ (I), intersystem crossing, and probably chemical relaxation. If, however, the pH and water content of the solution are appropriate so that protonation (and deprotonation) of I^* can take place during its lifetime, the formation of the energetically more favorable II^* is competing with these deactivation processes. The excited state II^* of the valence isomeric form subsequently decays to II, giving rise to a second fluorescence $h\nu_f$ (II). Ground-state II finally crosses over to the initial form I.

(4) H. A. Skinner and H. O. Pritchard, *Chem. Rev.*, **55**, 745 (1955).

(5) "Tables of Interatomic Distances and Configuration in Molecules and Ions," *Chem. Soc., Spec. Publ.*, No. 11 (1958).

Pioneering Research Laboratory
U. S. Army Natick Laboratories
Natick, Massachusetts 01760

J. R. Huber
M. Nakashima*
J. A. Sousa

Received August 9, 1972

Quenching of the $\text{Ru}(\text{dipy})_3^{2+}$ Phosphorescence by $\text{Cr}(\text{CN})_6^{3-}$. Evidence for a Diffusion-Controlled Mechanism

Sir: The quenching of the phosphorescence emission of $\text{Ru}(\text{dipy})_3^{2+}$ by anionic $\text{Cr}(\text{III})$ complexes has recently been investigated² and it was suggested that the observed quenching was a "static quenching," taking place between the counter ions in an ion pair formed by the ground-state complexes. To our knowledge, this would be the first example of a solely static quenching between complex ions in fluid solution. However, during a systematic investigation of the energy transfer between coordination compounds, we have found sure evidence against the static quenching hypothesis for the $\text{Ru}(\text{dipy})_3^{2+}$ - $\text{Cr}(\text{CN})_6^{3-}$ system.

Lifetime and phosphorescence intensity measurements were made on air-equilibrated aqueous solutions containing $\text{Ru}(\text{dipy})_3^{2+}$ ($1.2 \times 10^{-4} M$) and various amounts of $\text{Cr}(\text{CN})_6^{3-}$. Emission intensities were measured with a Turner Spectro 210 spectrofluorimeter, and lifetimes with an apparatus described elsewhere,³ which uses a Febetron 706 electron accelerator and a ZnSe target as a pulsed light source. We have thus observed that the triplet life-

(1) Work supported in part by the National Research Council of Italy through Contract No. 71.01610.03 115.4416.

(2) I. Fujita and H. Kobayashi, *Ber. Bunsenges. Phys. Chem.*, **76**, 115 (1972).

(3) A. Hutton, G. Giro, S. Dellonte, and A. Breccia, *Int. J. Radiat. Phys. Chem.*, submitted for publication.

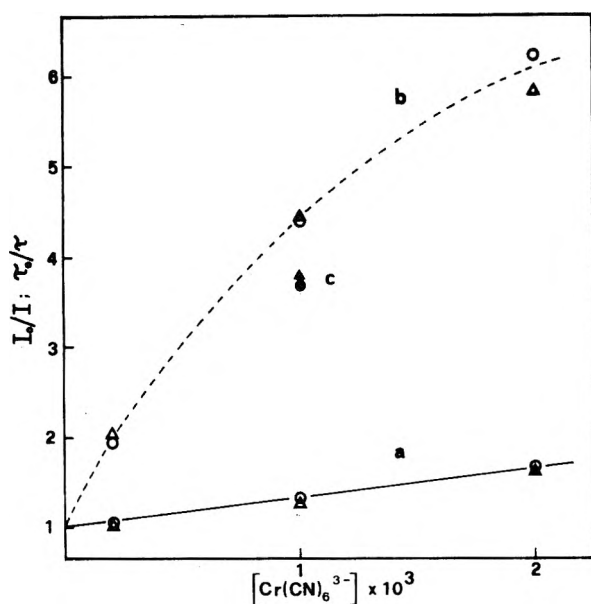


Figure 1. Quenching of the $\text{Ru}(\text{dipy})_3^{2+}$ phosphorescence emission (O) and lifetime (Δ) by $\text{Cr}(\text{CN})_6^{3-}$ in air-equilibrated solutions: a, aqueous solutions of constant ionic strength ($\mu = 0.5$); b, aqueous solutions of variable ionic strength (see text); c, 20% glycerol-water solutions.

time of $\text{Ru}(\text{dipy})_3^{2+}$ is quenched in parallel with the phosphorescence emission (Figure 1). This clearly demonstrates that the quenching of the emitting excited state of $\text{Ru}(\text{dipy})_3^{2+}$ occurs by a dynamic, diffusion-controlled process, and rules out the possibility of a static quenching, since this would affect the emission intensity but not the lifetime.

We have also found that the Stern-Volmer quenching constant, k_{sv} , shows a decrease with increasing ionic strength. This dependence is clearly shown in Figure 1, where the points in line a refer to solutions at constant ionic strength ($\mu = 0.5$, adjusted by adding KCl), and points in curve b refer to solutions whose ionic strength was not adjusted and, thus, increased with increasing $[\text{Cr}(\text{CN})_6^{3-}]$ ($\mu = 1.6 \times 10^{-3}$, 6.4×10^{-3} , 12.4×10^{-3} , respectively). The same effect had been observed by Fujita and Kobayashi² and it was taken as evidence for the static quenching since, of course, μ influences the association constant of the ion pair.⁴ However, the ionic strength is also expected to influence the encounter rate constant between two ionic species in the same way, so that the dependence of k_{sv} on μ cannot discriminate between the static and dynamic mechanism. The k_{sv} value calculated from the quenching data of our most dilute solution is $4.9 \times 10^3 \text{ M}^{-1}$, and the corresponding value at $\mu = 0$ (calculated with the usual equation⁵ $\log k = \log k_0 + 1.02z_A z_B u^{1/2}$) is $k_{sv}^0 = 8.6 \times 10^3 \text{ M}^{-1}$. This value is in good agreement with that obtained by extrapolation in ref 2.

The bimolecular quenching rate constant ($k_q = k_{sv}/\tau^0$), obtained from k_{sv}^0 and the experimentally determined lifetime of $\text{Ru}(\text{dipy})_3^{2+}$,^{6,7} is $2.1 \times 10^{10} \text{ M}^{-1} \text{ sec}^{-1}$, which is in good agreement with the encounter rate constant ($3.2 \times 10^{10} \text{ M}^{-1} \text{ sec}^{-1}$) calculated from the Debye equation for ionic species.⁸

As shown by points c in Figure 1, the quenching by $\text{Cr}(\text{CN})_6^{3-}$ is less efficient in 20% glycerol aqueous solution than in pure water. This result is mainly due to the increase of the viscosity of the medium, and thus, it supports the hypothesis of a dynamic quenching. Fujita and Kobayashi² found no difference between the quenchings in the two media reported above; since the association constant is not affected by the viscosity, these authors took this fact as another proof in favor of the static quenching. It is to be noted, however, that even the association constant may be influenced by a change of the medium, because of variations in the dielectric constant. For the $\text{Ru}(\text{dipy})_3^{2+}-\text{Cr}(\text{CN})_6^{3-}$ system, calculations based on the Bjerrum⁹ or the Fuoss¹⁰ equation show that the association constant, and thus the Stern-Volmer quenching constant if the static mechanism were to operate, should be about 30% higher in 20% glycerol-water than in water solutions.

In conclusion, it appears evident that several parameters of the medium (such as, *e.g.*, viscosity, dielectric constant, and ionic strength) must be taken into appropriate consideration in order to interpret correctly a quenching process between ionic species. Studies are now in progress in our laboratory in order to clarify the role played by these parameters.

Acknowledgments. We wish to thank Professor V. Balzani for helpful discussions and Professors A. Breccia and G. Semerano (Laboratorio di Fotochimica e Radiazioni d'Alta Energia del CNR, Bologna) for the suggestion to use the Febetron equipment for lifetime measuring.

- (4) In a static mechanism, k_{sv} is, under certain conditions, equal to the association constant of the ion pair.
- (5) S. Glasstone, "Physical Chemistry," 2nd ed, Macmillan, London, 1953, p 1116.
- (6) $\tau^0 = 0.40 \mu\text{sec}$ in air-equilibrated solution; we also obtained a lifetime of $0.65 \mu\text{sec}$ for deoxygenated solution, in good agreement with a previous report.⁷
- (7) N. J. Demas and A. W. Adamson, *J. Amer. Chem. Soc.*, **93**, 1800 (1971).
- (8) P. Debye, *Trans. Electrochem. Soc.*, **82**, 265 (1942); in this calculation we assumed an encounter radius value of 5 \AA for both complexes.
- (9) N. Bjerrum, *Kgl. Dan. Vidensk. Selsk., Mat.-Fys. Medd.*, **7**, 3 (1926).
- (10) R. M. Fuoss, *J. Amer. Chem. Soc.*, **80**, 5059 (1958).

Istituto Chimico "G. Ciamician"
dell' Università
40126 Bologna, Italy

F. Bolletta
M. Maestri
L. Moggi*

Received December 4, 1972

Journal of Chemical and Engineering Data

JANUARY 1973, Vol. 18, No. 1

TABLE OF CONTENTS

Editorial	1
List of Reviewers	2
A Guide to Procedures for the Publication of Thermodynamic Data	3
Volumetric Behavior, Vapor Pressures, and Critical Properties of Neopentane. P. P. Dawson, Jr., I. H. Silberberg, and J. J. McKetta	7
Scaling of Equilibrium Properties of Inorganic Substances. A. Bondi	16
Thermochemistry of <i>N,N</i>-Dimethyl-<i>p</i>-nitrosoaniline Complexes. S. Gurrieri, R. Cali, and G. Siracusa	22
Dissociation Constants of Pyro- and Tripolyphosphoric Acids at 25°C. C. W. Edwards, T. D. Farr, R. L. Dunn, and J. D. Hatfield	24
Enthalpies of Formation of Some Fluoronitroethyl Derivatives and 2,2',4,4',6,6'-Hexanitrobenzene. E. E. Baroody and G. A. Carpenter	28
Heat of Combustion of 5-Amino-3,4-dimethylisoxazole. W. S. Hamilton and G. M. Mitchell	36
Heat of Combustion of <i>N,N'</i>-bis(<i>o</i>-methoxyphenyl)terephthalamide. W. S. Hamilton and G. M. Mitchell	38
Viscosity Data of Binary Mixtures System: Methyl Isobutyl Ketone-<i>n</i>-butanol. P. Dakshinamurty, K. V. Rao, P. V. Rao, and C. Chiranjivi	39
Total Pressure Method: Binary Systems Cyclohexane-<i>n</i>-Pentanol, -<i>n</i>-Heptanol, and -<i>n</i>-Octanol. D. C. Minh and M. Ruel	41
Vapor-Liquid Equilibria in Mixtures of Water, <i>n</i>-Propanol, and <i>n</i>-Butanol. R. A. Dawe, D. M. T. Newsham, and S. B. Ng	44
Integral Isobaric Heat of Vaporization of Benzene-1,2-Dichloroethane System. Y. J. Rao and D. S. Viswanath	49
Effect of Water on Enthalpies of Solution of Electrolytes in <i>N,N</i>-Dimethylformamide. Y. A. Tsai and C. M. Criss	51
Excess Gibbs Free Energies for Binary Systems Isopropanol with Benzene, Cyclohexane, and Methylcyclohexane. I. Nagata, T. Ohta, and Y. Uchiyama	54
Liquid-Phase Diffusion Coefficients for Dissolved Gases: Systems Chlorine-Carbon Tetrachloride and Hydrogen Chloride-Ethylene Glycol. G. T. Clegg and M. A. Tehrani	59

Use of a new cell to Measure Diffusion Coefficients for the systems Benzene–Carbon Tetrachloride and Sucrose–Water at 25°C. G. R. Staker and P. J. Dunlop	61
Excess Enthalpies, Volumes, and Surface Tensions of Isomeric Butanol–<i>n</i>-Decanol Mixtures. V. T. Lam, H. D. Pflug, S. Murakami, and G. C. Benson	63
Heats of Fusion and Heat Capacities of Lithium Chloride–Potassium Chloride Eutectic and Potassium Nitrate. R. P. Clark	67
Solubility of Hydrogen Sulfide in Aqueous Diethanolamine Solutions at High Pressures. J. I. Lee, F. D. Otto, and A. E. Mather	71
Miscibility of Liquid Metals with Salts. XI. System Yttrium Metal–Yttrium Trichloride at High Temperatures. A. S. Dworkin and M. A. Bredig	74
Surface Tension of LiCl–KCl Eutectic Mixtures. D. A. Nissen and R. W. Carlsten	75
Thermodynamic Properties of Neopentane. P. P. Dawson, Jr., J. J. McKetta, and I. H. Silberberg	76
Theoretical Calculations of Equilibrium Concentrations for Species Generated in Analytically Important Flames. L. L. Reigle, W. J. McCarthy, and A. C. Ling	79
Prediction of Excess Heat Capacities of Alcohol–Hydrocarbon Mixtures. I. Nagata and T. Yamada	87
Thermodynamic Properties of Liquid Gallium Alloys. I. Gallium–Lead. A. Desideri and V. Piacente	90
Survey of Alkanone Reactivity Based on Time Required for 50% Oximation. P. G. Kletzke	93
Preparation and Spectral Characterization of Substituted 2-Aminothiazoles. G. Y. Sarkis and S. Al-Azawe	99
Synthesis and Spectral Data for Quinoxaline Derivatives. G. Y. Sarkis and S. Al-Azawe	102
Preparation of 4,4',5,5'-Tetranitro-1,1'-binaphthyl. L. A. Jones and C. T. Joyner	105
Synthesis of Tris (<i>N,N</i>-dimethyl-2-carbamoylethyl)phosphine Oxide. D. J. Daigle, T. L. Vigo, and L. H. Chance	108
Synthesis and Spectral Characterization of 2-Substituted Indole Derivatives. S. Al-Azawe and G. Y. Sarkis	109
New Data Compilations	112

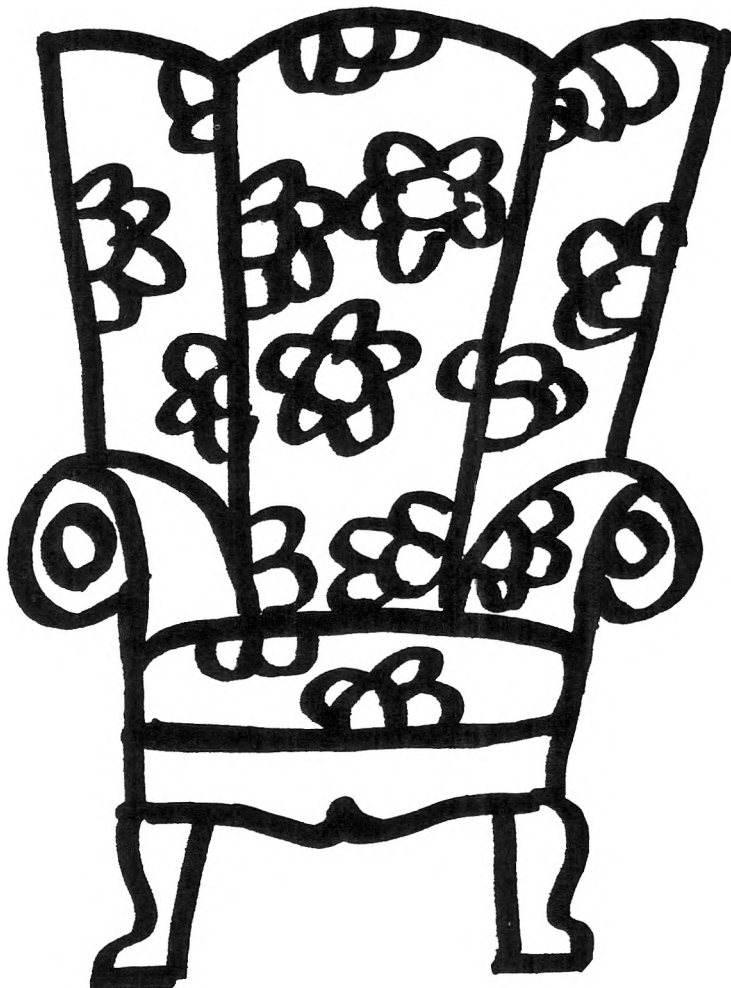
**You
don't have
to search
the archives
for data . . .**

JOURNAL OF CHEMICAL AND ENGINEERING

DATA

THE ACS JOURNAL FOR DATA

JANUARY 1973 VOL 18 NO 1
ISSUED QUARTERLY



. . . because THE JOURNAL OF CHEMICAL AND ENGINEERING DATA will bring precise, reliable, useful technical information right to your fingertips quarterly! With a year's subscription, you'll receive a total of over 500 pages of valuable science and engineering data that are especially relevant now in light of today's new instrumentation. The information in JCED includes:

- experimental data relating to pure compounds or mixtures covering a range of states;
- manuscripts based on published experimental information which make tangible contributions through their presentation or which set forth a sound method of prediction of properties as a function of state;

- experimental data which aid in identifying or utilizing new organic or inorganic compounds; and
- papers relating primarily to newly developed or novel synthesis of organic compounds and their properties.

Start to benefit now from this "arm-chair" source of pertinent technical data—with your own personal

subscription to JCED . . . just complete and return the form below . . . get your data without the dust.



. . . another ACS service

**Journal of Chemical & Engineering Data
American Chemical Society**

1155 Sixteenth Street, N.W.
Washington, D.C. 20036

Yes, I would like to receive the JOURNAL OF CHEMICAL & ENGINEERING DATA at the one-year rate checked below:

ACS Member Personal-Use	U.S.	Canada	Latin America	Other Nations
One-Year Rate	<input type="checkbox"/> \$15.00	<input type="checkbox"/> \$18.00	<input type="checkbox"/> \$18.00	<input type="checkbox"/> \$18.50
Nonmember	<input type="checkbox"/> \$45.00	<input type="checkbox"/> \$48.00	<input type="checkbox"/> \$48.00	<input type="checkbox"/> \$48.50

Bill me Bill company Payment enclosed

Name _____

Street _____

Home
Business

City _____

State _____

Zip _____

**Journal
of Chemical
& Engineering
Data**

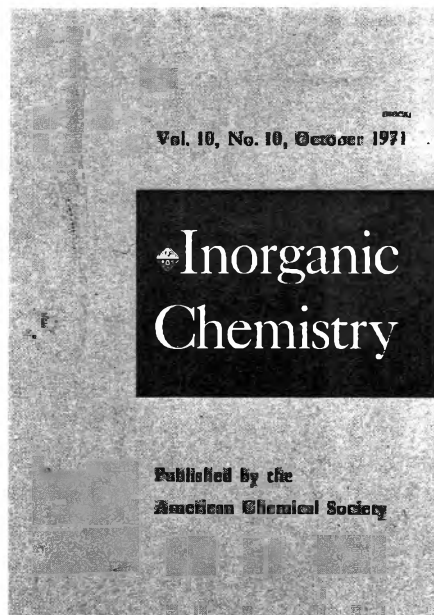
Inorganic Chemistry is the one...

that publishes both experimental and theoretical fundamental studies in *all phases of inorganic chemistry*.

These studies include synthesis and properties of new compounds, quantitative studies regarding structure, and thermodynamics and kinetics of inorganic reactions. Articles may range from the borders of organic chemistry to the borders of theoretical physics . . . giving you a broad expanse of authoritative information.

Besides the 35 or more papers presented in each monthly issue, you'll also profit from the shorter *Notes* and the *Correspondence* sections, that provide an informal medium of exchange for scientific views and ideas.

Inorganic Chemistry is the one . . . to order right now for your own professional interests. Simply complete and return the form below.



American Chemical Society / 1155 Sixteenth Street, N.W., Washington, D.C. 20036

Please enter my subscription to **Inorganic Chemistry** at the rates checked below:

ACS Members: U.S. \$18.00 Canada, PUAS \$22.00 Other Nations \$23.00
Nonmembers: U.S. \$54.00 Canada, PUAS \$58.00 Other Nations \$59.00
 Bill me Bill employer Payment enclosed (Payable to American Chemical Society)

Name _____ Title _____

Employer _____

Address: Home Business _____

City _____ State/Country _____ Zip _____

Nature of employer's business? Manufacturing or processing Academic Government
 Other _____

(Please indicate)

Note: Subscriptions at ACS Member Rates are for personal use only.

I am an ACS member I am not an ACS member

Payment must be made in U.S. currency, by international money order, UNESCO coupons, U.S. bank draft; or order through your book dealer.

P3A